HIGHWAY RESEARCH
RECORD

Number 76

Design—Bridges and Structures

10 Reports

Presented at the
43rd ANNUAL MEETING
January 13-17, 1964

HIGHWAY RESEARCH BOARD
of the
Division of Engineering and Industrial Research
National Academy of Sciences—
National Research Council
Washington, D. C.
1965

Department of Design

T. E. Shelburne, Chairman
Director of Research, Virginia Department of Highways
University of Virginia, Charlottesville

COMMITTEE ON BRIDGES

(As of December 31, 1963)

J. N. Clary, Chairman
Bridge Engineer, Virginia Department of Highways, Richmond

W. C. Anderson, Chief, Research and Development Engineer, The Union Metal Manufacturing Company, Canton, Ohio
Raymond Archibald, Kalispell, Montana
W. E. Baumann, Engineer of Bridge and Traffic Structures, Illinois Division of Highways, Springfield
J. M. Biggs, Associate Professor of Structural Engineering, Massachusetts Institute of Technology, Cambridge
Vernon J. Burns, Assistant Deputy Chief Engineer (Bridge), New York Department of Public Works, Albany
E. M. Cummings, Manager of Sales, Bethlehem Steel Company, Bethlehem, Pennsylvania
Frederick H. Dill, Assistant to Vice President—Engineering, United States Steel Corporation, Pittsburgh, Pennsylvania
E. S. Elcock, Bridge Engineer, Kansas State Highway Commission, Topeka
Arthur L. Elliott, Bridge Engineer—Planning, California Division of Highways, Sacramento
Eric L. Erickson, Chief, Bridge Division, Office of Engineering, U. S. Bureau of Public Roads, Washington
R. S. Fountain, Bridge Engineer, Portland Cement Association, Chicago, Illinois
F. M. Fuller, Assistant Vice President, Raymond International, Inc., New York, New York
H. deR. Gibbons, The Union Metal Manufacturing Company, Canton, Ohio
T. R. Higgins, Director of Engineering and Research, American Institute of Steel Construction, New York, New York
Rudolph Hofer, Jr., Highway Products and Structural Section, Sales Development Division, Aluminum Company of America, New Kensington, Pennsylvania
John J. Hogan, Consulting Structural Engineer, Portland Cement Association, New York, New York
C. L. Hulsbos, Department of Civil Engineering, Fritz Laboratory, Lehigh University, Bethlehem, Pennsylvania
J. J. Kozak, Supervising Bridge Engineer, California Division of Highways, Sacramento
W. T. Lankford, Applied Research Laboratory, United States Steel Corporation, Monroeville, Pennsylvania
C. A. Marmelstein, Bridge Engineer, Georgia State Highway Department, Atlanta
William H. Munse, Jr., Department of Civil Engineering, University of Illinois, Urbana
LeRoy T. Oehler, Physical Research Engineer, Michigan State Highway Department, Lansing
D. H. Overman, Columbus, Ohio
Adrian Pauw, Professor of Civil Engineering, University of Missouri, Columbia
M. N. Quade, Consulting Engineer, Parsons, Brinckerhoff, Quade and Douglas, New York, New York
William H. Rabe, Columbus, Ohio
W. T. Robertson, Bridge Design Engineer, Washington Department of Highways, Olympia

Charles F. Scheffey, Department of Civil Engineering, University of California, Berkeley
C. P. Seiss, Department of Civil Engineering, University of Illinois, Urbana
Charles B. Trueblood, Armco Drainage and Metal Products, Inc., Middletown, Ohio
Ivan M. Viest, Structural Engineer, Bethlehem Steel Corporation, Bethlehem, Pennsylvania
George S. Vincent, U. S. Bureau of Public Roads, Washington, D. C.

Contents

OVERLOAD BEHAVIOR OF PRETENSIONED PRESTRESSED CONCRETE I-BEAMS WITH WEB REINFORCEMENT
John M. Hanson and C. L. Hulsbos 1

STRUCTURAL BEHAVIOR OF A CONCRETE BOX GIRDER BRIDGE
Raymond E. Davis, John J. Kozak and Charles F. Scheffey 32

BEHAVIOR OF ELASTOMERIC BEARING PADS UNDER SIMULTANEOUS COMPRESSION AND SHEAR LOADS
William B. Nachtrab and Robert L. Davidson 83

ECONOMIC POSSIBILITIES OF CORROSION-RESISTANT LOW-ALLOY STEEL IN BOX GIRDER HIGHWAY BRIDGES
J. M. Hayes and S. P. Maggard 102

FIELD TESTS OF A THREE-SPAN CONTINUOUS HIGHWAY BRIDGE
James W. Baldwin 140

A NEW MATRIX-ENERGY METHOD FOR ANALYZING ALL STRESSES IN RIGIDLY CONNECTED HIGHWAY BRIDGE TRUSSES
Shu-t'ien Li, Ing-Chang Jong, James E. Russell and Malvinder Samra 168

DESIGN OF ALUMINUM SIGN STRUCTURES BY ELECTRONIC COMPUTATION
Rudolph Hofer, Jr., and Alan H. Knoll 227

THERMAL BEHAVIOR OF COMPOSITE BRIDGES—INSULATED AND UNINSULATED
William Zuk 231

FATIGUE TESTS OF PLATES AND BEAMS WITH STUD SHEAR CONNECTORS
J. E. Stallmeyer, W. H. Munse and K. A. Selby 254

FIELD DYNAMIC LOADING STUDIES OF HIGHWAY BRIDGES IN THE U. S., 1948—1965
R. F. Varney and C. F. Galambos 285

Overload Behavior of Pretensioned Prestressed Concrete I-Beams With Web Reinforcement

JOHN M. HANSON and C. L. HULSBOS
Respectively, Research Instructor of Civil Engineering and Research Professor of Civil Engineering, Lehigh University

The results of ultimate static strength tests on 18 pretensioned prestressed concrete I-beams with web reinforcement are presented. The principal variables in the test program were the shear-span-to-effective-depth ratio, which varied between 2.54 and 6.34, and the percentage of web reinforcement. The beams had an overall depth of 18 in. and the majority of the tests were conducted on a shear-span-to-effective-depth ratio of 3.39, for which the web reinforcement percentage was varied from 0 to 1.22. The behavior of the test beams under overloads to failure is discussed in detail. Requirements for the amount of web reinforcement based on the current AASHO specifications are compared with the test results. In addition, procedures for improved design of the web reinforcement are considered.

•AN ULTIMATE strength design of a concrete structure must be based generally on the following five factors: static strength, fatigue strength, stability, deflection, and durability. To be satisfactory, a structure must have the desired degree of safety with respect to each of these factors. For prestressed concrete bridge beams, stability, deflection, and durability are generally factors of lesser importance. The ultimate static strength is usually the factor of paramount importance. However, where many repeated loads of large magnitude can be expected, the fatigue strength of the member may be of equal importance.

This investigation (1) was undertaken to study the ultimate static strength of prestressed concrete I-beams with web reinforcement. The results of 18 tests on simply supported beams subjected to a symmetrical two-point loading, designated as the E Series and given in Table 1, are presented in this report. Sixteen of these tests were single-cycle static load tests; that is, the load was increased in increments, without unloading, until the ultimate capacity of the member was reached. The remaining two tests were repeated load tests. Only data taken from the first load cycle of the repeated load tests are included herein.

The principal variables in the test program were the shear-span-to-effective-depth ratio, which ranged between 2.54 and 6.34, and the percentage of web reinforcement. Concrete strength and prestressing were held as nearly constant as possible. Most of the tests, however, were conducted on a shear-span-to-effective-depth ratio of 3.39, for which the web reinforcement percentage ranged from 0 to 1.22. Corresponding to this particular shear span, No. 3 stirrups with a yield point of 55,500 psi, and the average concrete strength of 7,000 psi, the percentage of web reinforcement required by Paragraph 1.13.13 of the Standard Specifications for Highway Bridges (AASHO) is 0.85.

Paper sponsored by Committee on Bridges.

TABLE 1
OUTLINE OF TESTS

Shear Span, a (ft)	Web Reinforcement Size (no.)	Spacing (in.)	Percent	Beam Designation
3	2D	8.75	0.374	E.14
	2D	8.75	0.374	E.15
4	-	-	0	E.4
	3D	6	1.22	E.5
	3D	8	0.917	E.6
	3D	10	0.733	E.7
	3S	6	0.611	E.8
	3S	8	0.458	E.9
	3S	6	0.611	E.10F[a]
	3S	8	0.458	E.11F[a]
	3S	10	0.367	E.12
	2D	8.75	0.374	E.13
	2S	6	0.272	E.16
	2S	8	0.204	E.17
	2S	10	0.163	E.18
5	-	-	0	E.3
6	-	-	0	E.2
7.5	-	-	0	E.1

[a] F indicates two repeated load tests.

NOTATION

a = length of shear span;
A = area of beam cross-section;
A_v = area of vertical stirrup;
b = width of compression flange;
b′ = width of web;
d = distance from concrete top fibers to centroid of strand;
e = eccentricity of c.g.s. with respect to c.g.;
E_c = modulus of elasticity of the concrete;
f_c' = ultimate compressive strength of concrete at test;
f_{ci}' = ultimate compressive strength of concrete at prestress release;
f_r' = modulus of rupture strength of concrete at test;
f_t' = flexural tensile strength of concrete at test;
f_u' = ultimate tensile strength of stirrups;
f_y' = yield point of stirrups;
F = prestress force at test;
F_i = initial prestress force, before prestress release;
ℓ_e = distance from junction of web and top flange to lowest level at which stirrups may be regarded as effective;
M_d = dead load moment;
M_u = static ultimate moment;
M_c^f = flexural cracking moment;

Q = moment about the c.g. of the area on one side of horizontal section on which shearing stress is desired;
r = percentage of web reinforcement, $100\ A_v/b's$;
s = spacing of vertical stirrups;
V_c = shear carried by concrete;
V_d = dead load shear;
V_w = shear carried by stirrups;
V_u = ultimate shear;
V_c^f = shear causing flexural cracking;
V_c^{dt} = shear causing diagonal tension cracking;
V_c^{fs} = shear causing flexure shear cracking;
V_u^f = shear causing flexural failure;
Z = section modulus;
β = dimensionless factor which, when multiplied by d, determines effective horizontal projection of inclined crack;
θ = angle, with respect to horizontal, of compressive stress trajectory;
σ = normal stress;
σ_t = principal tensile stress;
σ_t^{cg} = principal tensile stress at c.g. of beam cross-section; and
τ = shearing stress.

TEST SPECIMENS

Description

A doubly symmetric I-shaped cross-section with a total-depth-to-flange-width ratio of 2 and a flange-to-web-width ratio of 3 was used for all 18 beam specimens. Each beam was 17 ft 6 in. in length, providing a test span of 15 ft and an overhang at each reaction of 1 ft 3 in. Details of the test beams are shown in Figure 1.

Size, spacing, and percentage of web reinforcement are given in the outline of tests in Table 1. Except for E.13 and E.14, each stirrup consisted of either one or two U-shaped bars, referred to as S or D. Where only one bar was used, each successive bar was placed so that the U opened to the opposite side of the test beam. In E.13 and E.14 inverted L-shaped bars were used, and each stirrup consisted of two bars.

Six 7/16-in. diameter strands were used as the prestressing elements in each beam. All strands were straight, and each strand was pretensioned to a nominal initial force of 18.9 kips, providing a total initial design prestress force of 113.4 kips. Assuming losses of 8 percent in the prestress force at transfer, the initial stresses in the top and bottom concrete fibers, based on the transformed section and neglecting dead weight, are 210-psi tension and 2,150-psi compression, respectively.

Materials

Ready-mixed concrete was used in casting the test beams, having a cement-to-sand-to-coarse-aggregate ratio of approximately 1:1.8:2.3. The mix contained 7.5 sk/cu yd of Type III portland cement. The maximum size of the coarse aggregate was ¾ in. Gradation of the aggregate conformed to Pennsylvania Department of Highways specifications. Mixes were made in either 2 or 2.5 cu yd batches, sufficient to cast three test beams at one time. Slump varied between 1 ½ and 2 ¾ in., and concrete strength at the time of test of all beams was approximately 7,000 psi.

The prestressing strand was a 7/16-in. diameter, seven wire, uncoated, stress-relieved, high tensile strength strand. A stress-strain curve for the strand, determined from a tension test conducted in the laboratory, is shown in Figure 2. Failure occurred in the testing machine grips at an ultimate load of 26.3 kips. The stress-strain curve in Figure 2 was virtually identical with the stress-strain curve provided by the manufacturer, which indicated that the strand had an ultimate load of 27.5 kips, corresponding

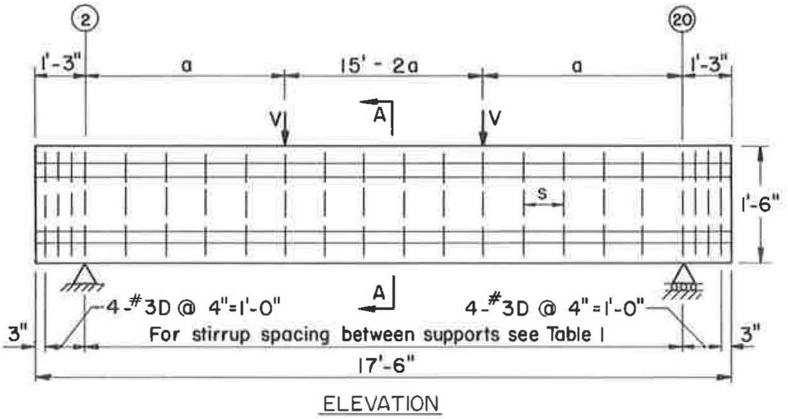

2
20
1'-3"
a
15' - 2a
a
1'-3"
V
A
V
s
1'-6"
4-#3D @ 4"=1'-0"
A
4-#3D @ 4"=1'-0"
3"
For stirrup spacing between supports see Table I
3"
17'-6"
ELEVATION

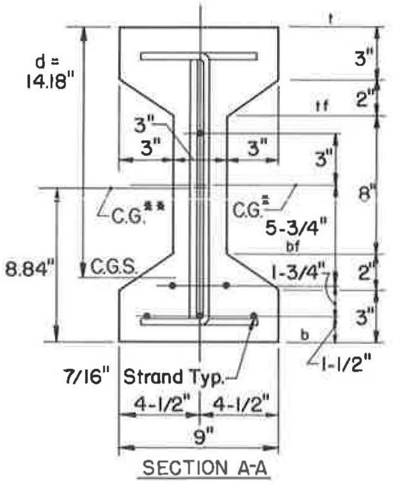

d =
14.18"
t
3"
2"
tf
3"
3"
3"
3"
8"
C.G.**
C.G.*
5-3/4"
bf
8.84"
C.G.S.
1-3/4"
2"
3"
b
1-1/2"
7/16" Strand Typ.
4-1/2"
4-1/2"
9"
SECTION A-A

SECTION PROPERTIES		
PROPERTY	CONCRETE SECTION	TRANSFORMED SECTION
A	102.0 in.^{2}	105.3 in.^{2}
I	3854 in.^{4}	3986 in.^{4}
Z^t	428.2 in.^{3}	435.2 in.^{3}
Z^b	428.2 in.^{3}	450.9 in.^{3}
Q^{tf}	262.5 in.^{3}	270.9 in.^{3}
Q^{cg}	286.5 in.^{3}	298.5 in.^{3}
Q^{bf}	262.5 in.^{3}	276.3 in.^{3}

* Concrete Section
** Transformed Section

Figure 1. Details of test beams.

to an ultimate stress equal to 252.5 ksi, and 5.1 percent elongation in 24 in. The surface of the strand was free from rust, and care was taken to avoid getting any grease on the strand during the fabrication operation.

The web reinforcement was fabricated from hot rolled No. 2 or No. 3 deformed bars. For the No. 2 bar, the yield point stress, f'_y, was 59,500 psi and the ultimate stress, f'_u, was 85,700 psi, based on an area of 0.049 sq in. For the No. 3 bar, f'_y was 55,500 psi and f'_u was 82,700 psi, based on an area of 0.11 sq in. The values of f'_y and f'_u for the No. 2 and No. 3 bars are an average of 12 and 3 tension tests, respectively.

Fabrication

The test beams were fabricated in a prestressing bed set up in the laboratory. The length of the bed was sufficient to permit three beams to be cast end to end. The sequence of operations in casting the test specimens was as follows: tensioning the strands, positioning the web reinforcement, form erection, casting, curing, form removal, instrumentation, and prestress release.

Two 50-ton mechanical jacks were used to tension the strands to approximately the desired value of 113.4 kips. A special hydraulic jacking arrangement was subsequently used to adjust the tension in individual strands if required.

Wire ties were used to secure the web reinforcement to the strand. In addition, it was found necessary to use a wire tie between successive projecting elements of the

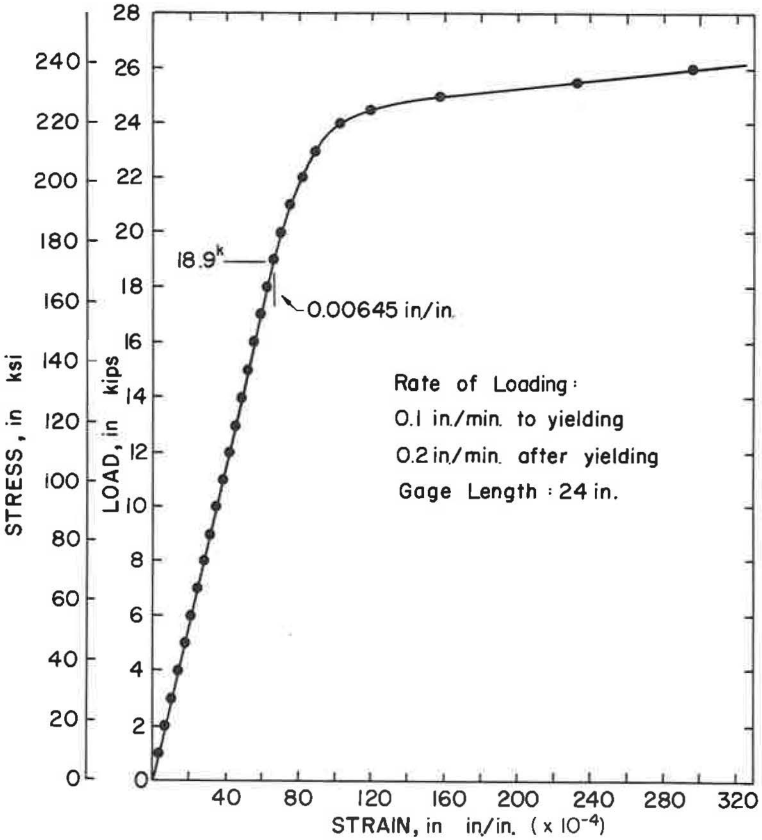

Figure 2. Stress-strain curve for prestressing strand.

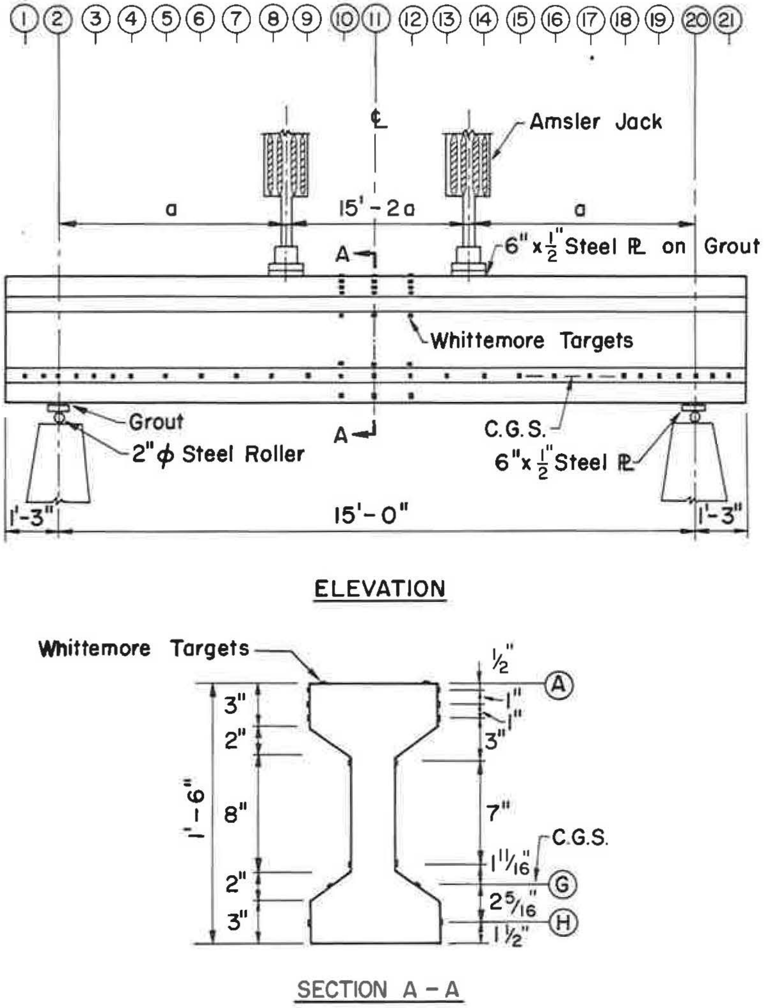
① ② ③ ④ ⑤ ⑥ ⑦ ⑧ ⑨ ⑩ ⑪ ⑫ ⑬ ⑭ ⑮ ⑯ ⑰ ⑱ ⑲ ⑳ ㉑
℄
Amsler Jack
a
15'-2a
a
6"x½" Steel ℞ on Grout
A
Whittemore Targets
Grout
2"ϕ Steel Roller
A
C.G.S.
6"x½" Steel ℞
1'-3"
15'-0"
1'-3"
ELEVATION
Whittemore Targets
½"
A
1"
1"
3"
3"
2"
1'-6"
8"
7"
C.G.S.
1 1/16"
G
2"
2 5/16"
3"
1½"
H
SECTION A - A

Figure 3. Test setup and principal instrumentation.

stirrups, in the compression flange area, to prevent movement of the stirrups during the casting operation.

Wood forms were used to cast the test beams. Dimensional checks made on the finished product indicated that, in general, dimensions were maintained within 1/8 in., and consequently, the nominal dimensions of the cross-section given in Figure 1 were used in all calculations. With each test beam were cast six or more cylinders and three modulus of rupture beam specimens. Vibrators were used to place the concrete in both the test beams and the modulus of rupture specimens; the cylinders were rodded.

All specimens were covered with wet burlap and plastic sheeting for 5 days, after which the forms were stripped. Whittemore targets were positioned on the test beams on the sixth day. On the seventh day after casting, the prestress force was slowly released into the beams. The specimens were subsequently stored in the laboratory until the time of testing.

Instrumentation and Loading Apparatus

The test setup and principal instrumentation employed on the test beams is indicated in Figure 3. Loads for all test beams were symmetrically applied using two 55-kip Amsler hydraulic jacks bolted to a steel test frame. Vertical deflections were measured by both Ames dial gages and level readings. Deformation data were taken using a 10-in. Whittemore strain gage. The Whittemore targets were cemented to the test beams with an epoxy resin.

PROCEDURE AND RESULTS

Properties of the Concrete

Standard 6- by 12-in. cylinder tests were conducted to determine the ultimate compressive strength of the concrete associated with the test beams at the time to prestress release, f'_{ci}, and at the time of test, f'_c. Strains were measured on selected cylinders with a compressometer to determine the modulus of elasticity of the concrete, E_c. For comparison, values of E_c were also determined from the load deflection curves of the test beams. As a measure of the tensile strength of the concrete, the modulus of rupture, f'_r, was determined from 6- by 6- by 36-in. beams loaded at the third points of a 30-in. span.

Cylinder tests associated with prestress release were always carried out on the same day that the prestress force was released, usually within an hour or two of the actual operation. Cylinder and modulus of rupture tests associated with the beam test were carried out either on the same day, or in a very few instances, on the day after testing. The values of f'_{ci}, f'_c, f'_r, and E_c determined from these tests are given in Table 2. In general, each value is an average of three tests. As a typical example, the results of three cylinder tests associated with E. 5 at the time of test are shown in Figure 4.

Prestress Data

The initial strand tension was measured just before casting by load cells placed on each strand. The total initial prestress force, F_i, obtained for each test beam is given in Table 3.

Whittemore readings were taken along line G shown in Figure 3 to determine the elastic and inelastic losses in the prestress force, and the distance from the ends of the test beams, at the level of the center of gravity of the prestressing strand (c. g. s.), to the point at which 85 percent of the prestress force was effective. Readings were taken just before releasing the prestress force, after release, and again just before testing. The difference between these readings, converted to concrete strain, was plotted against location along the length of the test beam, a typical example of which is shown for E. 5 in Figures 5a and 5b.

Assuming that the concrete strain measured on the surface of the test beam at the level of the c. g. s. is equal to the average strain loss in the prestressing strand, the loss in the prestress force can be determined from the stress-strain curve of the strand. The

TABLE 2
PROPERTIES OF CONCRETE[a]

Beam	At Transfer			At Test				
	Age (days)	f'_c (psi)	E^1_c (ksi)	Age (days)	f'_c (psi)	f'_r (psi)	E^1_c (ksi)	E^2_c (ksi)
E.1	7	5.600	3,100	67	7,030	690	4,000	4,600
E.2	7	5,640	3,100	62	6,690	740	3,600	4,200
E.3	7	5,690	3,100	56	6,720	660	3,500	4,300
E.4	7	5,500	3,200	55	6,960	700	3,900	4,700
E.5	7	5,530	3,100	60	6,610	670	3,800	4,600
E.6	7	5,440	3,200	62	7,100	730	4,100	4,500
E.7	7	5,900	3,800	62	7,230	800	4,100	4,700
E.8	7	5,680	3,400	70	6,970	650	4,400	4,700
E.9	7	5,630	3,500	74	7,140	720	4,200	4,700
E.10F	7	6,160	3,600	228	7,360	950	4,400	5,100
E.11F	7	6,410	3,600	245	7,790	960	4,200	5,000
E.12	7	5,590	3,300	68	7,020	680	3,900	4,700
E.13	7	6,130	3,700	27	7,320	630	4,400	4,500
E.14	7	5,670	3,600	47	6,780	680	4,100	4,700
E.15	7	5,730	3,500	35	6,940	670	4,300	4,600
E.16	7	5,650	3,300	64	6,950	610	3,700	4,500
E.17	7	5,400	3,300	57	6,580	600	3,800	4,300
E.18	7	5,520	3,200	52	6,640	580	3,600	4,500
Avg	-	5,720	3,400	-	7,000	710	4,000	4,600

[a] Modulus of elasticity values are designated E^1_c if determined from cylinder tests and E^2_c if determined from load-deflection curve of test beam.

strain determined from the difference in the Whittemore readings before and after release of the prestress force was considered to be the elastic loss. Similarly, the strain determined from the difference in the readings after release of the prestress force and just before testing was considered to be the inelastic loss. The losses and the prestress force at test, F, for each beam are given in Table 3.

The distance from the end of the beam at the level of the c. g. s. to the point at which 85 percent of the prestress force was developed was determined by plotting the total concrete strain at the time of test along the length of the beam. An example of this is shown for E. 5 in Figure 5c. Transfer distances determined in this way for the test beams are given in Table 3.

Static Beam Tests

Load was symmetrically applied to the test beams in shear increments of 2 kips, except when near loads at which cracking was expected. In this case, the shear increment was reduced to 1 kip. Data taken during the test included primarily load-deflection reading, strain measurements by Whittemore readings, and a log of the loads at which flexural cracking, inclined cracking, and ultimate failure took place. In addition, crack patterns were marked on the test beams after the application of each load increment. After failure the test beams were photographed.

The principal results of these tests are presented in Table 4. Convenient parameters for comparing the two principal variables in this investigation, length of shear span and amount of web reinforcement, are tabulated as the shear-span-to-effective-depth

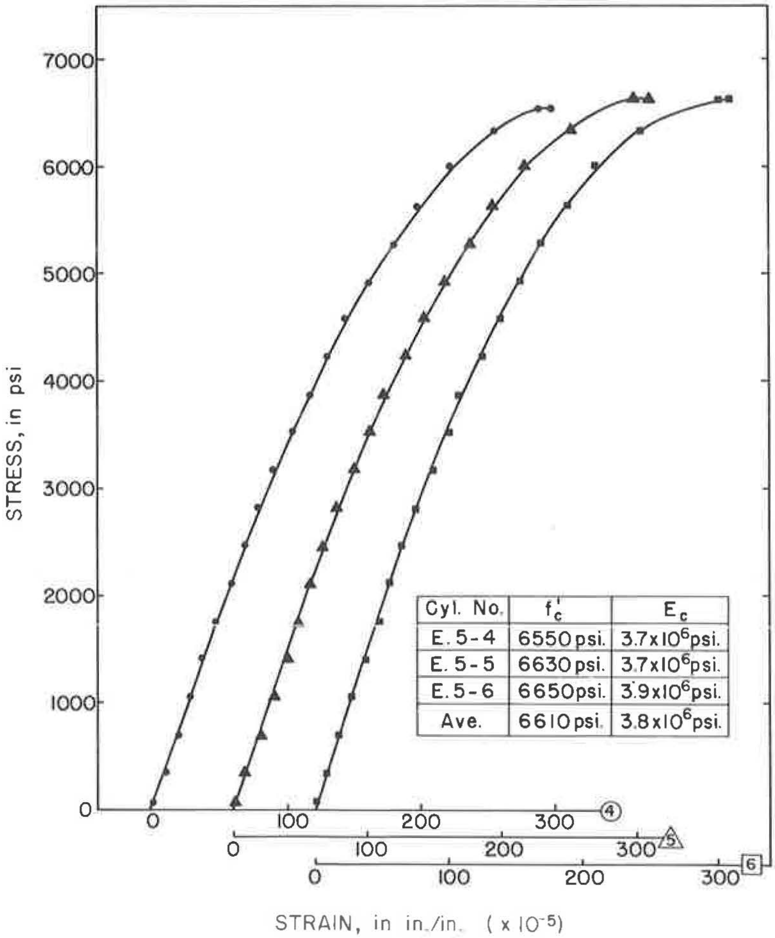

Figure 4. Cylinder tests for E.5 (at test).

ratio, a/d, and the web reinforcement index, $rf'_y/100$. The applied load shears at flexural cracking, inclined diagonal tension cracking, and at failure are given as V_c^f, and V_c^{dt}, and V_u, respectively.

Figures 6a and 6b show an overall view and a closer view of the right side, respectively, of E. 12. The crack patterns are marked to indicate extent of cracking for the value of shear marked on the beam, and the dark lines marked on the web of the test beams, perpendicular to the longitudinal axis, indicate the location of the web reinforcement. The values of V_c^f and and V_c^{dt} can be readily determined from Figure 6b as 24 and 30 kips, respectively. The mode of failure is flexure.

Inclined diagonal tension cracking occurred in all of the test beams. This cracking was characterized by its sudden

TABLE 3

PRESTRESS DATA

Beam	F_i (kips)	Losses (%)			F (kips)	Transf. Dist. (in.)	
		Elastic	Inelastic	Total		End 2	End 20
E.1	113.7	8.4	12.9	21.3	89.4	11	9
E.2	113.7	8.5	12.7	21.2	89.5	12	14
E.3	113.7	9.0	12.3	21.3	89.4	14	17
E.4	113.9	8.8	11.3	20.1	91.0	11	12
E.5	113.9	8.6	11.9	20.5	90.6	14	14
E.6	113.9	8.5	12.3	20.8	90.2	16	16
E.7	114.9	8.1	11.8	19.1	92.0	13	15
E.8	114.9	8.1	11.8	19.9	92.0	14	15
E.9	114.9	8.1	12.7	20.8	91.0	17	15
E.10F	113.7	8.4	15.3	23.7	86.7	15	15
E.11F	113.7	8.3	15.4	23.7	86.7	14	16
E.12	113.7	8.5	12.3	20.8	90.0	12	15
E.13	113.5	7.8	7.1	14.9	96.6	15	14
E.14	113.5	7.6	7.3	14.9	96.6	10	11
E.15	113.5	7.3	7.9	15.2	96.3	13	11
E.16	113.3	8.2	11.0	19.2	91.6	13	15
E.17	113.3	8.4	10.2	18.6	92.4	14	13
E.18	113.3	8.5	9.9	18.4	92.6	15	15
Avg	113.8	8.3	11.5	19.8	91.4	13.5	14.0

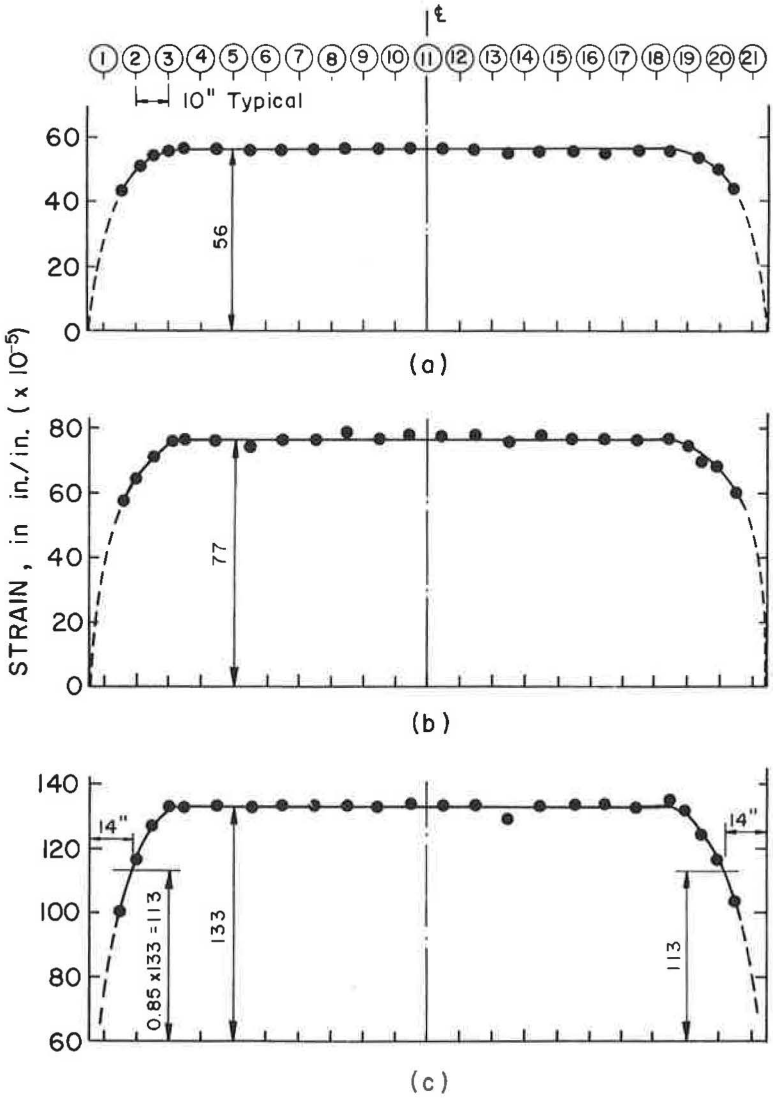

Figure 5. Concrete strain along c.g.s.: (a) after transfer, (b) from transfer to test, and (c) total strain to test.

appearance and by its initiation from an interior point in the web of the test beams. Because the hydraulic loading apparatus controlled the displacement introduced into the test beams and measured the corresponding applied force, a further characteristic of diagonal tension cracking was a noticeable drop-off in the measured applied load at the instant diagonal tension cracking formed.

In the test beams without web reinforcement, E. 1 through E. 4, the diagonal tension cracking load was, in effect, the ultimate load. Although the test beam did not collapse after the formation of diagonal tension cracking, failure appeared to be imminent. These four test beams were then unloaded and subsequently reloaded to failure. These final values of ultimate load are given as V_u in Table 4; however, the value of V_c^{dt} for these four test beams may be more appropriately regarded as the ultimate load.

The state of cracking in the test beams at the time of formation of the inclined diagonal tension cracks was reconstructed from photographs and is presented in the

TABLE 4
STATIC TEST RESULTS

Beam	$\frac{a}{d}$	$\frac{rf'_y}{100}$ (psi)	Shear, V (kips) V_c^f	V_c^{dt} End 2	V_c^{dt} End 20	V_u	Nominal Shear Stress at Ult. Load $v_u = \frac{V_u}{b'd}$ (psi)	Mode of Failure[a]
E.1	6.34	0	14.4	-	20.4	16.2	381	S
E.2	5.07	0	16	-	23.9	20.8	489	S
E.3	4.23	0	20	26	-	23.1	542	S
E.4	3.39	0	24.4	30	-	30.8	724	S
E.5	3.39	676	24	31.8	28	42.0	988	F
E.6	3.39	508	24	30	28	41.8	984	F
E.7	3.39	406	25	28	28	41.1	965	F
E.8	3.39	339	23.3	28.2	27.2	41.2	968	F
E.9	3.39	254	24	28	28	41.2	968	F
E.10F	3.39	339	24	30	30	-	-	-
E.11F	3.39	254	24	30	28	-	-	-
E.12	3.39	204	24	30	30	41.2	968	F
E.13	3.39	222	24	30.6	29.2	41.7	981	F
E.14	2.54	222	33	33.8	32.3	53.8	1263	S
E.15	2.54	222	32	33	34	55.7	1310	F
E.16	3.39	162	24	30	30	39.9	939	F
E.17	3.39	121	24	26	29.4	38.0	894	S
E.18	3.39	97	24	27.1	31.5	38.7	911	S

[a] F = flexure; S = shear.

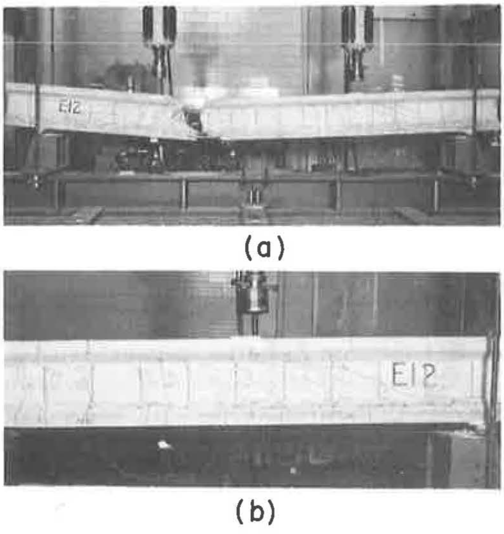

Figure 6. E.12 after failure: (a) elevation view, end 2 on right; and (b) end 2.

Appendix for selected test beams. Similar sketches of all of the test beams have been published previously (1). Diagonal tension cracking occurred on only one end of the test beams without web reinforcement because the diagonal tension cracking load was the ultimate load. Those beams with web reinforcement, however, had substantial load-carrying capacity beyond diagonal tension cracking; consequently, diagonal tension cracking would form, at different loads, in both shear spans.

In the figures in the Appendix, all cracking before the formation of diagonal tension cracking is indicated by solid heavy lines. The suddenly appearing diagonal tension cracking is indicated by dashed heavy lines, and the shear causing this cracking is indicated at the load point. Also shown in the figures, in the conventional way, is the location of the vertical web reinforcement.

The principal tensile stresses, σ_t, shown in the figures in the Appendix were calculated, assuming an uncracked section and using the properties of the transformed section, at the intersection of the grid lines within the shear span and the junction of the web and top flange, the center of gravity, and the junction of the web and bottom flange. It was assumed that the state of stress was defined by a horizontal normal stress, σ, and a shearing stress, τ, and that the vertical normal stress was zero. Therefore, σ_t was calculated from the equation:

$$\sigma_t = \sqrt{\left(\frac{\sigma}{2}\right)^2 + \tau^2} + \frac{\sigma}{2} \qquad (1)$$

in which the normal stress was calculated from:

$$\sigma = F\left(\frac{ey}{I} - \frac{1}{A}\right) - \frac{y}{I}\left(V_c^{dt}x + M_d\right) \qquad (2)$$

and the shearing stress was calculated from:

$$\tau = \frac{Q}{Ib'}\left(V_c^{dt} + V_d\right) \qquad (3)$$

In Eq. 2, x is the horizontal distance from the reaction and y is the vertical distance, positive upwards, from the center of gravity of the transformed section. The slope of the compressive stress trajectory was calculated from the equation:

$$\theta = \frac{1}{2}\tan^{-1}\left(\frac{2\tau}{\sigma}\right) \qquad (4)$$

Light dashed lines in the shear span show the compressive stress trajectories in the web of the test beams.

For some test beams, for example, E.14, there was no cracking in the shear span before diagonal tension cracking and, therefore, the given principal stresses represent the state of stress just before cracking. However, for other test beams, for example, E.3, inclined cracking which began as a flexural crack occurred in the shear span before diagonal tension cracking. Therefore, the calculated principal stresses in the region of the flexural cracking do not accurately represent the state of stress at the time of diagonal tension cracking.

Examination of the inclined cracking indicated that three test beams, E.1, E.2, and E.3, had a lower value of the inclined cracking load than the value of V_c^{dt} given in Table 4. These three test beams are shown in Figure 7. Inclined cracks may be seen which begin as flexural cracks but, because of the presence of shear, turn and become inclined in the direction of increasing moment. Inclined cracks of this type will be called flexure shear

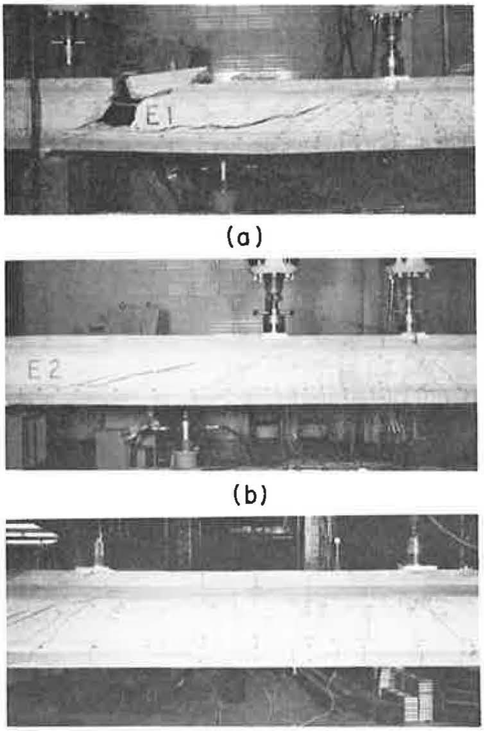

(a)

(b)

(c)

Figure 7. Beams after failure: (a) E.1, (b) E.2, and (c) E.3.

TABLE 5

SHEAR AT FLEXURE SHEAR CRACKING

Beam	a/d	V_c^{fs} (kips)
E.1	6.34	17.5
E.2	5.07	22
E.3	4.23	26

cracks and will be considered significant when they occur at a distance equal to or greater than the effective depth of the beam outside of the concentrated load point with which they are associated. From these figures, values of applied load shear, V_c^{fs}, in agreement with the definition of significant flexure shear cracking were determined; the values selected are given in Table 5. The value of V_c^{fs} equal to 26 kips for E. 3 is the same as the value of V_c^{dt} given in Table 4. In this case, the diagonal tension crack formed while holding the load on E. 3 constant at a shear of 26 kips. A significant flexure shear crack, however, had formed just before reaching the shear of 26 kips.

Modes of failure of the test beams were classified in Table 4 as flexure or shear. The flexural failures were all similar, being characterized by crushing of the concrete in the compression zone and sudden complete collapse of the test beam. Test beam E. 5 (Fig. 8) may be regarded as typical of the flexural failures.

The shear failures were dissimilar. In the beams without web reinforcement, E. 1 through E. 4, as previously noted, the formation of diagonal tension cracking caused the beam to appear unstable but did not trigger a collapse mechanism. Subsequent unloading and reloading to failure led to a collapse mechanism characterized in all four cases by crushing of concrete in the lower portion of the web and by the simultaneous development of a tension crack in the top flange. The failure in E. 4 typifies this description. The failure in test beams E. 1 through E. 3 was similar to that shown in Figure 9 for E. 4, and the failure region in all cases was located approximately the effective depth of the test beam from the reaction.

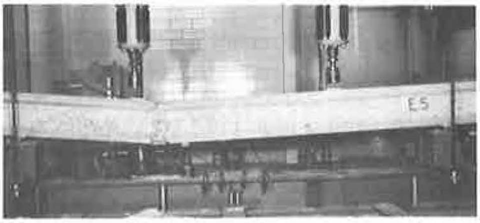

(a)

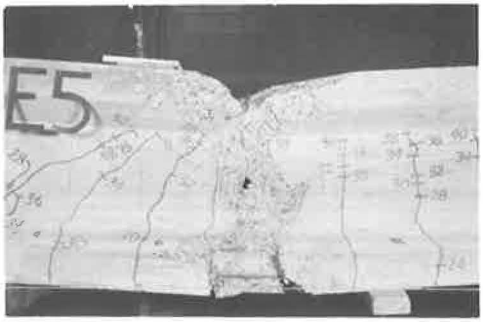

(b)

Figure 8. Flexural failure in E.5: (a) elevation view, end 2 on right; and (b) failure region.

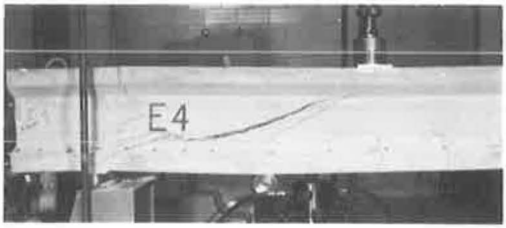

Figure 9. Shear failure in E.4.

Two beams with web reinforcement, E. 17 and E. 18, failed in shear. Overall and close-up views of the shear span in which the failure occurred are shown for both of these beams in Figures 10 and 11, respectively. Only the close-up view of E. 18 is taken (Fig. 11b) in the test setup. The other three pictures were taken after the beams were removed from the test setup, and artificial means are used to indicate the location of the reactions and load points.

The shear failure in E. 17 was gradual and nonviolent, being characterized by crushing of concrete in the web. No stirrups were broken. In contrast, the shear failure in E. 18 was sudden and violent. Examination of E. 18 after failure showed that the second and third stirrup from the reaction had fractured.

As previously noted, beams E. 13 and E. 14 had inverted L-shaped stirrups for web reinforcement, in contrast to the U-shaped stirrups used in the other test beams. Beam E. 13 failed in flexure. However, E. 14 failed in shear due to a bond failure in the web

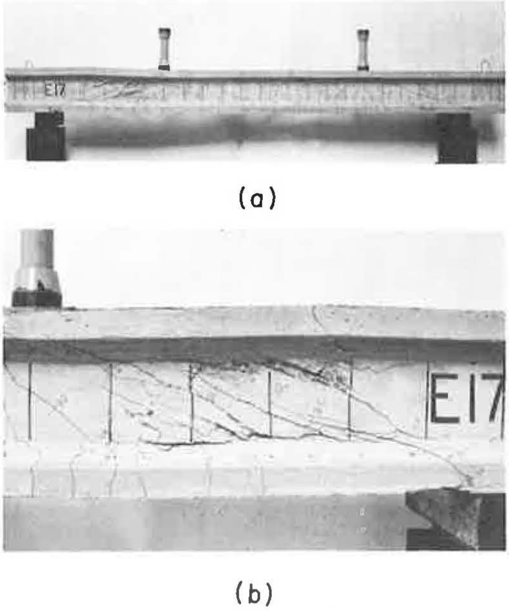

Figure 10. Shear failure in E.17: (a) elevation view, end 2 on left; and (b) opposite side of failure region.

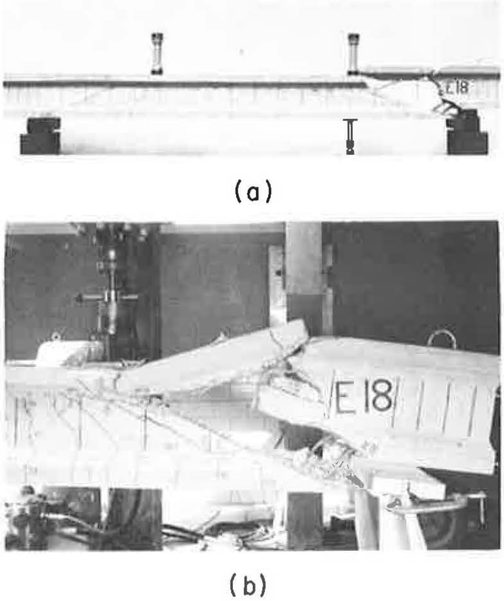

Figure 11. Shear failure in E.18: (a) elevation view, end 2 on right; and (b) failure region.

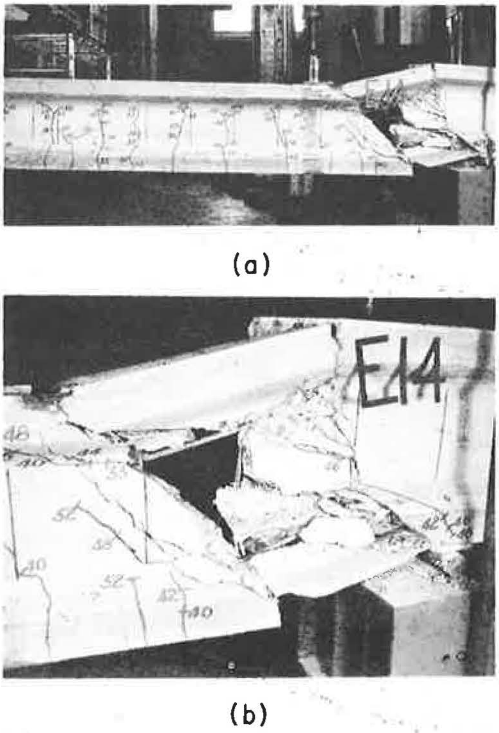

Figure 12. Failure in E.14: (a) part elevation view, end 20 on right; and (b) failure region.

reinforcement. As can be seen from the close-up view of the failure region in Figure 12, the second stirrup from the reaction had inadequate anchorage below the point at which it was crossed by an inclined crack to develop the strength of the stirrup, thereby triggering the shear failure.

Strain measurements were taken at selected intervals during the course of a beam test. As shown in Figure 3, the Whittemore targets can be separated into two groups. The first group may be considered to consist of the set of targets on the c.g.s., i.e., on the horizontal line G, and the second group to consist of the set of targets on vertical lines 10, 11, and 12.

The first group of targets was intended, in addition to determining prestress losses, to show the variation in concrete deformation with applied load along the c.g.s. Accordingly, strain data for E.16, which failed in flexure, and E.17 and E.18, which failed in shear, are presented in Figures 13, 14, and 15, respectively.

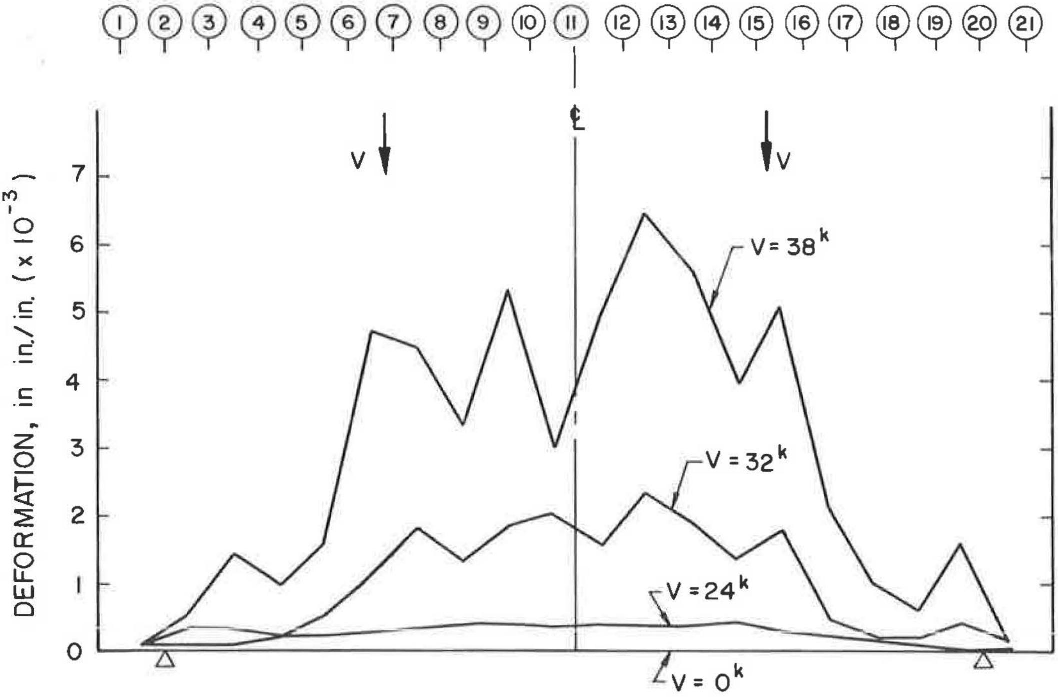

Figure 13. Concrete deformation along c.g.s. during test of E.16.

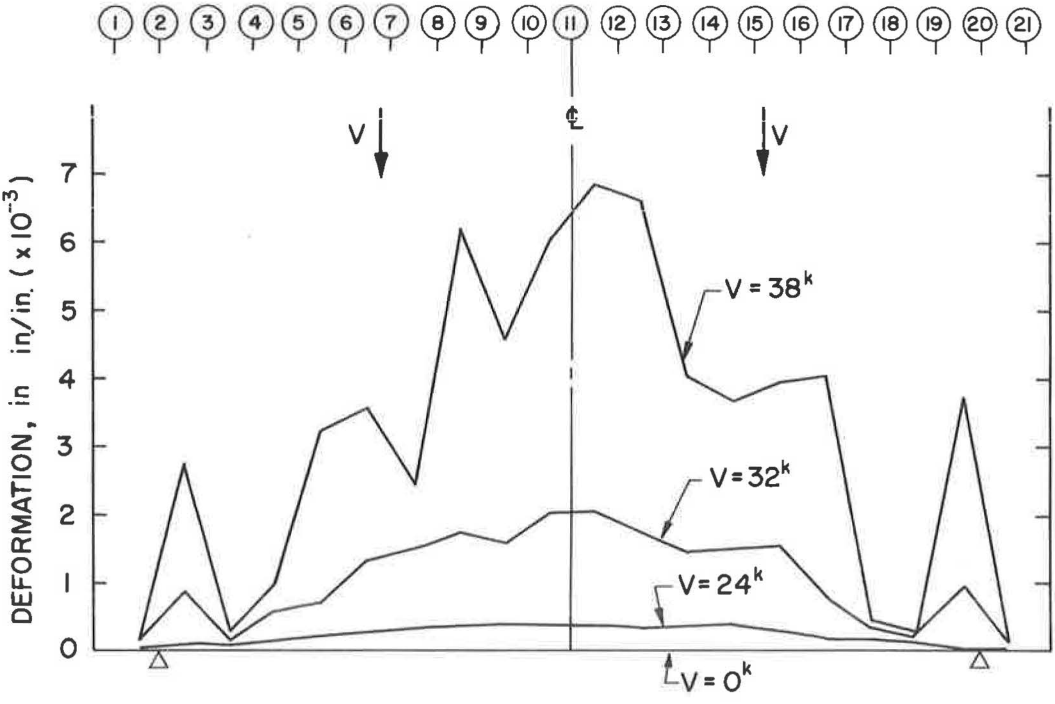

Figure 14. Concrete deformation along c.g.s. during test of E.17.

Data taken for the other test beams are not reported. In these figures, the variation in concrete deformation along the c.g.s. is given for three values of shear; 24, 32, and 38 kips. For all three test beams, the flexural cracking load, V_c^f, was equal to 24 kips; therefore, the deformation at this load may be regarded as concrete strain. At V = 32 kips, inclined diagonal tension cracking had occurred for all three beams, and flexural cracking had extended across the c.g.s. The deformations for V = 38 kips are, in all three cases, indicative of the deformations at ultimate load.

The second group of targets was intended to give the deformation at a vertical section in the constant moment region of the test beams. Test beam E.5 may be regarded as typical; the data for this beam are plotted in Figure 16. Each plotted point is an average of readings between lines 10 and 11 and 11 and 12 on both sides of the member. This plot includes data taken before and after transfer, as well as before and during the test. In Figure 16, the strains before and after transfer, from transfer to test, and during the test are plotted separately; e.g., the strain from after transfer to test is measured between the vertical zero line and the indicated line.

In Figure 17, the data in Figure 16 have been used to determine the elastic strain distribution in E.5 just before testing, i.e., at V = 0, and corresponding to selected magnitudes of shear during the test. The strain distribution determined from the Whittemore readings before and after transfer was assumed to be elastic strain. This was corrected to indicate the elastic strain just before testing by evaluating the effect of the change in prestress force due to the inelastic losses occurring from after transfer to time of test. The deformation corresponding to the different increments of shear were then added to the elastic strain at V = 0. From Figure 17, the strain in the top fibers of the test beams, ϵ_u, and the approximate location of the neutral axis at failure can be determined by extrapolation to the ultimate load, V_u, equal to 42.0 kips.

Values of ϵ_u, determined as indicated in the preceding paragraph, and ultimate moment, M_u, are given in Table 6 for those test beams failing in flexure. The values

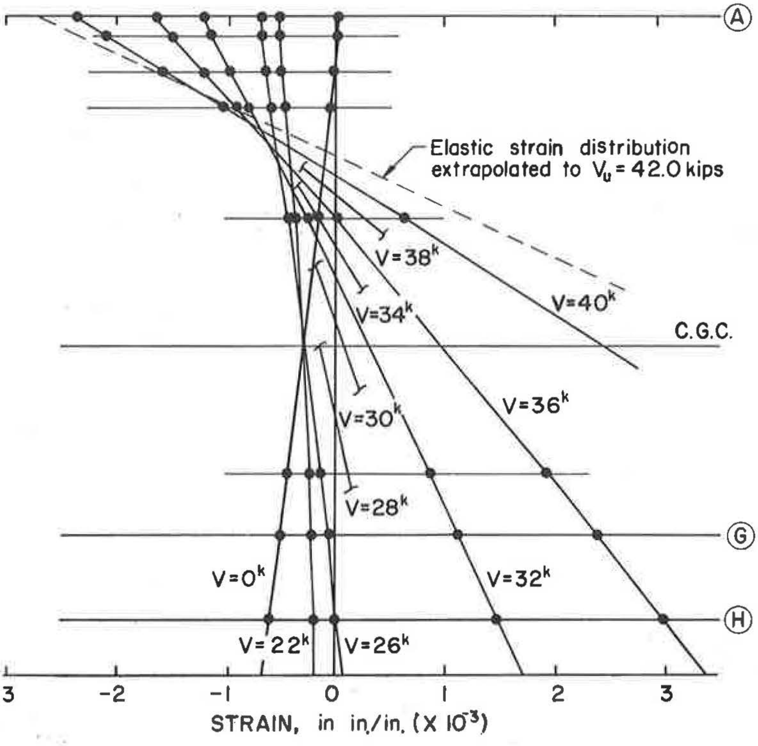

Figure 17. Elastic strain history of E.5.

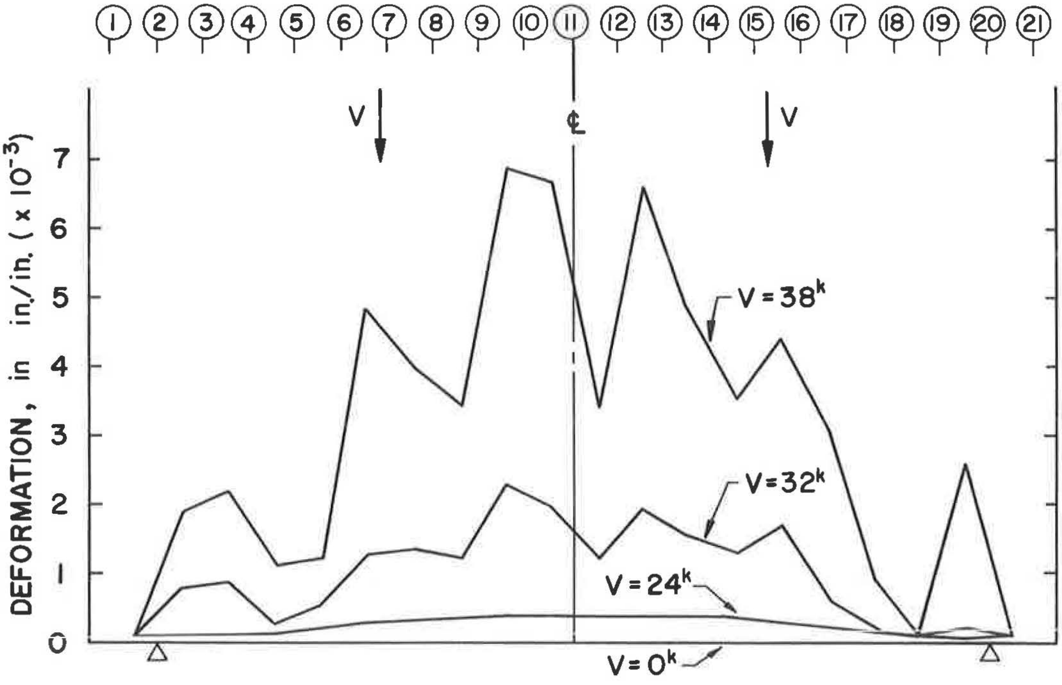

Figure 15. Concrete deformation along c.g.s. during test of E.18.

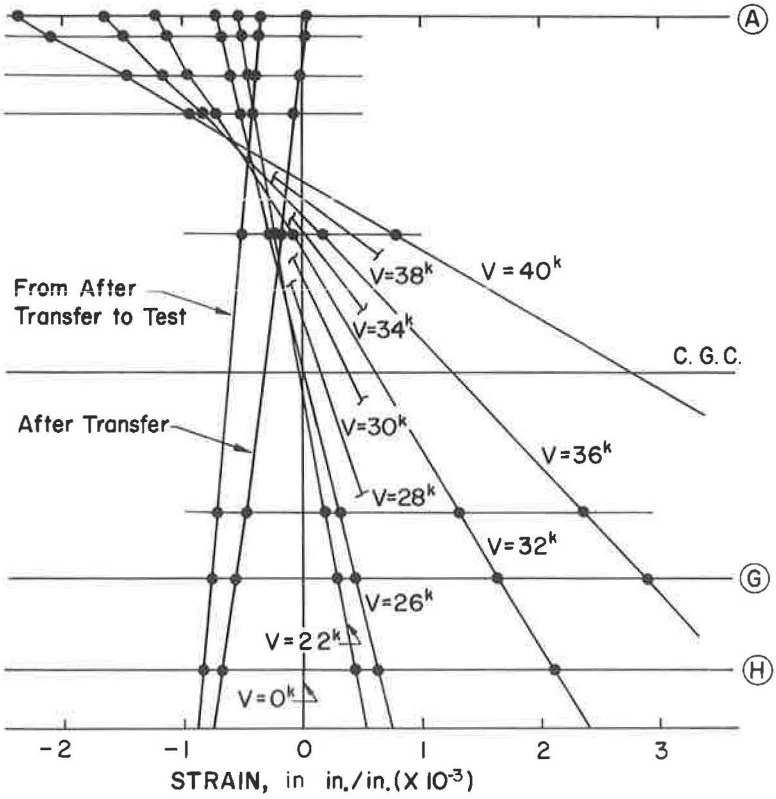

Figure 16. Strain distribution of E.5.

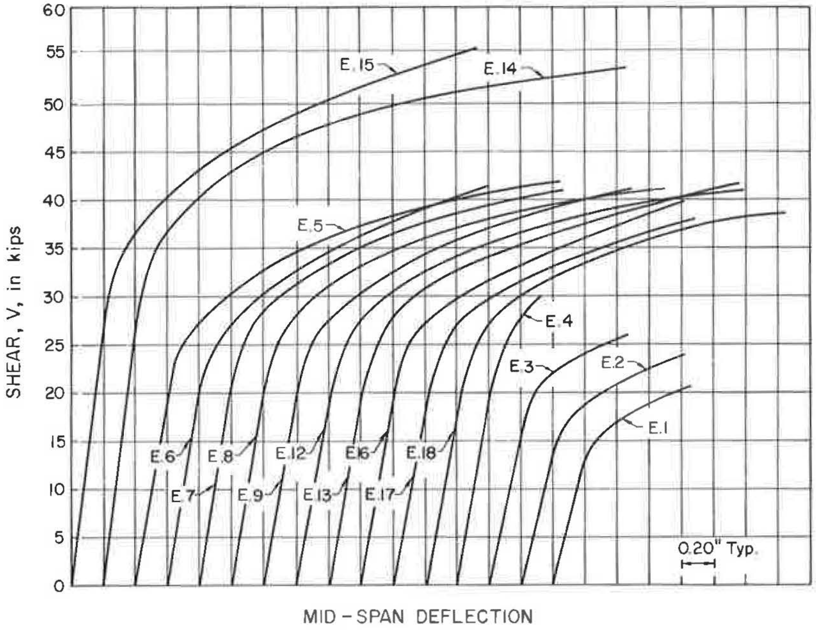

Figure 18. Load-deflection curves for test beams.

TABLE 6

BEAMS FAILING IN FLEXURE

Beam	ϵ_u (in./in.)	M_u (kip-ft)
E.5	0.0027	170.9
E.6	0.0027	170.1
E.7	0.0028	167.3
E.8	0.0025	167.7
E.9	0.0025	167.7
E.12	0.0028	167.7
E.13	0.0025	167.7
E.15	0.0025	170.0
E.16	0.0028	162.5

of M_u include an allowance of 2.9 kip-ft for dead load moment. The average experimental ultimate moment of these nine beams was 168.2 kip-ft. For comparison, the calculated ultimate flexural capacity according to Section 1.13.10 of the AASHO specification, assuming f'_c = 7,000 psi (average f'_c of all test beams) and f'_s = 252.5 ksi, was 164.5 kip-ft.

Load-deflection curves for the static tests are presented in Figure 18.

DISCUSSION

Overload Behavior of Prestressed I-Beams

Knowledge of the ultimate strength of a prestressed beam requires an understanding of the physical behavior of this type of member under load. This behavior may be described with reference to the uncracked or cracked loading range.

In the uncracked range, the familiar formulas of structural mechanics, based on an uncracked section and a linear strain distribution, are applicable. However, at cracking a fundamental change takes place in the way in which the prestressed beam carried load. Two cases are important. Where flexure predominates, the strain distribution remains linear after cracking up to failure. With this as a compatibility condition, the ultimate flexural capacity can be accurately determined. Where shear is significant, inclined cracks develop in the prestressed beam. In the zone of inclined cracking, the strain distribution is nonlinear. If shear is critical, the inclined cracking leads to a shear failure.

The ultimate shear strength of prestressed concrete members has been studied extensively in recent years. Three important conclusions may be drawn from these investigations:

1. The inclined cracking load in a prestressed beam without web reinforcement is the same as the inclined cracking load in a prestressed beam with web reinforcement;
2. The inclined cracking load in a prestressed beam without web reinforcement and subjected to moving loads is the ultimate load; and
3. The stress in web reinforcement is not significant unless crossed by an inclined crack.

Tests on 33 pretensioned I-beams without end blocks by Hulsbos and Van Horn (2) may be regarded as a basis for the first conclusion. The results of their tests indicated that the amount of web reinforcement had no apparent effect on the magnitude of shear causing the formation of inclined cracks. This conclusion is supported by the results presented in Table 4. Comparison of the values of V_c^{dt} for beams tested on an a/d ratio of 3.39 shows no significant trend with amount of web reinforcement.

McClarnon, Wakabayashi, and Ekberg (3) conducted tests on two pretensioned beams of rectangular cross-section without web reinforcement which were first symmetrically loaded until fully developed flexure shear cracking had occurred. The two beams were then unloaded and subsequently reloaded to failure on an increased shear span. The ultimate shear strength of the two beams was approximately equal to the shear causing significant inclined cracking in two other beams without the load points moved. The four E Series tests without web reinforcement, E.1 through E.4, also support the second conclusion, without the restriction that the loads be moving loads. As indicated in Table 4, the maximum shear sustained by these beams was either equal to or nearly equal to the shear causing diagonal tension cracking.

Work by Mattock and Kaar (4) on the shear strength of continuous prestressed girders with web reinforcement forms a basis for the third conclusion. Their investigation showed that before diagonal tension cracking, the web reinforcement was only slightly stressed, in either tension or compression. With diagonal tension cracking, web reinforcement crossed by the cracking yielded immediately.

The importance of the three conclusions discussed in the preceding paragraphs emphasizes the need to determine accurately the inclined cracking strength of a prestressed beam. There is first the flexure shear type of inclined cracking, which begins as a flexure crack but, because of the presence of shearing forces, becomes inclined in the direction of increasing moment. An important characteristic of this type of cracking is that its development is more rapid than a flexural crack. Therefore, the flexure shear inclined cracking load at a particular section may be realistically taken as the load which will cause a flexural crack to form first at some distance in the direction of decreasing moment from this section. The distance from the section must be sufficient to permit the development of a significant inclined crack which would lead to a critical shear condition.

Hulsbos and Van Horn (2) determined that the principal stress method was satisfactory for evaluating the diagonal tension cracking strength of pretensioned I-beams. Their conclusion was based on a study of the calculated state of stress in the web of the I-beam just before inclined cracking, and included an approximation of the stresses due to the stress concentration from the reaction and load point. The inclined cracking load was calculated as the load causing the principal tensile stress to reach a certain limiting value at any point in the web of the I-beam.

A very thorough study of the shear at inclined cracking of a large number of prestressed beams has been made by Hernandez, Sozen, and Siess. Their design proposals, based on the findings of this study, have been summarized by Mattock and Kaar (4) and state that the shear at inclined cracking shall be taken as equal to the least shear which will produce either of the following effects: (a) a net tensile stress of $6\sqrt{f_c'}$ in the extreme fiber in tension at a distance from the section considered equal to the effective depth of the section, measured in the direction of decreasing moment; or (b) a principal tensile stress of $4\sqrt{f_c'}$ at the intersection of the neutral axis with a 45° line drawn in the direction of decreasing moment from the extreme fiber in compression of the section considered.

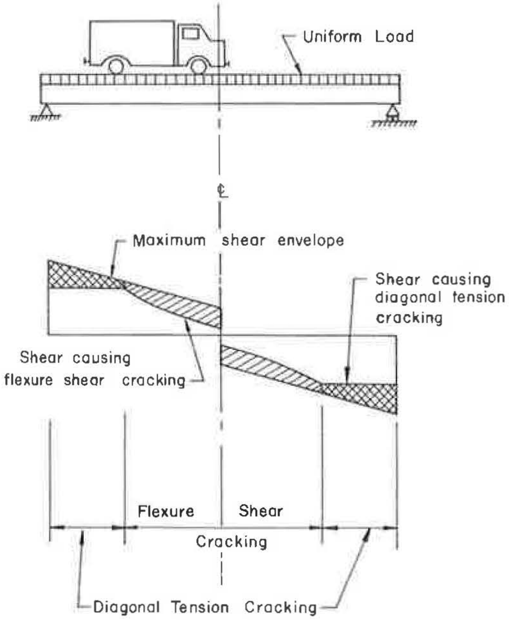
Uniform Load
℄
Maximum shear envelope
Shear causing diagonal tension cracking
Shear causing flexure shear cracking
Flexure
Shear
Cracking
Diagonal Tension Cracking

Figure 19. Behavior of simply supported prestressed beam with web reinforcement.

The significant feature of the proposals by Hernandez, Sozen, and Siess is that only the state of stress at the neutral axis of the member is considered in determining the inclined diagonal tension cracking load. Inasmuch as the state of stress at the bending neutral axis is simplified because flexural stresses are zero at that point, the inclined cracking load becomes a function of only two variables, the limiting tensile strength of the concrete and the effective prestress force, and can be readily calculated.

The discussion in the preceding paragraphs can form the basis of a consideration of the behavior of a simply supported prestressed beam with web reinforcement, as shown in Figure 19, subjected to a uniform load and a moving vehicle load. These applied loads can represent design loads multiplied by appropriate load factors, i. e., ultimate loads. The crack patterns may develop in several ways. For beams with the greater span lengths, the first cracking would be flexural, followed by flexure shear cracking. For intermediate span lengths, diagonal tension cracking may either precede or follow flexure shear cracking. For short span lengths, diagonal tension cracking may precede flexural cracking.

If the span is regarded as being of intermediate length, both flexure shear and diagonal tension cracking must be considered. Wherever the shear in the beam produces a stress in the web equal to the principal tensile strength of the concrete, or a stress in the bottom fibers equal to the flexural tensile strength of the concrete, diagonal tension or flexure shear cracking, respectively, may occur. A plot of the least value of shear causing either diagonal tension or flexure shear cracking on a diagram of the maximum shear envelope, as in Figure 19, indicates the amount of shear which must be carried at any section after inclined cracking. Because the web reinforcement does not begin working until an inclined crack forms, the amount of shear carried after inclined cracking must be a function of the amount of web reinforcement in the beam.

A section arbitrarily located in the beam in Figure 19 in the region where inclined cracking would exist is shown in Figure 20. A free body diagram of the portion of the beam to the left of this section may be drawn by separating the beam along the path of an inclined crack, say JK, and by a vertical cut through the concrete at the top of the inclined crack, say KL. Because the path of the inclined diagonal tension crack will not extend through to the bottom flange in the region of J, the section taken along JK may pass through some concrete. The principal forces at this section would be the two components of the resultant force in the strand, F_H and F_V, the two components of the resultant force in the web reinforcement, V_{W_H} and V_{W_V}, and the resultant force transmitted through the concrete, which may be represented by a horizontal compressive force, C, and a shearing force, V_c. For prestressed beams with web reinforcement, the horizontal component of the force in the web reinforcement is small, and therefore, V_{W_V} may be taken as simply V_W. Likewise, the vertical component of shear transmitted across the prestressing elements is small and may be neglected. Thus, the general free body diagram may be replaced by a simplified free body diagram, also shown in Figure 20.

V_u can be considered the ultimate shear on this section located x distance from the support. For equilibrium:

$$V_u = V_c + V_w \qquad (5)$$

But V_w may be regarded as known, based on the assumption that web reinforcement crossed by an inclined crack has yielded. Therefore, if A_v is the area of a single stirrup and s is the spacing:

$$V_w = A_v f_y' \frac{\beta d}{s} \qquad (6)$$

in which f_y' is the yield point of the web reinforcement. Solving for A_v gives the equilibrium requirement that:

$$A_v = \frac{\left(V_u - V_c\right) s}{f_y' \beta d} \qquad (7)$$

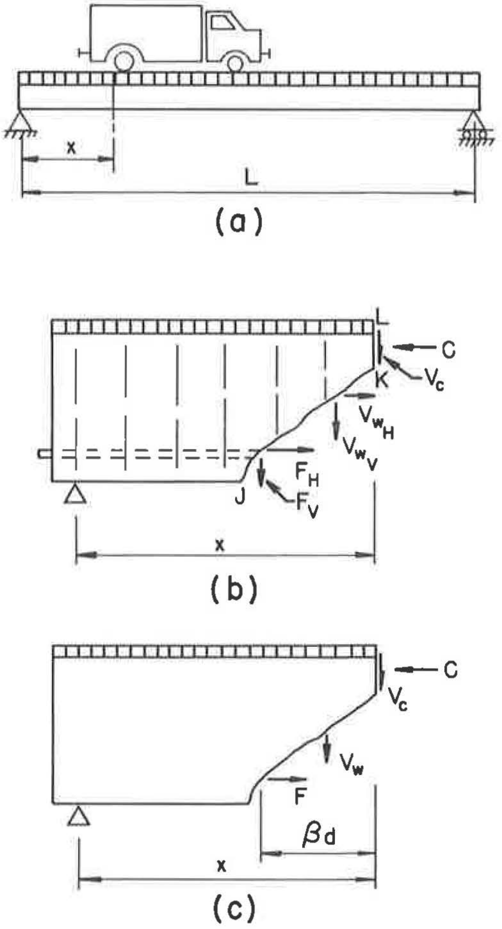

Figure 20. Shear equilibrium condition: (a) elevation, (b) general free body diagram, and (c) simplified free body diagram.

Eq. 7 has several significant features. If V_c and β were known, the form of Eq. 7 is such that it could readily be used as a design equation. In fact, with $\beta = 1$, Eq. 7 has been presented as a design proposal by Hernandez, Sozen, and Siess (4), in which V_c is assumed equal to the inclined cracking load and is calculated according to the recommendations previously given. Mattock and Kaar (4) have also presented a design equation of the form of Eq. 7, in which V_c is calculated according to the recommendations of Hernandez, Sozen, and Siess and the factor β is taken equal to $3.5 \sin(\tan^{-1} a/d)$.

The assumption that the shear just before inclined cracking is equal to the shear carried by the concrete at failure is supported by the tests on E. 1 through E. 4. These four beams, all without web reinforcements, were initially loaded until inclined diagonal tension cracking formed, indicated in Table 4 as V_c^{dt}. At this point in the test, the beams, which had become very unstable, were unloaded. Subsequently, the beams were reloaded to failure, indicated as the shear V_u in Table 4. In the reloading process, essentially all of the shear must have been carried by the concrete in the region above the top of the inclined crack. The lowest ratio of V_u to V_c^{dt} is 0.80, in the case of the beam with the longest shear span; the average ratio for these four tests is 0.90. Furthermore, there is reason to believe that with even a small amount of web reinforcement, the crack opening in the web would have been restricted and the ratio of V_u to V_c^{dt} would have increased to 1 or greater.

The angle of inclination of the inclined crack, for diagonal tension cracking, is closely associated with the direction of the compressive stress trajectory, as can be readily seen from the crack patterns presented in the Appendix. Observations from the tests reported herein indicated that before failure would occur, the inclined crack would have developed sufficiently to have crossed all web reinforcement in its projected path. Therefore, β may be calculated as the factor which, when multiplied by d, gives the horizontal projection of an inclined crack with inclination approximated as the slope

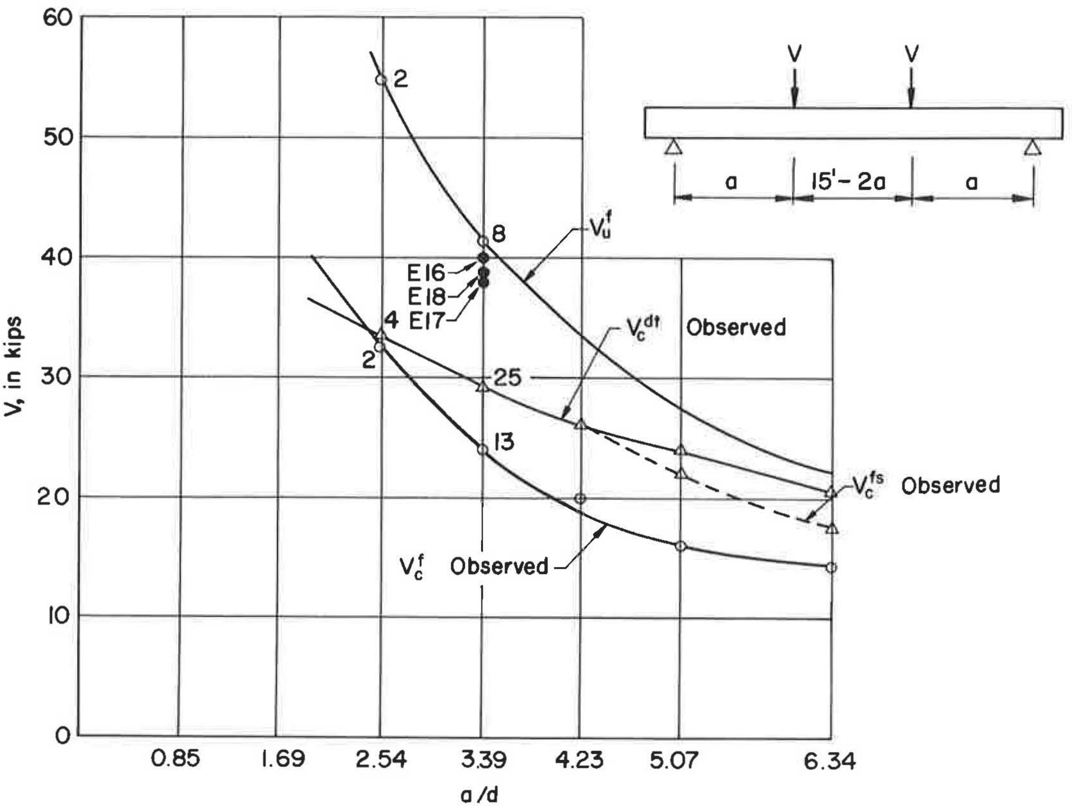

Figure 21. Static strength of test beams.

of the compressive stress trajectory at the bending neutral axis, and arbitrarily considered to extend from the junction of the web and the top flange to the lowest depth at which the web reinforcement may be regarded as effective. This may be expressed as:

$$\beta = \frac{\ell_e}{(\tan \theta)\, d} \tag{8}$$

in which ℓ_e is the distance from the intersection of the top flange and web to the lowest point at which the web reinforcement may be regarded as effective.

For flexure shear cracking, β could have values varying from 0 to greater than 1. Experimental observations indicated that flexure shear cracks forming at β values of less than 1 are supplanted by more critical flexure shear cracks with values of β greater than 1. Therefore, it is conservative to take $\beta = 1$ for all flexure shear cracking.

With V_c and β values determined according to the discussion in the preceding paragraphs, Eq. 7 becomes a criterion for proportioning vertical web reinforcement in a prestressed beam. But Eq. 7 has limitations as an ultimate shear strength equation. The purpose of web reinforcement is to permit an increase in the load-carrying capacity of the beam above the inclined cracking load. This is accomplished by effecting a redistribution of forces in the beam at inclined cracking. In effect, the beam action destroyed by inclined cracking must be restored by web reinforcement. The conditions required to insure that this restoration of beam action takes place must be met before Eq. 7 can be regarded as having any meaning; these conditions include limitations on the spacing of the web reinforcement, anchorage and bond requirements, which can be summed up under the heading of good dimensional proportioning. Assuming that the conditions required for the redistribution of forces are met, the prestressed beam

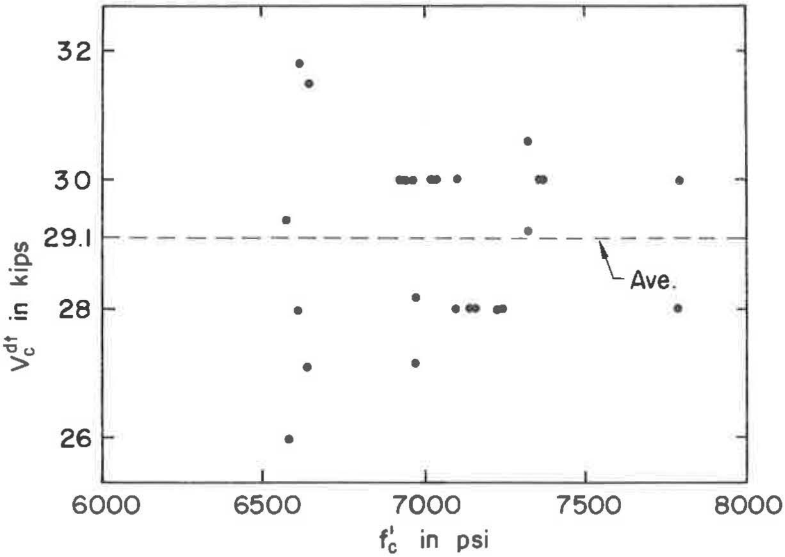

Figure 22. Variation in V_c^{dt} with concrete strength for a/d = 3.39.

critical in shear may fail in three ways: (a) by fracture of the web reinforcement, (b) by web distress, i.e., by crushing of concrete in the web, and (c) by shear compression. But if failure occurs as fracture of the web reinforcement, the critical stress would be the ultimate stress, f_u', which may be more than 50 percent greater than f_y'. Similarly, failure due to web distress or shear compression must be associated with the strength of the concrete. None of these indices, however, are an explicit part of Eq. 7.

Static Shear Strength of Test Beams

The preceding section discussed the overload behavior of prestressed I-beams with web reinforcement. The purpose of this section is to correlate the test results with the discussion in the preceding section.

For this purpose, the test results given in Tables 4 and 5 are plotted as applied load shear, V, vs the a/d ratio on which the test was conducted, as shown in Figure 21. In this form, the results represent the experimentally determined flexural cracking, inclined cracking, and ultimate strength of the type of member being tested. The number beside some of the plotted points indicates the number of tests for which that point is an average.

The test beams ranged in concrete strength from 6,580 to 7,790 psi; the average value of f_c' was 7,000 psi. The effective prestress force ranged from 86.7 to 96.6 kips; the average value of F was 91.4 kips. The 25 points, plotted as an average in Figure 21, indicating the diagonal tension cracking strength of the test beams on an a/d ratio of 3.39 are plotted as individual points in Figure 22 and indicate little variation in inclined cracking strength with concrete strength over the small range of concrete strengths being considered. Similarly, the flexural capacities of the static test beams failing in flexure, presented in Table 6, do not indicate any significant variation with concrete strength or prestress force. Therefore, the data plotted in Figure 21 may be regarded as representing an "average" test beam with a concrete strength of 7,000 psi and a prestress force of 91.4 kips.

The flexural cracking moment of the test beams would generally be calculated from the equation:

TABLE 7

FLEXURAL TENSILE STRENGTH AND PRINCIPAL TENSILE STRENGTH DETERMINED FROM TEST BEAMS

Beam	f'_t (psi)	$\frac{f'_t}{\sqrt{f'_c}}$	σ_t^{cg} (psi) End 2 (psi)	σ_t^{cg} (psi) End 20 (psi)	$\sigma_t^{cg}/\sqrt{f'_c}$ End 2	$\sigma_t^{cg}/\sqrt{f'_c}$ End 20
E. 1	-[a]	-	-[b]	-[c]	-	-
E. 2	710	8.68	-[b]	-[c]	-	-
E. 3	-[a]	-	-[c]	-[b]	-	-
E. 4	725	8.70	435	-[b]	5.22	-
E. 5	690	8.49	480	395	5.90	4.85
E. 6	695	8.26	445	405	5.29	4.81
E. 7	765	9.00	395	395	4.65	4.65
E. 8	585	7.01	405	375	4.86	4.50
E. 9	680	8.04	400	395	4.74	4.68
E. 10F	760	8.85	450	455	5.24	5.30
E. 11F	760	8.62	455	410	5.16	4.66
E. 12	700	8.35	440	445	5.25	5.31
E. 13	565	6.60	440	410	5.15	4.80
E. 14	640	7.77	480	500	5.83	6.08
E. 15	570	6.84	490	520	5.88	6.25
E. 16	665	7.97	440	440	5.28	5.28
E. 17	655	8.08	355	425	4.38	5.24
E. 18	645	7.82	370	475	4.54	5.83
Avg	675	8.07	430		5.16	

[a] Values of f'_t calculated for these beams regarded as unrealistically high and indicate that the corresponding experimentally determined values of V_c^f are too high.

[b] Diagonal tension cracking at other end only.

[c] Not applicable because of prior flexure shear cracking.

$$M_c^f = Z^b \left[f'_t + \frac{F}{A} + \frac{F(e)}{Z^b} \right] \tag{9}$$

Expressed in terms of the shear causing flexural cracking in the test beams, this equation becomes:

$$M_c^f = V_c^f(a) + M_d \tag{10}$$

Solving for f'_t yields,

$$f'_t = \frac{V_c^f(a) + M_d}{Z^b} - \frac{F}{A} - \frac{Fe}{Z^b} \tag{11}$$

Using Eq. 11, values of F from Table 3, and values of V_c^f from Table 4, f'_t was calculated, and the values determined are given in Table 7. M_d was taken as the maximum dead load moment, or 2.9 kip-ft. The average value of the flexural tensile strength determined in this manner was 675 psi, and corresponds to an average ratio of $f'_t/\sqrt{f'_c}$ of 8.07. The minimum ratio of $f'_t/\sqrt{f'_c}$ was 6.60, as determined for E. 13. Therefore, the recommendation of Hernandez, Sozen, and Siess that the critical tensile stress in the extreme fiber in tension be taken as $6\sqrt{f'_c}$ would have conservatively predicted the flexural cracking moment for all the E Series test beams. Their recommendation was based on an investigation which covered a much wider range of concrete strengths than were included in the E Series tests. However, Figure 23 shows a plot of f'_c vs $f'_t/\sqrt{f'_c}$, and indicates no significant trend in the range of concrete strengths investigated. Thus, for concretes similar to those tested in this investigation, the flexural tensile strength of the concrete may be determined as:

$$f'_t = 6.5\sqrt{f'_c} \tag{12}$$

The V_c^f design curve shown in Figure 24 was determined using Eq. 11, with f'_t calculated from Eq. 12, for an "average" test beam.

The calculated inclined cracking strength depends on whether the inclined cracking is classified as flexure shear or diagonal tension. With flexure shear cracking, assuming that the shear causing flexure shear cracking, V_c^{fs}, is equal to the shear causing a flexural crack to form a distance d from the load point:

$$V_c^{fs} = \frac{M_c^f - M_d}{a - d} \tag{13}$$

The V_c^{fs} design curve shown in Figure 24 was determined from Eq. 13. It is a conservative estimation of the V_c^{fs} observed curve, as it must be because the flexure shear cracking was not considered significant until it formed a distance d or greater away from the load point.

The transition from flexure shear to diagonal tension cracking may be seen, from Figure 21, to take place in the neighborhood of an a/d ratio of 4. From an examination

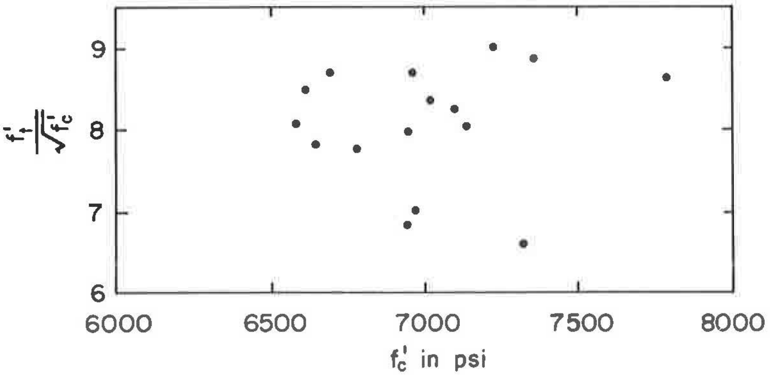

Figure 23. Variation in flexural tensile strength with compressive strength.

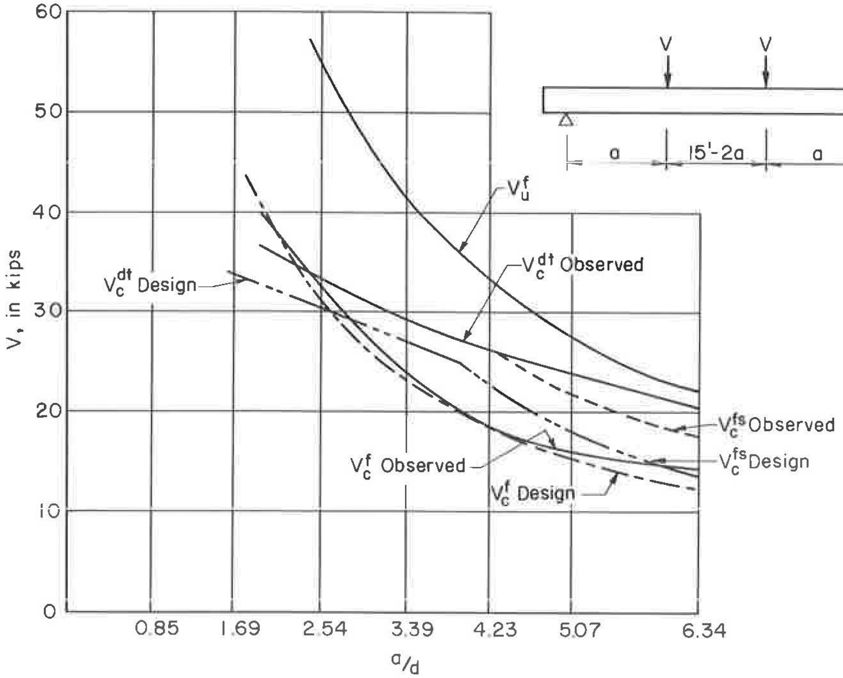

Figure 24. Comparison of observed and design strength of test beams.

of all test beams at inclined cracking (1), as shown for selected test beams in the Appendix, the critical principal tensile stresses at the intersection of the path of the diagonal tension cracks and the center of gravity of the cross-section, σ_t^{cg}, were estimated, and are recorded in Table 7. The average value of σ_t^{cg} determined in this manner was 430 psi, which corresponds to an average ratio of $\sigma_t^{cg}/\sqrt{f_c'}$ of 5.16. The minimum ratio of $\sigma_t^{cg}/\sqrt{f_c'}$ was 4.38, as determined for E.17. The recommendation of Hernandez, Sozen, and Siess was that diagonal tension inclined cracking should be considered to occur, for design purposes, when a principal tensile stress of $4\sqrt{f_c'}$ occurs at the intersection of the neutral axis with a 45° line drawn in the direction of decreasing moment from the extreme fiber in compression of the section considered. As may be noted from the figures in the Appendix, the values of the principal tensile

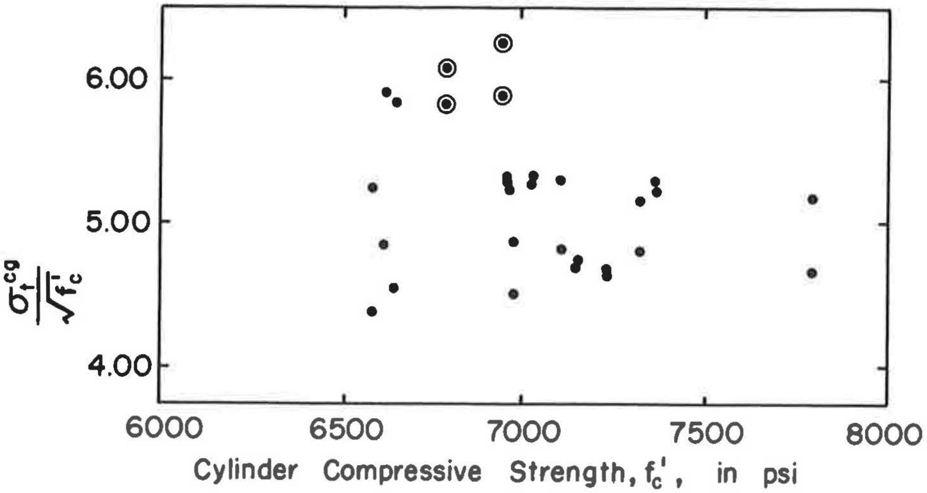

Figure 25. Relationship between principal tensile strength along cgc at diagonal tension cracking and compressive strength of concrete.

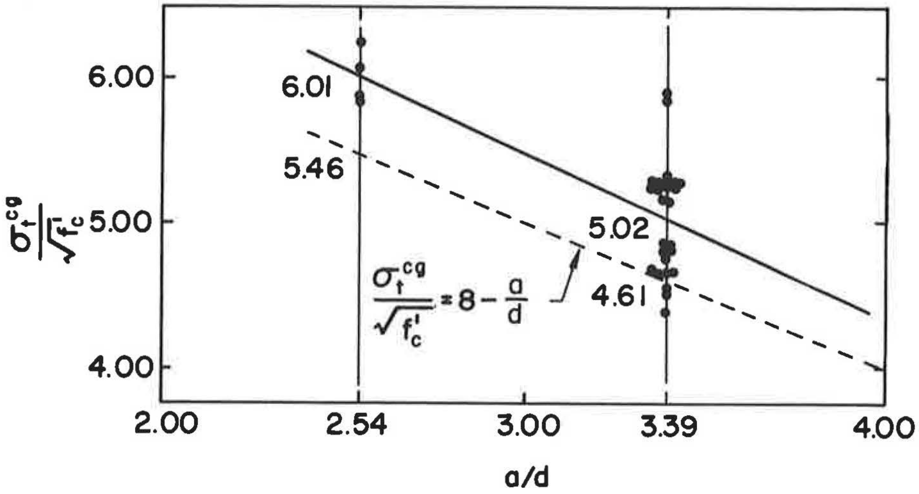

Figure 26. Relationship between tensile strength along cgc at diagonal tension cracking and a/d ratio.

stress along the neutral axis are relatively constant, because the dead load of the test beams is a small proportion of the total load at inclined cracking; therefore, the location of the section considered for diagonal tension cracking is not critical. Thus, it may be concluded that the recommendation of Hernandez, Sozen, and Siess would have conservatively predicted the diagonal tension inclined cracking of all of the test beams.

Values of $\sigma_t^{cg}/\sqrt{f_c'}$ are plotted against concrete strength in Figure 25 and the a/d ratio in Figure 26. In Figure 25, the four encircled points are for tests on an a/d ratio of 2.54; the remaining points are for tests on an a/d ratio of 3.39. Figure 25 indicates that, in the range of concrete strengths investigated, $\sigma_t^{cg}/\sqrt{f_c'}$ is relatively insensitive to changes in concrete strength. However, Figure 26 indicates that σ_t^{cg} varies with the a/d ratio. The following expression was selected for the principal tensile stress at the center of gravity causing diagonal tension cracking:

$$\sigma_t^{cg} = \left(8 - \frac{a}{d}\right)\sqrt{f_c'} \tag{14}$$

This expression has been plotted in Figure 26 for comparison with the test data. Based on Eq. 14, the applied load shear causing diagonal tension cracking may be calculated from the following equation, obtained from Eqs. 1, 2, and 3:

$$V_c^{dt} = \frac{Ib'}{Q^{cg}}\sqrt{\left(\sigma_t^{cg}\right)^2 + \left(\sigma_t^{cg}\right)\frac{F}{A}} - V_d \tag{15}$$

The V_c^{dt} design curve shown in Figure 24 was determined from Eq. 15 for an "average" test beam, assuming that V_d is equal to the dead load shear at the midpoint of the shear span. For a/d ratios of 2.54 and 3.39, V_c^{dt} is equal to 30.6 and 27.2 kips, respectively. Therefore, Eqs. 14 and 15 conservatively predicted all but two of the observed diagonal tension cracking shears on these a/d ratios. For the four observed diagonal tension cracking shears on an a/d ratio of 2.54, the average observed-to-predicted ratio was 1.09. For the 25 observed diagonal tension cracking shears on an a/d ratio of 3.39, the average observed-to-predicted ratio was 1.07.

Because $rf_y'/100$ is equal to $A_v f_y'/b's$, Eq. 7 may be written as:

$$\frac{rf_y'}{100} = \frac{V_u - V_c}{b'\beta d} \tag{16}$$

Flexural failures occurred in tests on a/d ratios of 2.54 and 3.39. Eq. 16 can be used to predict the least amount of web reinforcement required to develop the flexural capacity on these a/d ratios. The shear carried by the concrete, V_c, is assumed equal to the shear causing inclined cracking. For a/d ratios of 2.54 and 3.39, V_c^{dt} is less than V_c^{fs} and, therefore, V_c is equal to 30.6 and 27.2 kips, respectively. The applied load shear, V_u^f, required to develop the flexural capacity is 55.1 and 41.3 kips, respectively. Assuming that ℓ_e is equal to 11.5 in., β can be calculated from Eq. 8 after θ has been calculated using Eqs. 2, 3, and 4. β is equal to 1.38 and 1.46 for the a/d ratios of 2.54 and 3.39, respectively. Therefore, the amount of web reinforcement required to develop the flexural capacity of an "average" test beam on a/d ratios of 2.54 and 3.39 is $rf_y'/100$ equal to 417 and 226, respectively.

Four beams were tested on an a/d ratio of 3.39 with less web reinforcement than $rf_y'/100$ equal to 226. E.13 with $rf_y'/100$ equal to 222 and 162, failed in flexure, although it should be noted that the flexural capacity of E.16 was less than the other beams which failed in flexure. E.17 and E.18, with $rf_y'/100$ equal to 121 and 97, failed in shear.

Both beams tested on an a/d ratio of 2.54 had less web reinforcement than $rf_y'/100$ equal to 417. E.15, with $rf_y'/100$ equal to 222, failed in flexure. E.14 had the same amount of web reinforcement as E.15, except that the stirrups were not hooked in the tension flange. E.14 failed in shear because of inadequate anchorage of the stirrups below the inclined crack.

TABLE 8

BEAMS FAILING IN SHEAR

Beam	$\frac{rf_y'}{100}$ (psi)	$\frac{a}{d}$	V_c^{dt} (kips)	V_c^{fs} (kips)	V_c (kips)	V_u (kips)	$\frac{\text{Test}}{\text{Predicted}}$
E.1	0	6.34	14.4	13.8	13.8	13.8	1.48
E.2	0	5.07	20.0	18.0	18.0	18.0	1.33
E.3	0	4.23	23.5	22.9	22.9	22.9	1.13
E.4	0	3.39	27.2	31.8	27.2	27.2	1.10
E.17	121	3.39	26.8	32.0	26.8	34.4	1.10
E.18	97	3.39	27.0	32.0	27.0	33.1	1.17
E.14	222	2.54	30.8	51.6	30.8	40.1	1.34

Therefore, it can be concluded that Eq. 16 conservatively predicted the least amount of web reinforcement required to develop the flexural capacity of the test beams when loaded on a/d ratios of 2.54 and 3.39. Eq. 16 was more conservative for the lower a/d ratio, indicating that the closeness of the load point and the reaction had an influence on the amount of shear which was carried after diagonal tension cracking.

Eq. 16 can also be used to predict the shear strength of beams failing in shear. Solving for V_u:

$$V_u = V_c + b'\beta d \frac{rf'_y}{100} \tag{17}$$

The shear strength of the seven test beams which failed in shear was calculated from Eq. 17 and is given in Table 8. V_c^{dt} and V_c^{fs} were determined from Eqs. 13 and 15, respectively. V_c was assumed equal to the least value of V_c^{dt} and V_c^{fs}. Because the stirrups in E.14 were not hooked in the tension flange, ℓ_e was assumed equal to 8 in. The test-to-predicted ratios of shear strength ranged from 1.10 to 1.48; the average was 1.24. For the four beams without web reinforcement, the test to predicted ratios decreased from 1.48 to 1.10 as the a/d ratio decreased from 6.34 to 3.39, indicating that the prediction of the shear causing inclined cracking is more conservative for the higher a/d ratios. For the three beams with web reinforcement, the test-to-predicted ratios increased from 1.10 to 1.34 as the a/d ratio decreased from 3.39 to 2.54, indicating that the prediction of ultimate shear strength is more conservative for the lower a/d ratios.

CONCLUDING REMARKS

The following remarks are based on the tests on pretensioned I-beams reported herein and on the general discussion of overload behavior presented in this report. Concrete strengths of the tests reported herein varied between 6,500 and 7,800 psi.

1. Flexural cracking was observed at loads corresponding to computed tensile stresses in the extreme fiber in tension greater than that given by Eq. 12. The shear causing the development of significant inclined flexure shear cracking was greater than, although realistically predicted as, the shear expected to cause a flexural crack, based on Eq. 12, to form a distance from the concentrated load point in the direction of decreasing moment equal to the effective depth of the member.
2. The shear causing the development of inclined diagonal tension cracking in the tests reported herein was realistically predicted as the shear producing a principal tensile stress at the intersection of the path of the crack and the center of gravity given by Eq. 14.
3. Flexural failures occurred at strains in the extreme fiber in compression which varied between 0.0025 and 0.0028.
4. Of the seven test beams which failed in shear, five failed due to crushing of concrete in the web (four of which had no web reinforcement), one failed due to fracture of the web reinforcement, and the other failed due to inadequate anchorage of the web reinforcement in the tension flange.
5. The test results support the assumption that the ultimate shear which can be carried by the concrete above the top of an inclined crack is equal to the shear at inclined cracking.
6. The test results for a/d ratios of 2.54 and 3.39 indicated that the AASHO equation for design of web reinforcement:

$$A_v = \frac{1}{2}\,\frac{\left(V_u - V_c\right)s}{f'_y\, j\, d}$$

was conservative by a factor of roughly 3, with respect to a single cycle static load test.

7. An equation for the design of web reinforcement of the form of Eq. 7, in which β is determined from Eq. 8 for diagonal tension cracking or equals 1 for flexure shear cracking and V_c equals shear at inclined cracking, would have conservatively predicted the amount of web reinforcement required to prevent shear failures in the tests on an a/d ratio of 2.54 and 3.39 reported herein.

ACKNOWLEDGMENTS

This work has been carried out in the Department of Civil Engineering at Fritz Engineering Laboratory under the auspices of the Institute of Research of Lehigh University, as part of an investigation sponsored by the Pennsylvania Department of Highways, U. S. Bureau of Public Roads, and the Reinforced Concrete Research Council.

REFERENCES

1. Hanson, J. M., and Hulsbos, C. L. Overload Behavior of Prestressed Concrete Beams with Web Reinforcement. Fritz Engineering Laboratory Rept. No. 223.25, Lehigh Univ., Feb. 1963.
2. Hulsbos, C. L., and Van Horn, D. A. Strength in Shear of Prestressed Concrete I-Beams. Iowa State Univ., Engineering Experiment Station, Progress Rept. April 1960.
3. McClarnon, F. M., Wakabayashi, M., and Ekberg, C. E., Jr. Further Investigation into the Shear Strength of Prestressed Concrete Beams Without Web Reinforcement. Lehigh Univ., Fritz Engineering Laboratory Rept. No. 223.22, Jan. 1962.
4. Mattock, A. H., and Kaar, P. H. Precast-Prestressed Concrete Bridges 4. Shear Tests of Continuous Girders. Journal of the PCA Research and Development Laboratories, Vol. 3, No. 1, pp. 19-46, Jan. 1961.

Appendix

STATE OF CRACKING AT TIME OF INCLINED CRACKING

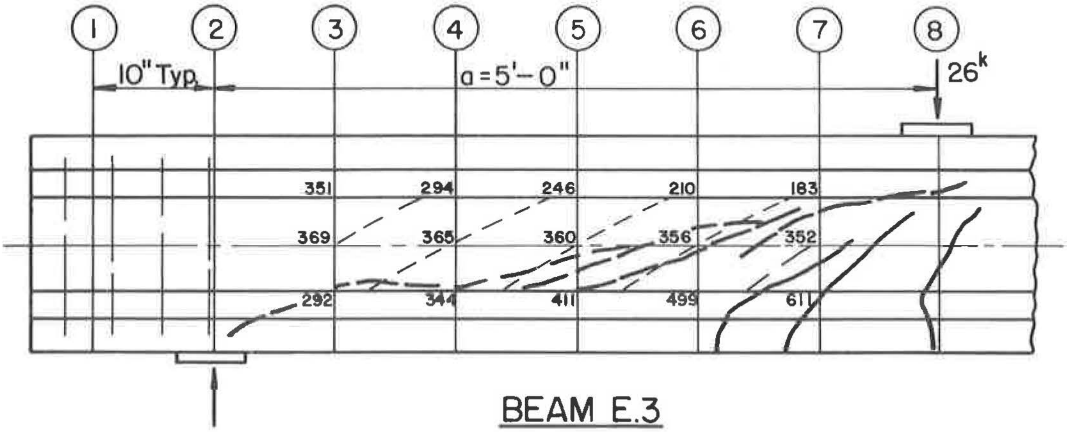

BEAM E.3

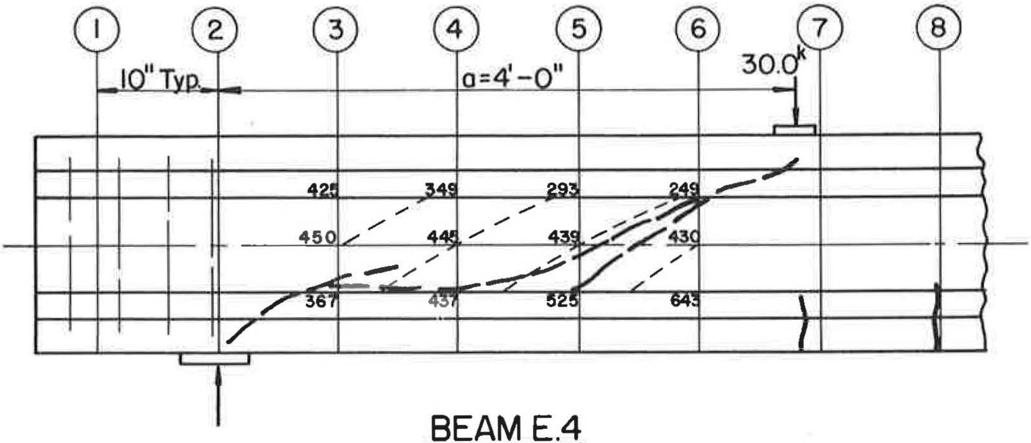
1
2
3
4
5
6
7
8
10" Typ.
a=4'-0"
30.0k
425
349
293
249
450
445
439
430
367
437
525
643

BEAM E.4

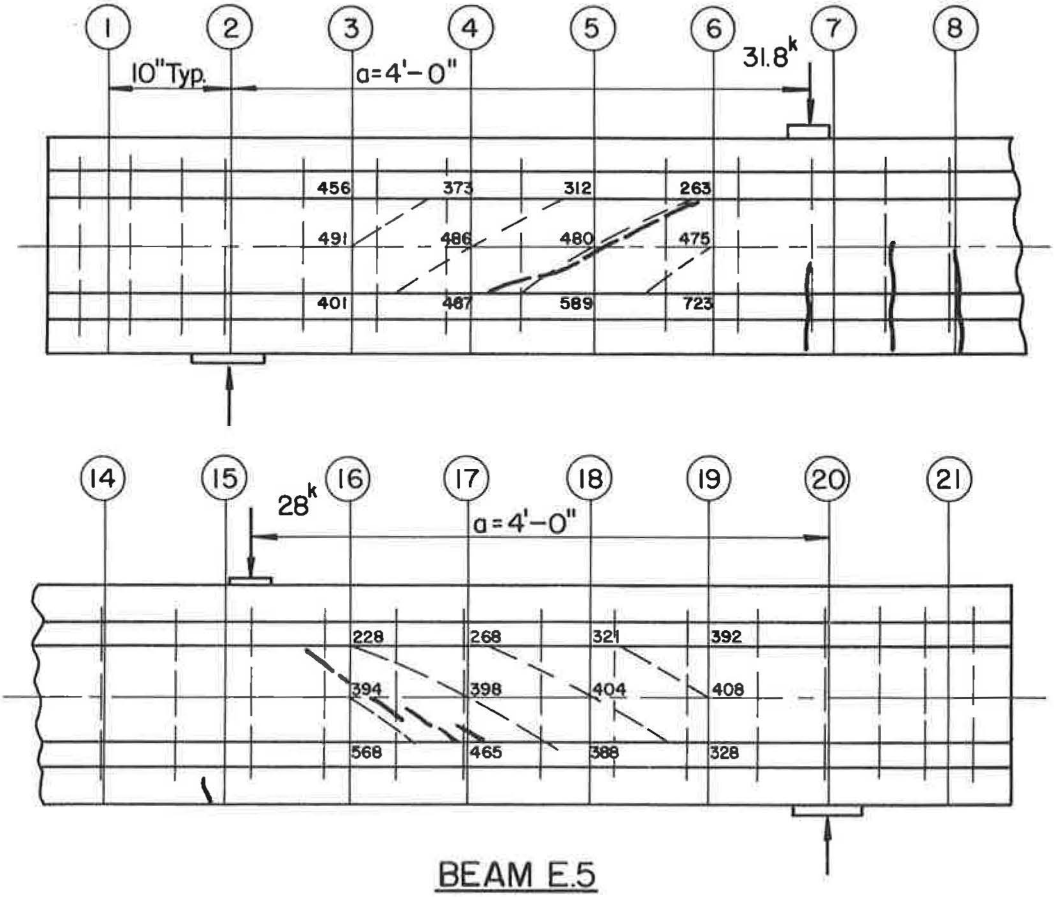
1
2
3
4
5
6
7
8
10" Typ.
a=4'-0"
31.8k
456
373
312
263
491
486
480
475
401
487
589
723
14
15
16
17
18
19
20
21
28k
a=4'-0"
228
268
321
392
394
398
404
408
568
465
388
328

BEAM E.5

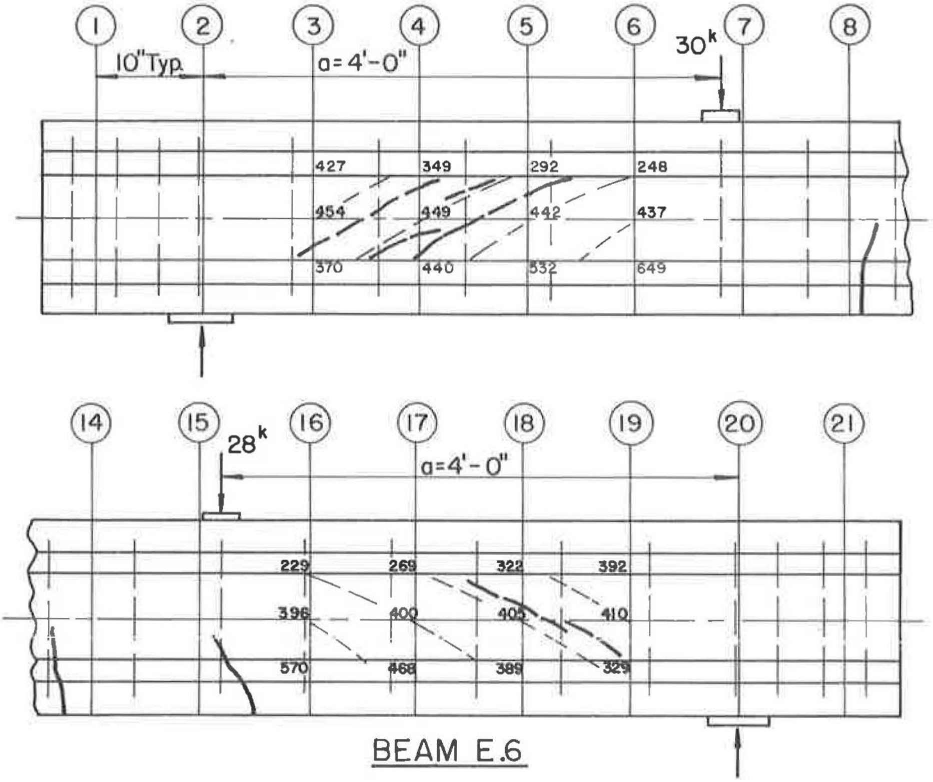
1
2
3
4
5
6
7
8
10"Typ.
a=4'-0"
30k
427
349
292
248
454
449
442
437
370
440
532
649
14
15
16
17
18
19
20
21
28k
a=4'-0"
229
269
322
392
396
400
405
410
570
468
389
329

BEAM E.6

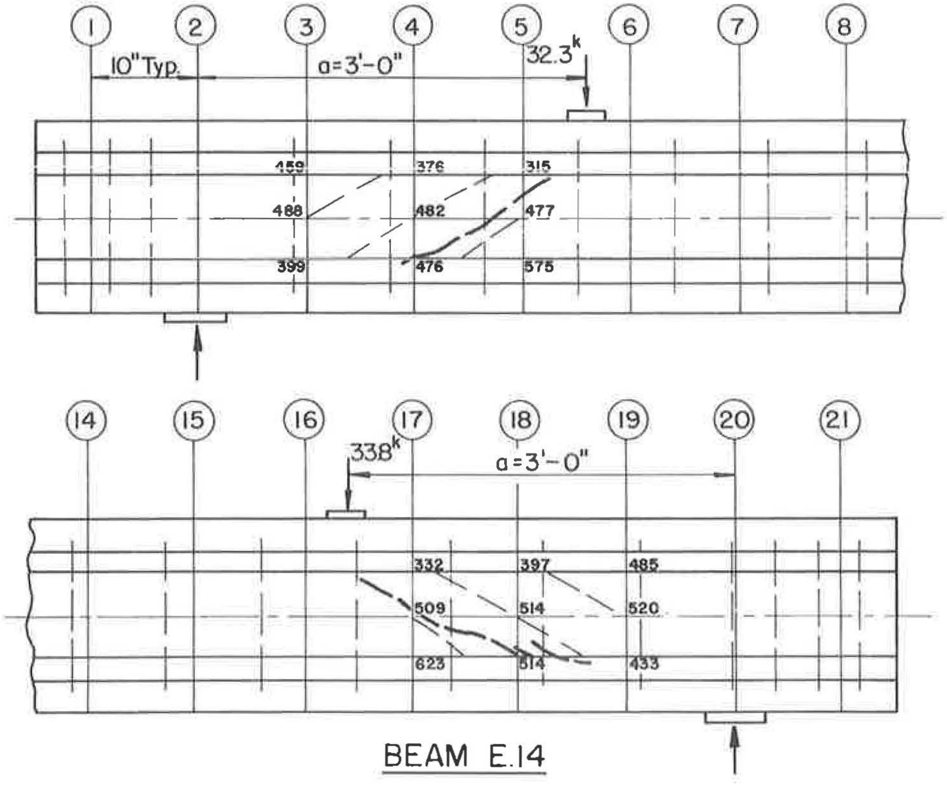
1
2
3
4
5
6
7
8
10"Typ.
a=3'-0"
32.3k
459
376
315
488
482
477
399
476
575
14
15
16
17
18
19
20
21
338k
a=3'-0"
332
397
485
509
514
520
623
514
433

BEAM E.14

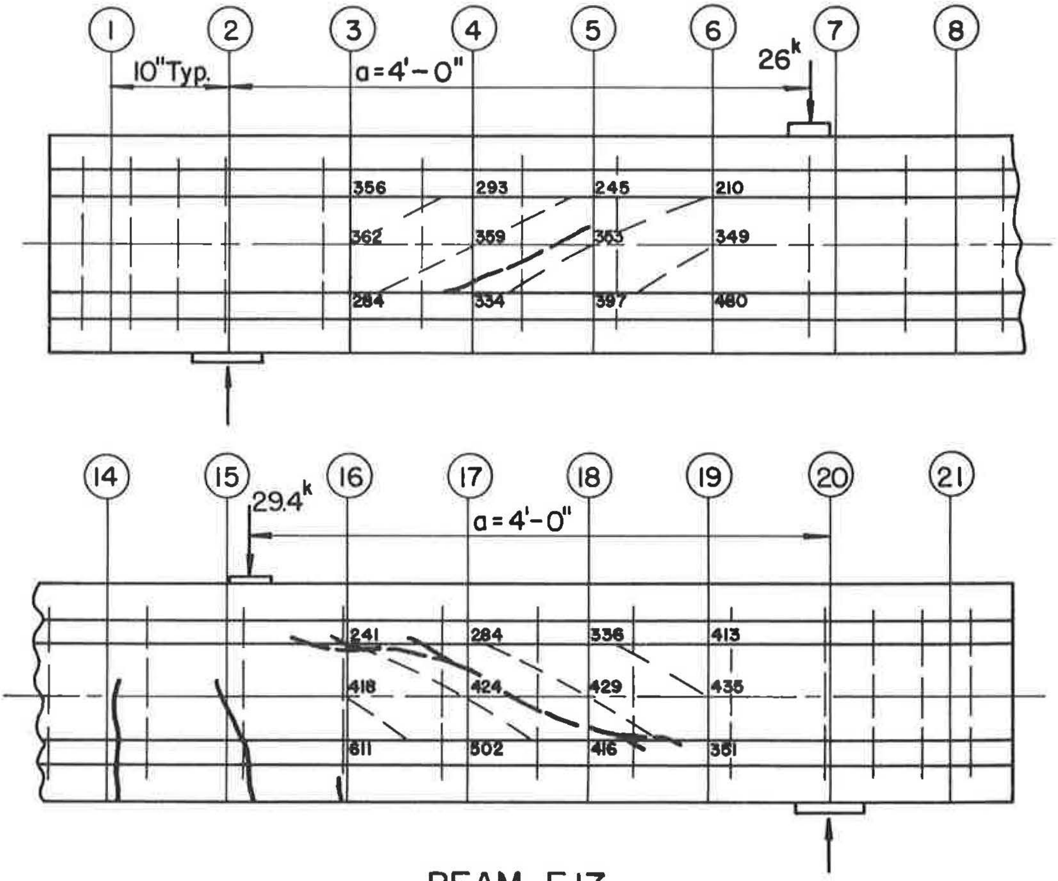
10"Typ.
a = 4'– 0"
26^k
29.4^k
a = 4'- 0"

BEAM E.17

Structural Behavior of a Concrete Box Girder Bridge

RAYMOND E. DAVIS and JOHN J. KOZAK, California Division of Highways, and
CHARLES F. SCHEFFEY, University of California, Berkeley

•DURING THE past three years the California Division of Highways and the University of California at Berkeley have carried out an extensive program of research pertinent to concrete box girder bridges. Although the program had a number of objectives, its primary goal was the study of the manner in which live loads are distributed transversely in a box girder. Secondary objectives involved the determination of: (a) dead load distribution, (b) influence of intermediate diaphragms on live load distribution, and (c) influence of barrier curbs and railings on live load distribution.

The University of California, in addition to providing consulting services in connection with the field test, conducted studies of models, including a small plastic model and a ¼-scale concrete model of the prototype. The program also included a study of analytical methods which might accurately describe the empirically determined behavior of the structure.

The box girder section is generally conceded to have high torsional rigidity with attendant efficient transverse distributional properties. There is, however, a lack of experimental evidence and analytical procedures which can produce quantitative answers to support design specification provisions for load distribution.

SCOPE

The principal experimental effort comprised the field test of a new structure on the State highway system, the Harrison Street Undercrossing, in Oakland, Calif. This structure was instrumented with SR-4 electrical resistance strain gages, Carlson strainmeters, and deflectometers to permit measurements of longitudinal and transverse strains and girder deflections resulting from a dynamic loading provided by a heavily loaded R-15 Euclid dump truck. Tests were conducted first without an intermediate diaphragm, secondly with a single intermediate diaphragm, and then after the addition of curbs and barrier railings.

Strains and deflections produced by the slowly moving test vehicle were recorded by oscillographs housed in an instrumentation trailer parked beneath the structure. Companion tests were conducted and supplementary instrumentation was provided to support the principal objectives and investigate secondary objectives, among which were the following:

1. Control tests were accomplished concurrently with the dynamic testing to evaluate physical properties of the component materials of the structure. Tests were conducted on four concrete control beams, on standard concrete cylinders, and on reinforcing steel coupons.
2. Laboratory tests were conducted by the University of California on a plastic model of ¹⁄₃₀-scale and a concrete model of ¼-scale.
3. A small amount of dynamic testing was performed, with the test vehicle traversing the structure at speeds of 5, 10, 15, and 20 mph and with various patterns of obstruction on the structure and its approach. In addition to selected strains and deflections, the accelerations of the structure and test vehicle were measured. This phase of the test was not included in original plans for the program and is not discussed here; however, it was considered a worthwhile adjunct to provide valuable information per-

---

Paper sponsored by Committee on Bridges.

tinent to impact effects on box girders for later use, when existing instrumentation permitted acquisition of the data at little additional expense.

4. Certain supplementary instruments were included within the structure to provide information concerning shears and temperature distribution. These included a group of thermocouples and five shear rosettes. Also, because of the questionable nature of the information provided by some of the internal gages, a group of linear variable differential transformers was used to evaluate vertical distribution of strain in the webs, and a curvemeter was used to verify slab curvatures indicated by the deck gages.

5. With the object in view of evaluating the validity of using distribution factors determined experimentally for this structure in the design of box girders with differing configurations of proportions, extensive analytical studies were conducted. Assuming that analytical methods could be derived which would accurately describe the empirically determined structural behavior of the prototype, such analytical methods could then be applied to other structures.

EXPERIMENTAL PROGRAM

Description of Field Prototype Structure

The structure chosen for testing was the Harrison Street Undercrossing, Bridge Number 33-289 OL, on Road IV-Alameda-5-Oakland (Fig. 1). The structure is part of the MacArthur Freeway, a major artery carrying traffic through the City of Oakland. Field tests were completed during the initial phases of construction of the freeway section in which the structure is located. A cross-section of the structure is shown in Figure 2.

The structure has one simple span of 80 ft, and rests on bearings which are normal to the centerline. Overall width is 34 ft, and width between barrier curbs and railings is 28 ft. There are five girder stems, inclosing four cells. Design was in accordance with the 1957 AASHO specifications. Design live loading was the H20-S16-44 and alternative loading.

After the structure had been chosen for testing, the following changes were made in the plans to conform to test requirements:

1. A rigid testing scaffold on timber piles just below the structure was added for support of the deflectometers.
2. Three-foot diameter holes were formed in the end diaphragms at the ends of each cell, and a gallery was added between each end diaphragm and the abutment backwalls.

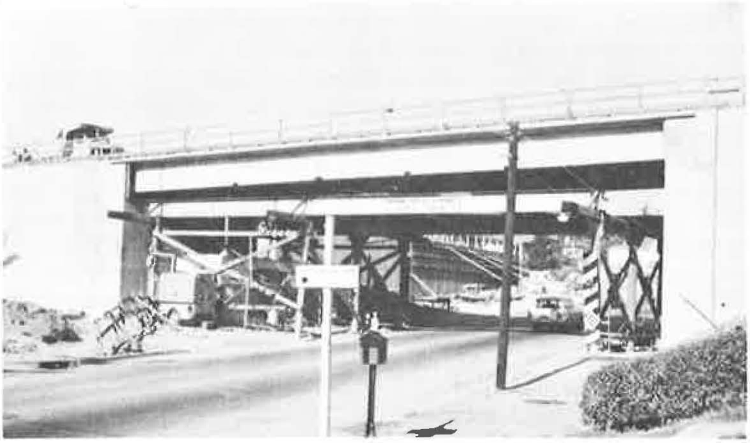

Figure 1. Overall view of prototype test structure, showing deflectometer scaffold, instrumentation trailer inclosure, and test vehicle.

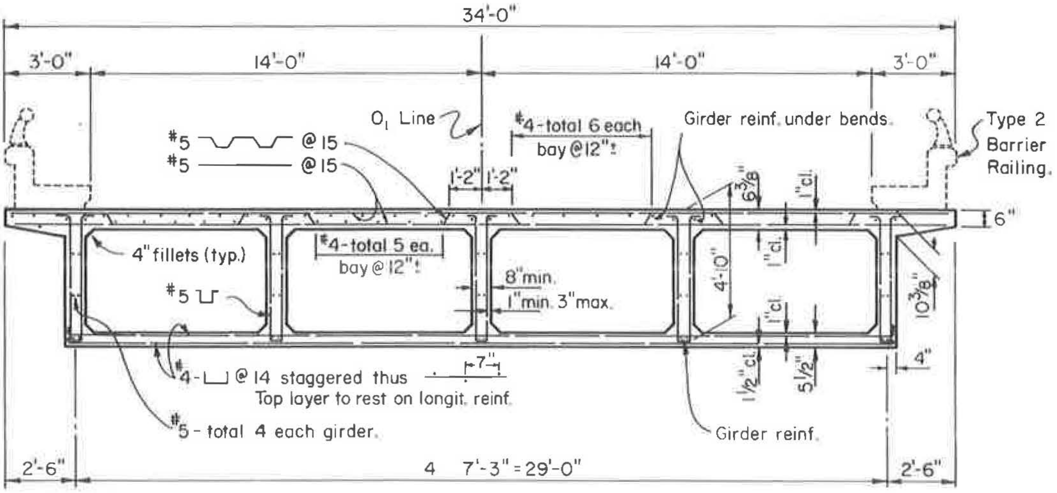

Figure 2. Cross-section of prototype test structure.

These features permitted access to the interior of the cells for removal of the forms from the soffit of the deck slab, for access to the gage installations, and for forming of the intermediate diaphragm.

3. Features were added to permit placement of the intermediate diaphragm after the deck slab was in place.
4. Blockouts, junction boxes, and gage installation were added.

With these exceptions, the plans remained unchanged, and the structure dimensions, reinforcement quantities, etc., were similar to what might be expected on any ordinary structure on the State highway system.

It is not standard procedure to remove the forms which support the deck slab within the cells, due to the inaccessibility of these forms after placing the slab. In this particular structure, these forms comprised plywood facing on closely spaced 2- by 6-in. beams resting on short posts supported on the bottom slab. Such support could be expected to contribute to the stiffness of the deck slab, and some question arose in the initial planning concerning the advisability of departing from the normal procedures in removing the forms; however, it is believed that under normal circumstances these forms will gradually deteriorate until the deck slab receives negligible support therefrom, and that removal of these forms would produce the worst, and most representative, condition for ultimate performance of the deck.

The manner of placing the intermediate diaphragm also represented a departure from normal procedures. This span length requires one diaphragm according to the 1957 and 1961 AASHO specifications, and it was felt that the test program would be enhanced by an attempt to evaluate the effects of inclusion of such a diaphragm on the distribution factors. Such an evaluation required that the structure be tested with and without this diaphragm. Ordinarily, of course, the intermediate diaphragm is placed monolithically with the stems and bottom slab. However, the intermediate diaphragm in this structure was placed after an initial series of crawl tests had been made without this structural component. Eight- and six-in. pipe nipples were placed in the deck slab above the diaphragm location (Fig. 3), and were closed at the tops by bar plugs, the lugs of which were placed about $\frac{1}{2}$ in. below the riding surface of the deck slab to prevent interference with finishing or riding qualities. Three nipples were placed in the slab in each bay, the larger one in the center to be used for placement of the diaphragm concrete, and the two smaller ones at the outer limits of the bays to be used in venting the forms to prevent formation of air pockets.

After the first series of crawl tests had been completed without the intermediate diaphragm in place, the concrete above the nipples was removed with a chipping gun,

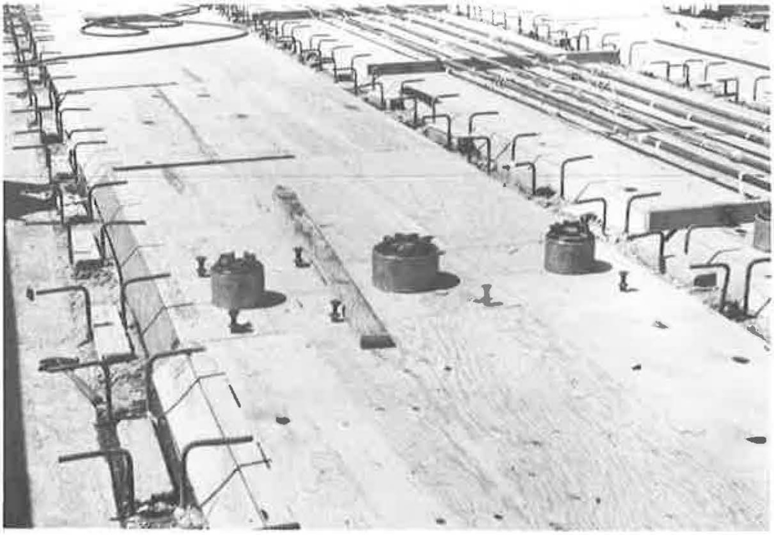

Figure 3. Pipe nipples placed in deck slab to permit interior diaphragm placement after first series of crawl tests.

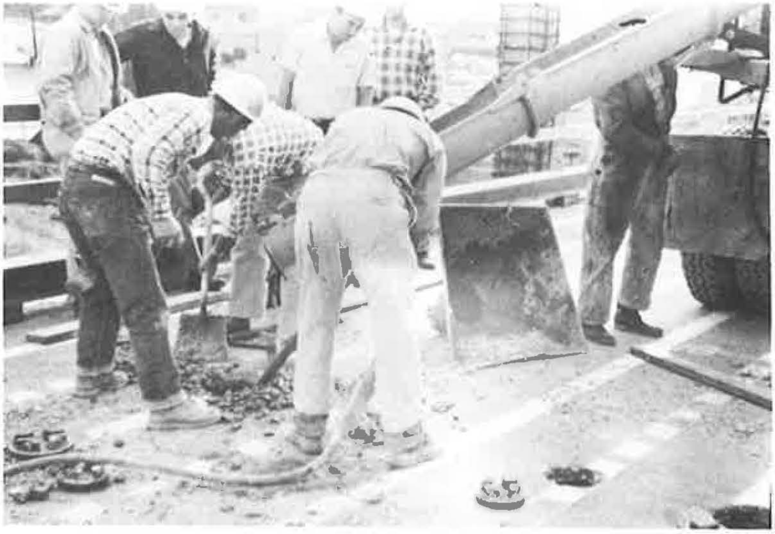

Figure 4. Pouring intermediate diaphragm within cells of prototype structure between Phases II and III.

and the bar plugs were removed. Forms for the diaphragms were placed within the cells and braced by timbers bolted to inserts embedded in the slabs and webs around the peripheries of the diaphragms. Concrete was placed through the open nipples and carefully vibrated (Fig. 4). As was anticipated, considerable effort was required to vent the forms just below the deck slab and to obtain a tight fit; however, this effort was expended, the forms were carefully checked from within the cells during the pour, and a tight fit was obtained on all boundaries of the diaphragm.

Description of Instrumentation

Instrumentation placed in or on the superstructure, exclusive of the recording equipment placed in the instrument trailer (Figs. 5 and 6), fell into the following categories:

1. Carlson strainmeters were placed in the top slab at 30 locations, over the girder stems and at the midpoints of the bays. The axes of all gages were placed parallel to the structure centerline.
2. SR-4, AX-5, electrical resistance strain gages were placed on the main #11 reinforcing bars at the tops and bottoms of the girder stems and at the centerlines of bays in the bottom slab.

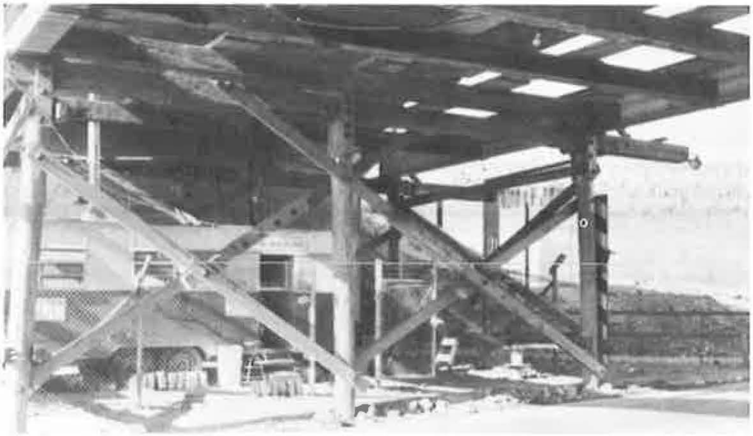

Figure 5. Exterior view of instrumentation trailer.

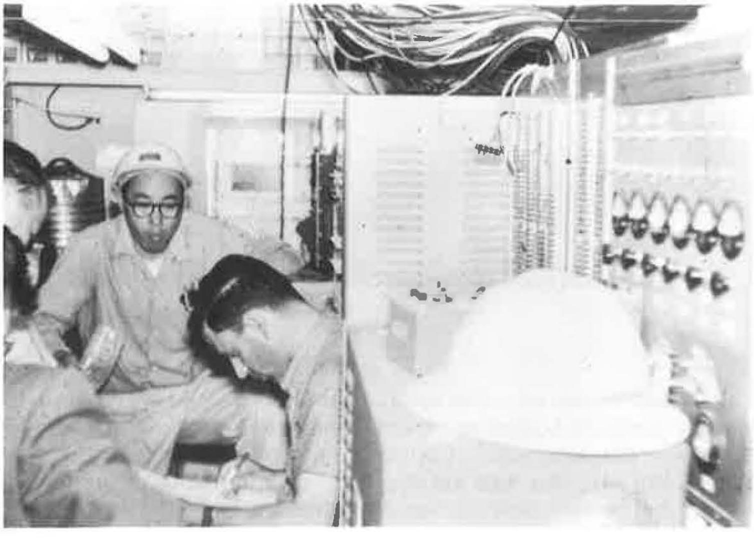

Figure 6. Interior view of instrumentation trailer with leads from 200 gages coming down through trailer ceiling.

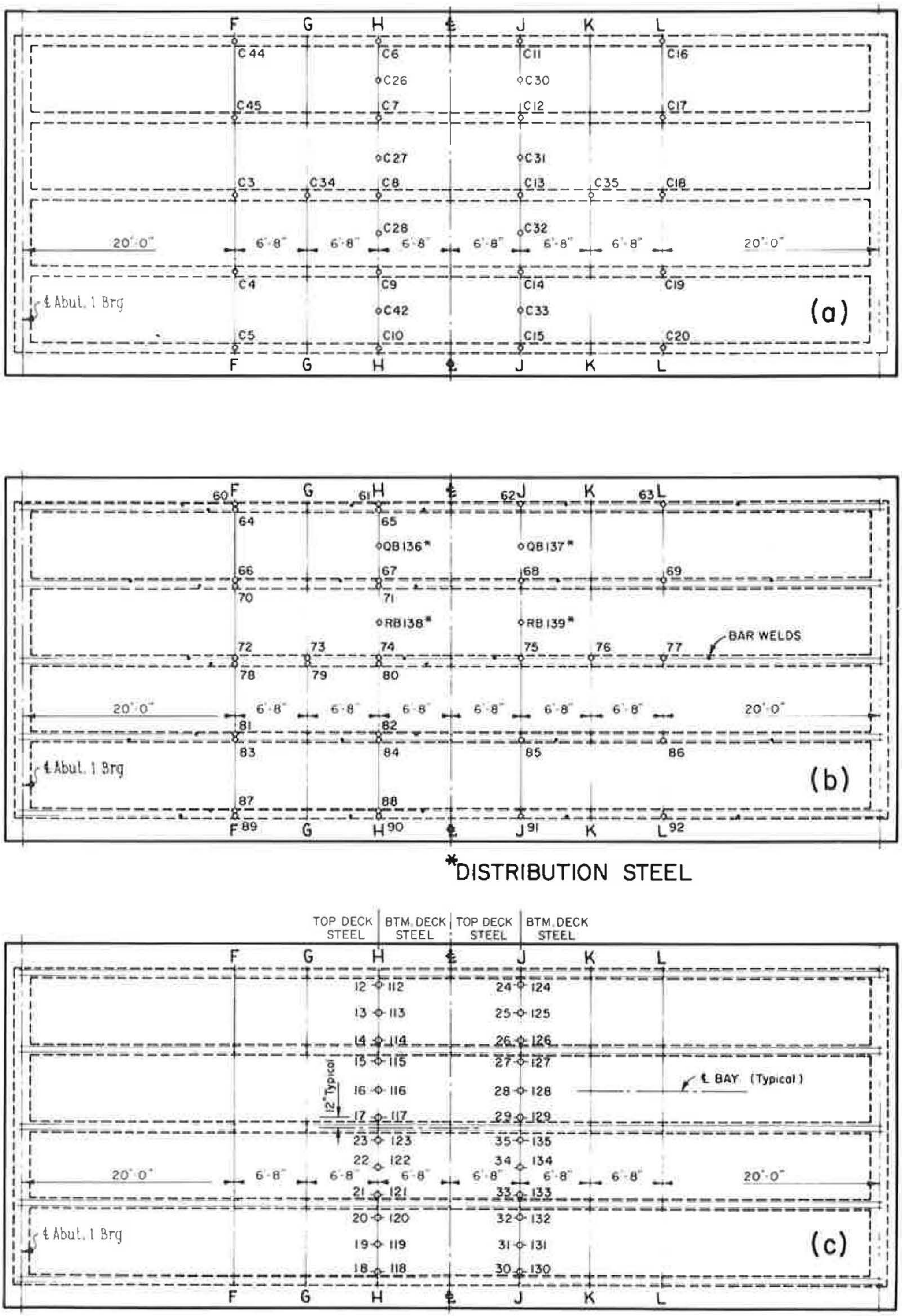
F G H ℄ J K L
C44 C6 C11 C16
C26 C30
C45 C7 C12 C17
C27 C31
C3 C34 C8 C13 C35 C18
C28 C32
20'-0" 6'-8" 6'-8" 6'-8" 6'-8" 6'-8" 6'-8" 20'-0"
C4 C9 C14 C19
℄ Abut. 1 Brg
C42 C33
(a)
C5 C10 C15 C20
60 61 62 63
64 65
QB136* QB137*
66 67 68 69
70 71
RB138* RB139*
72 73 74 75 76 77
BAR WELDS
78 79 80
81 82
83 84 85 86
(b)
87 88
89 90 91 92
*DISTRIBUTION STEEL
TOP DECK STEEL
BTM. DECK STEEL
TOP DECK STEEL
BTM. DECK STEEL
12 112 24 124
13 113 25 125
14 114 26 126
15 115 27 127
16 116 28 128
℄ BAY (Typical)
12" Typical
17 117 29 129
23 123 35 135
22 122 34 134
21 121 33 133
20 120 32 132
19 119 31 131
18 118 30 130
(c)

Figure 7. Prototype instrumentation: (a) Carlson strainmeters, top slab; (b) upper stem bars (#11) and distribution steel (#4); and (c) transverse gages, top slab.

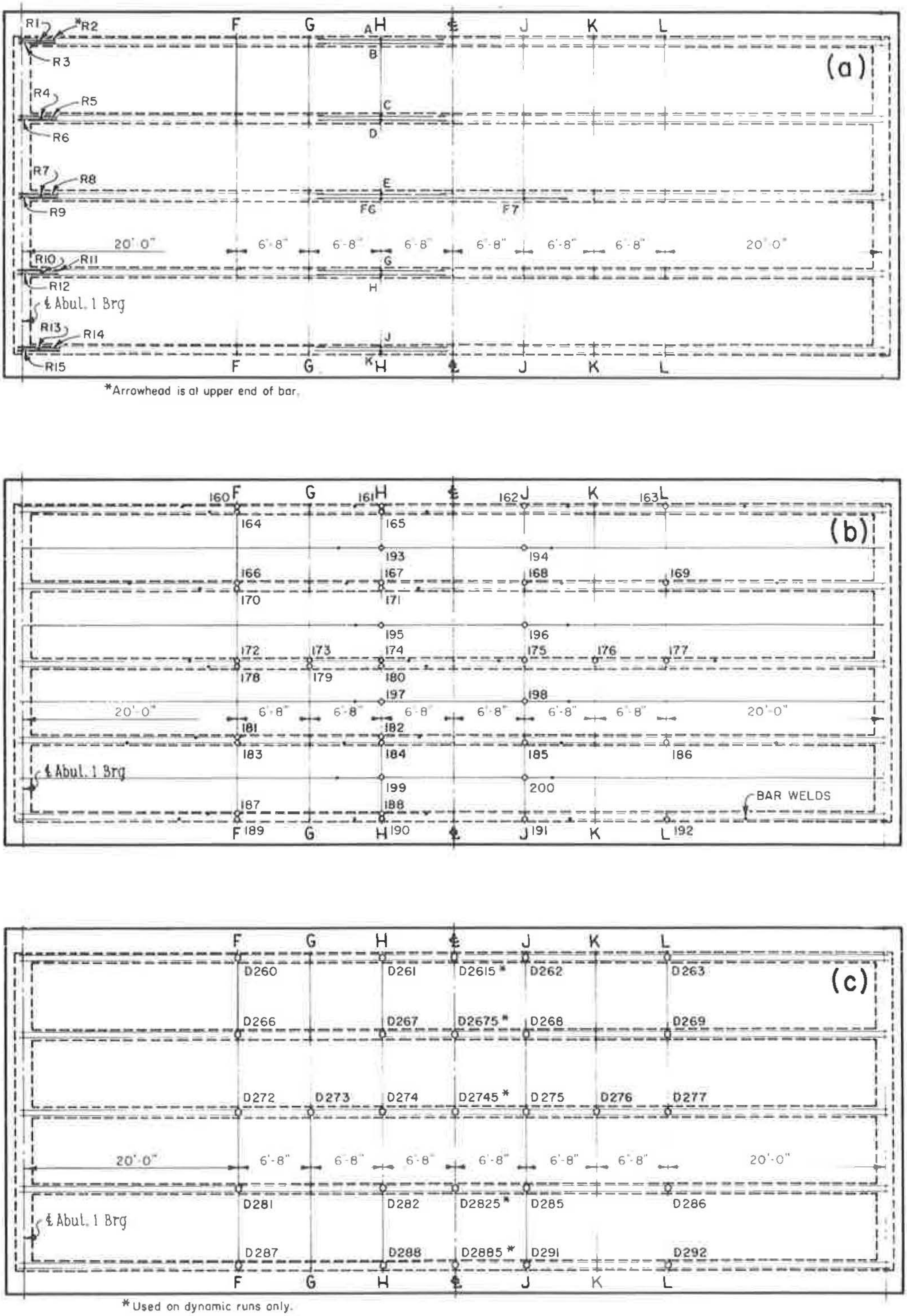
(a)
F G H ℄ J K L
R1 *R2 R3
R4 R5 R6
R7 R8 R9
R10 R11 R12
R13 R14 R15
A B C D E F6 F7 G H J K
20'-0" 6'-8" 6'-8" 6'-8" 6'-8" 6'-8" 6'-8" 20'-0"
℄ Abut. 1 Brg
(b)
160 161 162 163
164 165 166 167 168 169 170 171 172 173 174 175 176 177 178 179 180
181 182 183 184 185 186 187 188 189 190 191 192
193 194 195 196 197 198 199 200
BAR WELDS
(c)
D260 D261 D2615* D262 D263
D266 D267 D2675* D268 D269
D272 D273 D274 D2745* D275 D276 D277
D281 D282 D2825* D285 D286
D287 D288 D2885* D291 D292

*Arrowhead is at upper end of bar.

*Used on dynamic runs only.

Figure 8. Prototype instrumentation: (a) lower third point bars (#5) and shear rosettes; (b) bottom slab reinforcement; and (c) deflectometer.

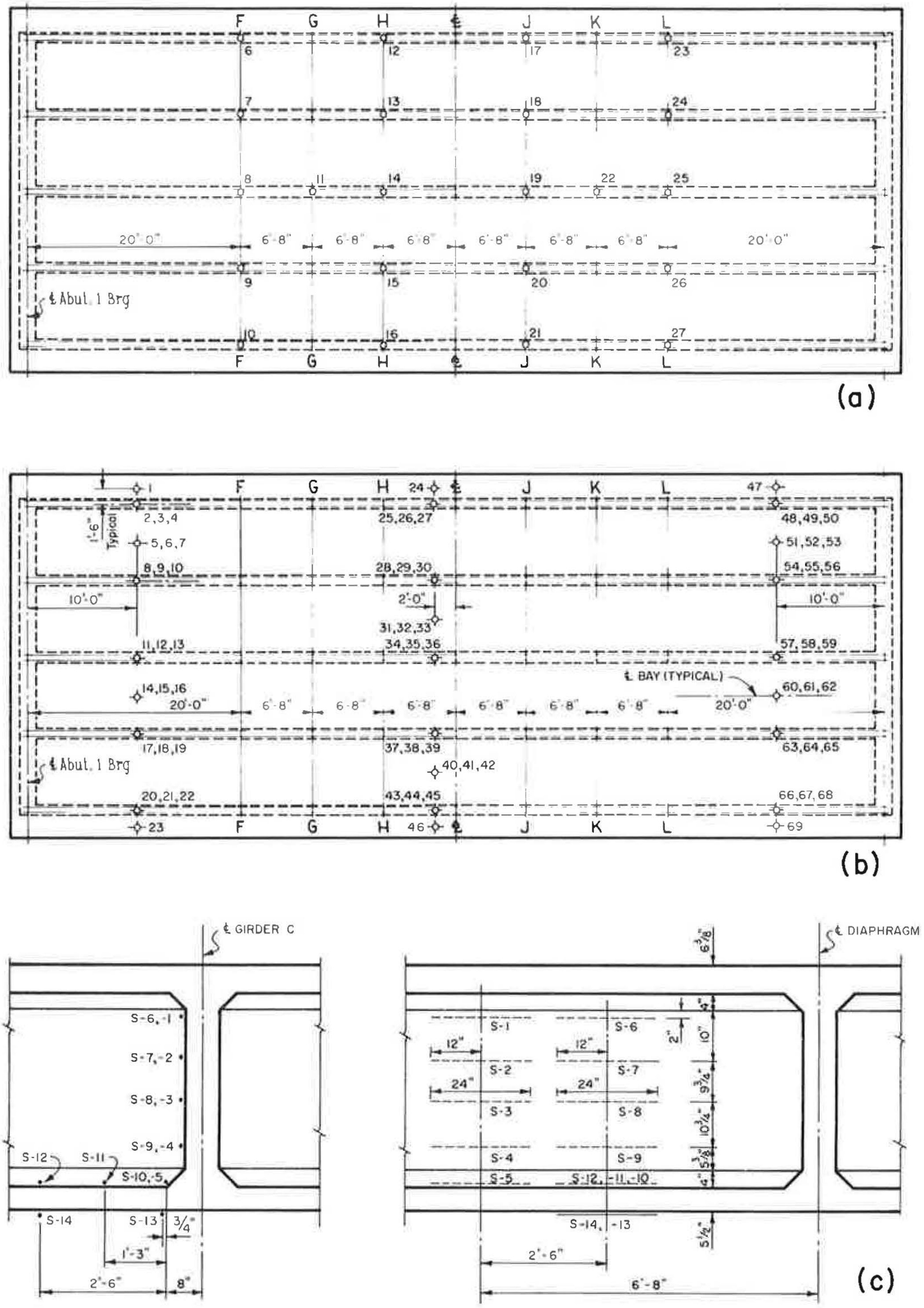
F G H ℄ J K L
6 12 17 23
7 13 18 24
8 11 14 19 22 25
20'-0" 6'-8" 6'-8" 6'-8" 6'-8" 6'-8" 6'-8" 20'-0"
9 15 20 26
℄ Abut. 1 Brg
10 16 21 27
F G H ℄ J K L
(a)
F G H 24 ℄ J K L 47
1
2,3,4
25,26,27
48,49,50
1'-6" Typical
5,6,7
51,52,53
8,9,10
28,29,30
54,55,56
10'-0"
2'-0"
10'-0"
31,32,33
11,12,13
34,35,36
57,58,59
℄ BAY (TYPICAL)
14,15,16
60,61,62
20'-0" 6'-8" 6'-8" 6'-8" 6'-8" 6'-8" 6'-8" 20'-0"
17,18,19
37,38,39
63,64,65
℄ Abut. 1 Brg
40,41,42
20,21,22
43,44,45
66,67,68
23 F G H 46 ℄ J K L 69
(b)
℄ GIRDER C
S-6, -1
S-7, -2
S-8, -3
S-9, -4
S-12
S-11
S-10, -5
S-14
S-13
3/4"
1'-3"
2'-6"
8"
6 3/8"
℄ DIAPHRAGM
4"
10"
2"
S-1
S-6
12"
12"
S-2
S-7
9 3/4"
24"
24"
S-3
S-8
10 3/4"
S-4
S-9
5 3/8"
S-5
S-12, -11, -10
4"
S-14, -13
5 1/2"
2'-6"
6'-8"
(c)

Figure 9. Prototype instrumentation: (a) copper bench nails; (b) thermocouples; and (c) LVDT locations.

3. SR-4, AX-7, electrical resistance strain gages were placed on the top and bottom transverse deck steel (#5 bars) over the edge of each fillet and at the centerlines of bays in two transverse sections.

4. At Abutment 1, a large shear rosette, comprising three gaged #5 bars, oriented at +45°, 0°, and -45° from the vertical, was placed in each of the five girder stems. Because the functional relationship of girder shear and skew is an unsolved problem, it was felt that the strain pattern in this area might prove valuable for latter comparison with other structures.

5. Deflectometers were placed on a rigid scaffold below the girders at 22 locations to permit measurement of live load deflections.

6. SR-4, AX-7, electrical resistance strain gages were placed on the #5 bars located in the stems 20 in. above the bottom slab soffit. The purpose of these gages was to determine the extent to which plane sections remained plane.

7. At four locations in the top slab, at the centerlines of bays, SR-4, AX-7, electrical resistance strain gages were placed on the longitudinal #4 distribution steel to measure local bending stresses in the deck slab in the longitudinal direction.

8. Thermocouples were placed at 69 locations in the superstructure to permit evaluation of internal temperature distribution.

9. Copper bench nails were placed at 32 locations in the deck surface for use in determination of dead load deflections of the superstructure by simple leveling methods.

10. A group of SR-4, A-9, electrical resistance gages and 12 inductance gages employing linear variable differential transformers were placed on one girder stem and at several locations on the bottom slab. These gages were added after it became evident that the gages at the lower third points of the stems were producing strain readings which were questionable.

11. Four "Tapeswitches" were placed on the riding surface to permit determination of longitudinal truck position.

Locations and numerical designations of the gages are shown in Figures 7, 8, and 9.

Because there were over 200 gages in the structure, and only 22 active recording channels on the oscillographs, it was necessary to group the gages in various combinations of 22 to be recorded simultaneously. A total of 28 combinations was established. An attempt was made to: (a) include every gage in at least one combination; (b) group the gages to produce simultaneous readings of the same types of stresses (e.g., girder shears, slab bending moments, longitudinal strains) at given transverse or longitudinal sections; and (c) provide sufficient overlap of gages from combination to combination to permit checks of reproducibility of strains.

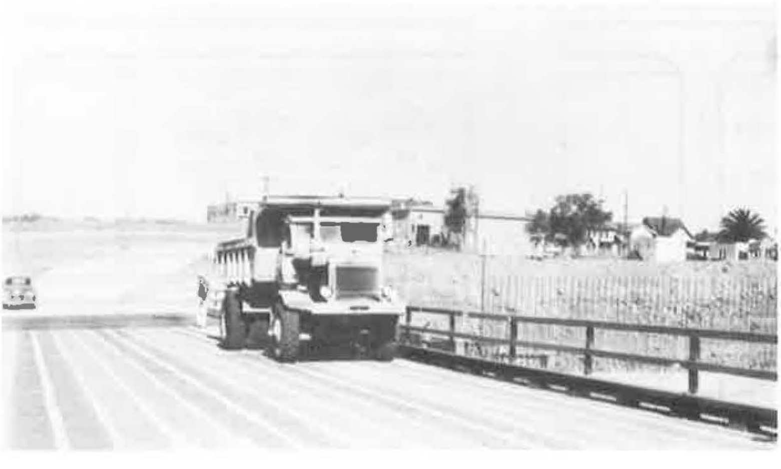

Figure 10. Test vehicle traversing prototype structure at crawl speed; painted striping on deck to facilitate transverse positioning.

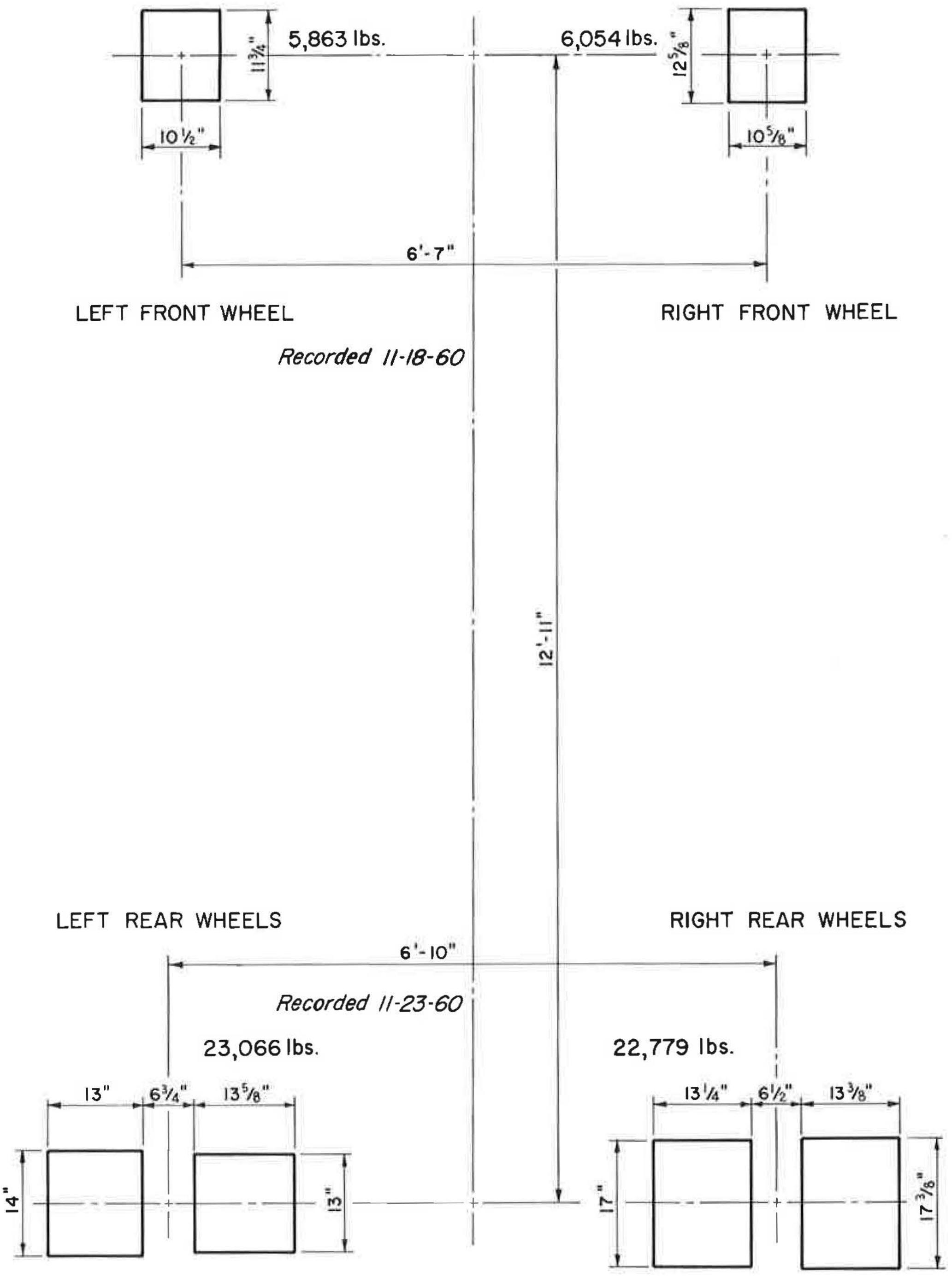
5,863 lbs.
6,054 lbs.
11¾"
12⅝"
10½"
10⅝"
6'-7"
LEFT FRONT WHEEL
RIGHT FRONT WHEEL
Recorded 11-18-60
12'-11"
LEFT REAR WHEELS
RIGHT REAR WHEELS
6'-10"
Recorded 11-23-60
23,066 lbs.
22,779 lbs.
13"
6¾"
13⅝"
13¼"
6½"
13⅜"
14"
13"
17"
17⅜"

Figure 11. Dimensions and average, measured wheel reactions of test vehicle.

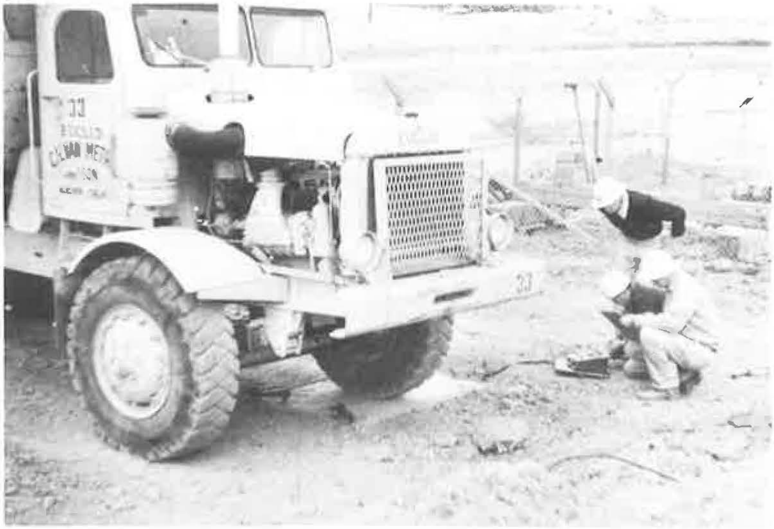

Figure 12. Typical measurement of test vehicle wheel reactions on Loadometer box.

Description of Test Vehicle

The vehicle employed in testing the structure was an R-15 rear dump Euclid truck loaded with steel ingots to a gross weight of 57 kips (Fig. 10). Pertinent dimensions and measured wheel reactions of the vehicle are shown in Figure 11, and a typical measurement of wheel reactions on the Loadometer box is shown in Figure 12.

Description of Materials Control Tests

Paralleling tests on the structure, tests were made to determine physical properties of the component materials used in its construction. Eighteen standard 6- by 12-in.

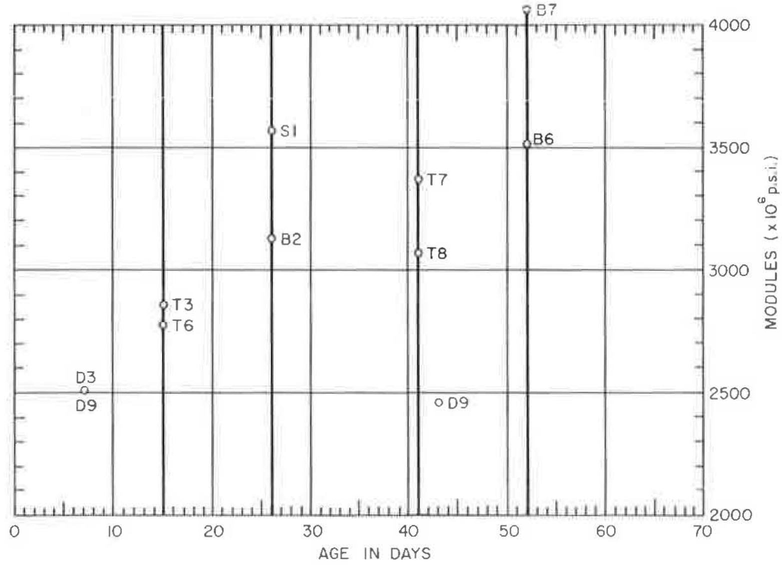

Figure 13. Axial concrete moduli based on 6-in. diameter by 12-in. cylinders.

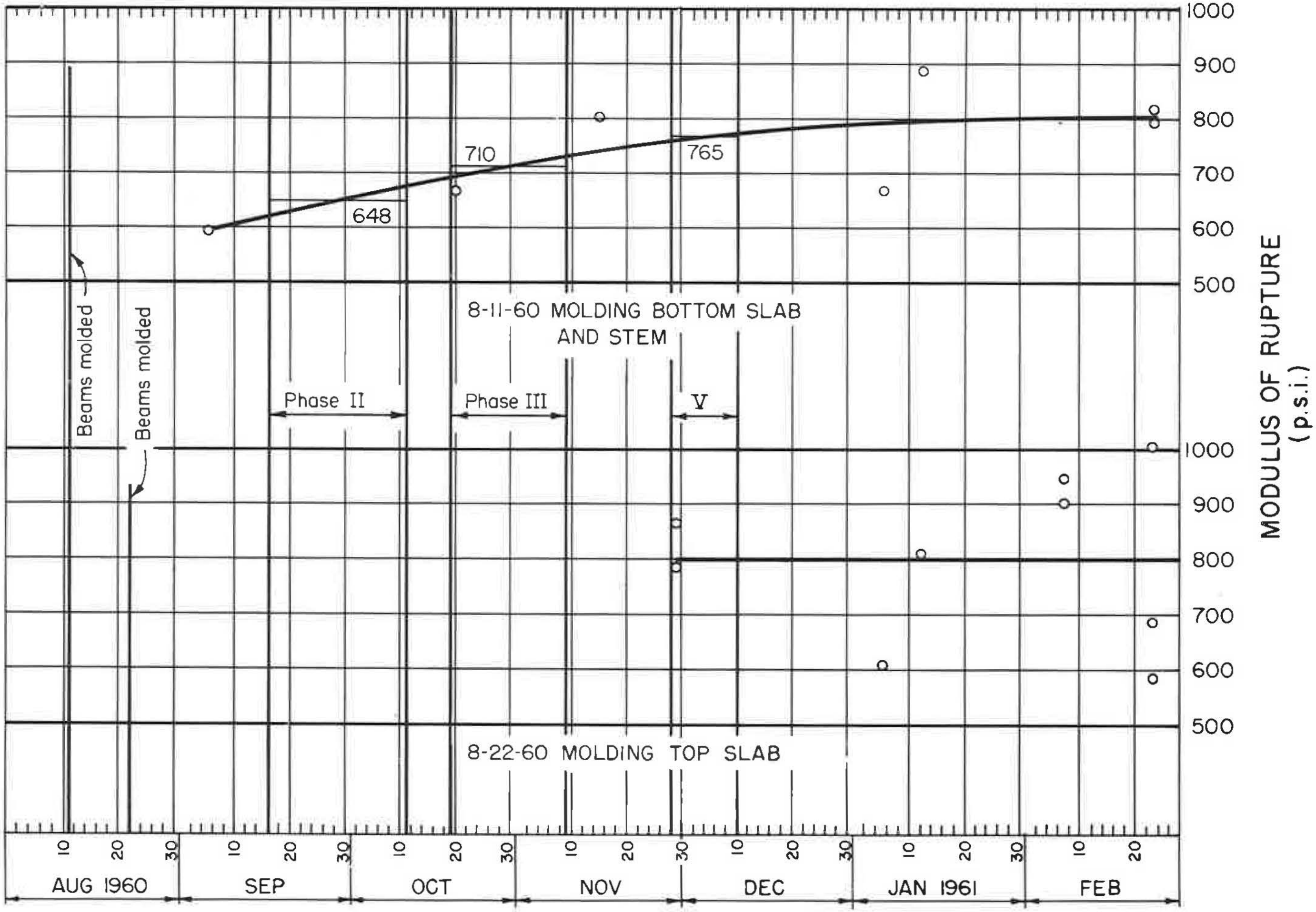

Figure 14. Modulus of rupture for prototype structure concrete.

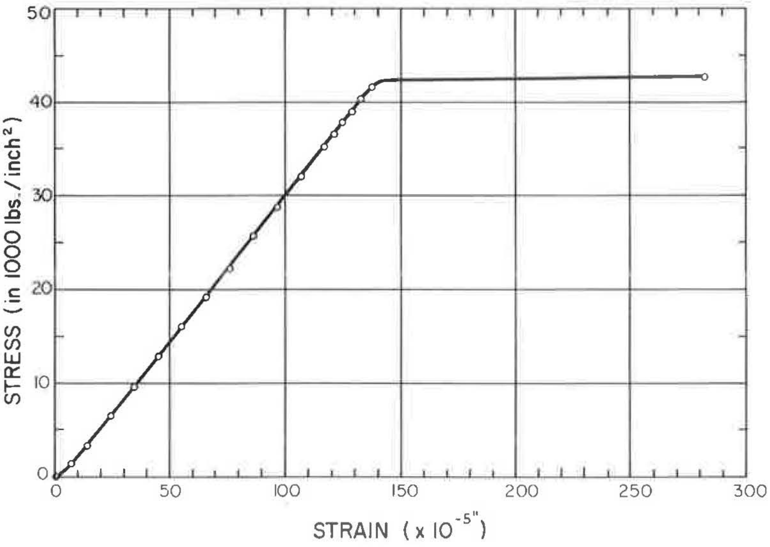

Figure 15. Typical stress-strain curve for #11 reinforcing bars placed in prototype structure.

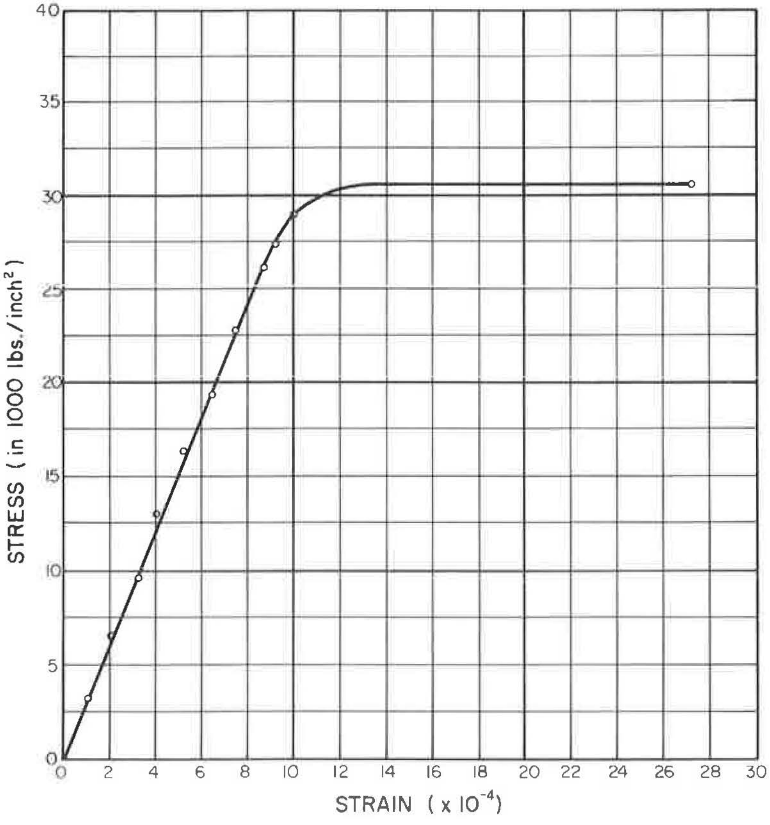

Figure 16. Typical stress-strain curve for #5 reinforcing bars placed in prototype structure.

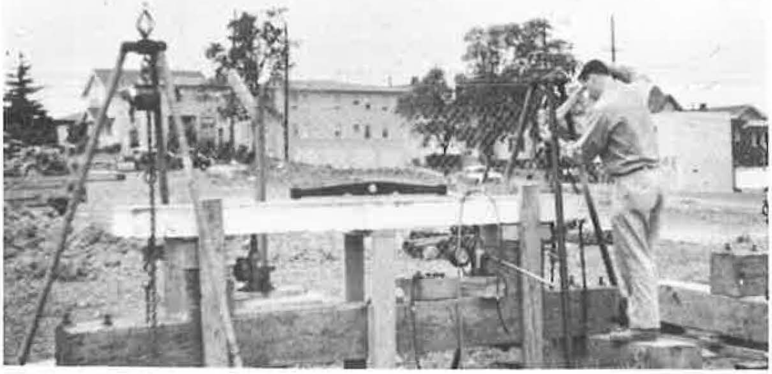

Figure 17. Making measurements on one of the control test beams.

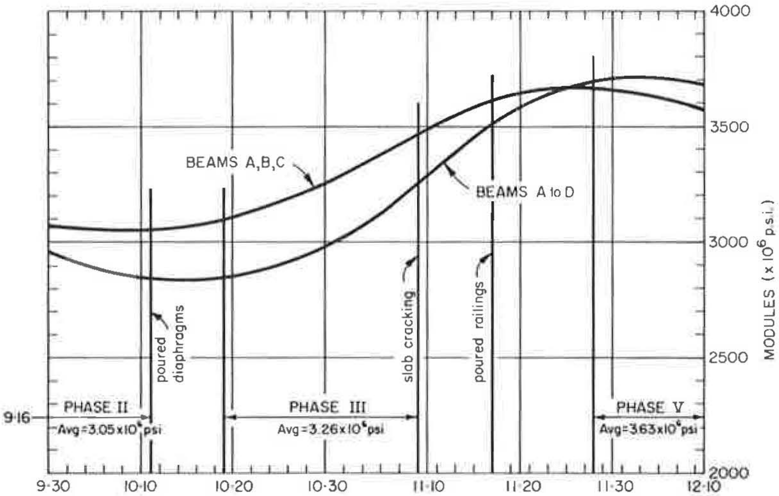

Figure 18. Axial moduli for prototype concrete based on measurements of control test beams.

diameter concrete cylinders were molded from each of the two main pours of the superstructure, four from the diaphragm pour, and seven from the barrier railing pour. Seven standard 6- by 6- by 34-in. modulus of rupture specimens were molded from the bottom slab and stem pour, and nine more from the top slab pour. Several tests were made of modulus of elasticity of the reinforcing steel used in the structure. Lastly, six $6\frac{3}{8}$- by 12-in. by 10-ft concrete control test beams were fabricated from batches chosen at random in the course of the deck pour.

Concrete Test Cylinders.—Test cylinders were fabricated in accordance with the instructions in the California Construction Manual. The specimens were kept in their metal molds under the structure until the time of testing when they were delivered to the University of California Engineering Materials Laboratory for determination of

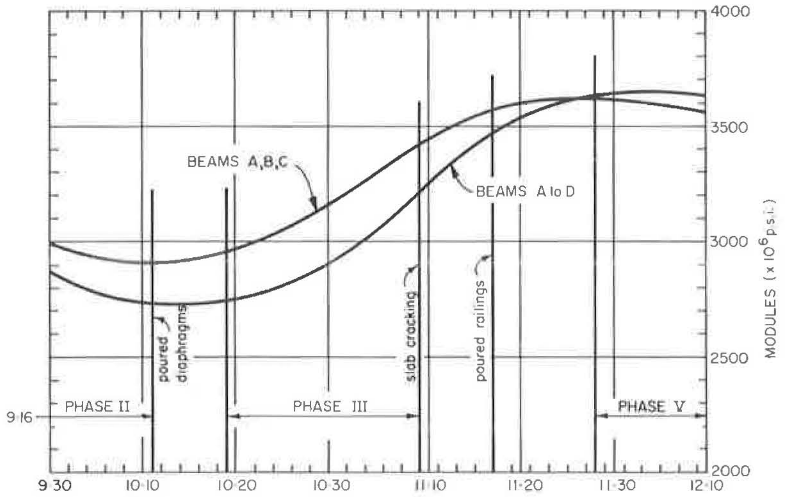

Figure 19. Bending moduli for prototype concrete based on measurements of control test beams.

elastic modulus, Poisson's ratio, and compressive strength. Measured values of modulus for the cylinders were erratic but are plotted in Figure 13.

Modulus of Rupture Specimens.—The 16 modulus of rupture specimens were fabricated in steel molds in accordance with instructions in the California Construction Manual. They were cured by burial in a pile of wet sand near the jobsite until they were broken in a three-point-loading beam-breaking machine. Plotted values of the modulus of rupture are shown in Figure 14.

Reinforcing Steel.—Figures 15 and 16 show stress-strain curves established by tests made by the Division of Highways Materials and Research Section for typical reinforcing bars chosen from the two primary sizes used in the structure. These curves were employed in the determination of the elastic moduli used in the data analysis.

Control Test Beams.—Four of the control test beams were tested on a continuing basis during the period the field prototype was being tested (Fig. 17). Final results of determinations of the elastic moduli of the concrete from these specimens are shown in Figures 18 and 19. The methods used to test the beams and derive these moduli are described in a final project report. The curves depict the mean values established from curves for three or four beams. The curves for Beam D were radically different from those of Beams A to C—it is believed this beam contained hairline cracks—so separate means were computed for Beams A to C and for all four beams.

Mean values of concrete modulus used in calculations for the three live load phases, taken from the three-beam curves of axial modulus, have been entered in Figure 18. Axial moduli differ from bending moduli because of marked variation of modulus through the slab depth. The axial modulus was used in resisting moment calculations because stresses of this type predominate in the top slab as a result of beam action.

EXPERIMENTAL RESULTS PERTINENT TO FIELD PROTOTYPE

The main portion of the research work pertinent to the prototype structure was divided into five phases, two of which were concerned with effects of live loads under varying conditions. In addition, slab stresses and deflections under wheel loads and very heavy concentrated loads were briefly studied, as well as the influence on the structure of heavy impact loadings. In all cases, interpretation of the data was complicated by pronounced departures from expectations based on idealized structural behavior and by the usual idiosyncracies of concrete behavior.

Dead Load Tests

Phase I was devoted to the study of deflections and bending strains under the influence of dead load of the bare box section and determination of the distribution of that load. During Phase IV, a similar study was made of the influence of the superimposed dead load of the barrier curbs and railings.

Each of these two phases entailed measurements, by simple leveling methods, of short- and long-term displacements of bench nails embedded in the deck slab over each stringer, as well as a continuing program of static measurement of internal strains.

Phase I Results.—Dead load deflection data were evaluated by plotting elevations of copper bench nails and computing displacements of each bench nail below the chords joining the abutment bench nails for the $\frac{1}{4}$-, $\frac{5}{12}$-, $\frac{7}{12}$-, and $\frac{3}{4}$-span points. Curves for the $\frac{5}{12}$ points of three girders are shown in Figure 20. "Instantaneous" values of dead load deflections were estimated by extrapolating the curves of best fit back to the time of striking falsework. Displacements obtained in this way are listed in Table 1. Values computed by theoretical methods described later in the report are tabulated for comparison.

To make distributions of bending strains more meaningful to the average designer, who is more familiar with specifications dealing with distributions of resisting moments, these moments were computed using stress components and moment arms based on the measured strains, employing the usual design assumptions for locating lateral limits of the stringers at midbays and edges of the deck slab. Computations of these resisting moments were subject to certain complications resulting from unanticipated anomalies in the strain measurements, coupled with the usual idiosyncrasies of concrete behavior. The former included: (a) the erratic distribution of dead load strains in the deck slab; (b) large, and obviously unrepresentative, temporary strains in the bottom slab reinforcement; and (c) larger discrepancies among stem and adjacent midbay strains than might reasonably be attributed to shear lag. The latter included the usual problems inherent in evaluating effects of creep, shrinkage, and cracking.

Twenty-four-hour strains for 16 midbay gages are listed in Table 2. The strains listed in each quadruplet were measured by gages located at the corners of a rectangle whose axes of symmetry coincided with those of the structure. Under the influence of the symmetrical dead load, the four readings might reasonably be expected to be the same. The erratic strain distribution which actually was manifested in the top slab readings probably resulted from variations in concrete modulus. Although a slump tolerance of $\pm 1\frac{1}{2}$ in. was maintained in superstructure construction, measurements for the control beams evidenced the fact that large variations in concrete modulus were possible; indeed, measured moduli varying by factors as great as $2\frac{1}{2}$ across the $6\frac{3}{8}$-in. beam depth were common. Such variations might result from different curing rates at top and bottom, nonhomogeneity and segregation of the vibrated mass, or differential shrinkage cracking.

Despite the possible existence of local "hard" and "soft" spots in the deck slab, it may be expected, because of the stiffness of the end diaphragms, that the longitudinal strains averaged over the entire span would be equal for symmetrically located cells. Although the determination of such average values would require knowledge of the entire longitudinal strain distribution, an insufficiency of gages precluded this; however, longitudinal averaging of strains measured at the $\frac{5}{12}$ and $\frac{7}{12}$ points produced marked transverse strain symmetry (Table 3). It may be argued, of course, that averaging for two sections does not necessarily produce a representative average.

Similar longitudinal averaging of bottom slab reinforcement strains measured 24 hr after striking falsework did not produce similar transverse symmetry. Compilations of strains at later periods, however, demonstrated that transverse symmetry was markedly improved after 24 hr (Table 4). This observation led to the plotting of strain-time curves for these bottom slab gages. These curves demonstrated that, after the initial 24-hr readings, the bottom slab reinforcement strains remained essentially constant with time; however, in general, the 24-hr strains differed radically from the ordinates of the curves extrapolated back to this time. Extrapolated strain values are also listed in Table 4.

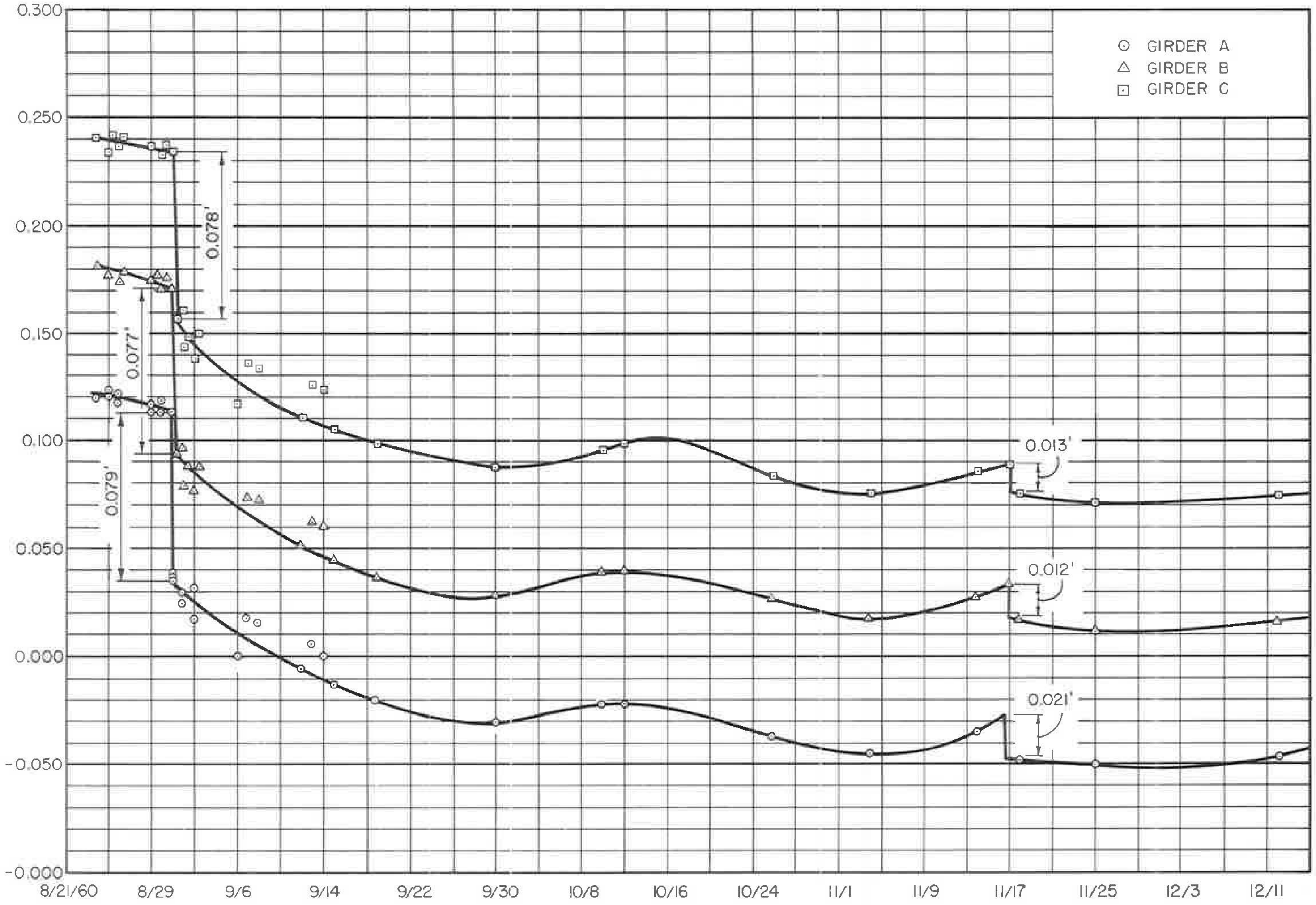

Figure 20. Dead load deflections of stringers A, B, and C, at 5/12 point of span taken from levels on copper bench nails embedded in deck.

TABLE 1

DEAD LOAD DEFLECTIONS

Girder	Deflection	
	Exper.[a] (ft)	Theor. (ft)
A	0.079	0.077
B	0.077	0.077
C	0.078	0.077
D	0.075	0.077
E	0.080	0.077

[a] Average of deflections 5/12 and 7/12 points.

TABLE 2

24-HOUR STRAINS FOR 16 MIDBAY GAGES

Gage	Strain (μ in./in.)	Gage	Strain (μ in./in.)
(a) Top Slab			
C26	-460	C27	-555
C30	-306	C31	-285
C42	-546	C28	-310
C33	-251	C32	-472
(b) Bottom Slab			
193	641	195	499
194	456	196	597
199	438	197	327
200	334	198	563

Large differences among stem and midbay strains necessitated assumption of a distribution pattern in the intervening slab area; a parabolic distribution was assumed.

An explicit evaluation of the effects of creep and shrinkage would have been very difficult for this field test. Existence of pronounced creep strains was evident from the deflection-time and deck slab strain-time curves, although little or no evidence existed for any influence of creep on the lower slab reinforcement strains. It is hypothesized that the creep strains were augmented by the closing of transverse cracks in the deck slab resulting from differential shrinkage of the deck slab against the restraint of the lower slab and stem section. The stems and lower slab were poured monolithically, and the deck slab was poured 11 days later.

Although an explicit determination of the effects of creep and shrinkage would be difficult, these effects may be accounted for implicitly in dead load moment calculations by one of two methods:

1. The strain pattern in the deck slab and stems may be used to determine the location of the resultant compressive total stress and moments due to total tensile stresses in the reinforcing steel computed about this location; or
2. An "effective" concrete modulus may be determined such that the total compressive stress, determined from this modulus and the measured strain distribution, is equal to the total tensile stress, and moments produced by the two types of stress may be computed about the experimentally determined neutral axis; moments due to total stresses in compressive reinforcement are, of course, computed explicitly.

After the aforementioned longitudinal averaging of strains for the 5/12 and 7/12 points, the resultant strains were also averaged transversely. The final strain distributions used in determination of dead load moments based on strains read at 24 hr and 15 days after striking falsework are shown in Figures 21 and 22, respectively. Resisting moments, total stresses, and the "effective" concrete moduli required to balance total stresses across the transverse section are shown in Table 5. Table 6 lists the moments due to the panel loads computed in accordance with 1961 AASHO specifications; these computed moments include the couples due to flared transitions in the ends of the stems. Table 7 lists dead load moments distributed to each stringer as computed by a theoretical method discussed later in this report.

The figures in the tables evidence the fact that, when values of concrete modulus compatible with static balance of total stresses across the transverse section were used in determination of resisting moments (moments computed implicitly in terms of reinforcing steel total stresses were essentially the same), the total section moments determined empirically agreed very closely with the total of computed dead load panel

TABLE 3

TOP SLAB STRAINS PRODUCED BY FALSEWORK REMOVAL

Location	Gage	9-1-60				9-15-60			
		Indicated Strain	I. S.[a] / 2.462	Mean	Mean	Indicated Strain	I. S.[a] / 2.462	Mean	Mean
Girder A	61	-				-1,268	-525		
H-H	C 6	-325				-546		-553	
	65	-863	-358	-342		-1,419	-588		
					-304				-522
J-J	62	-700	-290			-1,198	-497		
	C11	-241		-266		-456		-477	
Bay A-B:									
H-H	C26	-460				-699			-577
J-J	C30	-306			-383	-455			
Girder B	67	-815	-337			-1,356	-561		
H-H	C 7	-350				-565			
	71	-920	-380	-356		-1,450	-600	-575	
					-377				-613
J-J	68	-920	-380			-1,532	-634		
	C12	-440		-410		-706		-670	
Bay B-C:									
H-H	C27	-555				-802			
J-J	C31	-285			-420	-519			-661
Girder C	74	-940	-388			-1,459	-602		
H-H	C 8	-401				-643			
	80	-880	-363	-384		-1,408	-581	-609	
					-359				-581
J-J	75	-770	-319			-1,342	-555		
	C13	-324		-322		-524		-540	
Bay C-D:									
H-H	C28	-310				-484			
J-J	C32	-472			-391	-733			-609
Girder D	82	-815	-334			-1,374	-564		
H-H	C 9	-306				-531			
	84	-800	-328	-323		-1,355	-556	-550	
					-330				-555
J-J	C14	-345				-574			
	85	-815	-335	-340		-1,340	-550	-562	
Bay D-E:									
H-H	C42	-546				-809			
J-J	C33	-251			-399	-470			-640
Girder E	88	-915	-375			-1,416	-581		
H-H	C10	-350				-556			
	90	-820	-336	-354		-1,330	-546	-561	
					-328				-535
J-J	C15	-302				-509			
	91	-670	-275	-289		-1,179	-484	-497	

[a] Corrected for lead length resistance; lead length correction equal to $1 + 2RL/R_{SR4}$, and applies only to SR4 gages.

TABLE 4

BOTTOM SLAB STRAINS PRODUCED BY FALSEWORK REMOVAL

Location	Gage	9-1-60[a]				9-15-60[c]				9-1-60[b]		
		Indicated Strain	I. S.[c] / 2.462	Mean	Mean	Indicated Strain	I. S.[c] / 2.462	Mean	Mean	I. S.[c] / 2.462	Mean	Mean
Girder A	161	1,150	476	477	461	1,179	488	502	482	465	469	455
H-H	165	1,155	478			1,245	515			473		
J-J	162	1,035	429	429		1,068	442	442		428	428	
Bay A-B:												
H-H	193	1,550	641		549	1,010	418		396	410		391
J-J	194	1,100	456			900	373			372		
Girder B	167	1,290	532	492	489	1,330	549	541	526	535	527	513
H-H	171	1,095	452			1,290	532			519		
J-J	168	1,170	484	484		1,200	496	496		484	484	
Bay B-C:												
H-H	195	1,210	499		548	950	392		380	371		364
J-J	196	1,445	597			890	368			357		
Girder C	174	1,398	575	573	540	1,353	557	550	525	551	542	516
H-H	180	1,385	570			1,320	543			553		
J-J	175	1,150	475	475		1,150	475	475		465	465	
Bay C-D:												
H-H	197	795	327		445	890	366		366	366		359
J-J	198	1,365	563			885	365			351		
Girder D	182	1,260	518	537	538	1,245	512	513	506	492	498	488
H-H	184	1,350	555			1,250	514			504		
J-J	185	1,310	540	540		1,190	491	491		467	467	
Bay D-E:												
H-H	199	1,065	438		386	945	388		372	366		350
J-J	200	810	334			860	355			334		
Girder E	188	1,080	443	464	479	1,260	517	484	470	479	471	461
H-H	190	1,180	484			1,100	451			464		
J-J	191	1,240	511	511		1,075	443	443		426	426	

[a] Strains shown are actual differences between strains read just before striking false work and those read about 24 hr later, and those read 15 days later.

[b] Strains obtained by graphical extrapolation of best smooth curve drawn visually through strain reading from 8-31 through 10-10-60, in general disregarding first 24-hr reading.

[c] Readings corrected for lead length resistances.

moments. Moreover, the distribution factors for individual stringers agreed very favorably with factors computed on the basis of folded plate theory.

Inasmuch as the value of "effective" concrete modulus required to produce static balance is quite low compared with the 9-day cylinder test value of 2,600,000 psi, an attempt was made to evaluate possible relative magnitudes of creep and shrinkage. By assuming that any transverse cracks due to differential shrinkage would close immediately on striking falsework, after which combined creep and shrinkage occur, it is possible to establish a rough approximation of the magnitude of initial cracking by establishing an approximate value of instantaneous strain.

Figure 23 illustrates three typical plots of the strain-time relationship for deck slab gages. Curve-fitting methods were used to determine equations comparable to the following equation established by Billig (1) for the creep strain-time relationship in unreinforced concrete:

$$e_t = (1 + \phi_t)\ c/E_o \qquad (1)$$

where

e_t = strain due to creep,
ϕ_t = $1.26\ (t)^{1/3}$,

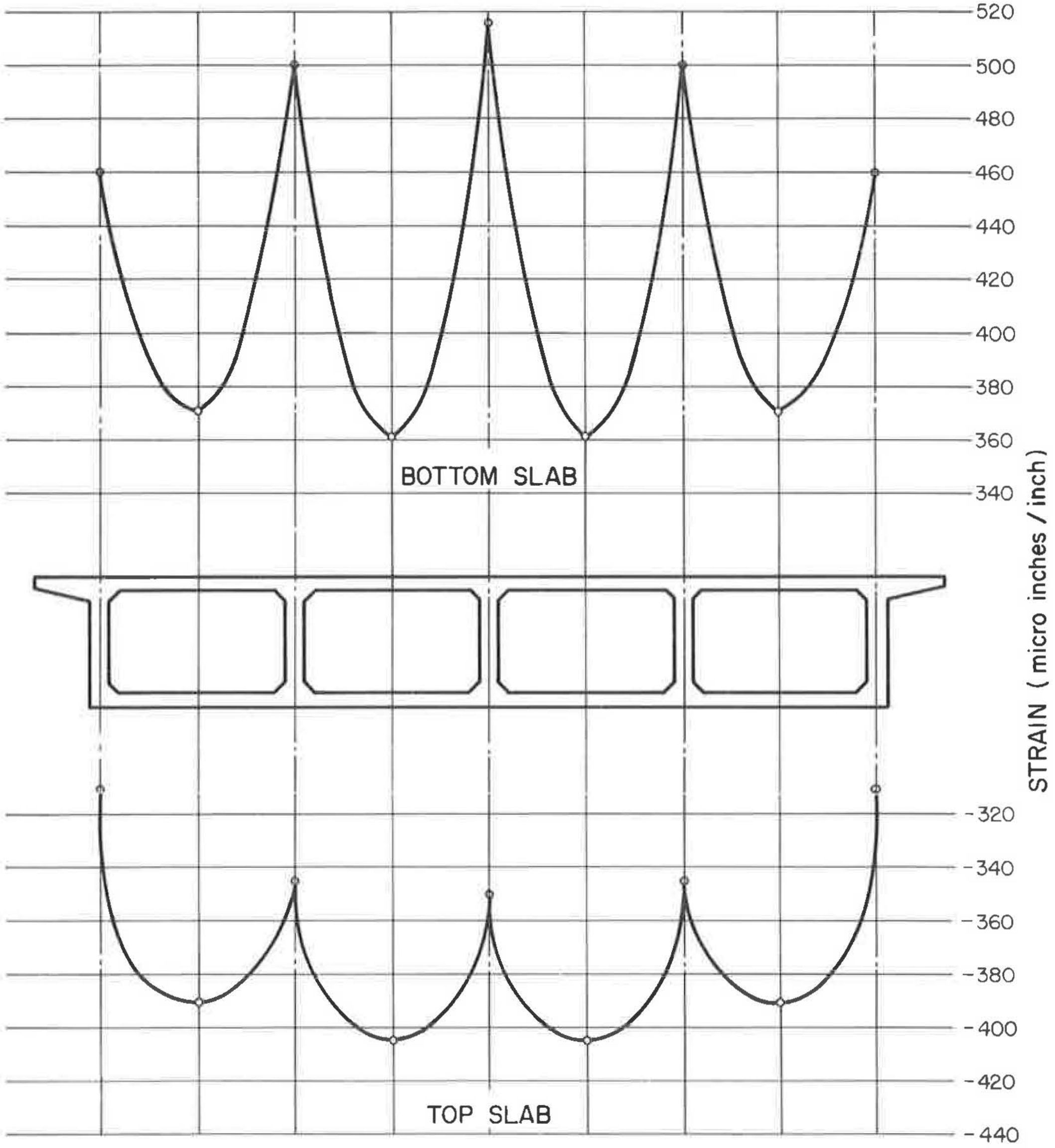

Figure 21. Assumed average distribution of dead load strains 24 hr after striking falsework.

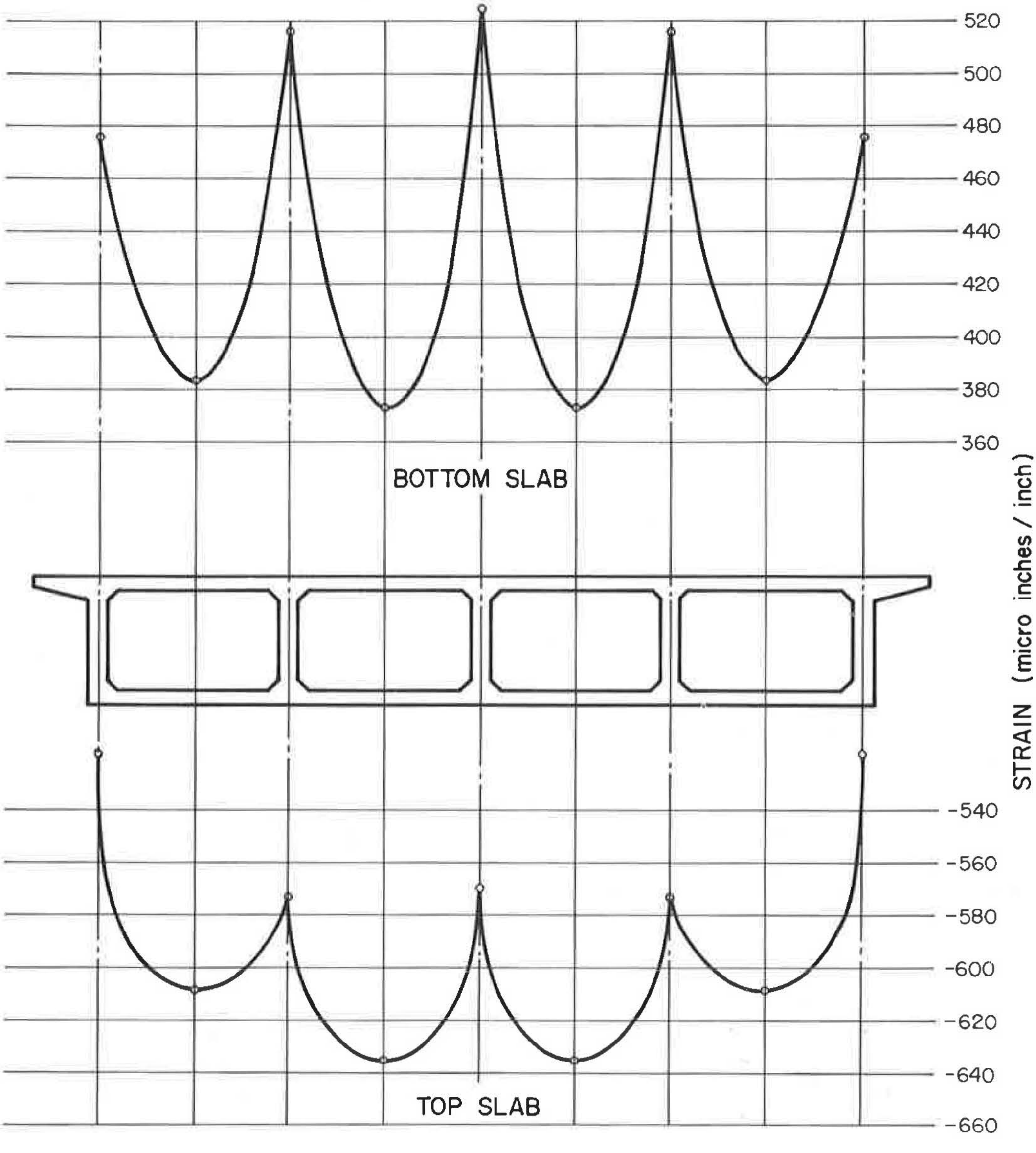

Figure 22. Assumed average distribution of dead load strains 15 days after striking falsework.

TABLE 5

COMPUTED DEAD LOAD MOMENTS AND TOTAL STRESSES

Time	E_c (ksi)	Girder	Moment (kip-ft)	Percent Total	Compressive Total Stress (kips)	Tensile Total Stress (kips)
24-hr	954.9	A, E	870	16.0	242	197
		B, D	1,231	22.6	277	296
		C	1,248	22.9	283	299
Total[a]			5,450	-	1,285	1,285
15-day	495.1	A, E	913	16.4	235	203
		B, D	1,245	22.4	283	305
		C	1,254	22.5	286	305
Total			5,570	-	1,322	1,321

[a] Five girders.

t = time after loading (mo),
c = stress, and
E_0 = design modulus of elasticity.

Although this particular equation could not be expected to hold for reinforced concrete, it was found that an equation of the same general form with different constants,

$$e_t = c(1 + kt^a) \tag{2}$$

produced curves conforming closely to the measured data. It has been assumed that if suitably chosen values of c, k, and a produced curves which closely approximated the empirical data, the values of c would approximate the instantaneous strain, free of creep. Using values taken from such curves, the ratios of instantaneous to 24-hr strains are listed in Table 8. The instantaneous strains average about 75 percent of the 24-hr strains.

The ratio (955,000/2,600,000) of modulus computed for static balance to the 9-day cylinder test value requires a reduction of strains to 37 percent of their 24-hr values for determination of instantaneous strain. The 24-hr strain would then comprise the following: (a) 90 μ in. of creep strain; (b) 37 percent of 365, or 135 μ in. of dead load strain; and (c) 140 μ in. of shrinkage crack closing. The latter figure compares

TABLE 6

DEAD LOAD MOMENTS COMPUTED ON BASIS OF 1961 AASHO SPECIFICATIONS

Girder	Moment (kip-ft)	Percent Total Moment
A, E	945	17.5
B, D	1,169	21.7
C	1,169	21.7
Total[a]	5,397	-

[a] Five girders.

TABLE 7

THEORETICAL DEAD LOAD MOMENTS
(Third Method)

Girder	Moment (kip-ft)	Percent Total Moment
A, E	846	0.158
B, D	1,218	0.228
C	1,215	0.227
Section total	5,343	-

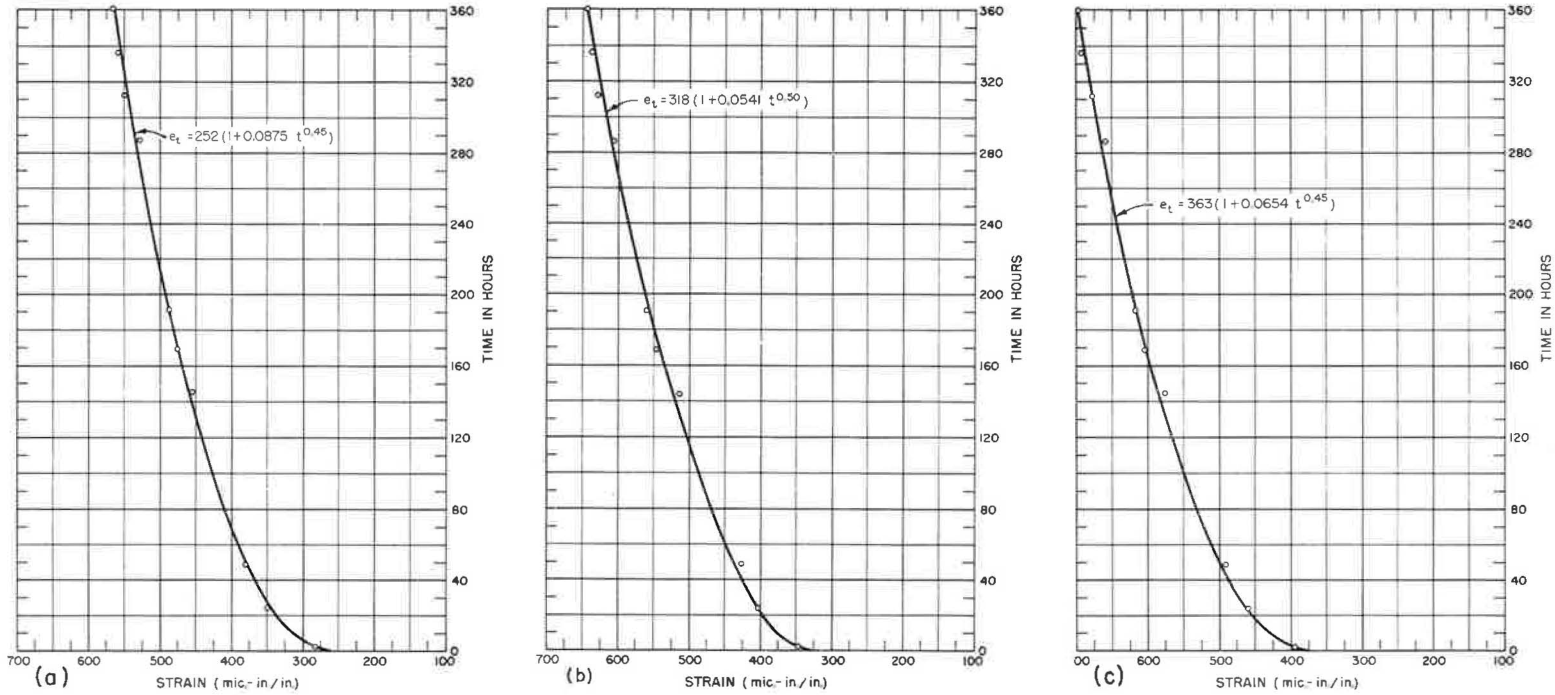

Figure 23. Typical dead load strains in top slab as functions of time using Carlson strainmeters: (a) C7, (b) C8, and (c) C26.

TABLE 8

RATIOS OF COMPUTED INSTANTANEOUS TO MEASURED 24-HOUR STRAINS

Gage	Strain (μ in./in.)		Ratio (%)
	Est. Instantaneous	24-Hr[a]	
C 6	230	322	71.4
C 7	252	344	73.3
C 8	318	403	78.9
C 9	227	305	74.4
C10	251	354	70.9
C26	363	463	78.4
Avg	274	365	74.6

[a]From curve.

favorably with the usual shrinkage coefficient of 0.0002 (200 μ in./in.) and with a measured shrinkage of 110 μ in. in Control Beam C between the ages of 16 and 29 days and about the same amount for Beam A between ages of 16 and 39 days.

Phase IV Results.—Strains measured during the application of the superimposed dead load of barrier curbs and railings were small and too erratic to be of value in determination of induced resisting moments.

Live Load Tests

Phases II, III, and V entailed evaluation of influences on deflections and internal bending strains of a heavily loaded test vehicle moving across the span at crawl speeds of 2 to 5 mph. Strains and deflections measured by internal gages and deflectometers were recorded on oscillographic equipment housed in the instrumentation trailer parked beneath the structure. Frequent static readings were taken with the test vehicle on the span to permit checking of calibration procedures. The resulting correlations were excellent; however, the dynamic loading methods were superior to the static methods for two reasons: (a) the intervals between loading and unloading were shorter and strain variations due to temperature changes were negligible; and (b) very large variations in the patterns of general bending strains, which result from local effects of wheel loads, could readily be evaluated or eliminated by smoothing the oscillographic traces. At the low speeds employed, dynamic effects on the strain patterns were negligible.

Phase II was devoted to the study of structural action of the bare box section. Between Phases II and III, a single intermediate diaphragm was placed within the structure at midspan to permit evaluating the influence during Phase III of such a diaphragm on structural behavior. Between Phases III and V, barrier curbs and railings were placed on the structure, and crawl testing was continued during Phase V to determine the extent to which strains and deflections were modified by these structural components.

Comparison of results based on test data obtained using only one test vehicle with stringer moments based on specifications which permit two vehicles to occupy the span required assumption of validity of the principle of superposition. Crawl tests were performed with the test vehicle occupying 12 transverse positions on the deck slab (Fig. 24), and longitudinal strains were plotted as functions of transverse position. The resulting curves were averaged graphically for symmetrically placed gages for symmetrical test vehicle positions; the symmetry of these strains was very marked, the variation of one curve from its symmetrical counterpart seldom exceeding 2 μ in./in. Strains for four hypothetical vehicle positions were established from the resulting average curves and superposed in the following two vehicle position combinations. (Position 4.10 denotes that the left rear dual wheel is centered at 0.10 of the distance between Positions 4 and 5 from Position 4; Position 11.43, that the right rear dual is located 0.43 of the distance between Positions 11 and 12 from Position 11.) Vehicles were assumed to be confined to separate lanes as in the specifications:

1. Position 4.10 + 11.43—critical loading for center girder;
2. Position 4.10 + 11.93—critical loading for first interior girder; and
3. Position 4.10 + 12.30—critical loading for exterior girder.

As in the case of dead load testing, data analysis was complicated by certain departures from idealized structural behavior. Chief difficulties were as follows:

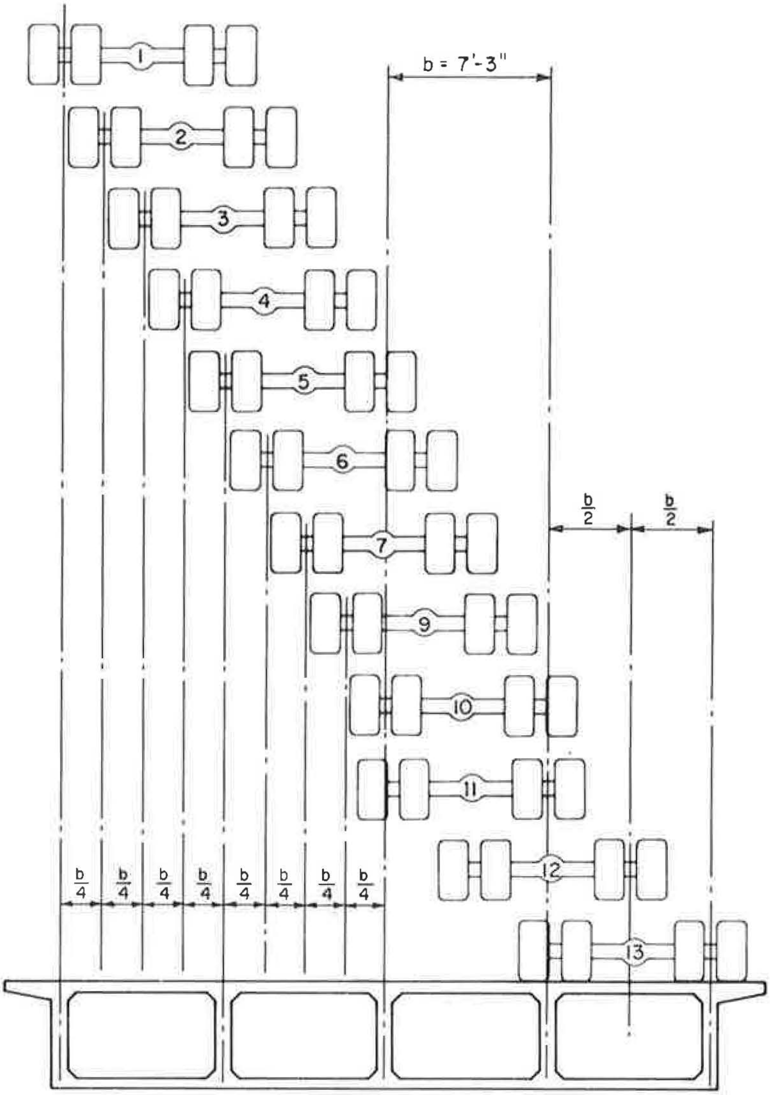

Figure 24. Transverse positions of test vehicle used in live loading of prototype structure.

1. Larger discrepancies among stem and midbay strains existed than those anticipated from shear lag considerations, necessitating assumption of a pattern of strain distribution in the intervening bars and slab sections; again a parabolic distribution was assumed between each midbay strain and the adjacent stem strain, the former being at the parabola's vertex.

2. Simultaneous satisfaction of statics was lacking for total stresses and total resisting moments across given transverse sections of the structure. The total compressive stresses, computed from the measured strain patterns and the concrete moduli determined for the control test beams, invariably exceeded the total tensile stresses computed from the measured steel strains and calibration factors established in the laboratory for total bar stresses as functions of measured strains, and from measured steel moduli. Arbitrary reduction of concrete moduli to effect static balance of total stresses only increased a large discrepancy between external and internal moments.

3. There was lack of agreement between the total internal resisting moments, computed from known concrete and reinforcement properties and measured strains, and the external moments which can be computed from known loads and positions of the test vehicle.

Depending on the manner in which empirical data from live load tests are treated in the computation of girder resisting moments, the discrepancies between summations of those moments for the five stringers and the external moments known to be acting on the structure due to the test vehicle can reach magnitudes as great as 30 percent or as little as 2 percent, the external moment exceeding the internal.

This latter departure from idealized structural behavior appears not to be unique to this particular study; it has probably occurred more frequently than published test results would indicate. Several possible contributing factors have been examined. Tests performed in 1958 by the University of Iowa (2) on a continuous, composite, steel girder bridge evidenced a 23 percent discrepancy between known external and measured internal resisting moments. In the authors' discussion of this discrepancy, the major portion (20 percent) was attributed to distributing effects of the concrete slab; that is, a concentrated wheel load was assumed to act as such on the girder over which it was placed, but, due to the presence of the concrete slab, as a distributed load on girders removed therefrom, resulting in a reduction of computed total resisting moment. Although this explanation has its appeal, it is believed that satisfaction of the principles of static equilibrium across a given transverse section demands that moments in the comparatively flexible slabs (the top slab stiffness being roughly 0.4 percent of the summation of girder stiffnesses) would have to contribute the deficient portion of the total moment.

The second possibility which suggests itself depends on the existence of possible tensile stresses in the concrete below the neutral axis. The resisting moments were computed for cracked sections. In connection with this argument, the following points should be considered:

1. Visible evidence existed, on stem faces, of cracking almost to the computed level of the neutral axis for the cracked section; moreover, the measured strains at tops and bottoms of stems verified these locations.

2. Computed total resisting moments for the gross section are much greater than the external moments. However, if the stems are assumed to remain uncracked down to the top of the lower slab, the computed resisting moment becomes nearly equal to the external moment. In this event, however, the total computed tensile stress becomes much greater than the total computed compressive stress. Also, with live load strains of roughly 60 μ in./in. combined with dead load strains of 450 μ in./in. at this upper limit of cracking, the concrete would be sustaining tensile stresses of about 1,550 psi. Using the usual assumption that tensile strength is about half the modulus of rupture, the limiting tensile strength should be about 400 psi.

As a third possibility, the measured strains in the gaged bars may not accurately represent those in the intervening bars. At each gage location, a blockout was cast into the concrete to permit gage replacement. If it may be logically assumed that the longitudinal strain distribution in a reinforcing bar is nonuniform, exhibiting maxima at the cracks and minima midway between cracks where tensile stress in the concrete participates in carrying load, then the average strain measured in a blocked-out bar would doubtlessly be slightly lower than the strains in adjacent bars at the locations of a crack running through the blockout. These latter strains should be the representative strains used in moment computations. The possibility of such a phenomenon having any significant effect on results was, for all practical purposes, eliminated by conducting tests on one girder stem with a special type of gage. These tests clearly demonstrated that the measured strains in the lower bars corresponded accurately with the vertical strain distribution observed in the stem.

A fourth possibility may be considered in that the strain distribution assumed between stems and midbays may not represent the true distribution. The differences exhibited between stem and midbay strains were much larger than theoretical considerations would indicate. The strain distribution in the intervening bars would have to be radically different from the parabolic distribution assumed, however, to produce any significant increase in computed resisting moments.

Much of the evidence observed in the box girder project favors an explanation of the discrepancy between computed total resisting moments and known external moments on the basis of results of some research work on flat slabs completed in recent years at the University of Illinois. In the course of this work it was observed that a reinforced concrete beam loaded into the cracking range and subsequently unloaded, would, on reloading, behave like an uncracked section, its stress-strain curve approximately paralleling the curve obtained before first cracking. It is hypothesized that, when the cracked structure is unloaded, cracks in the concrete do not close completely, leaving residual stresses in the tensile reinforcement which produce compressive stresses against whatever material is preventing closing of the cracks. Steel strains measured in the reinforcement during subsequent reloading of the beam, lacking consideration of these residual stresses, would be lower than strains commensurate with the moments applied to the beam.

Evidence favoring this explanation is furnished by the fact that, as will be noted below, when the steel stresses are eliminated from consideration in moment calculations by computing the moments of the compressive total stresses about the computed location of the tensile total stress resultants, the summation of computed resisting moments in the five girders is very nearly equal to the known acting moment. The fact that the computed total compressive stress across the transverse box girder section greatly exceeds the total tensile stress also favors the hypothesis that unmeasured residual stresses exist in the reinforcing steel. Lastly, the configuration of the oscillographic traces of strain in the lower slab reinforcing steel favors this hypothesis. If the phenomenon which keeps the cracks in the concrete from closing also permits the existence of temporary compressive stresses in the cracked area, the residual stresses in the tensile reinforcing steel would, in effect, cause the beam to behave like a partially prestressed beam, increasing the moment of inertia with respect to that of the fully cracked beam and lowering the neutral axis. As the beam is reloaded and the residual stresses are overcome, the cracks will re-open until the load reaches its former maximum value, when the beam again acts as a fully cracked section. This behavior would be manifested by a rising neutral axis, a decreasing moment of inertia, and an increasing "fiber distance" for the reinforcement. Under such circumstances, a linear change in bending moment would be accompanied by a curvilinear increase in reinforcement bending strains.

The influence line for bending moment or strain in a simple beam traversed by the two-axle test vehicle would normally be expected to be a broken line comprising the graphical summation of two dissimilar triangles whose vertices are displaced horizontally from one another by the wheelbase of the vehicle. The oscillographic traces in rare instances did assume such a configuration; however, in the general case, these traces exhibited a series of curvilinear traces with upward concavity, such as would be expected if the aforementioned phenomenon existed.

Unfortunately, at the time the oscillographic data were reduced, the possibility of such a phenomenon was not anticipated and the actual trace displacements were assumed to represent the strain patterns. In retrospect, it appears that the lower layer steel strains for each beam might more logically have been obtained by constructing an idealized influence line, based on the measured axle reactions, wheelbase, and bridge dimensions, on each oscillographic trace for which strains in a given gage reached the maximum strain in the course of the test. The ratios of influence line ordinates to trace displacements for various moments could then be used to correct the traces for any vehicle traverse. For one oscillographic trace treated in this manner, it was found that the strain at the $\frac{5}{12}$ths point, with the rear axle of the test vehicle at midspan, was increased by 30 percent.

It might reasonably be expected that, if this phenomenon did exist, the residual stresses after first loading would be readily observable on plots of dead load strain as functions of time and that overcoming these residual stresses would result in a delay in the appearance of strains on the oscillographic trace. Neither of these phenomena was explicitly observable; however, it should be noted that these residual strains would be most pronounced at a crack but would be averaged out over a considerable length where the gages were blocked out or extensively waterproofed. Moreover, the aforementioned curvilinear configuration of the oscillographic traces does, in effect, constitute a delayed appearance of strain, though lacking the more abrupt nature which might be expected if the strain were measured at a crack.

Any of the five effects mentioned constitutes a possible contributing factor to the discrepancy between external and internal moment. Little evidence exists among the prototype strains for the existence of some of them; insufficient instrumentation precludes the elimination of others from consideration. The best evidence points to the fifth reason given, and the excellent agreement noted between total external moment and total resisting moment based on compressive total stresses only, favors this argument. To avoid any loopholes, however, four sets of girder resisting moments were calculated, using various assumptions, to cover the various possibilities.

The first set of values was established from the raw test data with little modification. Mean strains in the tensile reinforcing bars, assuming parabolic distribution, and measured strains in compressive reinforcement were used in conjunction with laboratory calibrations to establish total steel stresses. Mean strains in the concrete slab were multiplied by elastic moduli determined from tests on unreinforced control beam specimens poured simultaneously with the slab and subjected to a similar environment. Resulting values of resisting moments are given in Table 9 and shown in Figure 25 for test vehicles in hypothetical positions 4.10 and 11.43, with the rear axle at midspan. In all cases, such curves were drawn for the aforementioned critical locations and for the rear axle at the quarterspan and at midspan. Only typical curves will be included herein.

The discrepancy between computed total resisting moment and known acting moment is roughly 25 percent for this case. Total computed compressive stresses are significantly larger than computed total tensile stresses across the transverse sections

TABLE 9

COMPUTED LIVE LOAD RESISTING MOMENTS AT $^{5}/_{12}$ POINT OF SPAN[a]

Phase	Position Comb.	Resisting Moment (kip-ft)						E_c (× 10^3 ksf)
		A	B	C	D	E	Total	
II	4.10 +	204	293	308	308	219	1,332	439.2
III	12.30	222	311	313	320	231	1,397	469.4
V	-	162	257	261	265	169	1,114	522.7
II	4.10 +	206	297	311	305	215	1,334	439.2
III	11.93	224	314	314	318	228	1,398	469.4
V	-	164	260	261	264	167	1,116	522.7
II	4.10 +	208	299	313	304	212	1,336	439.2
III	11.43	226	316	315	315	225	1,397	469.4
V	-	165	262	261	261	164	1,113	522.7

[a] Based on unmodified strain data and control beam moduli, rear wheels at midspan.

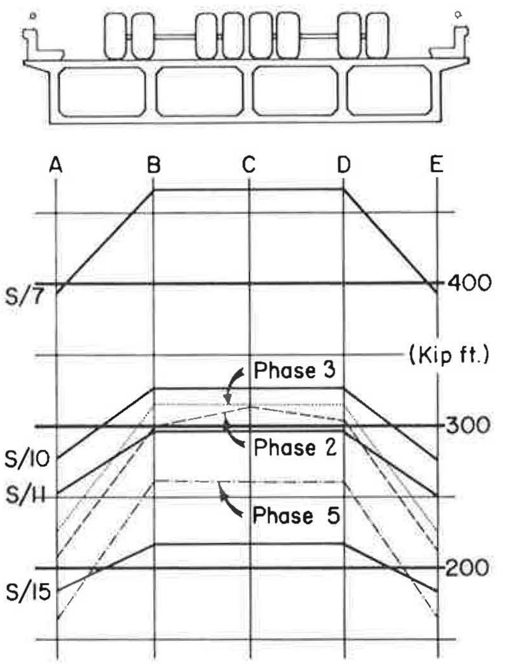

Figure 25. Computed live load resisting moments for two test vehicles in hypothetical transverse positions 4.10 and 11.43 (critical for center girder), with rear axle at midspan, taken about experimental neutral axis and based on control beam moduli.

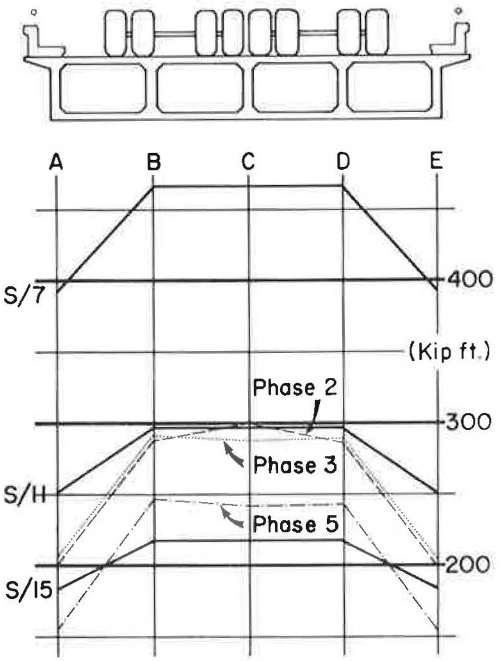

Figure 26. Computed live load resisting moments for two test vehicles in hypothetical transverse positions 4.10 and 11.43 (critical for center girder), with rear axle at midspan, taken about experimental neutral axis, with concrete moduli reduced to effect static balance between total tensile and compressive stresses.

studied. Two possible alternatives exist to effect static balance of the total stresses across the transverse section: (a) by decreasing the total computed compressive stress; or (b) by increasing the total computed tensile stress.

For the second set of resisting moments, the concrete modulus was assumed at a lower value than that measured for the control beams to effect static balance of total stresses by decreasing the total compressive stress. The control beams were, of necessity, tested in a much lower stress range than that to which the deck slab was subjected, possibly producing a higher figure for effective modulus. In addition, if it were possible for transverse deck cracks to exist in the high compressive stress field due to differential shrinkage of the deck slab against the restraint of the stems, the necessity for closing these cracks under live loading would reduce the effective modulus from that measured for the control beams. Resisting moments computed for the lower modulus are given in Table 10 and shown in Figure 26. Although static balance is established for total stresses by this method of computation, the discrepancy between external and internal moments is increased to 30 percent.

In the third calculation, resisting moments were computed explicitly in terms of concrete stresses using the control beam moduli in conjunction with measured strain patterns in the concrete and computing moments about the lower slab reinforcement. This method of calculation eliminates consideration of the tensile reinforcement stresses, assuming that these measured stresses are unrepresentative for reasons discussed previously. Results are given in Table 11 and shown in Figure 27. The discrepancy between internal and external moments is decreased to 8 percent for Phase II and 2 percent for Phase III.

TABLE 10

COMPUTED LIVE LOAD RESISTING MOMENTS AT $^5/_{12}$ POINT OF SPAN[a]

Phase	Position Comb.	Resisting Moment (kip-ft)						E_c (× 10^3 ksf)
		A	B	C	D	E	Total	
II	4.10 +	195	281	295	294	207	1,272	351.8
III	12.30	200	286	286	293	208	1,273	353.9
V	-	150	240	241	247	156	1,034	353.9
II	4.10 +	197	284	297	291	204	1,273	351.8
III	11.93	202	288	287	291	205	1,273	353.9
V	-	151	239	237	246	155	1,028	353.9
II	4.10 +	201	289	299	287	199	1,275	351.8
III	11.43	204	290	288	289	202	1,273	353.9
V	-	153	245	241	243	152	1,034	353.9

[a] With concrete moduli reduced to produce static balance of total stresses, rear wheels at midspan.

TABLE 11

COMPUTED LIVE LOAD RESISTING MOMENTS AT $^5/_{12}$ POINT OF SPAN[a]

Phase	Position Comb.	Resisting Moment (kip-ft)						E_c (× 10^3 ksf)
		A	B	C	D	E	Total	
II	4.10 +	282	342	370	357	301	1,652	439.2
III	12.30	313	364	376	378	328	1,759	469.4
II	4.10 +	286	346	375	354	297	1,658	439.2
III	11.93	317	366	377	375	325	1,760	469.4
II	4.10 +	291	350	380	351	291	1,663	439.2
III	11.43	320	370	379	370	320	1,759	469.4

[a] Based on control beam moduli and taken about resultant of total tensile stress.

In the fourth set of calculations, the resisting moments for individual stringers in each of the previously mentioned calculations were arbitrarily increased by the ratio of the known external moment to the summation of individual stringer moments. Envelopes of resulting maximum moments for each stringer are shown in Figures 28a and 29a for the rear axle at midspan and quarterspan, respectively. The latter calculation was not extended to Phase V because of the indeterminate nature of the contribution of the barrier curbs and railings to the individual stringers.

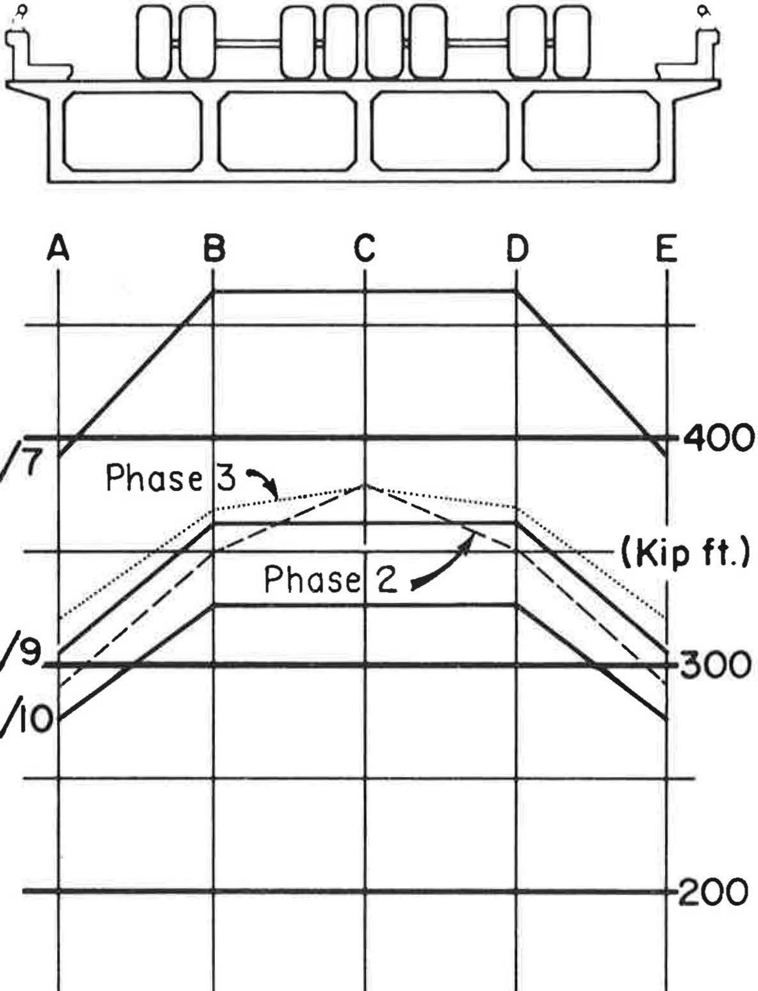

Figure 27. Computed live load resisting moments for two test vehicles in hypothetical transverse positions 4.10 and 11.43 (critical for center girder), with rear axle at mid-span, taken about resultant of total tensile stresses and using control beam moduli.

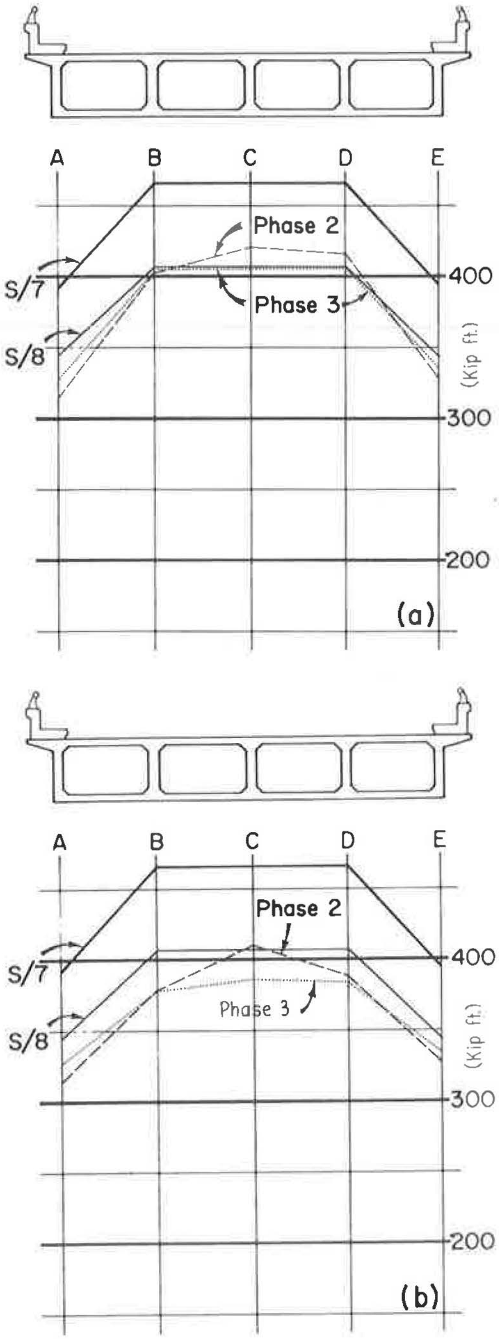

Figure 28(a). Envelopes of maximum augmented live load resisting moments for two test vehicles in hypothetical transverse positions critical for various girders, and with rear axle at midspan; and (b) using only moment of total compressive stresses about tensile resultant location.

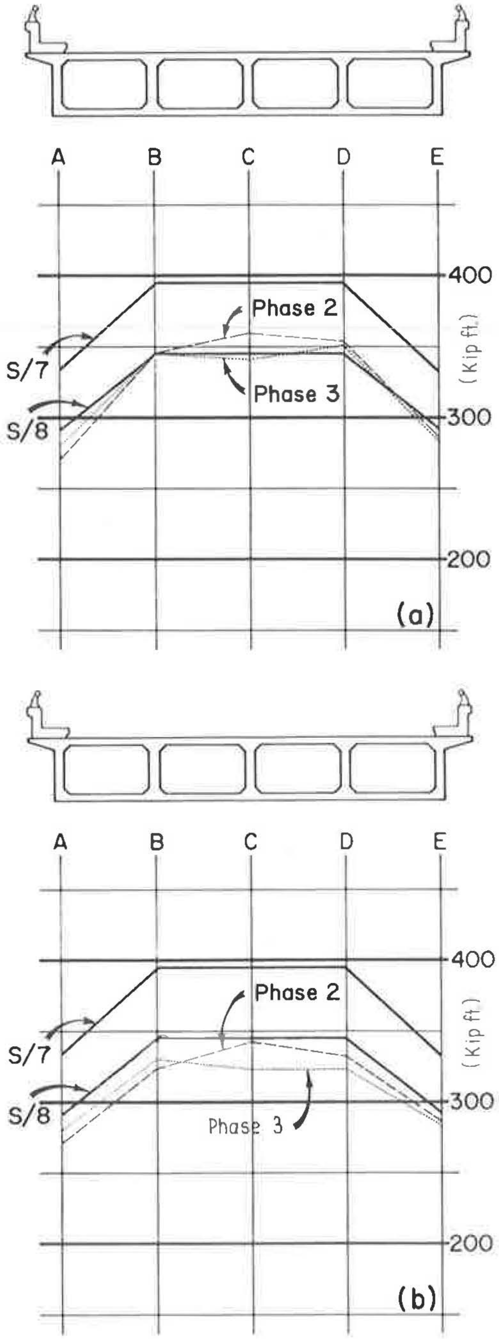

Figure 29(a). Envelopes of maximum augmented live load resisting moments for two test vehicles in hypothetical transverse positions critical for various girders, and with rear axle at quarterspan; and (b) using only moment of total compressive stresses about tensile resultant location.

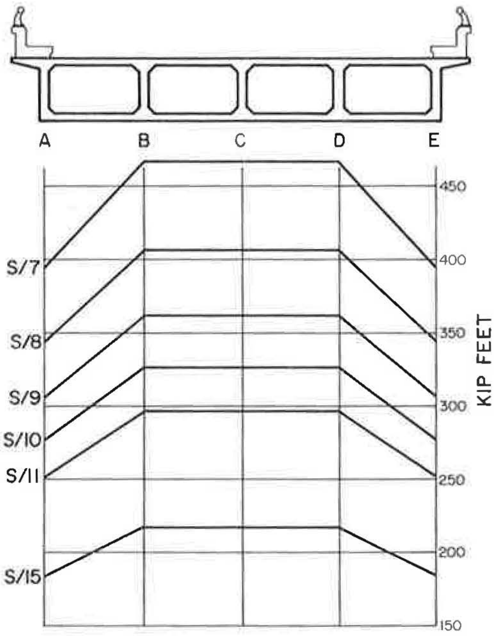

Figure 30. Live load resisting moments for various distribution factors, rear axle at midspan.

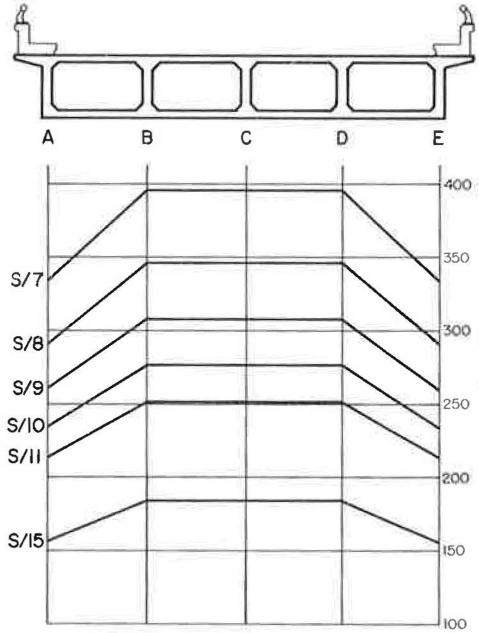

Figure 31. Live load resisting moments for various distribution factors, rear axle at quarterspan.

TABLE 12

EMPIRICAL VALUES OF DISTRIBUTION FACTOR, K

Stringer	No. of Wheel Lines, WL	WL/S	$\frac{WL/S}{W_e/S}$	K
(a) Phase II[a]				
A	$\frac{314}{449} = 0.699$	0.096	0.114	8.77
B	$\frac{407}{449} = 0.906$	0.125	-	8.00
C	$\frac{421}{449} = 0.938$	0.129	-	7.75
D	$\frac{416}{449} = 0.927$	0.128	-	7.82
E	$\frac{327}{449} = 0.728$	0.100	0.118	8.48
(b) Phase III[a]				
A	$\frac{327}{449} = 0.728$	0.100	0.118	8.48
B	$\frac{409}{449} = 0.911$	0.126	-	7.94
C	$\frac{406}{449} = 0.904$	0.125	-	8.00
D	$\frac{413}{449} = 0.920$	0.127	-	7.88
E	$\frac{335}{449} = 0.746$	0.103	0.122	8.20
(c) Phase II[b]				
A	$\frac{314}{449} = 0.699$	0.096	0.114	8.78
B	$\frac{378}{449} = 0.842$	0.116	-	8.62
C	$\frac{411}{449} = 0.915$	0.126	-	7.94
D	$\frac{388}{449} = 0.864$	0.119	-	8.40
E	$\frac{327}{449} = 0.728$	0.100	0.118	8.48
(d) Phase III[b]				
A	$\frac{327}{449} = 0.728$	0.100	0.118	8.48
B	$\frac{378}{449} = 0.842$	0.116	-	8.62
C	$\frac{387}{449} = 0.862$	0.119	-	8.40
D	$\frac{386}{449} = 0.860$	0.119	-	8.40
E	$\frac{335}{449} = 0.746$	0.103	0.122	8.19

[a] Based on envelopes of maximum augmented values of resisting moments computed by four methods.

[b] Based on maximum augmented values of resisting moments of total concrete stresses about location of tensile resultant.

TABLE 13

EXPERIMENTAL LIVE LOAD MOMENTS[a]

Girder	Resisting Moment (kip-ft)	Proportion of Total
A	208	0.156
B	299	0.224
C	313	0.234
D	304	0.228
E	212	0.159
Total	1,336	-

[a]From Table 9, Phase II; Position 4.10 + 11.43, rear axle at midspan, (calculated from control beams for Phase II).

TABLE 14

EXPERIMENTAL LIVE LOAD MOMENTS[a]

Girder	Resisting Moment (kip-ft)	Proportion of Total
A	291	0.175
B	350	0.210
C	380	0.228
D	351	0.211
E	291	0.175
Total	1,663	-

[a]Moments of compressive resultants about tensile resultant, Phase II, from Table 11, Phase II; Position 4.10 + 11.43, rear axle at midspan, E_c = 439,200 ksf (calculated from control beams for Phase II).

TABLE 15

EXPERIMENTAL LIVE LOAD MOMENTS[a]

Girder	Resisting Moment (kip-ft)	Proportion of Total
A	320	0.182
B	370	0.210
C	379	0.215
D	370	0.210
E	320	0.182
Total	1,759	-

[a]Moments of compressive resultants about tensile resultant, Phase III, from Table 11, Phase III; Position 4.10 + 11.43, rear axle at midspan, E_c = 439,200 ksf (calculated from control beams for Phase III).

TABLE 16

EXPERIMENTAL LIVE LOAD MOMENTS[a]

Girder	Resisting Moment (kip-ft)	Proportion of Total
A	201	0.157
B	289	0.227
C	299	0.235
D	287	0.225
E	199	0.156
Total	1,275	-

[a]Position 4.10 + 11.43; rear axle at midspan; E_c = 351,800 ksf (value required to satisfy statics for total longitudinal stresses).

A similar augmentation was performed using only the moment of the total compressive stresses about the tensile resultant location. Envelopes are plotted in Figures 28b and 29b for the rear axle at midspan and quarterspan, respectively.

For comparison purposes, each of the previous graphs depicts the resisting moment in each girder as it would be computed for a fractional distribution of S/7. In addition, Figures 30 and 31 depict computed moments for several other fractional distributions up to S/15.

The aforementioned maximum bending moments in the stringers may be translated into more familiar design terms. If S/K is the number of wheel lines distributed to each interior stringer for an average stringer spacing, S, and $(W_e/S)(S/K)$ is the corresponding factor for the exterior stringer, where W_e is one-half the panel width plus the width of slab overhang; the factor, K, may be computed as shown in Table 12. The moment per wheel line, with rear axle at midspan = 449 ft-kips. A similar calculation

TABLE 17

THEORETICAL LIVE LOAD MOMENTS[a]

(First Method)

Girder	Resisting Moment (kip-ft)	Proportion of Total
A	261	0.144
B	430	0.237
C	444	0.244
D	423	0.233
E	258	0.142
Total	1,816	-

[a] Position 4.10 + 11.43; rear axle at midspan; E_c = 432,000 ksf.

TABLE 18

THEORETICAL LIVE LOAD MOMENTS[a]

(Second and Third Methods)

Girder	Resisting Moment (kip-ft)	Proportion of Total
A	280	0.153
B	420	0.229
C	430	0.235
D	420	0.229
E	280	0.153
Total	1,830	-

[a] Position 4.10 + 11.43; rear axle at midspan; E_c = 432,000 ksf.

TABLE 19

EXPERIMENTAL LIVE LOAD MOMENTS[a]

Girder	Resisting Moment (kip-ft)	Proportion of Total
A	204	0.153
B	293	0.220
C	308	0.231
D	308	0.231
E	219	0.164
Total	1,332	-

[a] From Table 9, Phase II; Position 4.10 + 12.30; rear axle at midspan; E_c = 439,200 ksf (calculated from control beams for Phase II).

TABLE 20

EXPERIMENTAL LIVE LOAD MOMENTS[a]

Girder	Resisting Moment (kip-ft)	Proportion of Total
A	282	0.171
B	342	0.207
C	370	0.224
D	357	0.216
E	301	0.182
Total	1,652	-

[a] Moments of compressive resultants about tensile resultants, Phase II, from Table 11, Phase II; Position 4.10 + 12.30, rear axle at midspan, E_c = 439,200 ksi (calculated from control beams for Phase II).

was made using only augmented moments of total compressive stresses about the location of the tensile resultant. Values of K for this calculation are also listed in Table 12.

Selected results of calculations of experimental live load moments are listed in Tables 13 through 18. Table 13 lists the ratios of individual stringer to total moments computed by the aforementioned first method and listed in Table 9. Similar ratios for moments of total compressive stresses about tensile resultant locations are listed in Tables 14 and 15 for Phases II and III, respectively—the moments in the latter two tables were taken from Table 11. Table 16 lists these ratios for moments computed by the second method, wherein all moments are increased by the ratio of known external moment to computed internal moment. Tables 19 through 22 list similar ratios for a different critical position of the test vehicles.

It should be emphasized that the results shown are for a structure with the particular configuration of the test structure, and that these results may require modification for structures with other configurations if theoretical considerations so indicate.

TABLE 21

EXPERIMENTAL LIVE LOAD MOMENTS[a]

Girder	Resisting Moment (kip-ft)	Proportion of Total
A	313	0.178
B	364	0.207
C	376	0.214
D	378	0.215
E	328	0.186
Total	1,759	-

[a] Moments of compressive resultants about tensile resultants, Phase III, from Table 11, Phase III; Position 4.10 + 12.30, rear axle at midspan, E_c + 439,200 ksf (calculated from control beams for Phase III).

TABLE 22

EXPERIMENTAL LIVE LOAD MOMENTS[a]

Girder	Resisting Moment (kip-ft)	Proportion of Total
A	195	0.154
B	281	0.221
C	295	0.232
D	294	0.231
E	207	0.163
Total	1,272	-

[a] Position 4.10 + 12.30; rear axle at midspan; E_c = 351,800 ksf (value required to satisfy statics for total longitudinal stresses).

THEORETICAL ANALYSIS

In order that the results of field and model studies might be extended to permit application of these results to structures varying in configuration from the field prototype, certain analytical procedures were investigated. The first method comprises an attempt to apply a distribution procedure developed by Newmark (3). Because some of the assumptions used in Newmark's development do not hold true in the case of the box girder, some modifications of the method have been required. The third method entails an application to the box girder of folded plate equations developed by Goldberg and Leve (4), using matrix algebra. The second method combines portions of the first and third methods, treating the transverse rigidity phase by Newmark's method, and the longitudinal rigidity phase by folded plate equations. Whereas the mathematical approach used in the second method differs considerably from that used in the third, the results of these two solutions are the same.

Because all three procedures involve much tedious arithmetic, the use of an electronic computer is essential. The computational burden connected with the work described herein was, in large measure, carried out by programming in FORTRAN language for an IBM 704 owned by the Division of Highways.

Description of Analytical Procedures

The distribution procedure developed by Newmark was designed for application to slabs on steel I-beams, wherein the assumption can be made that there exists negligible transfer of longitudinal shear at the beam-slab interface. Transverse slab moments and shears are distributed by the moment distribution method, modified for application to the slab elements. Effects of the torsional rigidities of the supporting beams may be included. The analysis may, in effect, be separated into two phases, in which the effects of transverse slab rigidity and of longitudinal girder rigidities are evaluated separately.

This brief description evidences some of the shortcomings of the method in its application to the box girder. For one thing, the torsional rigidity of the supporting beams becomes indeterminate in the box girder section due to the restraint at the bottom of the web resulting from the presence of the lower slab. An attempt has been made to surmount this difficulty by treating the webs and lower slab in a manner comparable to that used by Newmark for the top slab. The transverse section thus becomes analogous to a Vierendeel truss with rigid joints, with the slabs and webs comprising the truss members.

A second difficulty arises from the fact that the webs are integral with the upper and lower slabs, and longitudinal shear is inevitable at the joints. Although the assumption of no longitudinal shear transfer is basic in Newmark's method, he suggests as an approximation, where "T-beam" action is present, the use of a modified moment of inertia in the calculation of the longitudinal girder stiffness. In the first method, the moment of inertia of the entire I-section between vertical planes at the midbays has been used in the computation of the longitudinal stiffness. This expedient, however, does not adequately take into account the longitudinal rigidity of the closed box section; this is believed to be the reason for the poor results from the use of this method. In the second method, the longitudinal stiffness is treated by use of those folded plate equations treating the membrane stresses, with considerably improved results.

The third method does not deal with transverse and longitudinal rigidities in separate steps but employs all of the folded plate equations to permit evaluation of a stiffness matrix for the section. This procedure provides a convenient method for evaluation of girder deflections and internal stresses for various applied loads.

An ordered description of steps involved in the three procedures follows. Outlines of the first and second methods are combined because the first phase of each method, considering only the effects of transverse rigidity, is the same.

Analytical Procedures—First and Second Methods

1. Resolve the external loading forces into component terms of a Fourier series. Use equations furnished by Newmark (3) where applicable. (It is convenient to defer inclusion of the sine terms in the series expansions and to deal only with amplitudes of the forces until the final stages of the analysis.)

2. Replace the transverse box girder section with an "analogous Vierendeel truss" with vertical sections of the slabs and webs replaced by the truss members. It is assumed that the slabs are framed into diaphragms at the bearings only and that these end diaphragms provide only simple support without moment restraint in a longitudinal direction.

3. Compute stiffness and carry-over characteristics for each member of the analogous truss for determination of fixed end moments and reactions. Because these factors apply to truss members which are, in reality, sections of slabs, they will differ numerically from similar factors for beams. Values may be found by interpolation from tables provided by Newmark (3), or they may be computed from equations furnished for the purpose. Although these coefficients include hyperbolic functions for which accurate tables are not always available, computation by electronic computer makes the use of the equations more convenient than use of Newmark's tables.

4. Using the coefficients from Step 3 and the loading components from Step 1 for known values of the loading, fixed edge moments and reactions may be computed for each value of the Fourier module.

5. Assume that the slabs are inextensible between joints. At the bottom of each web and at one end of each slab, introduce constraints which permit longitudinal movements and joint rotations but prevent transverse or vertical translations.

6. Compute unbalanced moments at each joint and, by successive relaxations, distribute moments around the analogous truss using the carry-over factors from Step 3.

7. Calculate modifications of the fixed end reactions resulting from the relaxation of the joints in the course of distributing moments. The analogy with the Vierendeel truss breaks down here because the reaction changes cannot be computed by statics. A description of the applicable procedure is given by Newmark (3).

8. Summation of the modified fixed end reactions along horizontal or vertical planes will produce a total of seven external reactions at the points of constraint. The loading producing these reactions may be replaced by a set of seven hypothetical external loads (R_{10}, R_{20}, . . . , R_{70}) acting at the panel points. These loads are equal and opposite to the external reactions (Fig. 32).

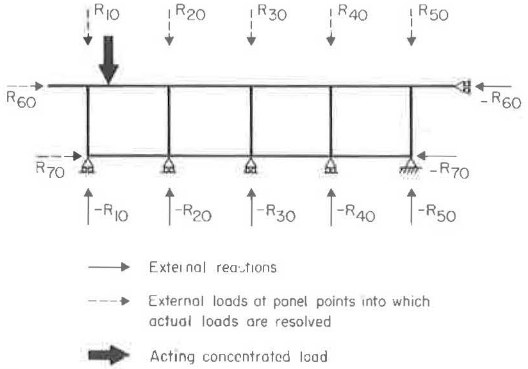
R10
R20
R30
R40
R50
R60
-R60
R70
-R70
-R10
-R20
-R30
-R40
-R50
External reactions
External loads at panel points into which actual loads are resolved
Acting concentrated load

Figure 32. Resolution of external actions with joints restrained.

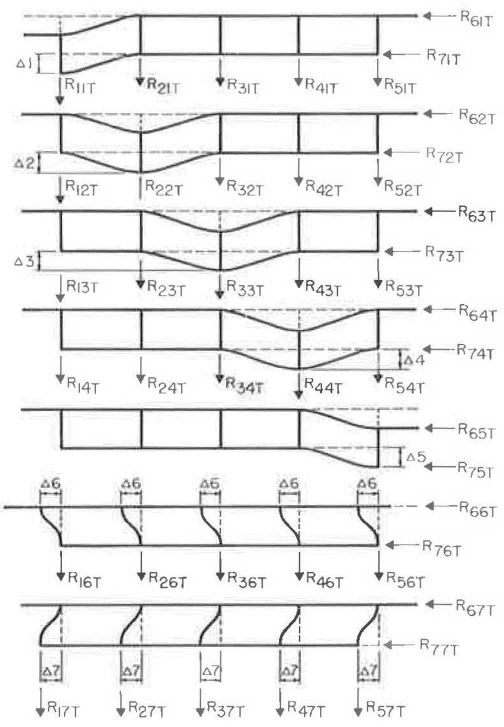
R61T
R71T
Δ1
R11T
R21T
R31T
R41T
R51T
R62T
R72T
Δ2
R12T
R22T
R32T
R42T
R52T
R63T
R73T
Δ3
R13T
R23T
R33T
R43T
R53T
R64T
R74T
Δ4
R14T
R24T
R34T
R44T
R54T
R65T
Δ5
R75T
Δ6
R66T
R76T
R16T
R26T
R36T
R46T
R56T
R67T
R77T
Δ7
R17T
R27T
R37T
R47T
R57T

Figure 33. Hypothetical displacement patterns assumed in analysis: transverse rigidity phase.

9. Assume a set of seven independent patterns of deflection, in which each girder stem (two joints) and each slab (five joints each) are deflected through known distances.

10. Compute a new set of fixed end moments and reactions commensurate with each deflection pattern. This calculation will require coefficients applicable to slab deflections computed from Step 3.

11. Distribute unbalanced moments as before and compute the changes in the new fixed end reactions due to joint relaxations.

12. Compute a second set of reactions (R_{11T}, R_{21T}, ..., R_{71T}; R_{12T}, R_{22T}, ..., R_{72T}; etc.) required to hold the analogous truss in equilibrium in each distorted configuration (Fig. 33). (R_{ij} is the reaction at panel point i due to a deflection at panel point j.)

13. The reactions determined in Step 12 are based on the assumption that the structure has large transverse rigidity compared to its longitudinal rigidity; the first and second methods are identical to this point.) A second component of reaction must be calculated at each panel point assuming that the structure has large longitudinal rigidity compared to its transverse rigidity. Superposition of the two reaction components will result in reactions required to produce the deflected configurations for a structure with rigidity in both directions.

14. The method used to compute the reaction components for the structure with large longitudinal rigidity constitutes the basic difference between the first and second methods.

a. First Method.—The individual girders are assumed to be cut at the midpoints of the bays by vertical planes or at the mid-depths of the stems by horizontal planes (Fig. 34). Girder stiffnesses are computed and multiplied by the same deflections used in Step 9. Because this girder stiffness is a function of the girder moment of inertia, this method permits the use of any desired section, be it cracked or uncracked. The procedure possesses the disadvantage that it neglects the longitudinal rigidity of the closed box section, which may be appreciable.

b. Second Method.—The webs and slabs are assumed to be membranes which can sustain longitudinal shears and normal stresses but no transverse moments or shears; the latter two components are covered in the first step for both methods. Values of S, the longitudinal shears, and of N, the normal stresses, will depend on the longitudinal displacements of the joints, u, and transverse displacements, v. Goldberg and Leve (4) have developed equations for N and S in terms of u and v. With values of v established for the seven aforementioned displacement patterns, it is possible, through use of these equations, to compute corresponding values of u by formulating equilibrium

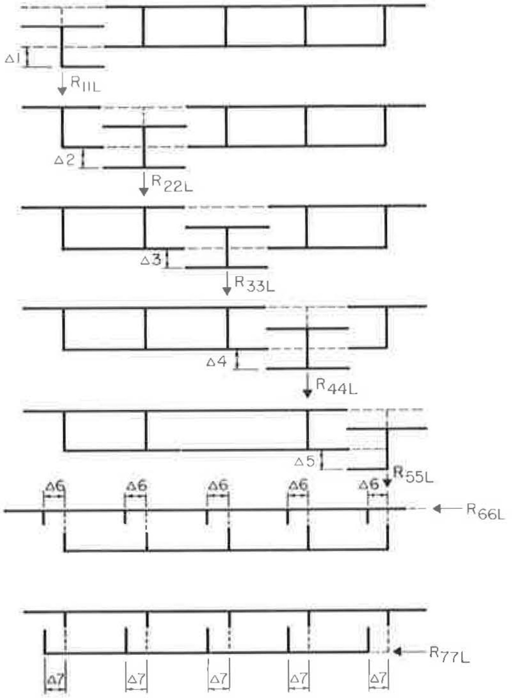

Figure 34. Hypothetical displacement patterns assumed in analysis: longitudinal rigidity phase.

equations for the longitudinal shears at each joint. The resulting values of u, together with the corresponding assumed values of v, may be employed to determine the N forces for each member at the joints. The N forces may be summed along vertical and horizontal lines to produce the second components of reactions, R_{11L}, R_{21L}, ..., R_{71L}; R_{12L}, R_{22L}, ..., R_{72L}; etc. This method permits an evaluation of the longitudinal shears at the joints but possesses the disadvantage that it deals purely in terms of the gross concrete section.

15. Values of R_{ijT} established from Step 12 for the structure with assumed negligible longitudinal rigidity and values of R_{ijL} established by one of the two methods in Step 14 for a structure with assumed negligible transverse rigidity may be summed to produce the external actions required to hold a structure with rigidity in both directions in the assumed deflected configurations. The internal actions resisting these displacements will be equal and opposite to the external actions:

$$R_{11} = -\left(R_{11L} + R_{11T}\right)$$

$$R_{21} = -\left(R_{21L} + R_{21T}\right), \text{ etc.} \qquad (3)$$

16. If, under a given loading condition, k, the deflections of the girders and slabs are Δ_{1k}, Δ_{2k}, ..., Δ_{ik}, ... Δ_{7k}, the total internal action at Joint i is the summation of the component internal actions at Joint i due to deflections at the other joints. Expressed as an equation, the total internal resisting force at Joint i is:

$$R_{i1}\,\Delta_{1k} + R_{i2}\,\Delta_{2k} + \ldots + R_{i7}\,\Delta_{7k} \qquad (4)$$

For equilibrium to exist, the internal action at each panel point must be equal and opposite to the external load at the same panel point, the latter having been computed in Step 8. Thus,

$$-R_{10} = R_{11}\,\Delta_{1k} + R_{12}\,\Delta_{2k} + \ldots + R_{17}\,\Delta_{7k}, \text{ etc.,} \qquad (5)$$

or

$$R_{10} = \left(R_{11L} + R_{11T}\right)\Delta_{1k} + \left(R_{12L} + R_{12T}\right)\Delta_{2k} + \ldots + \left(R_{17L} + R_{17T}\right)\Delta_{7k} \qquad (6)$$

Similar equations may be written for each of the seven girders (slabs), producing seven equations in seven unknown deflections for each loading condition.

17. The seven equations are solved for the seven unknown deflections of the girders and slabs for each condition of loading. The procedure must be repeated for a sufficient number of values of the Fourier module to result in convergence.

18. At this point the proper sine functions are applied as factors to component terms of the Fourier series and summations are calculated to produce the total theoretical deflections at each panel point. These deflections may then be employed to compute the girder resisting moments or the desired slab stresses (depending on the method used) for comparison with empirically determined values. Results of the first method are in terms of individual girder resisting moments, whereas the second and third methods result in longitudinal slab stresses, there being no way to evaluate resisting moments directly by these two methods. Combined effects of the separate wheel loadings may be most conveniently evaluated by making the calculations for a single concentrated load in a large number of positions and then evaluating the effects of the measured wheel reactions through the use of influence lines and surfaces.

Solution by Matrix Formulation of Folded Plate Equations—Third Method

1. The folded plate equations published by Goldberg and Leve (4) are in the general form:

$$P_{ijm} = F_{Fijm} + Q(= \Sigma C \delta) \tag{7}$$

where P_{ijm} is a final edge force, F_{Fijm} is a fixed edge force, and Q represents the internal edge force due to edge displacements. For equilibrium to exist at a joint, the final edge forces and moments produced by all members framing into the joint must sum to zero. Therefore, a relationship may be established between the fixed edge forces produced by external forces acting on the plates and the forces resulting from edge displacements. It is also possible to establish a relationship between the external joint displacements and the internal edge displacements. The external system having forces and displacements are conveniently related to a coordinate system having a constant orientation in space. The folded plate equations are related by Goldberg and Leve (4) to coordinate systems whose orientations vary with the orientations of the plates. The external forces and displacements are, in general, also designated in a different manner than are the internal forces and displacements. The fixed edge and external forces are related in the analysis through an equilibrium matrix:

$$\left[\Sigma F_{Fijm}\right] + [A]\,[Q] = \left[\Sigma P_{ijm}\right] = 0 \tag{8}$$

The internal edge displacements, δ, are related to the joint displacements, Δ, by the geometry matrix:

$$[\delta] = [B]\,[\Delta] \tag{9}$$

The [A] and [B] matrices are formulated so that one is the transpose of the other.

2. A stiffness matrix is formulated to relate the internal edge forces to the internal edge displacements:

$$[Q] = [S]\,[\delta] = [S]\,[B]\,[\Delta] = [S]\,[A]^T\,[\Delta] \tag{10}$$

and

$$[P] + [A]\,[Q] = 0 \tag{11a}$$

$$[P] + [A]\,[S]\,[A]^T\,[\Delta] = 0 \tag{11b}$$

3. If the matrix product, $[A]\,[S]\,[A]^T$ is designated by the single matrix, [K],

$$[P] + [K][\Delta] = 0 \tag{12a}$$

and

$$[\Delta] = -[K]^{-1}[P] \tag{12b}$$

4. Substitution of Eq. 12b in Eq. 10 yields

$$[Q] = [S][A]^{T}\left(-[K]^{-1}[P]\right) \tag{13}$$

5. Final edge forces are represented by the summations of the fixed edge forces and the forces due to edge displacements.

6. Forces at any point within the plates may be evaluated through use of equations furnished by Goldberg and Leve (4).

7. To reduce the sizes of the matrices employed, symmetric and antisymmetric load systems are employed, the box section being split at the center web. A discussion of this treatment of loads is given by Newell (5). As applied to the box section, this treatment of loads has the following implications at Joints C and H, at the top and bottom of the center web:

a. Symmetric Case.—Displacements and rotations perpendicular to the plane of symmetry, and external forces producing shears parallel to the plane of symmetry are zero (Fig. 35). External moments and forces normal to the plane of symmetry, resulting from the hypothetical loads on the removed half of the structure, produce, in effect, built-in restraints which prevent the normal displacements and rotations. Because these external forces nullify similar but oppositely disposed forces in the half structure, these oppositely disposed forces need not appear in the F-matrix, nor do the zero displacements appear in the Δ-matrix. There are no bending moments or normal shears in the web, CH, but there may exist longitudinal shears and membrane stresses. Therefore, the stiffness factor used in computing S and N must be halved.

b. Antisymmetric Case.—Displacements parallel to the plane of antisymmetry, and forces and moments normal to the plane of symmetry are zero (Fig. 36). There exist vertical and longitudinal shears parallel to the plane of antisymmetry, resulting from the hypothetical antisymmetric loads, restraining the Joints C and H from movements parallel to the plane of antisymmetry. These external forces nullify similar but oppositely directed forces in the half structure, which need not be included in the F-matrix. Displacements parallel to the plane of antisymmetry are not included in the Δ-matrix. There exist no longitudinal shears or planar stresses in the center web, but there may exist transverse moments and shears. The transverse flexural stiffness used in computing M and V must be halved.

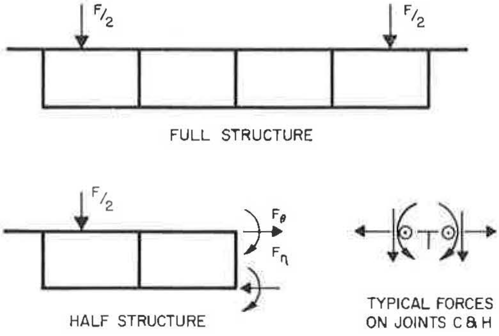

Figure 35. Force distribution for symmetric loading.

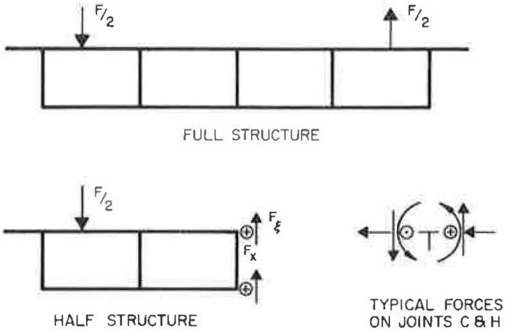

Figure 36. Force distribution for antisymmetric loading.

c. The displacements and internal forces may be found by superposing the results of the two cases.

As has been stated before, the mathematical work involved in the theoretical analysis was performed in large measure by an IBM 704 through the use of FORTRAN programs. The machine work entailed calculation of frame constants for slab components of the analogous Vierendeel truss, including distribution and carry-over factors for loads and displacements; calculation of coefficients for fixed edge moments and reactions; distribution of moments through the truss by the Bridge Department's Multi-story Frame Distribution Program; modification of fixed edge reactions due to joint relaxations during the distribution process; solution of simultaneous or matrix equations for panel point displacements; and calculation of resisting moments or longitudinal slab stresses. The actual mechanics of applying these methods are described only briefly herein. The theoretical methods will be discussed in more detail in a final project report.

For dead load, the calculations were made for the actual loads of the components of the structure (expressed, of course, in terms of their Fourier components). For live loads, calculations were first made for a 1,000-kip concentrated load placed on the upper slab at the fifth points of the bays. The results of these calculations were used to plot influence lines or surfaces of deflections, and resisting moments (first method) or longitudinal stresses (second and third methods). Transparent overlays depicting the test vehicle wheel locations in plan or section were used in conjunction with these charts to permit computation of deflections and resisting moments or stresses for the test vehicle in various transverse locations. In general, the calculations were made for two longitudinal locations of the vehicle, i.e., with the rear axle at the quarterspan and midspan, for comparison with the empirically determined values.

COMPARISON OF THEORETICAL AND EMPIRICAL RESULTS

To test the relative applicability of the three analytical methods employed, computed theoretical results were compared with values measured experimentally. Such comparisons may be made in several ways. Certain complications arise in establishing the comparisons.

Results of theoretical calculations are given in terms of resisting moments or longitudinal stresses, and deflections, whereas the experimental measurements comprised strains and deflections. Establishment of a comparison between any measurement and its theoretical counterpart requires knowledge of an effective modulus of elasticity for the concrete in the structure, which may be difficult to assess.

As noted earlier, measured strains and deflections do not accord fully with expectations based on idealized structural behavior. Dead load, total, tensile and compressive stresses, and external and internal moments may be made to satisfy static equilibrium principles simultaneously only by using a somewhat arbitrary system of longitudinal strain averaging and by assuming a relatively low value for effective concrete modulus. Live load, total, tensile and compressive stresses cannot be made to satisfy statics simultaneously, regardless of choice of concrete modulus. External and internal moments may be made nearly equal for experimental moduli if the moments of the total compressive stresses are computed about the locations of the total tensile stress resultant. The known external moments always exceed the summations of internal stringer resisting moments computed from strain patterns and measured concrete moduli or reinforcing steel calibration factors. By contrast, the various theoretical methods employed produce results complying with the principles of static equilibrium. Comparisons between actual, theoretical and measured strains and deflections will, therefore, be of less importance than comparisons of the relationships these individual values, translated into resisting moments, bear to their summations.

When comparisons are made between measured strains for the lower slab reinforcement and strains computed by the second and third analytical methods, consideration must be given to the fact that these methods deal with the gross concrete section. The problem has been treated herein by increasing the theoretical strains computed for the lower slab by the ratio of the gross area of the lower slab to the transformed area of the lower layer of reinforcing steel. This ratio is of smaller magnitude

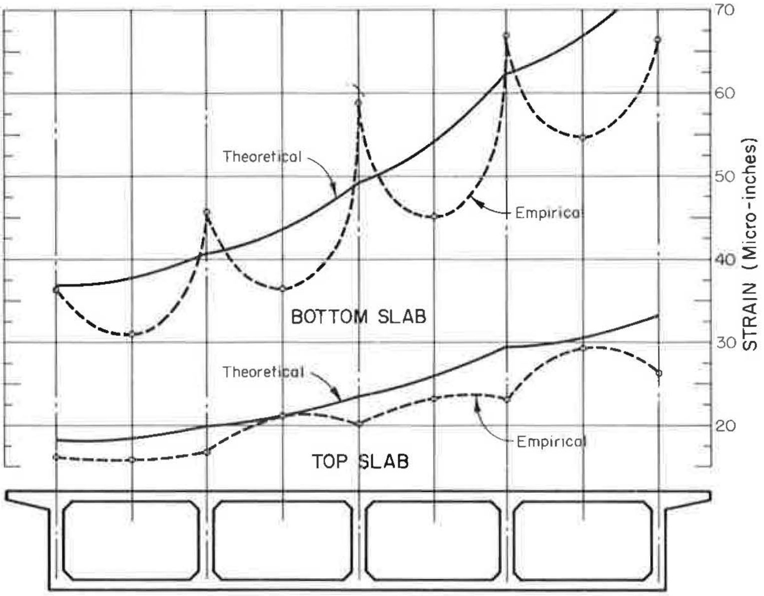

Figure 37. Comparison of theoretical and experimental live load strain distributions for test vehicle in transverse Position 13.

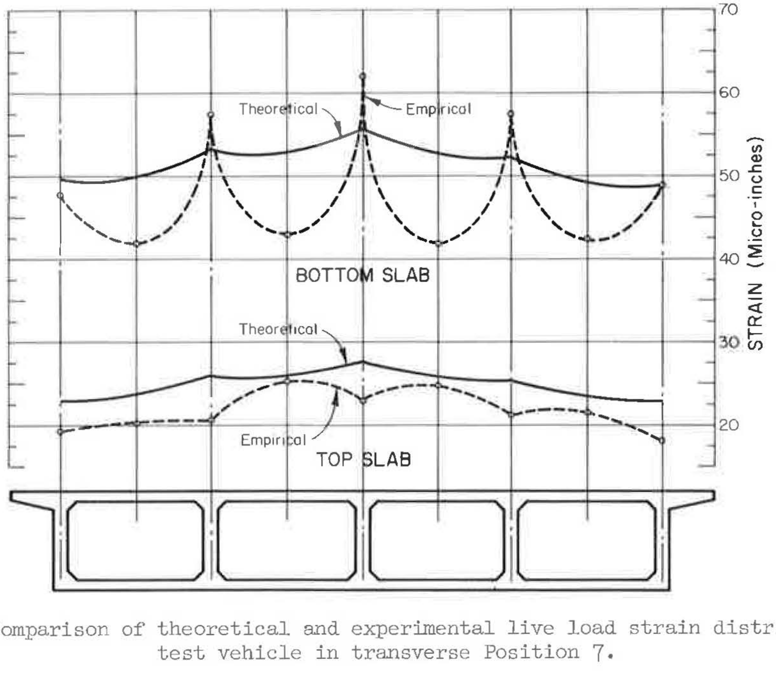

Figure 38. Comparison of theoretical and experimental live load strain distributions for test vehicle in transverse Position 7.

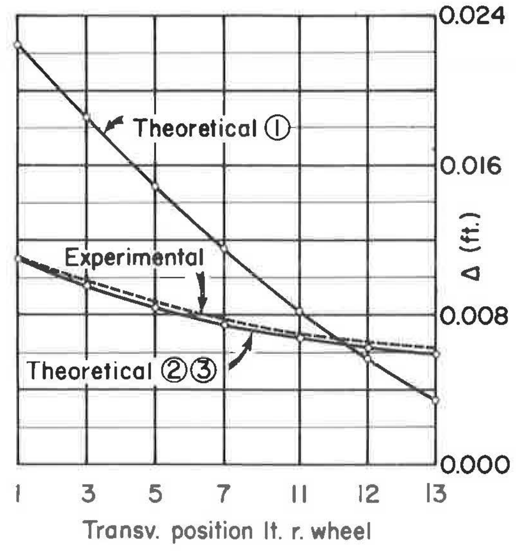

Figure 39. Comparisons of theoretical and experimental live load deflections as functions of transverse position of test vehicle; Girder A.

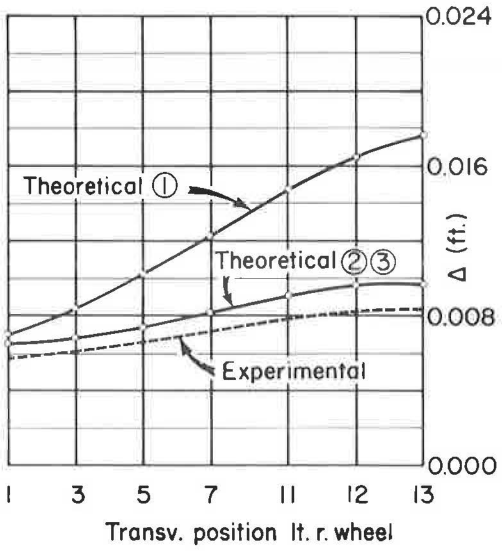

Figure 40. Comparisons of theoretical and experimental live load deflections as functions of transverse position of test vehicle; Girder D.

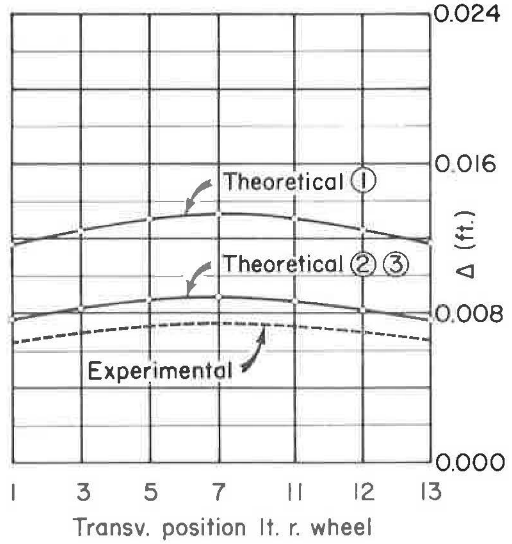

Figure 41. Comparisons of theoretical and experimental live load deflections as functions of transverse position of test vehicle; Girder C.

than it should be because a significant area of the concrete stems has been neglected. The discrepancies between theoretical and measured strains will, therefore, not appear commensurate with the discrepancies between measured and computed moments.

Because the folded plate equations do not take into consideration the orthotropy of the reinforced slab, this approximation is not rigorous. However, because the lower slab was cracked only transversely and the gross section is likely to be the applicable section for the other types of forces treated by the folded plate equations, the approximation, based on the assumption that all longitudinal stress computed for the lower slab is concentrated in the reinforcing steel, should closely predict the true strain pattern. In Figures 37 and 38, theoretical live load strains (the lower slab strains having been augmented as discussed previously) are compared with strains determined experimentally for the test vehicle in Positions 7 and 13.

Theoretical vs Empirical Live Load Deflections

Figures 39, 40 and 41 depict the comparisons between theoretical and measured deflections for the exterior, interior, and center girders. Deflections computed by the first method show very little agreement with the experimental values. Results of

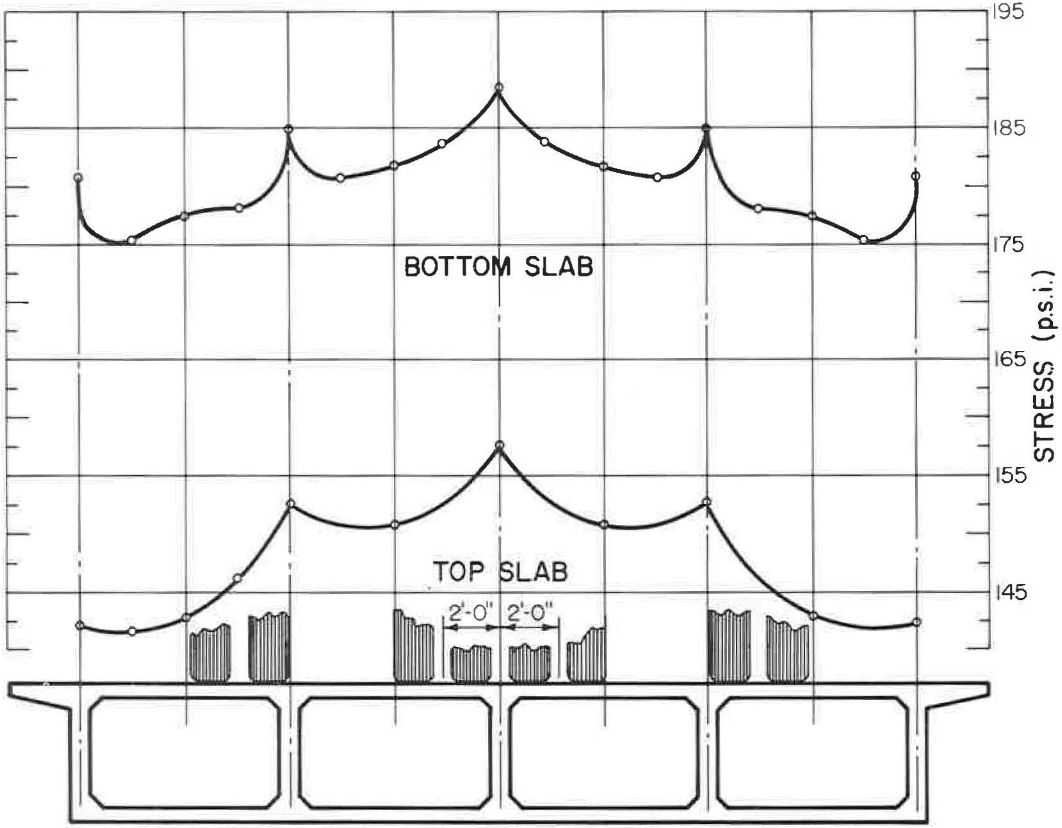

Figure 42. Theoretical live load stress distribution computed by third method for test vehicles in hypothetical positions 4.10 and 11.43 (critical for center girder), with rear axles at midspan.

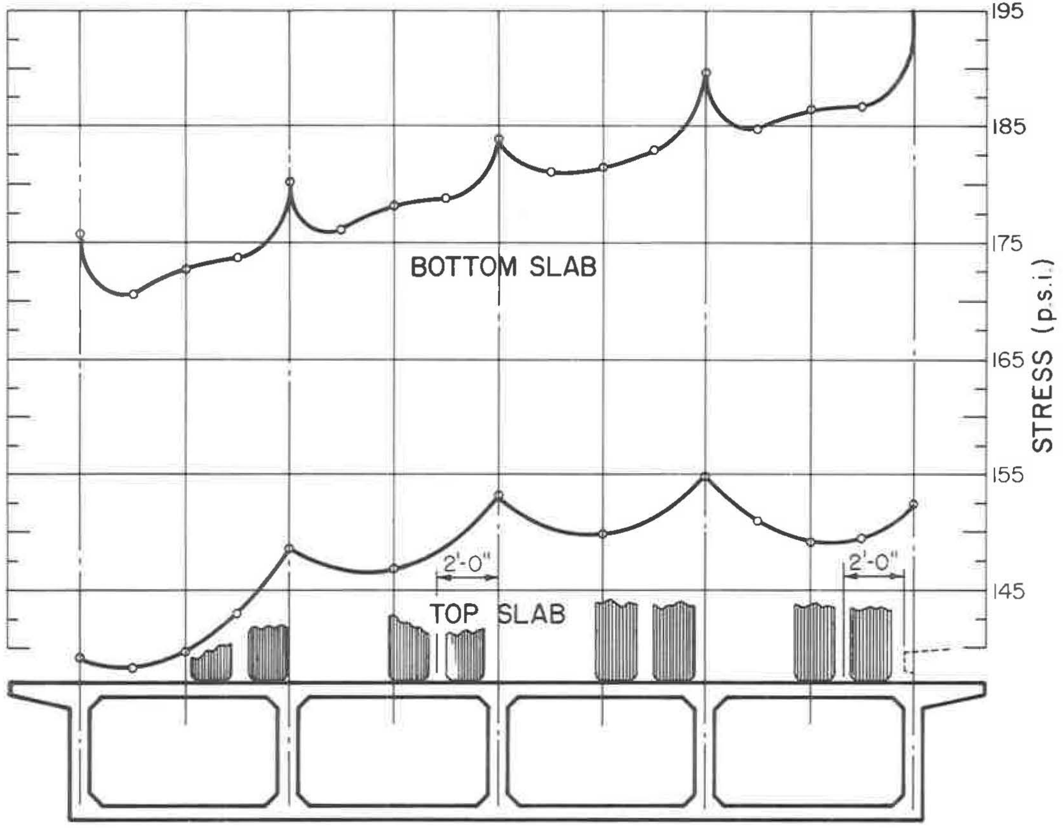

Figure 43. Theoretical live load stress distribution computed by third method for test vehicles in hypothetical positions 4.10 and 12.30 (critical for exterior girder), with rear axles at midspan.

TABLE 23

THEORETICAL LIVE LOAD MOMENTS[a]
(First Method)

Girder	Resisting Moment (kip-ft)	Proportion of Total
A	238	0.131
B	403	0.222
C	423	0.233
D	448	0.247
E	301	0.166
Total	1,813	-

[a] Position 4.10 + 12.30; rear axle at midspan; E_c = 432,000 ksf.

TABLE 24

THEORETICAL LIVE LOAD MOMENTS[a]
(Second and Third Methods)

Girder	Resisting Moment (kip-ft)	Proportion of Total
A	273	0.150
B	408	0.223
C	420	0.230
D	427	0.234
E	298	0.163
Total	1,827	-

[a] Position 4.10 + 12.30; rear axle at midspan; E_c = 432,000 ksf.

the second and third methods were plotted as one curve. Although trends of the latter and experimental curves show considerable parallelism, the magnitudes may differ by as much as 20 percent. Theoretical deflections were computed for an elastic modulus of concrete of 432,000 ksf (3,000,000 psi).

Theoretical vs Empirical Dead Load Deflections

Dead load deflections, as experimentally determined and as computed by the second and third methods, are listed in Table 1. Because the falsework was removed when the concrete was only 9 days of age, an elastic modulus of 288,000 ksf (2,000,000 psi) was used in the theoretical calculations.

Theoretical vs Empirical Live Load Moments

Figures 42 and 43 depict stress patterns computed by the second and third analytical methods for test vehicles in Positions 4.10 and 11.43, and 4.10 and 12.30, critical for center and exterior girders, respectively. These stresses were computed at the quarter-points, midpoints, and panel points of each slab using equations developed by Goldberg and Leve (4) for folded plates, for a 1,000-kip concentrated load moving transversely across the structure, and using the resulting influence lines in conjunction with a transparent overlay showing the test vehicle wheel locations in section. Mean stresses in each bay were computed by Simpson's rule, and these were used to compute internal resisting moments.

Resisting moments for the two conditions mentioned in the previous paragraph were also calculated by the first analytical method. Because resisting moments are the direct result of this method, the results for the 1,000-kip load were used to plot an influence surface, which was used in conjunction with a transparent overlay showing the test vehicle wheels in plan to determine moments as functions of transverse position of the left rear wheel. Results of these calculations are listed in Tables 13 through 24.

Theoretical vs Empirical Dead Load Moments

The theoretical dead load strain distribution, computed by the third analytical method, is depicted in Figure 44. Mean strains and stresses were computed for the gross concrete section for each half-bay by Simpson's rule and were used in computing dead load resisting moments, which are listed in Table 7.

A method of evaluation of the effects of slab cracking on load distribution is shown in Figure 45.

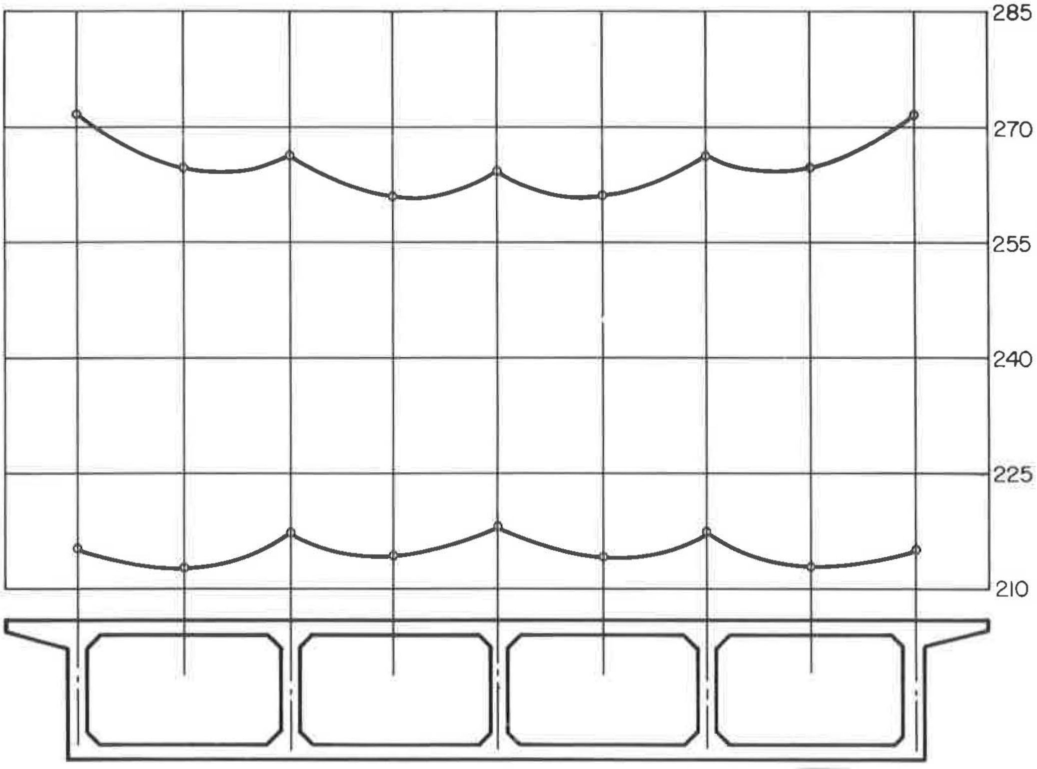

Figure 44. Theoretical dead load stress distribution computed by third method.

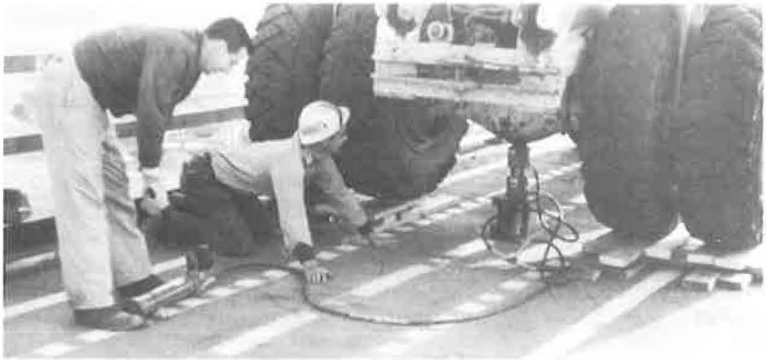

Figure 45. Cracking deck slab with 47-kip rear axle reaction on 10- by 14-in. plate to evaluate effects of slab cracking on load distribution.

Model Tests

Results of tests on plastic and concrete models by the University of California will be discussed in a separate report to be published at a future date.

CONCLUSIONS

The following conclusions may be drawn from studies of the results of testing the full-sized prototype:

1. Dead load deflections measured in the field agreed closely with those computed theoretically.
2. Correlation of total dead load resisting moments with known acting moments is good, provided that suitable modifications of concrete modulus are made to account for the effects of creep and shrinkage cracking. A satisfactory correlation exists among the ratios of individual stringer moments to the total resisting moment, based on 1961 AASHO specifications and similar ratios determined experimentally (Tables 5 and 6).
3. Live load distribution without an intermediate diaphragm indicated about 15 percent greater transverse distribution in the box girder than allowed in the 1961 AASHO specifications (Figs. 28 and 29). For this particular structure and test vehicle, the distribution factor determined experimentally approximated one-eighth of the stringer spacing.
4. Addition of a diaphragm at midspan resulted in a very small change in the distribution of moments across the transverse section; average change was 2 percent.
5. Addition of curbs and railings resulted in a large increase of total section stiffness. Changes in bottom main reinforcement strains were insignificant. Large reductions in top slab compressive strains were measured.
6. Theoretical analysis by the first method, in which the longitudinal stiffness of the structure is based on discrete stringer stiffnesses, thus neglecting the inherent longitudinal rigidity of the closed box section, is poor. This lack of correlation is more amply demonstrated by comparison of theoretical and empirical deflections in Figures 39, 40 and 41 than it is by consideration of Tables 13, 16, 17, 19, 22, and 23. The hypothetical placement of two trucks on the span in the latter calculation spreads the live loading over a relatively large proportion of the structure's width and tends to obscure the lack of consideration of torsional rigidity in this analytical approach.
7. The third analytical method did not accurately predict the patterns of transverse strain distribution in the deck slab or the lower layer of reinforcing steel for dead load (compare Figs. 21 and 22 with Fig. 34) or for live load (Figs. 37 and 38). However, when the theoretical or empirical strain patterns are used to compute stringer resisting moments, correlation between theoretical and experimental ratios is excellent (compare Tables 13 and 16 with 18, 19 and 22 with 24, and 5 with 7). This correlation is much poorer when the moments of the compressive resultants are taken about the tensile resultants (compare Tables 14 and 15 with 18, and 20 and 21 with 24).

ACKNOWLEDGMENTS

This research was financed in part with Federal-aid highway funds and was conducted with the approval of the U. S. Bureau of Public Roads. The work described herein was accomplished by the California Division of Highways, Bridge Department, of which J. E. McMahon is head. Instrumentation of the field prototype was accomplished by the California Division of Highways, Materials and Research Section, directed by F. N. Hveem. Professor A. C. Scordelis of the University of California furnished a valuable outline of possible analytical methods to be applied in studying behavior of the structure.

Acknowledgment is gratefully made to the following for their assistance in field work, data reduction and other services: H. R. Myers, William Chow, H. Bornhorst, J. Gates, J. Haug, P. Ibold, J. McKee, G. Matchette, A. Nelson, H. Stup, T. Suyetsugu, R. Tomlinson, J. Wing and J. Wyles, Violet Asano, Don Lancaster and the Judson Steel Corporation.

REFERENCES

1. Billig, Kurt. Structural Concrete. New York, St. Martins Press, 1960.
2. Hulsbos, C. L., and Linger, D. A. Dynamic Tests of a Three-Span Continuous I-Beam Highway Bridge. Highway Research Board Bull. 279, pp. 18-46, 1961.
3. Newmark, N. M. A Distribution Procedure for the Analysis of Slabs Continuous Over Flexible Beams. Univ. of Illinois Engineering Experiment Station, Bull. 304, June 17, 1938.
4. Goldberg, J. E., and Leve, H. L. Theory of Prismatic Folded Plate Structures. Publications, Int. Assoc. of Bridge and Structural Eng., Vol. 17, 1957.
5. Newell, J. S. Symmetric and Anti-symmetric Loadings. Civil Engineering, April 1939.
6. Holcomb, R. M. Distribution of Loads in Beam-and-Slab Bridges. Iowa Highway Research Board Bull. 12.

Behavior of Elastomeric Bearing Pads Under Simultaneous Compression and Shear Loads

WILLIAM B. NACHTRAB and ROBERT L. DAVIDSON
Bureau of Materials, Testing and Research, Pennsylvania Department of Highways

A study of elastomeric bearing pad performance was conducted on laboratory-size test pieces but under conditions which approached as nearly as feasible the cyclic shear conditions found on actual structures rather than the initial shear conditions of currently published investigations. It is shown that the current definition of shear modulus is not applicable to elastomeric materials. A simple formula is developed and the constants are determined by which a satisfactorily close approximation of the stress/strain curve can be reconstituted mathematically. The parameters that affect such curves were found to be testing rate, degree of strain, and previous deformation history of the sample. Other parameters such as grain direction and shape factors of less than unity are suspected of affecting these curves but present study was not conclusive. With a knowledge of the effects of these parameters and a stress/strain curve established by a standard procedure, it is possible to compute pier shear forces as the engineering problem dictates.

•PRACTICAL KNOWLEDGE of shear/strain curves, their composition, derivation, and interpretation with a knowledge of the factors which influence deviations from these curves and the extent of such deviations is essential to intelligent elastomeric bridge pad design. The response of elastomers to external force is not the same as the response of other construction materials. This difference can lead to erroneous and costly conclusions unless the difference is recognized by the engineer and the pad is designed accordingly.

OBJECTIVE

The objective of the current investigation was to determine the shear strain characteristics of molded neoprene slabs on laboratory-size test pieces and as far as possible to interpret such results in terms of design performance. The properties primarily investigated were the characters of the compressive and shear stress/strain curves (hereinafter referred to as the compression and shear curves, respectively). Other properties investigated were the effect of shape factor, hardness, grain direction, variable cyclic loading and loading rate.

METHOD

The method of investigation consisted of cutting laboratory test samples from sheet stock submitted by various suppliers and subjecting these samples to the tests indicated. The maximum size of sample that could be accommodated in the current test equipment was 3 by 3 in. All compression and shear deformation rates were 0.05 in./min unless otherwise stated.

In general, the method employed was to cycle the samples in compressive deformation to reproducibility at 500-psi compressive stress and then, while maintaining this

---

Paper sponsored by Committee on Bridges.

compressive load, to cycle the samples in shear deformation, alternately in both a positive and a negative direction from this initially compressed position to a numerical distance equal to one-half, or other stated factor, of the original uncompressed thickness. A standard method of test was developed and is included as Appendix B.

EQUIPMENT

The equipment consisted of a shear modulus device similar in design to the Maguire machine (1) with 4- by 4-in. steel compression heads and a steel drawplate. The compression heads and drawplate were machined, ground, and polished in the earlier investigations, but knurled (40 lines to the inch) heads and plate were substituted in the later work. Four dial gages were used to determine pad compressed thickness, one dial on each side of each pad. The average of the readings of the two dials on the opposite sides of each pad was taken as pad compressed thickness. Vertical deformations were produced by mounting the shear modulus device in a twin-screw Tinius Olsen universal testing machine of 20,000-lb capacity.

One dial gage, centered on the draw axis, was used to determine shear deformation, accomplished with a double-acting hydraulic cylinder. Rate of shear loading was controlled by a needle valve which controlled the rate of fluid feed to the hydraulic cylinder. Shear forces in the positive shear direction were measured with a tension ring. Compression rings were not available; therefore, shear forces in the negative shear direction were not measured.

COMPRESSION CHARACTERISTICS

Figure 1 is a typical compression curve. Line abc represents the initial cycle. It originates at the origin, a, and proceeds to the maximum, b, along line ab. The unloading portion is represented by line bc. The curve of the second cycle originates at point c, proceeds to d at maximum load, and returns to e when unloaded. Succeeding cycles follow a similar pattern. The increment of increase in both the maximum compressive strain and the compressive strain at zero load decreases with each succeeding cycle until eventually the cycles reproduce. For the purpose of this study, all

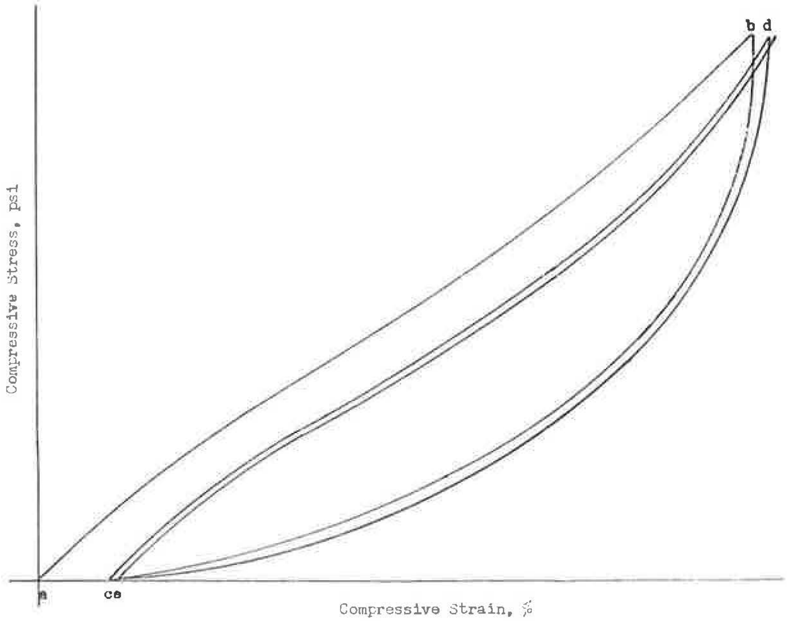

Figure 1. Typical compression curve.

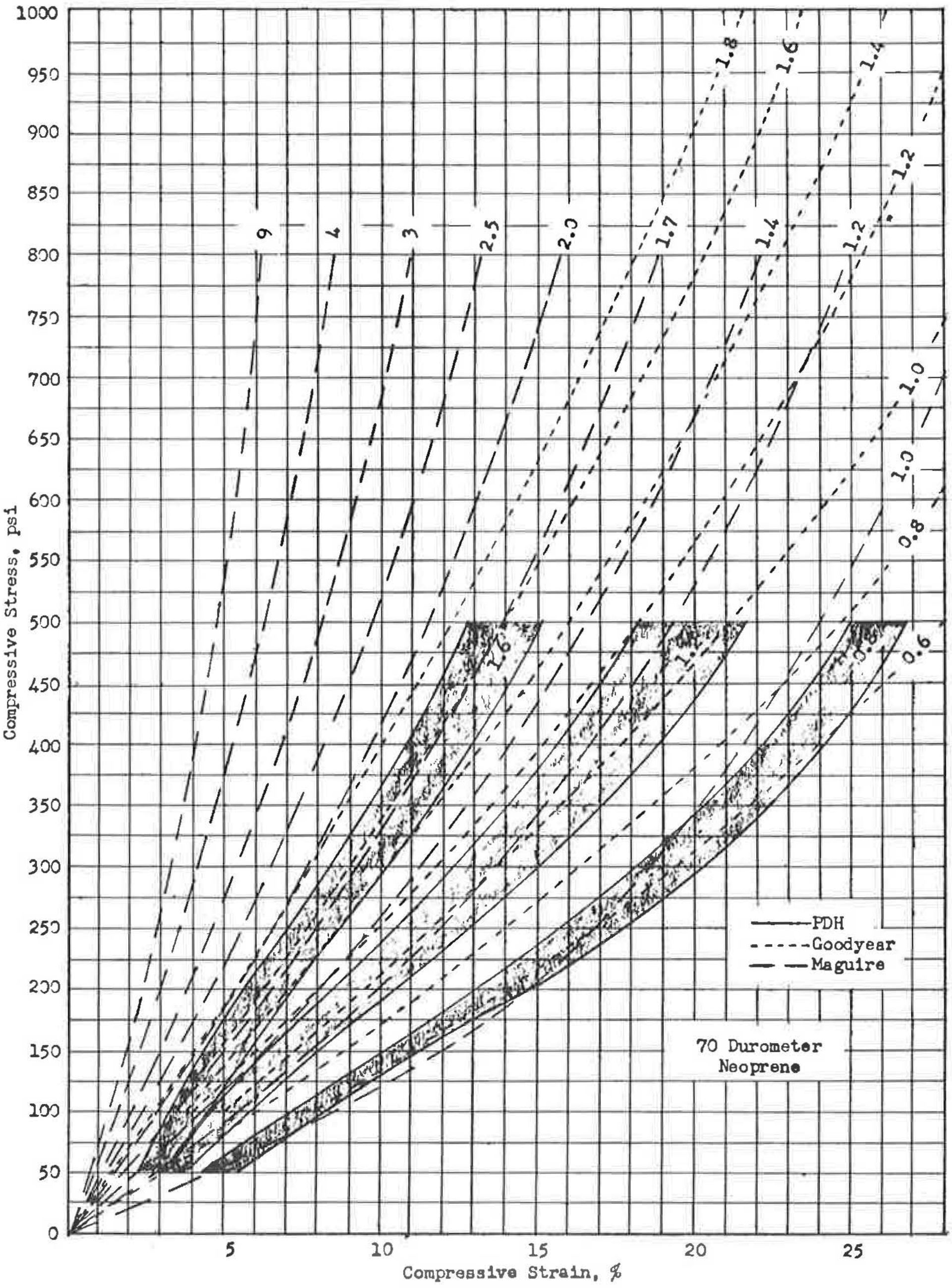

Figure 2. Composite compression curves.

samples were cycled in compressive loading to reproducibility before shear loading to minimize the effects of stress relaxation and creep.

Figure 2 is a composite of the loading portions of the reproducible compression curves of 74 durometer neoprene compressed to 500-psi stress each cycle. The solid line on either side of each shape factor designation represents the high and low value obtained at that shape factor. Values from the literature (1, 2) are plotted for comparison. Compressive deformation values are in some measure dependent on the condition of the compressing surfaces (2): the smoother the surface, the higher the deformation values. The Goodyear values were based on bonded samples presumably compressed to 1,000 psi. The Maguire values (1) were obtained on concrete and steel surfaces and were compressed to 2,000 psi.

In general, it was found that the area of the compression diagrams increased with percent compressive strain; i.e., lower shape factor or softer materials gave greater hysteresis curves (Figs. 3 and 4). It was also found that ff', the relative energy loss between the input and recovery portions of the hysteresis curves, was independent of the shape factor and hardness per se but dependent on the testing rate if the testing rate exceeded the recovery rate. Recovery rates were exceedingly low; consequently, practical testing rates were always greater than the recovery rates. Therefore, the value of ff' was dependent on the difference between these two rates and increased as the difference increased. In addition, ff' was dependent on surface condition; the smoother the compressive surfaces, the greater the freedom of compressive expansion and corresponding increase in the hysteresis curve.

The effect of increasing the maximum value of the cyclic load is illustrated in Figure 5. Line ab represents the loading portion of the initial cycle to 250-psi compressive stress; line bc represents the unloading portion. Line $\overline{cd}$ represents the loading portion of the reproducible cycle to 250-psi compressive stress, and line $\underline{dc}$ represents the unloading portion. Line cde represents the loading portion of the initial cycle to 500-psi compressive stress, as well as the loading portion $\overline{cd}$ of the reproducible cycle to 250-psi compressive stress plus its extension de. Such a cycle whose maximum compressive stress is different from the maximum compressive stress of the previous cycle is referred to as a transition cycle. Line ef represents the unloading portion of the transition cycle to 500-psi compressive stress. Line $\overline{fg}$ represents the loading portion of the reproducible cycle to 500-psi compressive stress, and line $\underline{gf}$ is the unloading portion. Each successively increasing increment of compressive stress follows a similar pattern with the additional loading portion of the curve of the transition cycle being an extension of the reproducible loading portion of the previous loading and with

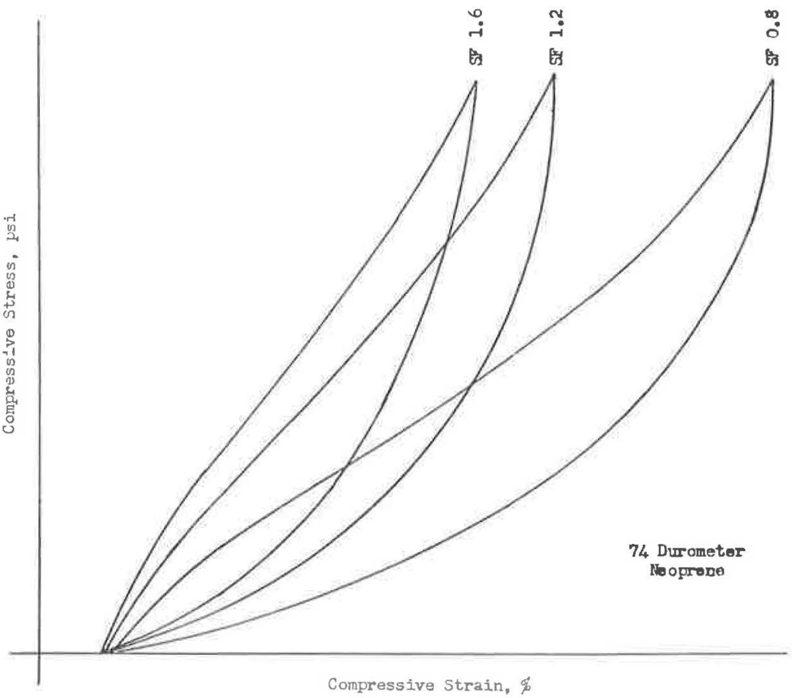

Figure 3. Effect of shape factor on compression curves.

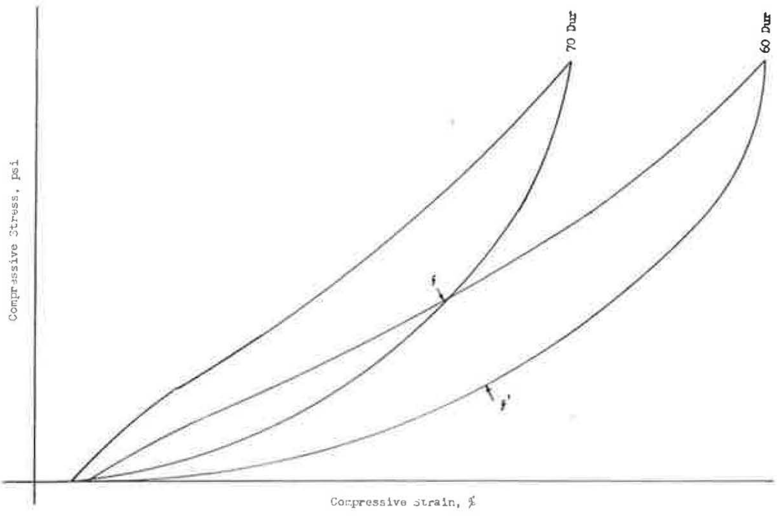

Figure 4. Effect of hardness on compression curves.

the reproducible curve falling below the transition curve. From this it can be seen that cyclic compression curves are dependent on the maximum load at which cycled; therefore, the maximum stress values must be stated when such curves are presented.

The effect of decreasing cyclic load is illustrated in Figure 6. Line $\overline{aba}$ represents the loading portion of the reproducible cycle of the maximum compressive stress at which cycled (in this case, 1,750 psi). Line $\overline{aca}$ represents both the transition and the reproducible loading portions of the cycle at the next succeeding decreasing increment of load (1,500-psi compressive stress), line $\overline{ada}$ at the next increment, etc. In all cases, the loading portion of the curve follows the curve of the maximum cyclic load to which the sample was compressed and does not return to the loading portion of the corresponding reproducible curve for increasing loads from Figure 5. From this it follows that compression curves are dependent on the previous compressive history of the sample (3).

The effect of loading amplitude is illustrated in Figure 7. By loading amplitude is meant the difference between the minimum and maximum compressive stress of any one cycle. A sample may be loaded in a single increment from the minimum to the maximum compressive stress on each cycle as illustrated in Figures 1, 3 and 4, or it may be loaded in successively changing increments as illustrated in Figure 5. The first type of loading is referred to as a single increment cycle and the second type of loading is a multiple increment cycle. The dotted line ab is a plot of the maximum values obtained from the transition curves of a uniformly increasing incremental compression similar to that illustrated in Figure 5 and as determined by points a, b, e, etc. The dotted line cd represents the maximum incremental reproducible values as determined by points c, d, g, etc. The solid line ae represents the loading portion of the actual initial cycle of a duplicate sample of the same material loaded from zero to maximum in a single increment. The solid line fg represents the loading portion of the actual single increment reproducible cycle and is identical with the loading portion of the final increment of the multiple increment reproducible cycle as represented by xy (Fig. 5).

It is apparent from Figure 7 that small, uniformly increasing loading has a stiffening effect on elastomers. Line ae should initially follow line ab and then deviate to the left. This deviation is proportional to the time differential required by the two testing methods to reach the same point being compared because elastomers take a permanent set under load and this set increases with loading time. Line ae is initially less than ab and remains so for a substantial length of the curve. The low rate of testing was

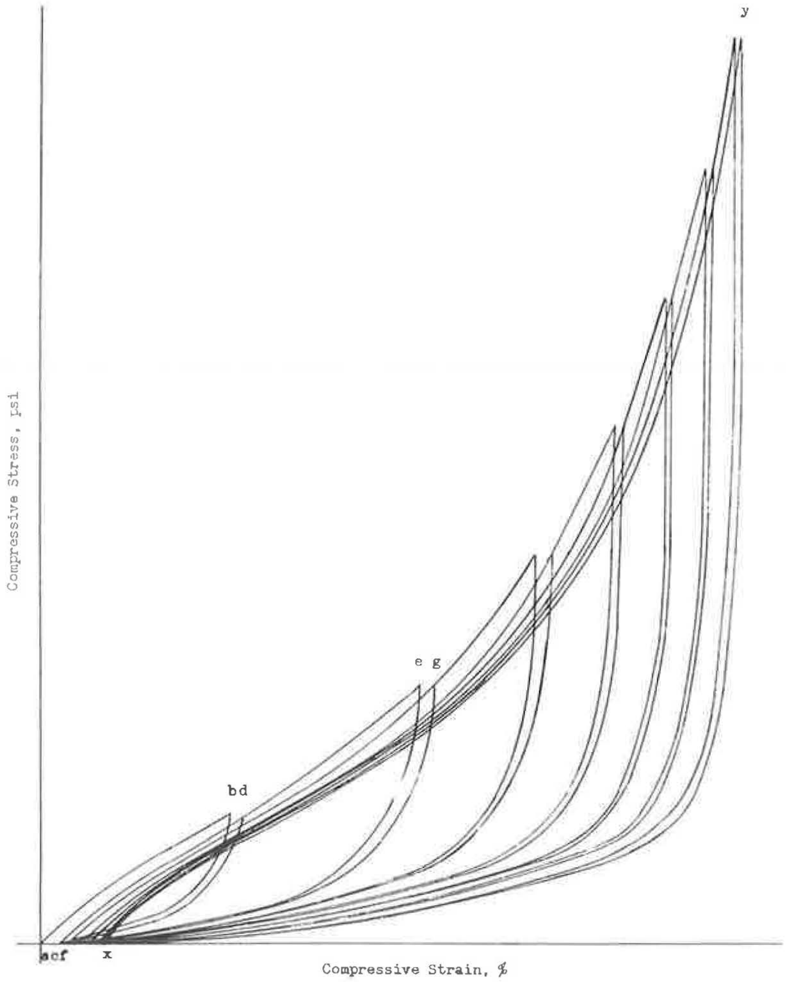

Figure 5. Effect of increasing compressive loads.

insufficient to produce any heat buildup in the samples; thus, this stiffening cannot be accounted for by the Joule effect. This increase or stiffening in ab can only be explained by some other phenomenon associated with the mechanical working of the sample.

The fact that the loading portion of the single increment reproducible curve is identical with that of the final multiple increment reproducible curve is encouraging. In fact, not only were the loading portions of the curves identical, but the entire hysteresis loops were also identical; this means that although compression curves are dependent on previous compressive history of the sample, they are dependent only on the previous maximum values and not on the sequence in which the maximums are obtained.

Successive determinations of percent compression on the same sample often give progressively smaller values for percent compression with each determination (all calculations based on original uncompressed thickness). This may be another manifestation of the same stiffening due to mechanical working previously indicated.

It must be pointed out that this study was made entirely under compressive loads. A true study of the compressive character of an elastomer should be made on a tension/compression diagram wherein the sample is stretched as much in one direction as it is compressed in the other. However, the study herein presented is valid for the

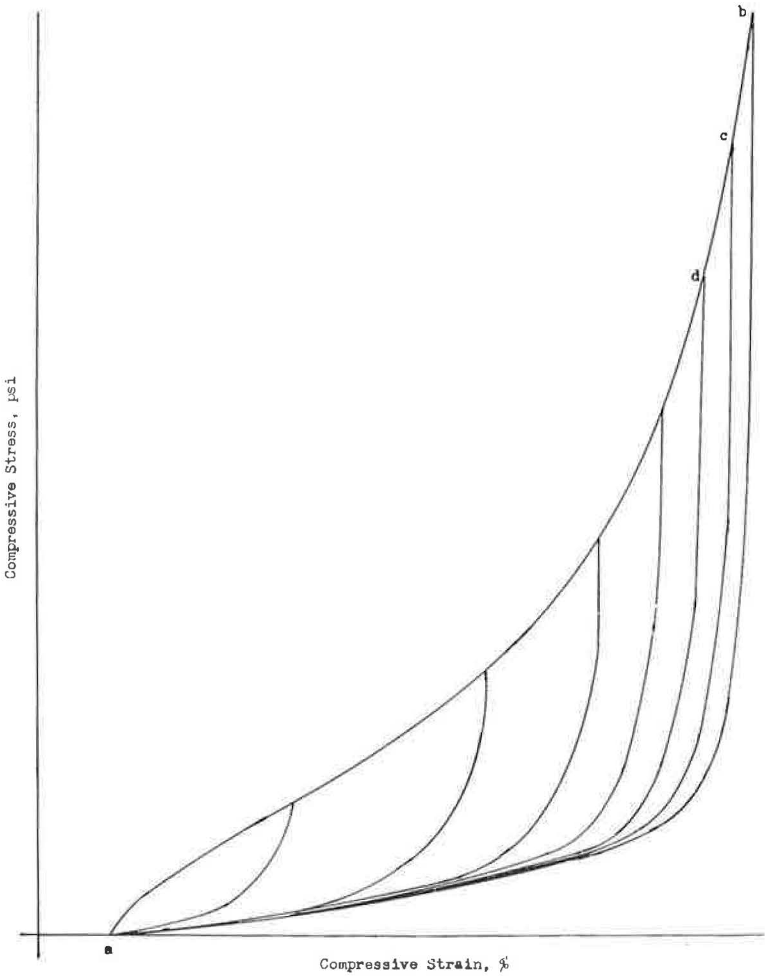

Figure 6. Effect of decreasing compressive loads.

intended application because only compressive loads varying from zero to maximum will be encountered and it is the cumulative effects of this continual compression that must be evaluated.

SHEAR CHARACTERISTICS

Typical shear curves were of two types. Figure 8 is typical of the first type. The portion above the horizontal axis is under positive shear load and the portion below the horizontal axis is under negative shear load. Line abcde represents the initial cycle. It originates at the origin, a, and increases to b along the line ab which represents the positive loading portion of the first cycle. The unloading portion is represented by line bc. At point c, the positive shear load becomes zero and the negative shear load is applied. The negative loading portion of the cycle is represented by line cd. The negative unloading portion is represented by de which completes the initial cycle.

The stress values of the negative loading could not be determined with present equipment, but the value of D/T at maximum negative load was determinable since D is deformation and T is compressed thickness at D deformation (Appendix A), both of which can be measured; therefore, the dotted lines were plotted to indicate the extent to which samples were cycled.

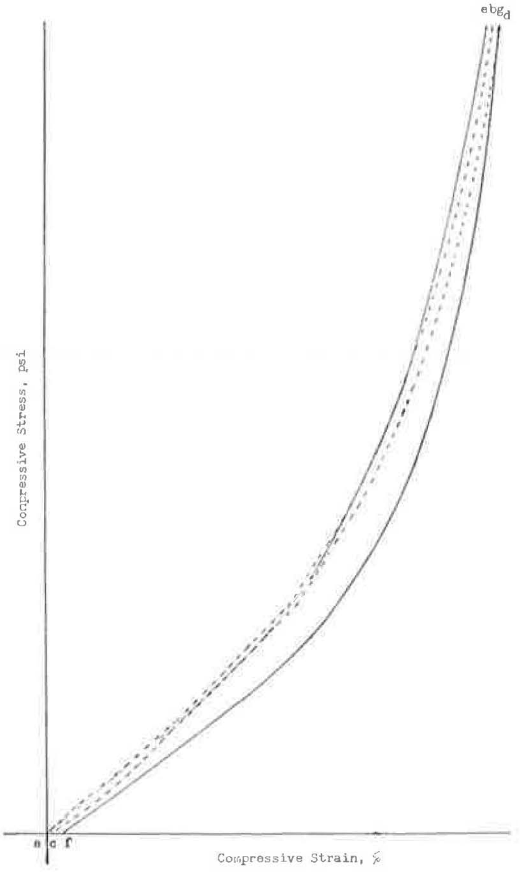

Figure 7. Effect of loading amplitude.

The second cycle is represented by the curve efghi. Succeeding cycles approach the curve ijklm with the following characteristic trends: (a) point f becomes increasingly greater along both axes; (b) a portion of ef approaches linearity and this linear portion increases with each cycle; and (c) the incremental increase in the values of f as well as the increase in the linear portion of ef becomes less with each cycle until eventually succeeding cycles reproduce. The curve ijklm represents the reproducible cycle. Unless otherwise stated, all shear computations are made from values taken from these reproducible cycles.

The characteristics of Type 1 shear curves are as follows:

1. The curve of the initial cycle is not linear over any portion of its path.

2. The horizontal (shear) force transmitted to the piers at any given deformation is greater for the same deformation on the second and succeeding cycles than on the initial cycle.

3. If the bearing pad is once deformed, there always remains a residual shear force on the pier at zero horizontal deformation.

4. The reproducible shear curves approach linearity over that portion of the curve from D/T = 0 to a point at which the sample starts to slip (within the limits herein investigated) but do not pass through the origin. With equipment capable of obtaining negative as well as positive loading values from maximum negative position to maximum positive position, and vice versa, on continuously loaded cycles at uniform loading rate, it is expected that the linear portion would begin well into the negative portion of the curve and continue to the positive maximum.

5. As with compression deformations, the hysteresis curves for shear deformations and the values computed from these curves are dependent on testing rate, if rate of shear exceeds recovery rate.

6. The slope of the curve, and again the values computed therefrom, are dependent on the degree of deformation at which cycled and on the previous deformation history of the sample.

7. Deformations in direction of the grain give more uniform values than those computed from cross-grain deformations.

This type of curve is in agreement with the work of Wilkinson and Gehman (4).

The second type of shear curve is represented in Figure 9. In this type, the curves of the second and succeeding cycles lie very near the curve of the initial cycle and may quite often undercut the curve of the initial cycle. The curve of the initial loading cycle may even approach linearity over a portion of its length. This type of curve is in agreement with the Maguire report (1). The curves from the Maguire report are essentially linear after the first 10 to 20 percent deformation. In this type of curve, the curve of the second cycle will approach linearity, but normally the slope will be less than that of the curve of the initial cycle. With each succeeding cycle, the slope of the

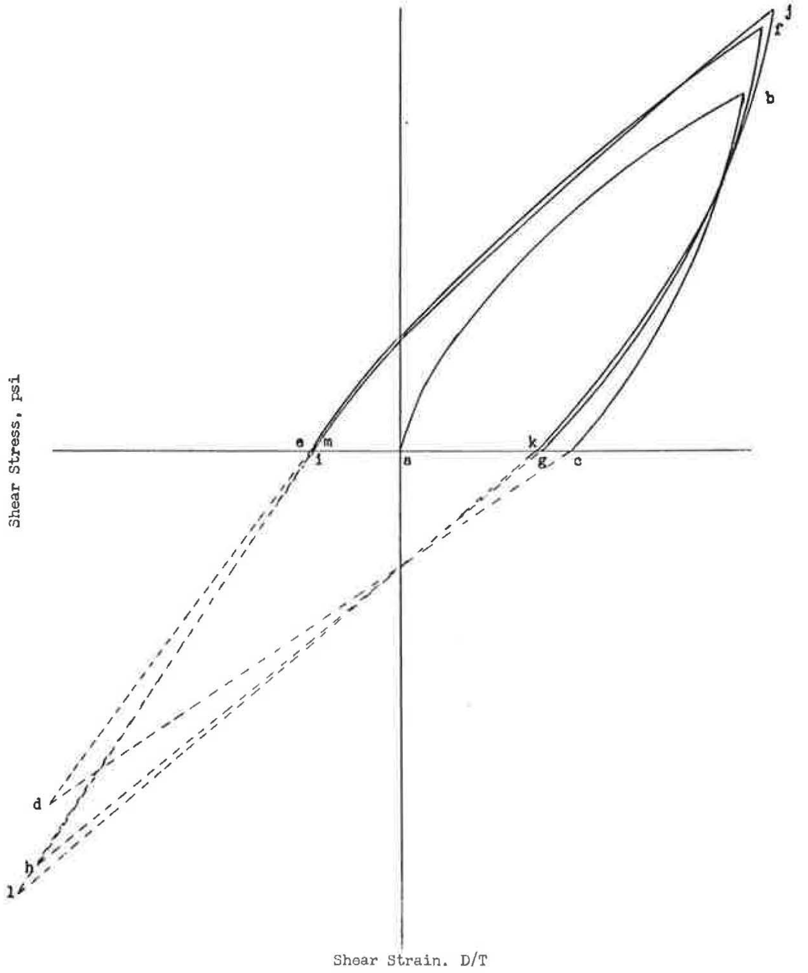

Figure 8. Typical shear curve, Type 1.

curve decreases, but the amount of decrease becomes less and less until the cycles eventually reproduce. The shear force transmitted to the piers is greatest on the first cycle, except for those small deformations of the initial cycle in the vicinity of zero deformation. Other curve characteristics are similar to the first type of curve.

The effect of increasing the cyclic load is illustrated in Figures 10 and 11. Figure 10 represents a sample that conforms to a typical curve of the first type of material and Figure 11 represents a sample that conforms to a curve of the second type. In both types, as with compressive strains, the transition curves are extensions of the previous reproducible curves. The differences between the two are as follows:

1. In the first type the extensions are curved lines, and in the second type the extensions approach straight lines, providing the increments of load increase are moderate. With large load increments, the extensions for the second type of material are not entirely linear.
2. In both types, the slopes decrease with increased strain and the stress axis intercepts at D/T = 0 increase. The effect of the change in slope is that in the first type of material, the deviation is greater at strain D/T = 0; in the second type of material, the deviation is greater at strain D/T maximum.

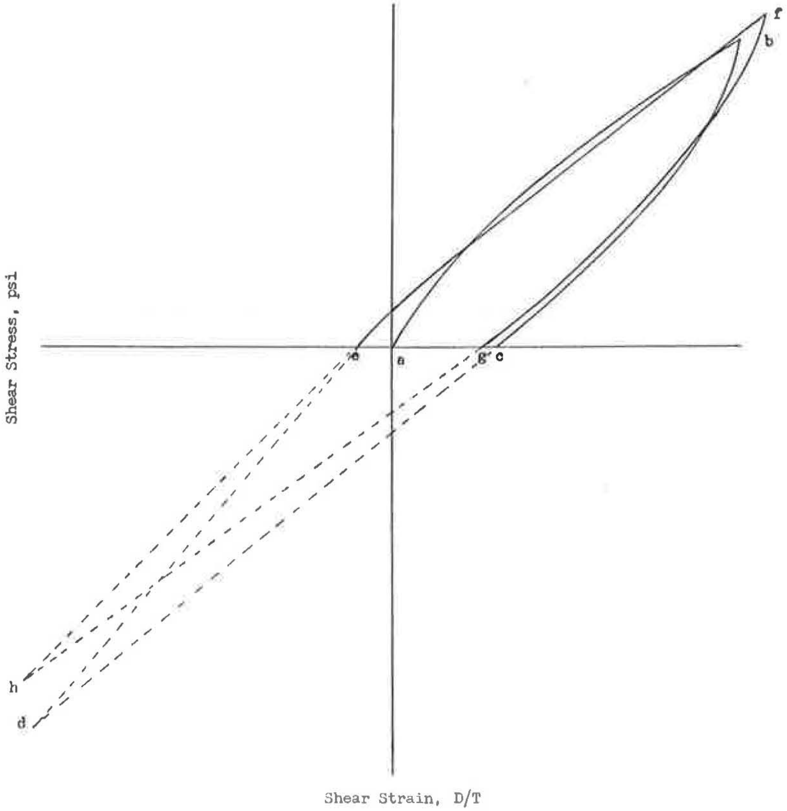

Figure 9. Typical shear curve, Type 2.

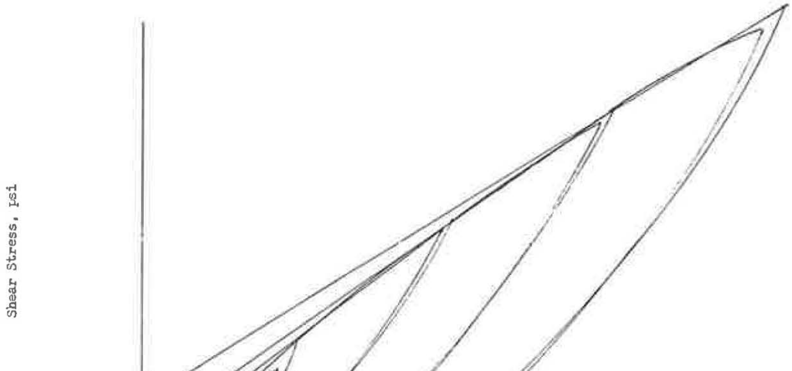

Figure 10. Effect of increasing shear loads.

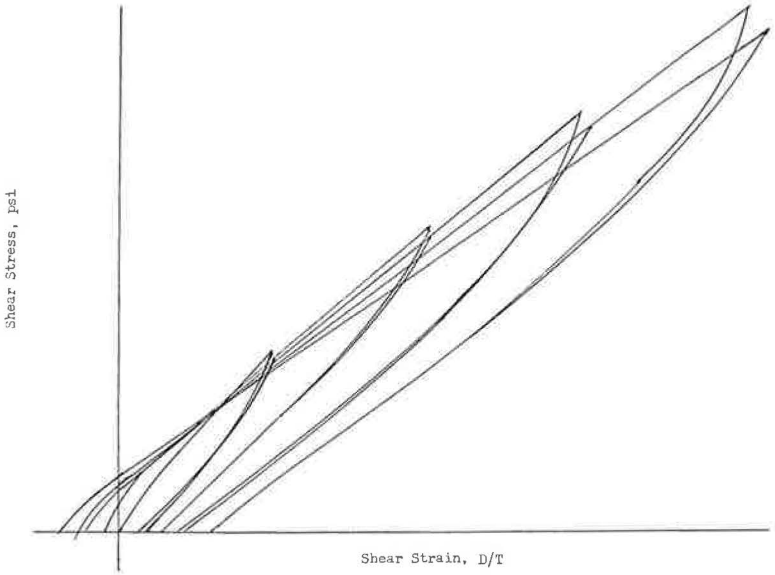

Figure 11. Effect of increasing shear loads.

The effect of decreasing cyclic loads in both types of curves is similar to that obtained with compression curves in that the curves do not return to the corresponding reproducible curves for increasing loads from Figures 10 and 11, nor do they follow the cyclic load curve for maximum stress. The curves lie between these two values. This is probably due to the completely reversible cycling (both positive and negative) and not to a higher recovery rate in shear as compared to compression. Once again the values obtained are dependent on the previous history of the sample, but with complete reversibility technique this difference is reduced.

The effects of shear loading rate, hardness, shape factor, and grain direction can be estimated from Table 1. The effect of shear loading rate is immediately apparent and is one of the most critical parameters of the method of test. Many of the variations in Table 1 are directly attributable to fluctuations in shear loading rate. This is especially true on small samples (SF less than 1.0). The numerical data given in Table 1 also illustrate the apparent stiffening of the sample under stepwise increases in stress.

In general, at the same strain, samples with higher durometer hardness have higher stress values, but the deviations at any one hardness are greater than the average differences between samples at two separate hardnesses (60-70 durometer). Therefore, stress cannot be estimated from durometer values.

There are indications that grain direction has an influence on stress values. At least the variations in stress values with shape factor are not as pronounced in one direction as in the other. Where grain direction has been identified, the "with grain" has been the more stable. However, this may be an indirect result of loading rate control because "with grain" deformations and the larger samples were found to be the easier to control.

The effect of testing temperature was not evaluated. These tests were made during a time span of more than one year and were made at the prevailing room temperatures.

DEFINITION OF SHEAR MODULUS FOR ELASTOMERS

Modulus in general is defined as unit stress per unit strain:

$$\text{Modulus} = \frac{\text{Stress}}{\text{Strain}} \tag{1}$$

TABLE 1

Sample	Size (in.)	SF	Direction of Shear	Run	Head	(%) Shear	f	k	λ	M_r	M_i
(a) BH-36509, Type 1, 74 Durometer											
3/4	3 × 3	1.57	w/g	1	M	50	-	-	-	-	-
				2	M	50	80.6	21.6	118.0	161.2	-
				3	M	25	53.0	12.0	164.0	212.0	-
						50	84.0	22.2	123.6	168.0	-
						25	51.5	12.6	155.6	206.2	-
13/14	3 × 1	0.77	w/g	1	M	50	-	-	-	-	-
				2	M	50	90.9	32.7	116.4	181.8	-
1/2	3 × 3	1.57	c/g	1	M	50	-	-	-	-	-
				2	M	50	79.0	24.4	109.2	158.0	-
				3	M	25	55.0	11.7	173.2	220.0	
						50	81.2	20.0	122.4	162.4	-
						25	48.9	7.6	165.2	195.6	-
						50	93.8	18.1	151.4	187.6	-[a]
						50	76.8	15.9	121.8	153.6	-[b]
				4	M	12.5	28.8	2.4	211.2	230.4	-
						25	49.0	8.8	160.8	196.0	-
						50	79.4	20.7	117.4	158.8	-
						100	136.8	58.4	78.4	136.8	-
						50	87.0	34.6	104.8	174.0	-
5/6	3 × 3	1.54	c/g	1	M	50	83.4	29.0	108.8	166.8	148.1
				2	M	50	77.9	24.8	106.2	155.8	-
						25	-	-	-	-	-[c]
				3	M	50	81.6	24.9	113.4	163.2	-
7/8	3 × 2	1.23	c/g	1	M	50	-	-	-	-	-
				2	M	50	87.0	27.6	118.8	174.0	-
11/12	3 × 1	0.78	c/g	1	M	50	-	-	-	-	-
				2	M	50	97.7	35.7	124.0	195.4	-
(b) BJ-29109, Type 2, 62 Durometer											
1/2	3 × 3	1.51	w/a	1	M	50	55.4	7.9	95.0	110.8	117.4
5/6	3 × 3	1.56	w/a	1	K	50	58.6	8.1	101.0	117.2	119.2
						100	94.8	19.5	75.3	94.8	-
				2	K	50	59.1	5.9	106.4	118.2	-
						100	98.4	12.4	86.0	98.4	-
7/8	3 × 3	1.54	w/a	1	K	25	34.6	2.8	127.2	138.4	-
						50	60.8	6.7	108.2	121.6	-
						75	80.6	10.0	94.1	107.5	-
						100	97.9	13.2	84.7	97.9	-
						75	77.0	10.8	88.3	102.7	-
						50	55.3	7.9	94.8	110.6	-
						25	31.3	5.2	104.4	125.2	-
9.1/10.1	2 × 2	1.06	w/a	1	K	50	53.8	8.9	89.8	107.6	111.4
9.2/10.2	3 × 1	0.79	w/a	1	K	50	61.6	10.8	101.6	123.2	129.4
3/4	3 × 3	1.52	c/a	1	M	50	53.7	6.6	94.2	107.4	113.3
9.3/10.3	2 × 1	0.71	c/a	1	K	50	53.9	11.3	85.2	107.8	110.4
(c) BJ-29110, Type 1, 75 Durometer											
1/2	3 × 3	1.55	w/a	1	M	50	118.7	27.4	182.6	237.4	226.6
				2	M	50	120.1	30.3	179.6	240.2	-
						100	-	-	-	-	-[d]
3/4	3 × 3	1.53	c/a	1	M	50	117.8	31.7	172.2	235.6	211.9
(d) BJ-29108, Type 1, 74 Durometer											
5/6	3 × 3	1.36	w/a	1	K	6.25	28.8	4.7	385.6	460.8	-
						12.5	44.6	7.2	299.2	356.8	-
						18.75	56.9	10.8	245.9	303.5	-
						25	69.2	12.2	228.0	276.8	-
						31.25	79.8	14.4	209.3	255.4	-
						37.5	87.3	16.6	188.5	232.8	-
						43.75	100.3	15.8	193.2	229.3	-
				2	K	6.25	23.0	2.0	336.0	368.0	-
						12.5	37.6	5.6	256.0	300.8	-
						18.75	50.4	8.1	225.6	268.8	-
						25	62.5	11.2	205.2	250.0	-
						31.25	74.5	13.1	196.5	238.4	-
						37.5	85.2	15.0	187.2	227.2	-
						43.75	95.9	18.1	177.9	219.2	-
						50	107.2	21.1	172.2	214.4	-
						62.5	124.5	26.6	156.6	199.2	-
						75	140.3	34.0	141.7	187.1	-
						100	176.8	33.2	143.6	176.8	-
7/8	3 × 3	1.38	w/a	1	K	50	110.4	35.4	150.0	220.8	203.4
13.1/14.1	2 × 2	0.92	w/a	1	K	50	101.2	35.7	131.0	202.4	192.6
13.2/14.2	3 × 1	0.70	w/a	1	K	50	120.5	48.0	145.0	241.0	189.4
9/10	3 × 3	1.37	c/a	1	K	50	108.0	37.4	141.2	216.0	195.2
						100	-	-	-	-	-[d]
				2	K	50	102.3	28.1	148.4	204.6	-
11/12	3 × 3	1.39	c/a	1	K	50	111.8	39.1	145.4	223.6	200.2
13.3/14.3	2 × 1	0.62	c/a	1	K	50	108.8	41.7	134.2	217.6	194.8

[a] Fast rate. [b] Slow rate. [c] Initial cycle only. [d] Sample slipped.

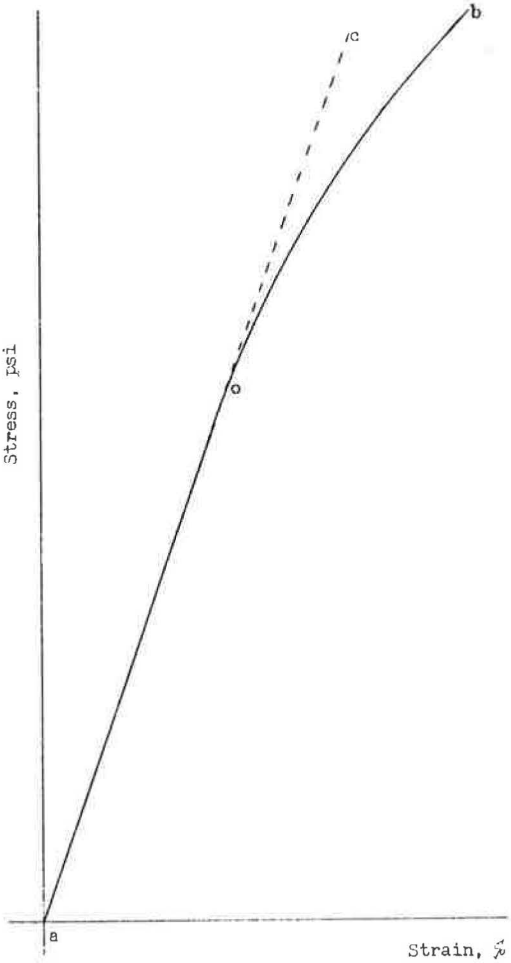

Figure 12. Stress/strain curve—elastic material.

Because for elastomers the unit stress is equal to the shearing force divided by the bearing area and the unit strain is the shear deformation divided by the pad thickness, Eq. 1 becomes:

$$\text{Modulus} = \frac{\dfrac{\text{Shearing Force}}{\text{Bearing Area}}}{\dfrac{\text{Shear Deformation}}{\text{Pad Thickness}}} \qquad (2)$$

This is the definition of shear modulus for elastomers (5).

If the stress is plotted vs strain for a perfectly elastic material, the plot would be as indicated in line aob of Figure 12. The portion of the plot within the elastic limit of the material in linear as represented by the straight line, ao, whose value is indicated by the tangent aoc.

Elastomers under strain always have some permanent set, regardless of how small the strain, and the plot of stress vs strain is not linear. The characteristic curve for rubber and rubber-like materials is not a straight line but an S curve (2), similar to line ab of Figure 13. This is a typical tensile curve. Line ab of Figure 14 is a typical compression curve from the literature (1, 2). Our experience has been that all elastomeric deformations (tensile, compression, and shear) exhibit the typical S character, some more than others; tensiles are the most pronounced, compressions the least. Furthermore, because these deformations are not straight-line functions, it is customary to identify the stated modulus by the degree of strain at which the modulus was determined (2), i.e., 300 percent modulus. This modulus value does not identify the stress/strain curve for elastomers as it does for an elastic material but actually identifies only the chord of the curve from the origin to a point on the curve at the degree of strain stated (straight lines aA, Figs. 13 and 14). For small strains, this cord is a reasonable and adequate approximation. Other values often quoted in the literature are the slope static moduli and the tangential modulus (lines c, Figures 13 and 14) which is the tangent to the curve at the point of strain designated.

For large strains, the modulus value identifies the chord only of an arc of appreciable curvature and has limited application. Data are comparable only at identical points on the curve. Elaborate calculations or an actual physical test must be resorted to in order to obtain the stress at any other desired point as dictated by the engineering problem.

RECOMMENDATIONS

We have shown that shear cycling produces curves that are reproducible and that a substantial length of the loading portion of these curves approach a straight line. Therefore, in lieu of the present practice of computing shear forces from the "chord shear

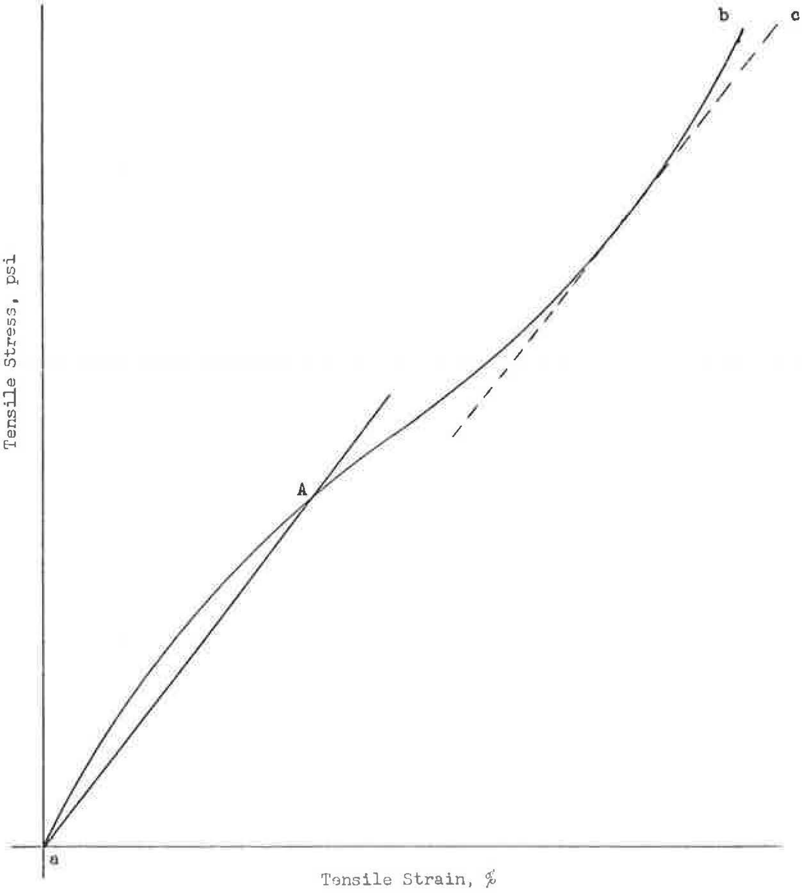

Figure 13. Tensile stress/strain curve—elastomeric material.

modulus," which are approximations only, it is proposed that standard curves be established from which the shear forces can be computed according to the following formula:

$$f = k + x\lambda \tag{3}$$

where f is the shear stress at shear strain D/T = x; k is a constant from the standard curve, which represents the stress axis intercept or residual pier stress at zero horizontal deformation; x is the ratio of the shear deformation to the pad compressed thickness at the same deformation at which f is being computed; and λ is the tangent to the loading portion of the standard curve at the point on the standard curve where the strain D/T based on the pad compressed thickness is equal to the decimal equivalent of the percent of shear based on the uncompressed pad thickness. Because the standard curves approach linearity from the stress intercept at the point where D/T = 0 to that at the point where D/T is equal to the decimal equivalent of the percent of shear, for practical purposes this tangent, λ, is equal to the slope of the chord between these two points. The values of λ in Table 1 are computed from this chord.

For a standard curve at 50 percent shear strain based on the uncompressed pad thickness (which is our test strain; 100 percent or any other desirable strain could be designated), the value of k is determined by the stress axis intercept, the value of f is determined at D/T = 0.500 (designated as the standard strain for 50 percent shear strain), and λ is computed from the slope of the chord according to:

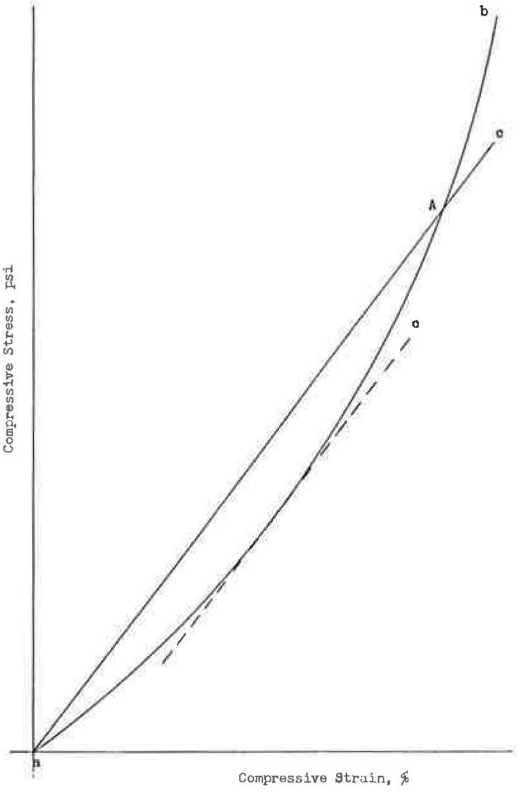

Figure 14. Compressive stress/strain curve—elastomeric material.

$$\lambda = \frac{f - k}{x} \tag{4}$$

With the values of k and λ known for a 50 percent shear strain, it is possible to reconstruct the loading portion of the shear curve and to compute the shear stress at any desired deformation within the limits to which the curve is applicable.

COMPILATIONS

Table 1 gives the values for the samples indicated of f, k and λ from standard curves at the percent of strain indicated and as computed by Eq. 3. It also gives the values of M_r, the reproducible chord shear modulus, as computed from the standard curve by:

$$M_r = \frac{f}{x} \tag{5}$$

where f is the shear stress from the reproducible cyclic curve at the standard strain x. Also given are the values of M_i, the initial chord shear modulus, as computed by:

$$M_i = \frac{f_i}{x} \tag{6}$$

where f_i is the shear stress from the initial cycle at the standard strain x. Appendix A gives a comparison of computations based on each of these three formulas.

ACKNOWLEDGMENTS

The authors wish to acknowledge the able assistance of Earl F. Heisler of our Physical Testing Laboratory in the collection of data and Heinz P. Koretzky and Hans L. Streibel of the Division of Bridge Engineering for their review of this study and their helpful criticism.

REFERENCES

1. Elastomeric Bridge Bearings—Report of Tests and Design Procedures. Charles A. Maguire and Assoc., Providence, R. I., 1958.
2. "Handbook of Molded and Extruded Rubber," Goodyear Tire and Rubber Co., Akron, Ohio, 1949.
3. Mullins, L. Trans. Inst. Rub. Ind, Vol. 26, p. 27, 1950.
4. Wilkinson, C. S., Jr., and Gehman, S. D. Anal. Chem, Vol. 22, p. 283, 1950.
5. Design of Neoprene Bridge Bearing Pads. E. I. duPont de Nemours and Co., Wilmington, Del., 1959.

Appendix A

COMPARISON OF COMPUTATIONS

Figure 15 illustrates a comparison of computations of the shear stress according to current practice and according to the recommendations proposed in the basic presentation. Figure 15 is a representation of the shear cycles of pads 7/8, Sample BJ-29108, from Table 1.

The arc abc represents the positive loading portion of the initial cycle of the pads cycled at 50 percent shear deformation as based on the uncompressed thickness of the pads. The arc ab represents the segment of this curve from D/T = 0 to D/T = 0.500. The stress coordinate of point b is f_i, 101.7 psi. The initial chord shear modulus, as represented by the chord ab and defined by Eq. 6, then becomes 203.4.

The arc khg represents the positive loading portion of the reproducible shear cycle of the same sample. The line kh is the chord of this curve from D/T = 0 to D/T = 0.500. The stress coordinates of k and h are k and f, respectively. Since k = 35.4

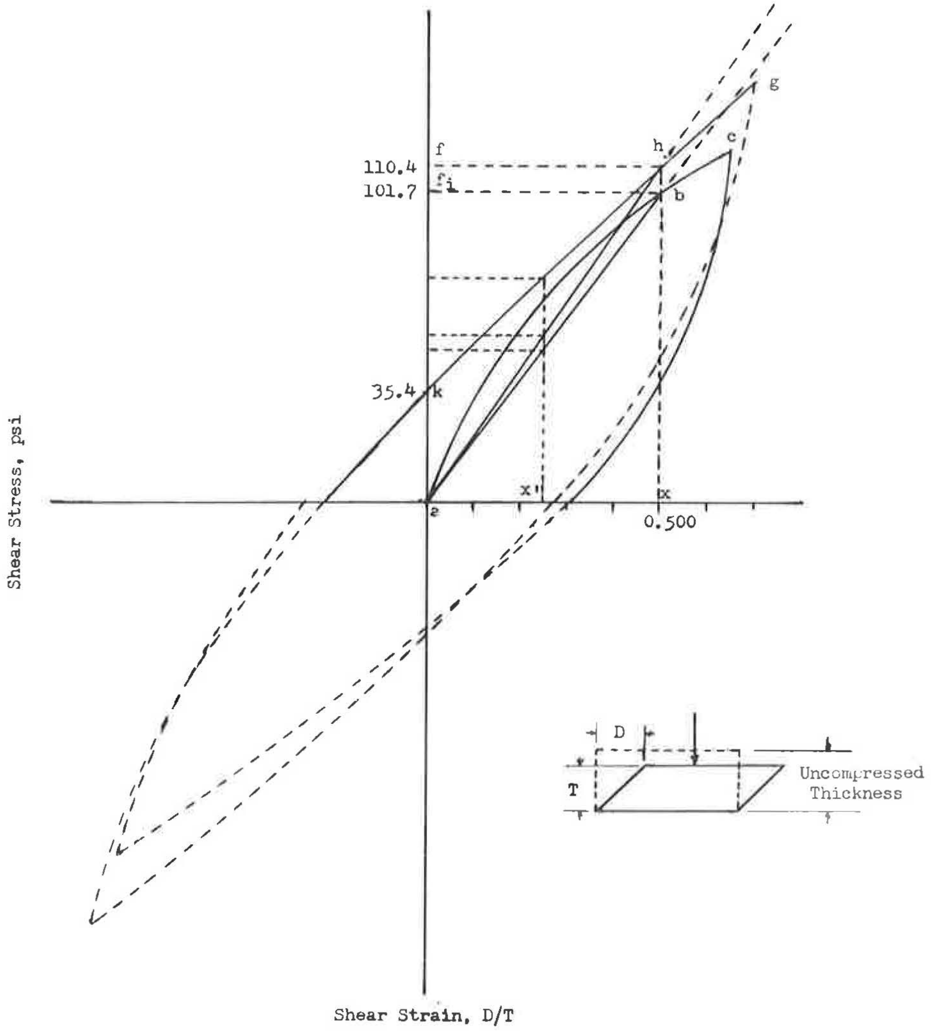

Figure 15. Comparison of shear stress computations.

and f = 110.4, the value of λ, as indicated in the basic presentation and as computed from Eq. 4, is as follows: $\lambda = \frac{110.4 - 35.4}{0.500} = 150.0$

The line ah represents the cyclic chord shear modulus as defined by Eq. 5 and, in this instance, has the value of 220.8.

These and similarly determined values for other samples and/or degrees of shear will be found in Table 1 of the basic presentation. Assuming we wish to compute the shear stress at some point, x', and we choose $x' = 0.250$, then from Eq. 3 which for the value x' becomes $f' = k + x'\lambda$, and with the substitution of the values of $k = 35.4$ and $\lambda = 150.0$, from the standard curve, $f' = 35.4 + (0.250 \times 150.0) = 35.4 + 37.5 = 72.9$, which is the computed shear stress by the method proposed in the basic presentation.

The computed shear stress based on the present practice of computing the shear stress from the chord shear modulus would be as follows:

1. For the cyclic chord shear modulus as defined by Eq. 5, with $M_r = 220.8$ as computed previously and x' chosen as 0.250, $f' = x' M_r = 0.250 \times 220.8 = 55.2$.
2. For the initial chord shear modulus as defined by Eq. 6, with $M_i = 203.4$ as computed previously and again with x' chosen as 0.250, $f_i' = x' M_i = 0.250 \times 203.4 = 50.8$.

The actual stress as determined experimentally at the strain $x' = 0.250$ was found to be 73.0 psi.

Appendix B

SHEAR DEFORMATION STANDARD METHOD OF TEST

Equipment

The equipment consists of a universal testing machine modified with two steel compression heads of 4 by 4 in. and a steel drawplate of approximately ½ by 8 by 12 in. The compression heads and sample areas of the drawplate are knurled at 40 lines to the inch. The heads are positioned so that they are matched and parallel at contact. Four gages are used to determine pad compressed thickness, one dial on each side of each pad. The universal testing machine must be capable of rapid adjustment, either manual or automatic, to maintain the specified compressive load within ±0.5 percent of actual load. Compressive loading rate must be 0.05 in./min. Total compressive load must exceed 15 percent and be less than 85 percent of the calibrated capacity of the universal testing machine.

Shear displacement must be accomplished at 0.050 ± 0.002 in./min. Mechanical control of shear loading rate is the most reliable. Shear displacement shall be measured by one gage centered on the draw axis. Shear load is determined by load cell, load rings or some other method and must be measurable to within 0.5 percent of actual load. The load measuring device shall be so selected that determined shear load exceeds 15 percent and is less than 85 percent of the calibrated capacity of the device.

Standard Conditions

The following conditions are considered standard, and any deviations must be noted:

1. Testing temperature—68 ± 5 F;
2. Compressive stress—500 psi;
3. Loading rate, both compressive and shear—0.050 ±0.002 in./min;
4. Degree of shear deformation—50 and 100 percent, respectively, of the uncompressed thickness; and
5. Standard sample—two samples, each ½ by 3 by 3 in., for each grain direction.

Method

1. Two samples, both of the same grain direction, are centered between the compression heads with the grain of both samples oriented in the same direction. The two samples are placed exactly one above the other with the drawplate between. The compression heads are brought together to zero load. The average thickness of each sample is calculated and compared with the original premeasured thickness. Deviation should not be more than ± 0.001 in.

2. The samples are loaded in compression at the rate of 0.050 ± 0.002 in./min to testing compressive load and then unloaded to zero load. The cycles are repeated until percent compressive strain at maximum load remains constant. The plane of the drawplate is maintained parallel with the plane of the compression heads during cycling. Percent compressive strain is assumed to be constant when, after three consecutive cycles, the compressive deformation has not changed more than ± 0.001 in.

3. After the percent compressive strain becomes constant, the compressive load and load in shear are maintained at the rate of 0.050 ± 0.002 in./min until the drawplate has been displaced a distance equal to one-half (± 0.005 in.) of the original uncompressed (premeasured) average thickness of the two samples under test. The drawplate is reserved and returned through the original position to a like negative distance. Then it is reversed again and displaced to the original positive position. These cycles are repeated until they reproduce. Samples are considered to have reproduced when the variations in shear load at zero shear deformation and the variations in slope at $D/T = 0.500$ (or 1.000 as appropriate) are less than 5 percent. The shear load, the shear deformation (D), and the thickness at shear (T) are recorded at sufficient intervals to plot the shear stress/strain curve.

4. After the shear stress values reproduce at 50 percent shear deformation, the samples are cycled at 100 percent shear deformation without change in the compressive load.

Calculations

The shear stress is plotted in psi against the shear strain, D/T, where D is the shear deformation in inches and T is the compressed thickness in inches at that deformation. The shear stress at the point $D/T = 0$ is then designated as k for the percent of shear deformation at which cycled. The slope of the chord of the shear stress/strain curve is determined from the point where $D/T = 0$ to the point where D/T is equal to the decimal equivalent of the percent of shear deformation at which cycled (0.500 or 1.000 as appropriate). This slope is designated as λ.

Appendix C

DESIGN COMPUTATIONS

The general formula as established is $f = k + x\lambda$ (Eq. 3). For 50 percent deflections and at the value $D/T = 0.500$, the specific formula for the standard curve becomes $F_{0.500} = k + 0.500\,\lambda$. It must be borne in mind that the constants of this specific formula are valid only under the conditions of test. Any deviations of actual conditions from standard test conditions must be compensated for by correction factors. Also, these constants are based on compressed thicknesses. Therefore, an estimate of the compressed thickness under service conditions must be made and such thickness is used in computations.

For example, to calculate various shear stresses on pads 5/6, Sample BJ-29190, from Table 1, we must first know the cyclic degree of strain at which the bearing is flexing to choose the proper values of k and λ. If the bearing is undergoing random cycling, values for k and λ appropriate to the immediately previous cycle are used as a close approximation. If previous cycle is unknown, the next approximation is the design cycling value.

We may assume that it is desired to know the stress at deflection D/T = 0.250 at some future date. Because the sample will in all probability be undergoing random cycling in which the immediately previous cycle is unknown, we will use the values of k and λ appropriate to the design which we will assume to be 50 percent deflection. Then $f^{0.250}_{0.500}$, which is the stress at deflection D/T = 0.250 based on previous deflection (or standard curve) of 50 percent deflection, will be equal to the value of k at 50 percent deflection plus 0.250 multiplied by the value of λ at 50 percent deflection: $f^{0.250}_{0.500} = k + 0.250\,\lambda = 8.1 + 0.250 \times 101.0 = 8.1 + 25.2 = 33.3$ (actual value = 34.3).

If we assume we wish to know the stress at some future date at 25 percent deflection and it is assumed that at 25 percent deflection D/T = 0.343: $f^{0.343}_{0.500} = k + 0.343\,\lambda = 8.1 + 34.6 = 42.7$ (actual value = 43.3).

If we assume we now wish to know the stress at D/T = 0.250 after a maximum cycle at 100 percent deflections: $f^{0.250}_{1.000} = k + 0.250\,\lambda = 19.5 + 0.250 \times 75.3 = 38.3$ (actual value = 39.6).

If we assume we wish to know the stress at 50 percent deflection and it is assumed that at 50 percent deflection D/T = 0.700: $f^{0.700}_{0.500} = k + 0.700\,\lambda = 8.1 + 70.7 = 78.8$ (actual value = 77.5).

Under the standard conditions of test the 50 percent deflection curve is valid over values of D/T = 0.250 to 0.750 and 100 percent deflection curve is valid from D/T = 0.500 to approximately 1.300.

Economic Possibilities of Corrosion-Resistant Low-Alloy Steel in Box Girder Highway Bridges

J. M. HAYES and S. P. MAGGARD
Respectively, Professor of Structural Engineering, Purdue University, and Assistant Professor of Structural Engineering, New Mexico State University

An analytical study was made of the economic possibilities of the use of corrosion-resistant low-alloy steel for girders in composite action with a precast high-strength concrete deck for short and medium length highway bridges. A design procedure is presented. Structural quantities and cost data are developed for one- and three-cell steel boxes for 75- and 120-ft simple spans. The structures involve the integrated use of a nickel-copper grade of ASTM A242 and T-1 steels. Cost data are also given for the use of ASTM A441 steel, as well as of stainless-clad steel for the exterior plates of the steel box.

The results indicate that it is possible to design and erect a box structure for short and medium length highway bridges at a lower first cost than the conventional I-beam highway bridge with a poured-in-place concrete deck. It is recommended that a nickel-copper type of high-strength low-alloy steel be used due to its better resistance to atmospheric corrosion because thin plates are proposed in the steel box.

•THE OBJECTIVE of this work was to investigate the economic possibilities of nickel-copper high-strength alloy steels in short and medium length highway bridges. Two reports on this study have been published previously. In the first (1), designs for the superstructures of typical short-span concrete slab and rolled wide-flange steel stringer highway bridges fabricated from nickel-copper high-strength low-alloy steels were analytically compared with those fabricated from ASTM A7 and A373 structural steels. The results of this first study indicated that this type of highway bridge could, for all practical purposes, be constructed of nickel-copper types of high-strength low-alloy steels at the same first cost in dollars as if ASTM A7 or A373 structural steels were used.

The second report (2) was an analytical study of the comparative economic use of various steels for welded I-section stringers with concrete deck for short and medium length highway bridges within the framework of the standard design specifications. The results indicated that structures of this type could be fabricated and erected using a nickel-copper grade of high-strength low alloy steel at about the same first cost in dollars as if ASTM A373 structural steel were used.

Since the publication of these first two reports, changes in the chemical requirements in the specifications for ASTM A36 structural steel have resulted in its being accepted for welding in highway bridges. It is expected that ASTM A7 and A373 structural steels will be replaced by A36 structural steel. The cost of fabricating and erecting the types of structures covered in these first two reports using ASTM A36 structural steel will average about 95 percent of the same first cost in dollars

---

Paper sponsored by Committee on Bridges.

if a nickel-copper grade of high-strength low-alloy steel were used. However, it may be possible that the higher atmospheric corrosion resistance of the nickel-copper grades of high-strength low-alloy steels will result in overall economy due to savings in maintenance costs.

This report covers the third phase of the investigation, which was an analytical study of the use of high-strength steels, with particular attention to nickel alloy steels, in forms for short and medium length highway bridges independent of current standard practice and design specifications.

PROPOSED TYPE

Presupposing satisfactory dynamic properties, the most efficient steel highway bridge superstructure is one which incorporates a combination of the various grades of constructional steels with integral action in all directions. Design procedures and fabrication, erection, and maintenance problems must be considered in the overall economic evaluation. The intangible matter of esthetics should also receive attention.

One possible type of construction is a welded steel box girder with a deck unit acting compositely with it. This type results from an attempt to reduce the excess shear carrying capacity of the standard I-beam highway bridge. The deck unit could be either a steel orthotropic plate or a reinforced concrete slab. The types investigated in this study are shown in Figures 1 and 2. It is proposed that a high-strength concrete deck be precast in units of suitable length and held in place with high-strength

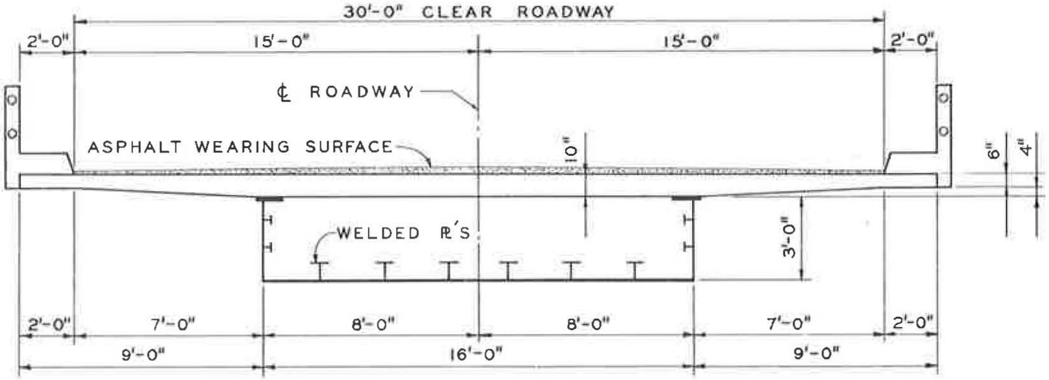
30'-0" CLEAR ROADWAY
2'-0"
15'-0"
15'-0"
2'-0"
℄ ROADWAY
ASPHALT WEARING SURFACE
10"
6"
4"
WELDED ⅊'S
3'-0"
2'-0"
7'-0"
8'-0"
8'-0"
7'-0"
2'-0"
9'-0"
16'-0"
9'-0"

Figure 1. Details of one-cell box.

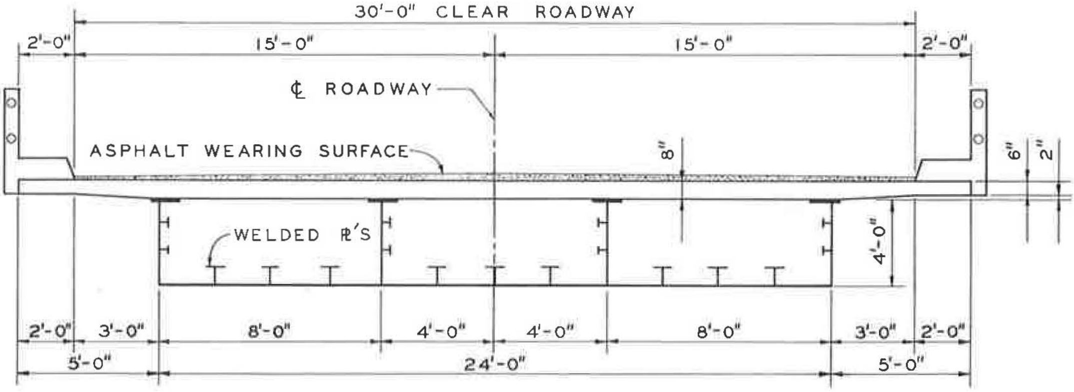
30'-0" CLEAR ROADWAY
2'-0"
15'-0"
15'-0"
2'-0"
℄ ROADWAY
ASPHALT WEARING SURFACE
8"
6"
2"
WELDED ⅊'S
4'-0"
2'-0"
3'-0"
8'-0"
4'-0"
4'-0"
8'-0"
3'-0"
2'-0"
5'-0"
24'-0"
5'-0"

Figure 2. Details of three-cell box.

grout and high-strength bolts to give integral action with either a one- or a three-cell steel box girder. These slab units are joined together with high-strength grout. Post-stressed strand might be feasible to hold the units together. This procedure has been used for highway structures in Europe (3, 4). A combination of high-strength bolts and epoxy resins has been used on one structure in Europe with a span of 7.38 meters, about 24 ft (5). The use of epoxy bonding compounds to secure composite action is being studied at Rensselaer Polytechnic Institute (6).

Steel Box Details

The various grades of constructional steels are combined to give the best possible balanced use of the material in the design of the steel box girder. The plates around the box have one-sided longitudinal stiffeners, which are continuous throughout the

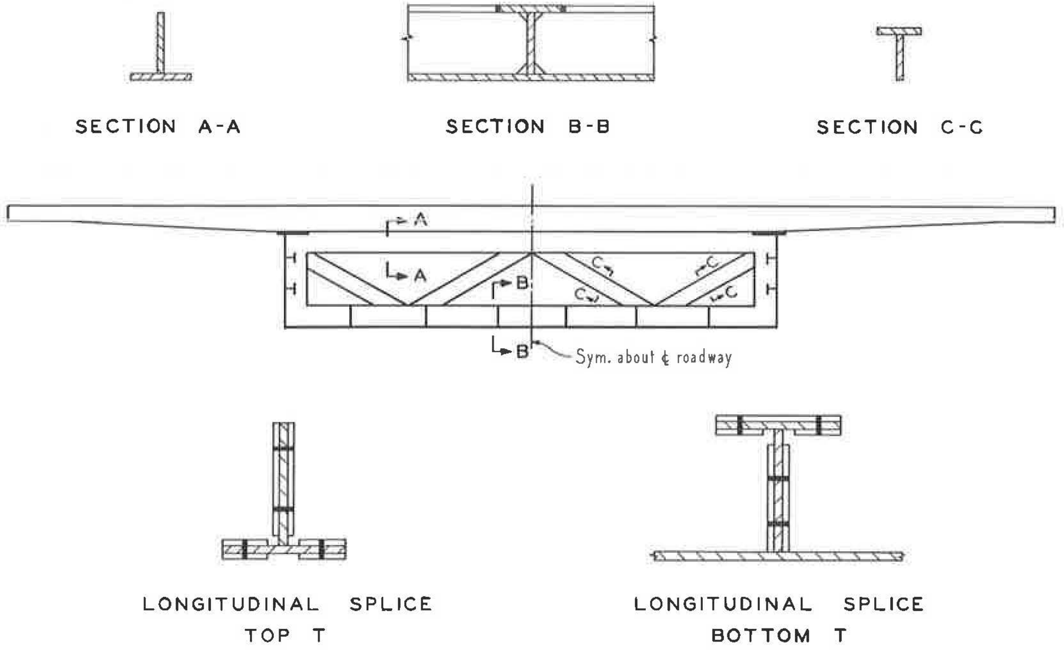
SECTION A-A

SECTION B-B

SECTION C-C

LONGITUDINAL SPLICE
TOP T

LONGITUDINAL SPLICE
BOTTOM T

Figure 3. Details of transverse stiffening ring.

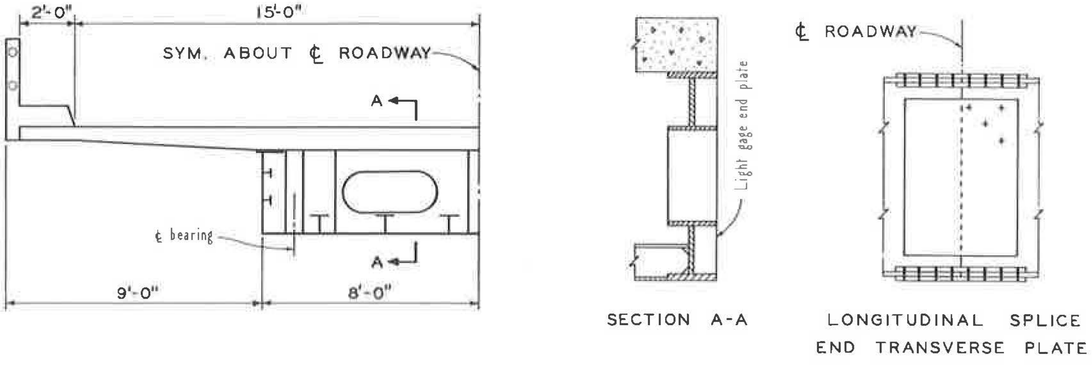
SECTION A-A

LONGITUDINAL SPLICE
END TRANSVERSE PLATE

Figure 4. Details of transverse end stiffening ring.

length of the girder and participate in direct structural action with the plates. A rolled structural T may be used for these longitudinal stiffeners instead of a welded T as shown in Figures 1 and 2.

Intermediate transverse stiffening ring diaphragms are spaced at about 12-ft intervals, (Fig. 3). Typical details of a transverse end stiffening ring diaphragm are shown in Figure 4. These details are also typical for a ring at an intermediate support in a continuous structure. At an abutment end, the box is completely sealed with a light gage seal plate. Access to the interior of the box girder is given by covered entrance holes in the bottom plate, near the abutments where the bending moment is small. The bearing details at an end or intermediate support vary, depending on the substructure configuration.

The steel box is shop fabricated into the largest units which can be shipped to a specific site. All shop fabrication is by an appropriate welding procedure and the side plates are joined by butt welding to form appropriate units of the box.

Field Splices

No transverse field splicing is usually required for short and medium length structures. Longitudinal sections, 120 ft long, can be shipped to the site. Details for a transverse splice at a stiffening ring are shown in Figure 5 for use in continuous spans and other places where splices might be required.

Usually longitudinal field splicing is required. The details of a high-strength bolted longitudinal splice are shown in Figure 6. Details of a complete penetration one-sided

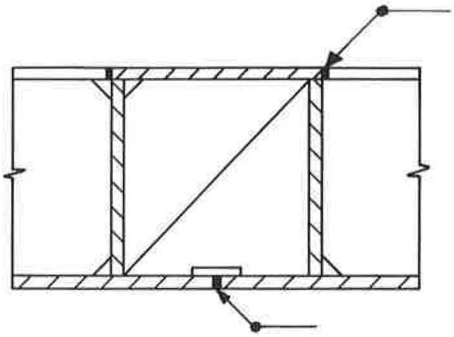

WELDED SPLICE

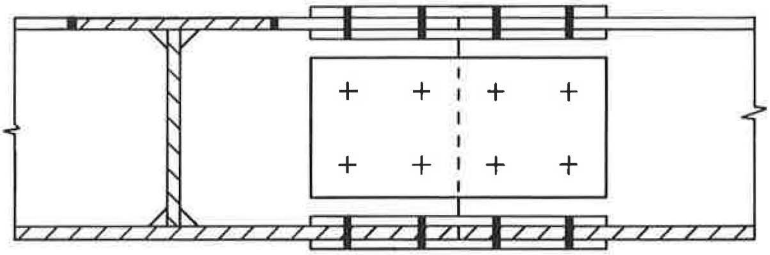

BOLTED SPLICE

Figure 5. Details of transverse splice.

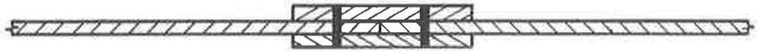

BOLTED SPLICE

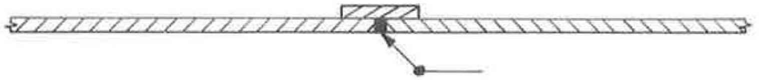

WELDED SPLICE

Figure 6. Details of longitudinal splice.

butt weld with backup strip are also shown. The bolted splice is preferred because of ease of erection. The details for the splicing of intermediate and end transverse stiffening rings due to longitudinal splicing are shown in Figures 3 and 4.

THEORETICAL ANALYSIS OF BOX

The units of the steel box, as shop fabricated, have to be braced for shipment to the site. Circumstances vary, and this matter is not given further attention here, because similar situations are now satisfactorily handled.

The complete steel box has to support its own weight and that of the precast slab, either for the full length of a span or between erection bents. It is assumed that the total deadweight of the structure is carried by the steel section and that the live load is carried by the complete cross-section when the precast slab acts compositely with the steel portion of the box girder.

Stress Analysis

The stress analysis of the steel portion of the box girder under the dead load of the structure presents no unusual problems. Both the flexural and the horizontal shear formulas are used, as well as the usual theory for combined stresses.

The stress analysis of the complete box girder under the live load differs somewhat from that of the standard I-beam highway bridge. The primary stresses in this composite section are those due to shear and flexure from symmetrical loading and those due to torsion from unsymmetrical loading, especially live and wind loads.

The precast slab is transformed to an equivalent steel section by using the ratio of the modulus of elasticity of the steel to that of the concrete (E_s/E_c). Using the ratio between the shearing moduli of the two materials gives a coefficient, $G_s/G_c = 0.92\ E_s/E_c$.

The membrane analogy (7) is used to determine the shearing stresses due to torsion and to locate the shear center of the box. The so-called shear flow forces (8) are computed by subdividing the cross-section of the box into segments. It is convenient to use segments corresponding to the discontinuities in the static moments caused by the longitudinal stiffeners. This gives an average shear flow force for each segment based on the following assumptions: (a) the plate thickness is small in comparison with other dimensions, (b) there are no re-entrant corners, and (c) the shear is uniform across the plate thickness. Figure 7 shows the distribution of these shear flow forces in the box for both a vertical load through the shear center and a horizontal load through some convenient point.

The loads acting on the box are broken into load through the shear center of the box and torsion about the shear center. The shear flow forces due to torsion are computed by a direct application of the membrane analogy. The shear flow due to torsion is given by:

$$q_t = T/2A_B \tag{1}$$

where

q_t = shear flow force due to torsion (lb/lin in.),
T = applied torsion (in.-lb), and
A_B = area enclosed by box section (sq in.).

The horizontal shearing stress formula may be written:

$$\tau t = VQ/I = q \tag{2}$$

where

τ = unit shearing stress,
t = thickness of plate at point in question,
V = total external shear at the transverse section under consideration,
I = total moment of inertia of the transverse cross-section about its centroidal axis,
Q = statical moment of the cross-sectional area of the transverse cross-section on either side of the point in question about the centroidal axis of the section, and
q = shear flow force per linear measure.

The units must be kept compatible. The box cross-section is assumed to be cut at some convenient point and a quantity q is computed for each segment into which the box is divided. The restoration of the cut section and torsional equilibrium are determined in one operation by taking moments about some convenient point.

Stability Analysis

The steel plates of the box must be stable at all times, both during and after erection. The top plates must have lateral stability until the precast slab units are in

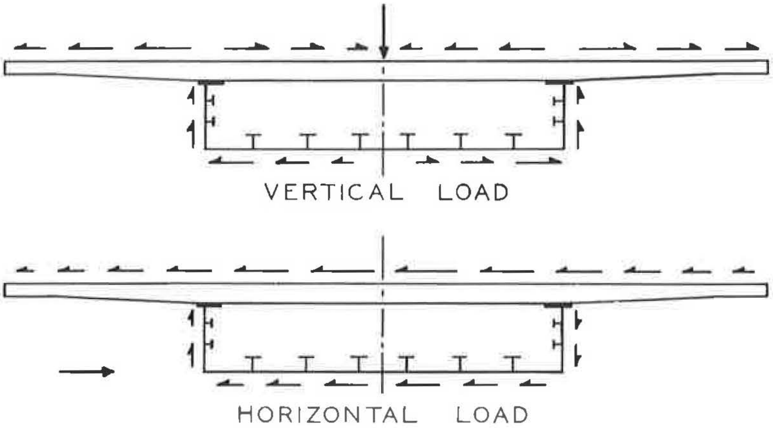

Figure 7. Distribution of shear flow forces.

place. Temporary braces may be used, or a slab unit might be bolted in position to serve as a temporary brace. The size and spacing of the stiffeners must be determined.

The upper limit of the elastic action of a plate may be either the theoretical elastic buckling stress or the yield strength of the material. A plate element, such as one of those comprising the box section, may carry additional load beyond the theoretical elastic buckling strength by transferring the additional load to the edge supports. This is usually referred to as the post-buckling strength of the plate and its magnitude depends on the strength of the edge supports.

In this study the limit of elastic action is used as an upper bound to determine the requirements for the stability of the plates in the steel box. The theoretical elastic buckling stress at which elastic instability takes place is given for a rectangular plate by the Bryan buckling formula (9, 10, 11):

$$\sigma_{cr} \text{ or } \tau_{cr} = \frac{k\pi^2 E}{12(1 - \mu^2)} \left(\frac{t}{b}\right)^2 \tag{3}$$

where

σ_{cr} = critical normal stress due to bending and/or axial load;

τ_{cr} = critical shearing stress;

a = long dimension of rectangular plate element;

b = short dimension of rectangular plate element;

α = aspect ratio, a/b;

E = modulus of elasticity;

μ = Poisson's ratio;

t = thickness of plate element; and

k = constant depending on type of loading, magnitude of aspect ratio, and edge support conditions of plate element.

The plates of the box may be considered as simply supported panels with lengths equal to the spacing of the intermediate transverse stiffening rings and widths equal to the spacing of the longitudinal stiffeners (12). Figure 8 shows the setup for a typical vertical side plate with flexural stress distribution. The setup for shear stress distribution is similar. The horizontal bottom plate will be in tension in a simple span and stability is no problem. In the regions of negative moment in a continuous span, the bottom plate will be in compression and may be treated similarly to the vertical plates.

Using $E = 30,000$ ksi and $\mu = 0.3$, the Bryan buckling formula reduces to σ_{cr} or $\tau_{cr} = 27,114.4k(t/b)^2$ ksi. The constant k may be determined from Table 36 of Bleich (11, Chap. 11). For varying normal stress distribution, linear interpolation may be made between the values of Cases 1 and 2 as given in this table. The theoretical elastic buckling stress for each panel of the side plates must be determined for each stress condition during and after erection. In a simple span the shearing and flexural stresses will not both be a maximum at the same transverse section of the structure and they may be considered separately. It is recommended that in no case should the theoretical elastic buckling stress for any panel be less than 1.5 times the actual comparable flexural or shearing stress in the panel.

High values of flexural and shearing stresses may occur simultaneously at a transverse section in continuous spans. The following interaction relationship may be used to determine safe ratios between the actual stresses and the theoretical elastic buckling stresses for the Panels 11 and 13:

$$\frac{\sigma^D}{\sigma^D_{cr}} + \left(\frac{\sigma^F}{\sigma^F_{cr}}\right)^2 + \left(\frac{\tau}{\tau_{cr}}\right)^2 \leq 0.67 \tag{4}$$

where σ^D, σ^F and τ are, respectively, the actual average direct stress, the maximum flexural stress, and the shearing stress in a panel; and σ^D_{cr}, σ^F_{cr}, and τ_{cr} are the corresponding theoretical elastic buckling stresses for each individual state of stress in the same panel.

Longitudinal Stiffener Rigidity

Based on the stipulation that a longitudinal stiffener remains straight until the theoretical elastic buckling stress is reached, with the panels and edge supports as previously assumed, studies (14, 15) indicate that the required minimum rigidity for a single-sided longitudinal stiffener in the case of pure flexure may be taken as follows:

1. stiffener at mid-depth of plate:

$$I = 0.1167t^3b \tag{5a}$$

2. stiffener at quarter-depth from compression flange:

$$I = t^3b\,(1.1 + 8.45\delta)\ (\alpha - 0.3) \tag{5b}$$

with a maximum value of $t^3b\,(1.4667 + 18.3333\delta)$; and

3. stiffener at one-fifth of the depth from compression flange

$$I = t^3b\left[0.354 + 0.467\alpha + (0.807 + 7.114\delta)\ \alpha^2\right] \tag{5c}$$

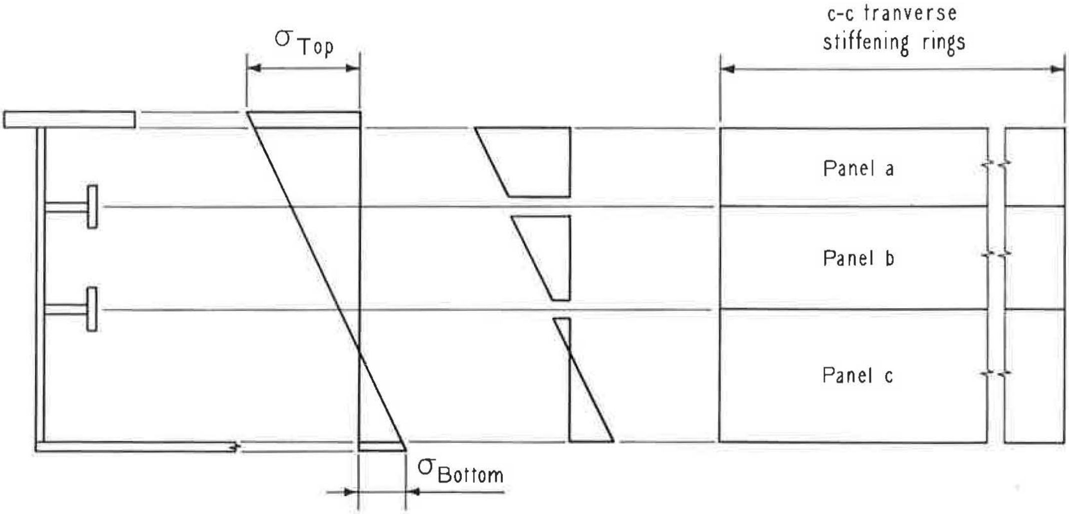

Figure 8. Assumptions for buckling of side plate.

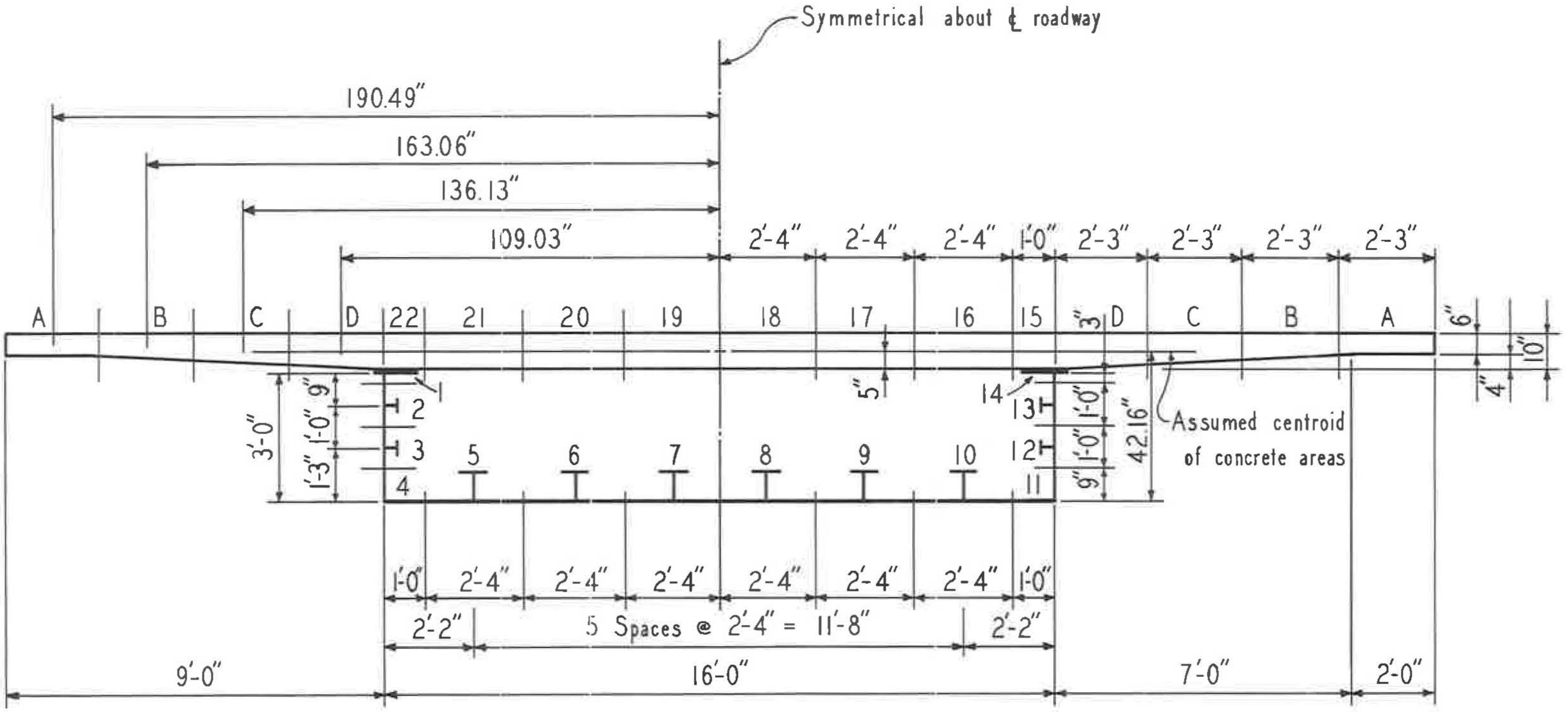
Symmetrical about ℄ roadway
190.49"
163.06"
136.13"
109.03"
2'-4"
2'-4"
2'-4"
1'-0"
2'-3"
2'-3"
2'-3"
2'-3"
A
B
C
D
22
21
20
19
18
17
16
15
3"
D
C
B
A
6"
10"
4"
5"
1
2
3
4
5
6
7
8
9
10
11
12
13
14
3'-0"
9"
1'-0"
1'-3"
1'-0"
1'-0"
9"
42.16"
Assumed centroid of concrete areas
1'-0"
2'-4"
2'-4"
2'-4"
2'-4"
2'-4"
2'-4"
1'-0"
2'-2"
5 Spaces @ 2'-4" = 11'-8"
2'-2"
9'-0"
16'-0"
7'-0"
2'-0"

BOX SECTION

Top Flange ℘ 12 x 1

Vertical Side ℘'s 36 x $\frac{1}{4}$

Bottom ℘ 192 x $\frac{5}{16}$

LONGITUDINAL STIFFENERS

Vertical Side Plates

2 ℘'s 4 x $\frac{1}{4}$ or Structural T's

Bottom Side Plates

2 ℘'s 8 x $\frac{5}{16}$ or Structural T's

Figure 9. Analysis details of one-cell box, 75-ft span.

The nomenclature is as previously used with the addition of δ as the ratio of the area of the stiffener to the cross-sectional area of the plate bt, and I as the moment of inertia of the stiffener taken about the surface in contact with the plate.

For the stress distribution as shown in Figure 8, the stiffener rigidity, I, may be computed using the plate width, b, for a hypothetical plate with width equal to twice the greatest distance from the neutral axis to the edge of the plate (12). Shear will not be a consideration in the determination of longitudinal stiffener rigidity for the aspect ratios involved. The minimum size longitudinal stiffener will undoubtedly be controlled by practical considerations and not by stability requirements, since the stiffeners participate in direct structural action with the side plates of the box.

Transverse Stiffening Rings

Transverse stiffening rings are required to help hold the steel box to its original configuration and control the aspect ratio of the side plates. Ring size would be set primarily by practical consideration of the fabrication and erection problems. They would probably be of the same size as the longitudinal stiffeners. Again, either a rolled structural T or a welded T could be used for these rings. It is recommended at present (1963) that width to thickness ratios follow current practice (16).

SUGGESTED DESIGN PROCEDURE FOR ONE-CELL BOX

A suggested design procedure is illustrated by the analysis of a 75-ft simple span structure consisting of a one-cell box for the H20-S16 live loading. The concrete slab must be designed and preliminary thicknesses for the side plates and spacings and sizes for the longitudinal stiffeners estimated. The flexural stresses may be determined from the flexure formula and the shearing stresses, including those due to torsion, computed by an application of the membrane analogy.

The details of the one-cell box for a 75-ft simple span are shown in Figure 9. The box is divided into segments, taken symmetrical with respect to the stiffeners. Segments A, B, C, and D in the cantilever portion of the slab resist shear, but torsion is resisted only by the box section, Segments 1 through 22. A modular ratio, E_s/E_c, of 6 is used for 5,000-psi concrete to obtain the equivalent steel area for the slab segments.

Vertical Load

The computation of the section moduli required to obtain the flexural stresses due to vertical loads and an analysis for the determination of shear flow forces for a shear of 100 kips due to a vertical load through the shear center of the box are given in Table 1. The assumption that each segmental area (Col. 2) is concentrated at the centerline of the side plate is considered to give sufficient accuracy to the computations. Dividing the sum of the vertical distances from each element to the center of the bottom plate, y', and the first moments of the segmental areas about the center of the bottom plate, Ay', by the total area locates the centroidal axis from the center of the bottom plate: $\bar{y} = 26,400.26/734.06 = 35.9647$ in. for the composite section; and $\bar{y} = 1,358.04/140.08 = 9.69$ in. for the steel section.

The values of Ay'^2 are for use in the determination of the moments of inertia about the centroidal x-axis from the following:

$$I_x = \sum Ay'^2 - y^2 \sum A \tag{6}$$

For the composite section:

$$I_x = 1,099,724.78 - 734.06\,(35.9647)^2 = 150,247.79 \text{ in.}^4$$

TABLE 1

VERTICAL LOAD—SHEAR STRESS ANALYSIS, ONE-CELL BOX, 75-FOOT SPAN

1 Segment	2 A Area (in.^{2})	3 y' Arm From ℄ Bott. ⅊ (in.)	4 Ay' (in.^{3})	5 Ay'^2 (in.^{4})	6 y Arm From Comp. C.G. (in.)	7 AY (in.^{3})	8 $\Delta q = \frac{V}{I} AY$ (lb / in.)	9 q_y (lb / in.)	10 L Length (in.)	11 a Arm (in.)	12 L·a (in.^{2})	13 $q_y \cdot L \cdot a$ (lb - in.)	14 $q_y + q_1$ (lb / in.)	15 $(q_y + q_1) \cdot L$ (lb)
1	12.75	36.66	467.42	17,135.43	0.5953	8.865	5.900	5.900	9.50	96.00	912.00	5,380.80	1230.518	11,734.21
2	5.00	27.16	135.80	3,688.33	- 8.8047	- 44.024	- 29.301	- 23.401	12.00	96.00	1152.00	- 26,957.95	1201.207	14,414.48
3	5.00	15.16	75.80	1,149.13	- 20.8047	- 104.024	- 69.235	- 92.636	15.16	96.00	1455.36	- 134,818.73	1131.982	17,160.85
4	6.04	0.0	0.0	0.0	- 35.9647	- 217.227	- 144.579	- 237.215	26.00	0.0	0.0	0.0	987.403	25,672.48
5	13.75	0.0	0.0	0.0	- 35.9647	- 494.515	- 329.133	- 566.348	28.00	0.0	0.0	0.0	658.270	18,431.56
6	13.75	0.0	0.0	0.0	- 35.9647	- 494.515	- 329.133	- 895.481	28.00	0.0	0.0	0.0	329.137	9,215.84
7	13.75	0.0	0.0	0.0	- 35.9647	- 494.515	- 329.133	- 1224.614	28.00	0.0	0.0	0.0	0.0	0.0
8	13.75	0.0	0.0	0.0	- 35.9647	- 494.515	- 329.133	- 1553.747	28.00	0.0	0.0	0.0	- 329.137	- 9,215.61
9	13.75	0.0	0.0	0.0	- 35.9647	- 494.515	- 329.133	- 1882.880	28.00	0.0	0.0	0.0	- 658.262	- 18,431.34
10	13.75	0.0	0.0	0.0	- 35.9647	- 494.515	- 329.133	- 2212.013	26.00	0.0	0.0	0.0	- 987.395	- 25,672.27
11	6.04	0.0	0.0	0.0	- 35.9647	- 217.227	- 144.579	- 2356.592	15.16	96.00	1455.36	- 3,429,689.73	- 1131.974	17,160.73
12	5.00	15.16	75.80	1,149.13	- 20.8047	- 104.024	- 69.235	- 2425.827	12.00	96.00	1152.00	- 2,794,552.70	- 1201.209	14,414.51
13	5.00	27.16	135.80	3,688.33	- 8.8047	- 44.024	- 29.301	- 2455.128	9.50	96.00	912.00	- 2,239,076.74	- 1230.510	11,689.85
14	12.75	36.66	467.42	17,135.43	0.6953	8.865	5.900	- 2449.228	5.50	96.00	528.00	- 1,293,192.38	- 1224.610	6,735.36
A	27.03	42.16	1139.58	48,044.89	6.1953	167.459	111.455	111.455					111.455	
B	30.67	42.16	1293.05	54,514.87	6.1953	190.010	126.464	237.919					237.919	
C	36.67	42.16	1546.01	65,179.66	6.1953	227.182	151.204	389.123					389.123	
D	42.61	42.16	1796.44	75,737.81	6.1953	263.982	175.698	564.821					564.821	
15	20.00	42.16	843.20	35,549.31	6.1953	123.906	82.468	- 1801.939	26.00	42.16	1096.16	- 1,957,213.45	- 577.321	- 15,010.35
16	46.67	42.16	1967.61	82,954.32	6.1953	289.135	192.439	- 1609.500	28.00	42.16	1180.48	- 1,899,982.56	- 384.882	- 10,776.70
17	46.67	42.16	1967.61	82,954.32	6.1953	289.135	192.439	- 1417.061	28.00	42.16	1180.48	- 1,672,812.17	- 192.443	- 5,388.40
18	46.67	42.16	1967.61	82,954.32	6.1953	289.135	192.439	- 1224.622	28.00	42.16	1180.48	- 1,445,641.78	0.0	0.0
19	46.67	42.16	1967.61	82,954.32	6.1953	289.135	192.439	- 1032.183	28.00	42.16	1180.48	- 1,218,471.39	192.435	5,388.18
20	46.67	42.16	1967.61	82,954.32	6.1953	289.135	192.439	- 839.744	28.00	42.16	1180.48	- 991,301.00	384.874	10,776.47
21	46.67	42.16	1967.61	82,954.32	6.1953	289.135	192.439	- 647.305	26.00	42.16	1096.16	- 709,549.85	577.313	15,010.14
22	20.00	42.16	843.20	35,549.31	6.1953	123.906	82.468	0.0	5.50	96.00	528.00	0.0	1224.618	6,735.40
D	42.61	42.16	1796.44	75,737.81	6.1953	263.982	175.698	- 564.821					- 564.821	
C	36.67	42.16	1546.01	65,179.66	6.1953	227.182	151.204	- 389.123					- 389.123	
B	30.67	42.16	1293.05	54,514.87	6.1953	190.010	126.464	- 237.919					- 237.919	
A	27.03	42.16	1139.58	48,044.89	6.1953	167.459	111.455	- 111.455					- 111.455	
Comp. Sec.	734.06		26,400.26	1,099,724.78							16,189.44	- 19,825,879.63		
Steel Sec.	140.08		1358.04	43,945.78							2 A_B			

and for the steel section:

$$I_x = 43,945.78 - 140.08(9.69)^2 = 30,792.81 \text{ in.}^4$$

The shear flow forces for a 100-kip shear due to a vertical load through the shear center may now be computed. The box is cut between Segments 22 and 1, and the resulting shear flow forces are computed around the box. The place the box is cut is a matter of convenience. Cutting where $q = 0$ simplifies the computations. The torque of these shear flow forces around a point is determined and used to restore equilibrium and continuity to the box section. The shear flow forces in Segments A, B, C, and D on the left are opposite hand to those on the right and may be neglected in computing any torque. The static moment, Ay, of the segmental area about the centroidal axis of the composite box is computed by using the distance, y, from the centroidal axis to the center of each segment. The average increment in shear flow force acting in each segment of the cut box, $\Delta q = (V/I) Ay$, is given ($V/I = 100,000/150,247.79 = 0.665567194 \text{ lb/in.}^4$).

The intensity of the shear flow force at the center of each segment in the cut section, q_y, is found by summation, beginning with Segment 1, and it is assumed constant between the centers of the segments. The subscript y is used on q to indicate that the shear flow forces are from vertical loads. The shear flow forces create a torque. Since there is no torque with the load acting vertically through the shear center, the forces must be corrected, except for those in Segments A, B, C, and D, and brought into equilibrium. This may be done by determining the torque of the total shear flow forces around the box section about some convenient point and making the necessary correction to reduce the torque to zero. The torque will be computed about the intersection of the centerline of the bottom plate and the vertical centroidal axis of the box; clockwise torque is taken as positive. Columns 10 through 13 of Table 1 contain the computations necessary to determine the correction coefficient to be added algebraically to the values of q_y in Column 9. The distances between the centers of adjacent segments are noted by L. The total shear flow force between the centers of adjacent segments is q_yL and, letting a denote the perpendicular arm to each q_yL from the assumed torque center, the total torque is Σq_yLa. The correction coefficient, q_1, is equal to $-\Sigma q_yLa/\Sigma La = 19,825,879.63/16,189.44 = 1,224.618$ lb/in., where $\Sigma La = 2A_B$, with A_B being the total area inclosed by the box section.

The corrected values of the shear flow forces from a 100-kip shear due to a vertical load through the shear center, $q_y + q_1$, may be used to determine the shear flow force due to any vertical loading symmetrical with respect to the shear center of the box. The unit shearing stress is obtained by dividing the shear flow force by the thickness in inches of the side plate.

A check for horizontal and vertical equilibrium is obtained by noting that the values of the total shear flow forces, $(q_y + q_1)L$, for segments of opposite hand should have the same magnitude but be of opposite sign. Another check on the computations is to note that twice the area inclosed by the box section, $2A_B$, is (2) (192) (42.16) = 16,189.44, which is the same as the summation of Column 12, $\Sigma La = 16,189.44$.

Horizontal Load and Location of Shear Center

In the analysis for a 100-kip horizontal load, it is convenient to assume that the load acts along the horizontal centerline of the bottom side plate of the box. It could be assumed to act along any horizontal line. The computations in Columns 1 through 13 of Table 2 correspond to those in Columns 1 through 15 of Table 1. The location of the vertical centroidal axis is known for the horizontal load. The intensity of the shear flow force at the center of each segment is designated by q_x to indicate that the shear flow force is from a horizontal load. The shear flow forces in Segments A, B, C, and D must be considered, since the shear flow forces on the left and the right cantilever sides of the box act in the same direction. They must not be corrected in

1	2	3	4	5	6	7	8	9
Segment	A Area (in.²)	X Arm From ℄ Box (in.)	A·X (in.³)	A·X² (in.⁴)	$\Delta q_x = \frac{H}{I} A x$ (lb/in.)	q_x (lb/in.)	a Arm (in.)	L Length (in.)
1	12.75	96.00	1 224.00	117,504.00	15.90	15.90	96.00	9.50
2	5.00	96.00	480.00	46,080.00	6.24	22.14	96.00	12.00
3	5.00	96.00	480.00	46,080.00	6.24	28.38	96.00	15.16
4	6.04	96.00	579.84	55,664.64	7.53	35.91	0.0	26.00
5	13.75	70.00	962.50	67,375.00	12.50	48.41	0.0	28.00
6	13.75	42.00	577.50	24,255.00	7.50	55.91	0.0	28.00
7	13.75	14.00	192.50	2,695.00	2.50	58.41	0.0	28.00
8	13.75	- 14.00	- 192.50	2,695.00	- 2.50	55.91	0.0	28.00
9	13.75	- 42.00	- 577.50	24,255.00	- 7.50	48.41	0.0	28.00
10	13.75	- 70.00	- 962.50	67,375.00	- 12.50	35.91	0.0	26.00
11	6.04	- 96.00	- 573.84	55,664.64	- 7.53	28.38	96.00	15.16
12	5.00	- 96.00	- 480.00	46,080.00	- 6.24	22.14	96.00	12.00
13	5.00	- 96.00	- 480.00	46,080.00	- 6.24	15.90	96.00	9.50
14	12.75	- 96.00	- 1224.00	117,504.00	- 15.90	0.0	96.00	5.50
A	27.03	-190.49	- 5148.84	980,787.27	- 66.89	- 66.89	42.16	27.43
B	30.67	-163.06	- 5 001.05	815,524.14	- 64.97	-131.86	42.16	26.93
C	36.67	-136.13	- 4 986.59	679,433.54	-64.83	-196.69	42.16	27.10
D	42.61	-109.03	- 4 647.05	508,971.91	-60.38	-257.07	42.16	13.03
15	20.00	- 96.00	- 1 920.00	184,320.00	-24.94	-282.01	42.16	26.00
16	46.67	- 70.00	- 3266.90	228,683.00	-42.44	-324.45	42.16	28.00
17	46.67	- 42.00	- 1960.14	82,325.88	-25.46	-349.91	42.16	28.00
18	46.67	- 14.00	- 653.38	9,147.32	- 8.49	-358.40	42.16	28.00
19	46.67	14.00	653.38	9,147.32	8.49	-349.91	42.16	28.00
20	46.67	42.00	1960.14	82,325.88	25.46	-324.45	42.16	28.00
21	46.67	70.00	3,266.90	228,683.00	42.44	-282.01	42.16	26.00
22	20.00	96.00	1 920.00	184,320.00	24.94	0.0	96.00	5.50
D	42.61	109.03	4647.05	508,971.91	60.38	-257.07	42.16	13.03
C	36.67	136.13	4986.59	679,433.54	64.83	-196.69	42.16	27.10
B	30.67	163.06	5001.05	815,524.14	64.97	-131.86	42.16	26.93
A	27.03	190.49	5148.84	980,787.27	66.89	- 66.89	42.16	27.43
	734.06			7,607,693.40				

restoring the cut section, as Segments A, B, C, and D do not resist torque. The correction is given by:

$$q_1 = - \Sigma q_x La / \Sigma La \tag{7}$$

In this case, $q_1 = 3,656,878.49/16,189.44 = 225.88$ lb/in.

Since only Segments 1 through 22 resist torque, the total shear forces in Segments A, B, C, and D must be considered an external load on the box section in location the shear center (Fig. 7). The general expression for the increment in angle of twist at the section is

$$d\theta/dz_1 = (1/2A_BG) \sum_{1}^{22} qL/t \tag{8a}$$

The increment in angle of twist at the section due to the external loading under consideration is

$$d\theta/dz_2 = (1/2A_BG) \sum_{1}^{22} (q_x + q_1)L/t \tag{8b}$$

LYSIS, ONE-CELL BOX, 75-FOOT SPAN

11	12	13	14	15	16	17	18	19	20
$q_x \cdot L \cdot a$	$q_x + q_1$	$(q_x + q_1) L$	$(q_x + q_1) \frac{L}{t}$	$\frac{L}{t}$	a'	$L \cdot a'$	$q_x \cdot L \cdot a'$	$q_x + q_2$	$(q_x + q_2) \frac{L}{t}$
(lb - in.)	(lb/ in.)	(lb)	(lb/in.)		(in.)	(in.^{2})	(lb - in.)	(lb/in.)	(lb/in.)
14,500.80	241.78	2,296.91	9,187.64	38.00	96.00	912.00	14,500.80	16.79	638.02
25,505.28	248.02	2,976.24	11,904.96	48.00	96.00	1 152.00	25,505.28	23.03	1105.44
41,303.12	254.26	3,854.58	15,418.33	60.64	96.00	1 455.36	41,303.12	29.27	1774.93
0.0	261.79	6,806.54	21,780.93	83.20	36.45	947.70	34,031.91	36.80	3061.76
0.0	274.29	7,680.12	24,576.38	89.60	36.45	1020.60	49,407.25	49.30	4417.28
0.0	281.79	7,890.12	25,248.38	89.60	36.45	1020.60	57,061.75	56.80	5089.28
0.0	284.29	7,960.12	25,472.38	89.60	36.45	1020.60	59,613.25	59.30	5313.28
0.0	281.79	7,890.12	25,248.38	89.60	36.45	1020.60	57,061.75	56.80	5089.28
0.0	274.29	7,680.12	24,576.38	89.60	36.45	1 020.60	49,407.25	49.30	4 417.28
0.0	261.79	6,806.54	21,780.93	83.20	36.45	947.70	34,031.91	36.80	3061.76
41,303.12	254.26	3,854.58	15,418.33	60.64	96.00	1455.36	41,303.12	29.27	1774.93
25,505.28	248.02	2,976.24	11,904.96	48.00	96.00	1 152.00	25,505.28	23.03	1105.44
14,500.80	241.78	2,296.91	9,187.64	38.00	96.00	912.00	14,500.80	16.79	638.02
0.0	225.88	1,242.34	745.40	3.30	96.00	528.00	0.0	0.87	2.87
77,354.94	- 66.89	- 1,834.79			5.71	156.63	- 10,476.98	-66.89	
149,709.89	-131.86	- 3,350.99			5.71	153.77	- 20,276.11	-131.86	
224,726.19	-196.69	- 5,330.30			5.71	154.74	- 30,435.81	-196.69	
141,218.83	-257.07	- 3,349.62			5.71	74.40	- 19,126.01	-257.07	
309,128.08	- 56.13	- 1,459.38	- 875.63	15.60	5.71	148.46	- 41,867.20	-281.12	- 4385.47
383,006.74	- 98.57	- 2,759.96	- 1 655.98	16.80	5.71	159.88	- 51,873.07	-323.56	- 5435.81
413,061.76	- 124.03	- 3,472.84	- 2083.70	16.80	5.71	159.88	- 55,943.61	-349.02	- 5,863.54
423,084.03	- 132.52	- 3,710.56	- 2226.34	16.80	5.71	159.88	- 57,300.99	-357.51	- 6,006.17
413,061.76	-124.03	- 3,472.84	- 2 083.70	16.80	5.71	159.88	- 55,943.61	-349.02	- 5,863.54
383,006.74	- 98.57	- 2,759.96	- 1655.98	16.80	5.71	159.88	-51,873.07	-323.56	- 5,435.81
309,128.08	- 56.13	- 1,459.38	- 875.63	15.60	5.71	148.46	-41,867.20	-281.12	- 4,385.47
0.0	225.88	- 1,242.34	745.40	3.30	96.00	528.00	0.0	0.87	2.87
141,218.33	-257.07	- 3,349.62			5.71	74.40	- 19,126.01	-257.07	
224,726.19	-196.19	- 5,330.30			5.71	154.74	- 30,435.81	-196.69	
149,709.89	-131.86	- 3,350.99			5.71	153.77	- 20,276.11	-131.86	
77,354.94	- 66.89	- 1,834.79			5.71	156.63	- 10,476.98	- 66.89	
,656,878.49			231,739.46			16,189.44 $2A_B$	- 14,065.10		

The general expression for torque about the shear center is

$$T_1 = 2qA_B \tag{9a}$$

The expression for torque about the shear center for the external loading under consideration is

$$T_2 = 71,868.60e \tag{9b}$$

where e is the distance from the resultant force to the shear center (Fig. 10). The computations necessary to locate the shear center are shown in Figure 10. The shear center is the point through which the line of action of the resultant external loading must pass in order to have no torsion. The point of application of the 100-kip horizontal force for zero torque about the shear center is located from $e_2 = (28,131.4)(7.95) / 100,000 = 2.24$ in. above the shear center (Fig. 10).

The shear flow forces in Column 7 must now be corrected to give torque equilibrium about the shear center with the external load of 100 kips. This load must act 2.24 in. above the shear center for zero torque. This is done by taking the torque of the external load and internal shear flow forces about some convenient point and determining the shear flow corrections to give torque equilibrium about the shear center for the internal shear flow forces. It is convenient to take moments about the line of action of the 100-kip load for zero torque—2.24 in. above the shear center. The correction is found from:

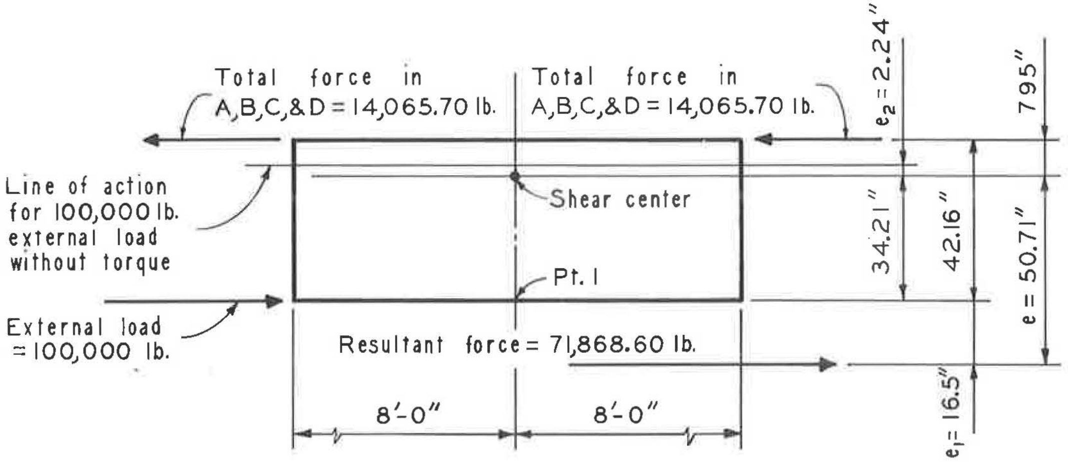
Total force in A,B,C,&D = 14,065.70 lb.
Total force in A,B,C,&D = 14,065.70 lb.
Line of action for 100,000 lb. external load without torque
External load = 100,000 lb.
Shear center
Pt. 1
Resultant force = 71,868.60 lb.
8'-0"
8'-0"
e2 = 2.24"
795"
34.21"
42.16"
e = 50.71"
e1 = 16.5"

$\sum H = 0$

$$100{,}000 - 2 \times 14{,}065.70 = 71{,}868.60 \text{ pounds}$$

$\sum M$ Pt. 1

$$e_1 = \frac{2 \times 14{,}065.70 \times 42.16}{71{,}868.60} = 16.5''$$

$$\frac{d\theta}{dZ_1} = \frac{1}{2A_B G} \sum_{1}^{22} q \frac{L}{t} \quad \& \quad T_1 = 2qA_B$$

$$\frac{d\theta}{dZ_2} = \frac{1}{2A_B G} \sum_{1}^{22} \left(q_x + q_1\right) \frac{L}{t} \quad \& \quad T_2 = 71{,}868.60\, e$$

$$\frac{T_2}{T_1} = \frac{d\theta / dZ_2}{d\theta / dZ_1}$$

$$\frac{71{,}868.60\, e}{16{,}189.44\, q} = \frac{231{,}739.46}{1{,}029.48\, q}$$

$$e = 50.71''$$

Figure 10. Location of shear center, one-cell box, 75-ft span.

$$q_2 = - \sum q_x La' / \sum La'$$

which is in this case 14,065.10/16,189.44 = 0.87 lb/in.

Torsion Only

The shear flow force for pure torsion about the shear center is equal to $T/2A_B$. This gives for a pure torsion of 100 ft-kips about the shear center, $q_t = (100,000)(12)/16,189.44 = 74.12$ lb/in.

Flexural and Shearing Stresses

The dead load per foot of bridge for the one-cell box on the 75-ft span to be used in the stress computations is as follows:

Railing and curb = 467.4 lb/ft
Asphalt wearing surface = 450.0 lb/ft
Precast concrete deck = 3,711.7 lb/ft
Steel box = 550.7 lb/ft
Total = 5,179.8 lb/ft

The maximum bending moments and shears for one lane of H20-S16 live loading are given in the AASHO specifications (16, p. 273). The impact factor is 0.25 in accordance with these specifications. The following maximum moments result from full loading of the structure, noting that the maximum live load moment occurs 2.33 ft from mid-span with 14-ft axle spacings for the live load:

Dead load at mid-span = $(5.1798)(75)^2/8$ = 3,642.1 ft-kips
Maximum live load plus impact = (2) (1075.1) (1.25) = 2,687.8 ft-kips
Dead load at point of maximum LL moment = $\left[(5.1798)(39.83)(35.17)\right]/2$ = 3,628.0 ft-kips

The following maximum shears occur under the same conditions:

Dead load at end of span = (5.1798) (37.5) = 194.2 kips
Live load plus impact = (2) (63.1) (1.25) = 157.8 kips

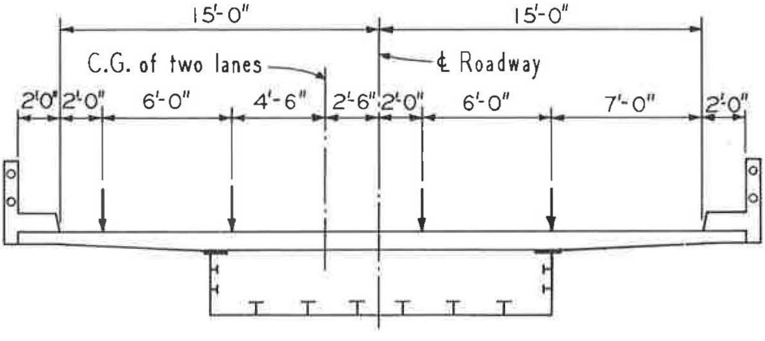

Figure 11. Transverse position of live load for maximum torque.

Torque is obtained by the unsymmetrical placing of the live load lanes on the roadway. Figure 11 shows the transverse position of the live load on the roadway deck for maximum torque, both lanes loaded, with the end heavy axle placed over the support. This gives the value of the maximum live load plus impact torque, with the value of the torque from each load distributed to the end similarly to its effect on end shear as:

$$\Big[(64)(2.5) + (64)(2.5)(61)/75 + (16)(2.5)(47)/75\Big](1.25) = 393.75 \text{ ft-kips.}$$

Assuming the dead load carried by the steel box alone and the live load and impact by the total composite section and using the moments of inertia previously computed to obtain the appropriate section moduli yields the unit flexural stresses given in Table 3.

By assuming the dead load shear to be uniformly distributed in the vertical side plates, and determining the maximum live load, impact and torque shearing effect by the use of the coefficients previously determined, the unit shearing stresses between Segments 1 and 2 are as follows:

$$\begin{aligned}
\text{DL} &= (194.2)/(2)(36)(1/4) &&= 10.79 \text{ ksi}\\
\text{LL} + \text{I} &= (1.578)(1.230518)/(1/4) &&= 7.76 \text{ ksi}\\
\text{Torque} &= (3.9375)(0.07412)/(1/4) &&= 1.17 \text{ ksi}\\
&\ \text{Total} &&= 19.72 \text{ ksi}
\end{aligned}$$

SUGGESTED DESIGN PROCEDURE FOR THREE-CELL BOX

The details of a three-cell box for a 75-ft simple span are shown in Figure 12. The box is divided into 32 segments around the cells with each cantilever portion of the slab divided into Segments A, B, and C, which resist shear but not torsion.

Vertical Load

Tables 4 through 7 contain most of the computations for the effect of a shear of 100 kips due to a vertical load through the shear center of the box. The nomenclature is the same as used for the analysis of the one-cell box. Columns 1 through 5 of Table 4 give the data for the location of the centroids of both the steel box alone and the composite section and the determination of the moments of inertia of each I_x about the centroidal axes. It is necessary to cut the three-cell box into three one-cell boxes

TABLE 3

FLEXURAL STRESSES, ONE-CELL BOX, 75-FOOT SPAN

Load	Top of Steel (ksi)	Bottom of Steel (ksi)	Top of Concrete (ksi)
Dead Load	38.84	13.93	-
Live Load and Impact	0.26	7.76	0.40
Total	39.10	21.69	0.40

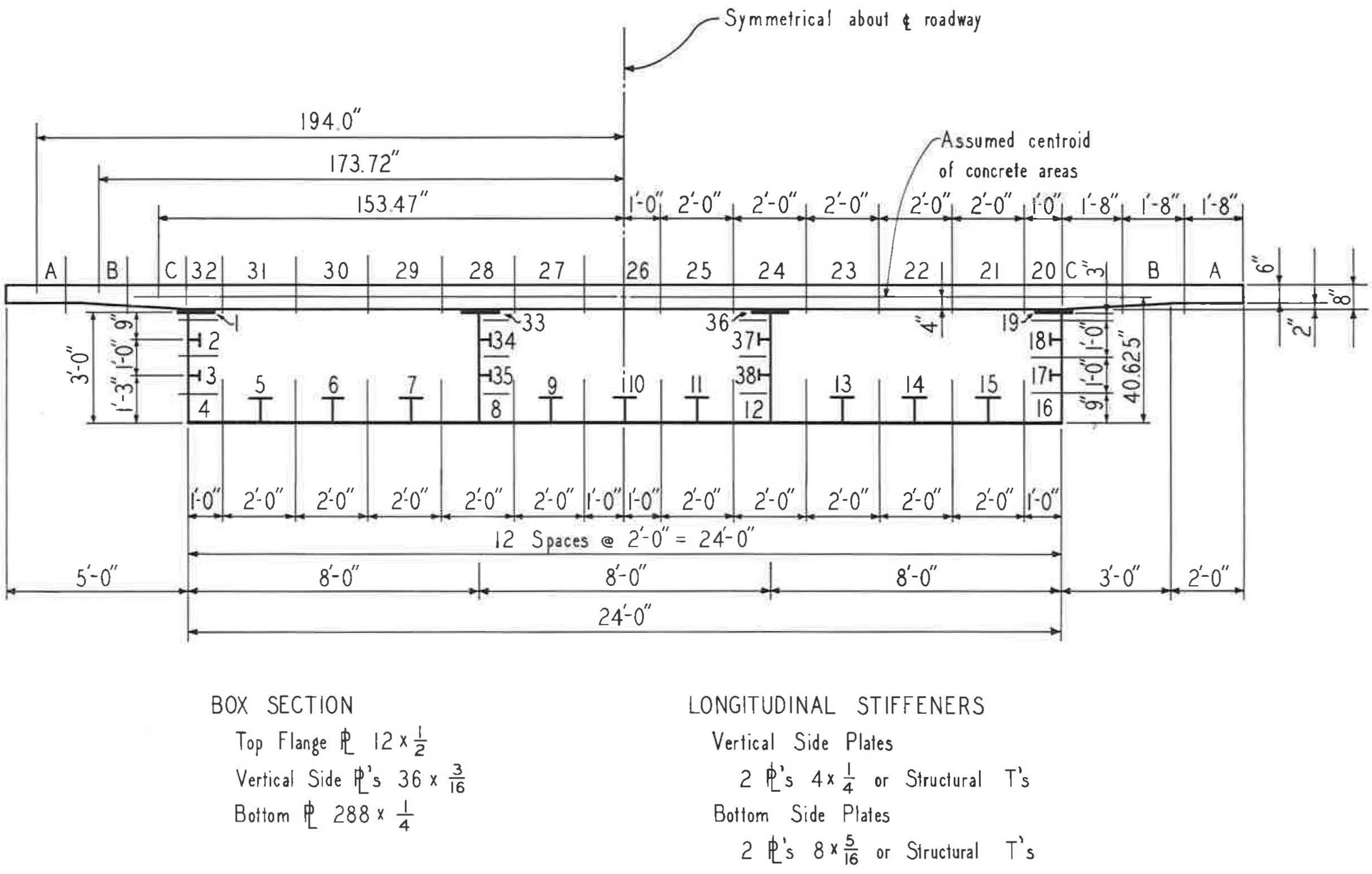
Symmetrical about ℄ roadway
Assumed centroid of concrete areas
194.0"
173.72"
153.47"
1'-0" 2'-0" 2'-0" 2'-0" 2'-0" 2'-0" 1'-0" 1'-8" 1'-8" 1'-8"
A B C 32 31 30 29 28 27 26 25 24 23 22 21 20 C 3" B A
6" 8" 2" 4"
1 2 3 4 5 6 7 8 9 10 11 12 13 14 15 16 17 18 19
33 34 35 36 37 38
3'-0" 9" 1'-0" 1'-3"
9" 1'-0" 1'-0" 40.625"
1'-0" 2'-0" 2'-0" 2'-0" 2'-0" 2'-0" 1'-0" 1'-0" 2'-0" 2'-0" 2'-0" 2'-0" 2'-0" 1'-0"
12 Spaces @ 2'-0" = 24'-0"
5'-0" 8'-0" 8'-0" 8'-0" 3'-0" 2'-0"
24'-0"
BOX SECTION
Top Flange ℘ 12 x 1/2
Vertical Side ℘'s 36 x 3/16
Bottom ℘ 288 x 1/4
LONGITUDINAL STIFFENERS
Vertical Side Plates
2 ℘'s 4 x 1/4 or Structural T's
Bottom Side Plates
2 ℘'s 8 x 5/16 or Structural T's

Figure 12. Analysis details of three-cell box, 75-ft span.

TABLE 4

VERTICAL LOAD–SHEAR STRESS ANALYSIS, THREE-CELL BOX, 75-FOOT SPAN

1 Segment	2 A Area (in.^{2})	3 y' Arm From ℄ Bott ⅊ (in.)	4 Ay' (in.^{3})	5 Ay'^2 (in.^{4})	6 y Arm From Comp C.G. (in.)	7 Ay (in.^{3})	8 $\Delta q = \frac{V}{I} Ay$ (lb/in.)	9 q_y (lb/in.)	10 L Length (in.)	11 a Arm (in.)	12 L·a (in.^{2})	13 q_y·L (lb)	14 q_y·L·a (lb-in.)	15 $q_y + q$ (lb/in.)
1	6.56	36.375	238.620	8,679.80	4.029	26.430	15.466	15.466	9.25	144.00	1,332.00	143.061	20,600.71	558.894 ↑
2	4.25	27.125	115.281	3,127.00	- 5.221	- 22.189	- 12.984	2.482	12.00	144.00	1,728.00	29.784	4,288.90	545.910 ↑
3	4.25	15.125	64.281	972.25	- 17.221	- 73.189	- 42.827	- 40.345	15.125	144.00	2,178.00	- 610.218	- 87,871.41	503.083 ↑
4	4.71	0.0	0.0	0.0	- 32.346	- 152.350	- 89.148	- 129.493	24.00	0.0	0.0	0.0	0.0	413.935 ←
5	11.00	0.0	0.0	0.0	- 32.346	- 355.806	- 208.201	- 337.694	24.00	0.0	0.0	0.0	0.0	205.734 ←
6	11.00	0.0	0.0	0.0	- 32.346	- 355.806	- 208.201	- 545.895	24.00	0.0	0.0	0.0	0.0	2.467 →
7	11.00	0.0	0.0	0.0	- 32.346	- 355.806	- 208.201	- 754.096	24.00	0.0	0.0	0.0	0.0	210.668 →
8	7.69	0.0	0.0	0.0	- 32.346	- 248.741	- 145.552	- 899.648	24.00	0.0	0.0	0.0	0.0	312.327 ←
9	11.00	0.0	0.0	0.0	- 32.346	- 355.806	- 208.201	- 1107.050	24.00	0.0	0.0	0.0	0.0	104.126 ←
10	11.00	0.0	0.0	0.0	- 32.346	- 355.806	- 208.201	- 1316.050	24.00	0.0	0.0	0.0	0.0	104.075 →
11	11.00	0.0	0.0	0.0	- 32.346	- 355.806	- 208.201	- 1524.251	24.00	0.0	0.0	0.0	0.0	312.276 →
12	7.69	0.0	0.0	0.0	- 32.346	- 284.741	- 145.552	- 1669.803	24.00	0.0	0.0	0.0	0.0	210.702 ←
13	11.00	0.0	0.0	0.0	- 32.346	- 355.806	- 208.201	- 1878.004	24.00	0.0	0.0	0.0	0.0	2.501 ←
14	11.00	0.0	0.0	0.0	- 32.346	- 355.806	- 208.201	- 2086.205	24.00	0.0	0.0	0.0	0.0	205.700 →
15	11.00	0.0	0.0	0.0	- 32.346	- 355.806	- 208.201	- 2294.406	24.00	0.0	0.0	0.0	0.0	413.901 →
16	4.71	0.0	0.0	0.0	- 32.346	- 152.350	- 89.148	- 2383.590	15.125	144.00	2178.00	- 36,051.799	- 5,191,459.02	503.089 ↑
17	4.25	15.125	64.281	972.25	- 17.221	- 73.189	- 42.827	- 2426.417	12.00	144.00	1728.00	- 29,117.004	- 4,192,848.58	545.912 ↑
18	4.25	27.125	115.281	3,127.00	- 5.221	- 22.189	- 12.984	- 2439.401	9.25	144.00	1332.00	- 22,564.459	- 3,249,282.13	558.896 ↑
19	6.56	36.375	238.620	8,679.80	4.029	26.430	15.466	- 2423.935	4.25	144.00	612.00	- 10,301.724	- 1,483,448.22	543.430 ↑
A	20.00	40.625	812.500	33,007.81	8.279	165.580	96.890	96.890						96.890 →
B	21.29	40.625	864.906	35,136.82	8.279	176.260	103.139	200.029						200.029 →
C	25.21	40.625	1024.156	41,606.35	8.279	208.714	122.130	322.159						322.159 →
20	16.00	40.625	650.000	26,406.25	8.279	132.464	77.512	- 2024.264	24.00	40.625	975.00		- 1,973,657.40	143.759 ←
21	32.00	40.625	1300.000	52,812.50	8.279	264.928	155.023	- 1869.241	24.00	40.625	975.00		- 1,822,509.98	11.264 →
22	32.00	40.625	1300.000	52,812.50	8.279	264.928	155.023	- 1714.218	24.00	40.625	975.00		- 1,671,362.55	166.287 →
23	32.00	40.625	1300.000	52,812.50	8.279	264.928	155.023	- 1559.195	24.00	40.625	975.00		- 1,520,215.13	321.310 →
24	32.00	40.625	1300.000	52,812.50	8.279	264.928	155.023	- 40.345	4.25			- 171.466		708.875 ↑
36	6.56	36.375	238.620	8,679.80	4.029	26.430	15.466	- 55.811	9.25			- 516.251		724.341 ↑
37	4.25	27.125	115.281	3,127.00	- 5.221	- 22.189	- 12.984	- 42.827	12.00			- 513.920		711.357 ↑
38	4.25	15.125	64.281	972.25	- 17.221	- 73.189	- 42.827							668.530 ↑
12														
24								- 1444.517	24.00	40.625	975.00		- 1,408,404.08	232.542 ←
25	32.00	40.625	1300.00	52,812.50	8.279	264.928	155.023	- 1289.494	24.00	40.625	975.00		- 1,257,256.65	77.519 ←
26	32.00	40.625	1300.00	52,812.50	8.279	264.928	155.023	- 1134.471	24.00	40.625	975.00		- 1,106,109.23	77.504 →
27	32.00	40.625	1300.00	52,812.50	8.279	264.928	155.023	- 979.448	24.00	40.625	975.00		- 954,961.80	232.527 →
28	32.00	40.625	1300.00	52,812.50	8.279	264.928	155.023	- 40.345	4.25			- 171.466		708.892 ↑
33	6.56	36.375	238.620	8,679.80	4.029	26.430	15.466	- 55.811	9.25			- 516.251		724.358 ↑
34	4.25	27.125	115.281	3,127.00	- 5.221	- 22.189	- 12.984	- 42.827	12.00			- 513.920		711.374 ↑
35	4.25	15.125	64.281	972.25	- 17.221	- 73.189	- 42.827							668.547 ↑
8														
28								- 864.770	24.00	40.625	975.00		- 843,150.75	321.342 ←
29	32.00	40.625	1300.00	52,812.50	8.279	264.928	155.023	- 709.747	24.00	40.625	975.00		- 692,003.33	166.319 ←
30	32.00	40.625	1300.00	52,812.50	8.279	264.928	155.023	- 554.724	24.00	40.625	975.00		- 540,855.90	11.296 ←
31	32.00	40.625	1300.00	52,812.50	8.279	264.928	155.023	- 399.701	24.00	40.625	975.00		- 389,708.48	143.727 →
32	16.00	40.625	650.00	26,406.25	8.279	132.464	77.512	0.0	4.25	144.000	612.00			543.428 ↑
C	25.21	40.625	1024.156	41,606.35	8.279	208.714	122.130	322.159						322.159 ←
B	21.29	40.625	864.906	35,136.82	8.279	176.260	103.139	200.029						200.029 ←
A	20.00	40.625	812.500	33,007.81	8.279	165.580	96.890	96.890						96.890 ←
Comp Sec	701.04		22,675.852	904,368.16							23,400.00	100,000.887	- 28,360,215.03	
Steel Sec	184.04		1,672.728	51,116.20							3(2 A_B)			

$V = 100{,}000$ lb ↓

$\frac{V}{I} = \frac{100{,}000}{170{,}895.44} = 0.58515312$ lb/in.^{4}

$\bar{y}_{steel} = \frac{1{,}672.728}{184.04} = 9.0889$ in above ℄ bott ⅊

$I_x = 51{,}116.20 - 184.04(9.0889)^2 = 35{,}913.00$ in.^{4}

$\bar{y}_{comp} = \frac{22{,}675.852}{701.04} = 32.346$ in. above ℄ bott ⅊

$I_x = 904{,}368.16 - 701.04(32.346)^2 = 170{,}895.44$ in.^{4}

and to tie them together again with the principle of consistent displacements, noting that the segments in the two interior vertical plates must be considered as a part of each adjacent cell. Columns 7 through 14 in Table 4 and Tables 5, 6, and 7 contain the data necessary to find the shear force corrections, q_1, q_2, and q_3, for the left, middle, and right cutback one-cell boxes, respectively.

The first of three equations necessary to find these corrections is based on the fact that $-\Sigma q_y La / \Sigma La = q_1 + q_2 + q_3$, where $\Sigma La = 2A_B$ for each cell. This gives $q_1 + q_2 + q_3 = 28,360,215.03/7,800 = 3,635.928$. $2A_B$, $40.625(96)(2) = 7,800$, checks one-third of the summation of Column 12 in Table 4.

The other two necessary equations are based on the fact that the adjacent cells must deform similarly. The equations are found by equating the movement for the left box in Table 5 to that of the middle box in Table 6 and the movement of the middle box to that of the right box in Table 7. This gives $-223,125.588 + 850.376q_1 - 197.188q_2 = -552,651.36 - 197.188q_1 + 850.376q_2 - 197.188q_3$ and $-552,651.36 - 197.188q_1 + 850.376q_2 - 197.188q_3 = -1,360,148.00 - 197.188q_2 + 850.376q_3$. These reduce to $1,047.564q_1 - 1,047.564q_2 + 197.188q_3 = -329,525.77$ and $-197.188q_1 + 1,047.564q_2 - 1,047.564q_3 = -807,496.44$. Their solution gives $q_1 = 543.428$ lb/in., $q_2 = 1,211.975$ lb/in., and $q_3 = 1,880.505$ lb/in. These values are used to obtain the corrected values of the shear flow forces given in Column 15 of Table 4.

Horizontal Load

Tables 8 through 11 contain most of the computations for the effect of a 100-kip horizontal load assumed to act along the horizontal centerline of a bottom side plate of

TABLE 5

DEFORMATIONS IN LEFT CELL

Segment	q total (lb/in.)	L (in.)	t (in.)	L/t	q total - L/t
1-2	$15.466 + q_1$	9.25	.1875	49.333	$762.984 + 49.333\ q_1$
2-3	$2.482 + q_1$	12.00	.1875	64.000	$158.848 + 64.00\ q_1$
3-4	$- 40.345 + q_1$	15.125	.1875	80.667	$- 3,254.510 + 80.667\ q_1$
4-5	$-129.493 + q_1$	24.00	.250	96.00	$-12,431.328 + 96.00\ q_1$
5-6	$-337.694 + q_1$	24.00	.250	96.00	$-32,418.624 + 96.00\ q_1$
6-7	$-545.895 + q_1$	24.00	.250	96.00	$-52,405.920 + 96.00\ q_1$
7-8	$-754.096 + q_1$	24.00	.250	96.00	$-72,393.216 + 96.00\ q_1$
8-35	$q_1 - q_2$	15.125	.1875	80.667	$80.667\ q_1 - 80.667\ q_2$
35-34	$- 42.827 + q_1 - q_2$	12.00	.1875	64.00	$- 2,740.928 + 64.00\ q_1 - 64.00\ q_2$
34-33	$- 55.811 + q_1 - q_2$	9.250	.1875	49.333	$- 2,753.324 + 49.333\ q_1 - 49.333\ q_2$
33-28	$- 40.345 + q_1 - q_2$	4.250	1.333	3.188	$- 128.620 + 3.188\ q_1 - 3.188\ q_2$
28-29	$-864.770 + q_1$	24.00	1.333	18.00	$-15,565.860 + 18.00\ q_1$
29-30	$-709.747 + q_1$	24.00	1.333	18.00	$-12,775.446 + 18.00\ q_1$
30-31	$-554.724 + q_1$	24.00	1.333	18.00	$- 9,985.032 + 18.00\ q_1$
31-32	$-399.701 + q_1$	24.00	1.333	18.00	$- 7,194.618 + 18.00\ q_1$
32-1	q_1	4.25	1.333	3.188	$3.188\ q_1$
			$2A_B G \frac{d\theta_1}{dz}$	=	$-223,125.588 + 850.376\ q_1 - 197.188\ q_2$

TABLE 6

DEFORMATIONS IN MIDDLE CELL

Segment	q total (lb/in.)	L (in.)	t (in.)	L/t	q total - L/t
8-9	$-899.648 + q_2$	24.0	.250	96.00	$-86{,}366.208 + 96.00\ q_2$
9-10	$-1{,}107.849 + q_2$	24.0	.250	96.00	$-106{,}353.504 + 96.00\ q_2$
10-11	$-1{,}316.050 + q_2$	24.0	.250	96.00	$-126{,}340.800 + 96.00\ q_2$
11-12	$-1{,}524.251 + q_2$	24.0	.250	96.00	$-146{,}328.096 + 96.00\ q_2$
12-38	$+ q_2 - q_3$	15.125	.1875	80.667	$+ 80.667\ q_2 - 80.667\ q_3$
38-37	$-42.827 + q_2 - q_3$	12.00	.1875	64.00	$-2{,}740.928 + 64.00\ q_2 - 64.00\ q_3$
37-36	$-55.811 + q_2 - q_3$	9.25	.1875	49.333	$-2{,}753.324 + 49.333\ q_2 - 49.333\ q_3$
36-24	$-40.345 + q_2 - q_3$	4.25	1.333	3.188	$-128.620 + 3.188\ q_2 - 3.188\ q_3$
24-25	$-1{,}444.517 + q_2$	24.00	1.333	18.00	$-26{,}001.306 + 18.00\ q_2$
25-26	$-1{,}289.494 + q_2$	24.00	1.333	18.00	$-23{,}210.892 + 18.00\ q_2$
26-27	$-1{,}134.471 + q_2$	24.00	1.333	18.00	$-20{,}420.478 + 18.00\ q_2$
27-28	$-979.448 + q_2$	24.00	1.333	18.00	$-17{,}630.074 + 18.00\ q_2$
28-33	$40.345 + q_2 - q_1$	4.25	1.333	3.188	$128.620 - 3.188\ q_1 + 3.188\ q_2$
33-34	$55.811 + q_2 - q_1$	9.25	.1875	49.333	$2{,}753.324 - 49.333\ q_1 + 49.333\ q_2$
34-35	$42.827 + q_2 - q_1$	12.00	.1875	64.00	$2{,}740.928 - 64.00\ q_1 + 64.00\ q_2$
35-8	$q_2 - q_1$	15.125	.1875	80.667	$-80.667\ q_1 + 80.667\ q_2$

$$2\ A_B G \frac{d\theta_z}{dz} = -552{,}651.36 - 197.188\ q_1 + 850.376\ q_2 - 197.188\ q_3$$

TABLE 7

DEFORMATIONS IN RIGHT CELL

Segment	q total (lb/in.)	L (in.)	t (in.)	L/t	q total - L/t
12-13	$-1{,}669.803 + q_3$	24.0	.25	96.00	$-160{,}301.088 + 96.0\ q_3$
13-14	$-1{,}878.004 + q_3$	24.0	.25	96.00	$-180{,}288.384 + 96.0\ q_3$
14-15	$-2{,}086.205 + q_3$	24.0	.25	96.00	$-200{,}275.680 + 96.0\ q_3$
15-16	$-2{,}294.406 + q_3$	24.0	.25	96.00	$-220{,}262.976 + 96.0\ q_3$
16-17	$-2{,}383.590 + q_3$	15.125	.1875	80.667	$-192{,}277.055 + 80.667\ q_3$
17-18	$-2{,}426.417 + q_3$	12.0	.1875	64.00	$-155{,}290.688 + 64.00\ q_3$
18-19	$-2{,}439.401 + q_3$	9.25	.1875	49.333	$-120{,}342.970 + 49.333\ q_3$
19-20	$-2{,}423.935 + q_3$	4.25	1.333	3.188	$-\ 7{,}727.504 + 3.188\ q_3$
20-21	$-2{,}024.264 + q_3$	24.0	1.333	18.00	$-\ 36{,}436.752 + 18.0\ q_3$
21-22	$-1{,}869.241 + q_3$	24.0	1.333	18.00	$-\ 33{,}646.338 + 18.0\ q_3$
22-23	$-1{,}714.218 + q_3$	24.0	1.333	18.00	$-\ 30{,}855.924 + 18.0\ q_3$
23-24	$-1{,}559.195 + q_3$	24.0	1.333	18.00	$-\ 28{,}065.510 + 18.0\ q_3$
24-36	$40.345 + q_3 - q_2$	4.25	1.333	3.188	$128.620 - 3.188\ q_2 + 3.188\ q_3$
36-37	$55.811 + q_3 - q_2$	9.25	.1875	49.333	$2{,}753.324 - 49.333\ q_2 + 49.333\ q_3$
37-38	$42.827 + q_3 - q_2$	12.0	.1875	64.00	$2{,}740.928 - 64.0\ q_2 + 64.0\ q_3$
38-12	$q_3 - q_2$	15.125	.1875	80.667	$-\ 80.667\ q_2 + 80.667\ q_3$
			$2\ A_B G \frac{d\theta_3}{dz} =$	$-\ 1{,}360{,}148.00$	$-197.188\ q_2 + 850.376\ q_3$

TABLE 8

HORIZONTAL LOAD—SHEAR STRESS ANALYSIS, THREE-CELL BOX, 75-FOOT SPAN

1	2	3	4	5	6	7	8	9	10	11	12	13	14	15	16	17
Segment	A Area (in.^{2})	X Arm (in.)	AX (in.^{3})	AX^2 (in.^{4})	$\Delta q = \frac{H}{I}AX$ (lb/in.)	q_x (lb/in.)	L Length (in.)	$q_x \cdot L$ (lb)	a (in.)	L·a (in.^{2})	$q_x \cdot L \cdot a$ (lb-in.)	a′ Arm (in.)	L·a′ (in.^{2})	$q_x \cdot L \cdot a'$ (lb-in.)	$q_x + q$ (lb/in.)	q_T (lb/in.)
1	6.56	144.00	944.640	136,028.16	11.454	11.454	9.25		144.000	1332.00	15,256.728	144.00	1332.00	15,256.728	2.909 ↓	48.254 ↑
2	4.25	144.00	612.000	88,812.00	7.421	18.875	12.00		144.000	1728.00	32,616.000	144.00	1728.00	32,616.000	4.512 ↑	48.254 ↑
3	4.25	144.00	612.000	88,812.00	7.421	26.896	15.125		144.000	2178.00	57,272.688	144.00	2178.00	57,272.688	11.933 ↑	48.254 ↑
4	4.71	144.00	678.240	97,666.56	8.333	34.629	24.00	831.096	0.0	0.0	0.0	34.637	831.29	28,786.741	20.266 ←	48.254 ←
5	11.00	120.00	1320.000	158,400.00	16.006	50.635	24.00	1215.240	0.0	0.0	0.0	34.637	831.29	42,092.369	36.272 ←	48.254 ←
6	11.00	96.00	1056.000	101,376.00	12.805	63.440	24.00	1522.560	0.0	0.0	0.0	34.637	831.29	52,737.038	49.077 ←	48.254 ←
7	11.00	72.00	792.000	57,024.00	9.604	73.044	24.00	1753.056	0.0	0.0	0.0	34.637	831.29	60,720.747	58.681 ←	48.254 ←
8	7.69	48.00	369.120	17,717.76	4.476	77.520	24.00	1860.480	0.0	0.0	0.0	34.637	831.29	64,441.601	62.444 ←	57.338 ←
9	11.00	24.00	264.000	6,336.00	3.201	80.721	24.00	1937.304	0.0	0.0	0.0	34.637	831.29	67,102.560	65.645 ←	57.338 ←
10	11.00	0.00	0.000	0.00	0.000	80.721	24.00	1937.304	0.0	0.0	0.0	34.637	831.29	67,102.560	65.645 ←	57.338 ←
11	11.00	-24.00	-264.000	6,336.00	-3.201	77.520	24.00	1860.480	0.0	0.0	0.0	34.637	831.29	64,441.601	62.444 ←	57.338 ←
12	7.69	-48.00	-369.120	17,717.76	-4.476	73.044	24.00	1753.056	0.0	0.0	0.0	34.637	831.29	60,720.747	58.681 ←	48.254 ←
13	11.00	-72.00	-792.000	57,024.00	-9.604	63.440	24.00	1522.560	0.0	0.0	0.0	34.637	831.29	52,737.038	49.077 ←	48.254 ←
14	11.00	-96.00	-1056.000	101,376.00	-12.805	50.635	24.00	1215.240	0.0	0.0	0.0	34.637	831.29	42,092.369	36.272 ←	48.254 ←
15	11.00	-120.00	-1320.000	158,400.00	-16.006	34.629	24.00	831.096	0.0	0.0	0.0	34.637	831.29	28,786.741	20.266 ←	48.254 ←
16	4.71	-144.00	-678.240	97,666.56	-8.333	26.296	15.125		144.000	2178.00	57,272.688	144.000	2178.00	57,272.688	11.933 ↓	48.254 ↓
17	4.25	-144.00	-612.000	88,812.00	-7.421	18.875	12.00		144.000	1728.00	32,616.000	144.00	1728.00	32,616.000	4.512 ↓	48.254 ↓
18	4.25	-144.00	-612.000	88,812.00	-7.421	11.454	9.25		144.000	1332.00	15,256.728	144.00	1332.00	15,256.728	2.909 ↑	48.254 ↓
19	6.56	-144.00	-944.640	136,028.16	-11.454	0.0	4.25		144.000	612.00	0.0	144.00	612.00	0.0	14.363 ↑	48.254 ↓
A	20.00	-194.00	-3880.000	752,720.00	-47.047	-47.047	20.28	-954.113	40.625	823.675	-38,760.847	5.988	121.44	-5,713.388	47.047 ←	0.0
B	21.29	-173.72	-3698.500	642,503.21	-44.847	-91.894	19.97	-1835.123	40.625	811.281	-74,551.856	5.988	119.58	-10,988.685	91.894 ←	0.0
C	25.21	-153.75	-3876.040	595,941.15	-46.999	-138.893	9.75	-1354.207	40.625	396.094	-55,014.684	5.988	58.38	-8,108.573	138.893 ←	0.0
20	16.00	-144.00	-2304.000	331,776.00	-27.937	-166.830	24.00	-4003.920	40.625	975.000	-162,659.250	5.988	143.71	-23,975.139	181.193 ←	48.254 →
21	32.00	-120.00	-3840.000	460,800.00	-46.562	-213.397	24.00	-5121.408	40.625	975.00	-208,057.200	5.988	143.71	-30,666.564	227.755 ←	48.254 →
22	32.00	-96.00	-3072.000	294,912.00	-37.250	-250.642	24.00	-6015.408	40.625	975.00	-244,375.950	5.988	143.71	-36,019.762	265.005 ←	48.254 →
23	32.00	-72.00	-2304.000	165,888.00	-27.937	-278.579	24.00	-6685.896	40.625	975.00	-271,614.525	5.988	143.71	-40,034.588	292.942 ←	48.254 →
24	32.00	-48.00	-1536.000	73,728.00	-18.629	-8.766	4.25		48.000	204.00	-1,788.264	48.00	204.00	-1,788.264	9.489 ↑	9.084 ↑
36	6.56	-48.00	-314.880	15,114.24	-3.818	-4.948	9.25		48.000	444.00	-2,196.912	48.00	444.00	-2,196.912	5.661 ↑	9.084 ↑
37	4.25	-48.00	-204.000	9,792.00	-2.474	-2.474	12.00		48.000	576.00	-1,425.024	48.00	576.00	-1,425.024	3.187 ↑	9.084 ↑
38	4.25	-48.00	-204.000	9,792.00	-2.474										0.713 ↑	9.084 ↑
12																
24						-305.970	24.00	-7343.280	40.625	975.00	-298,720.750	5.988	143.71	-43,970.949	321.046 ←	57.338 →
25	32.00	-24.00	-768.000	18,432.00	-9.313	-315.283	24.00	-7566.792	40.625	975.00	-307,400.925	5.988	143.71	-45,309.320	330.359 ←	57.338 →
26	32.00	0.0	0.0	0.0	0.0	-315.283	24.00	-7566.792	40.625	975.00	-307,400.925	5.988	143.71	-45,309.320	330.359 ←	57.338 →
27	32.00	24.00	768.000	18,432.00	9.313	-305.970	24.00	-7343.280	40.625	975.00	-298,720.750	5.988	143.71	-43,970.949	321.046 ←	57.338 →
28	32.00	48.00	1536.000	73,728.00	18.629	-8.766	4.25		48.000	204.00	-1,788.264	48.000	204.00	-1,788.264	9.489 ↓	9.804 ↓
33	6.56	48.00	314.880	15,114.24	3.818	-4.948	9.25		48.000	444.00	-2,196.912	48.000	444.00	-2,196.912	5.661 ↓	9.804 ↓
34	4.25	48.00	204.000	9,792.00	2.474	-2.474	12.00		48.000	576.00	-1,425.024	48.000	576.00	-1,425.024	3.187 ↓	9.804 ↓
35	4.25	48.00	204.000	9,792.00	2.474										0.713 ↓	9.804 ↓
8																
28						-278.579	24.00	-6685.896	40.625	975.00	-271,614.525	5.988	143.71	-40,034.588	292.942 ←	48.254 →
29	32.00	72.00	2304.000	165,888.00	27.937	-250.641	24.00	-6015.408	40.625	975.00	-244,375.950	5.988	143.71	-36,019.762	265.005 ←	48.254 →
30	32.00	96.00	3072.000	294,912.00	37.250	-213.392	24.00	-5121.408	40.625	975.00	-208,057.200	5.988	143.71	-30,666.564	227.755 ←	48.254 →
31	32.00	120.00	3840.000	460,800.00	46.562	-166.830	24.00	-4003.920	40.625	975.00	-162,659.250	5.988	143.71	-23,975.139	181.193 ←	48.254 →
32	16.00	144.00	2304.000	331,776.00	27.937	0.0	4.25		144.00	612.00	0.0	144.00	612.00	0.0	14.363 ↓	48.254 ↑
C	25.21	153.75	3876.040	595,941.15	46.999	-138.893	9.75	1354.207	40.625	396.094	-55,014.684	5.988	58.38	-8,108.573	138.893 ←	0.0
B	21.29	173.72	3698.500	642,503.21	44.847	-91.894	19.97	1835.123	40.625	811.281	-74,511.856	5.988	119.58	-10,988.685	91.894 ←	0.0
A	20.00	194.00	3880.000	752,720.00	47.047	-47.047	20.28	954.113	40.625	823.675	-38,760.847	5.988	121.44	-5,713.388	47.047 ←	0.0
	701.04			8,247,142.16				99,999.721		23,400.00	-3,122,041.54		23,400.00 $3(2A_B)$	341,658.608		

H = 100,000 lb. →

$\frac{H}{I} = \frac{100{,}000}{8{,}247{,}142.16} = 0.0121254124$ lb./in.^{4}

Col 9 : 2ΣA, B, C = 8286.886

TABLE 9

DEFORMATIONS IN LEFT CELL

Segment	q total (lb/in.)	L/t	q total - L/t
1-2	$11.454 + q_1$	49.333	$565.060 + 49.333\ q_1$
2-3	$18.875 + q_1$	64.000	$1{,}208.000 + 64.000\ q_1$
3-4	$26.296 + q_1$	80.667	$2{,}121.219 + 80.667\ q_1$
4-5	$34.629 + q_1$	96.000	$3{,}324.384 + 96.000\ q_1$
5-6	$50.635 + q_1$	96.000	$4{,}860.960 + 96.000\ q_1$
6-7	$63.440 + q_1$	96.000	$6{,}090.240 + 96.000\ q_1$
7-8	$73.044 + q_1$	96.000	$7{,}012.224 + 96.000\ q_1$
8-35	$q_1 - q_2$	80.667	$80.667\ q_1 - 80.667\ q_2$
35-34	$2.474 + q_1 - q_2$	64.000	$158.336 + 64.000\ q_1 - 64.000\ q_2$
34-33	$4.948 + q_1 - q_2$	49.333	$244.100 + 49.333\ q_1 - 49.333\ q_2$
33-28	$8.766 + q_1 - q_2$	3.188	$27.946 + 3.188\ q_1 - 3.188\ q_2$
28-29	$- 278.579 + q_1$	18.000	$- 5{,}014.422 + 18.000\ q_1$
29-30	$- 250.642 + q_1$	18.000	$- 4{,}511.556 + 18.000\ q_1$
30-31	$- 213.392 + q_1$	18.000	$- 3{,}841.056 + 18.000\ q_1$
31-32	$- 166.830 + q_1$	18.000	$- 3{,}002.940 + 18.000\ q_1$
32-1	$+ q_1$	3.188	$3.188\ q_1$

$$2\ A_B G \frac{d\theta_1}{dz} = 9{,}242.495 + 850.376\ q_1 - 197.188\ q_2$$

TABLE 10

DEFORMATIONS IN MIDDLE CELL

Segment	q total (lb/in.)	L/t	q total - L/t
8-9	$77.520 + q_2$	96.00	$7,441.920 + 96.00\ q_2$
9-10	$80.721 + q_2$	96.00	$7,749.216 + 96.00\ q_2$
10-11	$80.721 + q_2$	96.00	$7,749.216 + 96.00\ q_2$
11-12	$77.520 + q_2$	96.00	$7,441.920 + 96.00\ q_2$
12-38	$+ q_2 - q_3$	80.667	$+ 80.667\ q_2 - 80.667\ q_3$
38-37	$- 2.474 + q_2 - q_3$	64.00	$- 158.336 + 64.000\ q_2 - 64.000\ q_3$
37-36	$- 4.948 + q_2 - q_3$	49.333	$- 244.100 + 49.333\ q_2 - 49.333\ q_3$
36-24	$- 8.766 + q_2 - q_3$	3.188	$- 27.946 + 3.188\ q_2 - 3.188\ q_3$
24-25	$- 305.970 + q_2$	18.00	$- 5,507.460 + 18.00\ q_2$
25-26	$- 315.283 + q_2$	18.00	$- 5,675.094 + 18.00\ q_2$
26-27	$- 315.283 + q_2$	18.00	$- 5,675.094 + 18.00\ q_2$
27-28	$- 305.970 + q_2$	18.00	$- 5,507.460 + 18.00\ q_2$
28-33	$- 8.766 + q_2 - q_1$	3.188	$- 27.946 - 3.188\ q_1 + 3.188\ q_2$
33-34	$- 4.948 + q_2 - q_1$	49.333	$- 244.100 - 49.333\ q_1 + 49.333\ q_2$
34-35	$- 2.474 + q_2 - q_1$	64.00	$- 158.336 - 64.00\ q_1 + 64.00\ q_2$
35-8	$q_2 - q_1$	80.667	$-80.667\ q_1 + 80.667\ q_2$

$$2\ A_B G \frac{d\theta_2}{dz} = 7,156.400 - 197.188\ q_1 + 850.376\ q_2 - 197.188\ q_3$$

TABLE 11

DEFORMATIONS IN RIGHT CELL

Segment	q total (lb/in.)	L/t	q total - L/t
12-13	$73.044 + q_3$	96.00	$7{,}012.224 + 96.00\ q_3$
13-14	$63.440 + q_3$	96.00	$6{,}090.240 + 96.00\ q_3$
14-15	$50.635 + q_3$	96.00	$4{,}860.960 + 96.00\ q_3$
15-16	$34.629 + q_3$	96.00	$3{,}324.384 + 96.00\ q_3$
16-17	$26.296 + q_3$	80.667	$2{,}121.219 + 80.667\ q_3$
17-18	$18.875 + q_3$	64.00	$1{,}208.000 + 64.00\ q_3$
18-19	$11.454 + q_3$	49.333	$565.060 + 49.333\ q_3$
19-20	$+ q_3$	3.188	$+ 3.188\ q_3$
20-21	$-166.830 + q_3$	18.00	$-3{,}002.940 + 18.00\ q_3$
21-22	$-213.392 + q_3$	18.00	$-3{,}841.056 + 18.00\ q_3$
22-23	$-250.642 + q_3$	18.00	$-4{,}511.556 + 18.00\ q_3$
23-24	$-278.579 + q_3$	18.00	$-5{,}014.422 + 18.00\ q_3$
24-36	$8.766 + q_3 - q_2$	3.188	$27.946 - 3.188\ q_2 + 3.188\ q_3$
36-37	$4.948 + q_3 - q_2$	49.333	$244.100 - 49.333\ q_2 + 49.333\ q_3$
37-38	$2.474 + q_3 - q_2$	64.000	$158.336 - 64.000\ q_2 + 64.000\ q_3$
38-12	$q_3 - q_2$	80.667	$- 80.667\ q_2 + 80.667\ q_3$

$$2\ A_B G \frac{d\theta_3}{dz} = 9{,}242.495 - 197.188\ q_2 + 850.376\ q_3$$

the box. Again the three-cell box is cut into three one-cell boxes and the shear flow forces are computed as given in Columns 1 through 7 of Table 8. The shear flow forces in Segments A, B, and C must be considered because the shear flow forces on the left and right cantilever sides of the box act in the same direction. They must not be corrected in restoring the cut sections because Segments A, B, and C do not resist torque; also, the total shear flow forces in Segments A, B, and C must be considered as an external load on the box to locate the shear center.

Columns 8, 10, 11, and 12 of Table 8 and Tables 9, 10, and 11 contain the basic data for the restoration of the cut sections to equilibrium about the centerline of the bottom plate on the vertical centerline of the box. The summation of Column 9 in Table 8 is a check on horizontal equilibrium of the section under the 100-kip horizontal load. Again $- \Sigma q_x La / \Sigma La = q_1 + q_2 + q_3$, with $\Sigma La = 2A_B$, twice the area of each cell. This yield $q_1 + q_2 + q_3 = 3,122,041.54/7,800 = 400.2617$.

As before, the other two necessary equations are based on the principle of consistent displacements. Tables 9 and 10 yield $9,242.495 + 850.376q_1 - 197.188q_2 = 7,156.400 - 197.188q_1 + 850.376q_2 - 197.188q_3$. Tables 10 and 11 yield $7,156.400 - 197.188q_1 + 850.376q_2 - 197.188q_3 = 9,242.495 - 197.188q_2 - 850.376q_3$. These two equations reduce to $1,047.564q_1 - 1,047.564q_2 + 197.188q3 = - 2,-86.095$ and $- 197.188q_1 + 1,047.564q_2 - 1,047.564q_3 = 2,086.095$. Their solution gives $q_1 = 124.919$ lb/in., $q_2 = 150.424$ lb/in., and $q_3 = 124.919$ lb/in. Thus, $(2A_BG)(d\theta_1/dz) = 9,242.495 + 850.376 (124.919) - 197.188 (150.424) = 85,808.81$ and $(2A_BG)(d\theta_2/dz) = 7,156.394 - 197.188 (124.919) + 850.376 (150.424) - 197.188 (124.919) = 85,808.29$.

It is now necessary to compute the shear flow forces for pure torque about the shear center. Using an external torque of 1,200,000 in.-lb, with the three-cell box cut to give three single cells, it is seen from the data in Tables 9, 10, and 11 that the deformations due to torque are $(2A_BG)(d\theta_1/dz) = 850.376q_{T1} - 197.188q_{T2}$, $(2A_BG)(d\theta_2/dz) = -197.188q_{T1} + 850.376q_{T2} - 197.188q_{T3}$, and $(2A_BG)(d\theta_3/dz) = -197.188q_{T2} + 850.376q_{T3}$. By letting $d\theta_1/dz = d\theta_2/dz$ and $d\theta_2/dz = d\theta_3/dz$, and noting that $2A_B(q_{T1} + q_{T2} + q_{T3}) = 1,200,000$ where $2A_B = 7,800$ there results $q_{T1} = 48.254$ lb/in., $q_{T2} = 57.338$ lb/in., and $q_{T3} = 48.254$ lb/in. Thus, $(2A_BG)(d\theta_1/dz) = 850.376 (48.254) -197.188 (57.338) = 29,727.678$. These shear flow forces are used to determine the shear flow forces due to a pure torque of 100,000 ft-lb about the shear center. The final shear flow forces due to this 100,000 ft-lb torque about the shear center are given in Column 17 of Table 8.

The shear center is located by noting that the torque of the shear flow forces given in Column 7 of Table 8 must be zero about the shear center. The deformations $(2A_BG)(d\theta/dz)$ are not proportional to the torques involved. Thus, the magnitude of the torque, T, which must be reduced to zero is $T = (d\theta_1/dz)(1,200,000) / (d\theta_1/dz_T) = (85,808.29)(1,200,000) / 29,727.678 = 3,463,773.6$ in.-lb.

The total shear flow force in Segments A, B, and C due to the 100-kip horizontal load is 8,286.886 lb (Fig. 13; Table 8, Col. 9). The resultant force is 100,000 - 8,286.886 = 91,713.114 lb, and it must be applied to balance the 8,286.886 lb force in Segments A, B, and C about the line of application of the 100-kip load on the horizontal centerline of the bottom plate. Thus, the resultant is applied at a distance of $e_1 = (8,286.886)(40.625) / (91,713.114) = 3.671$ in. below the centerline of the bottom plate. This gives the distance from this point to the shear center of $e = 3,463,773.6/91,713.114 = 37.767$ in., which places the shear center as shown in Figure 13. The point of application of the 100-kip horizontal load for zero torque about the shear center is computed from $e_2 = (8,286.886)(6.529) / 100,000 = 0.541$ in. above the shear center (Fig. 13).

The shear flow forces in Column 7 of Table 8 must be corrected to give torque equilibrium about the shear center in combination with the 100-kip external horizontal load. The external load of 100 kips must act at 0.541 in. above the shear center for zero torque. This is done by taking the torque of the external load and the internal shear flow forces about some convenient point and determining the shear flow correction to give torque equilibrium about the shear center for the internal shear flow forces. It is convenient to take moments about the line of action of the 100-kip load. Again

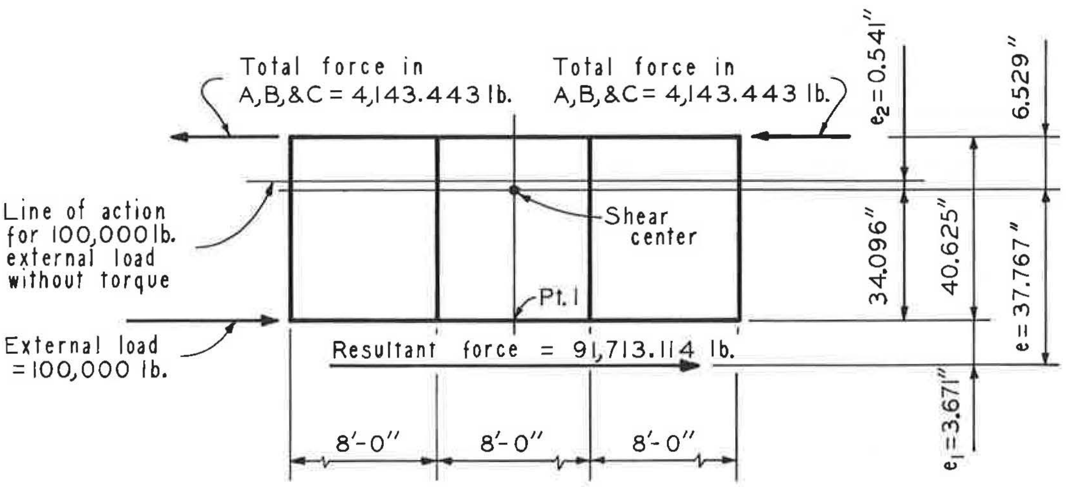
Total force in A,B,&C = 4,143.443 lb.
Total force in A,B,&C = 4,143.443 lb.
Line of action for 100,000 lb. external load without torque
Shear center
Pt. 1
External load = 100,000 lb.
Resultant force = 91,713.114 lb.
8'-0"
8'-0"
8'-0"
e2 = 0.541"
6.529"
34.096"
40.625"
e = 37.767"
e1 = 3.671"

Figure 13. Location of shear center, three-cell box, 75-ft span.

$-\Sigma q_x La' / \Sigma La' = q_1' + q_2' + q_3'$, with $\Sigma La' = 2A_B$ for each cell. Thus, $q_1' + q_2' + q_3' = -341{,}658.608/7{,}800 = -43.8024$. Again, based on the principle of consistent displacements, Tables 8, 9, and 10 yield $1{,}047.564q_1' - 1{,}047.564q_2' + 197.188q_3' = -2{,}086.095$ and $-197.188q_1' + 1{,}047.564q_2' - 1{,}047.564q_3' = 2{,}086.095$. Solution of these gives $q_1' = -14.363$ lb/in., $q_2' = -15.076$ lb/in., and $q_3' = -14.363$ lb/in. These corrections are applied to the shear forces in Column 7 of Table 8 to give the corrected shear flow forces for the 100-kip load with zero torque about the shear center as given in Column 16 of Table 8.

Flexural and Shearing Stresses

The dead load per foot of bridge for the three-cell box on the 75-ft span to be used in the stress computations is as follows:

Railing and curb	=	467.4 lb/ft
Asphalt wearing surface	=	450.0 lb/ft
Precast Concrete Deck	=	3,232.5 lb/ft
Steel box	=	743.1 lb/ft
Total	=	4,893.0 lb/ft

The maximum bending moments and shears for one lane of H20-S16 live loading are given in the AASHO specifications (16, p. 273). The impact factor is 0.25 in accordance with these specifications. The following maximum moments result from full loading of the structure, noting that the maximum live load moment occurs 2.33 ft from mid-span with 14-ft axle spacings for the live load:

Dead load at mid-span = $(4.893)(75)^2/8 = 3{,}440.4$ ft-kips

Maximum live load plus impact = $(2)(1075.1)(1.25) = 2{,}687.8$ ft-kips

Dead load at point of maximum LL moment = $\left[(4.893)(39.83)(35.17)\right]/2 = 3{,}427.1$ ft-kips

The following maximum shears occur under the same conditions:

Dead load at end of span = (4.893) (37.5) = 183.5 kips
Live load plus impact = (2) (63.1) (1.25) = 157.8 kips

The torque resulting from the unsymmetrical placing of the live load lanes on the roadway is the same as for the one-cell box—393.75 ft-kips. With the same assumptions as for the one-cell box, the unit flexural stresses are given in Table 12. Assuming the dead load shear to be uniformly distributed in the vertical plates, and determining the maximum live load and impact and torque shearing effect by the use of the coefficients previously determined, the unit shearing stresses between Segments 36 and 37 are as follows:

DL = (183.5) / (4) (36) (3/16) = 6.80 ksi
LL + I = (1.578) (0.724341) / (3/16) = 6.10 ksi
Torque = (3.9375) (0.009804) / (3/16) = 0.21 ksi
Total = 13.11 ksi

STABILITY ANALYSIS FOR ONE- AND THREE-CELL BOXES

The steel boxes acting alone in the carrying of the total dead load give the critical condition for the stability of the top flange and side plates. The theoretical elastic buckling stresses may be obtained with the Bryan buckling formula, Eq. 3, with $27{,}114.4k(t/b)^2$, as previously given.

Top Flange Plates

The top flange plates are assumed to have three simply supported edges and one free edge. The value of k = 0.43 is found by Bleich (11, p. 330). This gives $\sigma_{cr} = (27{,}114.4)(1/9)^2(0.43) = 143.9$ ksi, as compared to the actual extreme fiber stress of 38.8 ksi due to dead load for the one-cell box on the 75-ft span. It also gives $\sigma_{cr} = (27{,}114.4)(0.5/9)^2(0.43) = 72.0$ ksi, as compared to the actual total extreme fiber stress of 31.53 ksi due to dead load for the three-cell box on the 75-ft span.
It also gives $\sigma_{cr} = (27{,}114.4)(0.5/9)^2(0.43) = 72.0$ ksi, as compared to the actual total extreme fiber stress of 31.53 ksi due to dead load for the three-cell box on the 75-ft span.

Vertical Side Plates

The dead load flexural stresses for the panel subdivisions of the vertical side plates for both the one- and three-cell boxes on the 75-ft span are shown in Figure 14. The

TABLE 12

FLEXURAL STRESSES, THREE-CELL BOX, 75-FOOT SPAN

Load	**Top of Steel** (ksi)	**Bottom of Steel** (ksi)	**Top of Concrete** (ksi)
Dead Load	31.53	10.55	
Live Load and Impact	0.81	6.13	0.39
Total	32.34	16.68	0.39

theoretical elastic buckling stresses and comparisons with the actual maximum flexural stresses are given in Tables 13 and 14.

The theoretical elastic buckling stresses for the case of shear are given in Tables 15 and 16, as well as the comparisons with the actual total shearing stresses in each panel. The coefficient k = 5.3 is used for computing these buckling stresses due to shear.

Deflection Limitations

The total moments of inertia which a two-lane superstructure needs to meet the live load and impact deflection limitations of present standard specifications for highway bridges (16) are shown in Figure 15. Also shown are the moments of inertia furnished by the final composite structure for 75- and 120-ft spans with both one- and three-cell boxes. The basic background of this figure was presented previously (2, Fig. 4). It is evident that the steel box structures meet current practice with respect to live load and impact deflection limitations.

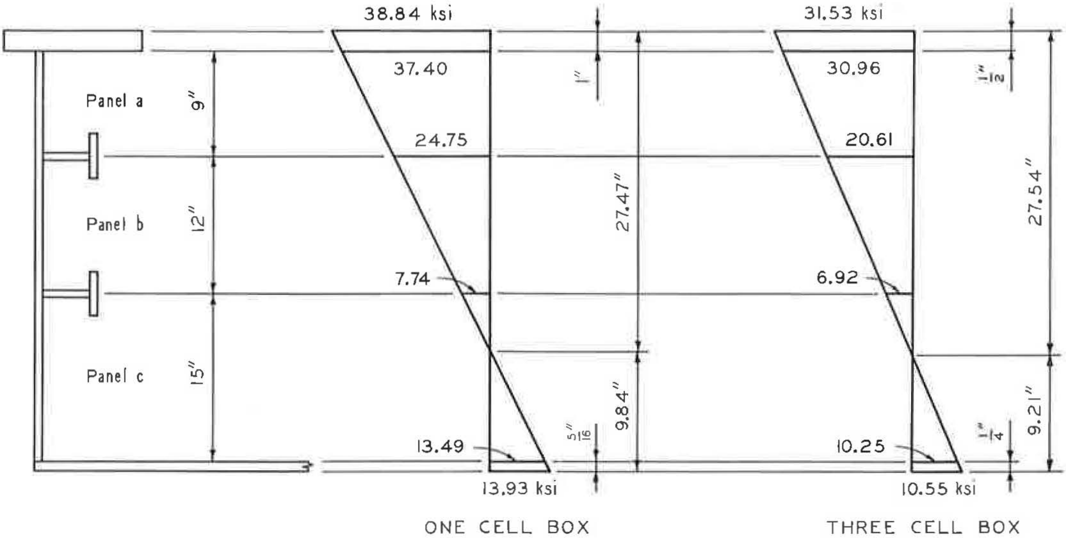
38.84 ksi
37.40
24.75
7.74
13.49
13.93 ksi
1"
27.47"
9.84"
5/16"
Panel a
9"
Panel b
12"
Panel c
15"
31.53 ksi
30.96
20.61
6.92
10.25
10.55 ksi
1/2"
27.54"
9.21"
1/4"
ONE CELL BOX
THREE CELL BOX

Figure 14. Setup of flexural stresses for buckling computations, 75-ft span.

TABLE 13

STABILITY OF SIDE PLATES, FLEXURAL STRESSES, ONE-CELL BOX, 75-FOOT SPAN

Panel	k	σ_{cr} (ksi)	Ratio to Max. EFS = 38.84 ksi
a	5.3	110.9	2.75
b	6.6	77.7	2.00
c	24.0	180.8	4.65

TABLE 14

STABILITY OF SIDE PLATES, FLEXURAL STRESSES, THREE-CELL BOX, 75-FOOT SPAN

Panel	k	σ_{cr} (ksi)	Ratio to Max. EFS = 31.53 ksi
a	5.2	61.2	1.94
b	6.5	43.0	2.08
c	24.0	101.7	3.22

Ratio to maximum stress in Panel b of 20.61 ksi.

TABLE 15

STABILITY OF SIDE PLATES, SHEARING STRESSES, ONE-CELL BOX, 75-FOOT SPAN

Panel	τ_{cr} (ksi)	Actual τ Panel	Ratio τ_{cr} to Actual τ in Panel
a	110.9	19.72	5.6
b	62.4	19.53	3.2
c	39.9	19.10	2.1

TABLE 16

STABILITY OF SIDE PLATES, SHEARING STRESSES, THREE-CELL BOX, 75-FOOT SPAN

Panel	τ_{cr} (ksi)	Actual τ Panel	Ratio τ_{cr} to Actual τ in Panel
a	62.4	13.1	4.7
b	35.1	13.0	2.7
c	22.5	12.6	1.8

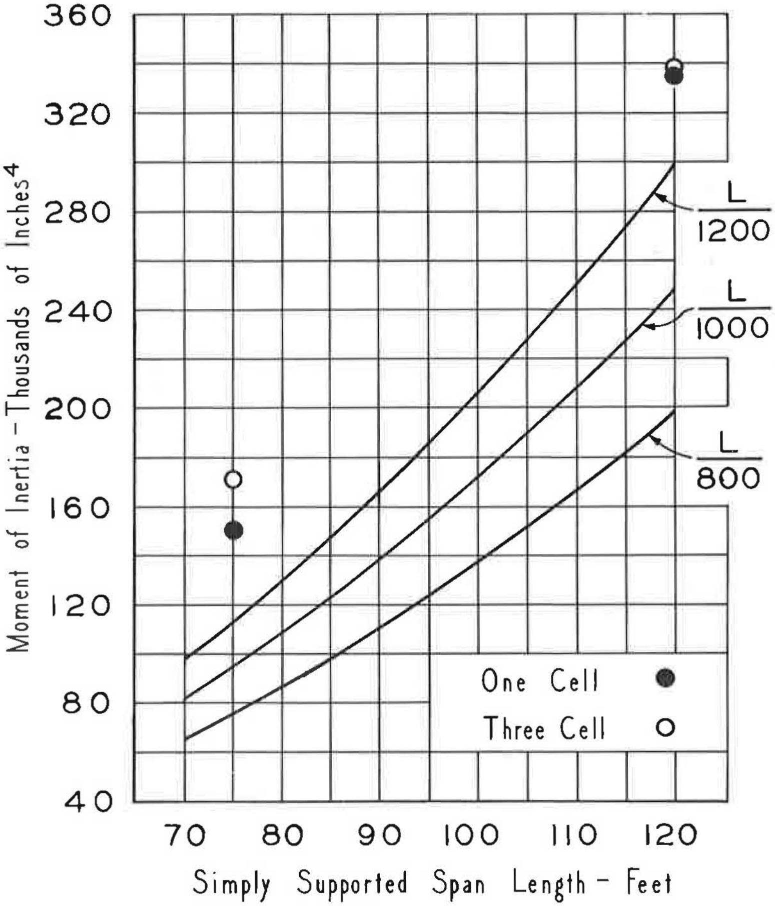

Figure 15. Deflection requirements H20-S16 live loading.

COST COMPARISONS

The structural steel quantities and cost estimates for one- and three-cell boxes on a 75-ft simple span are summarized in Tables 17 and 18. Also shown are the structural steel quantities and cost estimates for one- and three-cell boxes on a 120-ft simple span. The 120-ft span one-cell box has top flange plates of T-1 steel, 16 in. wide and 1¼ in. thick, with vertical side plates, 48 in. wide and ⅜ in. thick, and a bottom plate, 16 ft wide and ½ in. thick. The 120-ft span three-cell box has top flange plates of T-1 steel, 16 in. wide and 1 in. thick, with vertical side plates, 48 in. wide and ¼ in. thick, and a bottom plate, 24 ft wide and 5/16 in. thick. The other structural details are the same as those for the 75-ft span box structures.

In Figures 16 and 17, comparisons are made with results for the rolled wide-flange and welded I-stringer structures (1, 2). The cost comparisons include the concrete roadway deck, since the quantities involved vary with the type of structure. The railings and curbs are not included in the cost estimates, as their cost would be almost identical for all the structures compared. The cost of the shear connectors for the stringers are considered to balance that of the high-strength bolts used to help hold the precast deck in position on the steel boxes. Estimates are made for the use of either ASTM A242 and A441 steels with a heat-treated constructional alloy steel, designated T-1, used for top flange plates when required by high stresses.

TABLE 17

STRUCTURAL QUANTITIES AND COST ESTIMATES

75-FOOT SPAN

Description of Structure	Structural Steel						Concrete Deck		Total
	Type	Quantity (lb)	Estimated Cost ($)				Quantity[1] (cu yd)	Cost ($)	Cost ($)
			Fabrication	Erection	Freight	Total			
One Cell Box	T1, A242	46,353[2,3]	9,736	2,004	695	12,735[4]	69.42	7,636	20,871[5]
	T1, A441	46,353[2,3]	9,134	2,004	695	12,133[4]	69.42	7,636	20,269[5]
	T1, A242, SC	46,353[2,3,6]	14,572[7]	2,004	695	17,571[4]	69.42	7,636	25,707[5]
Three Cell Box	T1, A242	63,624[2,3]	13,960	2,750	954	17,964[4]	60.45	6,650	25,114[5]
	T1, A441	63,624[2,3]	13,139	2,750	954	17,143[4]	60.45	6,650	24,293[5]
	T1, A242, SC	63,624[2,3,8]	19,371[7]	2,750	954	23,375[4]	60.45	6,650	30,525[5]
Rolled WF Composite	A373	100,750				16,973	56.81	6,249	23,222
	A242	82,350				17,347	56.81	6,249	23,596
Rolled WF Non-Composite	A7	146,790				20,250	56.81	6,249	26,499
	A242	116,425				20,880	56.81	6,249	27,129
Welded-I Composite	A373	84,061				16,808	56.81	6,249	23,057
	A36	78,085				16,044	56.81	6,249	22,293
	A242	68,924				16,608	56.81	6,249	22,857
Welded-I Non Composite	A373	96,236				17,906	56.81	6,249	24,155
	A36	90,010				17,252	56.81	6,249	23,501
	A242	83,908				18,519	56.81	6,249	24,768

---

[1] Does not include curb.

[2] Includes 6,181 pounds of T-1 steel.

[3] Does not include bearing details.

[4] Includes $300 for bearing details.

[5] Includes $500 for asphalt roadway surface.

[6] Includes 21,026 pounds of stainless clad steel.

[7] Includes cost of stainless clad at an extra of $0.23 per pound.

[8] Includes 23,526 pounds of stainless clad steel.

TABLE 18

STRUCTURAL QUANTITIES AND COST ESTIMATES

120-FOOT SPAN

Description of Structure	Type	Structural Steel Quantity (lb)	Structural Steel Estimated Cost ($) Fabrication	Erection	Freight	Total	Concrete Deck Quantity[1] (cu yd)	Concrete Deck Cost ($)	Total Cost ($)
One Cell Box	T1,A242	103,823[2,3]	19,825	3,875	1,557	25,557[4]	110.90	12,199	38,576[5]
	T1,A441	103,823[2,3]	18,607	3,875	1,557	24,339[4]	110.90	12,199	37,338[5]
	T1,A242,SC	103,823[2,3,6]	32,504[7]	3,875	1,557	38,236[4]	110.90	12,199	51,235[5]
Three Cell Box	T1,A242	136,328[3,8]	28,055	5,090	2,045	35,490[4]	96.49	10,614	46,904[5]
	T1,A441	136,328[3,8]	26,197	5,090	2,045	33,632[4]	96.49	10,614	45,046[5]
	T1,A242,SC	136,328[3,8,9]	39,201[7]	5,090	2,045	46,636[4]	96.49	10,614	58,050[5]
Welded-I Composite	A373	207,570				36,242	90.56	9,962	46,204
	A36	189,392				34,185	90.56	9,962	44,147
	A242	170,393				36,583	90.56	9,962	46,545
Welded-I Non Composite	A373	244,476				40,241	90.56	9,962	50,203
	A36	224,052				37,596	90.56	9,962	47,558
	A242	201,358				40,352	90.56	9,962	50,314

[1] Does not include curb.

[2] Includes 16,422 pounds of T-1 steel.

[3] Does not include bearing details.

[4] Includes $300 for bearing details.

[5] Includes $800 for asphalt roadway surface.

[6] Includes 55,126 pounds of stainless clad steel.

[7] Includes cost of stainless clad at an extra of $0.23 per pound.

[8] Includes 26,275 pounds of T-1 steel.

[9] Includes 48,459 pounds of stainless clad steel.

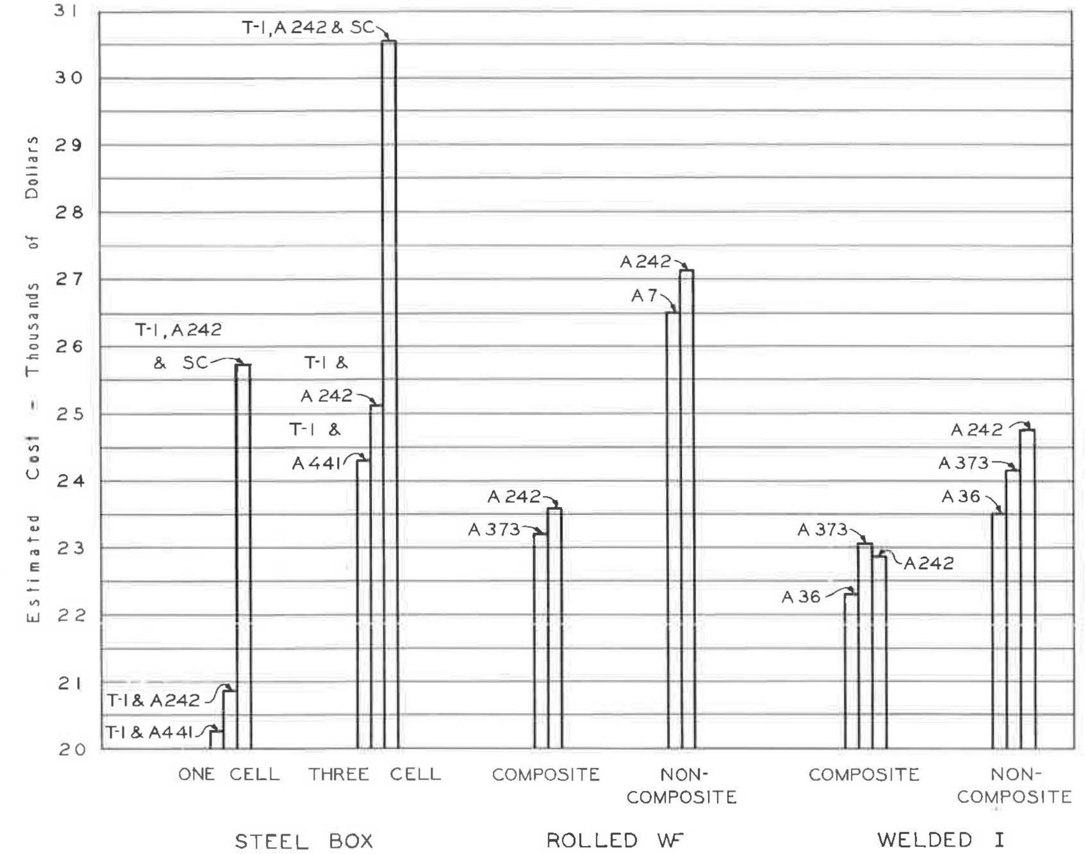

Figure 16. Cost comparison, 75-ft spans.

Cost Estimates—Steel Boxes

The fabrication cost of the steel box bridges was determined. It was assumed that the erection cost for the three-cell box would be the same as that for a welded I-stringer structure of the same length, which for the one-cell structure was computed on a tonnage ratio with the three-cell structure. Freight was taken as \$0.015/lb. The cost of steel bearing details was assumed to be \$300.00 for each of the steel box structures.

An estimate was made using stainless-clad steel for the outside side and bottom plates, as well as the outside longitudinal splice plate and the seal plates at the ends of the bridge. The base price for the stainless-clad material, after consultation with two leading manufacturers of stainless-clad plate, was taken as \$0.2665/lb. This compares with \$0.0785 as the base price of nickel-copper ASTM A242 steel. The fabricating costs for the stainless-clad plates were assumed to be about one-third higher than for plates of A242 steel. This gave an additional cost of \$0.23/lb for the stainless-clad plates over those of A242 steel. Structural T's were used for the longitudinal stiffeners and the stiffening rings in the cost estimates.

The asphalt wearing surface on the precast decks for the steel box structures was estimated at \$2.00/sq yd of roadway area.

Comparisons

The estimated cost of the one-cell box structure with the 75-ft simple span is less than the lowest cost structure with either rolled wide-flange or welded I-stringers,

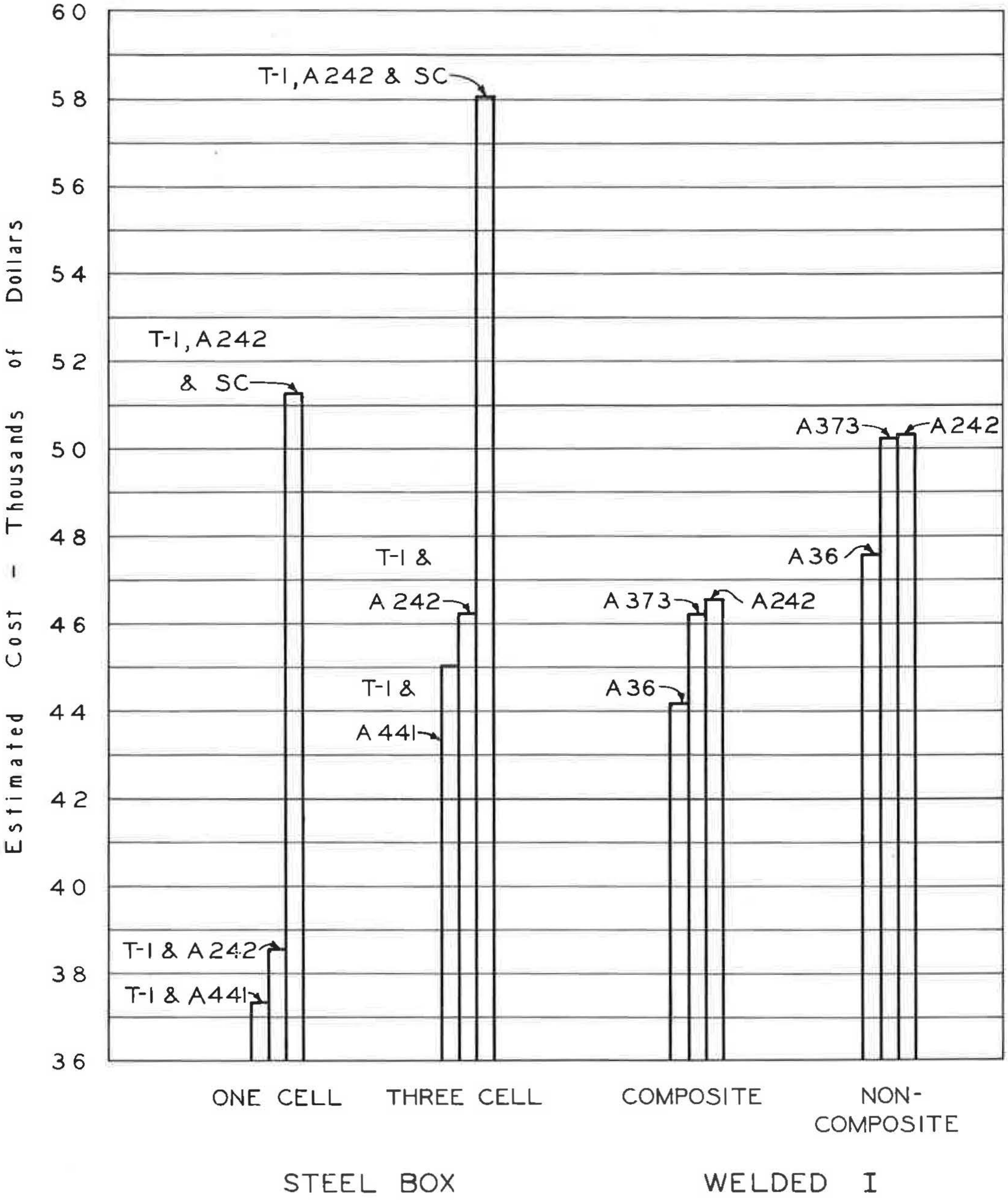

Figure 17. Cost comparisons, 120-ft spans.

except when stainless-clad steel is used in the outside plates. However, the three-cell box structure has, in general, a slightly higher estimated cost.

The estimated cost of the one-cell box structure with the 120-ft simple span is also less than the lowest cost for the welded I-structure, except when stainless-clad steel is used for the outside plates. The three-cell box structure has, in general, a slightly higher estimated cost, but the difference is less than in the case of the 75-ft simple span.

These estimates do not reflect any possible long-term maintenance savings due to the increased resistance to atmospheric corrosion or the better paint life of nickel-copper types of high-strength low-alloy steels.

CONCLUSIONS

The results of this study indicate that the steel box structure with a precast concrete deck has definite economic possibilities for use as a highway bridge. It is recommended that a nickel-copper type of high-strength low-alloy steel be used for these structures because of its better resistance to atmospheric corrosion (1), since thin plates are proposed. It should be noted that a heat-treated constructional alloy steel, designated T-1, is used for top flange plates where required.

ACKNOWLEDGMENTS

This study was made in the Engineering Experiment Station, Purdue University, in cooperation with the International Nickel Co. The authors gratefully acknowledge the assistance of F. W. Schroeder and J. F. W. Koch of the International Steel Co., Evansville, Ind., for their assistance in making the cost estimates and wish to thank L. Anselmini of the International Nickel Co. for his assistance in the investigation and the preparation of this report. David R. Raab, graduate assistant, helped in the final phases of this project.

REFERENCES

1. Hayes, J. M., and Maggard, S. P. Economic Possibilities of Corrosion-Resistant Low Alloy Steel in Short Span Bridges. Proc. A.I.S.C. Nat. Eng. Conf., pp. 59-68, 1960.
2. Hayes, J. M., and Maggard, S. P. Economic Possibilities of Corrosion-Resistant Low-Alloy Steel in Welded I-Section Stringer Highway Bridges. Highway Research Board Proc., Vol. 41, pp. 125-162, 1962.
3. Dörnen, K., and Meyer, A. Die Emsbrücke in dübellosem Stahlverbund. Der Stahlbau, pp. 199-206, July 1960.
4. Sattler, K. Betrachtungen über die Verwendung hochzugfester Schrauben bei Stahlträger-Verbundkonstruktionen. Preliminary Publ., 6th Congr. Int. Assoc. for Bridge and Structural Eng., pp. 333-350, 1960.
5. Postl, J. Klebung bei einer Verbundbrücke. Der Bauingenieur, pp. 390-391, Oct. 1962.
6. Epoxy Bonding Compounds as Shear Connectors in Composite Beams. New York Dept. of Public Works, Interim Rept., Physical Res. Proj. No. 13, Eng. Res. Ser. RR 62-2, Oct. 1962.
7. Seely, F. B., and Smith, J. O. Advanced Mechanics of Materials. 2nd Ed., New York, John Wiley and Sons, 1952.
8. Murphy, Glenn. Advanced Mechanics of Materials. 1st. Ed., New York, McGraw-Hill, 1946.
9. Bryan, G. H. On the Stability of a Plate under Thrusts in Its Own Plane with Application on the Buckling of the Sides of a Ship. Proc. London Math. Soc., Vol. 22, pp. 54-57, 1891.
10. Timoshenko, S. P., and Gere, J. M. Theory of Elastic Stability. 2nd Ed., New York, McGraw-Hill, 1961.
11. Bleich, F. Buckling Strength of Metal Structures. New York, McGraw-Hill, 1952.
12. Maggard, S. P. The Structural Analysis of Box-Like Girders for Highway Bridges. Unpubl. doctoral diss., Purdue Univ., Jan. 1963.
13. Kollbrunner, C. F., and Meister, M. Ausbeulen, Theorie und Berechnung von Blechen. Berlin, Springer-Verlag, 1958.
14. Rockey, K. C. Web Buckling and the Design of Web Plates. Brit. Aluminum Devel. Assoc., Res. Rept. No. 36, Sept. 1958.

15. Massonnet, C. Experimental Research on the Buckling Strength of the Webs of Solid Girders. Preliminary Publ., 4th Congr. Int. Assoc. for Bridge and Structural Eng., pp. 539-555, 1952.
16. AASHO. Standard Specifications for Highway Bridges. 8th Ed., 1961.

Field Tests of a Three-Span Continuous Highway Bridge

JAMES W. BALDWIN
Associate Professor of Civil Engineering, University of Missouri

A three-span continuous I-beam bridge of non-composite design was subjected to several series of static and dynamic tests. Strains and deflections in each stringer were recorded continuously during the tests. Moments in the bridge were calculated from the experimental strains by taking into account the semi-composite nature of the structure. These moments were compared with those calculated by elastic analysis. Measured deflections were also compared with those predicted by the elastic analysis. The nature of the semi-composite behavior was studied. The friction-link phenomenon provided an explanation of the rather unusual observed behavior. Lateral distributions of moment and deflection were compared with theoretical analyses and with the AASHO code.

Response of the structure to dynamic loads was compared with theoretical analyses and found to be in reasonable agreement. Within the limits of these tests, speed of the test vehicle was found to have only a slight effect on the impact factor. Severe roughness at the approach was found to have little effect on the maximum moments and deflections. Consideration of the damping characteristics of the vehicle suspension indicates that the effects of the roughness were damped out before the vehicle reached a critical position in the span.

•THE ACCEPTED design procedure for bridges subject to dynamic loads is based on a static analysis modified by an arbitrary factor called the impact factor. The introduction of new materials coupled with a desire for greater economy in design has resulted in the design of members which are much more flexible than those designed previously. This trend has created the need for a better understanding of the actual behavior of bridges under dynamic loads. Since 1953, the U. S. Bureau of Public Roads, in cooperation with various state highway departments, has conducted field dynamic tests on several highway bridges. The investigation reported herein is the result of such a cooperative undertaking with the Missouri State Highway Department. The test bridge, known as the Burris Fork Bridge, is located on Route 87 about five miles south of California in Moniteau County, Missouri.

Construction of the bridge was completed in July 1954, and the testing was carried out between August 24 and September 30, 1955. Preliminary reduction of the data was carried out by the Missouri State Highway Department and the U. S. Bureau of Public Roads between 1956 and 1960.

The bridge consists of three continuous spans and one simple approach span. A report (1) on the simple approach span was prepared by the Missouri State Highway Department. The analysis in the following report covers only the three continuous spans and was prepared by the Engineering Experiment Station of the University of Missouri between 1961 and 1963. The complete report has been published (13).

Paper sponsored by Committee on Bridges.

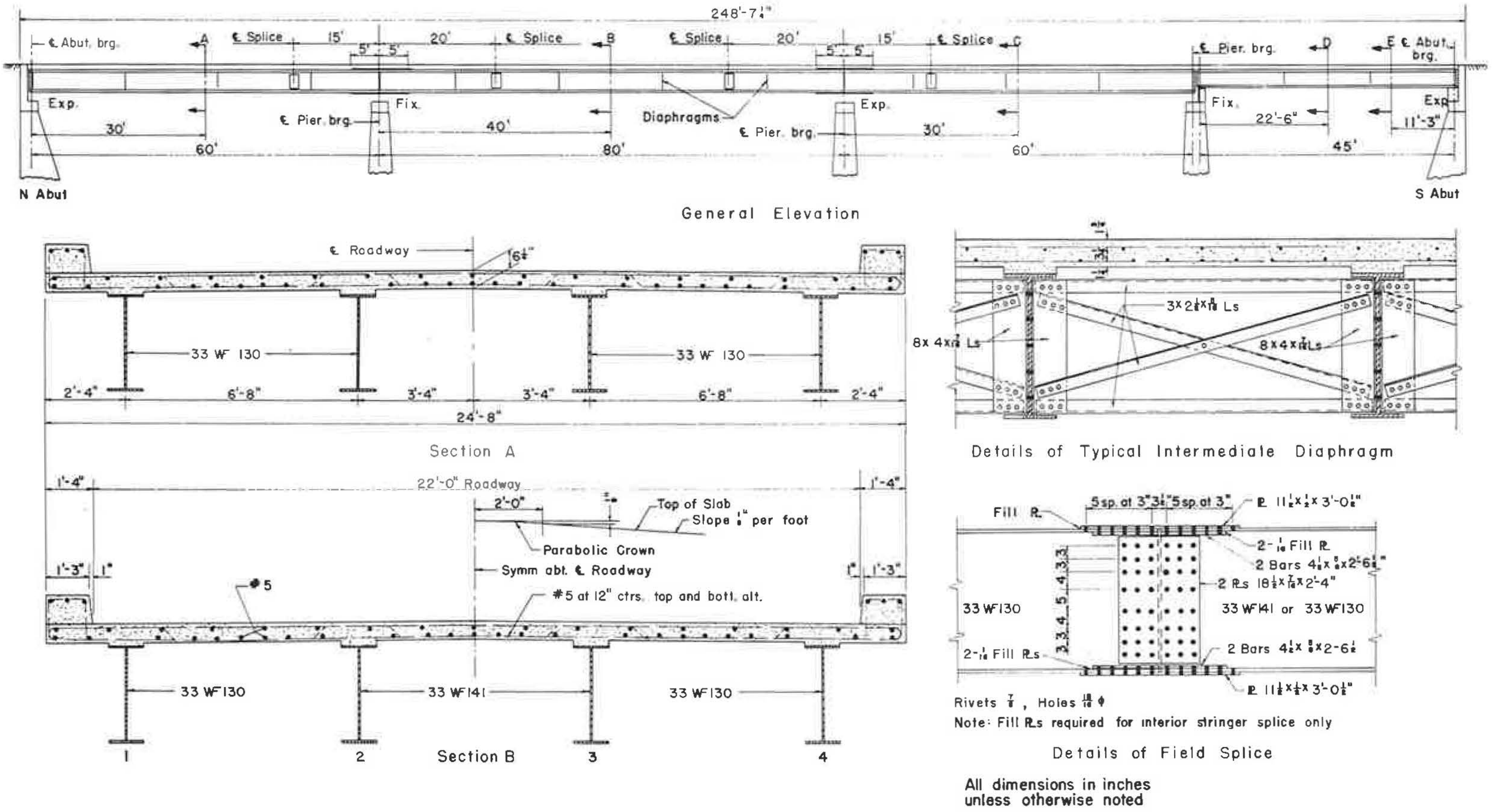
248'-7¼"
℄ Abut. brg.
A
℄ Splice
15'
5'
5'
20'
℄ Splice
B
℄ Splice
20'
5'
5'
15'
℄ Splice
C
℄ Pier. brg.
D
E
℄ Abut. brg.
Exp.
30'
60'
℄ Pier. brg.
Fix.
40'
80'
Diaphragms
℄ Pier. brg.
Exp.
30'
60'
Fix.
22'-6"
Exp.
11'-3"
45'
N Abut
S Abut
General Elevation
℄ Roadway
6¼"
33 WF 130
33 WF 130
2'-4"
6'-8"
3'-4"
3'-4"
6'-8"
2'-4"
24'-8"
Section A
1'-4"
22'-0" Roadway
1'-4"
2'-0"
Top of Slab
Slope ⅛" per foot
Parabolic Crown
Symm abt. ℄ Roadway
1'-3"
1"
#5
#5 at 12" ctrs. top and bott. alt.
1"
1'-3"
33 WF130
33 WF141
33 WF130
1
2
Section B
3
4
3x2½x5/16 Ls
8x4x7/16 Ls
8x4x7/16 Ls
Details of Typical Intermediate Diaphragm
Fill ℙ
5 sp. at 3" 3¼" 5 sp. at 3"
ℙ 11½x½x3'-0½"
2-1/16 Fill ℙ
2 Bars 4½x⅝x2'-6½"
2 ℙs 18½x7/16x2'-4"
33 WF130
33 WF141 or 33 WF130
3 3 4 3 3 4 5 4 3 3
2-1/16 Fill ℙs
2 Bars 4½x⅝x2-6½
ℙ 11½x½x3'-0½"
Rivets ⅞, Holes 15/16 ϕ
Note: Fill ℙs required for interior stringer splice only
Details of Field Splice
All dimensions in inches
unless otherwise noted

Figure 1. Details of test structure.

EXPERIMENTAL INVESTIGATION

Structure

The three-span test structure is of a non-composite design for H-15-44 loading. Details of the test structure are shown in Figure 1. The 22-ft wide deck is a $6\frac{1}{4}$-in. reinforced concrete slab supported on four steel I-beam stringers. The stringers are spaced 6 ft 8 in. on centers and consist of 33WF130 or 33WF141 rolled sections (Fig. 1). The 60- by 80- by 60-ft series of continuous bridge spans is supported on three dumbbell-type concrete piers and one open-type concrete end bent, all founded on rock. A photograph of the bridge site is shown in Figure 2.

Test Vehicle

The test vehicle (Fig. 3) was a standard commercial semitrailer truck loaded with gravel to produce approximately the AASHO H20-S16-44 truck loading. Wheel loading and axle spacing of the test vehicle are shown in Figure 4. Spring constants were 5.94 kips/in. for the driver axle and 16.5 kips/in. for the pair of tandem axles.

Instrumentation

Instrumentation was furnished, installed, and operated by the U. S. Bureau of Public Roads. The gages consisted of GE magnetic reluctance gages, SR-4 strain gages, and

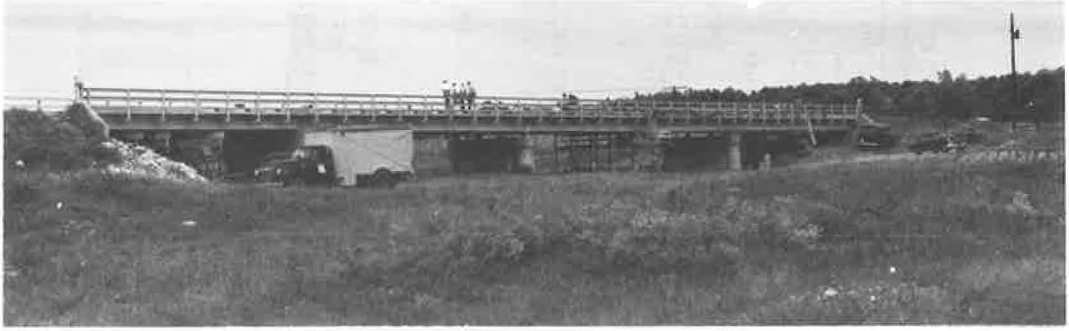

Figure 2. Bridge site.

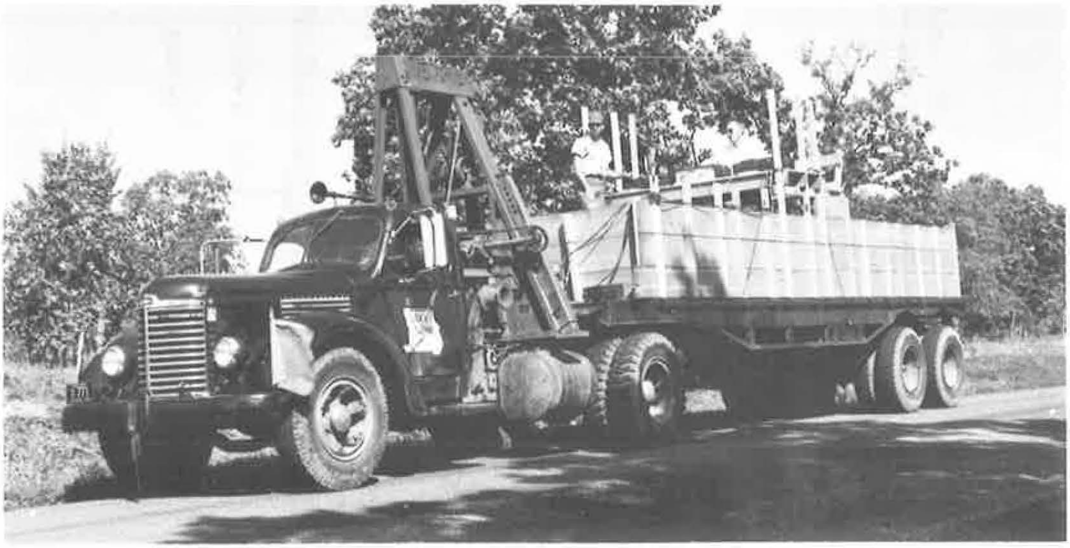

Figure 3. Test vehicle.

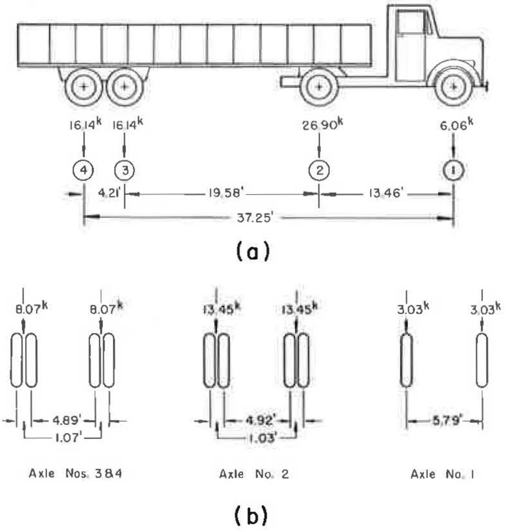
16.14^k
16.14^k
26.90^k
6.06^k
4
3
2
1
4.21'
19.58'
13.46'
37.25'
(a)
8.07^k
8.07^k
13.45^k
13.45^k
3.03^k
3.03^k
4.89'
1.07'
4.92'
1.03'
5.79'
Axle Nos. 3 & 4
Axle No. 2
Axle No. 1
(b)

Figure 4. Details of test vehicle: (a) axle spacing and loading, and (b) wheel spacing and loading.

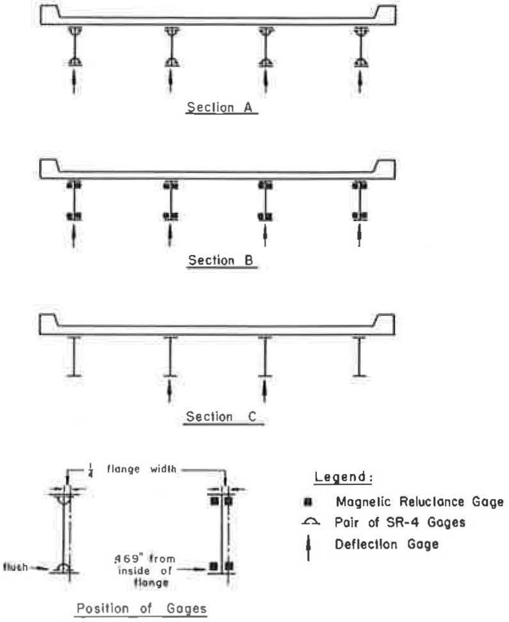
Section A
Section B
Section C
1/4 flange width
flush
.469" from inside of flange
Position of Gages
Legend:
Magnetic Reluctance Gage
Pair of SR-4 Gages
Deflection Gage

Figure 5. Instrumentation.

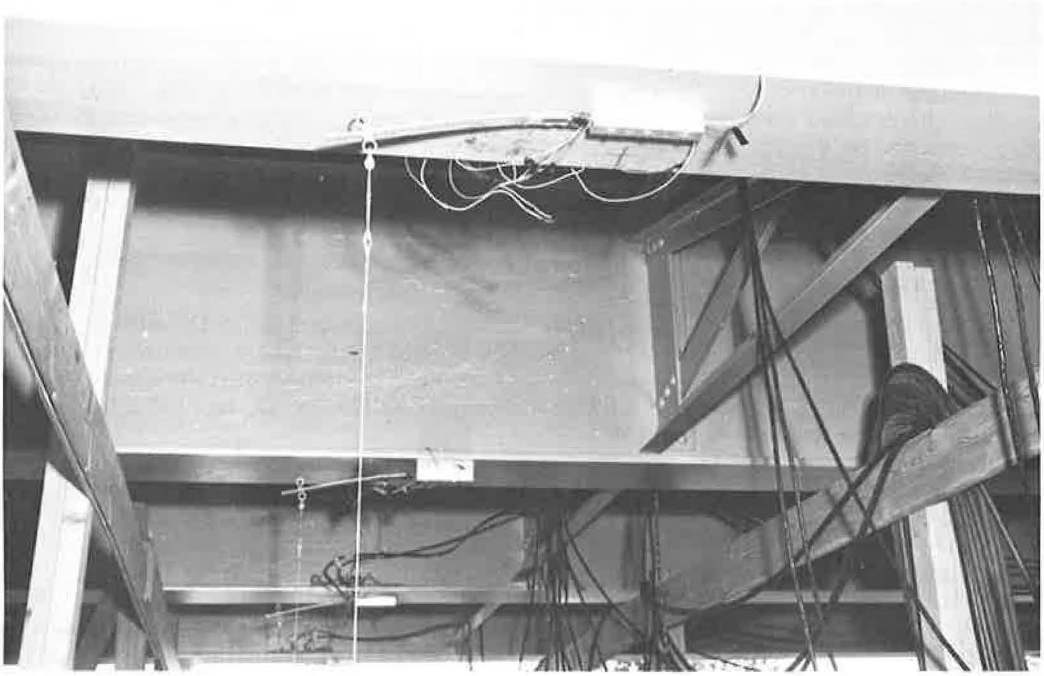

Figure 6. Deflection gages.

deflection gages located as shown in Figure 5. After carefully locating each gage position, paint and mill scale were removed from the steel beams. Resistance-type gages were attached to the structural steel members with a gage cement after the base metal was cleansed with a solvent. Reluctance-type gages were mechanically fastened to the bridge members which required drilling and tapping holes for the attaching screws. In this case the surface of the steel was faced to provide for proper seating of the gages.

Prior to mounting on the bridge the electromagnetic strain gages were calibrated in a test frame by varying the air gap in known increments with a micrometer screw. Since the calibration curves were not exactly linear, care was taken to reestablish the calibration zero position when the gages were attached to the test member.

Deflection gages consisted of SR-4 strain gages mounted on 12-in. aluminum cantilevers as shown in Figure 6. The free end of the cantilever was initially given a deflection greater than that expected in the beam and was fastened to a ground anchor by a light steel cable. Hence, the cable was in tension at all times during the test. Laboratory calibration curves were used to convert the strain-gage signals to deflections.

Four conductor shielded cables were used to connect the gages to the recording equipment which was located in an 18-ft housetrailer. Each gage when connected became one active leg of a Wheatstone bridge circuit. To complete the circuit, dummy gages of each type used were attached to small pieces of structural steel and located near the active gages for temperature compensation. The Wheatstone bridge circuits were arranged in groups of 8 or 12. Each group was energized by a 10-volt 3,000-cycle signal from one oscillator and the modulated return signals from the active gages were fed through individual amplifiers into the recording galvanometers of an oscillograph. There were two oscillographs, each capable of recording 18 signals simultaneously on a 7-in. wide strip of sensitized paper. Circuits were incorporated in each amplifier for calibrating an active variable-resistance gage, balancing the Wheatstone bridge, and regulating the amplifier output.

Additional information on the oscillograph records consisted of record identification numbers, axle position indicators, and 0.1- or 0.01-sec timing lines. The axle position indicators were triggered by air tubes laid across the bridge. The inside of the trailer is shown in Figure 7.

In addition to the instrumentation on the bridge, SR-4 gages were mounted on the axle housing of the truck. The purpose of these gages was to provide a qualitative indication of the force transmitted to the bridge by the truck. Signals from these gages were recorded by a direct writing Brush recorder mounted on the truck. As the truck entered the span, a switch on the underside of the truck was triggered by a flexible obstruction on the bridge. This switch triggered the event marker on the oscillograph, thus indicating the time at which the truck entered the span.

Test Procedure

The bridge was subjected to five series of tests, designated as 1a through 1e. Series 1a, 1b, and 1c were designed to investigate the effects of the lateral position of the truck lane on the bridge. The center of the truck lane coincided with the centerline of the bridge for Series 1a, was 6 ft east of the centerline for Series 1b, and 3 ft east of the centerline for Series 1c.

Series 1d and 1e were designed for the study of induced roughness. In Series 1d the centerline of the truck lane coincided with the centerline of the bridge and the east wheels passed through a 3-in. deep by 5-ft long trench at the north approach to the bridge. In Series 1e, the centerline of the truck lane coincided with the centerline of the bridge and both the east and west wheels passed through trenches at the north approach.

Each series consisted of several static and dynamic test runs. A static test run consisted of taking oscillograph readings from each of the gages with the truck remaining at rest in some position on the bridge. The truck was moved forward in increments of 4 ft between static runs. A dynamic run was conducted by making a continuous recording of each of the gage signals while the truck was driven at a constant rate of speed from one end of the bridge to the other. Nominal truck speeds ranged from 5 to

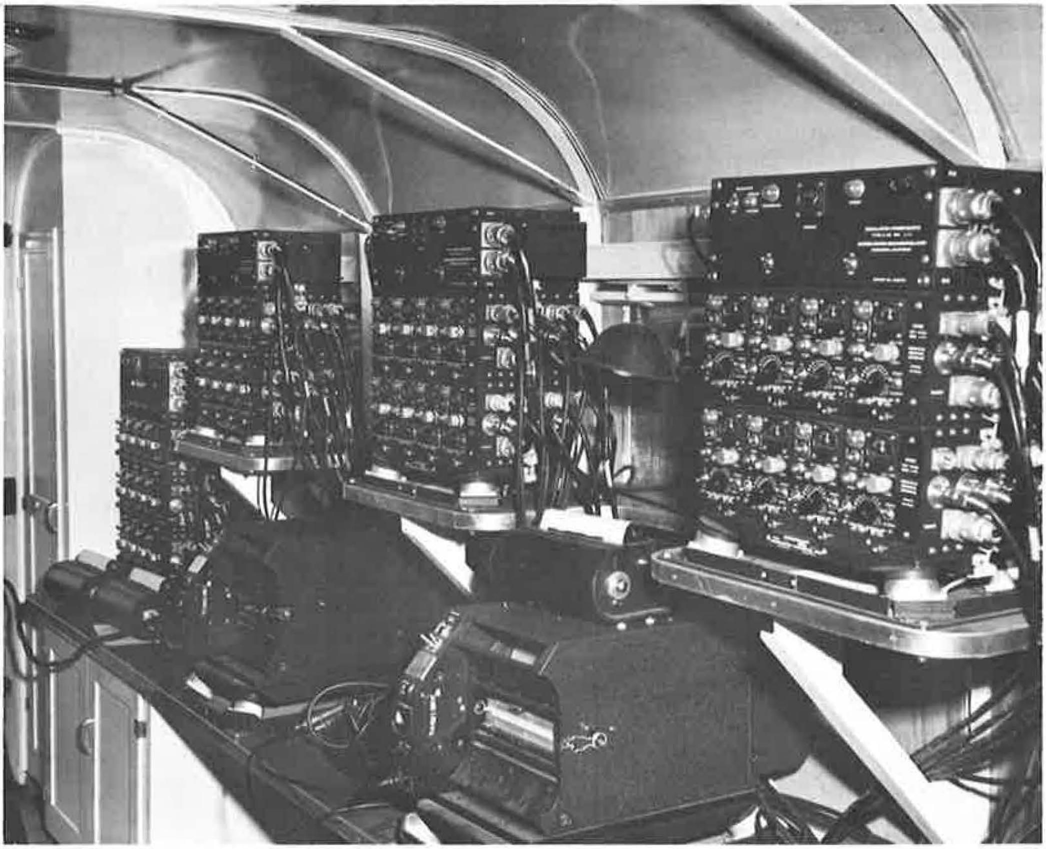

Figure 7. Recording equipment.

TABLE 1
TEST PROGRAM

Series	Displacement[a] (ft)	Static Runs		Dynamic Runs	
		NB	SB	NB	SB
1a	0	6	25	21	21
1b	6[b]	15	24	14	14
1c	3[b]	—	—	6	6
1d	0	—	—	—	10
1e	0	14	—	—	6

[a] Of truck lane from bridge centerline.
[b] East.

50 mph in 5-mph increments. In most cases two runs were made at each speed. A summary of the test program is given in Table 1.

During test runs, the recording equipment was operated through a remote control cable by the engineer on the bridge who also directed the test vehicle operation. Another engineer in the trailer observed the results on the screens of the oscillographs and made adjustments to the equipment when necessary.

Data

The tests described in the previous section resulted in several hundred feet of oscillograph records, each with 18 traces. Three typical oscillograph traces are shown in Figure 8. Because the truck was traveling at a constant rate of speed, the abscissa, time after the driver axle crossed the first support, determines the position of the truck on the bridge. The general shape of the trace is that for an influence line of the particular quantity being measured. In the cases shown in Figure 8, the quantity being measured was the stress in the bottom flange of an interior stringer in Span A. As the truck entered Span A from the north, the stress increased in the positive direction, reaching a maximum when the truck was somewhere near the center of Span A. As the truck proceeded into Span B, the stress became negative, reaching a maximum negative value when the truck was near the center of Span B. The stress reached another positive maximum as the truck passed through Span C.

A smooth curve through the trace (Fig. 8) is referred to as the mean curve, which is modulated by the vibration of the bridge. Thus, the bridge vibration is represented by the higher frequency, lower amplitude wave superimposed on this mean curve. The maximum curve is the outer envelope of the vibration as shown. Actually there are some other differences between the static influence line and the dynamic response not apparent from a cursory examination. These include phase shift and possibly some difference in amplitude.

For the remainder of the discussion the term mean will refer to the maximum value of the mean curve with the vehicle in a particular span; the term maximum will refer to the maximum value of the outer envelope with the vehicle in a particular span.

The first step in the reduction of the data was carried out by the State Highway Department and the U. S. Bureau of Public Roads. The critical ordinates shown in Figure 8

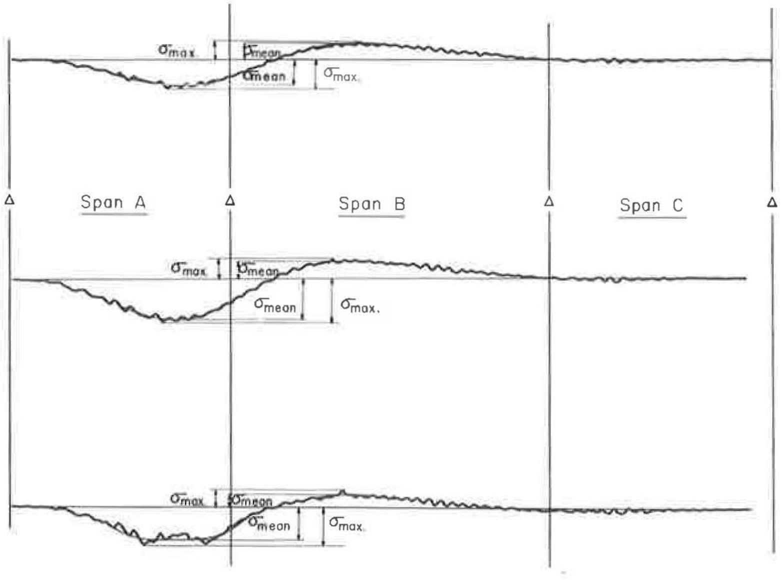

Figure 8. Typical oscillograph traces.

were taken off the oscillograph records. Stress or deflection conversion factors obtained from calibration curves were then used to convert these ordinates to stresses or deflections. The modulus of elasticity for the steel was assumed to be 30 × 10^6 psi. For each trace of each dynamic run, there was one maximum and one mean value as the truck passed through each span, making a total of six critical quantities for each trace of each run. (Benson-Lehner equipment was used by the U. S. Bureau of Public Roads for their part of the take-off work.) A slight variation in procedure was necessary because the maximum stress in the top flange did not necessarily occur at the same instant as the maximum stress in the bottom flange. To obtain simultaneous values, the stress in the top flange at the instant the stress in the bottom flange reached its maximum value was recorded as the maximum stress in the top flange. Take-off of the static data was much less complicated. A static trace was merely a short straight line representing a constant value.

This initial take-off resulted in approximately 20,000 pieces of data. It was decided that the use of punched cards and a high-speed digital computer would be the most economical method for handling such a large quantity of data. Consequently, the data were immediately punched on cards and all subsequent processing was done by machine. A straight-line extrapolation was used in computing the extreme fiber stresses from stresses at the gage locations.

ANALYSIS OF TEST RESULTS

Comparison of Experiments with Theory

The main objective of the investigation was to compare the experimental results with existing theory. To make satisfactory comparisons, experimental quantities must be compared with realistic theoretical quantities. Design stresses and deflections for the bridge under consideration are not satisfactory for comparison because the design was based on two H-15-44 loads, whereas the test conditions included only one H-20-S16-44 load. In a structure such as a bridge, the situation is complicated even further because several steps are involved in computing stresses for a given loading. First, the impact factor is applied to the load to account for the dynamic effects; next, the load is distributed to the stringers either through a rather complex analysis or by the use of a set of design coefficients. Moments in the stringers are then computed on the basis of elastic theory. Finally, the stresses in the stringers are computed on the basis of either a composite or non-composite section, depending on the type of construction. Completely non-composite action is never realized because the friction between the slab and the stringer always results in some degree of composite action. From a design standpoint, the assumption of completely non-composite action is conservative, whereas from a research standpoint this assumption introduces considerable difference between the experimental and theoretical values.

In comparing experiments with theory, it is desirable to separate the effects of these individual assumptions to determine which are satisfactory and which introduce error into the computations. The analyses in this report were performed in such a manner as to isolate as many individual effects as possible. This was accomplished as follows:

1. The static analysis was first compared with results from static tests, thereby eliminating the unknown effect of impact from the comparison.
2. Forces were compared on the basis of moment rather than stress to eliminate the uncertainties arising from the semi-composite action.
3. The uncertainties arising from lateral distribution were eliminated from these comparisons by considering the total moment in the entire cross-section of the bridge rather than that in a single stringer.
4. Average observed deflections for a given bridge section were compared with computed values for both composite and non-composite analyses.
5. The degree of composite action was evaluated in terms of effective section modulus.
6. Lateral distribution was compared directly with existing theory. Experimental moments were superimposed to produce a two-lane loading for comparison with the AASHO code provisions.

7. Base values for computing impact factors were determined from normalized plots of mean moment and mean deflection vs speed.

There was much scatter in the data where the readings were very small. This was almost always true when the gages were in an unloaded span. Values for Stringers 1 and 2 of Series 1b and 1c were also subject to this difficulty. Consequently, these data were not used in the analysis unless otherwise indicated.

Theoretical Moments

Conventional elastic theory was used in preparing influence lines for moments at Sections A and B due to a unit load passing across the bridge. Separate influence lines were prepared for the interior and exterior stringers. In each case completely non-composite action was assumed. The difference between the influence ordinates of the interior and exterior stringers was never more than 4 or 5 percent. As a result, it was decided that an influence line representing the average of the influence lines for an interior and an exterior stringer could be used satisfactorily as an influence line for

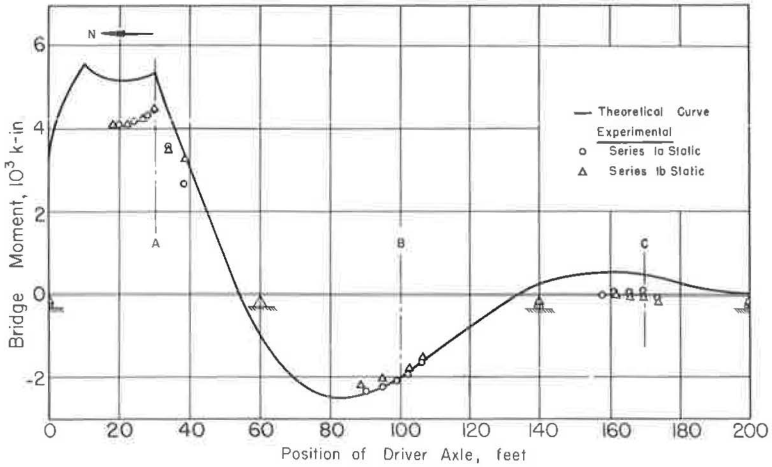

Figure 9. Influence line for bridge moment at Section A, truck northbound.

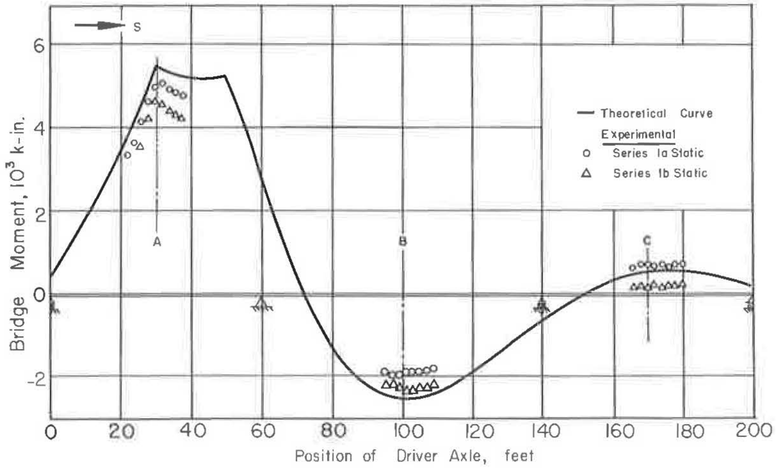

Figure 10. Influence line for bridge moment at Section A, truck southbound.

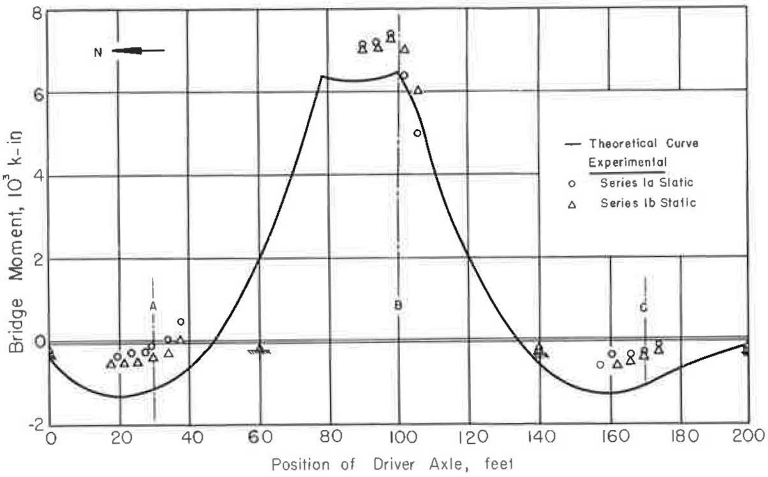

Figure 11. Influence line for bridge moment at Section B, truck northbound.

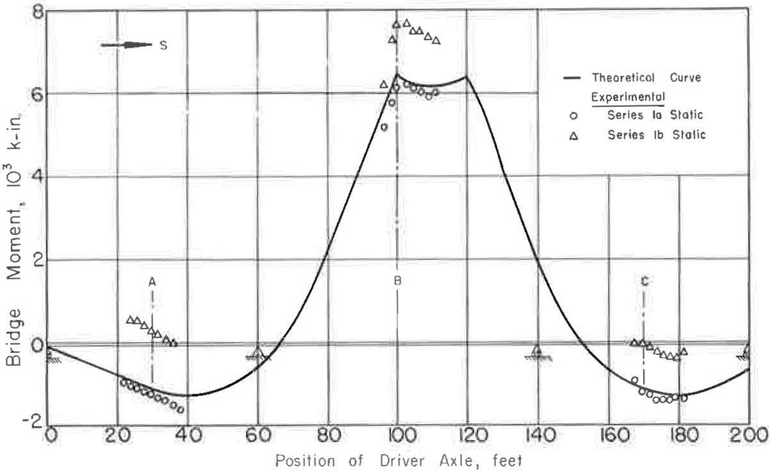

Figure 12. Influence line for bridge moment at Section B, truck southbound.

the entire bridge cross-section. Since such an influence line depends only on the ratios of the moments of inertia at various sections and not on the magnitude of the moment of inertia, these influence lines would be changed only a small amount by considering completely composite action.

Influence lines were then prepared for moments in the bridge at Sections A and B due to the test vehicle. This was accomplished by superimposing influence lines for the front axle, the driver axle, and the tandem axles, referring the position of each axle to the position of the driver axle. Influence lines for the test vehicle were not the same for northbound movement as for southbound movement because the axle loads were not symmetrical about the driver axle. Hence, influence lines for moments at Sections A and B were prepared for each direction of movement. These influence lines are shown in Figures 9 through 12. In each case there is a peak value when the driver axle is over the center of the span and another peak when the tandem axle is over the center of the span.

Experimental Moments

Since moments were not measured directly, the term experimental moment refers to the moment computed from the measured strains. These strains were converted to stresses in the initial data reduction, and all subsequent computations were based on these stresses. Computations for the experimental moments were based on the following assumptions:

1. There is an unknown amount of composite action between the slab and the steel beams.
2. There is no net axial force in the semi-composite section.
3. The slab and the steel beam always remain in contact, even though the slab may slide longitudinally on the beam (the curvature of the slab must be equal to the curvature of the steel beam).
4. The stress distributions on both the slab and the beam are linear with depth.

Assumptions 1 and 4 result in a stress distribution across the section as shown in Figure 13a. The stresses σ_t and σ_b are extreme-fiber stresses extrapolated from the original data. The analysis is equally valid for maximum or mean stresses. The stress distribution in the steel beam and the slab may be broken into axial and flexural components (Fig. 13b). From these stresses, both the axial force P and the bending moment in the steel beam M_S can be computed as follows:

$$P = \frac{\sigma_b + \sigma_t}{2} A_S \qquad (1a)$$

and

$$M_S = \frac{\sigma_b - \sigma_t}{d} I_S \qquad (1b)$$

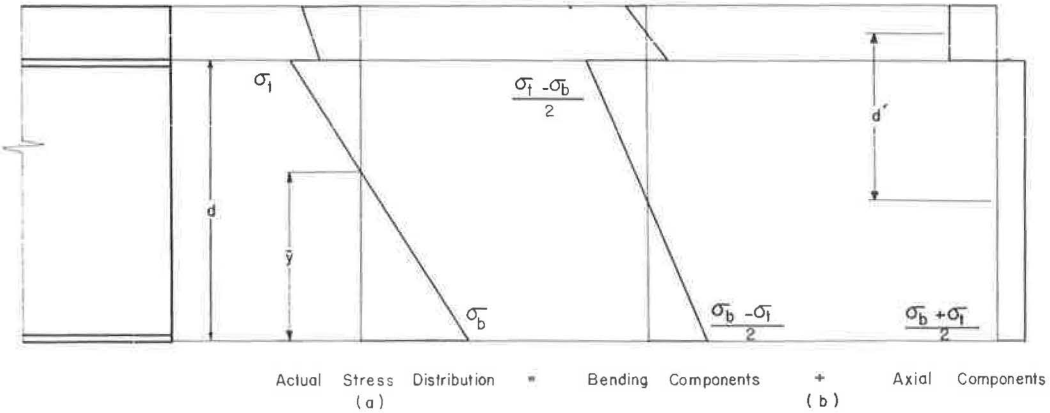
σ_t
d
$\bar{y}$
σ_b
$\frac{\sigma_t - \sigma_b}{2}$
$\frac{\sigma_b - \sigma_t}{2}$
d'
$\frac{\sigma_b + \sigma_t}{2}$
Actual Stress Distribution
(a)
=
Bending Components
+
(b)
Axial Components

$$\text{Total Moment} = M_{(\text{steel beam})} + M_{(\text{axial force})} + M_{(\text{slab})}$$

$$M = \frac{(\sigma_b - \sigma_t)}{d} I_s + \frac{(\sigma_b + \sigma_t)}{2} A_s d' + \frac{(\sigma_b - \sigma_t)}{d} \frac{I_c}{n}$$

Figure 13. Stress distribution on semi-composite section.

where A_s is the cross-sectional area of the I-beam, I_s is the moment of inertia of the I-beam, and d is the depth of the I-beam. To satisfy Assumption 2, the axial force in the slab must be equal in magnitude and opposite in sign to the axial force in the steel beam. Hence, moment due to composite action may be computed as follows:

$$M_P = Pd' = \frac{\sigma_b + \sigma_t}{2} A_s d' \tag{2}$$

where d' is the distance between the centroid of the slab and that of the I-beam. The only remaining bending component in the section is that in the slab itself. On the basis of Assumption 3, the moment in the slab may be computed by estimating its flexural rigidity and multiplying by the curvature of the beam. The flexural rigidity of the slab R may be expressed as

$$R = E_c I_c \tag{3}$$

where E_c is the modulus of elasticity of the concrete, and I_c is the moment of inertia of the transformed uncracked section of the slab. The curvature of the beam K may be expressed as

$$K = \frac{\sigma_b - \sigma_t}{E_s\, d} \tag{4}$$

where E_s is the modulus of elasticity of the steel. Hence, the moment in the slab M_c may be expressed as

$$M_c = RK = \frac{\sigma_b - \sigma_t}{d} \frac{I_c}{n} \tag{5}$$

where n is the modular ratio.

The accuracy of this last calculation may be questioned because of the uncertainties involved in determining both the effective width of the slab and the value of the modular ratio. However, calculations show that for the particular bridge in question, the moment in the slab can never exceed 4 percent of the total moment in the composite section. Thus, rather large errors in this particular component of the bending moment would result in only small changes in the total moment. The total experimental moment in the stringer M was calculated as the sum of the three components:

$$M = \frac{\sigma_b - \sigma_t}{d} I_s + \frac{\sigma_b + \sigma_t}{2} A_s d' + \frac{(\sigma_b - \sigma_t)}{d} \frac{I_c}{n} \tag{6}$$

Experimental moments were computed at Sections A and B of each stringer for each of the critical conditions.

Adding the experimental moments in the four stringers at a given section results in the total bending moment in the entire cross-section of the bridge at a particular instant. Under dynamic loading conditions this computed total is slightly in error because the moments computed for the individual stringers did not occur at exactly the same instant. Figures 9 through 12 show comparisons of the static experimental moments with the theoretical influence lines. In Figures 14 through 17, the dynamic experimental moments are compared with the theoretical values. The vertical bars

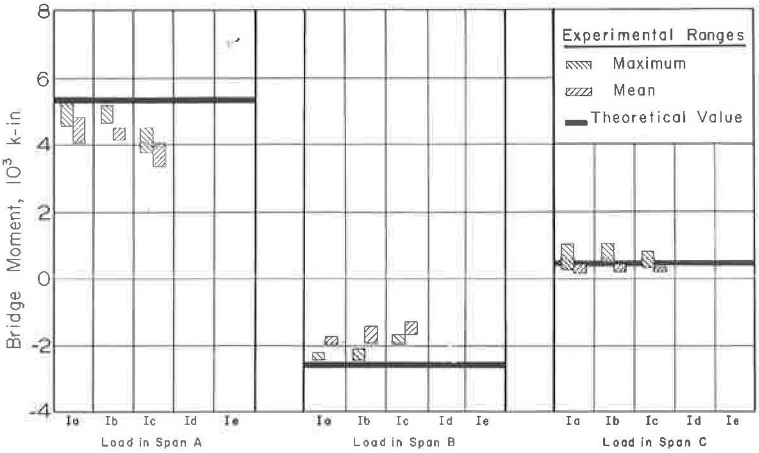

Figure 14. Dynamic ranges of bridge moment at Section A, truck northbound.

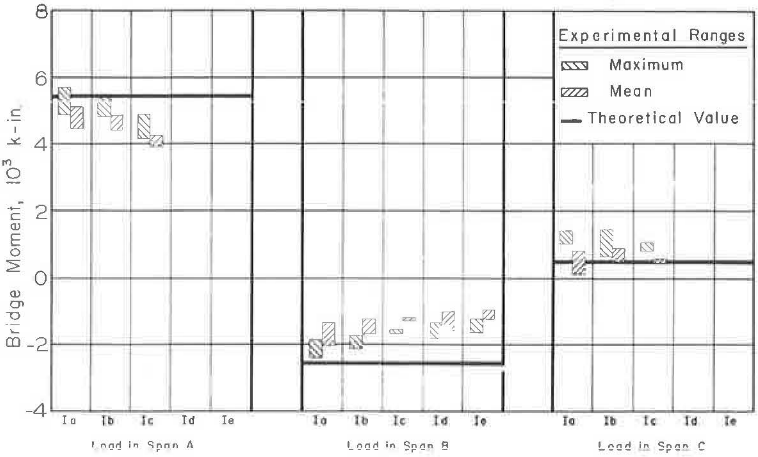

Figure 15. Dynamic ranges of bridge moment at Section A, truck southbound.

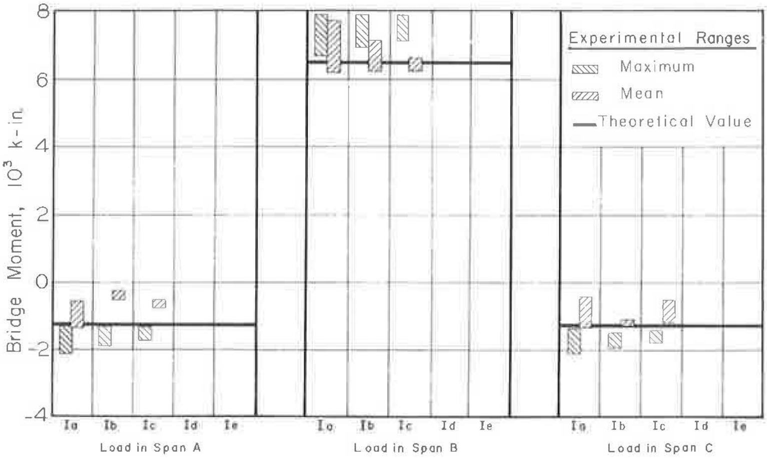

Figure 16. Dynamic ranges of bridge moment at Section B, truck northbound.

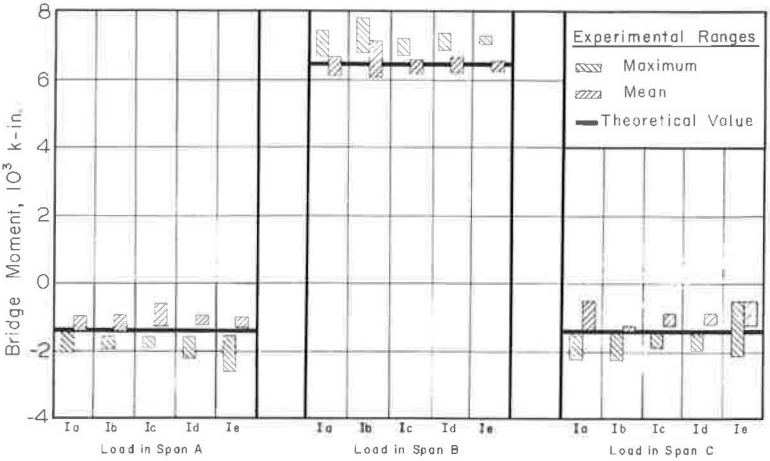

Figure 17. Dynamic ranges of bridge moment at Section B, truck southbound.

represent the ranges of total mean moments in the bridge whereas the heavy horizontal lines represent the peak values from the theoretical influence lines. The location of the truck at the time the peak moments occurred was not recorded.

In general, there is fair agreement between the experimental values and the theoretical influence lines. The static values at Section A with Span A loaded are approximately 15 percent lower than those predicted by the theory. It will be shown that the composite action in Span A was not as complete as in Span B; hence, the relative stiffness of Span A was actually less than that assumed in the analysis. This was probably the cause of the discrepancy.

The static moments at Section B from Series 1a southbound are in almost perfect agreement with the theoretical curve. The static moments at Section B from Series 1b southbound appear to be shifted approximately 1200 kip-in. in the positive direction. This shift is nearly constant for all points regardless of the span in which the truck was located and, therefore suggests some sort of a zero shift in the experimental data. One might immediately suspect such a shift in the gage readings, but more careful consideration reveals that several gage readings were incorporated in finding each of the moments plotted. None of these gage readings appear to be inconsistent with the rest of the gage readings, and it seems rather unlikely that there would be an accidental zero shift of about the same percentage in each of eight gages.

Another possible explanation of this shift is that there was a residual moment in the I-beam at the time the zero readings were taken. This residual could come about because of the friction between the slab and the steel beams. Mechanisms containing friction links normally have more than one equilibrium position. There is no proof of the cause of this apparent zero shift, but it seems to be inherent in the behavior of the bridge. This phenomenon is also present in the static runs of Series 1a and 1b northbound. The dynamic values seem to be in better agreement with the theory than the static values.

Theoretical Deflections

Elastic theory was used to prepare influence lines for deflections at Sections A and B due to a unit load passing across the bridge. This was done for both interior and exterior stringers and for both composite and non-composite action. A slab width of 80 in. and a modular ratio of 10 were used in computing the transformed section for composite action. The ordinates of the influence lines for interior and exterior stringers never differed more than 8 percent. By averaging the ordinates of these two influence lines, an influence line representing the average deflection of the four stringers was

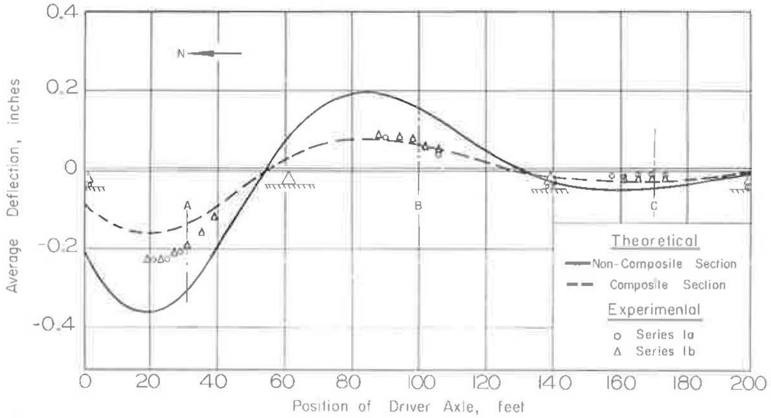

Figure 18. Influence lines for average deflection at Section A, truck northbound.

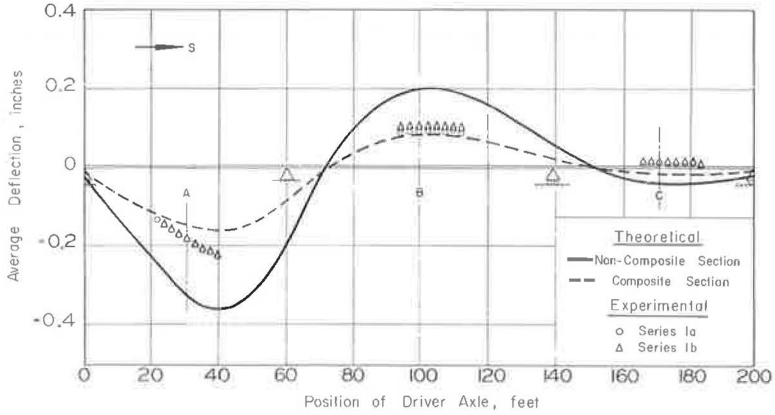

Figure 19. Influence lines for average deflection at Section A, truck southbound.

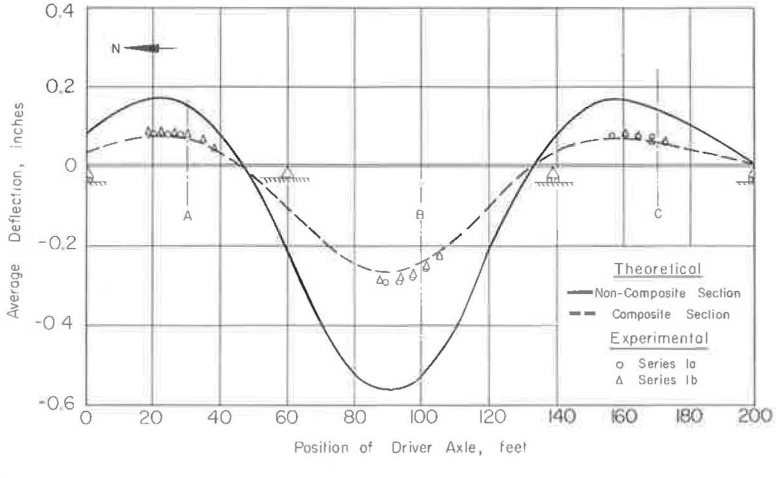

Figure 20. Influence lines for average deflection at Section B, truck northbound.

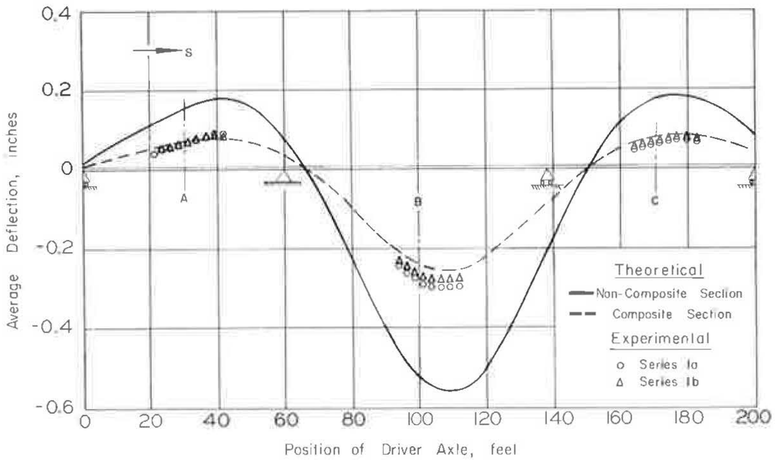

Figure 21. Influence lines for average deflection at Section B, truck southbound.

prepared. The procedure explained previously for preparing moment influence lines was then followed in preparing influence lines for average deflection due to the test vehicle. The resulting influence lines for the average deflection in the four stringers are shown in Figures 18 through 21. The solid line represents the deflections computed on the basis of non-composite action and the dashed line represents the deflections computed on the basis of composite action.

Experimental Deflections

Experimental deflections for the four stringers were averaged at each section for each critical condition. These average static deflections are compared with the theoretical values in Figures 18 through 21. Ranges of values for average deflection under dynamic loadings are compared with theoretical values in Figures 22 through 25. The position of the truck on the bridge at the time of the critical deflection was not recorded for these runs.

The static experimental deflections at Section B agree very well with the influence line for completely composite action. The deflections at Section A are somewhat greater

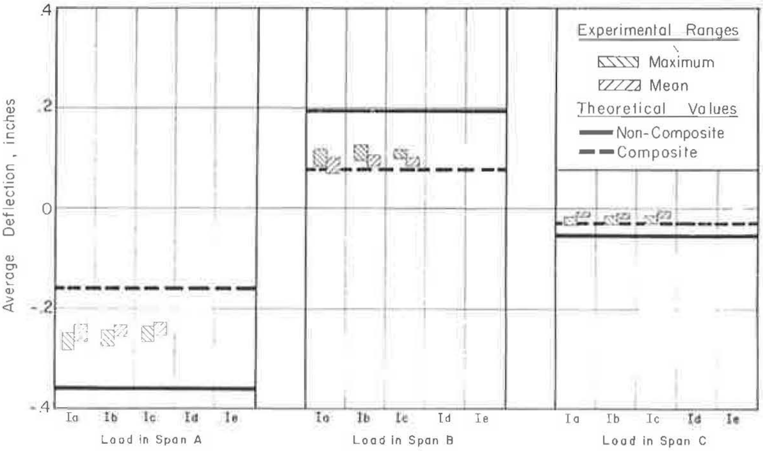

Figure 22. Dynamic ranges of average deflection at Section A, truck northbound.

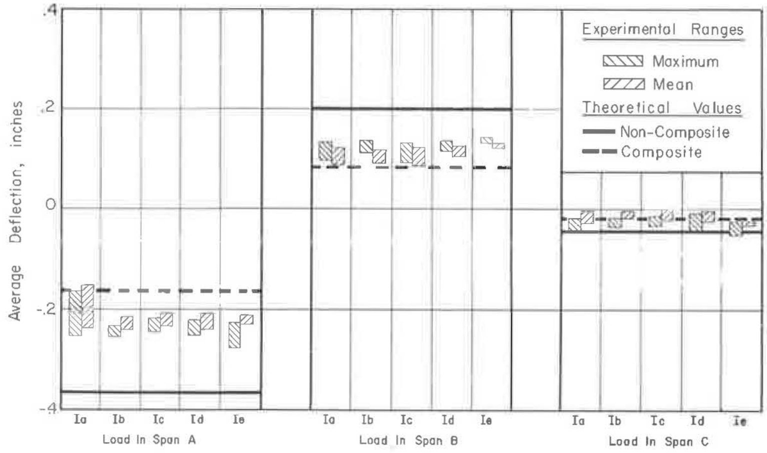

Figure 23. Dynamic ranges of average deflection at Section A, truck southbound.

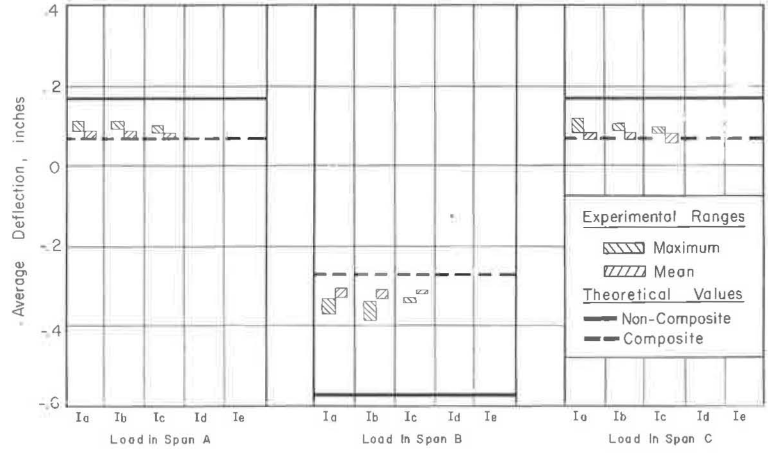

Figure 24. Dynamic ranges of average deflection at Section B, truck northbound.

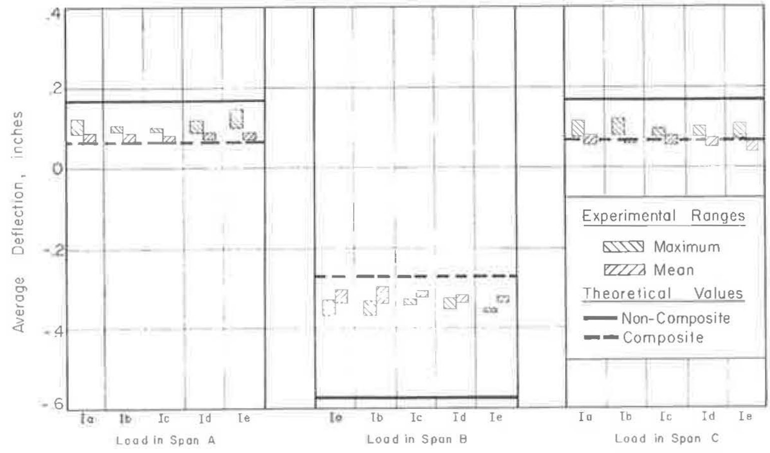

Figure 25. Dynamic ranges of average deflection at Section B, truck southbound.

than those predicted on the basis of completely composite action. This observation is further evidence that the degree of composite action was greater in the center span than in the end spans.

Figure 19 shows that the deflections at Section A were opposite in sign to those predicted by the theory when the truck was in Span C. This was probably another manifestation of the multiple-equilibrium position phenomenon of the system with a friction link. In this case the truck was southbound and had just left Span B. Thus, the deflections in Span A were changing from positive to negative. As shown in Figure 18, the deflections were in much better agreement with the theory when the truck was northbound. This phenomenon is not so noticeable in cases where the load was in Span A or B and the deflections due to load were of a much greater magnitude. In all cases the dynamic deflections were somewhat greater than the static deflections. Even so, there was still a high degree of composite action.

Moment vs Speed

To find the extent to which the impact factor was dependent on the speed of the vehicle crossing the bridge, some value on which to base the calculations had to be found. Static values were not considered desirable for this purpose because of the tendency for zero shift as indicated by the influence lines for static moment. Consequently, normalized moments based on mean stresses were plotted vs speed. The ordinate of this plot was normalized by dividing each moment value by the average of the 5-mph values for the same series, the same stringer, the same section, and the same loading conditions except for speed. By normalizing the moment values in this manner, it was possible to plot all available mean moments on a single plot (Fig. 26). A least-mean-squares fit of a straight line to all points shown in Figure 26 results in the following expression:

$$\frac{M_{\text{mean}}}{M_{\text{mean}_5}} = 1.01 - 0.000410 \times \text{speed (mph)} \tag{7a}$$

Although there is some scatter in the data, this plot indicates that the mean moment was essentially independent of speed. This is basically in agreement with the assumptions of other investigators (2, 3, 4, 5, 6, 7). On the basis of this finding it was decided that impact was a result solely of the vibration in the bridge and that the average of the

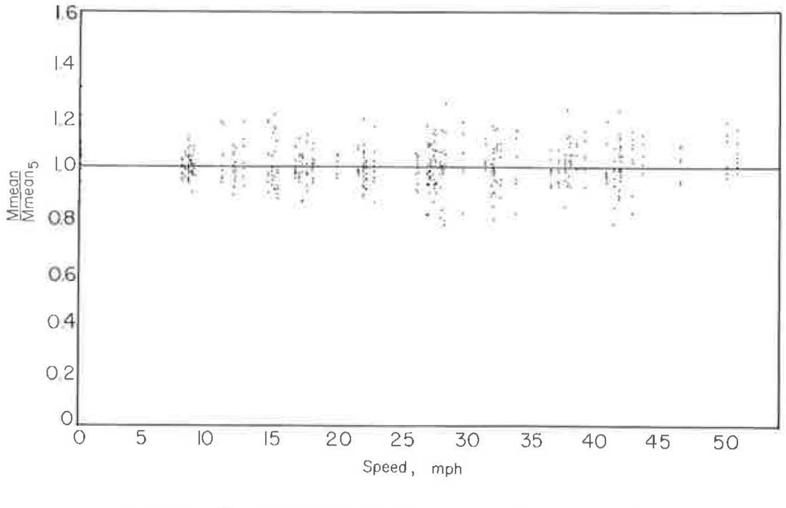

Figure 26. Normalized mean moment vs speed.

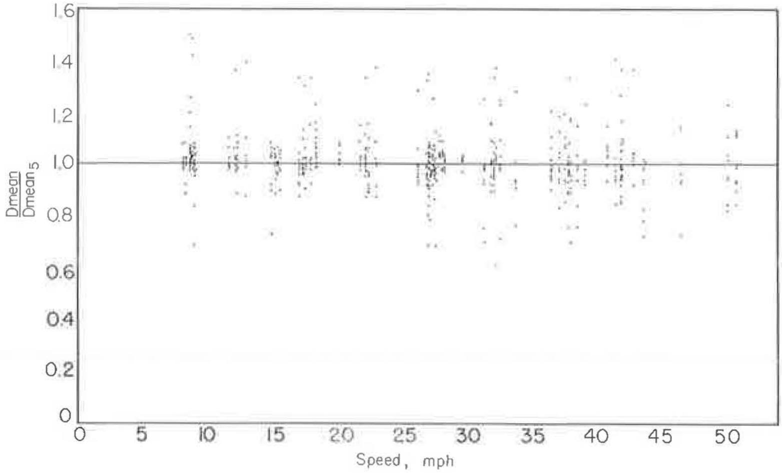

Figure 27. Normalized mean deflection vs speed.

corresponding mean moments was probably the best base value for determining impact factors.

Deflection vs Speed

In investigating the extent to which deflection was dependent on the speed of the vehicle, essentially the same procedure was followed as for moment. Each mean deflection was normalized by dividing it by the average of the corresponding deflections at 5 mph. Figure 27 was then prepared by plotting these normalized values of deflection against the speed of the vehicle, and the straight line shown represents a least-mean-squares fit. The equation of this line is:

$$\frac{D_{mean}}{D_{mean_5}} = 1.02 - 0.000327 \times \text{speed (mph)} \qquad (7b)$$

This expression again indicates that impact was due solely to the vibration of the bridge and the average of the mean values was probably the best base value for computing impact factors.

Lateral Distribution

Lateral distribution of the load was investigated by expressing the moment in each stringer as a percentage of the total moment in the section. These percentages for both static and dynamic runs are shown graphically in Figures 28 and 29. The ordinate of each of these plots represents the percentage of the total moment in the bridge section carried by each of the stringers, while the abscissa represents the four stringers of the bridge. The experimental data are represented by a band indicating the spread of values for all runs in a given series in both directions. The average values are very close to the center of the band in most cases.

The first plot in each line represents the distribution of moment in the bridge when the load was in the same span as the gages. Thus, the band designated "Gages in Span A" represents the distribution of moment in Span A when the load was in Span A, whereas the band designated "Gages in Span B" represents the distribution of moment in Span B when the load was in Span B. The second plot in each line represents the distribution of moment at the center of a given span when the load was in the adjacent span. Thus,

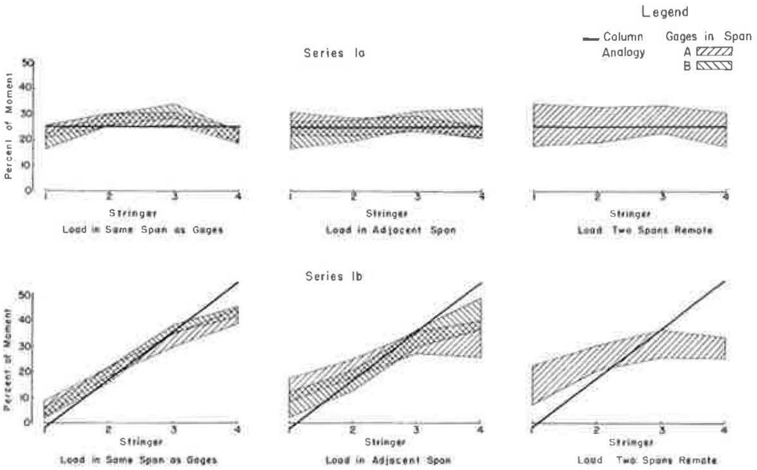

Figure 28. Lateral distribution of moment, Series 1a and 1b.

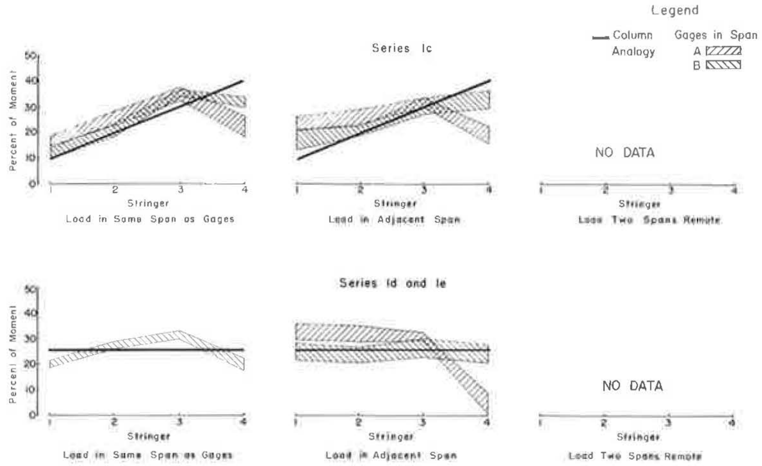

Figure 29. Lateral distribution of moment, Series 1c, 1d, and 1e.

the band designated "Gages in Span A" represents the distribution of moment in Span A when the load was in Span B, whereas the band designated "Gages in Span B" represents the distribution of moment in Span B when the load was either in Span A or Span C. Because these data were essentially the same whether the load was in Span A or Span C, the data were all indicated in a single band. The third plot in each line represents the distribution of moment in Span A when the load was in Span C. This was the only condition under which moment was measured in a span when the load was two spans remote from the gages. Malfunctioning of a few gages accounts for the missing plots in Series 1c, 1d, and 1e. The gages which did not function properly were on Stringer 4 in Span A. This difficulty may also account for the unusually low values for Stringer 4 in Span A of Series 1c, 1d, and 1e.

The most elementary of the theories for lateral distribution is based on the assumption of simple-beam action in the slab. The inaccuracy of this theory is obvious from inspection. Such a behavior would result in all the load being carried by the 2 interior stringers for Series 1a, 1d, and 1e. For Series 1b, 97 percent of the load would be carried by Stringers 3 and 4.

A form of column analogy suggested by Prentzas (8) gives a reasonably satisfactory prediction of the lateral distribution. This method predicts the load L_i carried by ith Stringer from the formula:

$$L_i = L_t \frac{I_i}{\sum\limits_k I_k} + L_t e \frac{y_i I_i}{\sum y_k{}^2 I_k} \tag{8}$$

where L_t is the load on the bridge, I_i and I_k are the moments of inertia of the ith and kth Stringers, y_i and y_k are the lateral distances from the center line of the bridge to

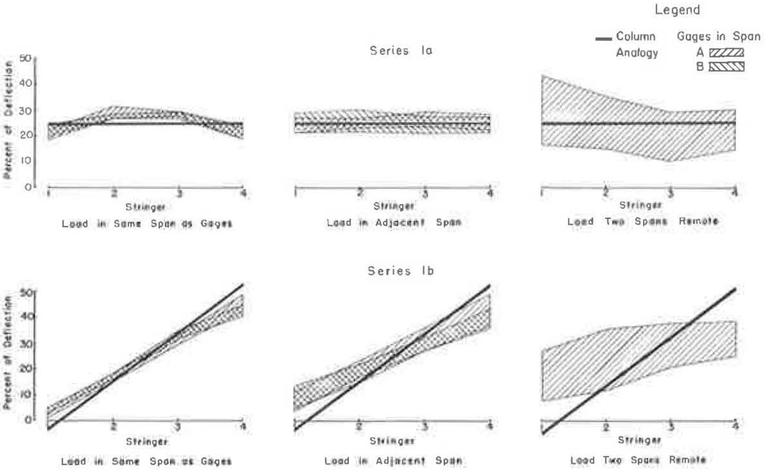

Figure 30. Lateral distribution of deflection, Series 1a and 1b.

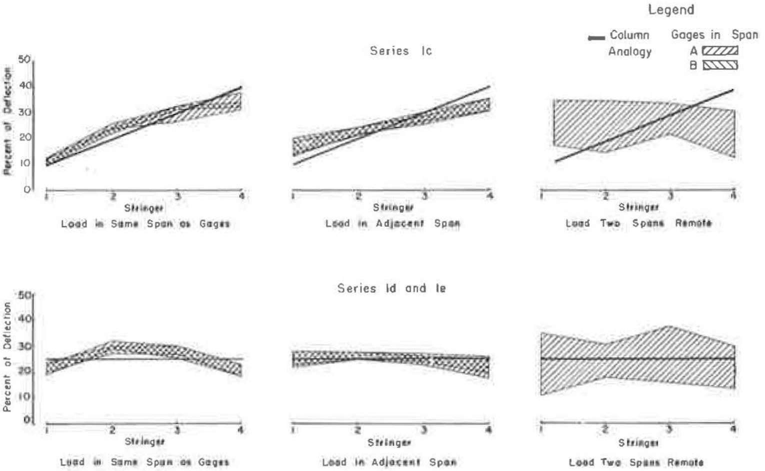

Figure 31. Lateral distribution of deflection, Series 1c, 1d, and 1e.

the ith and kth Stringers, and e is the lateral distance from the centerline of the bridge to the load (Figs. 28 and 29).

The portion of the current AASHO specifications relating to lateral distribution was developed on the basis of the work of Newmark and Siess (9, 10, 11). If one considers the effect of two trucks on the bridge by using the principle of superposition, the data agree reasonably well with these specifications. The code states that an interior stringer of the bridge under consideration should be designed for 1.21 wheel loads. Superimposing suitable data from Series 1b and 1c of the test results gives a range of 0.94 to 1.32 or an average of 1.14 wheel loads for an interior stringer. For an exterior stringer of the bridge under consideration, the code requires 1.18 wheel loads for design. Superimposing suitable data from Series 1b and 1c of the test data results in a range of 0.94 to 1.28 or an average of 1.11 wheel loads for an exterior stringer.

Lateral distribution was also investigated by comparing the deflections of individual stringers. The percent of deflection in a stringer was calculated as the deflection in the stringer divided by the sum of the deflections of the four stringers at the particular section. Figures 30 and 31 are identical to Figures 28 and 29 except that they represent the lateral distribution of deflections. This distribution was essentially the same as that for moment except for Stringer 4 of Series 1c, 1d, and 1e. This difference was undoubtedly due to some difficulty with the strain gages at Section A of Stringer 4. The comparison of the theoretical to experimental distribution of moments applies equally well to deflections.

The scatter of the data where the load was two spans remote from the gages may be explained by the very small gage readings under these conditions. With such small readings, the noise level in the instrumentation was a very large percentage of the measured quantity. There seemed to be a slight tendency for the distribution to become more uniform as the load moved farther from the section at which the moment was being measured.

Composite Action

The semi-composite action of the bridge was evaluated quantitatively on the basis of an effective section modulus. This modulus was calculated by dividing the experimental moment in a stringer by the stress in the bottom fiber. It should be noted that although the moment of inertia for a completely composite section is nearly twice as great as that for the same section with non-composite action, the effective section modulus is only 50 percent greater. The section modulus for a completely non-composite stringer in this bridge is approximately 400 cu in., whereas the section modulus for a completely composite stringer in this bridge is approximately 600 cu in.

Distributions of values of effective modulus are shown in Figures 32 and 33. The distributions calculated on the basis of mean values (Fig. 32) are essentially the same as the distributions calculated on the basis of maximum values (Fig. 33). However, the distributions of values for Span A are considerably different from the distributions of values for Span B. The values range from 400 to 540 for Span A and from 520 to 620 for Span B. Thus, the composite action was approximately 30 percent complete in Span A but more than 80 percent complete in Span B. These data are in agreement with the data for moments and deflections discussed previously. As mentioned before, the apparent reason for the much lower degree of composite action in Span A is the smaller surface over which the friction can develop composite action. This suggests that in long multispan bridges, completely composite action might be realized by placing shear developers in the end spans only. This hypothesis is purely conjecture and is intended only as a suggestion for future research.

Frequency of Vibration

The theoretical nature frequency for the fundamental mode of vibration of the bridge was calculated using the method developed by Darnley (12). This method for finding the natural frequency of multispan beams, with constant cross-section and uniformly distributed mass, results in the solution of the following equation:

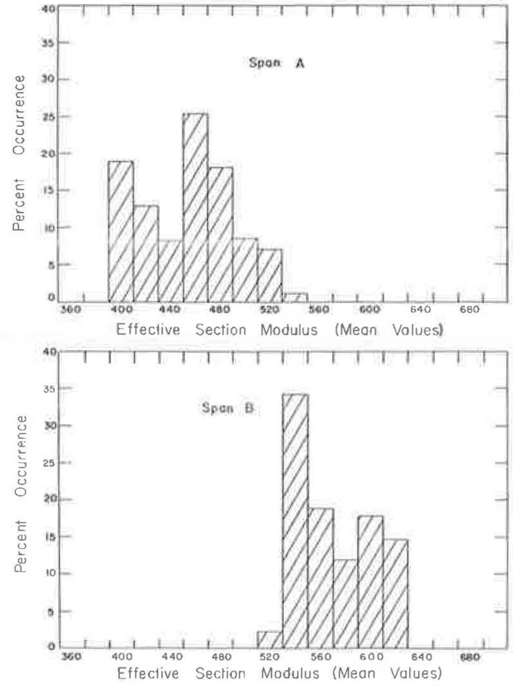

Figure 32. Distribution of values for effective section modulus (mean).

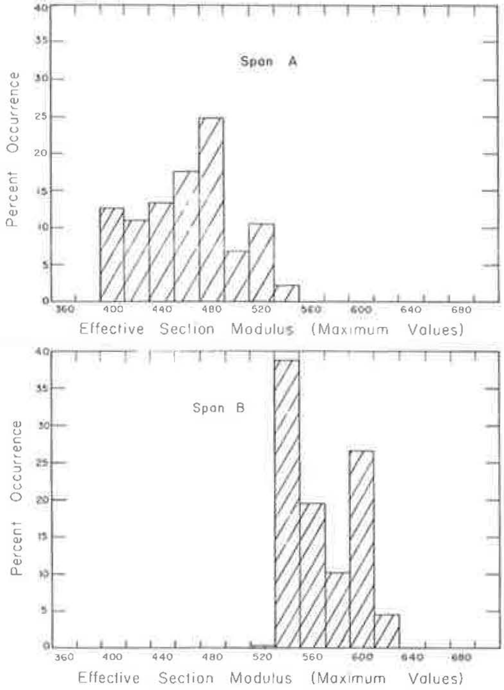

Figure 33. Distribution of values for effective section modulus (maximum).

$$F_1 = \frac{(k_1 L_1)^2}{2\pi L_I^2} \frac{\sqrt{EIg}}{w} \tag{9}$$

where $k_1 L_1$ is the smallest root of the equation

$$\phi_1 + \phi_2 = \psi 2 \tag{10}$$

where

ϕ_r = Coth kL_r - cot kL_r,
ψ_r = Csch kL_r - csc kL_r,
L_r = length of the r th span,
E = modulus of elasticity,
I = moment of inertia of bridge,
w = weight per unit length of bridge, and
g = acceleration of gravity.

Although the moment of inertia of the bridge under investigation varied as much as 15 percent from one cross-section to another, it was decided that calculations for a constant cross-section, based on an average of the cross-sections for the bridge would be suitable. The completely composite section was expected to give the best prediction of natural frequency because of the high degree of composite action indicated by the moment analysis. The following quantities were used in the calculation:

$E = 30 \times 10^6$ psi,
$I = 64{,}969$ in.^{4},
$L_1 = 720$ in.,
$L_2 = 960$ in.,
$g = 386$ in./sec^2, and
$w = 243.5$ lb/in.

Using these values, the natural frequency was found to be 4.00 cycles/sec. Considering non-composite action with an I of 32,332 in.^{4} resulted in a calculated natural frequency of 2.82 cycles/sec.

The natural frequency of the bridge as determined from the oscillograph records varied from 4 to 4.9 cycles/sec with an average of about 4.2 cycles/sec. There seemed to be no perceptible difference between the natural frequencies under loaded and unloaded conditions, which agreed with the analysis. Consideration of the weight of the truck distributed over the entire length of the bridge would have changed the calculated natural frequency by only 3.3 percent.

Amplitude of Vibration

According to the findings of Hayes et al. (3), one might expect some degree of resonance at speeds of 11.5, 36.6, and 53.4 mph by considering the distance between the two tandem axles, between the front axle and the driver axle, and between the driver axle and the first of the tandem axles. This resonance would result in substantial increases in the amplification factor at these speeds.

The amplification factor may be defined as the ratio of the maximum moment, stress, or deflection to the mean moment, stress, or deflection. It follows from the previous discussions that the impact factor IF may be computed from this amplification factor as follows:

$$IF = \text{amplification factor} - 1 \tag{11}$$

Impact factors were computed on the basis of both moment and deflection for each of the sets of critical values. The impact factor IF_M based on moment was computed from the equation

$$IF_M = \frac{M_m - M_a}{M_a} \tag{12}$$

where M_m is the maximum moment and M_a is the average of all the corresponding mean moments. The impact factor IF_D based on deflection was computed from the equation

$$IF_D = \frac{D_m - D_a}{D_a} \tag{13}$$

where D_m is the maximum deflection and D_a is the average of all the corresponding mean deflections.

The impact factors at each nominal speed were averaged and these were plotted against speed in Figure 34. This graph indicates no significant increase in the impact factor at speeds of 11.5 or 36.6 mph. There is some indication that the impact factor was increasing as the 53.4-mph speed was approached. Unfortunately, the greatest nominal test speed was 50 mph. The lack of sensitivity to the repeated loads applied by the tandem axles might be expected because of the extremely short distance between the two axles. Lack of sensitivity to repeated loads applied by the front axle and the driver axle might be attributed to the low load on the front axle.

Figure 35 shows the distributions of impact factors at all speeds. The peak of the distribution curve for impact factors based on moment falls between 0.10 and 0.12,

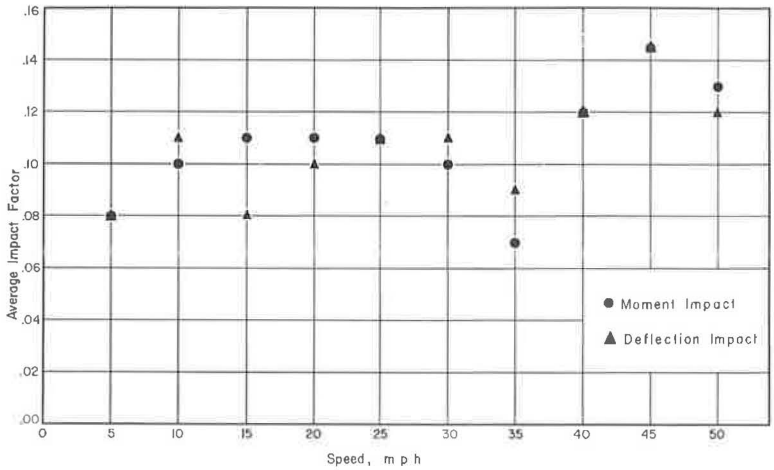

Figure 34. Average impact vs speed.

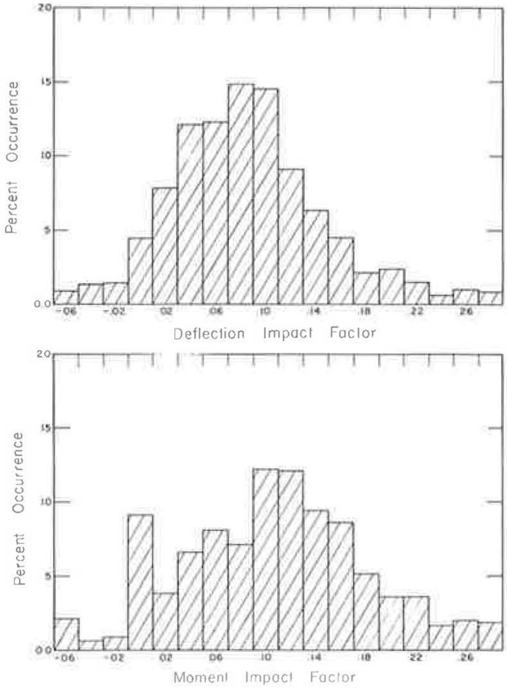

Figure 35. Distribution of impact factors.

whereas the peak of the distribution curve for impact factor based on deflection falls between 0.08 and 0.10. One might expect impact factors for moment to be slightly greater than those for deflection because the moment is a local condition and the deflection is an integral of the moments over the length of the span. Although the peaks of the distribution curves are considerably less than the values of 0.238 and 0.27 required by AASHO specifications for the bridge under investigation, there is a great deal of scatter in the data with some values more than twice the mean value. For this particular set of tests, 96.5 percent of the impact factors fell below the 0.25 level. Thus, one might well consider the currently accepted design impact factor as a suitable and conservative limit.

Induced Roughness

Series 1d and 1e of the test program were conducted to determine the effect of induced roughness at the bridge approach on the impact factor. The data indicate no significant increase in the impact factors for Series 1d and 1e. An examination of the records taken from the axle housings of the truck revealed such great damping of the suspension system of the truck that the initial oscillations produced by the induced roughness were damped out in approximately 1 to $1\frac{1}{2}$ cycles. The time required for these oscillations to be damped out was much less than the time required for the truck to move from the approach to the center of the span. Therefore, the high forces produced by these initial oscillations were not applied to the bridge at a location that would produce large moments in the bridge.

SUMMARY AND CONCLUSIONS

Data from the five series of tests outlined in Table 1 were analyzed and compared with existing theories and design codes. Mean moments in the test structure were calculated from the observed strains and compared with the moments predicted by elastic theory. These comparisons were generally in good agreement. The greatest discrepancies occurred in the static data and were presumably the result of the multiple-equilibrium positions of the bridge, a result of the friction link between the slab and the steel I-beam.

The average experimental deflection at each section in the bridge for each series of tests was compared with the average deflection calculated on the basis of elastic theory for both composite and non-composite action. The actual behavior of the structure was much closer to completely composite action than to non-composite action. The deflections in the center span were almost identical to those predicted on the basis of completely composite action, whereas the deflections in the end span were approximately ⅓ of the way between completely composite and non-composite action.

Mean moments and mean deflections were found to be essentially independent of speed. This indicated that the effect of impact on the bridge was entirely due to the vibrations of the bridge. Hence, moment impact factors were calculated as the difference between the maximum and the mean moments divided by the average of the corresponding mean moments. Deflection impact factors were calculated in the same manner. A plot of these impact factors against speed shows that the impact factor was independent of speed for speeds less than about 40 mph. Some indication exists that the impact factor was increasing beyond that speed, but no data are available beyond 50 mph. Assuming that the period of time between the passage of two wheels over a given point of the bridge may be treated as the period of a repeated forcing function on the bridge, and considering the measured natural frequency of vibration of the bridge, one might predict that a resonance would be reached at a speed of approximately 55 mph. The lateral position of the truck on the bridge seemed to have little effect on the impact factors.

The measured natural frequency of the bridge was approximately 5 percent greater than that predicted by Darnley's analysis (12) considering completely composite action.

The lateral distributions of moments and deflections were compared with an analysis suggested by Prentzas (8) and also with the AASHO code. Both of these comparisons showed reasonable agreement. However, comparison with the code required using superposition, a procedure subject to some criticism. Computing lateral distribution on the basis of simple beam action in the slab resulted in very poor agreement with the test results.

An analysis of the amount of composite action based on an effective section modulus revealed essentially the same information as the comparison of deflections. The section modulus in the center span was nearly equal to that of a completely composite section. The amount of composite action in the end span was approximately 30 percent. This difference perhaps was due to the difference in the amount of surface between the slab and the I-beam available for the development of composite action. In the end span, the surface available to develop the composite action through friction was limited to the surface between the center and end of the span, whereas in the case of the center span the surface available for developing composite action extended from the center of the center span through the entire length of the end span.

The test results indicated that induced roughness at the approach of the bridge had little or no effect on the maximum moments observed in the bridge. The oscillations of the truck induced by roughness at the approach were damped out before the truck reached a position on the bridge which would produce large moments.

The observed behavior of the structure was not materially different from that predicted by current theory and design codes. The idea of an impact factor to account for the effects of dynamic loading is rather crude and does not take into account the possibility of resonant vibration. However, present specifications were reasonable for the design of this particular bridge under the particular loading conditions of this investigation. This might not have been the case if the test runs had continued to slightly higher speeds.

Continuous Span vs Simple Span

There were two significant differences between the simple and continuous spans. The 45-ft simple span was only 75 percent as long as the shortest of the continuous spans. The mass of the simple span was approximately 25 percent as great as the mass of the combined continuous spans.

Both stresses and deflection indicate that there was much less composite action in the simple span than in the continuous spans. This may be accounted for in the same manner as the difference in composite action between continuous Spans A and B. Much less surface was available in the short simple span to develop the composite action through friction.

Impact factors for the simple span were slightly higher than those for the continuous spans. This might be expected because of the span length and, in fact, is indicated by the code provisions. Impact factors for the simple span seem to be somewhat more dependent on the speed and direction of the vehicle than are those for continuous spans. This may be an indication that the simple span was much more sensitive to the oscillations of the truck. The ratio of the mass of the truck to the mass of the structure was much higher for the simple span than for the continuous spans. The short span length also made it possible for the truck to reach the center of the bridge before the oscillations of the vehicle were damped out. Induced roughness caused significant increases in the impact factors for the simple span, which was not true for the continuous spans.

The frequency of free vibration of the unloaded simple span was observed to be 9 cycles/sec. The calculated natural frequency for the unloaded simple span, based on completely composite action and a modular ratio of 10 for the concrete, was 7.12 cycles/sec. The observed frequency of the loaded simple span was 8 cycles/sec, whereas the calculated natural frequency for the loaded simple span was 5.76 cycles/sec. Differences between the calculated and observed natural frequencies of the simple span were considerably greater than those for the continuous spans. This may have been due in part to the sensitivity of the bridge to the oscillations of the truck.

During creep runs the simple span was observed to vibrate at a frequency of 3.5 cycles/sec. This is in fairly close agreement with the calculated value of 3.61 cycles/sec for the loaded simple span if it were behaving in a completely noncomposite manner. The lateral distributions of both moment and deflection in the simple span and in the continuous spans were essentially the same.

REFERENCES

1. Impact Study of a Simple I-Beam Span of a Highway Bridge. Missouri State Highway Department, Div. of Bridges, 1958.
2. Biggs, John M., and Suer, Herbert S. Vibration Measurements on Simple Span Bridges. Highway Research Board Bull. 124, pp. 1-15, 1955.
3. Hayes, John M., and Sbarounis, John A. Vibration Study of Three-Span Continuous I-Beam Bridge. Highway Research Board Bull. 124, pp. 47-78, 1955.
4. Edgerton, Roy C., and Beecroft, Gordon W. Dynamic Studies of Two Continuous Plate-Girder Bridges. Highway Research Board Bull. 124, pp. 33-46, 1955.
5. Scheffey, Charles F. Dynamic Load Analysis and Design of Highway Bridges. Highway Research Board Bull. 124, pp. 16-32, 1955.
6. Foster, George M., and Oehler, Leroy T. Vibration and Deflection of Rolled-Beam and Plate-Girder Bridges. Highway Research Board Bull. 124, pp. 79-110, 1955.
7. Fenves, S. J., Veletsos, A. S., and Siess, C. P. Dynamic Studies of Bridges on the AASHO Test Road. Univ. of Illinois, Civil Eng. Studies, Structural Res. Ser. No. 227, 1962.
8. Prentzas, Elias George. Dynamic Behavior of Two Continuous I-Beam Bridges. Iowa State Highway Commission, Material Dept., 1958.
9. Newmark, N. M. A Distribution Procedure for the Analysis of Slabs Continuous over Flexible Beams. Univ. of Illinois, Exper. Sta., Bull. 304, 1938.
10. Newmark, N. M., and Siess, C. P. Moments in I/Beam Bridges. Univ. of Illinois, Exper. Sta., Bull. 336, 1942.

11. Newmark, N. M. Design of I-Beam Bridges. Trans. ASCE, Vol. 114, pp. 997-1022, 1949.
12. Darnley, E. R. The Transverse Vibrations of Beams and the Whirling of Shafts Supported at Intermediate Points. Phil. Mag., Vol. 41, p. 81, 1921.
13. Baldwin, J. W., Jr. Impact Study of a Steel I-Beam Highway Bridge. Univ. of Missouri, Eng. Exper. Sta., Bull. 58, 1964.

A New Matrix-Energy Method for Analyzing All Stresses in Rigidly Connected Highway Bridge Trusses

SHU-T'IEN LI, ING-CHANG JONG, JAMES E. RUSSELL, and MALVINDER SAMRA
Respectively, Professor of Civil Engineering and Research Associates, South Dakota School of Mines and Technology, Rapid City

An effort is made to advance a unified logical method for analyzing the true stress states in rigidly connected bridge trusses. The report is divided into two parts: (a) basic research and development, and (b) integrated synthetic application with automatic logical checks.

The theoretical development of the proposed matrix-energy method and examples for the orientation of its exact and simplified versions are set forth. The method of panel-load superposition is advanced as a powerful substitute for influence lines and the methods of substitution and transformation as efficient ways for reducing the number of unknowns and the unavoidable solution of large sets of simultaneous equations is clarified. Also included is an integrated synthetic application of those points developed to a complication analysis. To illustrate a comprehensive scheme with only a small computer available, a three-span continuous highway bridge truss has been selected for the objective analysis. The close correspondence of all maximum design axial stresses to these determined by the conventional method demonstrates the validity of the proposed method.

The proposed method yields most expediently two maximum stress states: (a) maximum axial stresses and simultaneous end moments and transverse shears; and (b) maximum end moments and simultaneous axial stresses and transverse shears. The larger requirement of the two constitutes the absolute maximum stress state that should govern the design. Automatic logical checks for programmed computation are presented. An independent proof for the symmetric coefficient matrix and a validity demonstration for the method of transformation are included.

•FOR MORE THAN eight decades, methods originally developed for analyzing pin-connected trusses have inappropriately continued to be used in determining stresses in modern rigidly connected trusses. Pinned joints were being replaced by riveted joints in the 1870's and became almost completely obsolete about half a century ago. Since World War II, additional versions of rigidly jointed trusses—welded and bolted—have gained increasing importance. All these modern rigidly connected trusses, with or without internal or external redundancy, are inherently highly statically indeterminate rigid frames. The rigidity of the joints constitutes the main cause for end moments, transverse shear, and axial stress in each member.

Paper sponsored by Committee on Bridges.

THEORETICAL DEVELOPMENT

Including Manderla's (1) first enunciation of a method 85 years ago, at least nine independent methods have been developed for the solution of the so-called "secondary stresses," stresses caused by conditions ignored in the conventional analysis of "primary stresses." The problem of secondary stress has actually arisen from improper solution of rigidly connected trusses, rather than from its being truly secondary in nature. By analyzing a rigidly connected truss under a given loading as an assemblage or chain of rigid frames, only one true set of perfectly normal genuine stresses will be found, thus dispelling the misnomer of secondary stresses.

To achieve the ideal of solving all genuine stresses including secondary stresses in each member of a rigidly connected truss of any configuration with any redundancy under any externally applied loading, a matrix-energy formulation is proposed. The method enables the determination of all genuine stresses in a unified setup; it adapts to programmed electronic computation, provides both exact and simplified solutions, and applies to both determinate and indeterminate rigidly connected bridge trusses.

BASIC CONCEPTS

A rigidly connected truss under a given loading is structurally much more complicated than an otherwise ideal pin-connected version identically loaded. There exist, as the truss deflects, couples acting on the bar ends (equal to the internal resisting moments at those points) plus transverse shears. Any determinate truss thus becomes indeterminate in its logical correct solution.

In the most general case, a rigidly connected indeterminate truss of any redundancy would be completely determined by statics, if all of the following were known: (a) the internal resisting moments at the ends of the members, (b) the axial stresses in the redundant members, and (c) the redundant reactions at the supports. These three types of quantities are treated as unknowns in the proposed method. To insure that all unknowns are statically independent, equations of static equilibrium must be fully applied to eliminate dependent unknowns. Consequently, the number of statically independent unknowns is just equal to the degree of statical indeterminateness of the truss viewed as an assemblage of rigid frames.

In general, for an asymmetrical rigidly connected truss of m members under asymmetrical loading, there will be 2m unknown end moments. In a symmetrical rigidly connected truss and under symmetrical loading, if n is the number of joints, the number N of statically independent unknown end moments is given by

$$N = \frac{1}{2}(2m - n) = m - \frac{n}{2} \tag{1}$$

All internal axial stresses, bending moments, and shears in the members, and hence, the total strain energy of the truss can be expressed in terms of the externally applied panel loads and the independent unknowns. ("Axial stress" denotes "total axial stress" or "total internal axial force" as distinguished from "unit axial stress.") By appropriate partial differentiations, all the necessary simultaneous equations will be evolved. On these basic concepts is founded the development of the problem solution in its operative sequence.

Fundamental Notations and Sign Convention

The exaggerated elastic curve of any truss member I-J in the plane of the truss is represented in Figure 1. Symbols applying to this member are as follows:

M_{ij}, M_{ji} = unknown internal resisting end moment at I- and J-end, respectively (kip-in.);

N_{ij} = axial stress (kips);

Q_{ij} = transverse shear (kips);

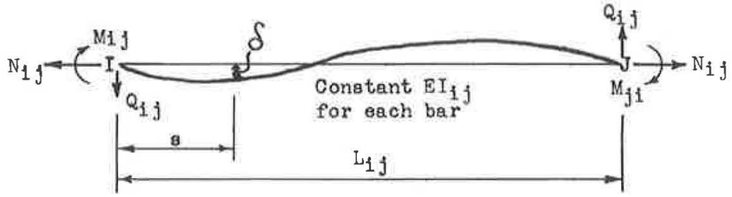

Figure 1.

A_{ij} = cross-sectional area (sq in.);
I_{ij} = moment of inertia (in.^{4});
L_{ij} = length (in.);
s = distance from I-end (in.);
δ = displacement at s, normal to line I-J (in.);
E = modulus of elasticity of material (ksi);
G = modulus of rigidity of material (ksi);
μ = Poisson's ratio of material (may be taken as 0.03 for structural steel); and
U_{ij}, V_{ij}, W_{ij} = strain energy due to bending moment, transverse shear, and axial stress, respectively (in.-kip).

The sign convention is defined such that (a) positive end moments produce clockwise rotation of the member ends; (b) positive axial stresses are in tension; and (c) a positive pair of shears forms a counterclockwise couple.

Constituent Strain-Energy Matrix

The matrix of constituent strain-energy expressions may now be formulated. In Figure 1, recognizing that the moment due to axial stress and deviation from the line I-J is usually negligibly small, the true moment about any point at a distance s from the I-end,

$$M_s = M_{ij} - Q_{ij}\, s - N_{ij}\, \delta \tag{2}$$

may take the simplified form of

$$M_s = M_{ij} - Q_{ij}\, s \tag{3}$$

where

$$Q_{ij} = \frac{M_{ij} + M_{ji}}{L_{ij}} \tag{4}$$

Following the original suggestion of Ménabréa (2) (containing the earliest suggestion in the use of the expression for the strain energy of the truss), but in the present-day complete form, we may write the matrix of the constituent strain-energy expressions of any member I-J as:

$$\begin{bmatrix} W_{ij} \\ \\ U_{ij} \\ \\ V_{ij} \end{bmatrix} = \frac{1}{2} \begin{bmatrix} \int_0^{L_{ij}} \frac{N_{ij}^2}{EA_{ij}} ds \\ \\ \int_0^{L_{ij}} \frac{M_s^2}{EI_{ij}} ds \\ \\ \int_0^{L_{ij}} \frac{Q_{ij}^2}{GA_{ij}} ds \end{bmatrix} = \frac{1}{E} \begin{bmatrix} \frac{1}{2} \frac{L_{ij}}{A_{ij}} N_{ij}^2 \\ \\ \frac{L_{ij}}{6I_{ij}} \left(M_{ij}^2 - M_{ij}M_{ji} + M_{ji}^2\right) \\ \\ \frac{1+\mu}{A_{ij}L_{ij}} \left(M_{ij} + M_{ji}\right)^2 \end{bmatrix} \tag{5}$$

where $G = E/2(1 + \mu)$ in the last equation.

Summing up $\{W\ U\ V\}_{ij}$ for all members of the truss, the total strain energy U of any truss is then

$$U = \sum_{1}^{m} \lfloor 1\ 1\ 1 \rfloor \left\{W_{ij}\ U_{ij}\ V_{ij}\right\} \tag{6}$$

where m is the number of members in the truss.

Matrix Equation of Unknowns and Their Solution

With all joints enormously rigid, all components ideally fit, and all supports unyielding, the application of Castigliano's second theorem (3), or the theorem of least work, to the problem of trusses with any degree of redundancy, will yield the following relations:

$$\left\{\frac{\partial U}{\partial M}\ \frac{\partial U}{\partial N}\ \frac{\partial U}{\partial R}\right\} = \{0\ 0\ 0\} \tag{7}$$

where M is any statically independent unknown end moment, N is the unknown axial stress in any redundant member, and R is any unknown redundant reaction.

Whereas Eqs. 7 represent minimization of strain energy or zero "relative" displacements, the last also denotes the condition of zero settlement of support. In the case of non-zero settlement, according to Castigliano's first theorem (3), $\frac{\partial U}{\partial M}$ would be equal to the rotation, $\frac{\partial U}{\partial N}$ to an over- or underrun, and $\frac{\partial U}{\partial R}$ to the support settlement.

The unknown M's, N's, and R's of any loaded plane truss of any configuration may be generalized as the unknown column vector $\{X_i\}$, where $i = 1, 2, \ldots, n$. Repeated application of $\frac{\partial U}{\partial X_i} = 0$ yields a set of n nonhomogeneous simultaneous algebraic linear equations:

$$\left[a_{ij}\right] \left\{X_i\right\} = \left\{C_i\right\} \tag{8}$$

in which both i and j = 1, 2, . . . , n and the constant vector $\{C_i\}$ has been transposed to the righthand side.

It follows analogously from Maxwell's theorem of reciprocity (4) that the coefficient a_{ji} of X_i in the j th equation is identical both in sign and magnitude as the coefficient a_{ij} of X_j in the i th equation, and, consequently,

$$a_{ij} = a_{ji} \tag{9}$$

where $i \neq j$, giving a symmetric coefficient matrix. An independent proof for the symmetry of the coefficient matrix is given in Appendix A.

The system of Eqs. 8 will always have a general solution by inverting $[a_{ij}]$ unless it is singular; i.e., if $|a_{ij}| \neq 0$, the solution will be

$$\{X_i\} = [a_{ij}]^{-1}\{C_i\} \tag{10}$$

Because the premultiplication of a matrix by its inverse is uniquely equal to a unit matrix, the vector of solutions given by the right side of Eqs. 10 constitutes the only solutions.

By virtue of a symmetric matrix in Eqs. 8, only $\frac{1}{2}n(n + 1)$ coefficients must be evaluated and, consequently, the computer time for inverting the matrix will be correspondingly reduced. In inverting large matrices, an efficient and fast method such as Li's algorisms (5) is recommended.

ANALYSIS OF A BRIDGE TRUSS BY MATRIX-ENERGY METHOD

An Example for Orientation of Exact Method

To exemplify the numerical process and compare the results with those obtained by recognized conventional methods, the simple bridge truss given by Sutherland and Bowman (6) is first solved by the proposed exact matrix-energy method.

It is desired to find all genuine stresses at the ends of each member of the rigidly connected truss shown in Figure 2 due to vertical loads of 166 kips at each lower panel point except supports. The makeup of members is given in Table 1. For simplicity,

TABLE 1

MAKEUP OF MEMBERS AND SECTION PROPERTIES

Bar	Section	A(in.^{2})	I(in.^{4})	L(in.)	I/c(in.^{3})	Sketch
1-3	2-[15 × 33.9 1-Pl 18 × 7/16	27.68	961.0	450.44	167.5 99.1	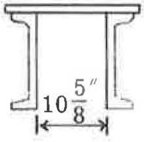
3-5	2-[15 × 33.9 1-Pl 18 × 3/8	26.55	922.8	300.00	156.0 97.6	
1-2 2-4	4-⌊s 6 × $3\frac{1}{2}$ × $\frac{1}{2}$	18.00	175.3	300.00	27.5	
2-3	4-⌊s 6 × $3\frac{1}{2}$ × 7/16	15.88	153.8	336.00	24.1	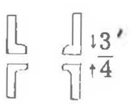
3-4	4-⌊s 6 × $3\frac{1}{2}$ × 3/8	13.68	131.8	450.44	20.7	
4-5	4-⌊s 5 3 × 3/8	11.44	79.1	336.00	14.7	

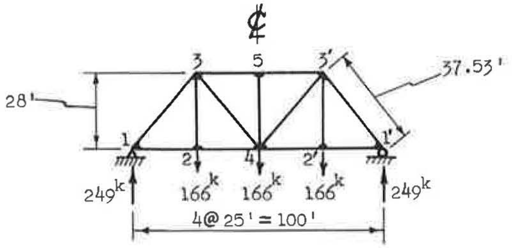

Figure 2.

centroidal axes of members are taken as intersecting exactly at theoretical panel points, thus eliminating eccentric moments.

Independent and Dependent Unknowns.—In the present case, referring to Eq. 1, m = 13 and n = 8; therefore, N = 13 - 4 = 9. That is, the present truss is determinate when pin connected, but becomes indeterminate to the 9th degree when rigidly connected. The nine statically independent unknown end moments may be represented, element for element, by the matrix:

$$\begin{bmatrix} X_1 & X_2 & X_3 \\ X_4 & X_5 & X_6 \\ X_7 & X_8 & X_9 \end{bmatrix} = \begin{bmatrix} M_{13} & M_{21} & M_{24} \\ M_{31} & M_{32} & M_{35} \\ M_{42} & M_{43} & M_{53} \end{bmatrix} = -\begin{bmatrix} M_{1'3'} & M_{2'1'} & M_{2'4'} \\ M_{3'1'} & M_{3'2'} & M_{3'5'} \\ M_{4'2'} & M_{4'3'} & M_{5'3'} \end{bmatrix} \tag{11}$$

Then, by $\Sigma M = 0$ at joints 1, 2, 3 and 1′, 2′, 3′, six of the remaining dependent unknown end moments can be expressed as:

$$\begin{bmatrix} M_{12} \\ M_{23} \\ M_{34} \end{bmatrix} = -\begin{bmatrix} M_{1'2'} \\ M_{2'3'} \\ M_{3'4'} \end{bmatrix} = -\begin{bmatrix} X_1 \\ X_2 + X_3 \\ X_4 + X_5 + X_6 \end{bmatrix} \tag{12}$$

By symmetry, this yields:

$$\{M_{45}\ M_{54}\ Q_{45}\} = \{0\ 0\ 0\} \tag{13}$$

Extended Methods of Moments, Shears, and Joints. —The axial stress in each member is readily determined by the extended methods of moments, shears, or joints, which are illustrated for members 1-2, 1-3, and 2-3 in the following paragraphs.

In the extended method of moments, by passing a section just to the left of member 2-3 and considering the equilibrium of the free body to the left, as shown in Figure 3, we have by $\Sigma M = 0$ about joint 3,

$$\lfloor -N_{12}\ X_2\ 249\ X_4 \rfloor \{336\ 1\ 300\ 1\} = 0 \text{ and}$$

$$N_{12} = \lfloor X_2\ X_4\ 1 \rfloor \{0.002976\ 0.002976\ 222.321\}$$

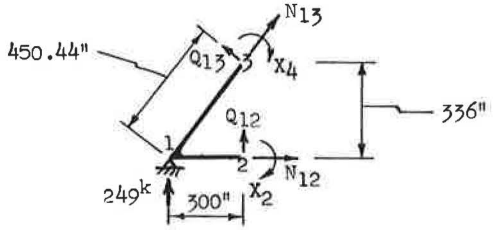

Figure 3.

The extended method of shears, taking the same free body as shown in Figure 3, yields:

$$\{Q_{12}\ Q_{13}\} = \left\{\frac{-X_1 + X_2}{300.00}\ \frac{X_1 + X_4}{450.44}\right\}$$

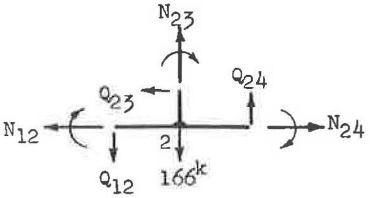

Figure 4.

and by $\Sigma Y = 0$,

$$\lfloor N_{13} \quad X_1 + X_4 \quad -X_1 + X_2 \quad 249 \rfloor \left\{ \frac{28}{37.53} \quad \frac{25}{450.44(27.53)} \quad \frac{1}{300} \quad 1 \right\} = 0$$

Therefore,

$$N_{13} = \lfloor X_1 \quad -X_2 \quad -X_4 \quad -1 \rfloor \{0.002486 \quad 0.004469 \quad 0.001982 \quad 333.808\}$$

In the extended method of joints, by passing a horseshoe section around joint 2, as shown in Figure 4, we have by $\Sigma Y = 0$,

$$\lfloor N_{23} \quad Q_{24} \quad Q_{12} \quad 166 \rfloor \{1 \quad 1 \quad -1 \quad -1\} = 0$$

Substitution of the values of Q_{24} and Q_{12} yields:

$$\lfloor N_{23} \quad X_3 + X_7 \quad -X_1 + X_2 \quad 166 \rfloor \left\{ 1 \quad \frac{1}{300} \quad -\frac{1}{300} \quad -1 \right\} = 0$$

or

$$N_{23} = \lfloor -X_1 \quad X_2 \quad -X_3 \quad -X_7 \quad 1 \rfloor \{0.003333 \quad 0.003333 \quad 0.003333 \quad 0.003333 \quad 166.000\}$$

Axial-Stress Expressions and Strain-Energy Constants. —By applying the preceding methods, axial stresses in all members of the truss may be found as given in Table 2. The constant term in each N expression is exactly equal to the "primary stress" in the same bar if it is pin jointed. Constants in the strain-energy expressions of Eqs. 5 are given in Table 3, taking Poisson's ratio μ as 0.3. With the aid of Tables 2 and 3, $(10)^6$ E times the strain energy in each truss member as given by Eqs. 5 is recorded in Table 4.

TABLE 2

AXIAL-STRESS EXPRESSIONS

Member	$(10)^3$ Times Axial-Stress Expressions
1-2	$2.976X_2 + 2.976X_4 + 222321$
1-3	$2.486X_1 - 4.469X_2 - 1.982X_4 - 333808$
2-3	$-3.333X_1 + 3.333X_2 - 3.333X_3 - 3.333X_7 + 166000$
2-4	$-2.976X_3 + 2.976X_4 + 2.976X_5 + 222321$
3-4	$4.469X_3 - 1.982X_4 - 1.982X_5 + 2.486X_6 + 4.469X_7 + 1.982X_8 + 4.469X_9 + 111269$
3-5	$-2.976X_7 - 2.976X_8 - 2.976X_9 - 296429$
4-5	$-6.667X_6 - 6.667X_9$

TABLE 3
CONSTANTS IN STRAIN-ENERGY EXPRESSIONS

Member	L/A	L/6I	$2(1 + \mu)/AL$
1-2	16.66667	0.285225	0.000481
1-3	16.27311	0.078120	0.000209
2-3	21.15869	0.364109	0.000487
2-4	16.66667	0.285253	0.000481
3-4	32.92689	0.569600	0.000422
3-5	11.29944	0.054183	0.000326
4-5	29.37063	0.707965	0.000676

TABLE 4
STRAIN ENERGY OF TRUSS MEMBERS

Member	$(10)^6$ E Times Strain Energy in Member I-J = $10^6 E(W_{ij} + U_{ij} + V_{ij})$
1-2	$\frac{1}{2}(16.66667)(2.976X_2 + 2.976X_4 + 222321)^2 + 285225(X_1^2 + X_1X_2 + X_2^2) + \frac{1}{2}(481)(-X_1 + X_2)^2$
1-3	$\frac{1}{2}(16.27311)(2.486X_1 - 4.469X_2 - 1.982X_4 - 333808)^2 + 78120(X_1^2 - X_1X_4 + X_4^2) + \frac{1}{2}(209)(X_1 + X_4)^2$
2-3	$\frac{1}{2}(21.15869)(-3.333X_1 + 3.333X_2 - 3.333X_3 - 3.333X_7 + 166000)^2 + 364109\left[(-X_2 - X_3)^2 + (X_2 + X_3)X_5 + X_5^2\right] + \frac{1}{2}(487)(-X_2 - X_3 + X_5)^2$
2-4	$\frac{1}{2}(16.66667)(-2.976X_3 + 2.976X_4 + 2.976X_5 + 222321)^2 + 285253(X_3^2 - X_3X_7 + X_7^2) + \frac{1}{2}(481)(X_3 + X_7)^2$
3-4	$\frac{1}{2}(32.92689)(4.469X_3 - 1.982X_4 - 1.982X_5 + 2.486X_6 + 4.469X_7 + 1.982X_8 + 4.469X_9 + 111269)^2 + 569600\left[(-X_4 - X_5 - X_6)^2 + (X_4 + X_5 + X_6)X_8 + X_8^2\right] + \frac{1}{2}(422)(-X_4 - X_5 - X_6 + X_8)^2$
3-5	$\frac{1}{2}(11.29944)(-2.976X_7 - 2.976X_8 - 2.976X_9 - 296429)^2 + 54183(X_6^2 - X_6X_9 + X_9^2) + \frac{1}{2}(326)(X_6 + X_9)^2$
4-5 center vertical	$\frac{1}{2}(29.37063)(-6.667X_6 - 6.667X_9)^2$ (use one-half in computing $\frac{1}{2}$ EU)

Simultaneous Equations and Their Solution. —Because of symmetry in both structure and loading in this particular example, it is necessary to write only one-half of the total strain energy. After eliminating 1/2 and E, repeated application of $\frac{\partial U}{\partial X_i} = 0$ yields Eqs. 10 where

$$\left\{X_i\right\} = \left\{X_1\ X_2\ X_3\ X_4\ X_5\ X_6\ X_7\ X_8\ X_9\right\},$$

$$\left[a_{ij}\right]^{-1} = \begin{bmatrix} 727716 & 284328 & 235 & -77992 & 0 & 0 & 235 & 0 & 0 \\ & 1300346 & 728471 & 292 & 363622 & 0 & -235 & 0 & 0 \\ & & 1300734 & -439 & 363183 & 366 & -283879 & 292 & 658 \\ & & & 1296559 & 1139899 & 1139460 & -292 & 569049 & -292 \\ & & & & 1868605 & 1139460 & -292 & 569049 & -292 \\ & & & & & 1249171 & 366 & 569340 & -52838 \\ \text{a_{ij} below main diagonal} & & & & & & 571981 & 392 & 758 \\ \text{$= a_{ji}$ above it} & & & & & & & 1139852 & 392 \\ & & & & & & & & 110103 \end{bmatrix}^{-1}$$

and

$$C_i = (10)^6\{25.2144\ -47.0097\ 6.3636\ -25.5609\ -3.7656\ -9.1098\ -14.6329\ -17.2309\ -26.3407\}.$$

The solution of $\{X_i\}$ in kips-inches by electronic digital computer or otherwise is recorded, element for element, as

$$\begin{bmatrix} X_1 & X_2 & X_3 \\ X_4 & X_5 & X_6 \\ X_7 & X_8 & X_9 \end{bmatrix} = \begin{bmatrix} 66.20 & -84.47 & 39.19 \\ -13.41 & 42.50 & -40.54 \\ -5.803 & -9.309 & -258.8 \end{bmatrix} = \begin{bmatrix} M_{13} & M_{21} & M_{24} \\ M_{31} & M_{32} & M_{35} \\ M_{42} & M_{43} & M_{53} \end{bmatrix} \tag{14}$$

TABLE 5

BENDING STRESSES AT MEMBER ENDS

Member	End	End Moment (kips-in.) Cross' Method	End Moment (kips-in.) Proposed Method	$\frac{I}{c}$ (in.^{3})	Unit Bending Stress (ksi)
1	2	-67	-66.20	27.5	2.262
	3	67	66.20	167.5	0.395^a
				99.1	0.668^b
2	1	-85	-84.47	27.5	3.072
	3	45	45.28	24.1	1.879
	4	40	39.19	27.5	1.425
3	1	-11	-13.41	167.5	0.080^a
				99.1	0.135^b
	2	43	42.50	24.1	1.763
	4	12	11.45	20.7	0.553
	5	-44	-40.54	156.0	0.260^a
				97.6	0.415^b
4	2	-5	-5.803	27.5	0.211
	3	-9	-9.309	20.7	0.450
	5	0	0	14.7	0
5	3	-263	-258.7	156.0	1.658^a
				97.6	2.651^b
	4	0	0	14.7	0

[a] Top.

[b] Bottom.

TABLE 6

AXIAL STRESSES AND TRANSVERSE SHEARS

Member	N_{ij} (kips)	N_{ij}/A_{ij} (ksi)	Q_{ij} (kips)
1-2	222.030	12.335	-0.502
1-3	-333.239	-12.039	0.118
2-3	165.387	10.415	0.261
2-4	222.291	12.350	0.111
3-4	110.085	8.047	0.005
3-5	-295.614	-11.134	-0.998
4-5	1.996	0.174	0

Bending Stresses. —Dividing end moments of members thus found by their respective section moduli (I/c) given in Table 1 yields the unit bending stresses at member ends recorded in Table 5. These correspond to the so-called secondary stresses. Values of end moments for the same truss members as found by Sutherland and Bowman (6) by the Cross method are also given. The closeness of end-moment values by both methods testifies to the validity of the proposed method. But the results of the proposed method are "truer" because more accurate axial-strain energy has been used and shearing-strain energy has been taken into consideration.

Axial Stresses and Transverse Shears.—Axial stresses and transverse shears, simultaneously obtained by substituting the values of X_i into Table 2 and Eq. 4, are recorded in Table 6. Unit axial stresses are also calculated.

Streamlining and Simplification. —By treating the rigidly connected truss as an assemblage of rigid frames, the exact matrix-energy method proposed herein, as demonstrated by the former example, has yielded the solution of axial, bending, and shearing stresses in all members of the truss in one unified single setup. With widespread use of electronic computers, the entire process can be programmed from given data to end results. It is shorter and more straightforward than the conventional methods when secondary stresses are considered.

Although the exact method should be used for special investigations and particular designs requiring a high degree of accuracy, for ordinary design purposes a simplified method should be used.

An Example for Orientation of Simplified Method

A study of the equations obtained from $\frac{\partial U}{\partial X_i} = 0$ suggests a simplified method which saves much time in writing the energy expressions and in evaluating the elements of the coefficient matrix.

The process for obtaining the first equation of Eqs. 10, after dividing $(10)^6$ EU by the planted $(10)^6$, from the true value of

$$\frac{1}{2} E \frac{\partial U}{\partial X_1} = 0$$

yields, on rearrangement, the relation:

$$
\begin{array}{lll}
0 = & \left.\begin{array}{l} 0.285225(2X_1 + X_2) \\ +0.078120(2X_1 - X_4) \end{array}\right\} & \text{contribution by moments} \\
& \left.\begin{array}{l} -16.27311(0.002486)\,(333.808) \\ -21.15869(0.003333)\,(166.000) \end{array}\right\} & \begin{array}{l}\text{axial stress (corresponding to} \\ \text{primary stress)}\end{array} \\
\hdashline
& \left.\begin{array}{l} +16.27311(0.002486)\,(0.002486X_1 \\ \qquad\qquad - 0.004469X_2 \\ \qquad\qquad - 0.001982X_4) \\ +21.15869(0.003333)^2(X_1 - X_2 + X_3 + X_7) \end{array}\right\} & \begin{array}{l}\text{axial stress (affected by} \\ \text{end moments and transverse} \\ \text{shears)}\end{array} \\
& \left.\begin{array}{l} +0.000481(-1)\,(-X_1 + X_2) \\ +0.000209(X_1 + X_4) \end{array}\right\} & \text{transverse shears}
\end{array}
$$

It is evident that the coefficients of the unknowns X_1, X_2, and X_4 above the dashed line are about 1,000 times greater than those below the dashed line.

An approximate but much simplified solution sufficiently accurate for usual engineering purposes can, therefore, be most expediently obtained by deleting all strain-energy terms contributed by transverse shears in writing the energy expressions and all terms affecting axial stress contributed by end moments and transverse shears after partial differention. All terms contributed by moments and the term corresponding to the primary stress should be retained.

The simplified form of the first equation thus becomes

$$\lfloor 7262 \quad 2852 \quad -781 \rfloor \; \{X_1 \; X_2 \; X_4\} \;=\; 25.214\,(10)^4$$

and the symmetric matrix equation reduces to:

$$\begin{bmatrix} 7262 & 2852 & 0 & -781 & 0 & 0 & 0 & 0 & 0 \\ & 12987 & 7282 & 0 & 3641 & 0 & 0 & 0 & 0 \\ & & 12988 & 0 & 3641 & 0 & -2853 & 0 & 0 \\ & & & 12954 & 11392 & 11392 & 0 & 5696 & 0 \\ & & & & 18674 & 11392 & 0 & 5696 & 0 \\ & & & & & 12476 & 0 & 5696 & -542 \\ \multicolumn{6}{l}{a_{ij} \text{ below main diagonal}} & 5705 & 0 & 0 \\ & & & & & & & 11392 & 0 \\ \multicolumn{6}{l}{\quad = a_{ji} \text{ above it.}} & & & 1084 \end{bmatrix} \begin{bmatrix} X_1 \\ X_2 \\ X_3 \\ X_4 \\ X_5 \\ X_6 \\ X_7 \\ X_8 \\ X_9 \end{bmatrix} = (10)^4 \begin{bmatrix} 25.214 \\ -47.010 \\ 6.364 \\ -25.561 \\ -3.766 \\ -9.110 \\ -14.633 \\ -17.231 \\ -26.341 \end{bmatrix}$$

whose solution by electronic digital computer yields:

$$\begin{bmatrix} X_1 & X_2 & X_3 \\ X_4 & X_5 & X_6 \\ X_7 & X_8 & X_9 \end{bmatrix} = \begin{bmatrix} 66.9 & -84.9 & 39.0 \\ -10.7 & 43.4 & -44.5 \\ -6.15 & -9.25 & -265 \end{bmatrix} = \begin{bmatrix} M_{13} & M_{21} & M_{24} \\ M_{31} & M_{32} & M_{35} \\ M_{42} & M_{43} & M_{53} \end{bmatrix} \qquad (15)$$

after which all axial, bending, and shearing stresses in each member of the truss can be determined by statics. The accuracy of the simplified method can be seen by comparing Eqs. 15 with Eqs. 14. The closeness of the results testifies to the validity of the simplified method.

SPECIALLY DEVELOPED TECHNIQUES FOR CONTINUOUS HIGHWAY BRIDGE TRUSSES

Method of Panel-Load Superposition for Continuous Trusses

In determining the maximum tensile or compressive stress, or maximum and minimum stresses in case of reversal, in all members of a determinate truss due to moving live loads, there are available two methods of approach—the influence-line method and the maximum-stress load-position criterion method—both giving the live-load positions producing maximum tensile or compressive stresses.

Due to its inherently complicated nature in an indeterminate system, however, the maximum-stress load-position criterion method has never been heretofore applied to a continuous bridge truss. Theoretically, such a criterion can be deduced for any continuous truss, but the resulting expression would be unwieldy. This explains why the influence-line method has remained the only means by which live-load positions are determined for computing the maximum tensile and compressive stresses in any member of a continuous truss.

Nevertheless, it must be recognized that continuous bridge trusses are usually built only for comparatively long-span crossings. Even in a moderate three-span continuous deck truss, such as the Hawk Falls Bridge (on the Northeast Extension of the Pennsylvania Turnpike) which measures 616 ft horizontally between end bearings and is built on a 1.54 percent grade, there are altogether 113 members if taken unsymmetrically and 57 members when considered as symmetrical about the centerline of the bridge. The formulation of influence-line equations, computation of influence ordinates, and plotting of influence broken lines for so many different members in the composition of the said continuous truss are all very time-consuming tasks.

It must be further recognized that influence lines constituted a visual aid in determining live-load positions in the days of manual computation. With modern electronic computation, typing out influence ordinates, plotting them into influence broken lines, and then retyping in positioned loads for maximum tensile and compressive stresses form the slowest links in automatically programmed continuous computation.

Moreover, it is evident that there are far less live-load panel points than stress-carrying members. In the case of the Hawk Falls Bridge, if considered symmetrical, there are only 15 (14 in a pin-connected truss) live-load panel points vs 57 members (55 if L_0U_0 and U_0U_1 are excepted which would be true in a pin-connected truss) in one-half of the continuous truss. It is, therefore, much more expedient to compute the stresses in all members under each of the 14 or 15 live panel loads than to compute 29 influence ordinates for each of the 55 or 57 members of the truss.

For the reasons just stated, it is proposed to abandon the classical influence-line method and, in its place, use the panel-load superposition method. The procedure is as follows:

1. Convert the lane loadings and concentrated loads for moment and shear, for a given number of lanes and specified reduction, and for a given roadway width to panel loads and concentrations when the lane loadings are placed nearest to the truss;
2. Load the bridge truss with one stress-producing live panel load at a time;
3. Compute the axial, bending, and shearing stresses in each member according to the proposed matrix-energy method;
4. Repeat the process until all stress-producing live-load panel points are covered from one end of the truss to and including the center panel point, if there is one, and if the truss is symmetrical about its centerline;
5. Tabulate the stresses thus found, labeling members symmetrically on the other side of the bridge centerline as primed members;
6. Add all plus-sign tensile stresses and minus-sign compressive stresses for each of the umprimed and primed members;
7. Obtain the concentrated load factors for moment and shear by dividing the respective converted concentrated load by the converted lane-loading panel load;
8. Multiply the appropriate concentrated load factor with the maximum stress among the plus-sign tensile stresses and among the minus-sign compressive stresses caused by single live panel loads, using the concentrated load factor for shear or for moment, respectively, as the stress in the member is dictated by shear or by moment, applying one or two concentrations for moment according to the specifications in use; and
9. Determine the maximum live-load stress of plus sign and minus sign in any member by summing up the plus-sign or minus-sign stresses obtained in Step 6 for the unprimed member and for the corresponding primed member, and in Step 8 for the unprimed member.

The maximum live-load stress obtained by this method will be almost identical with that obtained with the true lane-loading length as deduced from influence broken lines. We shall prove by a random example that the difference is generally less than one percent which is well within engineering accuracy because neither modulus of elasticity, moments of inertia, most probable load estimation, nor allowable stresses are probably more accurate than within one percent.

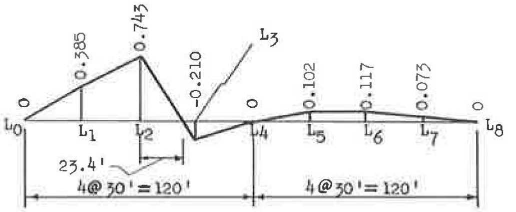

Figure 5.

Panel-Load Superposition Method vs Classical Influence-Line Method

A random proof of the closeness of the results obtained by these two methods is based on the influence line of the diagonal L_2U_3 of a two-span parallel-chord Warren-type continuous truss with verticals consisting of 4 panels at 30 ft in each span. This influence line was constructed to a close order of approximation by the three-moment theorem which can be applied to the case with expediency. An excerpt (7) of the correct influence line is shown in Figure 5.

For unit panel load, the corresponding fractional load over 23.4 ft of the stringer from L_2 to L_3 will be 23.4/30 = 0.780 and, therefore, the right stringer reaction = 0.78(23.4)/2(30) = 0.304 and the left stringer reaction = 0.780 - 0.304 = 0.476, making the panel load at L_2 = 0.476 + 0.500 = 0.976 instead of unity.

If the trusses were spaced at 38 ft c. to c., carrying two roadways of 26 ft each with an additional 4-ft divider, as in the Hawk Falls Bridge, applying the maximum lane live loading (converted from H20-S16-44) that may act on one truss, 1.26 kips/ft plus one concentration of 51.1 kips for shear, to this influence line will give the maximum tension in L_2U_3 as T_i and T_s, respectively, for the influence-line method and the panel-load superposition method. Thus,

$$\begin{bmatrix} T_i \\ T_s \end{bmatrix} = 1.26(30) \begin{bmatrix} 1 & 0.976 & 1 & 1 & 1 \\ 1 & 1 & 1 & 1 & 1 \end{bmatrix} \begin{bmatrix} 0.385 \\ 0.743 \\ 0.102 \\ 0.117 \\ 0.073 \end{bmatrix} + 51.1 \begin{bmatrix} 0.743 \\ 0.743 \end{bmatrix} = \begin{bmatrix} 90.97 \\ 91.65 \end{bmatrix} \text{ kips}$$

which shows that the proposed panel-load superposition method results in a stress error of only (91.65 - 90.97)/90.97 = 0.00747, on the order of $^7\!/_{10}$ of one percent. This is sufficiently accurate for all designing purposes. Similar verification may be shown for any member in any truss.

The panel-load superposition method is recommended for use in all analyses of indeterminate highway bridge trusses, especially when the maximum axial stresses are governed by lane loading plus concentrations.

Methods for Reducing the Number of Unknowns

Large-capacity computers, if available, can usually solve large systems of nonhomogeneous algebraic linear equations. The number of unknowns is generally immaterial. A process of solution which is easier to formulate and program will prove more expedient. However, when a moderately large set of equations has to be solved with a small-size computer, the capacity may not be enough to handle the necessary numerical operations. In addition, larger rounding-off errors are as a rule associated with a larger number of unknowns. Working with the smallest possible number of unknowns has the advantages that the solution is more easily accommodated by most computers, and the rounding-off errors are kept to a minimum.

Method of Substitution. —This consists of substituting an unsymmetrical loading by symmetrical and antisymmetrical loadings. This method has been developed to reduce to only one-half the number of statically independent unknowns in symmetrical longer span continuous trusses under unsymmetrical loading.

Figure 6a shows arbitrarily a symmetrical three-span continuous bridge truss carrying an unsymmetrical load of 2P applied at a certain panel point (e.g., the first panel point), with redundant reactions R_1 and R_2 indicated at interior supports. By the prin-

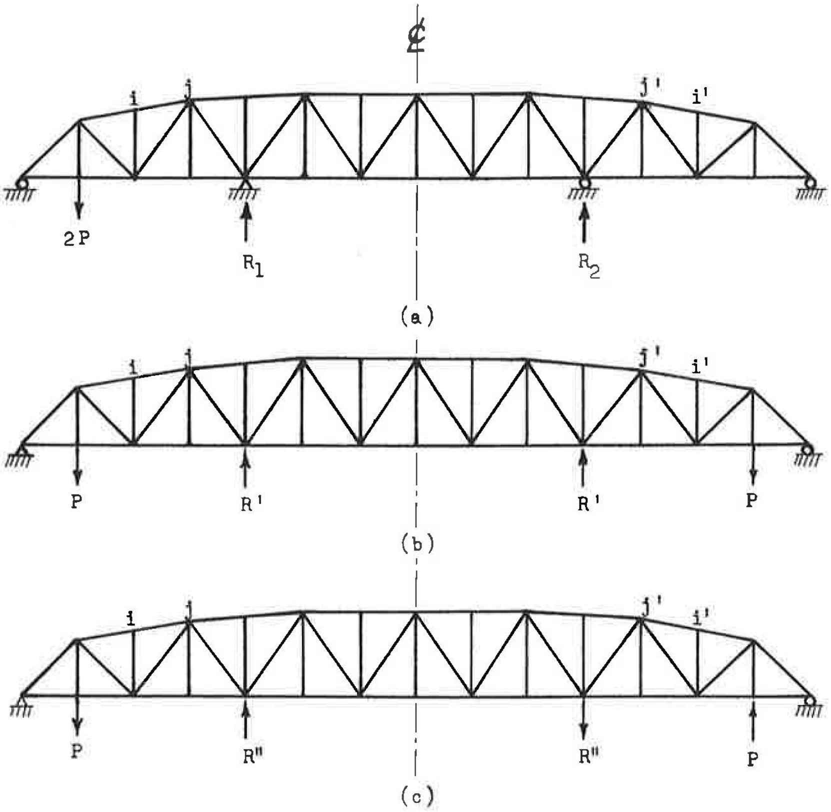

Figure 6.

ciple of superposition, R_1, R_2 and 2P, viewed as a loading system acting on the symmetrical bridge structure, can be represented as the sum of a set of symmetrical loading and a set of antisymmetrical loading acting separately on the same structure as indicated in Figures 6b and 6c. The magnitudes of R' and R'' are related to R_1 and R_2 by

$$\begin{bmatrix} R' + R'' \\ R' - R'' \end{bmatrix} = \begin{bmatrix} R_1 \\ R_2 \end{bmatrix} \tag{16}$$

Solving for R' and R'' yields

$$\begin{bmatrix} R' \\ R'' \end{bmatrix} = \frac{1}{2} \begin{bmatrix} R_1 + R_2 \\ R_1 - R_2 \end{bmatrix} \tag{17}$$

In the case of symmetrical trusses, the number of statically independent unknowns in the matrix-energy method for symmetrical loading will be just equal to one-half of that for unsymmetrical loading. By using unprimed subscripts for joints on the left half of the structure and primed subscripts for those on the right half, we have

$$\begin{bmatrix} N_{ij} \\ M_{ij} \\ Q_{ij} \end{bmatrix} = \begin{bmatrix} N_{i'j'} \\ -M_{i'j'} \\ -Q_{i'j'} \end{bmatrix} \tag{18}$$

In even-panel symmetrical trusses with a center-vertical member, the internal bending moments and shearing stress in this member under symmetrical loading will be equal to zero. But the axial stress in the center-vertical member will not be equal to zero due to axial stresses and shears of inclined chord members meeting at the center joints, or due to shears alone if those chord members are parallel. In computing the strain energy in one-half of the truss, of course, only one-half the strain energy in the center vertical should be counted. The same applies if a center top chord exists instead of a center vertical.

In the same symmetrical truss under the substituted antisymmetrical loading, the number of statically independent unknowns will also be equal to one-half of that under unsymmetrical loading; that is, using the unprimed and primed subscripts as before, we have

$$\begin{bmatrix} N_{ij} \\ M_{ij} \\ Q_{ij} \end{bmatrix} = \begin{bmatrix} -N_{i'j'} \\ M_{i'j'} \\ Q_{i'j'} \end{bmatrix} \tag{19}$$

where the absolute values of axial stresses, bending moments, and shearing stresses are the same in corresponding unprimed and primed members. As the strain energy is a scalar quantity, it may again be computed for only one-half of the truss.

Thus, in symmetrical bridge trusses, any unsymmetrical loading may be substituted by a set of symmetrical loading and a conjugate set of antisymmetrical loading, whereby not only are the unknowns reduced to one-half of the original number but also one-half of the total strain energy of the truss will be needed in later formulation. The algebraic sum of the solutions under the substituted symmetrical and antisymmetrical loadings will give the desired solution under the original unsymmetrical loading.

Method of Transformation. —If, after reducing the number of unknowns by the method of substitution, the size of the system of equations is still greater than the capacity of the computer available, further reduction of unknowns can be effected by the method of transformation, i.e., transformation of unknown end moments into unknown reference tangential deflection angles. In the matrix-energy method for analyzing rigidly connected trusses, the recognized unknowns, except redundants, are the statically independent end resisting moments of members. There are three such unknowns in each triangular closed figure. But there are fewer joints than independent unknown end moments. At each joint there is only one unknown rotation, which in rigid frames is the principal advantage of the slope-deflection method.

In a truss, however, it is more expedient to choose Manderla's (1) approach which was the origin of the modern slope-deflection method. To adapt his approach to the problem under consideration, the number of unknowns may be reduced by applying the relationship

$$M_{ij} = \frac{2EI_{ij}}{L_{ij}} \left(2\tau_{ij} + \tau_{ji}\right) \tag{20}$$

between the unknown end moment and the tangential deflection angle τ, which is the angle between the tangent at the end of the deformed member and the straight line joining the ends of that deformed member.

There are as many τ's as twice the number of members in a truss. However, all the τ's around a joint can be expressed in terms of the angle changes ($\Delta\alpha$'s) between the straight lines joining the ends of the neighboring members which experience deformations under a given loading, and a selected reference τ. Thus, all end moments can be expressed in terms of reference τ's which are the new intermediate unknowns. As there is only one reference τ at each joint, the number of τ's will be exactly equal to the number of truss joints, which is far less than the number of unknown end moments in the set of simultaneous equations in the energy method.

Hence, when all end moments are substituted by their corresponding equivalent expressions represented by Eq. 20, the set of n simultaneous equations will result in n equations with j unknowns, where n is the number of original equations or statically independent unknowns in the energy method, j is the number of unknown reference τ's plus the number of redundants, and $n > j$.

As both the original n equations with n unknowns and the present n equations with j unknowns are all genuinely correct and exact equations, there is no need to normalize (8) the n equations into a new set of j equations for solving the j new unknowns. The n equations are to be distinguished from "conditional equations" of observation. Instead of normalizing, any j equations out of the n equations that contain the j unknowns will give identically correct solutions. With the j unknowns (reference τ's and any redundant reactions and/or axial stress) solved, back substitution into M-τ relations represented by Eq. 20 will give all end moments.

To utilize a given computer capacity, partial reduction of unknown end moments may also be permissible with the result of mixed unknowns consisting of all redundants, some reference τ's, and some end moments. A numerical demonstration of the method of transformation for reducing the number of unknowns is given in Appendix B, where identical results are obtained as by the simplified energy method.

SOLUTION OF SIMULTANEOUS ALGEBRAIC LINEAR EQUATIONS

Scores of direct and indirect (or iterative) methods have been developed for solving simultaneous algebraic linear equations. Proper choice of method to suit the problem, to adapt to the computer capacity, and to attain the desired accuracy and efficiency lies in the skill of the programmer.

The well-known direct methods include (a) determinants of matrices (slowest); (b) lower triangular matrices; (c) upper triangular matrices including unit upper triangular matrices; (d) post multipliers; (e) elimination; (f) row operation; (g) row operator with and without augmentation; (h) decomposition; (i) submatrices, escalator, or block decomposition; (j) symmetrical matrices; (k) Cayley-Hamilton theorem; (l) Gauss-Doolittle method and Crout method of LDU decomposition; (m) orthogonalization; (n) inverting modified matrices; and (o) Li's algorisms for mono- and polyset constant terms with and without inversion for both asymmetrical and symmetrical matrices (5, 9, 10, 11).

Among the indirect or iterative methods, the following may be cited from the geometrical approach: (a) Wittmeyer process, (b) special Wittmeyer processes, (c) Seidel, (d) back-and-forth Seidel process, (e) optimum or steepest gradients, (f) conjugate gradient, (g) relaxation, (h) hyperplane interpretation, and (i) residual vector. From the analytic approach are (a) Cesari's method, (b) method of von Mises and Geiringer, and (c) method of Hotelling and Bodewig. To these, must be added the Monte Carlo method, a nondeterministic or statistical method. No attempt is made to exhaust the list (5, 9, 10, 11).

To choose the best method for a given set of equations requires a clear comprehension of the underlying theory, the synthesis of the procedures, and the formulation of the algorism of the preceding methods. Whenever a large-capacity high-speed computer is available, because computing time is generally insignificant, the most easily programmed method (except the slowest) should be chosen. With low-speed small-capacity computers the fastest method requiring the least storage capacity should be used. When the capacity is too limited, a flexible method that can be adapted to the computer should be chosen, such as "Simultaneous Equations A La King" for the IBM 1620 or the relaxation method.

Large Sets of Equations and Computing Time

Two- or three-span continuous highway bridge trusses of moderate length may easily run into the inversion of a matrix of the order of more than 100 × 100. The largest set of simultaneous linear equations solved by a computer in the United States up to June 1963 consisted of a matrix of 700 × 700.

Using STRETCH at the highest speed yet built (500,000 multiplications per second) and Li's algorism for a symmetrical coefficient matrix of a set of 199 equations, the computing time will be about 4 sec. With STRETCH and using an already inverted symmetric matrix according to Li's algorisms, the time of solution of 199 equations for each set of constant terms will be further reduced to only 0.115 sec.

To solve the same $n = 199$ equations by the conventional determinental method would require $(n + 1)!$ or approximately $789(10)^{372}$ multiplications, plus $(n + 1)(n)(n - 1) = n(n^2 - 1) = 7,880,400$ additions or 3,940,200 equivalent multiplications, taking each addition time as approximately equal to one-half of each multiplication time. Even using the fastest computer, STRETCH, it would still require $1,578(10)^{368}$ sec or slightly more than $5(10)^{361}$ yr. Before the advent of the electronic digital computer, the task would have been impossible.

Structural analyses generally involve symmetrical matrices. Using Li's algorism for symmetrical matrices with one set of constant terms, the solution of n unknowns requires an equivalent number of multiplications on the order of about $\frac{n^3}{2}$.

Simultaneous Equations A La King

Usually, computers available to bridge engineers are of moderate or smaller size than STRETCH and have limited storage capacity. For instance, in the use of the basic IBM 1620 computer, having only a storage capacity of 20,000, the solution of a moderately large set of linear equations will need special programming. "Simultaneous Equations A La King," developed by D. N. Leeson and designated Program Number 5.0.008 in the 1620 General Program Library, can solve a set of 58 linear equations requiring a core storage of 55,510 and 58,937, respectively, for the recommended mantissa length of 12 or a longer length of 13 (the latter for more accuracy). To facilitate the use of this program, the Source Program Deck (Cards) and the SPS II Processor Deck (or Assembly Deck) should be prepared or secured in advance.

Relaxation Method

This method of successive approximations has the inherent advantage of easy programming, may be broken into as many segments as any small computer can hold—especially if the coefficient matrix is band-like—and can attain any desired accuracy. The mathematical technique and the physical facility of the computer can be used in an infinite variety of ways to accelerate the convergence of the process of solution. Besides use as a mathematical tool for solving simultaneous linear equations, the method may be directly applied to stress calculation in frameworks (12).

A system ready for relaxation with the main diagonal elements equal to -1 and the constant K vector shifted to the left of the equations may be written:

$$\begin{bmatrix} -1 & a_{12} & \cdots & a_{1n} \\ a_{21} & -1 & \cdots & a_{2n} \\ \cdot & \cdot & \cdots & \cdot \\ \cdot & \cdot & \cdots & \cdot \\ \cdot & \cdot & \cdots & \cdot \\ a_{n1} & a_{n2} & \cdots & -1 \end{bmatrix} \begin{bmatrix} x_1 \\ x_2 \\ \cdot \\ \cdot \\ \cdot \\ x_n \end{bmatrix} + \begin{bmatrix} k_1 \\ k_2 \\ \cdot \\ \cdot \\ \cdot \\ k_n \end{bmatrix} = \begin{bmatrix} 0 \\ 0 \\ \cdot \\ \cdot \\ \cdot \\ 0 \end{bmatrix} \qquad (21)$$

The difference of the left-hand side of the ith equation may be denoted by r_i (residuals) for any reasonably assumed set of starting values $x_j^{(o)}$; thus,

$$\begin{bmatrix} -1 & a_{12} & \cdots & a_{1n} \\ a_{21} & -1 & \cdots & a_{2n} \\ \cdot & \cdot & \cdots & \cdot \\ \cdot & \cdot & \cdots & \cdot \\ \cdot & \cdot & \cdots & \cdot \\ a_{n1} & a_{n2} & \cdots & -1 \end{bmatrix} \begin{bmatrix} x_1^{(o)} \\ x_2^{(o)} \\ \cdot \\ \cdot \\ \cdot \\ x_n^{(o)} \end{bmatrix} + \begin{bmatrix} k_1 \\ k_2 \\ \cdot \\ \cdot \\ \cdot \\ k_n \end{bmatrix} = \begin{bmatrix} r_1 \\ r_2 \\ \cdot \\ \cdot \\ \cdot \\ r_n \end{bmatrix} \tag{22}$$

The relaxation procedure simply consists of altering the starting values of $x_j^{(o)}$, one or more at a time, until all the r_i become zero or negligibly small for the desired accuracy. If a given $x_j^{(o)}$, e.g., $x_k^{(o)}$, is altered by an amount Δx_k, then r_k alters by $-\Delta x_k$ and the other r_i alter by $a_{ik}\,\Delta x_k$. Consequently, to reduce a given r_i, e.g., r_k, to zero, we alter $x_k^{(o)}$ by $x_k = r_k$. Simultaneously, the other r_i will also alter and must be reduced to zero, one by one, by suitable alterations, Δx_j. It is expedient to eliminate the largest residual appearing in the system at any stage in the process.

The entire procedure may be most conveniently carried out in tabular form by entering the starting value of each $x_j^{(o)}$ and its successive alterations Δx_j in a left column (or computer locations), and the residuals in the right column (on another location of the computer). Thus, the relaxation table has two columns (or sequential locations) for each x_j. As soon as the residuals have gradually vanished to the degree of accuracy desired, the sum of $x_j^{(o)}$ and of all the Δx_j gives the final value of x_j. With this outline of the procedure, the relaxation method may be programmed for any particular version of the computer.

CONTINUOUS TRUSS, LOADINGS AND UNKNOWNS

Continuous Highway Bridge Truss and Loadings

Applicability of the proposed matrix-energy method to an indeterminate highway structure is demonstrated using as an example the three-span continuous bridge over the Missouri River near Wolf Creek, Montana, on Federal Aid Project 172D Unit 2. The bridge is an economical structure and has a pleasing appearance, mainly due to its excellent proportions and simplicity in details. The main reason for choosing this bridge truss to exemplify the indeterminate analysis lies in its having only two redundant reactions symmetrical in arrangement, a moderate number of members and, hence, comparatively few unknowns, which can be handled by the smaller digital computers possessed by most engineering organizations.

As shown in Figure 7, the skeleton truss of the bridge is of the Warren type with verticals and slightly inclined upper chords. It has spans of 135 ft: 180 ft: 135 ft, carrying a roadway of 20 ft. It was designed in 1932 for Standard H15 loading according to Montana State Highway Commission Standard Design Specifications for Highway Structures as revised in February 1932, which are the same as the AASHO Standard Specifications for Highway Bridges and Incidental Structures, 1931.

Makeup of Members. —Section components of each member, its gross sectional area, gross moment of inertia, theoretical length, and section modulus are as given in Table 7 for use in later computations. Centroidal axes are taken as intersecting at theoretical panel points, thus eliminating eccentric moments.

Dead Panel Loads. —These have been duly distributed to lower and upper panel points as given in Table 8.

Live Loads and Impact Formula. —The design live load for the bridge as used in 1932 was Standard H15 loading. The equivalent loading by which the design was then governed, as it is today, consists of a uniform load of 480 lb/lin ft of loaded lane plus a concentrated load of 13, 500 lb for moment or of 19, 500 lb for shear. That is, the

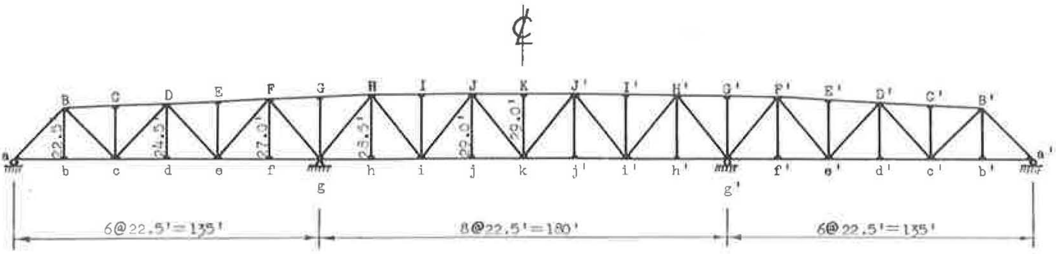

Figure 7.

TABLE 7

MAKEUP OF MEMBERS AND SECTION PROPERTIES

Member	Section	A(in.^{2})	I(in.^{4})	L(in.)	$\frac{I}{c}$(in.^{3})
ab to jk	2 - 12 [20.7	12.06	256.2	270	42.8
BC CD DE EF FG GH HI IJ JK	2 - 12 [20.7 1 - Pl 15 × $\frac{5}{16}$	16.75	384.1	270.26654 270.41635 270.14996 270.01667 270	83.7^a 49.7^b
Bb Dd Ff Hh Jj	8$\frac{1}{16}$ CB 31	9.12	37.0	270 294 324 342 348	9.2
Cc	4 - ⌊s 4 × 3 × $\frac{5}{16}$	8.36	30.3	282	7.3
Ee Gg Ii Kk	4 - ⌊s 5 × 3 × $\frac{5}{16}$	9.60	57.4	309 333 345 348	11.1
aB	2 - 12 [20.7 1 - Pl 15 × $\frac{5}{16}$	16.75	384.1	381.83766	83.7^a 49.7^b
Bc cD	2 - 9 [15	8.78	101.4	381.83766 399.16914	22.6
De	2 - 12 [20.7	12.06	256.2	399.16914	42.8
eF	2 - 12 [25	14.64	287.0	421.75349	47.8
Fg	2 - 12 [30 1 - Pl 16 × $\frac{3}{8}$	23.58	493.7	421.75349	102.8^a 65.2^b
gH	2 - 12 [35 1 - Pl 16 × $\frac{3}{8}$	26.44	618.4	435.73387	124.4^a 83.5^b
Hi iJ	2 - 12 [25	14.64	287.0 287	435.73387 440.45886	47.8
Jk	2 - 12 [20.7	12.06	256.2	440.45886	42.8

^{a}Top. ^{b}Bottom.

TABLE 8

DEAD PANEL LOADS

Lower Panel Pt.	D. L. (kips)	Upper Panel Pt.	D. L. (kips)
a	19.93	—	—
b	33.11	B	5.22
c	33.62	C	4.25
d	33.59	D	4.42
e	34.17	E	4.28
f	33.22	F	6.03
g	38.69	G	3.21
h	33.96	H	6.58
i	34.95	I	4.71
j	33.27	J	4.98
k	35.04	K	4.50

lighter concentrated load is used in computing the stresses in members in which the greater part of the stress is produced by bending moments; the heavier concentrated load is used when the greater part of the stress in a member is produced by shearing forces or when it is to be in equilibrium with that in a member such as at the end joint. There seems no stipulation, at the time when the bridge was designed, that two concentrations be placed in adjacent spans for the maximum stresses of chord members near the intermediate supports.

To conform further with the provisions for obtaining the greater maximum stress in a member at the time when the bridge was designed, the roadway is considered loaded over its entire width of 20 ft with both uniform and concentrated loads per foot of width equal to one-ninth (the lane width then being 9 ft) of the load of one traffic lane; but the load intensity is reduced by 20 (roadway in feet) - 18 (two-lane width in feet) = 2 percent. As the result of this method of applying live loads, the lane loading will be increased by a factor of $\frac{10}{9}(1 - 0.02) = 1.08889$.

For the bridge under consideration with a typical panel length of 22.5 ft, the typical live panel load is P = 480(22.5) = 10,800 lb, or 10.8 kips. The transversely modified live panel load P_m for producing maximum stresses is, therefore, $P_m = 10.8(1.08889) = 11.76$ kips.

The dynamic vibratory and impact effects will be accounted for as a fraction of the live-load stress by the formula:

$$I = \frac{50}{L + 125} \tag{23}$$

in which I is impact fraction and L is length, in feet, of the portion (or portions) of the span (or spans) which is loaded to produce the maximum stress in the member considered. There was no 30 percent impact ceiling when the bridge was designed.

By tracing the most possible former loading conditions as summarized previously one insures the closest check of maximum axial stresses determined by the proposed method with those obtained by the Montana State Highway Commission when the bridge was designed. This check will testify to the validity of the proposed method.

Reduction of Statically Independent and Dependent Unknowns

Statically Independent Unknowns. —There are 38 closed triangular figures (f) and two redundant supports (r) in the truss. If the structure is viewed as a chain of rigid frames, it is statically indeterminate to the $(3f + r) = 3(38) + 2 = 116$th degree under unsymmetrical loading. By using the method of substitution for an unsymmetrical loading by a set of symmetrical loading and a set of antisymmetrical loading, the number of statically independent unknowns are reduced to only one-half of 116, or 58.

With the letter designations for joints and numeral designations for independent unknown-end-moment subscripts as indicated in Figure 8, the 58 statically independent unknowns under any unsymmetrical loading are as defined in the following:

1. For the set of symmetrical loading,

$$\begin{bmatrix} X_1 \\ X_2 \\ \cdot \\ \cdot \\ \cdot \\ X_{57} \\ X_{58} \end{bmatrix}_s = \begin{bmatrix} M_{ab} \\ M_{Ba} \\ \cdot \\ \cdot \\ \cdot \\ M_{kJ} \\ R_g \end{bmatrix}_s = - \begin{bmatrix} M_{a'b'} \\ M_{B'a'} \\ \cdot \\ \cdot \\ \cdot \\ M_{k'J'} \\ -R_{g'} \end{bmatrix}_s \tag{24}$$

2. For the set of antisymmetrical loading,

$$\begin{bmatrix} X_1 \\ X_2 \\ \cdot \\ \cdot \\ \cdot \\ X_{57} \\ X_{58} \end{bmatrix}_a = \begin{bmatrix} M_{ab} \\ M_{Ba} \\ \cdot \\ \cdot \\ \cdot \\ M_{kJ} \\ R_g \end{bmatrix}_a = \begin{bmatrix} M_{a'b'} \\ M_{B'a'} \\ \cdot \\ \cdot \\ \cdot \\ M_{k'J'} \\ -R_{g'} \end{bmatrix}_a \tag{25}$$

Statically Dependent Unknowns. —The dependent unknown end moments are given by joint equilibrium as follows:

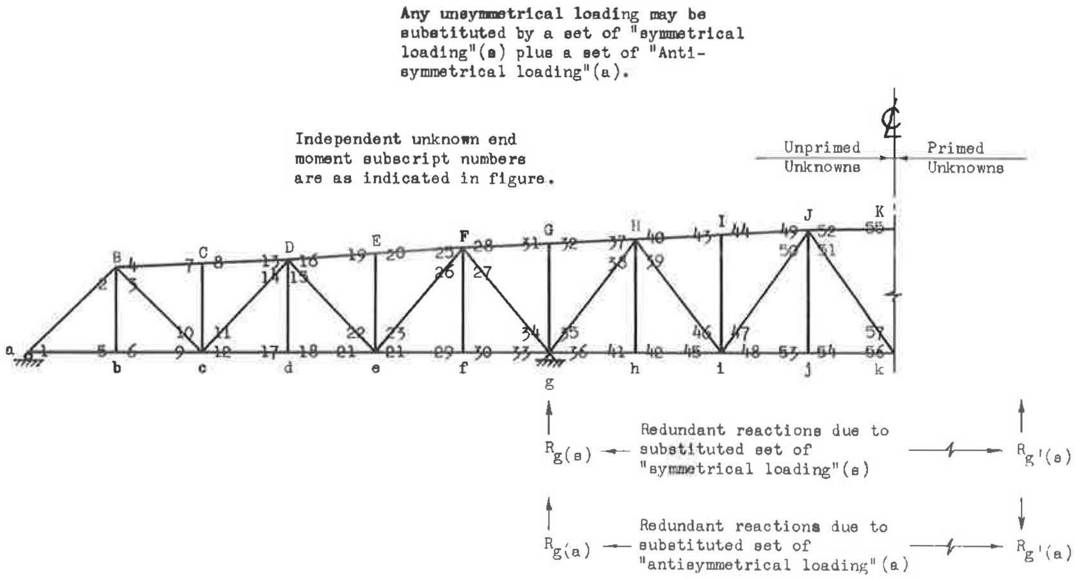
Any unsymmetrical loading may be substituted by a set of "symmetrical loading"(s) plus a set of "Antisymmetrical loading"(a).
Independent unknown end moment subscript numbers are as indicated in figure.
℄
Unprimed Unknowns
Primed Unknowns
B
C
D
E
F
G
H
I
J
K
a
b
c
d
e
f
g
h
i
j
k
Redundant reactions due to substituted set of "symmetrical loading"(s)
R_g(s)
R_g'(s)
Redundant reactions due to substituted set of "antisymmetrical loading"(a)
R_g(a)
R_g'(a)

Figure 8.

1. For the set of symmetrical loading,

$$\begin{bmatrix} M_{aB} \\ M_{Bb} \\ M_{bB} \\ \cdot \\ \cdot \\ \cdot \\ M_{jJ} \\ M_{Kk} \\ M_{kK} \end{bmatrix}_s = - \begin{bmatrix} M_{a'B'} \\ M_{B'b'} \\ M_{b'B'} \\ \cdot \\ \cdot \\ \cdot \\ M_{j'J'} \\ M_{K'k'} \\ M_{k'K'} \end{bmatrix}_s = - \begin{bmatrix} X_1 \\ X_2 + X_3 + X_4 \\ X_5 + X_6 \\ \cdot \\ \cdot \\ \cdot \\ X_{53} + X_{54} \\ 0 \\ 0 \end{bmatrix}_s \tag{26}$$

2. For the set of antisymmetrical loading,

$$\begin{bmatrix} M_{aB} \\ M_{Bb} \\ M_{bB} \\ \cdot \\ \cdot \\ \cdot \\ M_{jJ} \\ M_{Kk} \\ M_{kK} \end{bmatrix}_a = \begin{bmatrix} M_{a'B'} \\ M_{B'b'} \\ M_{b'B'} \\ \cdot \\ \cdot \\ \cdot \\ M_{j'J'} \\ M_{K'k'} \\ M_{k'K'} \end{bmatrix}_a = - \begin{bmatrix} X_1 \\ X_2 + X_3 + X_4 \\ X_5 + X_6 \\ \cdot \\ \cdot \\ \cdot \\ X_{53} + X_{54} \\ 2X_{55} \\ 2(X_{56} + X_{57}) \end{bmatrix}_a \tag{27}$$

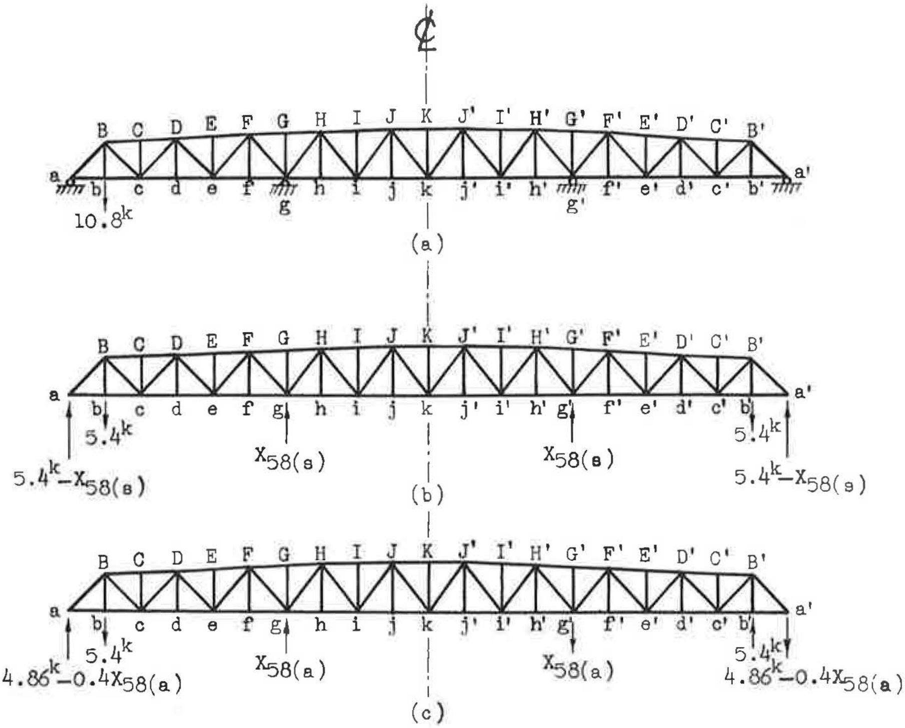
℄
B C D E F G H I J K J' I' H' G' F' E' D' C' B'
a b c d e f g h i j k j' i' h' g' f' e' d' c' b' a'
10.8^k
(a)
5.4^k
$X_{58(s)}$
$5.4^k - X_{58(s)}$
(b)
5.4^k
$X_{58(a)}$
$4.86^k - 0.4X_{58(a)}$
(c)

Figure 9.

Application of Method of Substitution

When the computer available is of small capacity, to analyze the truss under unsymmetrical loading with the reduced number of 58 statically independent unknowns, solutions of stresses in truss members for the substituted sets of symmetrical and antisymmetrical loadings must first be carried out. The solutions for the original unsymmetrical case may then be obtained at once by the principle of superposition.

As shown in Figure 9a, any unsymmetrical typical live panel load of 10.8 kips applied, e.g., at b may be substituted by two sets of loadings shown in Figures 9b and 9c. The reactions in Figure 9b are obvious; R_a in Figure 9c follows directly from the equation of couple equilibrium:

$$20R_a + 8X_{58} = 18(5.4)$$

If a sufficiently large computer is at hand for solving all the unknowns under any unsymmetrical loading, the process will be faster without resort to this method of substitution.

FORMULATION OF AXIAL-STRESS EXPRESSIONS AND CHARACTERISTIC SIMPLIFICATIONS

The basic techniques for formulating axial-stress expressions have been presented under "Extended Methods of Moments, Shears, and Joints." As a general rule, the axial stress in each of the top and bottom chord members and each of the diagonal members in the panels having inclined upper chords may be determined by the extended method of moments; that of the end posts and of the diagonal members in panels having parallel chords, by the extended method of shears; and that of the verticals, by the method of joints.

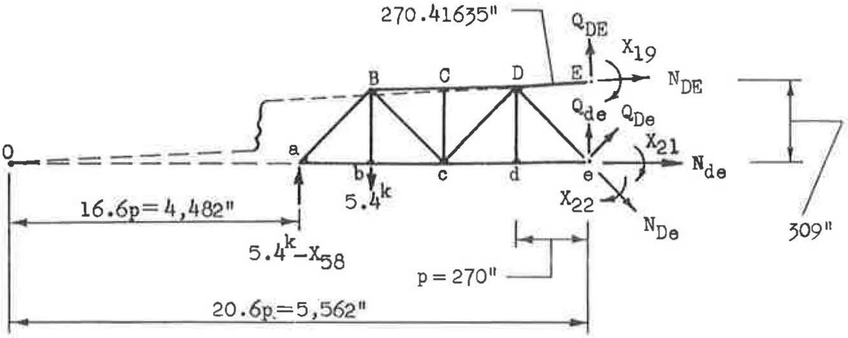

Figure 10.

As typical examples of application of this general rule, we may formulate the axial-stress expressions for members De, DE, aB, Jk, Bb, and Cc in the truss shown in Figure 9b under the substituted set of symmetrical half-panel loads.

Diagonal De and Upper Chord DE

These two axial stresses may be determined most expediently by the extended method of moments. Taking the free body diagram just to the left of member Ee, as shown in Figure 10, and noting that

$$\left\{Q_{de} \quad Q_{De} \quad Q_{DE}\right\} = \left\{\frac{X_{18}+X_{21}}{p} \quad \frac{X_{15}+X_{22}}{De} \quad \frac{X_{16}+X_{19}}{DE}\right\} \tag{28}$$

we have, by $\Sigma M_O = 0$,

$$\lfloor \text{Row vector of stresses} \rfloor \; \{\text{Column vector of lever arms}\} = 0$$

or

$$\lfloor N_{De} \quad -Q_{De} \quad -Q_{de} \quad -Q_{DE} \quad (X_{19}+X_{21}+X_{22}) \quad 5.4 \quad -(5.4-X_{58}) \rfloor$$

$$\left\{\frac{Dd(oe)}{De} \quad \frac{de(oe)}{De} \quad oe \quad 20.6(DE) \quad 1 \quad 17.6p \quad oa\right\} = 0 \tag{29}$$

Substituting Q's from Eq. 28 and all known distances into Eq. 29, and transposing, yields:

$$N_{De} = \frac{\lfloor X_{15} \quad (X_{16}+X_{18}) \quad (X_{19}+X_{21}) \quad X_{22} \rfloor}{(10)^{10}} \begin{bmatrix} 23006973 \\ 50285858 \\ 47844797 \\ 20565912 \end{bmatrix} - \lfloor X_{58} \quad 1 \rfloor \begin{bmatrix} 1.0940836 \\ 0.35590670 \end{bmatrix} \tag{30}$$

where the last product of two vectors corresponds to the conventional primary stress in member De.

Taking the same free body diagram shown in Figure 10, by $\Sigma M_e = 0$, we have again the product of a row vector and a column vector equal to zero,

$$\lfloor N_{DE} \quad -Q_{DE} \quad (X_{19} + X_{21} + X_{22}) \quad -5.4 \quad (5.4 - X_{58}) \rfloor$$

$$\left\{ Ee \quad \frac{p}{DE} \quad \frac{Ee(Ee - Dd)}{DE} \quad 1 \quad 3p \quad 4p \right\} = 0 \qquad (31)$$

Substituting Q's from Eq. 28 and all known distances into Eq. 31 and transposing, yields:

$$N_{DE} = \frac{\lfloor X_{18} \quad -X_{19} \quad -(X_{21} + X_{22}) \rfloor}{(10)^{10}} \begin{bmatrix} 2054445.1 \\ 30357919 \\ 32412364 \end{bmatrix} + \lfloor X_{58} \quad -1 \rfloor \begin{bmatrix} 3.5005353 \\ 4.7257226 \end{bmatrix} \qquad (32)$$

where the last product of two vectors also corresponds to the conventional primary stress in member DE.

End Post aB and Center Diagonal Jk

These two axial stresses may most expediently be determined by the extended method of shears. Taking the free body diagram just to the left of member Bb (Fig. 11), and noting that

$$\left\{ Q_{ab} \quad Q_{aB} \right\} = \left\{ \frac{X_1 + X_5}{p} \quad \frac{-X_1 + X_2}{aB} \right\} \qquad (33)$$

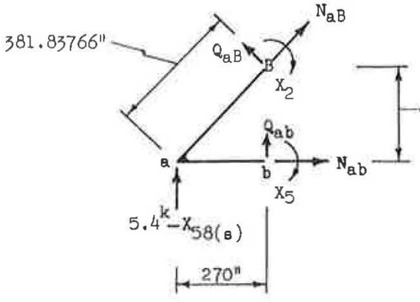

Figure 11.

we have, by $\Sigma Y = 0$,

$$N_{aB} \frac{1}{\sqrt{2}} + \frac{Q_{aB}}{\sqrt{2}} + Q_{ab} + 5.4 - X_{58} = 0 \qquad (34)$$

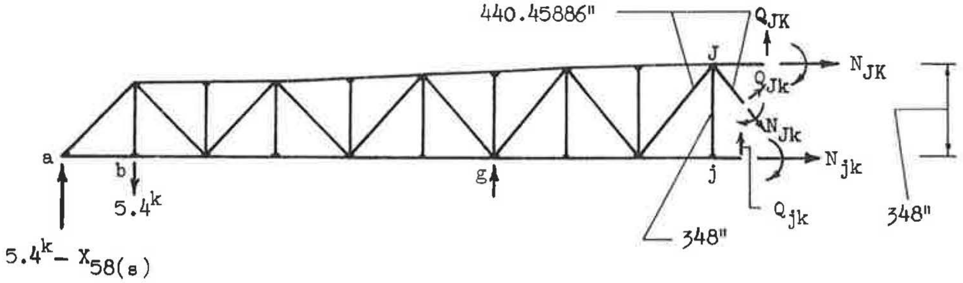

Figure 12.

Substituting Q's from Eq. 33 and known distances into Eq. 34, and transposing, yields:

$$N_{aB} = -\frac{\lfloor (X_1 + X_2)\ \ X_5 \rfloor}{(10)^{10}} \begin{bmatrix} 26189140 \\ 52378280 \end{bmatrix} + \lfloor X_{58}\ \ -1 \rfloor \begin{bmatrix} 1.4142136 \\ 7.6367532 \end{bmatrix} \tag{35}$$

in which the last product of two vectors is again the conventional primary stress in member aB.

To determine N_{Jk}, taking the free body diagram to the left of panel jk, as shown in Figure 12, and noting that

$$\left\{ Q_{jk}\ \ Q_{Jk}\ \ Q_{JK} \right\} = \left\{ \frac{X_{54} + X_{56}}{p}\ \ \frac{X_{51} + X_{57}}{Jk}\ \ \frac{X_{52} + X_{55}}{p} \right\} \tag{36}$$

we have, by $\Sigma Y = 0$,

$$-N_{Jk} \frac{Jj}{Jk} + Q_{Jk} \frac{p}{Jk} + Q_{JK} + Q_{jk} + X_{58} - 5.4 + (5.4 - X_{58}) = 0 \tag{37}$$

Substituting Q's from Eq. 36 and all known distances into Eq. 37, and transposing, yields:

$$N_{Jk} = \frac{\lfloor X_{51}\ \ (X_{52}\ X_{54}\ X_{55}\ X_{56})\ \ X_{57} \rfloor}{(10)^{10}} \begin{bmatrix} 17614859 \\ 46877273 \\ 17614859 \end{bmatrix} + 0 \tag{38}$$

where the last term means the conventional primary stress in member Jk is zero.

Vertical Members Bb and Cc

The extended method of joints may most advantageously be applied to determine the axial stresses in vertical members Bb and Cc. Taking the free body diagram around joint b (Fig. 13a), and noting that

$$\left\{ Q_{ab}\ \ Q_{bc} \right\} = \left\{ \frac{X_1 + X_5}{p}\ \ \frac{X_6 + X_9}{p} \right\} \tag{39}$$

we have, by $\Sigma Y = 0$,

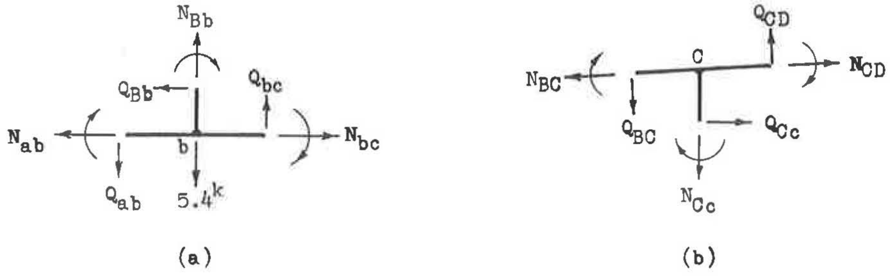

Figure 13.

$$N_{Bb} - Q_{ab} - 5.4 + Q_{bc} = 0 \qquad (40)$$

Substituting Q's from Eq. 39 and the known panel length into Eq. 40, and transposing, yields:

$$N_{Bb} = \frac{37037037}{(10)^{10}} (X_1 + X_5 - X_6 - X_9) + 5.4 \qquad (41)$$

where the last term represents the conventional primary stress in member Bb.

In the free body diagram shown in Figure 13b, noting that

$$\begin{bmatrix} Q_{Cc} \\ \\ Q_{CD} \\ \\ Q_{BC} \end{bmatrix} = \begin{bmatrix} -\dfrac{\sum\limits_{i=7}^{12} X_i}{Cc} \\ \\ \dfrac{X_8 + X_{13}}{CD} \\ \\ \dfrac{X_4 + X_7}{BC} \end{bmatrix} \qquad (42)$$

we have, by summing up the stress components along the axis perpendicular to member BC (or CD),

$$-N_{Cc}\left(\frac{p}{BC}\right) + Q_{Cc}\left(\frac{12}{BC}\right) + Q_{CD} - Q_{BC} = 0 \qquad (43)$$

Substituting Q's from Eqs. 42 and all known distances into Eq. 43, and transposing, yields:

$$N_{Cc} = \frac{\left\lfloor -X_4 \quad -X_7 \quad X_8 \quad \sum\limits_{i=9}^{12} X_i \quad X_{13} \right\rfloor}{(10)^{10}} \begin{bmatrix} 37037037 \\ 35460993 \\ 38613081 \\ 15760441 \\ 37037037 \end{bmatrix} + 0 \qquad (44)$$

where the last term denotes that the conventional primary stress in member Cc is zero.

Summary of Axial-Stress Expressions

The axial stresses in all other members of the left half of the truss shown in Figure 9b under typical symmetrical half live panel loads at b and b′, have been similarly determined. They are summarized in Eqs. 45:

Least Significant Part of Axial Stress — Most Significant Part of Axial Stress

Lower Chords

$$\begin{bmatrix} N_{ab} \\ N_{bc} \end{bmatrix} = \frac{37037037}{(10)^{10}} \begin{bmatrix} X_2 + X_5 \\ -(X_3 + X_4 + X_6) \end{bmatrix} + \begin{bmatrix} -X_{58} & 1 \\ -X_{58} & 1 \end{bmatrix} \begin{bmatrix} 1 \\ 5.4 \end{bmatrix}$$

$$\begin{bmatrix} N_{cd} \\ N_{de} \end{bmatrix} = \frac{34013605}{(10)^{10}} \begin{bmatrix} X_{13} + X_{14} + X_{17} \\ -(X_{15} + X_{16} + X_{18}) \end{bmatrix} + \begin{bmatrix} -X_{58} & 1 \\ -X_{58} & 1 \end{bmatrix} \begin{bmatrix} 2.7551020 \\ 4.9591837 \end{bmatrix}$$

$$\begin{bmatrix} N_{ef} \\ N_{fg} \end{bmatrix} = \frac{30864198}{(10)^{10}} \begin{bmatrix} X_{25} + X_{26} + X_{29} \\ -(X_{27} + X_{28} + X_{30}) \end{bmatrix} + \begin{bmatrix} -X_{58} & 1 \\ -X_{58} & 1 \end{bmatrix} \begin{bmatrix} 4.1666667 \\ 4.5000000 \end{bmatrix}$$

$$\begin{bmatrix} N_{gh} \\ N_{hi} \end{bmatrix} = \frac{29239766}{(10)^{10}} \begin{bmatrix} X_{37} + X_{38} + X_{41} \\ -(X_{39} + X_{40} + X_{42}) \end{bmatrix} + \begin{bmatrix} -X_{58} & 1 \\ -X_{58} & 1 \end{bmatrix} \begin{bmatrix} 4.7368422 \\ 4.2631579 \end{bmatrix}$$

$$\begin{bmatrix} N_{ij} \\ N_{jk} \end{bmatrix} = \frac{28735632}{(10)^{10}} \begin{bmatrix} X_{49} + X_{50} + X_{53} \\ -(X_{51} + X_{52} + X_{54}) \end{bmatrix} + \begin{bmatrix} -X_{58} & 1 \\ -X_{58} & 1 \end{bmatrix} \begin{bmatrix} 4.6551724 \\ 4.1896552 \end{bmatrix}$$

Upper Chords

$$N_{BC} = \frac{\lfloor X_4 \quad -X_7 \quad -(X_9 + X_{10}) \rfloor}{(10)^{10}} \begin{bmatrix} 1644467.1 \\ 33851532 \\ 35495999 \end{bmatrix} + \lfloor X_{58} \quad -1 \rfloor \begin{bmatrix} 1.9167840 \\ 5.1753167 \end{bmatrix}$$

$$N_{CD} = \frac{\lfloor X_8 \quad (X_{11} + X_{12}) \quad X_{13} \rfloor}{(10)^{10}} \begin{bmatrix} 37140466 \\ 35495999 \\ 1644467.1 \end{bmatrix} + \lfloor X_{58} \quad -1 \rfloor \begin{bmatrix} 1.9167840 \\ 5.1753167 \end{bmatrix}$$

$$N_{DE} = \frac{\lfloor X_{16} \quad -X_{19} \quad -(X_{21} + X_{22}) \rfloor}{(10)^{10}} \begin{bmatrix} 2054445.1 \\ 30357919 \\ 32412364 \end{bmatrix} + \lfloor X_{58} \quad -1 \rfloor \begin{bmatrix} 3.5005352 \\ 4.7257226 \end{bmatrix}$$

$$N_{EF} = \frac{\lfloor X_{20} \quad (X_{23} + X_{24}) \quad X_{25} \rfloor}{(10)^{10}} \begin{bmatrix} 34466809 \\ 32412364 \\ 2054445.1 \end{bmatrix} + \lfloor X_{58} \quad -1 \rfloor \begin{bmatrix} 3.5005352 \\ 4.7257226 \end{bmatrix}$$

$$N_{FG} = \frac{\lfloor X_{28} \quad -X_{31} \quad -(X_{33} + X_{34}) \rfloor}{(10)^{10}} \begin{bmatrix} 1233882.6 \\ 28812826 \\ 30046709 \end{bmatrix} + \lfloor X_{58} \quad -1 \rfloor \begin{bmatrix} 4.8675668 \\ 4.3808102 \end{bmatrix}$$

Least Significant Part of Axial Stress

Most Significant Part of Axial Stress

Upper Chords (Cont'd)

$$N_{GH} = \frac{\lfloor X_{32} \quad (X_{35} + X_{36}) \quad X_{37} \rfloor}{(10)^{10}} \begin{bmatrix} 31280592 \\ 30046709 \\ 1233882.6 \end{bmatrix} + \lfloor X_{58} \quad -1 \rfloor \begin{bmatrix} 4.8675668 \\ 4.3808102 \end{bmatrix}$$

$$N_{HI} = \frac{\lfloor X_{40} \quad -X_{43} \quad (X_{45} + X_{46}) \rfloor}{(10)^{10}} \begin{bmatrix} 411497.23 \\ 28575800 \\ 28987297 \end{bmatrix} + \lfloor X_{58} \quad -1 \rfloor \begin{bmatrix} 4.6959420 \\ 4.2263451 \end{bmatrix}$$

$$N_{IJ} = \frac{\lfloor X_{44} \quad (X_{47} + X_{48}) \quad X_{49} \rfloor}{(10)^{10}} \begin{bmatrix} 29398794 \\ 28987297 \\ 411497.23 \end{bmatrix} + \lfloor X_{58} \quad -1 \rfloor \begin{bmatrix} 4.6959420 \\ 4.2263451 \end{bmatrix}$$

$$N_{JK} = -0.0028735632(X_{55} + X_{56} + X_{57}) + \lfloor X_{58} \quad -1 \rfloor \begin{bmatrix} 4.6551724 \\ 4.1896552 \end{bmatrix}$$

Verticals

$$N_{Bb} = 0.0037037037(X_1 + X_5 - X_6 - X_9) + 5.4000000$$

$$N_{Cc} = \frac{\left\lfloor X_4 \quad -X_7 \quad X_8 \quad \sum_{i=9}^{12} X_i \quad X_{13} \right\rfloor}{(10)^{10}} \begin{bmatrix} 37037037 \\ 35460993 \\ 38613081 \\ 1576044.1 \\ 37037037 \end{bmatrix} + 0$$

$$N_{Dd} = 0.0037037037(X_{12} + X_{17} - X_{18} - X_{21}) + 0$$

$$N_{Ee} = \frac{\left\lfloor X_{16} \quad -X_{19} \quad X_{20} \quad \sum_{i=21}^{24} X_i \quad X_{25} \right\rfloor}{(10)^{10}} \begin{bmatrix} 37037037 \\ 35239123 \\ 38834951 \\ 1797914.4 \\ 37037037 \end{bmatrix} + 0$$

$$N_{Ff} = 0.0037037037(X_{24} + X_{29} - X_{30} - X_{33}) + 0$$

$$N_{Gg} = \frac{\left\lfloor -X_{28} \quad -X_{31} \quad X_{32} \quad \sum_{i=33}^{36} X_i \quad X_{37} \right\rfloor}{(10)^{10}} \begin{bmatrix} 37037037 \\ 36036036 \\ 38038038 \\ 1001001.0 \\ 37037037 \end{bmatrix} + 0$$

$$N_{Hh} = 0.0037037037(X_{36} + X_{41} - X_{42} - X_{45}) + 0$$

Least Significant Part of Axial Stress | Most Significant Part of Axial Stress

Verticals (Cont'd)

$$N_{Ii} = \frac{\left\lfloor -X_{40} \quad -X_{43} \quad X_{44} \quad \sum_{i=45}^{48} X_i \quad X_{49} \right\rfloor}{(10)^{10}} \begin{bmatrix} 37037037 \\ 36714976 \\ 37359098 \\ 322061.19 \\ 37037037 \end{bmatrix} + 0$$

$$N_{Jj} = 0.0037037037(X_{48} + X_{53} - X_{54} - X_{56}) \qquad + 0$$

$$N_{Kk} = 0.0074074074(X_{52} + X_{55}) \qquad + 0$$

Diagonals

$$N_{aB} = \frac{\left\lfloor -(X_1 + X_2) \quad -X_5 \right\rfloor}{(10)^{10}} \begin{bmatrix} 26189140 \\ 52378280 \end{bmatrix} + \left\lfloor X_{58} \quad -1 \right\rfloor \begin{bmatrix} 1.4142135 \\ 7.6367532 \end{bmatrix}$$

$$N_{Bc} = \frac{\left\lfloor X_3 \quad (X_4 + X_6) \quad (X_7 + X_9) \quad X_{10} \right\rfloor}{(10)^{10}} \begin{bmatrix} 26189140 \\ 52378280 \\ 50149417 \\ 23960277 \end{bmatrix} - \left\lfloor X_{58} \quad 1 \right\rfloor \begin{bmatrix} 1.2938550 \\ 0.32496822 \end{bmatrix}$$

$$N_{cD} = \frac{-\left\lfloor X_8 \quad X_{11} \quad X_{12} \quad X_{13} \quad X_{14} \quad X_{17} \right\rfloor}{(10)^{10}} \begin{bmatrix} 52425682 \\ 25146797 \\ 52425682 \\ 50285858 \\ 23006973 \\ 50285858 \end{bmatrix} + \left\lfloor X_{58} \quad 1 \right\rfloor \begin{bmatrix} 1.2421677 \\ 0.31198630 \end{bmatrix}$$

$$N_{De} = \frac{\left\lfloor X_{15} \quad (X_{16} + X_{18}) \quad (X_{19} + X_{21}) \quad X_{22} \right\rfloor}{(10)^{10}} \begin{bmatrix} 23006973 \\ 50285858 \\ 47844797 \\ 20565912 \end{bmatrix} - \left\lfloor X_{58} \quad 1 \right\rfloor \begin{bmatrix} 1.0940836 \\ 0.35590670 \end{bmatrix}$$

$$N_{eF} = \frac{-\left\lfloor X_{20} \quad X_{23} \quad X_{24} \quad X_{25} \quad X_{26} \quad X_{29} \right\rfloor}{(10)^{10}} \begin{bmatrix} 50551779 \\ 22099137 \\ 50551779 \\ 48211419 \\ 19758777 \\ 48211419 \end{bmatrix} + \left\lfloor X_{58} \quad 1 \right\rfloor \begin{bmatrix} 1.0489494 \\ 0.34122451 \end{bmatrix}$$

$$N_{Fg} = \frac{\left\lfloor X_{27} \quad (X_{28} + X_{30}) \quad (X_{31} + X_{33}) \quad X_{34} \right\rfloor}{(10)^{10}} \begin{bmatrix} 19758777 \\ 48211419 \\ 46908408 \\ 18455766 \end{bmatrix} - \left\lfloor X_{58} \quad 1 \right\rfloor \begin{bmatrix} 1.0906205 \\ 0.18997905 \end{bmatrix}$$

Least Significant Part of Axial Stress — Most Significant Part of Axial Stress

Diagonals (Cont'd)

$$N_{gH} = \frac{-\lfloor X_{32} \quad X_{35} \quad X_{36} \quad X_{37} \quad X_{38} \quad X_{41} \rfloor}{(10)^{10}} \begin{bmatrix} 48463338 \\ 19393605 \\ 48463338 \\ 47187987 \\ 18118254 \\ 47187987 \end{bmatrix} + \lfloor -X_{58} \quad 1 \rfloor \begin{bmatrix} 0.20660686 \\ 0.18594617 \end{bmatrix}$$

$$N_{Hi} = \frac{\lfloor X_{39} \quad (X_{40} + X_{42}) \quad (X_{43} + X_{45}) \quad X_{46} \rfloor}{(10)^{10}} \begin{bmatrix} 18118254 \\ 47187987 \\ 46777657 \\ 17707924 \end{bmatrix} + \lfloor X_{58} \quad -1 \rfloor \begin{bmatrix} 0.066473512 \\ 0.059826161 \end{bmatrix}$$

$$N_{iJ} = \frac{-\lfloor X_{44} \quad X_{47} \quad X_{48} \quad X_{49} \quad X_{50} \quad X_{53} \rfloor}{(10)^{10}} \begin{bmatrix} 47284901 \\ 18022487 \\ 47284901 \\ 46877273 \\ 17614859 \\ 46877273 \end{bmatrix} + \lfloor -X_{58} \quad 1 \rfloor \begin{bmatrix} 0.066035812 \\ 0.059432230 \end{bmatrix}$$

$$N_{Jk} = \frac{\lfloor X_{51} \quad (X_{52} + X_{54} + X_{55} + X_{56}) \quad X_{57} \rfloor}{(10)^{10}} \begin{bmatrix} 17614859 \\ 46877273 \\ 17614859 \end{bmatrix} + 0 \qquad (45)$$

Those axial stresses in members on the right half of the truss shown in Figure 9b under typical symmetrical half live panel loads at b and b′ may be obtained by using these axial-stress expressions and Eqs. 18.

Most and Least Significant Parts of Axial Stresses

As indicated in Eqs. 45, the most significant part of each axial stress represented by the last product of two vectors (or otherwise zero) consists of a constant term and another containing the redundant reaction X_{58}, and corresponds to the conventional primary stress in each member. The least significant part of each axial stress is due to end moments and transverse shears by virtue of rigid-frame action.

The entirety of an axial-stress expression should be used in writing the strain-energy expression due to each axial stress before partial differentiation, but thereafter the least significant part may be neglected in formulating the equations and in computing axial stresses.

It should be noted that the coefficients of the unknown end moments in the axial-stress expressions are dependent only on the properties of the composition of the truss. They are independent of any external loading. The coefficients of the unknown end moments in the axial-stress expressions are, therefore, always the same regardless of loading conditions. Only the most significant or primary-stress terms are subject to change for different loadings. This important fact necessitates determination of only a single set of coefficients of unknown end moments in the axial-stress expressions for all members under various loading conditions. For each different loading condition, only those coefficients in the most significant (or primary-stress) terms need further calculation, thus saving much time and labor.

Since the reactions at the end supports due to the redundant reactions (treated as loads) at the interior supports always have -1 as the coefficient of $X_{58(s)}$ for any substituted set of symmetrical loading and -0.4 as the coefficient of $X_{58(a)}$ for any substituted set of antisymmetrical loading, as shown in Figure 9, the coefficient of $X_{58(s)}$, in the axial-stress expressions will always be the same as will that of $X_{58(a)}$. Therefore, axial-stress expressions under any different symmetrical or antisymmetrical loading can be readily determined by revising only the constant terms in the most significant part of axial stresses, or primary stresses.

As has been pointed out, the least significant terms in the axial-stress expressions for antisymmetrical loadings are the same as for those for symmetrical loadings given previously (this applies even to unsymmetrical loading). To formulate the axial-stress expressions for the antisymmetrical set of loadings at b and b′, as shown in Figure 9c, we need only write explicitly the most significant part of axial stresses (corresponding to primary stresses) as grouped in Eqs. 46:

Lower Chords

$$N_{ab} = N_{bc} = \frac{1}{(10)^8} \lfloor -X_{58} \quad 1 \rfloor \{40,000,000 \quad 486,000,000\}$$

$$N_{cd} = N_{de} = \frac{1}{(10)^8} \lfloor -X_{58} \quad 1 \rfloor \{110,204,080 \quad 347,142,860\}$$

$$N_{ef} = N_{fg} = \frac{1}{(10)^8} \lfloor -X_{58} \quad 1 \rfloor \{166,666,670 \quad 225,000,000\}$$

$$N_{gh} = N_{hi} = \frac{1}{(10)^8} \lfloor -X_{58} \quad 1 \rfloor \{142,105,260 \quad 127,894,740\}$$

$$N_{ij} = N_{jk} = \frac{1}{(10)^8} \lfloor -X_{58} \quad 1 \rfloor \{46,551,724 \quad 41,896,552\}$$

Upper Chords

$$N_{BC} = N_{CD} = \frac{1}{(10)^8} \lfloor X_{58} \quad -1 \rfloor \{76,671,359 \quad 414,025,340\}$$

$$N_{DE} = N_{EF} = \frac{1}{(10)^8} \lfloor X_{58} \quad -1 \rfloor \{140,021,410 \quad 283,543,360\}$$

$$N_{FG} = N_{GH} = \frac{1}{(10)^8} \lfloor X_{58} \quad -1 \rfloor \{194,702,670 \quad 175,232,410\}$$

$$N_{HI} = N_{IJ} = \frac{1}{(10)^8} \lfloor X_{58} \quad -1 \rfloor \{93,918,842 \quad 84,526,957\}$$

$$N_{JK} = 0$$

Verticals

$$N_{Bb} = +5.4$$

$$N_{Cc} = N_{Dd} = N_{Ee} = N_{Ff} = N_{Gg} = N_{Hh} = N_{Ii} = N_{Jj} = N_{Kk} = 0$$

Diagonals

$$N_{aB} = \frac{1}{(10)^8} \lfloor X_{58} \quad -1 \rfloor \left\{ 56,568,542 \quad 687,307,790 \right\}$$

$$N_{Bc} = \frac{-1}{(10)^8} \lfloor X_{58} \quad 1 \rfloor \left\{ 51,754,198 \quad 102,364,990 \right\}$$

$$N_{cD} = \frac{1}{(10)^8} \lfloor X_{58} \quad 1 \rfloor \left\{ 49,686,707 \quad 98,275,685 \right\}$$

$$N_{De} = \frac{-1}{(10)^8} \lfloor X_{58} \quad 1 \rfloor \left\{ 43,763,343 \quad 94,671,183 \right\}$$

$$N_{eF} = \frac{1}{(10)^8} \lfloor X_{58} \quad 1 \rfloor \left\{ 41,957,976 \quad 90,765,719 \right\}$$

$$N_{Fg} = \frac{1}{(10)^8} \lfloor -X_{58} \quad -1 \rfloor \left\{ 43,624,819 \quad 77,891,410 \right\}$$

$$N_{gH} = \frac{1}{(10)^8} \lfloor -X_{58} \quad 1 \rfloor \left\{ 84,708,813 \quad 76,237,932 \right\}$$

$$N_{Hi} = \frac{1}{(10)^8} \lfloor X_{58} \quad -1 \rfloor \left\{ 77,774,009 \quad 69,996,608 \right\}$$

$$N_{iJ} = \frac{1}{(10)^8} \lfloor -X_{58} \quad 1 \rfloor \left\{ 77,261,899 \quad 69,535,709 \right\}$$

$$N_{Jk} = \frac{1}{(10)^8} \lfloor X_{58} \quad -1 \rfloor \left\{ 75,941,183 \quad 68,347,064 \right\} \qquad (46)$$

The most significant part of axial stresses in members on the right half of the truss may be obtained by using these products of vectors and Eqs. 19.

STRAIN-ENERGY EXPRESSIONS, REDUNDANT REACTIONS, AND SETS OF SIMULTANEOUS EQUATIONS

To apply the simplified matrix-energy method for analyzing the three-span continuous truss under consideration, the constants in the strain-energy expressions of truss members have been computed and the results are given in Table 9. With axial-stress expressions formulated as shown previously and strain-energy constants of truss members as given in Table 9, the strain-energy expressions can be readily formulated in practically the same manner as given in Table 4, except that to conform with the simplified matrix-energy method used herein the strain energy due to transverse shears will be neglected in the present analysis; the error so introduced will be negligible.

With the axial-stress expression for member ab represented by N_{ab}, that for member bc by N_{bc}, etc., the general strain-energy expressions may be written, according to Eqs. 5, using U to denote total internal strain energy in the member represented by the subscripts:

TABLE 9

CONSTANTS IN STRAIN-ENERGY EXPRESSIONS OF TRUSS MEMBERS

Member	$\frac{L}{A}$	$\frac{L}{6I}$	Member	$\frac{L}{A}$	$\frac{L}{6I}$
ab	22.388060	0.17564403	Cc	33.732057	1.5511551
bc	22.388060	0.17564403	Dd	32.236842	1.3243243
cd	22.388060	0.17564403	Ee	32.187500	0.89721254
de	22.388060	0.17564403	Ff	35.526316	1.4594595
ef	22.388060	0.17564403	Gg	34.687500	0.96689895
fg	22.388060	0.17564403	Hh	37.500000	1.5405405
gh	22.388060	0.17564403	Ii	35.937500	1.0017422
hi	22.388060	0.17564403	Ji	38.157895	1.5675676
ij	22.388060	0.17564403	Kk	36.250000	1.0104530
jk	22.388060	0.17564403	aB	22.796278	0.16568500
BC	16.135316	0.11727265	Bc	43.489483	0.62760957
CD	16.135316	0.11727265	cD	45.463456	0.65609655
DE	16.144260	0.11733765	De	33.098602	0.25967287
EF	16.144260	0.11733765	eF	28.808298	0.24492073
FG	16.128356	0.11722206	Fg	17.886068	0.14237847
GH	16.128356	0.11722206	gH	16.480101	0.11743582
HI	16.120398	0.11716422	Hi	29.763242	0.25303941
IJ	16.120398	0.11716422	iJ	30.085988	0.25578331
JK	16.119403	0.11715699	Jk	36.522294	0.28653322
Bb	29.605263	1.21621620	—	—	—

$$
E \begin{bmatrix} U_{ab} \\ U_{bc} \\ U_{cd} \\ U_{de} \\ U_{ef} \\ U_{fg} \\ U_{gh} \\ U_{hi} \\ U_{ij} \\ U_{jk} \end{bmatrix} = \begin{bmatrix}
\frac{1}{2} N_{ab}^2 & (X_1^2 - X_1X_5 + X_5^2) \\
\frac{1}{2} N_{bc}^2 & (X_6^2 - X_6X_9 + X_9^2) \\
\frac{1}{2} N_{cd}^2 & (X_{12}^2 - X_{12}X_{17} + X_{17}^2) \\
\frac{1}{2} N_{de}^2 & (X_{18}^2 - X_{18}X_{21} + X_{21}^2) \\
\frac{1}{2} N_{ef}^2 & (X_{24}^2 - X_{24}X_{29} + X_{29}^2) \\
\frac{1}{2} N_{fg}^2 & (X_{30}^2 - X_{30}X_{33} + X_{33}^2) \\
\frac{1}{2} N_{gh}^2 & (X_{36}^2 - X_{36}X_{41} + X_{41}^2) \\
\frac{1}{2} N_{hi}^2 & (X_{42}^2 - X_{42}X_{45} + X_{45}^2) \\
\frac{1}{2} N_{ij}^2 & (X_{48}^2 - X_{48}X_{53} + X_{53}^2) \\
\frac{1}{2} N_{jk}^2 & (X_{54}^2 - X_{54}X_{56} + X_{56}^2)
\end{bmatrix} \begin{bmatrix} 22.388060 \\ \\ 0.17564403 \end{bmatrix}
$$

$$E\begin{bmatrix} U_{BC} \\ U_{CD} \end{bmatrix} = \begin{bmatrix} \frac{1}{2} N^2_{BC} & (X_4^2 - X_4X_7 + X_7^2) \\ \frac{1}{2} N^2_{CD} & (X_8^2 - X_8X_{13} + X_{13}^2) \end{bmatrix} \begin{bmatrix} 16.135316 \\ 0.11727265 \end{bmatrix}$$

$$E\begin{bmatrix} U_{DE} \\ U_{EF} \end{bmatrix} = \begin{bmatrix} \frac{1}{2} N^2_{DE} & (X_{16}^2 - X_{16}X_{19} + X_{19}^2) \\ \frac{1}{2} N^2_{EF} & (X_{20}^2 - X_{20}X_{25} + X_{25}^2) \end{bmatrix} \begin{bmatrix} 16.144260 \\ 0.11733765 \end{bmatrix}$$

$$E\begin{bmatrix} U_{FG} \\ U_{GH} \end{bmatrix} = \begin{bmatrix} \frac{1}{2} N^2_{FG} & (X_{28}^2 - X_{28}X_{31} + X_{31}^2) \\ \frac{1}{2} N^2_{GH} & (X_{32}^2 - X_{32}X_{37} + X_{37}^2) \end{bmatrix} \begin{bmatrix} 16.128356 \\ 0.1172220 \end{bmatrix}$$

$$E\begin{bmatrix} U_{HI} \\ U_{IJ} \end{bmatrix} = \begin{bmatrix} \frac{1}{2} N^2_{HI} & (X_{40}^2 - X_{40}X_{43} + X_{43}^2) \\ \frac{1}{2} N^2_{IJ} & (X_{44}^2 - X_{44}X_{49} + X_{49}^2) \end{bmatrix} \begin{bmatrix} 16.120398 \\ 0.11716422 \end{bmatrix}$$

$$E\ U_{JK} = \begin{bmatrix} \frac{1}{2} N^2_{JK} & (X_{52}^2 - X_{52}X_{55} + X_{55}^2) \end{bmatrix} \begin{bmatrix} 16.119403 \\ 0.11715699 \end{bmatrix}$$

$$E\ U_{Bb} = \begin{bmatrix} \frac{1}{2} N^2_{Bb} \begin{bmatrix} \sum_{i=2}^{4} X_i & -\sum_{i=2}^{4} X_i & \sum_{i=5}^{6} X_i \end{bmatrix} \begin{bmatrix} \sum_{i=2}^{4} X_i \\ \sum_{i=5}^{6} X_i \\ \sum_{i=5}^{6} X_i \end{bmatrix} \end{bmatrix} \begin{bmatrix} 29.605263 \\ 1.2162162 \end{bmatrix}$$

$$E\ U_{Cc} = \left[\frac{1}{2} N^{2}_{Cc} \begin{bmatrix} \sum\limits_{i=7}^{8} X_i & -\sum\limits_{i=7}^{8} X_i & \sum\limits_{i=9}^{12} X_i \end{bmatrix} \begin{bmatrix} \sum\limits_{i=7}^{8} X_i \\ \sum\limits_{i=9}^{12} X_i \\ \sum\limits_{i=9}^{12} X_i \end{bmatrix} \right] \begin{bmatrix} 33.732057 \\ 1.5511551 \end{bmatrix}$$

$$E\ U_{Dd} = \left[\frac{1}{2} N^{2}_{Dd} \begin{bmatrix} \sum\limits_{i=13}^{16} X_i & -\sum\limits_{i=13}^{16} X_i & \sum\limits_{i=17}^{18} X_i \end{bmatrix} \begin{bmatrix} \sum\limits_{i=13}^{16} X_i \\ \sum\limits_{i=17}^{18} X_i \\ \sum\limits_{i=17}^{18} X_i \end{bmatrix} \right] \begin{bmatrix} 32.236842 \\ 1.3243243 \end{bmatrix}$$

$$E\ U_{Ee} = \left[\frac{1}{2} N^{2}_{Ee} \begin{bmatrix} \sum\limits_{i=19}^{20} X_i & -\sum\limits_{i=19}^{20} X_i & \sum\limits_{i=21}^{24} X_i \end{bmatrix} \begin{bmatrix} \sum\limits_{i=19}^{20} X_i \\ \sum\limits_{i=21}^{24} X_i \\ \sum\limits_{i=21}^{24} X_i \end{bmatrix} \right] \begin{bmatrix} 32.187500 \\ 0.89721254 \end{bmatrix}$$

$$E\ U_{Ff} = \left[\frac{1}{2} N^2_{Ff} \begin{bmatrix} \sum\limits_{i=25}^{28} X_i & -\sum\limits_{i=25}^{28} X_i & \sum\limits_{i=29}^{30} X_i \end{bmatrix} \begin{bmatrix} \sum\limits_{i=25}^{28} X_i \\ \sum\limits_{i=29}^{30} X_i \\ \sum\limits_{i=29}^{30} X_i \end{bmatrix} \right] \begin{bmatrix} 35.526316 \\ 1.4594595 \end{bmatrix}$$

$$E\ U_{Gg} = \left[\frac{1}{2} N^2_{Gg} \begin{bmatrix} \sum\limits_{i=31}^{32} X_i & -\sum\limits_{i=31}^{32} X_i & \sum\limits_{i=33}^{36} X_i \end{bmatrix} \begin{bmatrix} \sum\limits_{i=31}^{32} X_i \\ \sum\limits_{i=33}^{36} X_i \\ \sum\limits_{i=33}^{36} X_i \end{bmatrix} \right] \begin{bmatrix} 34.687500 \\ 0.96689895 \end{bmatrix}$$

$$E\ U_{Hh} = \left[\frac{1}{2} N^2_{Hh} \begin{bmatrix} \sum\limits_{i=37}^{40} X_i & -\sum\limits_{i=37}^{40} X_i & \sum\limits_{i=41}^{42} X_i \end{bmatrix} \begin{bmatrix} \sum\limits_{i=31}^{40} X_i \\ \sum\limits_{i=41}^{42} X_i \\ \sum\limits_{i=41}^{42} X_i \end{bmatrix} \right] \begin{bmatrix} 37.500000 \\ 1.5405405 \end{bmatrix}$$

$$E\ U_{Ii} = \begin{bmatrix} \frac{1}{2} N_{Ii}^{2} \begin{bmatrix} \sum\limits_{i=43}^{44} X_i & -\sum\limits_{i=43}^{44} X_i & \sum\limits_{i=45}^{48} X_i \end{bmatrix} \end{bmatrix} \begin{bmatrix} \sum\limits_{i=43}^{44} X_i \\ \sum\limits_{i=45}^{48} X_i \\ \sum\limits_{i=45}^{48} X_i \end{bmatrix} \begin{bmatrix} 35.937500 \\ 1.0017422 \end{bmatrix}$$

$$E\ U_{Jj} = \begin{bmatrix} \frac{1}{2} N_{Jj}^{2} \begin{bmatrix} \sum\limits_{i=49}^{52} X_i & -\sum\limits_{i=49}^{52} X_i & \sum\limits_{i=53}^{54} X_i \end{bmatrix} \end{bmatrix} \begin{bmatrix} \sum\limits_{i=49}^{52} X_i \\ \sum\limits_{i=53}^{54} X_i \\ \sum\limits_{i=53}^{54} X_i \end{bmatrix} \begin{bmatrix} 38.157895 \\ 1.5675676 \end{bmatrix}$$

$$E \begin{bmatrix} U_{Kk(s)} \\ U_{Kk(a)} \end{bmatrix} = \begin{bmatrix} \frac{1}{2} N_{Kk}^{2} & & & \\ \frac{1}{2} N_{Kk}^{2} & 4 \begin{bmatrix} X_{55} & -X_{55} & \sum\limits_{i=56}^{57} X_i \end{bmatrix} \end{bmatrix} \begin{bmatrix} 0 \\ \begin{bmatrix} X_{55} \\ \sum\limits_{i=56}^{57} X_i \\ \sum\limits_{i=56}^{57} X_i \end{bmatrix} \end{bmatrix} \begin{bmatrix} 36.250000 \\ 1.0104530 \end{bmatrix}$$

where (s) denotes symmetrical set of loading, and (a) denotes antisymmetrical set of loading. Only one-half of EU_{Kk} should be used in computing $\frac{1}{2}EU$.

$$E\begin{bmatrix}U_{aB}\\ U_{Bc}\\ U_{cD}\\ U_{De}\\ U_{eF}\end{bmatrix} = \begin{bmatrix} \left\lfloor \frac{1}{2} N_{aB}^2 \quad (X_1^2 + X_1X_2 + X_2^2) \right\rfloor & \begin{bmatrix}22.796278\\ 0.16568500\end{bmatrix} \\ \left\lfloor \frac{1}{2} N_{Bc}^2 \quad (X_3^2 - X_3X_{10} + X_{10}^2) \right\rfloor & \begin{bmatrix}43.489483\\ 0.62760957\end{bmatrix} \\ \left\lfloor \frac{1}{2} N_{cD}^2 \quad (X_{11}^2 - X_{11}X_{14} + X_{14}^2) \right\rfloor & \begin{bmatrix}45.463456\\ 0.65609655\end{bmatrix} \\ \left\lfloor \frac{1}{2} N_{De}^2 \quad (X_{15}^2 - X_{15}X_{22} + X_{22}^2) \right\rfloor & \begin{bmatrix}33.098602\\ 0.25967287\end{bmatrix} \\ \left\lfloor \frac{1}{2} N_{eF}^2 \quad (X_{23} - X_{23}^2X_{26} + X_{26}^2) \right\rfloor & \begin{bmatrix}28.808298\\ 0.24492073\end{bmatrix} \end{bmatrix}$$

$$E\begin{bmatrix}U_{Fg}\\ U_{gH}\\ U_{Hi}\\ U_{iJ}\\ U_{Jk}\end{bmatrix} = \begin{bmatrix} \left\lfloor \frac{1}{2} N_{Fg}^2 \quad (X_{27}^2 - X_{27}X_{34} + X_{34}^2) \right\rfloor & \begin{bmatrix}17.886068\\ 0.14237847\end{bmatrix} \\ \left\lfloor \frac{1}{2} N_{gH}^2 \quad (X_{35}^2 - X_{35}X_{38} + X_{38}^2) \right\rfloor & \begin{bmatrix}16.480101\\ 0.11743582\end{bmatrix} \\ \left\lfloor \frac{1}{2} N_{Hi}^2 \quad (X_{39}^2 - X_{39}X_{46} + X_{46}^2) \right\rfloor & \begin{bmatrix}29.763242\\ 0.25303941\end{bmatrix} \\ \left\lfloor \frac{1}{2} N_{iJ}^2 \quad (X_{47}^2 - X_{47}X_{50} + X_{50}^2) \right\rfloor & \begin{bmatrix}30.085988\\ 0.25578331\end{bmatrix} \\ \left\lfloor \frac{1}{2} N_{Jk}^2 \quad (X_{51}^2 - X_{51}X_{57} + X_{57}^2) \right\rfloor & \begin{bmatrix}36.522294\\ 0.28653322\end{bmatrix} \end{bmatrix} \tag{47}$$

Solution of Redundant Reactions

In the simplified matrix-energy method which we are now applying, not only is the strain energy due to transverse shears neglected but also the part other than the conventional primary stress (the most significant part) in the axial-stress expression is deleted after partial differentiation. Thus, the 58th equation obtained from

$$\frac{1}{2} E \frac{\partial U}{\partial X_{58}} = 0 \tag{48}$$

assumes the form of an algebraic linear equation with X_{58} as the "unique unknown." This redundant reaction may now be solved. The size of the set of simultaneous equations is consequently reduced to 57 equations with 57 unknowns.

The pair of symmetrical half-panel loads applied at b and b′, and c and c′, etc., may be represented by b++, c++, etc., respectively; the pair of antisymmetrical half-panel loads applied at b and b′, c and c′, etc., may be represented by b+-, c+-, etc., respectively; the panel load symmetrically applied at k may be represented by k; and the symmetrically located dead loads may be represented by DL. The redundant reactions at the interior supports are found as in Table 10. The left redundant reaction is upward positive, and the right redundant reaction is upward positive under symmetrical loadings and downward positive under antisymmetrical loadings.

It must be noted that the redundant reactions can first be solved independently only in the simplified matrix-energy method. In the exact matrix-energy method, Eq. 48 will contain some of the unknown end moments X_i; it must be solved simultaneous with the other 57 equations.

TABLE 10

REDUNDANT REACTIONS AT INTERIOR SUPPORTS

Due to	X_{58} (kips)	Due to	X_{58} (kips)
a+-	0	DL	269.39998
b++	1.0696012	a+-	0
c++	2.1265065	b+-	1.5125273
d++	3.1326161	c+-	2.9914410
e++	4.0066760	d+-	4.2743738
f++	4.7827808	e+-	5.0799756
g++	5.4000000	f+-	5.5290950
h++	5.8704096	g+-	5.4000000
i++	6.1854863	h+-	4.5959812
j++	6.3893981	i+-	3.2634630
k++	6.4439991	j+-	1.7249734

Formulation of Sets of Simultaneous Equations

For the present problem, the complete systems of simultaneous equations in polyset unknown and constant vectors, after partially differentiating the total strain energy given by Eq. 6 with respect to each unknown, take the following general matrix forms:

1. For symmetrical loadings,

$$\left[a_{ij}\right]_{\overline{57} \times 57} \left[X_{ik}\right]_{\overline{57} \times 10} = \left[c_{ik}\right]_{\overline{57} \times 10} \tag{49}$$

2. For antisymmetrical loadings,

$$\left[a_{ij}\right]_{\overline{57} \times 57} \left[X_{ik}\right]_{\overline{57} \times 8} = \left[c_{ik}\right]_{\overline{57} \times 8} \tag{50}$$

The solutions of these equations by matrix inversion are, respectively,

$$\left[X_{ik}\right]_{\overline{57} \times 10} = \left[a_{ij}\right]^{-1}_{\overline{57} \times 57} \left[c_{ik}\right]_{\overline{57} \times 10} \tag{51}$$

and

$$\left[X_{ik}\right]_{\overline{57} \times 8} = \left[a_{ij}\right]^{-1}_{\overline{57} \times 57} \left[c_{ik}\right]_{\overline{57} \times 8} \tag{52}$$

where the barred subscripts denote number of rows, the unbarred subscripts denote number of columns, and $[a_{ij}]$'s of Eqs. 51 and 52 differ by a 3 × 3 trailing sub-matrix as will be explained later by Eq. 53. There are as many unknown column vectors and known constant column vectors as there are loading conditions.

To explain the formulation of these matrices, Table 10 is used to express all primary axial stresses in truss members under the 18 different sets of loading conditions in their numerical values.

After substituting each of the 18 sets of axial stresses for N_{ij}'s in Eqs. 47, repeated operations of $\frac{1}{2} E \frac{\partial U}{\partial X_i} = 0$, where $i = 1, 2, \ldots, 57$, will yield two sets of 57 × 57 coefficient matrices with 57 × (10 + 8) known constant matrix to solve the 57 × (10 + 8) unknown end-moment matrix in two inversions.

It is especially noteworthy that, in the exact matrix-energy method, the coefficient matrix has to be determined from coefficients of all unknowns in the strain-energy expressions. But in the simplified matrix-energy method, the coefficient matrix is dependent only on coefficients of unknown bending moments.

Because the center vertical member has no bending moment under any symmetrical loading and experiences certain bending moment under each antisymmetrical loading, the coefficient matrix for symmetrical loadings will be different from that for antisymmetrical loadings but limited only to a 3 × 3 trailing sub-matrix:

TABLE 11

SOLUTION-VECTOR MATRIX

X_i	b++	c++	d++	e++	f++	h++	i++	j++	k++	DL	b+-	c+-	d+-	e+-	f+-	h+-	i+-	j+-
1	-2.4055712	-0.65158492	-0.44561134	-0.23444840	-0.10281838	0.07771276	0.12956796	0.16319313	0.17218851	-22.601890	-2.3931343	-0.62683546	-0.41309940	-0.20388586	-0.08156693	0.03615346	0.03720177	0.02475908
2	-1.7866888	1.2635521	-0.00829977	0.12806769	0.02666502	-0.03225614	-0.05127491	-0.06454358	-0.06799405	-3.1196718	-1.7915954	1.2537955	-0.02112347	0.11601286	0.01828284	-0.01589822	-0.01490431	-0.00996878
3	-0.12838390	0.30899713	0.50109965	0.16925690	0.08274663	-0.05746442	-0.09636843	-0.12137484	-0.12808581	4.6758872	-0.13763611	0.29056382	0.47691270	0.14652010	0.06693673	-0.02654108	-0.02764315	-0.01838373
4	2.0213862	-2.3228607	-0.77416475	-0.52292620	-0.20159021	0.16349613	0.27021036	0.34029667	0.35895171	-7.5058655	2.0473085	-2.2712827	-0.70640325	-0.45922739	-0.15729772	0.07691076	0.07775873	0.05179775
5	-5.5822360	0.23300047	-0.64982916	-0.12064142	-0.07776867	0.04548907	0.07763424	0.09778671	0.10324706	-39.382299	-5.5747760	0.24785096	-0.63032579	-0.10230734	-0.06502020	0.02053776	0.02218832	0.01472642
6	5.5762074	-1.0276941	0.33612084	-0.13566824	-0.02840189	0.03913274	0.06309882	0.07947646	0.08377560	32.352004	5.5822554	-1.0156644	0.35192910	-0.12102762	-0.01806876	0.01894826	0.01822875	0.01218260
7	-0.14146649	-6.1964330	-0.13404790	-0.60869145	-0.12603469	0.15040469	0.23852585	0.30022241	0.31624145	-48.248630	-0.11864673	-6.1510599	-0.07440935	-0.55262857	-0.08705185	0.07434184	0.06940060	0.04642552
8	0.51965699	6.1409189	-0.52303822	0.33346171	-0.01619998	-0.05099498	-0.07087894	-0.08903395	-0.09332900	47.292198	0.51314131	6.1275989	-0.54057605	0.31697538	-0.02766347	-0.02877603	-0.02141083	-0.01452296
9	2.7011943	-3.9179179	1.0103041	-0.58201852	-0.14454435	0.17205030	0.27924865	0.35172813	0.37082656	-2.3316837	2.7279681	-3.8646588	1.0802870	-0.51623142	-0.09879972	0.08267367	0.08057331	0.05380428
10	-0.71528609	-0.41386032	0.75245478	0.10433609	0.07735723	-0.04128430	-0.07107946	-0.08952959	-0.09455194	-2.9366250	-0.72212068	-0.42746347	0.73459116	0.08754351	0.06568061	-0.01842425	-0.02028336	-0.01344771
11	-0.57948913	0.45681994	0.67337035	0.28241392	0.09992315	-0.08028630	-0.13130510	-0.16530588	-0.17429783	3.1734162	-0.59207308	0.43178650	0.64047785	0.25149354	0.07842287	-0.03828237	-0.03793236	-0.02528706
12	-0.95407966	3.8190626	-3.1465206	-0.06017790	-0.16707785	0.04139364	0.07815523	0.09838119	0.10413855	1.1380347	-0.94654636	3.8340780	-3.1268192	-0.04165787	-0.15420002	0.01612041	0.02202245	0.01442974
13	0.13521703	1.7095313	-5.5289161	-1.0823744	-1.0644630	0.58575011	1.0290680	1.2970930	1.3708844	-10.988757	0.23432973	1.9069313	-5.2697549	-0.83875134	-0.89506024	0.25371412	0.29143947	0.19296750
14	-0.47341413	-0.33616160	-0.34742034	0.07611524	-0.06878610	0.01570982	0.03544835	0.04482901	0.04770800	-7.2444291	0.46995109	-0.32924072	-0.33835554	0.08463658	-0.06286068	0.00398718	0.00945325	0.00611846
15	-0.13595642	-0.81489770	0.73211959	0.65764024	0.74431732	-0.24785093	-0.43876494	-0.55210111	-0.58335930	-2.6551421	-0.17811526	-0.89885374	0.62189436	0.55402363	0.67226772	-0.10677054	-0.12528398	-0.08265829
16	0.66309564	0.05100597	5.2407294	0.04150114	0.34812161	-0.27882113	-0.50847040	-0.64217696	-0.67975665	27.716671	0.61389651	-0.04705766	5.1120449	-0.07946800	0.26400567	-0.11352240	-0.14144507	-0.09353500
17	-0.50572645	0.66396883	-6.9620071	-0.72383399	-0.79625230	0.32868463	0.58074216	0.73140022	0.77295665	-41.065560	-0.44985226	0.77524823	-6.8159131	-0.58649915	-0.70075685	0.14158637	0.16506028	0.10907590
18	0.68775553	-0.02889219	7.0588445	0.40253191	0.75530715	-0.24444154	-0.44750584	-0.56360808	-0.59619890	48.330125	0.64463767	-0.11480698	6.9460900	0.29653762	0.68160404	-0.09987727	-0.12639183	-0.08317717
19	0.03822173	-0.30927867	1.0461165	-3.6899920	0.03037325	0.33733584	0.36983475	0.48610521	0.50485224	-14.147154	0.07433210	-0.23600011	1.1402660	-3.6014875	0.09191095	0.21979247	0.12736597	0.08763112
20	0.22310959	0.75279677	-0.00712064	4.0755531	-0.33992840	-0.29167934	-0.27224320	-0.33730822	-0.34606176	29.827371	0.19854237	0.70462057	-0.07104321	4.0150633	-0.38170732	-0.21335799	-0.09669358	-0.06802215
21	0.37725826	0.28439378	4.2117706	-1.9441958	1.1035305	0.29177691	0.35375152	0.45586580	0.46543850	34.753101	0.41069719	0.35057497	4.2990603	-1.8621398	1.1605854	0.18159577	0.10828211	0.07523870
22	-0.31072201	-0.73354224	-1.1953132	-0.85735860	0.98054577	0.06662861	0.02183810	0.02795683	0.02620353	-14.063428	-0.30894417	-0.73024294	-1.1907454	-0.85306459	0.98353002	0.06168564	0.01047638	0.00916413
23	-0.16793446	-0.12371195	-1.5571038	0.38604819	0.82993214	-0.20611611	-0.25297200	-0.31311734	-0.32529684	-11.413357	-0.19117679	-0.16959811	-1.6176845	0.32909981	0.79033548	-0.13069681	-0.08445275	-0.05701338
24	0.33158936	0.94571633	-0.41108908	2.7515356	-3.3334884	-0.11706900	-0.02085407	-0.03223272	-0.02905207	-4.2307470	0.32959863	0.94211539	-0.41622042	2.7467119	-3.3368399	-0.11131401	-0.00777019	-0.01066295
25	0.40111082	0.86978292	0.98779296	2.2548192	-2.4273704	0.01402609	0.75701785	0.97291025	1.0603415	34.942066	0.47917216	1.0275663	1.1928871	2.4476172	-2.2932952	-0.25981274	0.15350067	0.06965335
26	-0.19673197	-0.32652911	-1.0465026	-0.66768542	-0.57281358	-0.09788775	0.18214831	0.24013352	0.26973795	-16.923849	-0.17651921	-0.28512399	-0.99315271	-0.61753402	-0.53793424	-0.17136928	0.02025696	0.00796719
27	-0.26184031	-0.57667665	-0.50045100	-1.3279476	0.13174628	0.15053370	-0.71563464	-0.85158727	-0.92116705	-31.692732	-0.32858927	-0.71116089	-0.67507342	-1.4921005	0.01759149	0.37510673	-0.21669832	-0.10979957
28	0.16441224	0.25829069	0.82620075	0.23137432	3.0702096	0.05084900	-0.13369718	-0.24931959	-0.29496071	25.607025	0.14094568	0.20930721	0.76332559	0.17226839	3.0290996	0.14867415	0.07569294	0.03621399
29	0.17437499	0.42170487	0.04990060	0.89715714	-5.4328576	-0.02608133	0.53327507	0.65929161	0.71417252	-13.112572	0.22648363	0.52674697	0.18648019	1.0255481	-5.3435729	-0.20469918	0.13790239	0.07536310
30	-0.05333637	-0.16780892	0.24734709	-0.36025800	5.6518827	0.15081458	-0.43710928	-0.53753457	-0.58981060	26.207579	-0.09660475	-0.25555640	0.13377853	-0.46701761	5.5776374	0.30112742	-0.10510967	-0.05077649
31	0.47559890	0.91400610	1.4405461	1.4840139	2.4092233	2.2919404	2.1362276	2.4957959	2.5120882	104.11260	0.65021333	1.2522162	1.8921983	1.9085864	2.7044008	1.7693453	0.95003622	0.62525704
32	-0.42480843	-0.81627582	-1.2741754	-1.3178571	-1.9888553	-2.7252284	-2.3603637	-2.7577936	-2.7635036	-105.29828	-0.61641789	-1.1879933	-1.7694389	-1.7834260	-2.3125289	-2.1561345	-1.0667521	-0.70973806
33	0.33310457	0.63521013	1.0624476	1.0937395	5.1828471	1.9172024	0.84442922	1.1086160	1.0925378	87.719904	0.40975158	0.78213605	1.2812547	1.2806270	5.3127621	1.6805194	0.31136616	0.27287611
34	0.07048108	0.11640711	0.22011957	-0.00923143	-0.62373044	2.2556948	0.80042410	1.0805594	1.0475374	32.275207	0.14365220	0.25529315	0.40969313	0.16897617	-0.49985916	2.0324040	0.29666898	0.28381705
35	-0.21118262	-0.38880163	-0.67893268	-0.55074967	-2.4503809	0.79538343	-0.27388066	-0.57630781	-0.60789832	-33.123103	-0.25501463	-0.47392634	-0.79353310	-0.65847944	-2.5252397	0.94262050	0.05112506	-0.08633756
36	-0.15282103	-0.28764806	-0.48888944	-0.40992221	-1.6572565	-5.4398604	-1.5431580	-1.8265748	-1.7331765	-87.959510	-0.27239143	-0.51515579	-0.79753106	-0.70005871	-1.8589602	-5.0898924	-0.74546971	-0.54138506
37	0.04095351	0.08964540	0.05200698	-0.00689930	-0.13473939	-2.9692443	-0.55428409	-1.1753670	-0.99495951	-34.139866	-0.02295553	-0.04322767	-0.10968101	-0.15889282	-0.24022918	-2.8220371	-0.20585081	-0.52472739
38	0.16144737	0.32970206	0.38444753	0.40937812	-0.34348754	0.23653954	1.9566442	1.4008345	1.5725211	38.714136	0.27316557	0.53804340	0.67485743	0.68237523	-0.15346573	-0.11364589	1.1608078	0.20908886
39	-0.06340884	-0.11629529	-0.13799928	-0.12652243	0.13110234	0.47355231	0.77658286	1.3225113	0.88871784	20.025351	-0.00567651	-0.01339034	0.00658039	0.01126941	0.22678453	0.33410540	0.44885581	0.66488646
40	-0.14601067	-0.31748473	-0.32227210	-0.29798550	0.26882753	2.0390582	-2.7216111	-1.9807853	-1.9303057	-36.078333	-0.28320848	-0.55597775	-0.67895167	-0.63327943	0.03539365	2.4693764	-1.7422989	-0.47806857
41	0.09425310	0.18344889	0.21151241	0.21324714	-0.25157926	-5.6121169	0.50893052	-0.01362089	0.33328523	-29.075157	0.12038331	0.23843637	0.21801333	0.27858021	-0.20600460	-5.7126972	0.28526575	-0.27175321
42	-0.10103609	-0.19682162	-0.23412354	-0.23313583	0.17362356	5.3690614	-1.1155331	-0.47517065	-0.86670422	16.358942	-0.16357697	-0.32176649	-0.39724215	-0.38647320	0.06682804	5.5709852	-0.65667928	0.15471104
43	-0.07948148	0.06015082	0.21736944	0.20575054	0.28212552	0.30350409	-3.9015765	-0.51858638	-0.50152356	-30.405164	0.04511832	0.08627907	0.13017144	0.12378291	0.22421059	0.37490326	-3.6895819	-0.21107886
44	-0.07965307	-0.07090397	-0.21549129	-0.20396396	-0.25739744	-0.10974162	3.4007691	-0.69422558	-0.58212544	15.816520	-0.11871576	-0.22968882	-0.31705721	-0.29944278	-0.32268874	0.02571563	3.6583517	-0.21078768
45	0.04893288	0.09213600	0.13075044	0.11762796	0.18076167	3.3537017	-2.8669826	-0.11241000	-1.3051976	-2.2794002	-0.04029740	-0.07943475	-0.09777128	-0.09718722	0.03079375	3.5834232	-2.3025323	0.59673903
46	0.03925561	0.07782856	0.10793250	0.10392450	0.13397896	-0.78559190	-0.04992132	1.9151619	1.0068163	14.621883	0.10740699	0.20826127	0.28363052	0.26909121	0.24840713	-0.98763141	-0.49312500	1.0417684
47	-0.03401738	-0.06979503	-0.09139617	-0.08476517	-0.11452342	-0.96656059	0.96805857	1.8392039	0.98414658	13.912573	0.03295626	0.06469364	0.08022139	0.07656355	-0.00183479	-1.1418466	0.53950895	1.0379950
48	-0.05390201	-0.10470336	-0.14441411	-0.13429427	-0.17466042	-1.2927190	1.5188031	-4.8334508	-1.6321349	-38.815250	-0.16382687	-0.31780032	-0.42780849	-0.40070669	-0.35922198	-0.96442703	2.2351068	-3.1572898
49	0.17121155	0.35944863	0.43300239	0.40638420	0.24935031	-0.39709212	-0.09373528	-5.2460866	-4.8009543	-41.926645	-0.14346427	-0.27873920	-0.37202312	-0.35037916	-0.27311483	0.47068516	1.7741729	-1.8466660
50	0.08261970	0.15168972	0.20954801	0.19757789	0.12084320	-0.64753623	-0.35549312	-0.16234413	-0.41069584	-4.5931378	0.06014301	0.11714411	0.15357134	0.14495579	0.08597193	-0.58986080	-0.28365599	0.05790758
51	0.07384836	-0.14837182	-0.18704346	-0.17580545	-0.10885632	0.29191092	0.15183665	1.5031540	1.4287052	14.274203	0.01460782	0.02828850	0.03870577	0.03644096	0.03700170	0.03348163	-0.35935557	0.58936284
52	-0.18061244	-0.36287597	-0.45745599	-0.42997095	-0.26623211	0.71393246	0.37134997	3.6762942	3.4942132	29.753810	0.04732155	0.09174071	0.12438311	0.11695914	0.10982178	0.09951566	-0.91453444	1.0872526
53	0.11720172	0.22557943	0.29684052	0.27947709	0.16956973	-0.72751213	-0.33315265	-7.5161612	-3.3279276	-61.517262	-0.09884623	-0.19202850	-0.25592636	-0.24017268	-0.18937191	-0.12209875	0.96133051	-3.9217534
54	-0.11797132	-0.22655631	-0.29912591	-0.28158345	-0.17462995	0.67745227	0.39865353	7.2611762	3.0016079	58.549610	0.07460945	0.14492849	0.19327295	0.18132147	0.14438861	0.13160722	-0.73629605	3.7353447
55	0.06576978	0.11903060	0.16938816	0.15925937	0.12711374	-0.03836554	-0.74793431	0.26396040	-0.60506109	-6.7231919	0.00306067	0.00593757	0.00800552	0.00752193	0.00670405	0.00608558	-0.04936143	0.03808340
56	0.04511919	0.08713853	0.11598601	0.10883475	0.08626189	0.07503440	-0.42340351	4.7530400	-0.06812434	29.971847	0.01196322	0.02326183	0.03075854	0.02882204	0.02080152	0.01903548	-0.06039943	-0.28763932
57	0.02689179	0.04866894	0.06925901	0.06511758	0.05197395	-0.01568681	-0.30581352	0.10792745	-0.24739589	-0.64042248	-0.00823036	-0.01691669	-0.02103010	-0.01968646	-0.01298277	-0.01192791	0.00897120	0.30519093

$$\text{sub} - \begin{bmatrix} a_{ij} \end{bmatrix} = \begin{bmatrix} a_{55,55} & a_{55,56} & a_{55,57} \\ a_{56,55} & a_{56,56} & a_{56,57} \\ a_{57,55} & a_{57,56} & a_{57,57} \end{bmatrix} \qquad (53)$$

which is a diagonal matrix for symmetrical loadings or a symmetrical matrix for antisymmetrical loadings. This difference is evident by inspecting the strain-energy expressions of the center-vertical member Kk in Eqs. 47.

Coefficient Matrices and Constant-Vector Matrices

The two sets of 57 × 57 coefficient matrices for symmetrical and antisymmetrical loadings and the 57 × 10 and 57 × 8 constant-vector matrices for the 18 basic loading conditions are regimented arrays of numbers. To save space, they are not shown herein.

Solution by Inversion Using Electronic Digital Computer

Eqs. 51 and 52 were solved by matrix inversion with the program "Simultaneous Equations A La King" furnished by IBM for use in the IBM 1620 computer (capacity, 60,000 core storage) available at the South Dakota Department of Highways.

Solutions of end moments of all members for substituted symmetrical and antisymmetrical sets of loadings are given in Table 11, from which full panel-load end moments may be obtained.

Appropriate combinations of panel-load end moments will yield all end moments simultaneous with maximum design stresses and maximum end moments of all members.

COMPOSITION OF MAXIMUM DESIGN AXIAL STRESSES

Dead-Load Stresses

Dead-load stresses are computed by the same general rule and in a similar manner as described previously by applying all upper and lower dead panel loads given in Table 8 simultaneously.

Maximum and Minimum Live-Load Stresses

Maximum live-load stresses, and minimum live-load stresses or maximum live-load stresses of the opposite sign, of all members of the truss are the most important part of live-load-stress analysis for later stress combination to arrive at maximum design stresses and maximum range of stress reversals.

In a programmed computation by the basic scheme of the proposed method, if the computer available is of sufficient capacity, neither method of substitution nor method of transformation would be needed. The procedure would be to load the truss with live panel loads, one at a time, from b to f, then from h to k, as shown in Figure 9a. By the panel-load superposition method, summation of all-plus-sign stresses and of all-minus-sign stresses in each member will give, respectively, the maximum tensile and compressive stresses.

From Figures 9b and 9c, with the method of substitution introduced in the present case because only a smaller computer is available, half live panel loads will be placed for both symmetrical and antisymmetrical sets, one pair at a time, at b and b′ to f and f′, then at h and h′ to j and j′, but one full panel load will be placed at k only once. Then from Eqs. 18 and 19, the axial stress, N, in member IJ is given by

$$\underset{\substack{\text{(due to any P}\\ \text{at any panel}\\ \text{point x)}}}{N_{ij}} = \underset{\substack{\text{(due to symm.}\\ \text{set of } \frac{1}{2}\text{P at}\\ \text{x and x}')}}{N_{ij(s)}} + \underset{\substack{\text{(due to antisymm.}\\ \text{set of } \frac{1}{2}\text{P at x}\\ \text{and x}')}}{N_{ij(a)}} \qquad (54)$$

and

$$\begin{array}{ccccccc} N_{ij} & = & N_{i'j'} & = & N_{ij}(s) & - & N_{ij}(a) \\ \text{(due to any P} & & \text{(due to any P} & & \text{(due to symm.} & & \text{(due to antisymm.} \\ \text{at panel} & & \text{at panel} & & \text{set of } \frac{1}{2}\text{P at} & & \text{set of } \frac{1}{2}\text{P at x} \\ \text{point x')} & & \text{point x)} & & \text{x and x')} & & \text{and x')} \end{array} \tag{55}$$

It follows, therefore, that

$$\begin{bmatrix} \text{Max. Total Pos. } N_{ij} \\ \\ \text{Max. Total Neg. } N_{ij} \end{bmatrix} = \begin{bmatrix} \sum_{b}^{b'} (\text{Pos. } N_{ij}) + (\text{Max. Pos. } N_{ij})\, F_c \\ \\ \sum_{b}^{b'} (\text{Neg. } N_{ij}) + (\text{Max. Neg. } N_{ij})\, F_c \end{bmatrix} \tag{56}$$

where the concentrated-load factors for moment and for shear are given by

$$\begin{bmatrix} F_c \text{ for moment} \\ F_c \text{ for shear} \end{bmatrix} = \frac{1}{10.8} \begin{bmatrix} 13.5 \\ 19.5 \end{bmatrix} \tag{57}$$

and in Eqs. 56 b to b′ attached to the Σ sign means summation of all positive or negative axial stresses when panel points from b to b′ are loaded such that like-sign stresses are produced.

Impact Stresses

The loaded length L in the impact formula of Eq. 23 will be obtained for either the maximum plus-sign or maximum negative-sign live-load stress by summing up the corresponding panel lengths. Impact stresses are then obtained from

$$\text{Impact stress} = \text{Max. L. L. stress} \left(\frac{50}{L + 125} \right) \tag{58}$$

Maximum and Minimum Design Stresses

These will be determined by summing up dead-load, maximum or minimum live-load (or maximum of opposite sign), and impact stresses in the usual manner.

Provision for Overload Stresses

These stresses are differently stipulated in different design specifications according to the judgment of those who have jurisdiction over formulating the specifications. The 100 percent increase of maximum live-load and impact fraction was stipulated in the 1932 design specifications. Because under this provision there is usually reversal of stresses, both the algebraic sum of one sign and that of the opposite sign are increased by 50 percent of the smaller value. When so increased for overload provision, the results of the analysis of this study check almost identically with those of a study conducted by the Montana State Highway Commission.

Summary of Axial Stresses

Dead-load, maximum live-load, impact, and maximum design stresses together with certain overload and reversal stresses are summarized in Tables 12 and 13. Results of the proposed method are given as well as those of the Montana study for comparison.

As shown in these tables, all dead-load, maximum and minimum (or of opposite sign) live-load, impact, and overload stresses check almost identically with the corresponding results of the Montana State Highway Commission. This further testifies to the validity and soundness of the proposed method.

All numerical values, except the minimum DL stresses for overload provision, were independently computed. To conform with the original design provisions, Montana values were used under "energy method."

TABLE 12

SUMMARY OF MAXIMUM AXIAL STRESSES, NO OVERLOAD

Member	Montana (kips)				Energy Method (kips)			
	D. L.	L. L.	I.	Total	D. L.	L. L.	I.	Total
ab	63.9	42.8	5.4	112.1	63.9	42.8	5.4	112.1
bc	63.9	42.8	5.4	112.1	63.9	42.8	5.4	112.1
cd	70.9	55.1	7.0	133.0	71.0	55.2	7.0	133.2
de	70.9	55.1	7.0	133.0	71.0	55.2	7.0	133.2
ef	-51.6	-32.2	-4.6	-88.4	-51.4	-32.2	-4.6	-88.2
fg	-51.6	-32.2	-4.6	-88.4	-51.4	-32.2	-4.6	-88.2
gh	-40.8	-26.3	-3.8	-70.9	-40.6	-26.3	-3.8	-70.7
hi	-40.8	-26.3	-3.8	-70.9	-40.6	-26.3	-3.8	-70.7
ij	80.7	55.3	9.1	145.1	81.0	55.3	9.1	145.4
jk	80.7	55.3	9.1	145.1	81.0	55.3	9.1	145.4
BC	-85.7	-55.0	-7.0	-147.7	-85.8	-55.0	-7.0	-147.8
CD	-85.7	-55.0	-7.0	-147.7	-85.8	-55.0	-7.0	-147.8
FG	154.0	58.0	6.6	218.6	153.9	57.9	6.6	218.4
GH	154.0	58.0	6.6	218.6	153.9	57.9	6.6	218.4
JK	-96.0	-61.1	-10.	-167.1	-96.2	-61.1	-10.	-167.2
Bb	33.1	33.0	9.9	76.0	33.1	33.0	9.7	75.8
Cc	-4.2	—	—	-4.2	-4.3	—	—	-4.3
Dd	33.6	33.0	9.9	76.5	33.6	33.0	9.7	76.3
Ee	-4.3	—	—	-4.3	-4.3	—	—	-4.3
Ff	33.2	33.0	9.9	76.1	33.2	33.0	9.7	75.9
Gg	-3.2	—	—	-3.2	-3.2	—	—	-3.2
Hh	34.0	33.0	9.9	76.9	34.0	33.0	9.7	76.7
Ii	-4.7	—	—	-4.7	-4.7	—	—	-4.7
Jj	33.3	33.0	9.9	76.2	33.3	33.0	9.7	76.0
Kk	-4.5	—	—	-4.5	-4.5	—	—	-4.5
aB	-90.4	-60.4	-7.7	-158.5	-90.4	-60.5	-7.7	-158.6
De	-70.1	-44.9	-6.0	-121.0	-70.0	-44.9	-6.0	-120.9
eF	117.3	60.4	7.7	185.4	117.2	60.4	7.6	185.2
Fg	-160.0	-74.2	-8.4	-242.6	-160.0	-74.2	-8.4	-242.6
gH	-182.6	-84.2	-9.6	-276.4	-182.6	-84.3	-9.6	-276.5
Hi	123.9	64.5	8.2	196.6	123.9	64.6	8.2	196.7
iJ	-72.9	-49.1	-6.6	-128.6	-72.9	-49.1	-6.6	-128.6

TABLE 13

SUMMARY OF MAXIMUM AXIAL STRESSES, OVERLOAD

Member	Loads	Montana (kips)		Energy Method (kips)	
Bc	D. L.	30.8	21.6	30.8	21.6
	L. L.	75.4	-37.2	75.4	-37.2
	I.	10.8	-5.6	10.8	-5.6
	Reversal	10.6	-10.6	10.6	-10.6
	Total	127.6	-31.8	127.6	-31.8
cD	D. L.	21.9	15.3	21.8	15.3
	L. L.	63.4	-45.0	63.4	-45.0
	I.	9.0	-6.8	9.0	-6.8
	Reversal	18.3	-18.3	18.3	-18.3
	Total	112.6	-54.8	112.5	-54.8
DE	D. L.	-23.5	-16.5	-23.6	-16.5
EF	L. L.	-82.4	53.2	-82.4	53.2
	I.	-10.4	8.8	-10.4	8.8
	Reversal	-22.8	22.8	-22.8	22.8
	Total	-139.1	68.3	-139.2	68.3
HI	D. L.	-36.0	-25.2	-36.2	-25.2
IJ	L. L.	-76.8	42.6	-76.8	42.6
	I.	-12.6	5.4	-12.6	5.4
	Reversal	-11.4	11.4	-11.4	11.4
	Total	-136.8	34.2	-137.0	34.2
Jk	D. L.	25.0	17.5	25.0	17.5
	L. L.	71.4	-48.6	71.4	-48.6
	I.	10.2	-7.4	10.2	-7.4
	Reversal	19.3	-19.3	19.3	-19.3
	Total	125.9	-57.8	125.9	-57.8

Further Merits of Panel-Load Method

Eqs. 54 and 55 give live-load stress in any truss member due to any typical panel load. For the investigation under consideration, a typical full live panel load was used so that the panel-load stresses may be later used to redesign the same bridge under current lane width of 10 ft, although the orginal design was made for the 1932 specifications of 9-ft lane-loading width. The transverse effect of shifting the 9-ft lane-loading width on the 10-ft lane width could have been directly obtained by multiplying the typical live panel load by the previously determined factor of 1.08889.

Influence-line ordinates for all members, although not needed in the proposed method of analysis, can be easily obtained from Eqs. 54 and 55 by simply using unit panel load instead of typical full live panel load. Moreover, the panel-load method makes it extremely expedient to obtain bending stresses (secondary stresses) simultaneous with maximum design axial stresses, and maximum bending stresses (maximum secondary stresses) together with simultaneous axial stresses.

END MOMENTS IN TRUSS MEMBERS

The essence of this study is to develop a unified, streamlined matrix-energy method so that engineers can analyze any rigidly connected truss, determinate or indeterminate, under any combination of loadings, and ascertain in each member the two possible governing states of required internal resistances: (a) under loadings of maximum axial stress—maximum axial stress, the larger of the bending stresses simultaneous with maximum axial stress, and transverse shear simultaneous with maximum axial stress; (b) under loadings of maximum bending stress—axial stress simultaneous with the larger of the maximum bending stresses, the larger of the maximum bending stresses, and transverse shear simultaneous with the larger of the maximum bending stresses. The term "bending stress," as used herein, corresponds to conventional secondary stress. It is evident that whichever of these two states requires the larger section should govern the design.

The problem involved is no longer academic. It deserves more serious practical considerations today than ever before: as longer spans of bridges are built, more brittle high-strength steels are used, welded connections are introduced, steel prestressing is applied, more dynamic effects are experienced from high-speed heavy wheel loads, more economical designs are stressed, and thinner sections, plates, and sheets are called for on plans. To best meet all these exacting demands and to insure public safety at minimum cost, the closest analysis of complicated bridge structures must be made.

Since the earliest introduction of a method for analyzing secondary stresses (1), although at least nine independent methods have been developed, the complicated and tedious analysis of secondary stresses has remained mainly of academic interest and even as such has been only rarely performed. Not many already constructed rigidly connected trusses have been given a secondary-stress analysis. None of particular importance have ever been given as thorough an analysis as required to investigate thoroughly the two governing states.

Even with today's technological development coupled with the availability of high-speed electronic digital computers, generally only a conventional maximum axial-stress analysis is made for rigidly connected trusses. By the time the analyst has achieved this conventional task using Müller-Breslau's (13) principle of influence lines, he is reluctant to undertake a secondary-stress analysis. The chief obstacle has been lack of a straight-forward, unified, streamlined method whereby axial stresses, end moments, and transverse shears will be obtained in one single setup. In this manner, all desired results will be yielded once the problem has been formulated and fed into the computer.

With the approach used in the present study, the formidable task of performing and iterating all necessary calculations for all members of a truss under all conceivable loading conditions will become simple. This advantage is inherent to the proposed method of panel-load superposition because at this stage of the analysis, each axial stress in every member due to each individual panel load as well as both end moments in every member due to each same individual panel load has been determined. The remaining computation of simultaneous end moments and shears under loadings of maximum axial stress and of maximum end moments and simultaneous shears and axial stresses under loadings of maximum bending stress is merely a simple arithmetic chore.

Simultaneous End Moments and Transverse Shears

End moments of a member simultaneous with its maximum axial stress may be readily obtained by the method of substitution used in this study, after converting X_i to M_{ij} according to Eqs. 24 to 27, in a manner analogous to Eqs. 54 and 55 for axial stresses. Thus,

$$\underset{\substack{\text{(due to any P}\\ \text{at any panel}\\ \text{point x)}}}{M_{ij}} = \underset{\substack{\text{(due to symm.}\\ \text{set of } \frac{1}{2}\text{P at}\\ \text{x and x}')}}{M_{ij(s)}} + \underset{\substack{\text{(due to antisymm.}\\ \text{set of } \frac{1}{2}\text{P at x}\\ \text{and x}')}}{M_{ij(a)}} \tag{59}$$

$$\underset{\substack{\text{(due to any P}\\ \text{at panel}\\ \text{point x}')}}{M_{ij}} = \underset{\substack{\text{(due to same P}\\ \text{at panel}\\ \text{point x)}}}{-M_{i'j'}} = \underset{\substack{\text{(due to symm.}\\ \text{set of } \frac{1}{2}\text{P at}\\ \text{x and x}')}}{M_{ij(s)}} - \underset{\substack{\text{(due to antisymm.}\\ \text{set of } \frac{1}{2}\text{P at x}\\ \text{and x}')}}{M_{ij(a)}} \tag{60}$$

Then, by the method of superposition,

$$\text{Simul. L. L. } M_{ij} = \sum_{b}^{b'} M_{ij} + F_c\, M_{ij} \text{ (due to the panel load producing max. } N_{ij}) \tag{61}$$

where b to b$'$ and F_c carry the same significances as defined with Eqs. 56 and 57. And by Eq. 23,

$$\text{Simul. Impact } M_{ij} = \text{Simul. L. L. } M_{ij} \left(\frac{50}{L + 125}\right) \tag{62}$$

Hence,

$$\text{Simul. Total } M_{ij} = \text{D. L. } M_{ij} + \text{Simul. L. L. } M_{ij} \left(1 + \frac{50}{L + 125}\right) \tag{63}$$

Simultaneous transverse shears for any member IJ may be obtained from simultaneous end moments, by Eq. 4, as

$$\text{Simul. } Q_{ij} = \frac{\text{Simul. Total } M_{ij} + \text{Simul. Total } M_{ji}}{L_{ij}} \tag{64}$$

Maximum End Moments and Simultaneous Shears

Maximum end moments represent the state in which the resisting moment at either end of a member reaches its possible maximum by loading certain panel points plus a concentration, all producing moments of the same sign. This state has its own simultaneous axial stresses and transverse shears. One of the two maximum end moments of each member will produce maximum secondary stresses.

Maximum live-load end moments M_{ij} and M_{ji} of any member IJ may be obtained from

$$\begin{bmatrix} \text{Max. L. L. } M_{ij} \\ \\ \text{Max. L. L. } M_{ji} \end{bmatrix} = \begin{bmatrix} \sum_{b}^{b'} \begin{matrix}\text{Pos.}\\ \text{or}\\ \text{Neg.}\end{matrix} \; M_{ij} + \left(\text{Max. } \begin{matrix}\text{Pos.}\\ \text{or}\\ \text{Neg.}\end{matrix} \; M_{ij}\right) F_c \\ \\ \sum_{b}^{b'} \begin{matrix}\text{Pos.}\\ \text{or}\\ \text{Neg.}\end{matrix} \; M_{ji} + \left(\text{Max. } \begin{matrix}\text{Pos.}\\ \text{or}\\ \text{Neg.}\end{matrix} \; M_{ji}\right) F_c \end{bmatrix} \tag{65}$$

in which the summations are to cover all positive or all negative M_{ij}, whichever gives the larger maximum live-load M_{ij}. M_{ji} is treated in the same manner. F_c and b to b′ are as defined before.

Then, maximum total end moments M_{ij} or M_{ji} of any member IJ is given by

$$\text{Max. Total } M_{ij} \text{ or } M_{ji} = \text{D. L. } M_{ij} \text{ or } M_{ji} + \text{Max. L. L. } M_{ij} \text{ or } M_{ji} \left(1 + \frac{50}{L + 125}\right) \tag{66}$$

Simultaneous transverse shear in member IJ under this state is given by

$$Q_{ij} = \frac{\text{Max. Total } M_{ij} \text{ or } M_{ji} + \text{Simul. Total } M_{ji} \text{ or } M_{ij}}{L_{ij}} \tag{67}$$

Governing Maximum Design Stress State

Under usual conditions, especially when the truss members are slender and light, the state under maximum axial-stress loadings will govern the design. But if the members are extremely short and heavy and the joints are enormously rigid, the state under maximum end-moment loadings may require a larger section. To be absolutely sure, both states of stress should be analyzed and compared by the sections required.

Summary of End Moments, Shears, and Unit Fiber Stresses

A summary of end moments, shears, and unit fiber stresses is given in Table 14 for all members of the three-span continuous highway bridge truss. Values are tabu-

TABLE 14

SUMMARY OF MAXIMUM STRESS STATES

		Maximum Axial-Stress Loading					Maximum End-Moment Loading				
Member	M. at End	M. (kips-in.)	Max. Axial Stress (ksi)	Bend. Stress (ksi)	Max. Fiber Stress (ksi)	Shear (kips)	M. (kips-in.)	Max. Bend. Stress (ksi)	Axial Stress (ksi)	Max. Fiber Stress (ksi)	Shear (kips)
Lower chord:											
ab	a	-37.88					-37.99				
	b	-68.80	9.28	1.61	10.89	-0.394	-69.20	1.62	8.86	10.48	-0.396
bc	b	61.10	9.28	1.43	10.71	0.240	64.70	1.51	7.16	8.67	0.298
	c	3.70					16.10				
cd	c	-9.63					-19.53				
	d	-82.87	11.00	1.94	13.03	-0.343	-85.17	1.99	10.32	12.31	-0.398
de	d	91.60	11.04	2.14	13.18	0.553	92.40	2.16	10.32	12.48	0.553
	e	57.71					56.80				
ef	e	6.83	-7.31	-0.16	-7.47	0.001	-14.91				
	f	-6.47					-44.43	-1.04	-3.16	-4.20	-0.220
fg	f	21.79					52.91				
	g	103.58	-7.31	-2.42	-9.73	0.465	135.00	-3.15	-5.18	-8.33	0.697
gh	g	-103.22	-5.86	-2.41	-8.27	-0.477	-136.20	-3.18	-4.06	-7.24	-0.715
	h	-25.73					-56.90				
hi	h	7.85	-5.86	-0.18	-7.74	0.009	48.41	-1.13	-2.49	-3.62	0.249
	i	-5.47					18.82				
ij	i	-65.26					-67.92				
	j	-105.75	12.10	2.47	14.57	-0.635	-106.09	2.48	11.13	13.61	-0.645
jk	j	100.89	12.06	2.36	14.42	0.551	101.86	2.38	11.39	13.77	0.392
	k	47.86					48.97				
Upper chord:											
BC	B	-23.98					-23.98				
	C	-84.34	-8.82	-1.01	-9.83	-0.401	-84.34	-1.01	-8.82	-9.83	-0.401
CD	C	-12.57	-8.82	-0.25	-9.07	-0.120	83.86	-1.00	-8.10	-9.10	0.296
	D	-19.75					-3.98				
DE	D	43.10	-4.19	-0.51	-4.19	0.032	59.21	-0.71	-3.21	-3.92	0.181
	E	-34.39					-10.27				
EF	E	53.77					54.93				
	F	47.26	-4.19	-0.95	-5.14	0.374	50.49	-1.02	-3.50	-4.52	0.389
FG	F	33.82					44.46				
	G	147.04	13.04	1.76	14.80	0.669	150.06	1.80	12.88	14.68	0.720
GH	G	-149.31	13.04	1.78	14.82	-0.738	-151.45	1.81	12.84	14.65	-0.768
	H	-49.98					-56.17				
HI	H	-52.36	-4.83	-1.05	-5.88	-0.392	-59.96	-1.21	-3.71	-4.92	-0.416
	I	-53.51					-52.46				
IJ	I	32.84					10.66				
	J	-59.90	-4.83	-0.72	-5.55	-0.100	-76.06	-0.91	-3.47	-4.38	-0.242
JK	J	51.79	-9.98	-0.62	-10.60	0.153	54.49	-0.65	-9.26	-9.91	0.175
	K	-10.35					-7.33				
Vert.:											
Bb	B	5.06					12.60				
	b	6.97	8.31	0.76	9.07	0.045	14.16	1.54	3.63	5.17	0.099
Cc	C	0.96					6.61				
	c	0.96	-0.51	-0.13	-0.65	0.007	6.92	-0.95	-0.51	-1.46	0.048
Dd	D	-7.71					12.88				
	d	-8.16	8.37	0.89	9.26	-0.054	13.63	1.48	5.14	6.62	-0.090
Ee	E	-15.68	-0.45	-1.41	-1.86	-0.095	-26.53	-2.39	-0.45	-2.84	-0.163
	e	-13.51					-23.89				
Ff	F	-13.57					-18.12				
	f	-14.89	8.32	1.62	9.94	-0.088	-20.05	2.18	3.79	5.97	-0.118
Gg	G	1.19	-0.33	-0.11	-0.44	0.007	5.72	-0.52	0.33	-0.85	0.034
	g	1.09					5.61				
Hh	H	12.86					17.60				
	h	14.25	8.41	1.55	9.96	0.079	19.53	2.12	5.16	7.28	0.109
Ii	I	14.59	-0.49	-1.31	-1.80	0.079	24.69	-2.22	-0.49	-2.71	0.136
	i	12.56					22.22				
Jj	J	3.82					4.53				
	j	4.70	8.33	0.51	8.84	0.024	5.57	0.61	7.56	7.17	0.029
Kk	K	0.00	-0.47	0.00	-0.47	0.000	0.54	-0.05	-0.47	-0.52	0.003
	k	0.00					0.51				
Diag.:											
aB	a	-42.55	-9.47	-0.86	-10.33	-0.143	-42.55	-0.86	-9.47	-10.33	-0.143
	B	-11.99					-11.99				
Bc	B	8.68	8.43	0.38	8.81	0.014	9.54	0.42	7.73	8.15	0.029
	c	-3.53					1.71				
cD	c	3.87					0.47				
	D	-10.22	6.61	0.45	7.06	-0.016	-12.42	0.55	3.69	4.24	-0.028
De	D	-1.00					-6.83				
	e	-24.26	-10.02	-0.57	-10.59	-0.063	-27.04	-0.63	-9.04	-9.67	-0.085
eF	e	-22.48					-20.34				
	F	-23.93	12.65	0.50	13.15	-0.110	-28.59	0.60	11.66	12.26	-0.116
Fg	F	-42.85					-42.21				
	g	43.03	-10.29	-0.66	-10.95	0.0004	54.52	-0.84	-8.55	-9.39	0.029
gH	g	-41.07					-39.34				
	H	53.18	-10.46	-0.64	-11.10	0.028	60.35	-0.72	-10.28	-11.00	0.046
Hi	H	29.06	13.44	0.61	14.05	0.115	32.60	0.68	12.82	13.50	0.134
	i	21.42					25.80				
iJ	i	26.64	-8.78	-0.56	-9.34	0.051	29.25	-0.61	-8.25	-8.86	0.051
	J	-4.26					-6.76				
Jk	J	20.86	5.46	0.49	5.95	0.043	26.26	0.61	2.19	2.80	0.059
	k	-1.92					-0.10				

TABLE 15

MAXIMUM BENDING STRESSES IN STRUT VERTICALS

Member	End	Max. Axial-Stress Loading[a]	Max. End-Moment Loading[b]
Cc	C	25.5	119
	c		127[c]
Ee	E	316[c]	52.7
Gg	G	33.3	93.2
Ii	I	267	49.7
Kk	K	0	10.6
	k		

[a] Bending stress in percent of maximum axial stress.

[b] Maximum fiber stress (%) over that due to maximum axial-stress loading.

[c] Highest.

lated for two maximum-stress states: (a) under maximum axial-stress loading—maximum axial stress and simultaneous bending stress, and (b) under maximum end-moment loading—maximum bending stress and simultaneous axial stress. Simultaneous shears are given for each stress state. Average and maximum shearing stresses may be obtained by established methods.

Discussion of Results

In Table 14 are underlined the larger of the maximum fiber stresses which should govern the design of the 39 members in one-half of the truss under each of the maximum stress loadings. Although for two members, both maximum stress states produce identical maximum fiber stresses, the maximum axial-stress loading (or state) produces the larger maximum fiber stress in 31 members, and there are as many as six members whose maximum fiber stresses are governed by the maximum end-moment loading (or state) conditions.

The hypothesis previously advanced that the governing state is that of maximum bending stress (maximum secondary stress) and simultaneous axial stress and shearing stress is fully substantiated. In the three-span continuous truss under analysis, the following observations are pertinent:

1. Highest bending stresses (secondary stresses) occur in strut verticals Cc, Ee, Gg, Ii, and Kk (Table 15). In all these strut verticals, maximum end-moment loadings govern. The extraordinarily high bending stresses in these strut verticals would be very serious if these members were not governed by minimum size or slenderness ratio requirements.
2. Bending stresses in hangers increase toward the intermediate supports and reach a maximum of 19.5 percent in Ff of their maximum axial stresses. Maximum axial-stress loadings invariably govern. Bending stresses in these members are generally lower than those in strut verticals.
3. Among compression diagonals, the end posts aB and a'B' have the higher bending stresses which, however, amount to only 9.1 percent of their maximum axial stresses. Both maximum axial-stress and end-moment loadings produce identical results.
4. Among tension diagonals, those nearest the center of the middle span have the higher bending stresses which amount to only 9.0 percent of their maximum axial stresses under loadings for these stresses.
5. Among upper chords, the end upper-chord members BC and B'C' have the higher bending stresses at their inner ends, which amount to 11.5 percent of their maximum axial stresses. Both maximum axial-stress and maximum end-moment loadings produce the same results. The next upper-chord members, CD and C'D', are governed by the maximum end-moment loadings, but their maximum fiber stresses under these loadings are only 0.3 percent over those produced by the maximum axial-stress loadings.
6. Among the lower chords in this continuous truss, those in compression adjacent to the intermediate supports have medium-high bending stresses, i.e., 33.1 percent in fg and f'g', and 41.1 percent in gh and g'h' where g and g' are intermediate supports. Both members are governed by the maximum axial-stress loadings.
7. These stress observations apply only to vertical loadings of the continuous truss under analysis. Bending stresses would be increased when both chord members are analyzed to transmit wind loads (centrifugal forces) resisted by upper and lower lateral systems or when verticals and end posts are analyzed to transmit sway portal action due to lateral loads.

It is thus clear that in the design of any important structure, in any critical design, or in any important investigation, bending (or secondary) stresses in rigidly connected trusses should never be taken as negligible, nor should maximum axial stress plus simultaneous bending stress be assumed as adequate to dictate a safe design.

AUTOMATIC LOGICAL CHECKS

The development up to this point has been in proper logical sequence which allows an automatic computation program to be written from a few basic parameters (span lengths, panel lengths, truss heights, roadway width, median-divider width, sidewalk width, live load, impact-fraction formula, modulus of elasticity, and Poisson's ratio) for maximum design axial stresses and simultaneous end moments, or maximum end moments and simultaneous axial stresses, with simultaneous transverse shears.

Individual programs must be written for each particular electronic digital computer in its most efficient machine language and must be adapted by the individual engineer and programmer to their own machine. To include any specific program would be extraneous to this basic investigation and would detract from its importance.

However, for the sake of helping those who are going to apply the proposed method and associated techniques, some intermediate, sub-final, and final automatic logical checks are given. To provide more general applicability, an indeterminate highway bridge truss of the continuous type will be assumed as the hypothetical analysis to be programmed.

Accuracy Desired

As is inherent in any indeterminate structural analysis, the terms and coefficients involve very small linear and angular displacements and their arithmetic operations. The solution involves rather large sets of simultaneous equations. Unless more significant figures are retained in the initial and intermediate stages, the final answers may not have a three-figure accuracy. For instance, the subtraction of two eight-digit figures differing by the last three digits would become zero if only five digits were kept, and the solution of a large set of simultaneous equations would generate large rounding-off errors. For this reason, it is not only desirable, but even imperative, to use as many digits as the available computer can accommodate.

Logical Checks

Intermediate, sub-final, and final answers should be strategically checked by logical criteria, either mathematical, statical, or according to conservation of energy. At any stage of the machine computation, logical checks can be devised and incorporated into the program; typing out the checking indication may be programmed. In any plane truss, for instance:

1. Computation of lengths of inclined members may be carried out by any process but the results must conform to the Pythagorean rule:

$$a^2 + b^2 = c^2 \tag{68}$$

2. Reactions may be determined by any determinate or indeterminate methods, as the case may be, but they must satisfy statical requirements:

$$\left.\begin{aligned} \Sigma X &= 0 \\ \Sigma Y &= 0 \end{aligned}\right\} \tag{69}$$

where X and Y include, respectively, all horizontal and vertical components of all applied loads and reactions if the entire truss is considered, or of all applied loads and reactions on one side of a section and all stresses on the same side of the same section if such a section is under consideration.

3. Moments may be determined in any way that is expedient, but

$$\Sigma M = 0 \tag{70}$$

must hold when moments are taken about any joint, or about any point through any section.

4. To test for correct internal strain energy, its total must be a minimum, that is

$$\frac{\partial U}{\partial X} = 0 \tag{71}$$

A change from negative to positive implies that nature does not do any foolish work or any more than the minimum or least work.

5. In axial-stress computation with parallel chords at least in center panels, unless the center vertical is a hanger in a pony or through truss or a strut in a deck truss, its live-load axial stress (corresponding to primary stress) must be zero, or

$$N_{Oo} = 0 \tag{72}$$

where O and o are, respectively, upper and lower center joints.

6. For end joint equilibrium, under the present lane loading with shear concentration much larger than moment concentration, the compressive stress in the end-post is governed by shear, and hence, the maximum stress in the end segment of the lower chord in a through truss will not be governed by maximum moment, but by

$$\text{Max. } N_{ab} = -\text{Max. } N_{aB} \frac{L_{ab}}{L_{aB}} \tag{73}$$

where a and B, respectively, denote end and hip joints, and b the lower joint of the first hanger.

7. At all T-shape joints, e.g., j or J, chord stresses (corresponding to primary stresses) are always equal, i.e.,

or

$$\left.\begin{aligned} N_{ij} &= N_{jk} \\ N_{IJ} &= N_{JK} \end{aligned}\right\} \tag{74}$$

8. With the simplified energy method, all axial stresses, N, should check with the primary stresses, S, by the conventional method, i.e.,

$$N_{ij} = S_{ij} \tag{75}$$

where ij denotes any member.

9. With the exact energy method, the resulting exact N's are in equilibrium under the principle of extended methods of moments, shears, and joints, i.e., when all components of N, M, Q are considered, or

$$F(N, M, Q) = 0 \tag{76}$$

10. With the simplified energy method, all bending stresses, f, should check with the secondary stresses, s, by any of the classical methods, i.e.,

$$\left.\begin{aligned} f_{ij} &= s_{ij} \\ f_{ji} &= s_{ji} \end{aligned}\right\} \quad (77)$$

11. With the energy method, either exact or simplified, all bending stresses, f, should satisfy Eq. 72, a criterion for minimum internal strain energy, or least work of deformation, in conformity with which nature works.

12. In the method of panel-load superposition, when the panel load is replaced by unity, the summation of reactions, R, should give

$$\Sigma R = 1 \quad (78)$$

13. With any method of inversion for solving any set of nonhomogeneous linear equations, unless the matrix is singular, i. e.,

$$|a_{ij}| = 0,$$

$$\left[a_{ij}\right]^{-1} \left[a_{ij}\right] = U \quad (79)$$

In European usage, U is denoted as E or I.

14. An overall check of all independent, i, and dependent, d, unknown end moments, M_i and M_d, is given by

$$\Sigma M_i = -\Sigma M_d \quad (80)$$

15. In general, maximum design N, M, Q for all members meeting at a joint or acting through a section give the inequalities:

$$\begin{bmatrix} \Sigma X \\ \Sigma Y \\ \Sigma M \end{bmatrix} \neq \begin{bmatrix} 0 \\ 0 \\ 0 \end{bmatrix} \quad (81)$$

No attempt should ever be made to check the results in this manner.

Other logical check criteria may be added as suggested by the premises of a particular problem.

CONCLUSIONS

The entire investigation stands for its full justification on the ground that:

1. Engineers have been aware of the "illogical (loath to use the word 'wrong') assumption" in analyzing "rigidly connected trusses" as "frictionlessly pin-connected" for 85 years; why then should the status quo be indefinitely continued by any progressive engineer except the ignorant?
2. Nature has never made the artificial distinction between "primary stresses" and "secondary stresses" as the prevalent engineering parlance has labeled them; they exist by their very nature as axial stresses, bending stresses, and shearing stresses; why then should this misnomer not be dispelled?
3. With the larger versions of modern electronic computers, rigidly connected trusses can be analyzed as a chain of rigid frames in its true nature by the proposed method and associated techniques in not over a few minutes difference in time as compared with the conventional methods; why then should engineers continue to use nineteenth-century methods?

Suffice it to state only a few without exhausting the enumeration.

On the ground as firm as this, the investigators have proceeded:

1. To expound a new exact matrix-energy method for analyzing all stresses in rigidly connected trusses (exact, for the method is compatible with the nature-behavior of any physical system), this being the rational approach for refined analysis required in critical designs or investigations;
2. To synthesize the elegance and efficacy of matrix algebra founded by Authur Cayley with the necessary compatible condition of minimum strain energy in elastic structures propounded by Alberto Castigliano, their technological union constituting the most powerful tool in structural analysis, especially in this electronic age and when the coefficient matrix is symmetrical as proved in Appendix A;
3. To deduce a simplified matrix-energy method for analyzing all stresses in rigidly connected trusses to minimize time and effort for ordinary engineering purposes;
4. To set forth the extended methods of moments, shears, and joints, so that strain-energy expressions of the truss members will be compatible with the exact matrix-energy method expounded;
5. To demonstrate the truth in the validity and thoroughness of the exact matrix-energy method in the case of a determinate truss by comparing results with previous authorities;
6. To reveal the closeness and dependability of the simplified matrix-energy method, again in the case of a determinate truss, by comparing results with previous authorities;
7. To advance the method of panel-load superposition for continuous trusses in lieu of the classical influence-line method of Müller-Breslau, this method being especially adapted to longer span bridges where lane loading plus concentrations govern as a rule;
8. To resort to the method of substitution of an unsymmetrical loading by a set of symmetrical loading and a conjugate set of antisymmetrical loading, as a powerful analytical tool to reduce 2n unknowns to n unknowns, which is indispensable in using the smaller versions of computers;
9. To introduce further a method of transformation from one type of many more unknowns to another type of many fewer unknowns, which enables the solution of a still larger set of equations in a much smaller computer as demonstrated in Appendix B;
10. To elucidate the problem of solving very large sets of simultaneous equations, with reference also to four matrix methods developed by the principal investigator;
11. To apply the proposed simplified matrix-energy method and relevant techniques set forth above to the analysis of a three-span continuous highway bridge truss with inclined upper chords, and to demonstrate the validity and accuracy of the results vs those of the Montana State Highway Commission;
12. To pronounce that the methods advanced make it possible and expedient to determine two maximum stresses states: (a) maximum axial stress plus the larger simultaneous bending stress and simultaneous transverse shear, and (b) the larger of the maximum bending stress plus simultaneous axial stress and simultaneous transverse shear;
13. To indicate that either of these two stress states has the same frequency of occurrence, and that either has the likelihood to dictate the larger requirement for the section of a member; hence,
14. To conclude that either of these two stress states may govern the design, and that both should be computed in cases of important critical designs and investigations; and
15. To establish automatic logical checks for programmed electronic computation throughout its initial, intermediate, sub-final, and final stages.

ACKNOWLEDGMENTS

This research was instituted through a grant from the China Foundation for the Promotion of Education and Culture, and continued through a research subsidy from the South Dakota Department of Highways and U. S. Bureau of Public Roads. The general data for the Wolf Creek Bridge were furnished by Fred Quinnell, Jr., and Albert W. Jones, Montana State Highway Commission.

REFERENCES

1. Manderla, Heinrich. Welche Spannungen entstehen in den Streben eines Fachwerks dadurch, dass die Winkel der Fachwerkdreieck durch die Belastung eine Änderung erleiden? Preisarbeit, Jahresbericht der Technischen Hochschule München, p. 18, 1878-1879.
2. Ménabréa, L. F. A memoir presented to the Academy of Sciences, Turin, 1857.
3. Castigliano, Alberto. Nuova teoria interno dell'equilibrio dei sistemi elastici. Atti delle Academia delle Scienze, Torino, 1875.
4. Maxwell, James Clark. On the Calculation of the Equilibrium and the Stiffness of Frames. Phil. Mag., Series 4, Vol. 27, p. 294, 1864.
5. Li, Shu-t'ien. Converging Matric Algorisms for Solving Systems of Linear Equations. Trans. Nov. 1962 Conv. of Chinese Assoc. for the Advancement of Sci., Taipei, Vol. 1, pp. 16-22, Nov. 1962.
6. Sutherland, Hale, and Bowman, H. L. Structural Theory. 4th Ed., pp. 351-357. New York, John Wiley and Sons, Inc., 1961.
7. Parcel, John I., and Moorman, Robert B. B. Analysis of Statically Indeterminate Structures. Pp. 336-337. New York, John Wiley and Sons, 1962.
8. Richardson, M. College Algebra. Alt. Ed., pp. 475-477. Englewood Cliffs, N. J., Prentice-Hall, Inc., 1958.
9. Marcus, Marvin. Basic Theorems in Matrix Theory. Nat. Bureau of Standards Appl. Math. Ser. 57. Washington, D. C., U. S. Govt. Print. Office, 1960.
10. Householder, Alston S. Principles of Numerical Analysis. New York, McGraw-Hill, 1953.
11. Li, Shu-t'ien. Applied Determinants and Matrices. Limited issue of lecture notes, 1960.
12. Southwell, R. V. Stress-Calculation in Frameworks by the Method of "Systematic Relaxation of Constraints"—I, II, and III. Proc. Royal Soc., Ser. A, No. 872, Vol. 151, pp. 56-95, Aug. 1, 1935; No. 878, Vol. 153, pp. 41-76, Dec. 2, 1935.
13. Müller-Breslau, H. F. B. Die Neuren Methoden der Festigkeitslehre und der Statik der Baukonstruktionen. Berlin, 1886.

Appendix A

INDEPENDENT PROOF FOR SYMMETRY OF COEFFICIENT MATRIX

By generalizing the n unknowns in the matrix-energy method as the column vector $\{X_i\}$, it is seen, from the extended methods of moments, shears, and joints for determining the axial stress in each member of the truss, that the axial stress N_{ij} of any member IJ is represented by

$$N_{ij} = \Sigma q_i X_i + S_{ij} \tag{82}$$

where q_i is the coefficient of the unknown X_i, and S_{ij} corresponds to the conventional primary stress in member IJ.

Knowing the expression of N_{ij}, we conclude, from Eqs. 5 and 6, that the expression of the total strain energy, U, of a given loaded truss is an algebraic expression of the second degree in $\{X_i\}$. After collecting like terms in the expression of U, the total strain energy becomes

$$U = \Sigma c_{ii} X_i^2 + \Sigma c_{ij} X_i X_j + \Sigma c_i X_i + p \tag{83}$$

where c_{ii} is the coefficient of X_i^2, c_{ij} is the coefficient of $X_i X_j$, c_i is the coefficient of X_i, p is the constant term, and $i \neq j$.

By Castigliano's second theorem, we have

$$\frac{\partial U}{\partial X_i} = 0 = 2c_{ii}X_i + c_{ij}X_j + \Sigma\, c_{ik}X_k + c_i \tag{84}$$

and

$$\frac{\partial U}{\partial X_j} = 0 = 2c_{jj}X_j + c_{ij}X_i + \Sigma\, c_{kj}X_k + c_j \tag{85}$$

where c_{ik}, c_{jj}, c_{kj}, and c_j are, respectively, the coefficients of X_iX_k, X_j^2, X_kX_j, and X_j in the expression of U; and $i \neq k \neq j$. Therefore, if a_{ij} is the coefficient X_j in the equation obtained from $\frac{\partial U}{\partial X_i} = 0$, and a_{ji} is the coefficient of X_i in the equation obtained from $\frac{\partial U}{\partial X_j} = 0$, Eqs. 84 and 85 yield

$$a_{ij} = a_{ji} = c_{ij} \tag{86}$$

Eq. 86 implies that if the equation obtained from $\frac{\partial U}{\partial X_i} = 0$ is arrayed in the i th row of the set of simultaneous equations, the coefficient matrix $[a_{ij}]$ is always symmetrical about its main diagonal.

Appendix B

DEMONSTRATION OF IDENTICAL RESULTS

The purpose of this demonstration is to show that (a) the simplified matrix-energy method yields identical results as (b) the simplified Manderla's method, (c) the completely transformed energy method, and (d) the partially transformed energy method.

For the sake of mere demonstration, a very simple rigidly connected truss has been chosen as shown in Figure 14 with all dimensions and section properties indicated. The problem is to determine the unknown end moments in all truss members by these four methods and compare their results.

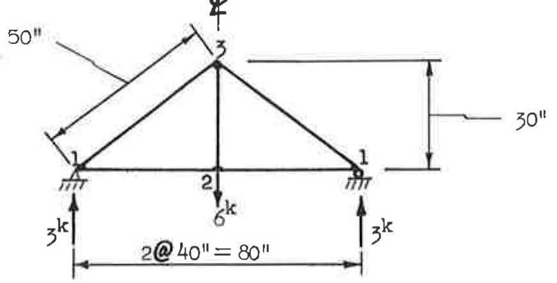

All A = 1 in^2

All I = 10 in^4

Figure 14.

Solution by Simplified Matrix-Energy Method

1. Choice of Independent Unknowns—The three statically independent unknowns are

$$\lfloor M_{12} \quad M_{21} \quad M_{31} \rfloor = \lfloor X_1 \quad X_2 \quad X_3 \rfloor$$

2. Determination of Axial Stresses—Axial stresses are determined by using the extended methods of moments, shears, and joints. Thus, for N_{12}, taking the free body diagram to the left of member 2-3, by $\Sigma M_3 = 0$, we have

$$\lfloor -N_{12} \quad X_2 \quad X_3 \quad 3 \rfloor \{30 \quad 1 \quad 1 \quad 40\} = 0$$

from which

$$N_{12} = 0.03\,(X_2 + X_3) + 4$$

Similarly,

$$N_{13} = -0.015X_1 - 0.0416X_2 - 0.026X_3 - 5$$

and

$$N_{23} = 0.05(X_1 + X_2) + 6$$

3. Tabulation of Constants for Strain-Energy Expressions:

Member	L/A	L/16
1-2	40	0.6
1-3	50	0.83
2-3	30	0.5

4. Formulation of Strain Energy:

$$E\,U = \sum\left[\frac{1}{2}\,\frac{L_{ij}}{A_{ij}}\,N_{ij}^2 + \frac{L_{ij}}{6I_{ij}}\left(M_{ij}^2 - M_{ij}\,M_{ji} + M_{ji}^2\right)\right]$$

Specific equations are given in Table 16.

5. Simultaneous Equations and Their Solution—Three simultaneous equations will be formed by taking partial derivatives of one-half the strain energy in the truss with respect to each independent unknown as stated in the simplified matrix-energy method. For example,

$$\frac{1}{2}E\,\frac{\partial U}{\partial X_1} = 0 = 0.6(2X_1 - X_2) + 50(-0.015)(-5) +$$

$$0.83(2X_1 + X_3) + \frac{1}{2}(30)(0.05)(6)$$

TABLE 16

Member	E Times Strain Energy
1-2	$\frac{1}{2}(40)\left[0.03(X_2 + X_3) + 4\right]^2 + 0.6(X_1^2 - X_1X_2 + X_2^2)$
1-3	$\frac{1}{2}(50)\left[-0.015X_1 - 0.0416X_2 - 0.026X_3 - 5\right]^2 + 0.83(X_1^2 + X_1X_3 + X_3^2)$
2-3	$\frac{1}{2}(30)\left[0.05(X_1 + X_2) + 6\right]^2 + 0$
	Use only one-half of the strain energy in this member by virtue of symmetry.

After taking similar derivatives with respect to X_2 and X_3, the following matrix equations result:

$$\begin{bmatrix} 3 & -0.6 & 0.83 \\ -0.6 & 1.3 & 0 \\ 0.83 & 0 & 1.6 \end{bmatrix} \begin{bmatrix} X_1 \\ X_2 \\ X_3 \end{bmatrix} = -\begin{bmatrix} 8.25 \\ 20.25 \\ 12 \end{bmatrix}$$

Being non-singular, the matrix has the solution:

$$\lfloor X_1 \quad X_2 \quad X_3 \rfloor = -\lfloor 5.5 \quad 17.9375 \quad 4.45 \rfloor$$

Solution by Simplified Manderla's Method

1. Unknowns—The same unknown moment vector $\lfloor X_1 \quad X_2 \quad X_3 \rfloor$ used in the energy method will be found here. Since these unknowns may be expressed in terms of tangent rotations, they result in one unknown reference τ vector $\lfloor \tau_{12} \quad \tau_{21} \quad \tau_{31} \rfloor$ at joints 1, 2, and 3. Using τ and $\Delta\alpha$ as defined for the method of transformation, the $\Delta\alpha$'s may be evaluated by the usual angle change formula. Thus,

$$E\,\Delta\alpha_{13} = \left\lfloor \left(f_a - f_b\right) \quad \left(f_a - f_c\right) \right\rfloor \left\{\cot\gamma \quad \cot\beta\right\}$$

where f is the unit stress and $\lfloor \alpha\ \beta\ \gamma \rfloor$ and $\lfloor a\ b\ c \rfloor$ are as defined in Figure 15.

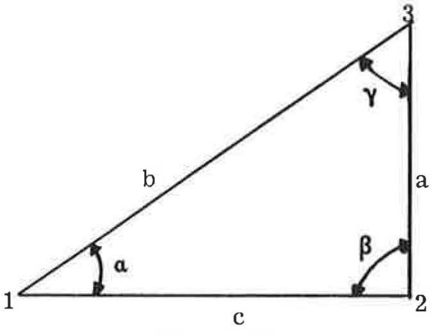

Figure 15.

2. Tabulation of Unit Stresses:

Member	N/A (ksi)
3-1′, 1-3	-5.0
2-1′, 1-2	4.0
2-3	6.0

3. Expressing All τ's in Terms of Reference τ's—In joint 1, the reference τ is τ_{12}. Then,

$$E\,\Delta\alpha_{13} = \lfloor (6 + 5) \quad (6 - 4) \rfloor \begin{Bmatrix} \frac{3}{4} & 0 \end{Bmatrix} = 8.25$$

Therefore, at joint 1,

$$E\begin{bmatrix} \tau_{12} \\ \tau_{13} \end{bmatrix} = \begin{bmatrix} E\tau_{12} \\ E\tau_{12} + 8.25 \end{bmatrix}$$

At joints 2 and 3, by symmetry,

$$E\begin{bmatrix} \tau_{23} \\ \tau_{32} \end{bmatrix} = \begin{bmatrix} 0 \\ 0 \end{bmatrix}$$

Applying the angle change formula, we have then:

$$\begin{array}{cc} \text{At joint} & \text{At joint} \\ 2 & 3 \end{array}$$

$$E\begin{bmatrix} \tau_{21} & \tau_{31} \\ \tau_{23} & \tau_{32} \\ \tau_{21} & \tau_{31} \end{bmatrix} = \begin{bmatrix} 20.25 & -12 \\ 0 & 0 \\ -20.25 & 12 \end{bmatrix}$$

4. Formulation of Equations and Evaluation of Unknown End Moments—The unknown end moments may be expressed as a function of τ's; thus,

$$X_k = M_{ij} = \frac{2EI_{ij}}{L_{ij}}\left(2\tau_{ij} + \tau_{ji}\right)$$

By joint equilibrium, at joint 1,

$$\Sigma M_{ij} = 0 = M_{12} + M_{13}$$

where j represents far end joints. On substituting M_{ij} in terms of τ's, we get

$$\frac{2(10)}{40}\left(2E\tau_{12} - 20.25\right) + \frac{2(10)}{50}\left[2\left(E\tau_{12} + 8.25\right) - 12\right] = 0$$

from which

$$E\tau_{12} = 4.625$$

All the unknown end moments may now be found by back substitution, resulting in:

$$\begin{bmatrix} X_1 \\ X_2 \\ X_3 \end{bmatrix} = -\begin{bmatrix} 5.5 \\ 17.9375 \\ 4.45 \end{bmatrix}$$

These results are identical with those of the energy method.

It should be noted that due to inherent simplicity, no simultaneous equations need be solved here in using Manderla's method. An unsymmetrical truss under any loading will result in a set of n equations in n unknowns, where n equals the number of joints in the truss.

Solution by Method of Complete Transformation

In this method, the unknown end moments will be written in terms of τ. There result, in this particular case, three equations involving one unknown τ_{12}. Any one of these equations will yield the correct value of $E\tau_{12}$.

1. End Moments as Functions of τ:

$$\begin{bmatrix} X_1 \\ \\ X_2 \\ \\ X_3 \end{bmatrix} = \begin{bmatrix} M_{12} \\ \\ M_{21} \\ \\ M_{31} \end{bmatrix} = 2 \begin{bmatrix} \frac{10}{40}\left[2(E\tau_{12}) - 20.25\right] \\ \\ \frac{10}{40}\left[2(-20.25) + E\tau_{12}\right] \\ \\ \frac{10}{50}\left[2(-12) + (E\tau_{12} + 8.25)\right] \end{bmatrix}$$

2. Transformation of Energy Equations—Making use of these equations, the set of simultaneous equations of the matrix-energy method may be transformed into a new set as functions of the mono-unknown $E\tau_{12}$:

$$\begin{bmatrix} 3 & -0.6 & 0.83 \\ -0.6 & 1.3 & 0 \\ 0.83 & 0 & 1.6 \end{bmatrix} \overset{\displaystyle X_i}{\overset{\shortparallel}{\begin{bmatrix} E\tau_{12} - 10.125 \\ 0.5\, E\tau_{12} - 20.25 \\ 0.4\, E\tau_{12} - 6.3 \end{bmatrix}}} = -\begin{bmatrix} 8.25 \\ 20.25 \\ 12 \end{bmatrix}$$

The solution of any one of these equations yields $E\tau_{12} = 4.625$. Back substitution into the column vector X_i yields:

$$\lfloor X_1 \quad X_2 \quad X_3 \rfloor = -\lfloor 5.5 \quad 17.9375 \quad 4.45 \rfloor$$

which are identical with the results of the simplified energy method and the simplified Manderla's method.

There is no advantage in using the completely transformed energy method since, after the end moments have been expressed in terms of the reference τ's, it is much easier to obtain relations between the end moments by using joint equilibrium equations than by using the simplified energy method.

Solution by Method of Partial Transformation

This method becomes useful in case it is necessary to reduce the number of simultaneous equations by a small number so that an existing program may be used.

The number of unknowns that will be reduced by substituting for part of X_i's depends on the configuration of the truss and the end moments chosen as unknowns. In the present simple case, X_1 and X_3 will be transformed resulting in two simultaneous equations with $E\tau_{12}$ and X_2 as unknowns, thus

$$\begin{bmatrix} 3 & -0.6 & 0.83 \\ -0.6 & 1.3 & 0 \end{bmatrix} \overset{\displaystyle X_i}{\overset{\|}{\begin{bmatrix} E\tau_{12} - 10.125 \\ X_2 \\ 0.4\ E\tau_{12} - 6.3 \end{bmatrix}}} = -\begin{bmatrix} 8.25 \\ 20.25 \end{bmatrix}$$

which by simplification becomes:

$$\begin{bmatrix} 10 & -2 \\ -2 & 4 \end{bmatrix} \begin{bmatrix} E\tau_{12} \\ X_2 \end{bmatrix} = \begin{bmatrix} 82.125 \\ -81 \end{bmatrix}$$

whose solution gives

$$\lfloor E\tau_{12} \quad X_2 \rfloor = \lfloor 4.625 \quad -17.9375 \rfloor$$

By back substitution into the X_i vector, the complete solution becomes

$$\lfloor X_1 \quad X_2 \quad X_3 \rfloor = -\lfloor 5.5 \quad 17.9375 \quad 4.45 \rfloor$$

which is identical with all preceding solutions.

Conclusions

This demonstration has conclusively shown that the simplified energy method yields results identical with the simplified Manderla's method which is the forerunner of the modern slope-deflection method. Thus, the simplified energy method has the same accuracy as the classical methods in the determination of secondary stresses, but it has dispensed with the unjustified assumption of analyzing rigidly connected trusses as ideally pin jointed in the determination of primary stresses, especially if its exact counterpart is applied.

It has also been demonstrated that the completely transformed and the partially transformed energy methods are equally valid, and each has its particular usefulness in reducing more or less unknowns to enable solution of a larger set of equations by a smaller computer.

Design of Aluminum Sign Structures By Electronic Computation

RUDOLPH HOFER, JR., and ALAN H. KNOLL
Aluminum Company of America

The design of overhead sign structures offers an ideal application for electronic computation because the efficiency of a computer is best utilized in the design of similar structures having a great variety of design loading conditions. This type of design work done by slide rule represents the ultimate in inefficient use of design talent.

In setting up a computer program, various suitable geometric configurations are considered for any given combination of span length and wind loading. The computer calculates the force in each member and then selects the lightest available section permitted by specifications. The total metal cost is calculated; this and a calculated fabrication cost make up the estimated total cost of the structure. It is then possible to select a truss for any span length and loading condition which has the correct configuration for the most economical balance of metal and fabrication costs.

•IN 1961 the American Association of State Highway Officials (AASHO) adopted "Specifications for the Design and Construction of Structural Supports for Highway Signs." These specifications, written by a joint AASHO-ARBA Committee, contain allowable design stresses for wrought aluminum alloys 6061-T6, 6062-T6, and 6063-T6 and for aluminum casting alloys 356-T6 and 356-T7. These specifications provide, for the first time, a recognized design and construction code for design and specifying agencies throughout the United States.

The AASHO specifications were adopted to provide for safe, reliable structures and to permit the standardization of designs. Standard designs afford the fabricator the advantages of carrying a minimum number of shapes in inventory and of using standard fabrication techniques. This can result in savings not only to the fabricator but also to his customer in the form of better, less expensive structures.

In 1962, Alcoa began a program designed to provide highway departments with a complete set of aluminum sign structure designs covering most conditions of span and loading. The variation in wind loads throughout the country and the range of span lengths and sign areas made this program a monumental task through any means other than by an electronic computer.

Consideration of the various cross-sections of roadways, including such things as median and shoulder width, led to the conclusion that span lengths for bridge-type structures of from 50 to 140 ft would satisfy most requirements. For example, this would provide a structure over a highway varying from four to twelve lanes. Cantilever and butterfly structures having spans of from 15 to 35 ft, measured from centerline of post, were thought to provide a full range of practical sizes for these types of structures.

Sign areas will vary for different structures having the same span length. Increase in sign area is generally in proportion to increase in span length. It was decided that a 50-ft span could carry a sign area as small as 100 sq ft but that it was highly unlikely

---

Paper sponsored by Committee on Bridges.

that a 140-ft span would carry anything smaller than about 400 sq ft and could easily carry as much as 1,000 sq ft of sign area. It was decided to design cantilever and butterfly structures for a sign area covering the full span length and having different sign depths.

The AASHO specifications governing the design of sign structures provide a map that gives the wind speeds in miles per hour for every area of the country. Thus, it is possible to select the design wind load for which a sign structure should be designed. Also provided by the specifications is a map showing the areas of the country in which an ice load is a consideration. Because design wind velocity can vary from 60 mph to a maximum of 120 mph, because only portions of the country are subjected to ice loads, and because some highway departments prefer trusses with walkways, the required number of sign structures can reach well up into the thousands.

Overhead sign structures, subjected to large design wind loads, are generally fabricated as four-chord box trusses. The horizontal-plane trusses carry the wind loads which are applied in either direction; the vertical-plane trusses carry the dead loads, live loads from walkways and ice loads, which are always applied in a downward direction. Consequently, it was decided that the vertical-plane trusses should be Pratt trusses in which the web diagonals normally carry tensile forces. Similarly, it was decided that the horizontal-plane trusses, whose bracing members carry either tension or compression, should be Warren trusses, and the diagonal members should be designed to carry either loading condition. A cost analysis proved these decisions to be economically advantageous.

Another factor of importance, for which a quick solution is possible through the use of a computer, is the correct balance of metal and fabrication costs to arrive at the most economical truss geometry. For example, for any given span length and sign area, the truss cross-section and its number of panel points will have an optimum value. Variation from this optimum will increase the cost of the structure, either in metal cost or cost of fabrication.

By including metal and fabrication costs for different ratios of depth to width of truss for various numbers of panel points, the optimum geometry can be reached. Theoretically, the geometry varies slightly for varying wind loads on any one truss. However, in the interest of standardization, it was deemed advisable to select a constant geometry for all trusses having a given span length, regardless of the wind loading conditions. This geometry was arrived at by trial runs which gave the variation in cost for a fabricated structure having different ratios of width to depth of truss. The selected cross-section and number of panel points per truss were arrived at by choosing the geometry that provided the greatest economy over the entire range of wind loadings. Though this decision will place a small penalty on the theoretical economy for a particular wind loading, it should be more than offset by economy afforded through standardization of fabrication.

Because tubular sections provide a much higher ratio of rigidity to weight of metal than angles or channels, they were chosen to be used for the chords and posts, as well as for the web bracing members. In the case of the chords and posts, this decision was made because these members are designed to resist compressive forces and are subject to column buckling in any plane. Because of the deflection limitations placed on sign structures by the AASHO specifications, and also because of the practical depth of the signs, the trusses have sufficient depth such that the web bracing members are often controlled by limiting values of slenderness ratio and are, therefore, designed on the basis of rigidity rather than stress. Thus, the efficiency of tubular sections is utilized for the entire structure. The more pleasing appearance of tubular members and welded construction is felt to provide an intangible value to the design.

An electronic computer can be used to select, according to such factors, from a list of available sizes the correct tube for each member of a truss. From a practical standpoint, it is desirable to keep the number of tube sizes to a workable minimum so that the fabricator is not faced with the problem of unavailability or of stocking a too-large variety of sizes. In the Alcoa program, trial designs were run in which the computer picked the tube size from a large list included in the input. The designs were then reviewed, with particular attention given to the number of times that each tube was used. The seldom-used sizes were eliminated from the program and the designs were rerun. This resulted in a usable number of tube sizes so that delivery of sections from the mill to the fabricator should not cause unnecessary delay of shipment to the purchaser.

To prepare for a wide variety of sign structure designs, four digital computer programs were written: (a) a program to design the truss portion of bridge-type sign structures, (b) a program to design the supports for bridge-type structures, (c) a program to design the truss portion of cantilever and butterfly-type structures, and (d) a program to design the supports for cantilever and butterfly-type structures. The operation of all four of these programs is basically similar; for purposes of illustration, the details of the program for the design of truss portions of bridge-type structures are described.

The designer begins by selecting a list of tube sections from which he wishes his structure to be fabricated. The properties (diameter, thickness, area, and radius of gyration) of the tubes in this list are fed into the computer. The designer then selects a trial configuration for the structure, including the vertical and horizontal depth of truss and the number of panels in the truss. These are fed into the computer along with the spans, wind load, sign area and estimated values of the deadweight of the structure, ice load on the structure, and area of the structural members exposed to the wind.

The computer proceeds to calculate the design loads for each type of member in the truss. For reasons of simplicity of fabrication and erection, the four chords of the truss are all made identical and of the same section over the entire span length, even though some reduction in section could take place near the ends of the span. Similarly, all diagonals in the vertical faces of the truss are identical, as are the struts in the vertical planes and the diagonals in the Warren trusses in the horizontal planes. In general, the chords are designed by the application of wind and gravity loads producing maximum stress at the center of the span, whereas, the web members in the horizontal and vertical trusses are governed by the shear loads near the ends of the span.

Since the gravity loads from the sign and walkway loadings are applied on one face rather than at the centroid of the truss, the torsional stiffness of a box truss is used to advantage to distribute a portion of this loading to the opposite vertical face. This produces additional shear loads in the horizontal planes of the truss which are accounted for in the design. To insure the torsional rigidity of the box structure, cross diagonals are included at the ends of each shop-assembled section of the truss. These cross diagonals also insure proper fitting of the field chord splices between the subassemblies.

After a design load is calculated for a particular member type, the minimum allowable radius of gyration based on the specification slenderness limit is calculated from the member length. The list of available tube sections is then scanned, starting at the lightest section and proceeding to sections of heavier weight, until a tube is found whose radius of gyration exceeds the calculated minimum radius of gyration. The allowable stress for this trial tube is calculated from the slenderness ratio and the diameter to thickness ratio, using the formulas given in the specification, and is then compared with the actual stress calculated from the design load and the area of the trial tube. If the actual stress exceeds the allowable stress, the trial tube is rejected. The list of tubes is scanned for the next heavier cross-section with an acceptable radius of gyration. This process is repeated until a tube is found whose allowable stress exceeds the actual stress. Because the list of available tubes is searched in order of increasing area and weight, the first section acceptable from a slenderness ratio and stress standpoint is necessarily the lightest tube in the list that can be used. This process is repeated for the chords, the vertical plane diagonals, the vertical plane struts, the horizontal plane diagonals, the horizontal plane struts and, finally, the end cross diagonals. To obtain the maximum economy, the chord and post members have been designed in aluminum alloy 6062-T6 and the web members have been designed in alloy 6063-T6 since they are generally governed by the basis of slenderness rather than strength considerations.

When the lightest acceptable tubes have been selected for each of these members, the dead weight of the truss is calculated. Also calculated are the truss ice load, which is a function of the exposed perimeter of the tubes, and the area of tubular members exposed to the wind. These calculated values of deadweight, ice load and wind area are compared with the corresponding values assumed at the beginning of the design. If any of the three estimates were low, the estimated values are revised and the entire design procedure is repeated. If the estimate for any of the quantities exceeded the calculated value by more than 5 percent, the design may be overly conservative and again the estimates are revised and the design procedure is repeated. The program may go through several cycles of design until the estimated and calculated values for deadweight, ice load and wind area are in agreement. When this point is reached, the estimated cost of the structure is calculated from the weight and unit cost of the metal plus an estimate of the fabrication cost based on the number of joints to be welded.

The following are then punched into a card from the computer memory: (a) the geometry information for the structure, including the span, sign area, vertical truss depth, horizontal truss depth, and number of panels; (b) the loading information, including the applied wind load, the actual dead load of the structure, actual ice load on the structure and actual area of the structures exposed to the wind; (c) the tube size for each of the member types; and (d) the calculated cost of the structure. The information on the card is provided to the designer on a printed sheet.

By selecting several trial geometrical configurations for a given structure and comparing the cost information for each, the designer can manipulate one or more of the geometric parameters to obtain a minimum cost structure. For example, it was found that the cheapest structure tended to be one with a small number of relatively long panels because this reduced the number of joints in the structure and thus lowered the fabricating cost, even though the sizes of the diagonals in the vertical and horizontal trusses increased with a corresponding increase in the metal cost. Similarly, for structures exposed to very light wind loads, the optimum cross-section of the truss tended to be deeper vertically than horizontally; the opposite tended to be true for very heavy wind loads. It was generally found that a square cross-section, that is, one with equal vertical and horizontal depths, was a good compromise when a single cross-section was to be selected for all wind loadings at a given span length.

The computer time required to produce a design for a given set of loading and geometric parameters varies considerably with the span length, loading, and the precision of the original estimates for deadweight, ice load and wind area. After some experience was acquired, these values could be estimated closely enough that one or two passes through the design portion of the program were sufficient. This meant that an average time to produce an acceptable design on a computer such as the IBM 650 or 1620 is on the order of one to two minutes. This time would be faster for short-span lightly loaded sign structures and somewhat longer for long-span heavily loaded structures.

This use of digital computation to produce standard designs for overhead sign structures was economical, efficient, and allowed a much greater degree of refinement in the designs than could have been included had they been prepared by hand. The successful application of this approach to sign structures suggests that similar techniques should be useful in the repetitive design of other types of structures.

Thermal Behavior of Composite Bridges—Insulated and Uninsulated

WILLIAM ZUK
Professor of Civil Engineering, University of Virginia, and Consultant to the Virginia Council of Highway Investigation and Research

Reported are theories and experimental data pertaining to various thermal aspects of composite bridge structures with steel beams and concrete decks or prestressed concrete beams and concrete decks, some of which are insulated on the underside with urethane foam. Heat conduction behavior as well as induced thermoelastic stresses and deformations are discussed in regard to these bridge types. Certain limited conclusions are drawn as affecting current design procedures.

•ALTHOUGH CURRENT bridge specifications in the United States, such as those of AASHO, do recognize the existence of thermal expansion and thermal forces, they are rather vague concerning values, particularly in regard to internally induced thermal stresses. Even though a bridge may have adequate provision for overall expansion and contraction, there could still exist large internal stresses due to non-uniformity in temperatures and material properties. Such is particularly true in composite structures exposed to solar radiation. German engineers and specifications were perhaps the first to deal with this subject. However, studies are now under way not only in the United States but also in Canada, England, Japan and Israel.

This paper is limited primarily to research efforts at the Virginia Council of Highway Investigation and Research located at the University of Virginia in Charlottesville. Although extensive field data have been taken in connection with this study, principal emphasis in the report is given the basic theoretical equations predicting bridge temperatures and stresses due to atmospheric weather conditions. These equations provide the greatest generality of application and are not necessarily restricted to the local conditions tested. However, as far as field conditions permit, the experimental data are compared to the theoretical to ascertain the general validity of such theories.

UNINSULATED BRIDGES

Theory of Temperature Distribution

Of first concern is the prediction of temperatures at the surface of a bridge deck. E. S. Barber (1) has developed a reasonably reliable equation to predict maximum surface temperatures of slabs, either concrete or bitumen. Although many complex factors such as solar radiation, ambient air temperature, wind velocity, insolation, reradiation, conductivity, diffusivity, and evaporation come into play, a simple but reasonable solution can be obtained on the basis of assuming average values of the secondary parameters and by assuming a sinusoidal effective daily temperature cycle.

Thus, for a normal concrete deck in the Middle Atlantic States, the maximum surface temperature in degrees Fahrenheit may be approximated by the formula

$$T_m = T_a + 0.018L + 0.667(0.50T_r + 0.054L) \quad (1a)$$

Paper sponsored by Committee on Bridges.

where

T_a = average daily air temperature (°F),
T_r = daily range in air temperature (°F), and
L = solar radiation received on a horizontal surface (cal/sq cm/day).

The equation for the maximum surface temperature of a bridge deck surfaced with a thin topping of bitumen would correspondingly be

$$T_m = T_a + 0.027L + 0.65\,(0.50\,T_r + 0.081\,L) \tag{1b}$$

For other regions and extreme conditions, the various constants may be appropriately adjusted as shown by Barber (1). The value of L (langleys of solar radiation) may be either determined from U. S. Weather Bureau maps or taken independently by a relatively inexpensive pyrheliometer which can be purchased commercially.

The effect of blacktopping can easily raise the surface temperature of decks 15 F or more above that of bare concrete decks. This factor is significant in relation to differential temperatures between the top and bottom of bridges, which in turn affect the induced internal thermal stresses.

The exact determination of the maximum differential temperature between the top of the slab and bottom of the supporting beam is also a complex matter. However, again with some simplifying assumptions, a rather simple but workable formula can be devised. In the case of steel beams, it is not too unreasonable to assume that the conduction of the steel is large enough that the lower outer fibers of the steel are at essentially the same temperature as the ambient air. However, there is a phase lag of several hours between the peak surface temperature (controlled primarily by solar radiation) and the air temperature, with the surface temperature generally leading the air temperature.

A simplified equation for predicting the maximum temperature differential between the top and bottom of a normal steel-concrete composite highway bridge may be assumed as

$$\Delta T_m = T_m - T_a \lambda T_r \tag{2}$$

where λ is the lag factor, varying from about one-fourth in the summer to about one-half in the winter. A value of three-eighths may be taken as an average for approximate analysis in Middle Atlantic States latitudes.

One other feature of interest is the character of the temperature distribution through the thickness of the deck slab itself. If the temperature at the top of the slab is equal to $T_t = B + C \sin(0.262t - \phi)$ and that at the bottom of the slab is $T_b = G + H \sin(0.262t)$, by superimposing the steady-state heat transfer solutions developed by Carslaw and Jaeger for periodic temperature states on an infinite plate (2), the following equation is obtained for the time-temperature-depth relation:

$$T = CY \sin(0.262t - \phi + \ln Y) + HY' \sin(0.262t) + (B - G)\frac{y}{h} + G \tag{3}$$

where

h = thickness of slab,
y = distance measured from bottom of slab,
t = time,

$$Y = \left[\frac{\cosh 2\,my - \cos 2\,my}{\cosh 2\,mh - \cos 2\,mh}\right]^{1/2}, \text{ and}$$

$$Y' = \left[\frac{\cosh 2\,m(h-y) - \cos 2\,m(h-y)}{\cosh 2\,mh - \cos 2\,mh}\right]^{1/2}.$$

In the last two terms, $m = \left(\frac{0.262}{2q}\right)^{1/2}$ where q is the diffusivity (an approximate value of m for concrete is 2.1 in units of feet, hours, pounds, British thermal units, and degrees Fahrenheit).

Generally speaking, in normal bridge structures, a temperature extreme (either hot or cold) at the top of the slab rapidly decays with depth, so that at approximately mid-depth the temperature is virtually the same as at the bottom of the slab.

Theory of Thermoelastic Stresses and Deformation—Composite Section with Steel Beam and Concrete Deck

The following theory follows in essence the derivations in a previous paper (3), except for the consideration of temperature varying as any function of depth instead of a linear function. The theory in this paper, therefore, represents a more generalized case. The slab and beam are assumed separated and free to deform independently according to the imposed temperature conditions. From basic thermoelastic theory, these separated induced thermal stresses may be easily determined. From these stresses, acting in conjunction with thermal expansion, the strains at any depth of the beam or slab may be found. However, in the actual composite beam, additional unknown forces in the nature of shears and couples exist at the interface between the slab and beam at the ends (3). These interface forces cause the two separated elements to join compositely, so that the strain of both the beam and the slab at the interface must be equal (assuming a no-slip condition) and the radius of curvature at the interface must be the same for the slab and the beam.

When the strain effects of the interface shears and couples are superimposed with the original thermal strains and the compatibility conditions of equal strain and curvature at the interface are met, the values of the interface shear and moment may be determined. Once these are established, the actual stresses and deformations in the composite section may be found by elementary beam theory.

Notations.—The symbols used in the following derivation are defined as follows:

A = cross-sectional area of beam,
a = half of depth of slab,
$b(y)$ = width of beam at various depths,
E_c = modulus of elasticity of concrete,
E_b = modulus of elasticity of steel beam,
ϵ_b = induced unit strain in beam,
ϵ_s = induced unit strain in slab,
F = interface shear force,
f_b = induced stress in beam,
f_s = induced stress in slab,
I = moment of inertia of beam section,
D = beam span,
μ = Poisson's ratio,
p = width of slab,
Q = interface couple,
ν = vertical deflection of beam at midspan,
α_c = coefficient of thermal expansion of concrete,
α_b = coefficient of thermal expansion of steel beam,
T = temperature, and
T_o = initial temperature.

Derivation.—From elastic theory, the general thermal stress-strain equations are as follows:

$$\epsilon_x = \frac{1}{E}\left[f_x - \mu(f_y + f_z)\right] + \alpha \Delta T$$

$$\epsilon_y = \frac{1}{E}\left[f_y - \mu(f_z + f_x)\right] + \alpha \Delta T$$

$$\epsilon_z = \frac{1}{E}\left[f_z - \mu(f_x + f_y)\right] + \alpha \Delta T \tag{4}$$

Referring to Figure 1 using a (x_1, y_1, z_1, T_1) coordinate system for the slab and considering the slab restrained in the z_1 direction ($\epsilon_{z_1} = 0$) by adjacent beams and free in the y_1 direction, one may derive from Eq. 1 the following relations for slab stresses:

$$f_{z_1 s} = \mu f_{x_1 s} - \alpha_c\, E_c \left[T_1(y_1) - T_o\right]$$

and

$$f_{y_1 s} = 0 \tag{5}$$

When the slab is assumed to be separated from the beam but subjected to the actual temperature distribution $T_1(y_1)$, the following general equation may be used to determine $f_{x_1 s}$ in the slab (3):

$$f_{x_1 s} = \frac{\alpha_c E_c\left[T_1(y_1) - T_o\right]}{1 - \mu} + \frac{\alpha_c E_c}{2a(1-\mu)} \int_{-a}^{+a} \left[T_1(y_1) - T_o\right] dy +$$

$$\frac{3\alpha_c E_c y_1}{2a^3(1-\mu)} \int_{-a}^{+a} \left[T_1(y_1) - T_o\right] y_1\, dy_1 \tag{6}$$

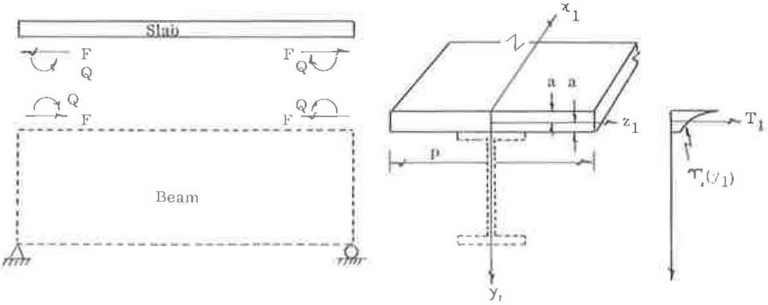

Figure 1.

The corresponding strain $\epsilon_{x_1 s}$ may be found from Eq. 4 as:

$$\epsilon_{x_1 s} = \frac{1}{E_c}\left[f_{x_1 s} - \mu f_{z_1 s}\right] + \alpha_c\left[T_1(y_1) - T_o\right] \tag{7}$$

Substituting Eq. 5 and 6 in Eq. 7, one may obtain the following expression to determine $\epsilon_{x_1 s}$ in the slab.

$$\begin{aligned}\epsilon_{x_1 s} = {} & \frac{(1+\mu)\,\alpha_c}{2a}\int_{-a}^{+a}\left[T_1(y_1) - T_o\right] dy_1 \; + \\ & \frac{3\,(1+\mu)\,\alpha_c\, y_1}{2a^3}\int_{-a}^{+a}\left[T_1(y_1) - T_o\right] y_1\, dy_1\end{aligned} \tag{8}$$

at $y_1 = 0$, making,

$$\epsilon_{x_1 s} = \frac{(1+\mu)}{2a}\int_{-a}^{+a}\left[T_1(y_1) - T_o\right] dy_1 \tag{9}$$

and at $y_1 = a$,

$$\begin{aligned}\epsilon_{x_1 s} = {} & \frac{(1+\mu)\,\alpha_c}{2a}\int_{-a}^{+a}\left[T_1(y_1) - T_o\right] dy_1 \; + \\ & \frac{3\,(1+\mu)\,\alpha_c}{2a^2}\int_{-a}^{+a}\left[T_1(y_1) - T_o\right] y_1\, dy_1\end{aligned} \tag{10}$$

The bottom slab strain (at $y_1 = a$) due to the interface shears and moments is

$$\epsilon'_{x_1 s} = \frac{(1 - \mu^2)}{ap\, E_c} \quad \frac{3Q}{2F - 2a} \tag{11}$$

Thus, the sum of Eqs. 10 and 11 gives the total interface strain of the slab:

$$\epsilon''_{x_1 s} = \frac{(1 - \mu^2)}{ap\, E_c} \quad 2\ F - \frac{3Q}{2a} \quad + \frac{(1 + \mu)\, \alpha_c}{2a} \int_{-a}^{+a} \left[T_1(y_1) - T_o \right] dy_1 \ + \frac{3\,(1 + \mu)\, \alpha_c}{2a^2} \int_{-a}^{+a} \left[T_1(y_1) - T_o \right] y_1\, dy_1 \tag{12}$$

Considering the beam separated from the slab, using a (x_1, y_1, z_1, T) coordinate system as shown in Figure 2, the following equation may be used to determine f_{xb} in the beam section due to the temperature change (3):

$$f_{xb} = \alpha_b E_b \left[T(y) - T_o \right] + \frac{\alpha_b E_b}{A} \int_{-d_1}^{+d_2} \left[T(y) - T_o \right] b(y)\, dy \ + \frac{\alpha_b E_b y}{I^2} \int_{-d_1}^{+d_2} \left[T(y) - T_o \right] b(y)\, y\, dy \tag{13}$$

Since the beam is free in both y and z directions ($f_{yb} = f_{zb} = 0$), one may derive from Eq. 4 the following stress-strain relation for the beam:

$$\epsilon_{xb} = \frac{f_{xb}}{E_c} + \alpha_b \left[T(y) - T_o \right] \tag{14}$$

Substituting Eq. 13 into Eq. 14, one may obtain the corresponding strain as

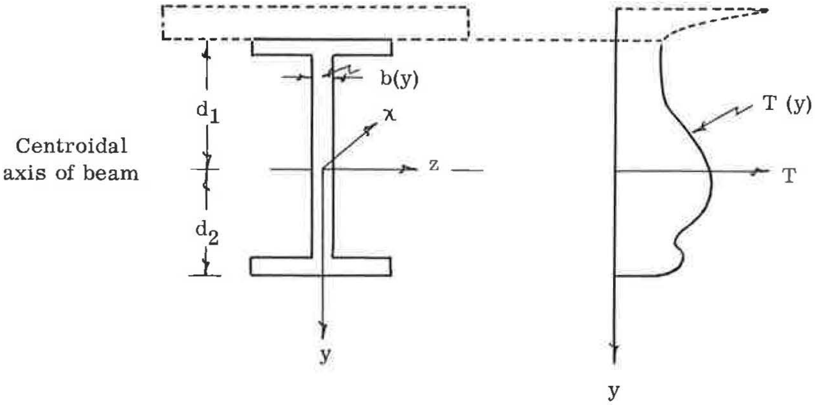

Figure 2.

$$\epsilon_{xb} = \frac{\alpha_b}{A}\int_{-d_1}^{+d_2}\left[T(y) - T_o\right] b(y)\,dy + \frac{\alpha_b y}{I}\int_{-d_1}^{+d_2}\left[T(y) - T_o\right] b(y)\,y\,dy \tag{15}$$

making, at $y = d_1$,

$$\epsilon_{xb} = \frac{\alpha_b}{A}\int_{-d_1}^{+d_2}\left[T(y) - T_o\right] b(y)\,dy - \frac{d_1\alpha_b}{I}\int_{-d_1}^{+d_2}\left[T(y) - T_o\right] d(y)\,y\,dy \tag{16}$$

The stress and strain in the beam caused by the interface forces are

$$f_{xb'} = \frac{Qy}{I} + F\left(\frac{d_1 y}{I} - \frac{1}{A}\right) \tag{17}$$

$$\epsilon_{xb'} = \frac{Qy}{IE_b} + \frac{F}{E_b}\left(\frac{d_1 y}{I} - \frac{1}{A}\right) \tag{18}$$

and at $y = -d_1$,

$$\epsilon_{xb'} = -\frac{Qd_1}{IE_b} - \frac{F}{E_b}\left(\frac{d_1^2}{I} + \frac{1}{A}\right) \tag{19}$$

Therefore, the sum of Eqs. 16 and 19 gives the total interface strain of the beam at $y = -d_1$ as follows:

$$\epsilon''_{xb} = -\frac{Qd_1}{IE_b} - \frac{F}{E_b}\left(\frac{d_1^2}{I} + \frac{1}{A}\right) + \frac{\alpha_b}{A}\int_{-d_1}^{+d_2}\left[T(y) - T_o\right] b(y)\,dy - \frac{d_1\alpha_b}{I}\int_{-d_1}^{+d_2}\left[T(y) - T_o\right] b(y)\,y\,dy \qquad (20)$$

For compatibility of horizontal strains between slab and beam at the interface, Eq. 12 must equal Eq. 20, which gives

$$\left[\frac{1}{AE_b} + \frac{d_1^2}{IE_b} + \frac{2(1-\mu^2)}{apEc}\right]F + \left[\frac{d_1}{IE_b} - \frac{3(1-\mu^2)}{2a^2\,pEc}\right]Q = -\frac{(1+\mu)\alpha_c}{2a}\left\{\int_{-a}^{+a}\left[T_1(y_1) - T_o\right]dy_1 + \frac{3}{a}\int_{-a}^{+a}\left[T_1(y_1) - T_o\right]y_1\,dy_1\right\} + \alpha_b\left\{\frac{1}{A}\int_{-d_1}^{+d_2}\left[T(y) - T_o\right]b(y)\,dy - \frac{d_1}{I}\int_{-d_1}^{+d_2}\left[T(y) - T_o\right]b(y)\,y\,dy\right\} \qquad (21)$$

Subtracting Eq. 9 from Eq. 10, one may obtain the strain difference between the midplane and bottom of slab induced by temperature change in the concrete section:

$$\epsilon_{x_1 s} \text{ (difference)} = \frac{3(1+\mu)\alpha_c}{2a^2} \int_{-a}^{+a} \left[T(y) - T_o\right] y\,dy \qquad (22)$$

The strain difference induced by the interface forces as the same positions is given by:

$$\epsilon_{x_1 s'} \text{ (difference)} = \frac{3(1-\mu^2)}{2a^2\, pE_c} (Fa - Q) \qquad (23)$$

Therefore, the total strain differential is the sum of Eqs. 22 and 23:

$$\epsilon_{x_1 s} \text{ (total difference)} = \frac{3(1-\mu^2)}{2a^2\, pE_c} (Fa - Q) + \frac{3(1+\mu)\alpha_c}{2a^2} \int_{-a}^{+a} \left[T_1(y_1) - T_o\right] y_1\, dy_1 \qquad (24)$$

This differential strain may then be related to the radius of curvature of the slab at the interface by simple geometry as follows:

$$R_s = \frac{2a^3\, p E_c}{3(1-\mu^2)(Fa - Q) + 3(1+\mu)\, p\alpha_c E_c \int_{-a}^{+a} \left[T_1(y_1) - T_o\right] y_1\, dy_1} + a \qquad (25)$$

Considering the beam alone, the total induced moment is

$$M_t = Fd_1 + Q + \alpha_b E_b \int_{-d_1}^{+d_2} \left[T(y) - T_o\right] b(y)\,y\,dy \tag{26}$$

The radius of curvature of the beam at the interface may be found by elementary flexure theory:

$$R_b = \frac{E_b I}{Fd_1 + Q + \alpha_b E_b \displaystyle\int_{-d_1}^{+d_2} \left[T(y) - T_o\right] b(y)\,y\,dy} - d_1 \tag{27}$$

The second term in both Eqs. 25 and 27 is so small in comparison to the first term that it can be omitted without introducing significant error. Thus, the vertical compatibility is written by equating Eqs. 25 and 27, which may be rearranged as follows:

$$\left[2pd_1 a^3 E_c - 3(1-\mu^2)\,aIE_b\right] F + \left[2pa^3 E_c + 3(1-\mu^2)\,IE_b\right] Q =$$

$$3(1+\mu)\,p\alpha_c IE_b E_c \int_{-a}^{+a} \left[T_1(y_1) - T_o\right] y_1\,dy_1 \; -$$

$$2pa^3 \alpha_b E_b E_c \int_{-d_1}^{+d_2} \left[T(y) - T_o\right] b(y)\,y\,dy \tag{28}$$

The unknown quantities F and Q may be obtained by solving Eqs. 21 and 28 simultaneously. For practical purposes, these equations are best solved numerically for particular problems.

With F and Q known, the stress f_{x_1s} in the slab is obtained by adding Eq. 6 to the stresses induced by the interface forces, giving:

$$f_{x_1s} = \frac{F}{2ap} + \frac{3(Fa - Q)\,y_1}{2a^3 p} - \frac{\alpha_c E_c \left[T_1(y_1) - T_o\right]}{1-\mu} +$$

$$\frac{\alpha_c E_c}{\mu} \int_{-a}^{+a} \left[T_1(y_1) - T_o\right] dy_1 + \frac{3\alpha_c E_c y_1}{\mu} \int_{-a}^{+a} \left[T_1(y_1) - T_o\right] y_1\,dy_1 \tag{29}$$

Similarly, the stress f_{xb} in the beam is the sum of Eqs. 13 and 17. The stress in the slab in the transverse or z_1 direction is obtained from Eq. 5.

The induced moment in Eq. 26 causes a deflection of the beam which may be obtained from the elementary equation of flexure of a simply supported beam acted on by a constant moment:

$$\nu_{\max} = \frac{Q^2}{8 E_b I} \left\{ F d_1 + Q + \alpha_b E_b \int_{-d_1}^{+d_2} \left[T(y) - T_o \right] b(y)\, y\, dy \right\} \tag{30}$$

Composite Section with Precast-Prestressed Concrete Beam and Concrete Deck

The detailed theory involved in this case is presented in a recent paper (4). In broad outline, the approach is similar to that explained in the steel-concrete composite section, except for the added stress and strain effects of the prestressing tendon. Although two cases of prestressing tendons were studied, one involving a straight tendon and the other involving a parabolically draped tendon, for brevity only the summary equations for the straight tendon are presented in this report. The pertinent equations are as follows:

$$\left(\frac{1}{AE_c} + \frac{1}{A_t E_t} + \frac{e^2}{IE_c}\right) F_t - \frac{e}{IE_c} Q + \frac{1}{E_c}\left(\frac{1}{A} - \frac{ed_1}{I}\right) F =$$

$$-\alpha_t \left[T(e) - T_o\right] + \frac{\alpha_c}{A} \int_{-d_1}^{+d_2} \left[T(y) - T_o\right] b(y)\, dy + \frac{e\alpha_c}{I} \int_{-d_1}^{+d_2} \left[T(y) - T_o\right] b(y)\, y\, dy \tag{31}$$

$$\left(\frac{1}{A} - \frac{ed_1}{I}\right) F_t + \left[\frac{d_1}{I} - \frac{3(1-\mu^2)}{2a^3 p}\right] Q + \left[\frac{1}{A} + \frac{d_1^{\,2}}{I} + \frac{2(1-\mu^2)}{ap}\right] F =$$

$$\alpha_c E_c \left\{ - \frac{1+\mu}{2a} \int_{-a}^{+a} \left[T_1(y) - T_o\right] dy_1 - \frac{3(1+\mu)}{2a^2} \int_{-a}^{+a} \left[T_1(y_1) - T_o\right] y_1\, dy_1 + \right.$$

$$\left. \frac{1}{A} \int_{-d_1}^{+d_2} \left[T(y) - T_o\right] b(y)\, dy - \frac{d_1}{I} \int_{-d_1}^{+d_2} \left[T(y) - T_o\right] b(y)\, y\, dy \right\} \tag{32}$$

and

$$2a^3 pe F_t - \left[2a^3 p + 3I(1 - \mu^2)\right] Q + \left[3aI(1 - \mu^2) - 2a^3 pd_1\right] F =$$

$$p\alpha_c E_c \left\{ - 3(1 + \mu) I \int_{-a}^{+a} \left[T_1(y_1) - T_o\right] y_1 \, dy_1 + 2a^3 \int_{-d_1}^{+d_2} \left[T(y) - T_o\right] b(y) \, y \, dy \right\} \qquad (33)$$

where e is the distance of the tendon from the centroidal axis of the beam, and the subscript t refers to the tendon.

Eqs. 31, 32, and 33 are solved simultaneously (best done numerically) for the factors F, Q, and F_t, where F_t is the change in prestressing force due to the temperature effects. The corresponding slab stresses are found by use of Eqs. 5 and 29.

The beam stresses are found as follows:

$$f_{xb} = F_t \left(\frac{1}{a} + \frac{ey}{I}\right) + \frac{Qy}{I} + F\left(\frac{d_1 y}{I} - \frac{1}{A}\right) - \alpha_c E_c \left[T(y) - T_o\right] +$$

$$\frac{\alpha_c E_c}{A} \int_{-d_1}^{+d_2} \left[T(y) - T_o\right] b(y) \, dy + \frac{\alpha_c E_c y}{I} \int_{-d_1}^{+d_2} \left[T(y) - T_o\right] b(y) \, y \, dy \qquad (34)$$

The maximum vertical deflection at the center of this simply supported prestressed beam due to the temperature is

$$\nu_{max} = \frac{D^2}{8 E_c I} \left\{ Fd_1 + Q - F_t e + \alpha_c E_c \int_{-d_1}^{+d_2} \left[T(y) - T_o\right] b(y) \, y \, dy \right\} \qquad (35)$$

Field Tests

To obtain data on actual field conditions of temperature and thermal strains on a bridge, a composite steel girder and concrete slab bridge over the Hardware River near Charlottesville was instrumented (Fig. 3).

Twenty-two iron-constantan thermocouples were embedded near the top of the slab, at the mid-depth of slab, at the top of the steel beams, at the mid-depth of the beam,

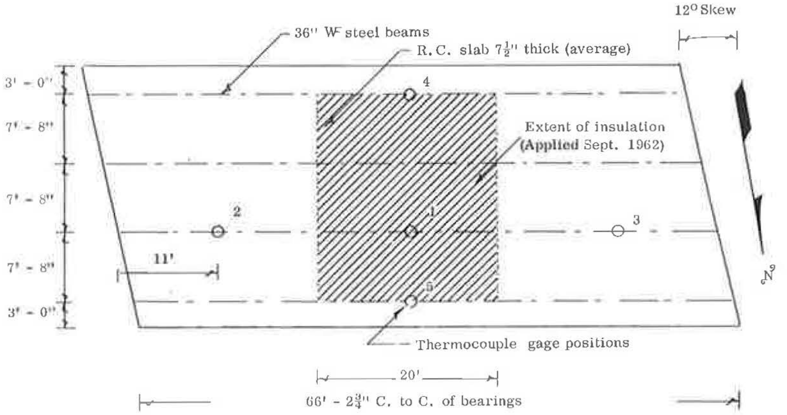

Figure 3. Plan of bridge.

and at the bottom of the beam at the positions shown in Figure 3. Two ambient air temperature gages were also installed at Positions 2 and 3. The thermocouples were all wired to a Minneapolis-Honeywell 24-point recorder which scanned and recorded all the points automatically once an hour.

Periodic strain readings were taken manually in the beam and slab at Position 1 by a 10-in. Whittemore strain gage, compensated by an invarient invar bar. A mechanical device instead of an automatic electrical device was selected for strain readings to insure greater long-term reliability. To isolate the temperature-induced strains, readings were taken only under dead load and constant moisture conditions in the slab. Slab moisture was detected by a nuclear moisture probe using a radium-beryllium source manufactured by Nuclear-Chicago.

When the testing was initiated, the bridge structure was 2 years old, so essentially all shrinkage had already taken place. Rod and level readings were taken at the same time strains were measured. All data were thus read and recorded for the period from September 1961 to August 1962, with the exception of June and July because of persistent instrument malfunctions. However, from September 1962 to May 1963 only temperature data were recorded (for reasons to be discussed later). As it is obviously impractical to present all accumulated data, only those believed to be meaningful or typical are presented.

The extreme low temperature, -6 F, was recorded in January 1962 from midnight to 6 A.M. at the bottom of the steel flanges. The air temperature at this time was also -6 F. The highest temperature recorded, 123 F, was in May 1963 at 3 P.M. at the top of the slab. The air temperature at this time was 97 F.

The maximum temperature differential through the depth of the bridge at an interior beam at any given time did not exceed 37 F, when the slab was warm and the beam was cool. This situation typically occurred during sunny afternoons when the sun's radiations coupled with high air temperatures warmed the top of the slab. Oddly enough, the reverse condition prevailed on outside beams exposed to the sun. A maximum differential temperature of 42 F was observed on such an exterior beam in January on a sunny but cold afternoon. The result was that the top of the slab remained relatively cool (although warmed to some degree by the sun) while the exposed lower portion of the steel beam with its high thermal conductivity was heated. Other than for these edge beams and isolated regions shaded by railings or trees, the temperature at any given strata of the bridge was practically constant.

Since it is the temperature gradient that contributed to high internal thermal stresses, high thermal differentials are most important. Large temperature fluctuations from winter to summer, although causing large overall expansion or contraction, do not normally play a large role in internal stresses.

As an adjunct experiment, temperature readings were taken at the surface of normal grey-white concrete and black-grey bituminous concrete. Due to color, the darker surface absorbed more short-wave solar radiation, raising the bituminous temperature approximately 15 F higher than that of the normal concrete on a sunny summer afternoon. On a sunny winter afternoon, only a 5 F differential was noted.

These experimental data correlate well with the theory presented in Eqs. 1a and 1b, in which solar radiation was measured near the site with a portable Belfort recording pyrheliometer.

A typical plot of temperatures on an interior region of the bridge for a day in March 1963 is shown in Figure 4. Based on the measured solar radiation for that day, L is 471.3. Using Eq. 1a, the maximum surface temperature is 102 F, compared to the true measured value of 98 F. Similarly, the maximum differential temperature based on Eq. 2 is 24 F, compared to the true measured temperature of 23 F. On sunny days, the sun's radiation often heats the top of the deck 20 or 30 F higher than the air temperature by mid-afternoon.

To illustrate the difference in thermal behavior between an interior and an exterior beam on a cool sunny day in January 1962, the log of temperatures in Figure 5 is presented. The general trends and distributions of temperature are about the same for a warm sunny day at any season of the year. There is a continuous variation due to conductivity and radiation.

Generally speaking, for an interior beam, the lower flanges rapidly assume the surrounding air temperature due to the steel's high conductivity. The conductivity of the concrete slab is lower, with the bottom surface and especially the middle temperatures generally lagging the air temperature. As is observed, the bottom slab temperature affects the temperature at the top of the steel beam, mostly through conduction. At night the temperature gradients are generally rather small, and it is occasionally observed that the top of the slab is at a temperature a few degrees lower than that of the air due to reverse long-wave radiation from the slab to the black sky. In the early hours of the morning, the entire bridge is often at a constant temperature, that of the air. This is also true during all the daylight hours on cloudy or rainy days.

The steep thermal gradients in the slab near the upper surface are characteristic. Spot check comparisons of the experimental data with the theory (Eq. 3) show agreement of about 10 percent. The most significant source of error lies in the theoretical assumption that the boundary temperatures vary as a sine wave, whereas a glance at a typical temperature curve as in Figure 4 shows this to be only approximately true.

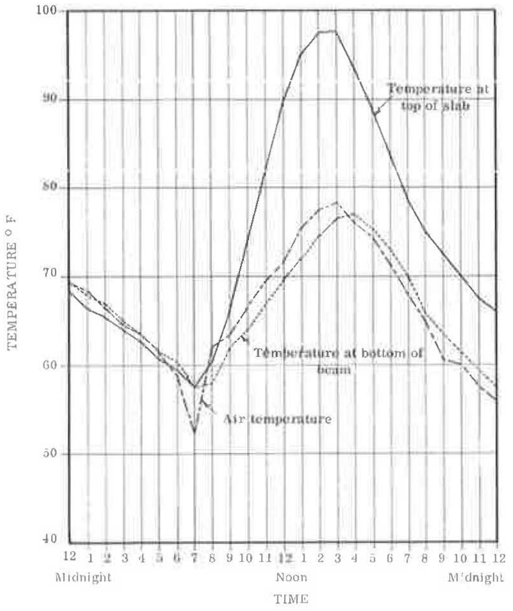

Figure 4. Plot of temperatures for March 18, 1963.

In regard to strain and deformation measurements, unexpected complications arose. Strain readings were not compared to theory until many months after the initiation of the testing program, at which time it was observed that (a) there was considerable interface slip between the steel and the concrete and (b) there were appreciable axial end restraints on the bridge at the positions of the slab and the bearing plate. The slip behavior was most erratic, precluding any easy explanation or correction. (This bridge has stud-type shear connectors.) As time progressed (particularly with the coming of warm weather) it was noticed that the entire bridge expanded to such an extent that several of the 1-in. diameter anchor bolts were bent and a 12-in. reinforced concrete

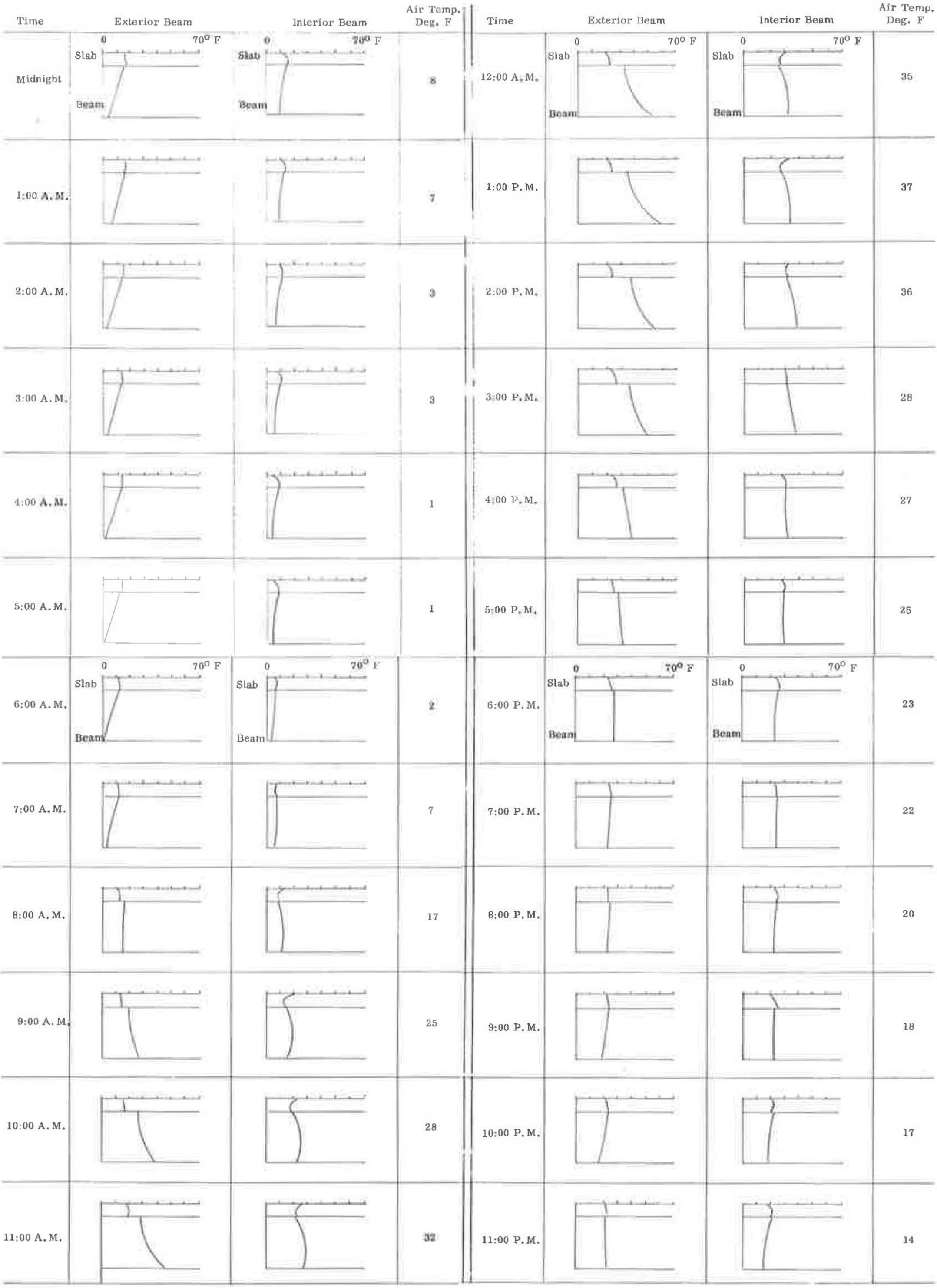

Figure 5. Temperature log.

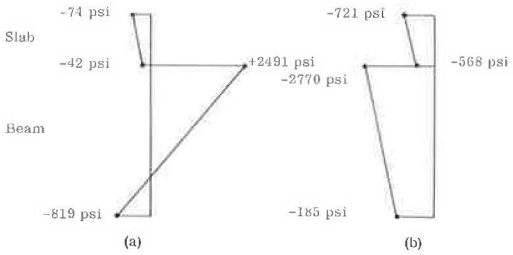

Figure 6. Stress distributions.

back wall was cracked from pressure transmitted through a 1-in. thick expansion filler at the slab level.

Because of these unexpected and unmeasured complications, attempts at reconciling the theory with experiments proved futile. As a case in point, for a temperature state with the top of the slab at 104 F and the beam and the bottom of the slab at 93 F, Figure 6a shows the theoretical stress distribution in the longitudinal direction. Figure 6b shows the actual stresses from measured strains.

To adjust these divergent results, theoretically there must exist an axial compressive stress at the end of the slab of 689 psi and a bearing force at the anchor bolts of 15,020 lb. Interface slip would tend to reduce these restraint values, but to an unknown extent as no reliable slip theory is yet available. A complete theory would also have to take into account creep and plasticity effects. For similar reasons, deformation measurements also had to be discarded.

INSULATED BRIDGES

In September 1962, a 1-in. thick coating of sprayed foam urethane insulation was applied to that portion of the Hardware River Bridge shown in Figure 3. The insulation was applied not only as is customary on the underside of the concrete deck, but also completely around the exposed portion of the supporting steel beams, including the webs and the lower flanges. As is seen in Figure 3, part of the bridge was left uninsulated for comparison.

The normal use of bridge insulation is to reduce the number of freeze-thaw cycles of the top surface of the deck and to delay or eliminate premature icing of the deck as compared to the adjacent soil-based road surface. However, the primary object of this experiment was to determine how insulation affects the induction of thermal stresses and, therefore, the full beam was coated.

Figures 7 and 8 show the comparative temperatures at the top and bottom of the bridge, insulated and uninsulated, for a cold sunny day in November 1962, with the air temperature near freezing during the early morning hours. The comparative behavior on a warm sunny day in April 1963 is shown in Figures 9 and 10. The trends on both cold and warm sunny days are the same.

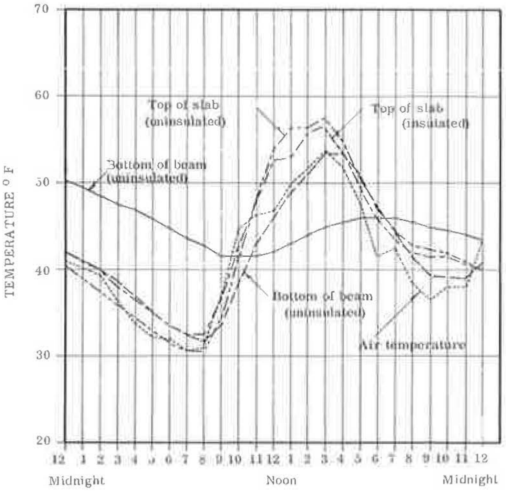

Figure 7. Plot of temperatures for November 23, 1962.

The observed data indicate that the presence of full insulation increases the maximum temperature differential between the top and bottom of the bridge by approximately 25 percent over uninsulated bridges. In building roof structures, the reverse is true (5). Although the thermodynamic theory explaining this bridge behavior quantitatively has not yet been fully worked out by the author, a qualitative explanation can be had from Figures 7 and 9. In regard to the bottom of the beam curve (insulated), the insulation serves to level out the extreme variations of the ambient air temperatures. Coupled with this, there is a time lag of many hours due to the insulating qualities around the steel. The net result is a decided increase in maximum temperature differential in the bridge oc-

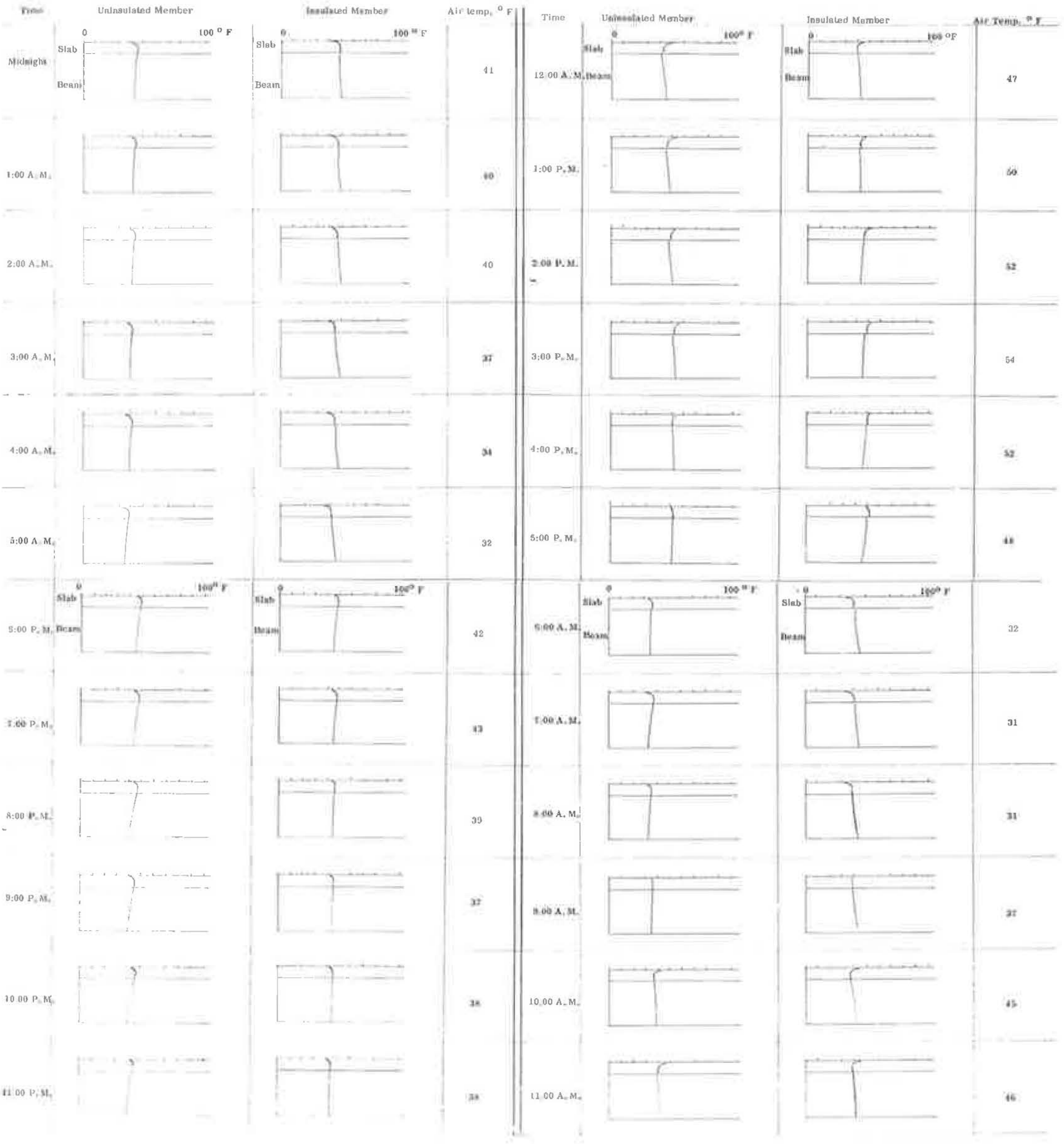

Figure 8. Temperature log, Hardware River Bridge.

curring in the early afternoon. The maximum differential temperature observed in these tests was 41 F in May 1963. Such a condition, therefore, appreciably increases the maximum induced internal thermal stresses in the structure, and is thus undesirable from a stress point of view.

During the colder non-daylight hours, the top of the insulated deck is a few degrees warmer than the uninsulated deck. For atmospheric conditions just below freezing, these few degrees could indeed make the difference between an iced or a non-iced deck. During the sunny daylight hours, the slab temperature conditions are reversed, with the uninsulated slab being warmer than the insulated one. Again, a qualitative explanation serves to explain this reversal. During the night, the warm stored heat flux in the insulated lower beam flows to the cooler surface where the heat warms the surface and

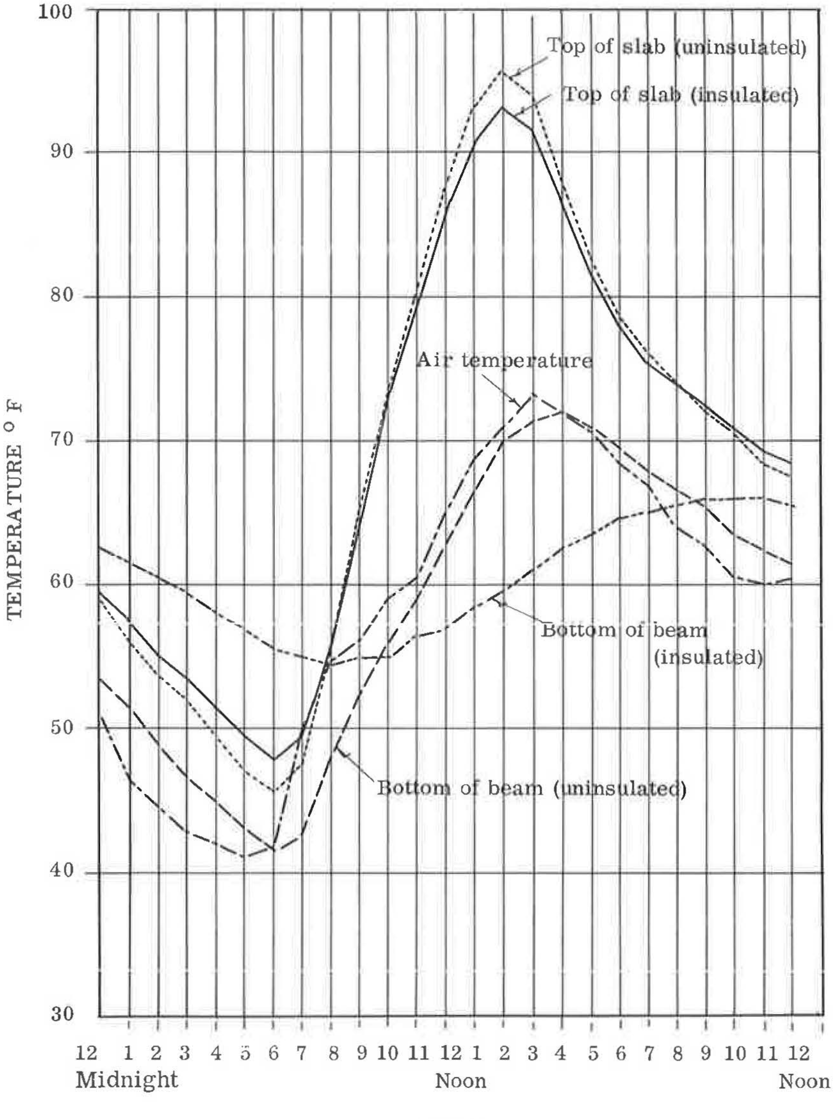

Figure 9. Plot of temperatures for April 8, 1963.

the boundary layer of air above it. However, during the day, the solar warmed boundary layer of air and the insulated slab surface are considerably hotter than the bottom of the beam, causing the heat flux to flow downward. This downward flow drains some heat energy from the surface of the slab, thereby slightly cooling it.

As a simple side experiment to test bounding characteristics, urethane foam was sprayed on test samples of bare aluminum, bare steel, and steel coated with aluminum paint. It is parenthetically noted that the insulation peeled off the aluminum in about 5 weeks, and off the bare steel in about 5 months of semi-protected outside exposure. The bond on the painted steel sample is still holding well as of this date, although some edge peeling is observed on the actual bridge.

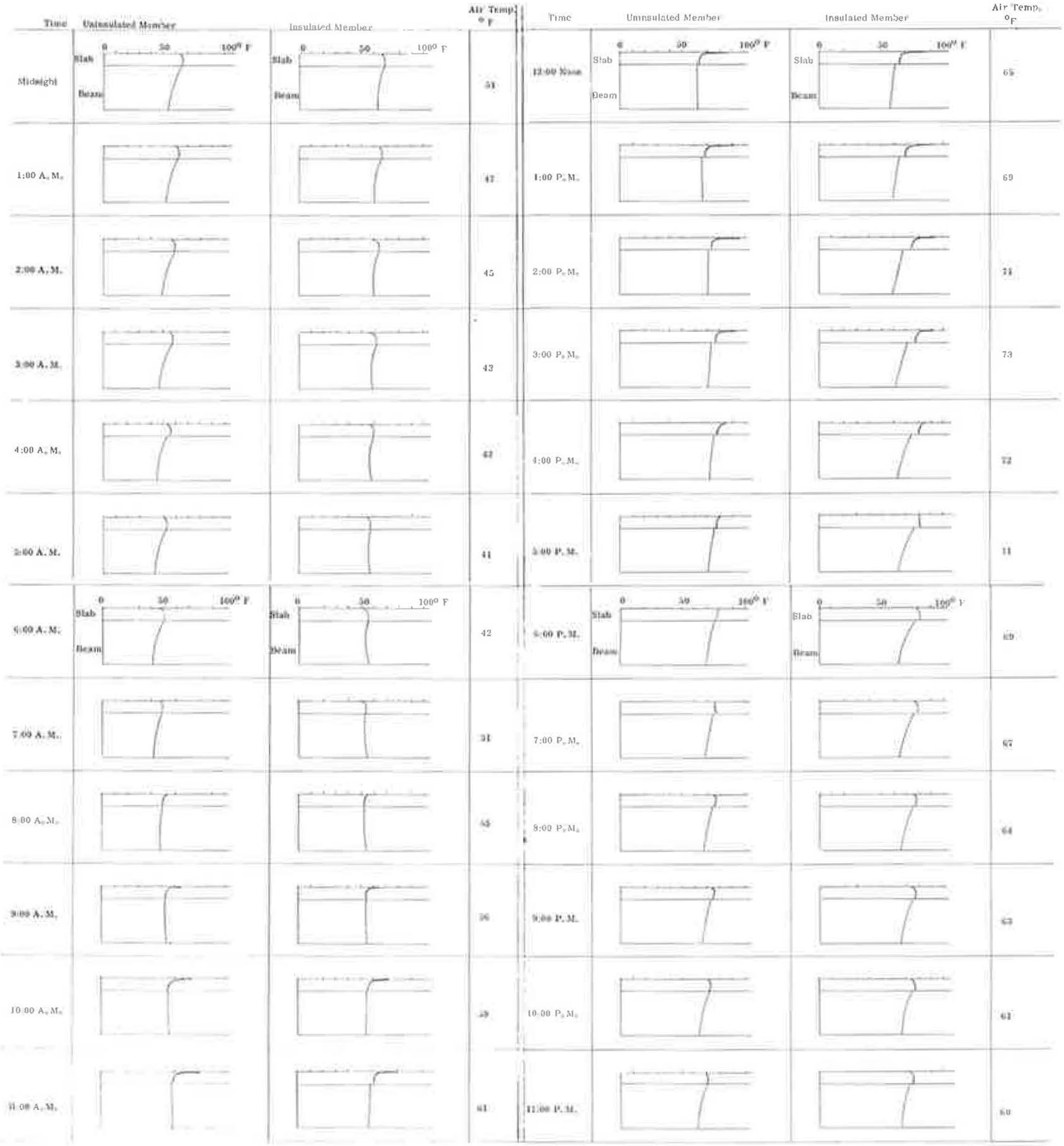

Figure 10. Temperature log, Hardware River Bridge.

EXAMPLES AND GENERAL CONCLUSIONS

It has been seen in earlier sections of this paper that the theoretical heat transfer equations have generally been supported by experiment. However, no confirmation or repudiation of the theoretical stress equations by experiment has been possible in this study. Therefore, a few typical numerical examples will be presented to obtain a "feel" for the thermoelastic stresses and deformations.

Consider a reasonable temperature distribution as shown in Figure 11a applied to the Hardware River Bridge. By use of the stress equations derived in this paper, assuming $T_0 = 60$ F and typical material properties, the resulting longitudinal stresses, f_x, developed will appear as in Figure 11b.

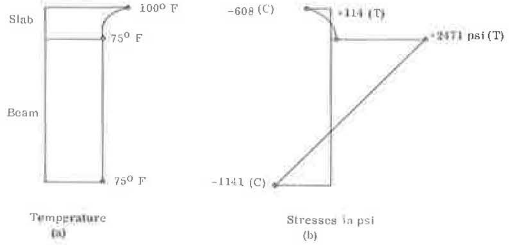

Temperature (a) Stresses in psi (b)

Figure 11.

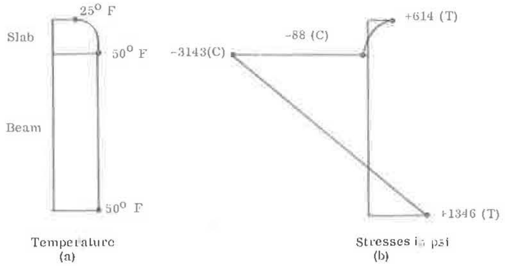

Temperature (a) Stresses in psi (b)

Figure 12.

The maximum transverse stress in the slab, f_{z_1s}, will be 109.6 psi (c), and the maximum thermal deflection, ν, will be 0.26 in. up. Of equal, if not more importance, is the development of theoretical large interface shears and couples concentrated within inches of the end. In this example the shear, F, equals 32, 042 lb, and the couple, Q, equals 396, 861 in.-lb. Q is physically manifested by the existence of normal pressures of compression and tension acting side by side on the interface surfaces or connectors within inches of the end of the beam. Since these large forces obviously cause slip and local yielding of the material, in actuality these interface stresses must be, to some unknown degree, less than predicted. This would then be followed by a decrease in all other thermal stresses and deflections.

For the temperature distribution in Figure 11a the stresses in the beam are of reverse sign to that of dead or live loads. Consequently, they would generally not be detrimental. However, should the temperature pattern be as shown in Figure 12a, the resulting stresses in Figure 12b would be additive to the dead and live load stresses. In this second example, F = 43, 273 lb, Q = 430, 563 in.-lb, ν = 0.32 in. down, and the maximum f_{z_1s} = 980 psi (T). Larger differential temperatures would obviously induce even higher stresses (although not proportionally) so that thermal differentials of 40 or 50 F could conceivably cause overstress of design allowables when coupled with dead loads, live loads and shrinkage.

Consideration too must be given to the eventuality of a concrete bridge deck being surfaced with blacktopping; this would generally increase the maximum thermal differential. Studies (5) show that a 2-in. topping is necessary before the insulating effect of the surfacing begins to offset the increase in temperature due to the darker color. Atmospheric conditions, such as air temperature, solar radiation, humidity, and wind velocity, at the time of construction also play a role in the induction of thermal stresses, complicated by complex relations of shrinkage and time-dependent changes in concrete properties during hardening.

German bridge specifications (6) do require provisions for temperature stresses in composite members. In particular, they specify for design (a) a temperature difference of ± 15 C (± 27 F) between the concrete slab and the steel beam, (b) special heavy end anchorages tieing the slab and the beam together at their interface, and (c) in the absence of more exact analysis, a distribution of end interface shear which is maximum at the end and linearly decreases to zero at a distance from the equal to the effective width of the slab. Sattler (7) has performed quantitative thermal analysis where the slab is at one uniform temperature and the beam at another uniform temperature. This condition only roughly approximates the actual nonlinear distribution of temperature considered in this paper.

An example of a prestressed-composite beam is a typical AASHO-PCI Type IV precast-prestressed beam shown in Figure 13 with a 100-ft span. Assuming a temperature distribution as shown in Figure 14a, the resulting longitudinal stresses (derived from the previous theoretical equations) are shown in Figure 14b. The initial temperature T_O is taken as 60 F. For this case, the interface shear is 19, 600 lb, the interface moment is 80, 300 in.-lb, the maximum transverse stress in the slab is 302 psi (c), the loss of prestress in the tendon is 0.86 percent, and the maximum center deflection is 0.36 in. down.

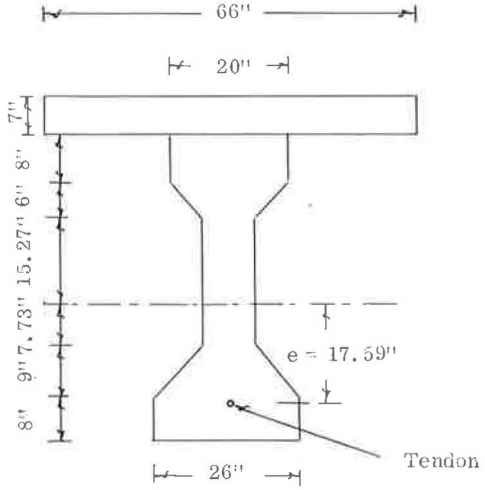

Figure 13.

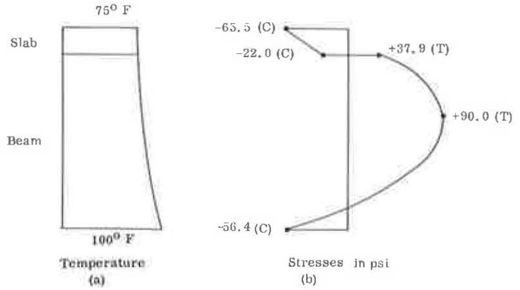

Figure 14.

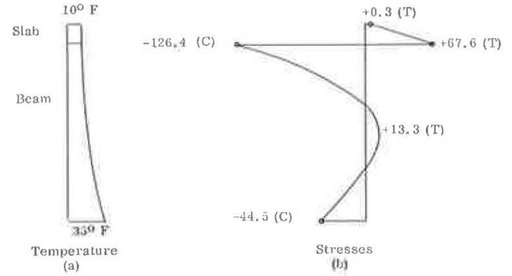

Figure 15.

For a different temperature distribution as shown in Figure 15a, the resulting longitudinal stresses are shown in Figure 15b. The interface shear is 16, 290 lb, the interface moment is 38, 890 in.-lb, the maximum transverse stress in the slab is 970-psi tension, the gain of prestress in the tendon is 0.70 percent, and the maximum center deflection is 0.53 in. down.

A review of the numerical examples (4) indicates that for conditions of moderate temperature variation (25 F) through the depth of prestressed beams, the induced thermal stresses and deflections in the concrete are generally within tolerable design limits.

Stresses in the concrete do not normally exceed the magnitude of about 200 psi in compression and about 100 psi in tension. The induced stress effects in the prestressing tendons range approximately from a 5, 000- (3 percent of initial prestress) to about a 8, 000-psi (5 percent of initial prestress) loss in stress. The deflections generally lie below 0.04 percent of the span length. Thus, for prestressed concrete beams which are used in bridge structures in moderate climates and are subject only to normal cyclic solar and atmospheric fluctuations, these thermally induced stresses appear to be absorbed by current design procedures and safety factors.

However, note is again made of the high theoretical values of interface shears and moments concentrated at the ends. The extent that these interface stresses are reduced by plasticity, slip, and creep is still an unsettled question. In Guyon's book on prestressed concrete (8), some experimental data are given for deflections of prestressed beams subject to the heat of fire. With the theory presented in this paper, agreement is excellent between theory and test for temperatures up to about 175 F. Since such a limit temperature encompasses normal conditions, it is believed that for those conditions as outlined, the theory set forth is adequate and reliable.

Because of the many complexities involved in the problem of predicting thermal stresses—including creep, slip, and plasticity—no specific recommendations for a simple design specification can be made at this time beyond what has been said. More studies must first be made. However, it is felt that the theories presented in this paper, although complex, can safely be applied, because the unknown effects mentioned will tend to reduce the severity of the induced stresses. Deflections, of course, are an exception, as they will tend to increase.

ACKNOWLEDGMENTS

This paper summarizes the principal findings to date of a long-range program of study sponsored jointly by the Virginia Council of Highway Investigation and Research and the U. S. Bureau of Public Roads. Individual acknowledgment is also made to K. Tatlidil and Y. N. Liu, who as graduate assistants aided in these studies.

REFERENCES

1. Barber, E. S. Calculation of Maximum Pavement Temperatures From Weather Reports. Highway Research Board Bull. 168, pp. 1-8, 1957.
2. Carslaw, H. S., and Jaeger, J. C. Conduction of Heat in Solids. 2nd Ed., pp. 105-106. London, Oxford University Press, 1960.
3. Zuk, W. Thermal and Shrinkage in Composite Beams. Jour. American Concrete Institute, pp. 327-340, Sept. 1961.
4. Liu, Y. N., and Zuk, W. Thermoelastic Effects in Prestressed Flexural Members. Jour. Prestressed Concrete Institute, pp. 64-85, June 1963.
5. Hendry, A. W., and Page, J. K. Thermal Movements and Stresses in Concrete Slabs in Relation to Tropical Conditions. RILEM Symposium on Concrete and R. C. in Hot Countries, Haifa, pp. 11-12, July 1960.
6. Verbundtrager; Strassenbrucken, Richtlinien fur Berechnung und Ausbildung—D1N1078 Blatt 1, Beton Kalender, 1958.
7. Sattler, K. Theorie der Verbundkonstruktionen, Spannbeton Stahltrager in Verbund mit Beton. Berlin, Wilhem Ernst und Sohne, 1959.
8. Guyon, Y. Prestressed Concrete. Pp. 110-112. New York, John Wiley and Sons, 1953.
9. RILEM Symposium on Concrete and R. C. in Hot Countries, Haifa, Part 2, July 1960.
10. Iwamoto, K. On the Continuous Composite Girder. Highway Research Board Bull. 339, pp. 80-90, 1962.
11. The AASHO Road Test, Report 41-1 Bridge Research. Highway Research Board Spec. Rept. 61D, 1962.
12. Hannant, D. J. Thermal Stresses in R. C. Slabs. Magazine of Concrete Research (London), Vol. 14, No. 41, July 1962.
13. Allan, D. W. The Calculation of Temperature Stresses. Concrete and Construction Engr., (London), Vol. 57, No. 9, Sept. 1962.
14. Hirschfeld, K. Der Temperatureinfluss bei der Verbund-Bauweise. Der Bauingenieur (Berlin), Vol. 25, No. 8, pp. 305-306, Aug. 1950.
15. Timoshenko, S., and Goodier. Theory of Elasticity. New York, McGraw-Hill, 1951.
16. Gatewood, B. E. Thermal Stresses. New York, McGraw-Hill, 1957.
17. Steinhardt. Temperaturversuche. Der Bauingenieur (Berlin), Vol. 27, No. 6, pp. 189-190, June 1952.
18. Aleck, B. J. Thermal Stresses in a Rectangular Plate Clamped Along an Edge. Trans. ASME, Vol. 71, pp. 118-122, 1949.
19. Tremmel, E. Temperaturspannungen im Plattenbalken. Osterreichische Bauzeitschrift (Vienna), Vol. 7, No. 1, pp. 1-5, Jan. 1952.
20. Boley and Weiner. Theory of Thermal Stresses. New York, John Wiley and Sons, 1960.
21. Eringer, A. C. Thermal Stresses in Multiple Layer Beam. Proc. 1st Midwestern Conf. of Solid Mechanics, Univ. of Illinois, pp. 69-73, April 1953.
22. Morsch, E. Der Spannbeton Trager. Stuttgart, 1943.
23. Hauelena, E. Brucken in Verbundausweise. Zeitschrift VDI (Dusseldorf), Vol. 90, No. 5, pp. 145-150, 1948.
24. Frohlich, H. Theorie der Stahlverbund-Tragwerke. Der Bauingenieur (Berlin), Vol. 25, No. 3, pp. 80-87, March 1950.
25. Walter, H. Der Einfluss des Schwindens und Kriechens bei Verbundtragern. Beton und Stahlbetonbau (Berlin-Wilmersdorf), Vol. 47, No. 5, pp. 110-115, May 1952.

26. Fritz et al. Discussion. Der Bauingenieur (Berlin), Vol. 25, No. 3, pp. 91-95, March 1950.
27. Tatlidil, K. G. Thermal Stresses in Composite Members Subjected to Temperature Variations Along the Length and in the Depth. C. E. Thesis, Univ. of Virginia, 1962.
28. Liu, Y. N. Thermoelastic Effects in Prestressed Flexural Members. C. E. Thesis, Univ. of Virginia, 1963.
29. England, G. L., and Ross, A. D. Reinforced Concrete Under Thermal Gradients. Magazine of Concrete Research (London), Vol. 14, No. 40, pp. 5-12, March 1962.
30. Zienkiewicz, O. C. Analysis of Visco-Elastic Behavior of Concrete Structures with Particular Reference to Thermal Stresses. Jour. ACI, Vol. 58, No. 4, pp. 383-394, Oct. 1961.
31. Rickenstorf, G. Structural Analysis of Temperature Stresses due to Non-Linear Temperature Distribution in Bars, Slabs, and Plates. Bauplanung-Bautechnik (Berlin), Vol. 13, No. 11, pp. 498-503, Nov. 1949.
32. Kato, M. The Calculation of the Stresses Caused by Shrinkage and Temperature Change in Composite Beams. (In Japanese). Japanese Civil Engineering Techniques, Vol. 14, No. 2, Feb. 1960.
33. Heilig, R. Zur Theorie des Starren Verbunds. Stahlbau, Vol. 22, p. 184, 1953.

Fatigue Tests of Plates and Beams With Stud Shear Connectors

J. E. STALLMEYER and W. H. MUNSE, Professors of Civil Engineering, University of Illinois, and K. A. SELBY, University of Toronto

•IN THE PAST few years there has been a great increase in the use of composite construction in both bridges and buildings. This increased use has produced some new proposals for shear connector design and more significantly, has resulted in applications of shear connectors in a variety of structures utilizing a number of different steels. Basic research work on composite construction was carried out several years ago, but the increased interest in this structural system has caused renewed interest in a number of questions not answered in the earlier studies.

Most of the research work conducted in the past has been carried out primarily for one of two purposes. Push-out tests (1) designed to determine the shear capacity of the many varieties of connectors and to study the load transfer distribution constitute the most common investigations. The second most common type of study has been conducted to determine the static flexural strength of composite beams. Very few fatigue tests were included in the earlier work.

This situation is not surprising since in most applications of composite construction the shear connectors are attached to a steel flange subjected to flexural stresses which are usually compressive or, at most, very small tensile stresses. In this case the fatigue problem is associated with the connector itself. The interest in the use of composite construction along the entire length of continuous structures and the desire to use higher strength steel in many applications has raised questions in connection with the fatigue resistance of such structures.

In these latter applications, a sufficient margin of safety must be provided to preclude fatigue failure of the flange of the beam. Shear connectors attached to the tension flange or to high-strength steels where a larger stress range is possible could serve as points of initiation for progressive failure. The program reported herein was undertaken to study this problem.

The primary objective of this program was to study the effect of shear connectors on the fatigue life under circumstances where the connectors are attached to the tension flange and to study the influence of flange material on this behavior. To study these two problems, work was undertaken on several different materials with varying chemical compositions and with different strength levels.

The program included a rather extensive series of tests on flat plate-type specimens. These specimens were fabricated from two different materials. For the different types of materials studied, one or more stud shear connectors were attached in a single line transverse to the direction of stress. Another variable, intended to permit a study of the effect of stud spacing, was the width of the plate. In one series of tests the welding procedure used to apply the studs was altered.

Flat-plate fatigue tests were conducted on stress cycles of complete reversal, zero-to-tension and partial tension-to-tension. A few supplementary tests were conducted to investigate the effect of geometry in the region of the connection between the plate and the stud shear connector.

The second phase of the program was carried out on nine beam specimens, divided into three groups of three beams each. All beams were loaded so that the flange to which the stud shear connectors were attached was subjected to a tensile stress. The first group of beams was tested without any stress applied to the shear connectors.

Paper sponsored by Committee on Bridges.

This series could then be directly related to the flat-plate tests to study the effect of stress gradient.

Bending of the beam and flexing of the stud simultaneously were studied in the other two series of beam tests. Two different methods were used to accomplish this loading condition. The studs of one group of beams were loaded by pre-tensioned mechanical flexors fabricated specifically for this purpose and provided with strain gages to monitor the load. In the final group of beams, a reinforced concrete slab was cast to resemble the situation as it actually exists in practice.

DESCRIPTION OF MATERIALS AND TESTS

Materials

Three different steels were used in the fabrication of the flat-plate and beam specimens reported herein. These three steels are referred to in the following discussion by their ASTM designations.

A7F Steel. —During the initial phases of the study reported, one series of eight plate specimens (GIA series) was fabricated from a steel which was available in the laboratory and had been purchased some time earlier to conform to ASTM A7-58T. Coupon tests carried out in the laboratory indicated that this steel failed to meet the tensile requirements of this specification.

A441 Steel. —All remaining flat-plate tests were carried out on specimens fabricated from a steel which satisfied the requirements of ASTM A441-60T. This material was also used as the flange material in the beam tests.

A373 Steel. —The third type of steel used served for the web material of the nine beam specimens. This steel met the requirements of ASTM A373-58T. Due to the location of this material in the beam specimens and the type of tests being conducted, this steel did not affect the fatigue life being studied.

The chemical composition and physical properties of all base materials are presented in Table 1. All specimens were fabricated in the Civil Engineering Shop at the University of Illinois and then shipped to Gregory Industries, Inc., in Lorain, Ohio, where the studs were affixed.

The entire test program was broken down into five different series of tests, designated GIA through GIE. Each specimen received a designation consisting of three letters to indicate the specific series followed by a number to distinguish the particular test specimen within that series (e.g., GIB12).

Plate Specimens

The dimensions of the various plate specimens are shown in Figures 1, 2 and 3. The details of the welding procedure used in the application of the studs to the individual specimens are given in Table 2.

GIA Series. —This series consisted of eight plate specimens machined from A7F steel. Each specimen was machined to the dimensions shown in Figure 1a before the stud was attached. Each specimen was provided with a single stud on a $3\frac{1}{2}$- by $\frac{1}{2}$-in.

TABLE 1

PROPERTIES OF BASE MATERIALS

Steel	Chemical Composition								Yield Pt.[a] (ksi)	Tensile[a] Strength (ksi)	Elongation[a, b] (%)
	C	Mn	P	S	Si	Cu	Va	Ni			
A7F[c]	0.20	0.28	0.009	0.041	0.01	0.05	-	0.01	30.3	52.8	29.5
A373	0.23	0.63	0.022	0.031	0.030	0.17	-	-	38.8	64.8	29.6
A441	0.20	1.14	0.015	0.031	0.06	0.23	0.06	-	61.6	84.1	22.2

[a] Based on average of three tests.

[b] Per 8 in.

[c] Failed to meet ASTM A7 tensile requirements.

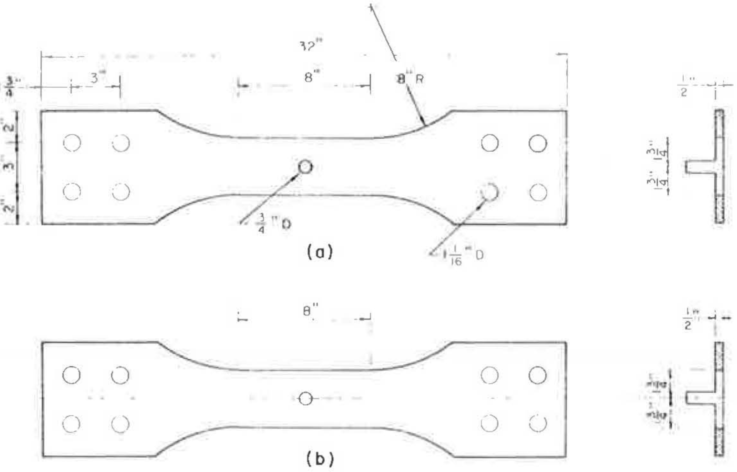

Figure 1. Dimensions of small plate specimens: (a) GIA specimens, and (b) GIB specimens.

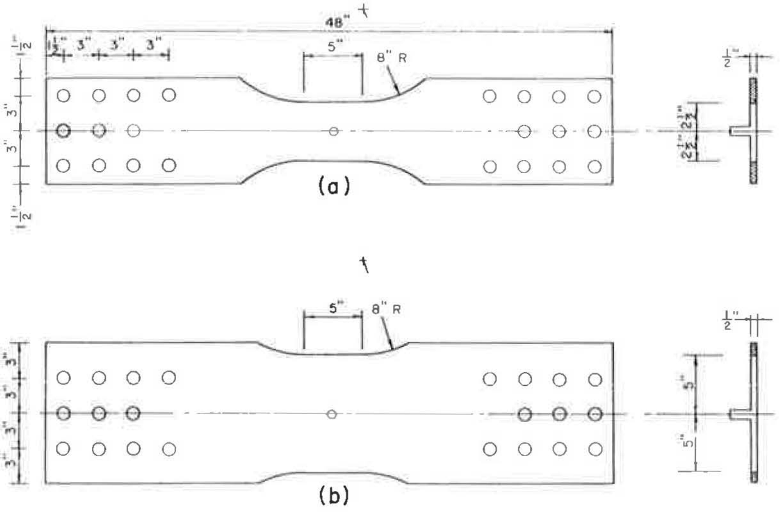

Figure 2. Dimensions of large plate specimens with a single stud: (a) GIC specimens, and (b) specimens GID1 through GID3.

cross-section. Throughout all five series, the material thickness was maintained constant at $\frac{1}{2}$ in. to reduce the number of variables involved.

GIB Series.—Basically, the GIB series, involving 20 specimens, was identical in all respects to the GIA series except that A441 steel was used instead of A7F. Specimens GIB16 through GIB20 were subjected to a slightly different welding procedure and several specimens had slight variations in geometry.

GIC Series.—The only significant difference between the five GIC specimens and those of the GIB series was the width of the cross-section. In this series of tests the width was increased to 5 in. Both series were fabricated from A441 steel and contained a single stud attached at the center of the flat-plate specimen.

GID Series.—To study the effect of multiple studs, ten flat-plate specimens were machined to a 10 in. width across the test section. These specimens were then provided with either one, three, or five studs attached in a single line transverse to the

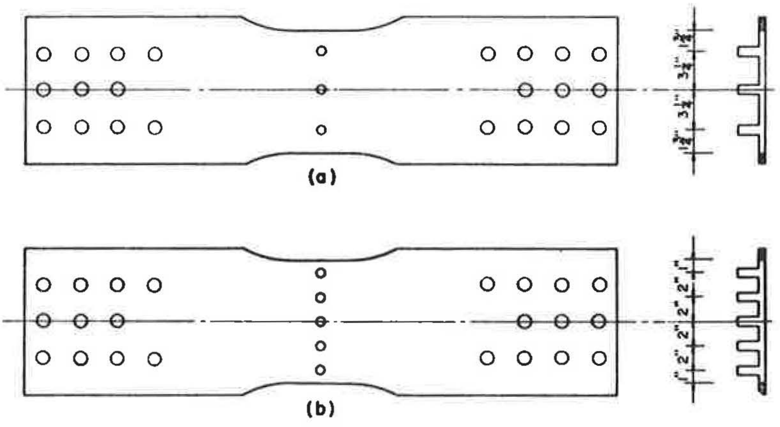

Figure 3. Dimensions of large plate specimens with multiple studs: (a) specimens GID4 through GID6, and (b) specimens GID3 through GID10.

TABLE 2

STUD-WELDING PROCEDURES

Specimens	Lift (in.)	Plunge (in.)	Weld Current (amp)	Arc Voltage (volts)	Weld Time (cycles)
GIA1-GIA8	3/32	3/16	1500	33	58
GIB1-GIB15	3/32	3/16	1500	33	58
GIB16-GIB20	3/32	3/16	1450	33	76
GIC1-GIC5	3/32	3/16	1750	31	43
GID1-GID10	3/32	3/16	1750	31	43

direction of applied stress. In addition to the increased width, these specimens, as well as those of the GIC series, were 4 ft long, whereas specimens of the GIA and GIB series were only 2 ft 8 in. long. The difference in length was necessitated by the increased cross-sectional area which required loadings of such a magnitude that they could only be produced by the larger testing machines.

The cross-sections of all flat-plate specimens through the line of studs are shown in Figure 4.

Beam Specimens

The nine steel beams used in this phase of the investigation were fabricated from three flat plates. The beams had an overall depth of 12 in., a flange thickness of $\frac{1}{2}$ in., and a web thickness of $\frac{3}{16}$ in. Each of the beams was then provided with two rows of studs spaced $2\frac{1}{2}$ in. apart. Each of the rows contained nine studs at a spacing of 10 in. along the length of the beam. These nine specimens were then subdivided into three groups of three specimens each and subjected to different loading conditions.

Specimens GIE1 through GIE3 were tested as simple flexural members with no external loads applied to the stud shear connectors. Specimens GIE4 through GIE6 were altered in such a manner as to remove the heads from the eight centrally located studs. Specially prepared and calibrated connectors were placed over four pairs of studs as shown in Figure 5b. These connectors were made so that they could be pretensioned to produce any desired shear force in the studs. The force in the connector was measured by strain gages attached to the connector and calibrated in a static testing machine. Additional strain gages were attached to specimens GIE4 and GIE5 to determine the strain distribution across two different cross-sections. The output from

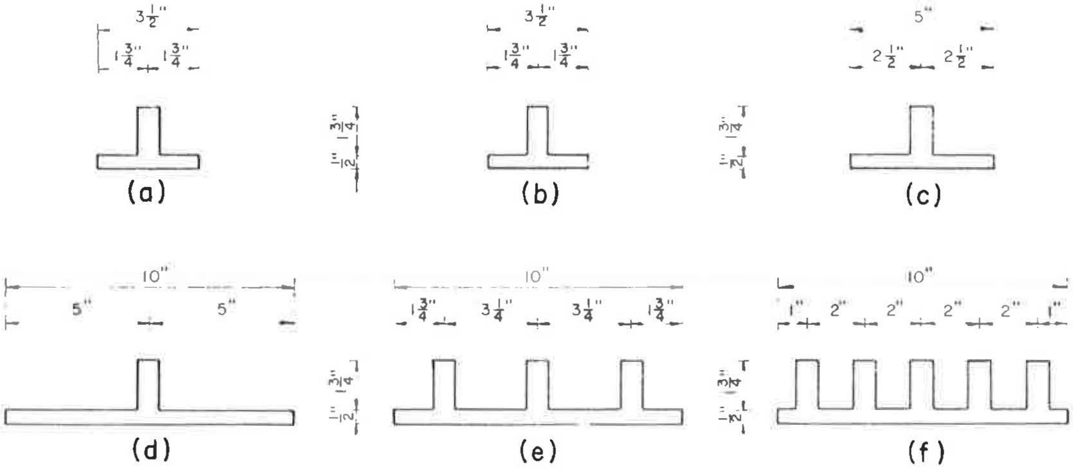
3 1/2"
1 3/4"
1 3/4"
1 3/4"
1/2"
5"
2 1/2"
2 1/2"
(a)
(b)
(c)
10"
5"
5"
1 3/4"
3 1/4"
3 1/4"
1 3/4"
1"
2"
2"
2"
2"
1"
(d)
(e)
(f)

Figure 4. Cross-sections of flat-plate specimens through line of studs: (a) GIA, (b) GIB, (c) GIC, (d) GID1 through GID3, (e) GID4 through GID6, and (f) GID7 through GID10.

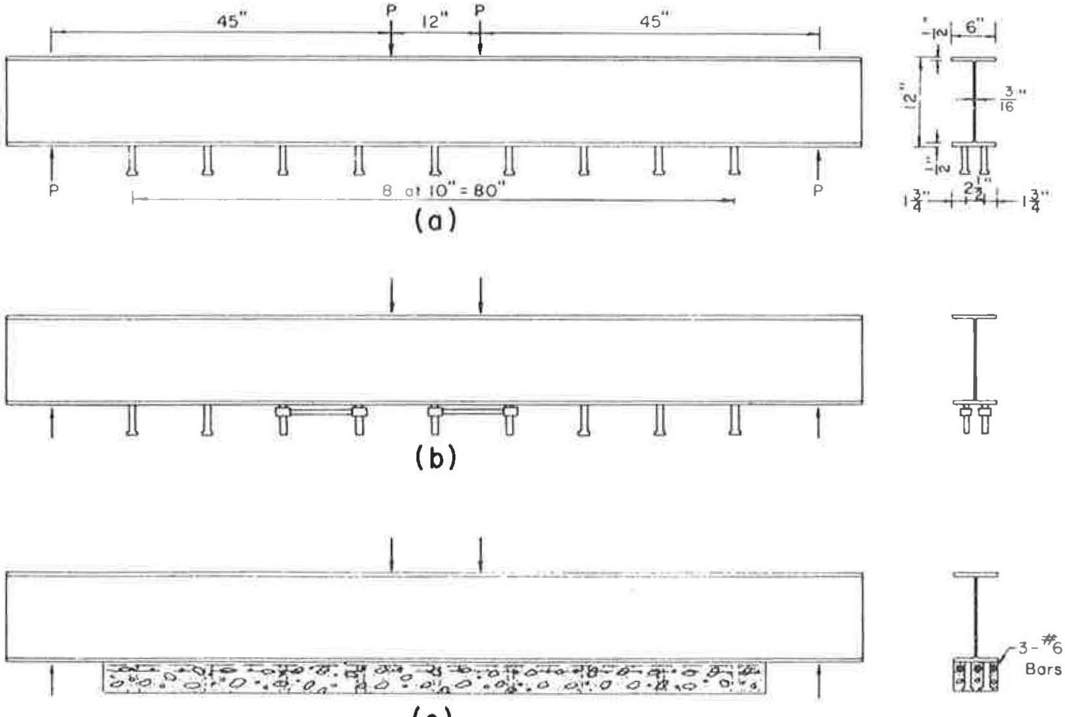
45"
P
12"
P
45"
P
8 at 10" = 80"
P
(a)
1/2"
6"
12"
3/16"
1/2"
1 3/4"
2 1/4"
1 3/4"
(b)
3-#6 Bars
(c)

Figure 5. Details of beam specimens: (a) GIE1 through GIE3, (b) GIE4 through GIE6, and (c) GIE7 through GIE10.

these strain gages was recorded during the period of the fatigue test on a Sanborn recorder.

The studs of specimens GIE7 through GIE9 were incased in a reinforced concrete slab as shown in Figure 5c. A mixture of graphite and linseed oil (one part graphite to 4.4 parts of linseed oil) was placed on the steel surface to destroy the steel-concrete bond. In this way all of the shear force must be transmitted through the studs. The reinforcing steel consisted of three No. 6 bars located $^3/_4$ in. below the lower flange of the steel beam. Beams GIE7 and GIE9 were instrumented with strain gages at various locations and through the depth of the steel beam to determine the strain distribution through the depth and the extent to which this strain distribution was altered as a result of the shear force transmitted through the shear connector.

Object of Individual Test Series

GIA Series. —The purpose of this series of tests was to obtain a basic S-N curve for A7F steel on a zero-to-tension stress cycle so that these results could be compared with similar tests on A441 steel.

GIB Series. —In this series S-N curves were to be established for both zero-to-tension stress cycles and a fully reversed stress cycle. On the basis of the results obtained on these two series of tests, an estimate was made of the stress cycle which would produce failure at 2,000,000 cycles on a one-half tension-to-tension stress cycle.

Specimens GIB16 through GIB20 were produced with a slightly different stud welding procedure from the rest of the specimens in this series. The purpose of these specimens was to investigate the effect of altering the stud welding procedure on the fatigue life and the fatigue behavior of this material. Two specimens, GIB11 and GIB12, were subjected to additional treatment after the studs had been attached. This treatment consisted of grinding the upset to produce a smooth transition from the plate to the stud to evaluate the significance of the geometry of the upset.

In two other specimens, GIB19 and GIB20, the studs were completely removed by grinding. The grinding was carried out so as to approximate the surface condition of the surrounding plate as nearly as possible. In these cases the notch effect of the upset and the presence of the stud had been completely removed, so that any difference in the results from plain-plate test results would indicate the effect of welding on the base material.

The tensile strength of GIA and GIB series specimens was checked by three static tests providing a basis for comparison of the various fatigue strengths with the static ultimate strength of similar specimens.

GIC Series. —The function of this series was to determine the fatigue strength for failure at 2,000,000 cycles on a one-half tension-to-tension stress cycle. Specimens in this series were 5 in. wide so that a comparison with the results of the GIB series would give some indication of the size effect. Specimen GIC5 was not subjected to any fatigue loading but was examined metallurgically to determine the hardness distribution near the stud.

GID Series. —All of these specimens were tested under a one-half tension-to-tension stress cycle. Specimens were provided with either one, three, or five studs on a single line transverse to the direction of applied stress. In all cases the fatigue strength for failure at 2,000,000 cycles was desired. The single-stud specimens, GID1 through GID3, provided data for a further evaluation of the effect of width since the cross-section was 10 in. wide in this series. Comparison of the three groups of specimens within this series provides an evaluation of stud spacing.

GIE Series. —This series was divided into three groups of three beams each. In every case the fatigue strength for 2,000,000 cycles under a one-half tension-to-tension stress cycle was desired. The purpose of the first group of tests, GIE1 through GIE3, was to compare the fatigue strength of the flange with the attached studs with the results of the axially loaded plate specimens. The other two groups were intended to show the effect of transmission of shear force through the stud connector while the beam is being subjected to primary bending. This, of course, is the loading condition occurring in actual composite construction. Some strain gages were attached to

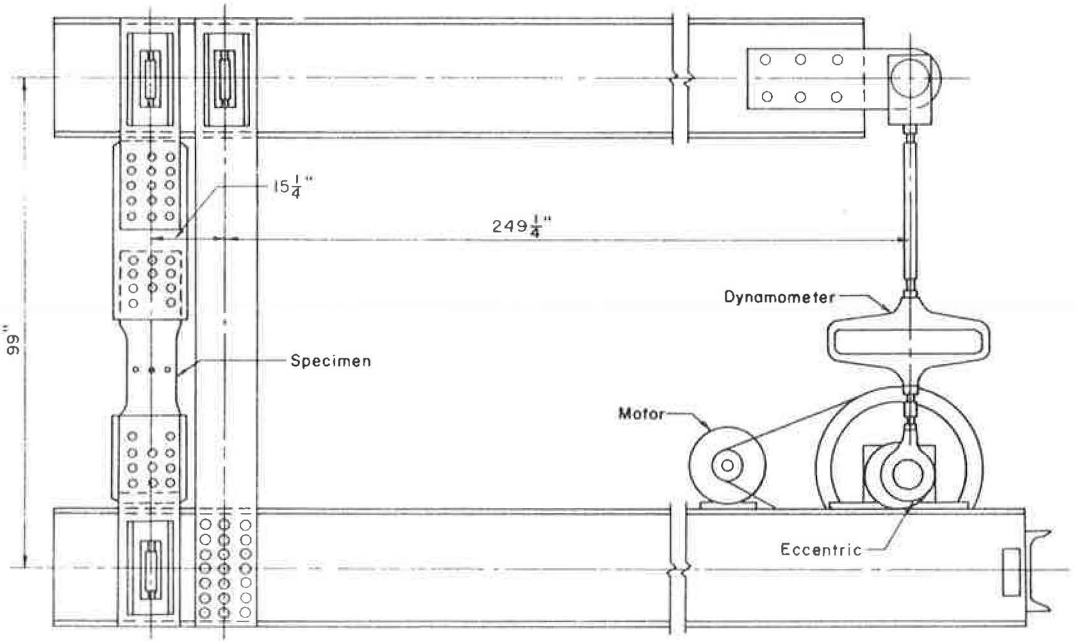
15 1/4"
249 1/4"
Dynamometer
99"
Specimen
Motor
Eccentric

Figure 6. Illinois' fatigue testing machine for axial loading.

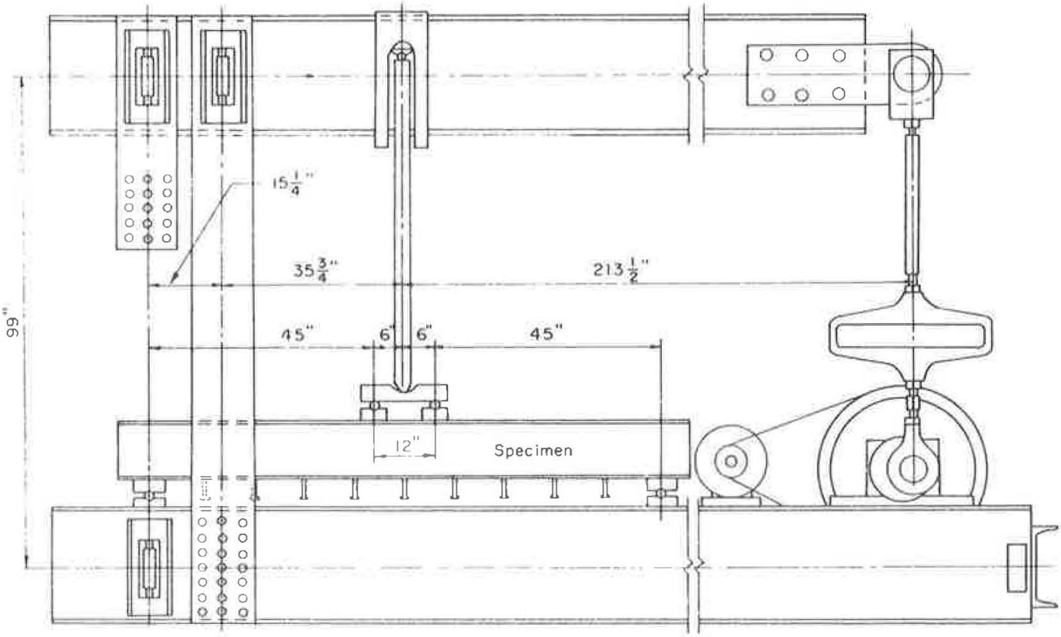
15 1/4"
35 3/4"
213 1/2"
99"
45"
6"
6"
45"
12"
Specimen

Figure 7. Illinois' fatigue testing machine modified for flexural loading.

several of these specimens to check the strain distribution across several cross-sections.

Test Procedures

All fatigue tests were conducted in University of Illinois lever-type fatigue machines. The small plate specimens, GIA and GIB series, were tested in machines with a total load capacity of 50,000 lb and all other tests were conducted in the larger 200,000-lb machines. These machines, while similar in their basic operation, varied in speed from 300 to 100 cycles/min.

Schematic diagrams of the University of Illinois fatigue testing machine adapted for axial or flexural loading can be seen in Figures 6 and 7, respectively. By adjusting the variable throw eccentric and the turnbuckle immediately above it, the required stress cycle can be applied to the specimen. The load is determined by an Ames dial which measures the deformation of the dynamometer.

A microswitch near the specimen end of the machine is adjusted so that excessive deflection of the specimen trips the switch and stops the machine. During the progress of the fatigue fracture the load is adjusted so that the specimen is subjected to a relatively constant load. Failure is defined as having occurred when the specimen could no longer withstand the prescribed load without yielding.

Before testing, the plate specimens were measured to determine the average cross-sectional area at the position of the stud. This area was then used to determine the load so that the desired average stress would exist at the expected failure location. In the case of the beam specimens, the loads and, therefore, the moments acting on the beam were calculated by the deformation of the dynamometer. The stresses were obtained by the simple flexural formula using the moment of inertia computed for the fracture section.

TABLE 3

FATIGUE RESULTS, ZERO-TO-TENSION, AXIAL LOADING

Specimen	Stress Cycle (ksi)	Life (cycle)
GIA1	0 to +16.5	1,320,000
GIA2	0 to +24.0	460,000
GIA3	0 to +24.0	840,000
GIA4	0 to +20.0	1,170,000
GIA5	0 to +16.5	1,480,000
GIA6	0 to +16.5	2,250,000
GIA7	0 to +15.0	3,240,000[a]
GIB1	0 to +20.0	820,000
GIB2	0 to +16.5	1,460,000
GIB3	0 to +16.5	2,410,000
GIB4	0 to +15.5	2,510,000
GIB11[b]	0 to +16.5	4,200,000
GIB12[b]	0 to +20.0	2,060,000
GIB16[c]	0 to +16.5	1,920,000
GIB17[c]	0 to +16.5	1,610,000
GIB19[d]	0 to +28.0	4,940,000[a]
GIB19[d]	0 to +40.0	810,000
GIB20[d]	0 to +38.0	550,000

[a] Did not fail.

[b] Upsets ground to form smooth transition.

[c] Welding procedure altered.

[d] Welding procedure altered and studs removed.

BEHAVIOR OF FLAT-PLATE SPECIMENS

The results of individual tests carried out on the plate specimens are given in Tables 3 through 6. These same results are shown as S-N diagrams in Figures 8 through 12. The data indicate a minimum amount of scatter and good consistency among the results.

The fatigue results showed amazingly little scatter so that relatively few tests gave a strong indication of the fatigue resistance of plate specimens with attached studs. Most of the tests carried out were intended to determine the magnitude of the stress cycle which would result in failure at 2,000,000 cycles. A study of the various S-N diagrams indicates that such stress cycles are as follows: for complete reversal a stress cycle from 8.0-ksi compression to 8.0-ksi tension (a range of 16.0 ksi), for the zero-to-tension stress cycle from 0 to 16.0 ksi (a range of 16.0 ksi), and for a stress cycle ranging from one-half tension-to-tension from +14.0 to +28.0 ksi (a range of 14.0 ksi). It should be noted that the stress range remains almost constant as the stress cycle changes.

Influence of Base Material on Fatigue Life

An indication of the effect of variations in base material is obtained by comparing the results of the GIA and GIB specimens. Figures 8 and 9 present the results for specimens which are similar in all respects except for base material. Seven GIA specimens, fabricated from A7F steel, and six GIB specimens, fabricated from A441 steel, were subjected to a zero-to-tension stress cycle. For each group of tests the results formed a very narrow scatter band, as indicated on the figures. When the data are superimposed, the two scatter bands coincide almost perfectly, as is seen in Figure 10. It must be noted that this excellent correlation involved only a few tests of two steels for one particular type of stress cycle. These results are similar to results previously obtained on these materials in studies of the effect of butt-welded joints.

Effect of Stud-Welding Procedure

To study the effect of variations in the stud-welding procedure, five specimens of the GIB series were fabricated with a substantially different welding procedure from that used for the preparation of the remainder of these specimens. For specimens GIB16 through GIB20, the weld current was 1,450 amperes, the arc voltage was 33 volts, and the weld time was 76 cycles. The remainder of the series, specimens GIB1 through GIB15, were prepared with a weld current of 1,500 amperes and an arc voltage of 33 volts for 58 cycles. This means simply that specimens GIB15 through GIB20 were subjected to 26 percent more heat than other specimens of this type.

Two of these specimens, GIB16 and GIB17, were subjected to a zero-to-tension stress cycle in the as-produced condition. The results of these tests are presented in Figure 9 and no significant difference in fatigue life was obtained. One specimen, GIB18, was subjected to a one-half tension-to-tension stress cycle in the as-welded condition and a study of the results given in Table 5 indicates that

TABLE 4

FATIGUE RESULTS, COMPLETE REVERSAL, AXIAL LOADING

Specimen	Stress Cycle (ksi)	Life (cycles)
GIB5	-20.0 to +20.0	190,000
GIB6	-20.0 to +20.0	180,000
GIB7	-10.0 to +10.0	960,000
GIB8	- 8.5 to + 8.5	1,730,000
GIB9	- 8.5 to + 8.5	1,660,000

TABLE 5

FATIGUE RESULTS, ONE-HALF TENSION-TO-TENSION, AXIAL LOADING

Specimen	Stress Cycle (ksi)	Life (cycles)
GIB13	+14.0 to +28.0	1,950,000
GIB14	+14.0 to +28.0	2,560,000
GIB15	+14.0 to +28.0	2,140,000
GIB18[a]	+14.0 to +28.0	2,690,000
GIC1	+27.9 to +55.8	280,000
GIC2	+14.0 to +28.0	2,220,000
GIC3	+14.0 to +28.0	2,700,000
GIC4	+14.0 to +28.0	2,590,000

[a] Welding procedure altered.

TABLE 6

FATIGUE RESULTS, ONE-HALF TENSION-TO-TENSION, AXIAL LOADING

Specimen	No. of Studs	Stress Cycle (ksi)	Life (cycles)
GID1	1	+14.0 to +28.0	3,260,000[a]
GID1	1	+15.0 to +30.0	1,730,000
GID2	1	+14.0 to +28.0	2,710,000
GID3	1	+15.0 to +30.0	1,840,000
GID4	3	+14.0 to +28.0	1,630,000
GID5	3	+14.0 to +28.0	1,900,000
GID6	3	+14.0 to +28.0	1,890,000
GID7	5	+14.0 to +28.0	1,410,000
GID8	5	+14.0 to +28.0	1,880,000
GID9	5	+14.0 to +28.0	1,570,000
GID10	5	+14.0 to +28.0	1,460,000

[a] Specimen did not fail.

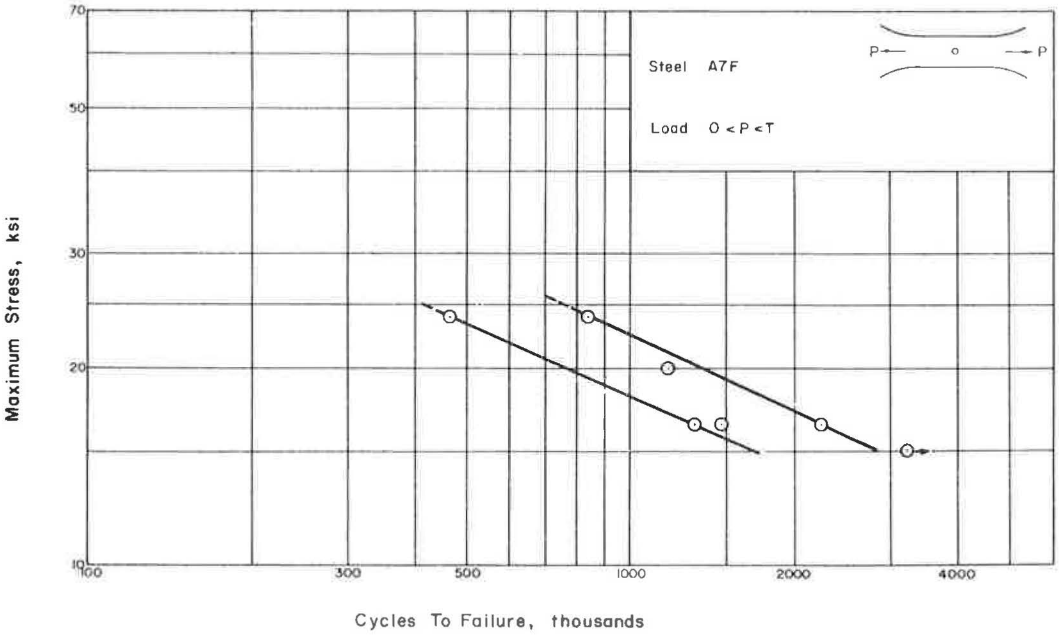

Figure 8. Fatigue results for GIA specimens, zero-to-tension stress cycle.

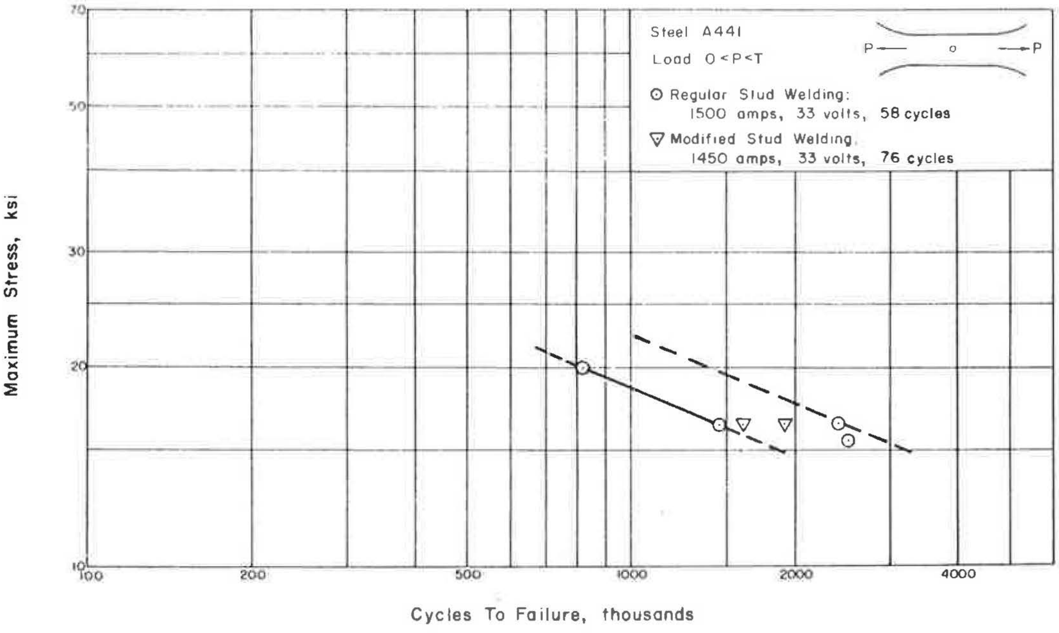

Figure 9. Fatigue results for GIB specimens, zero-to-tension stress cycle.

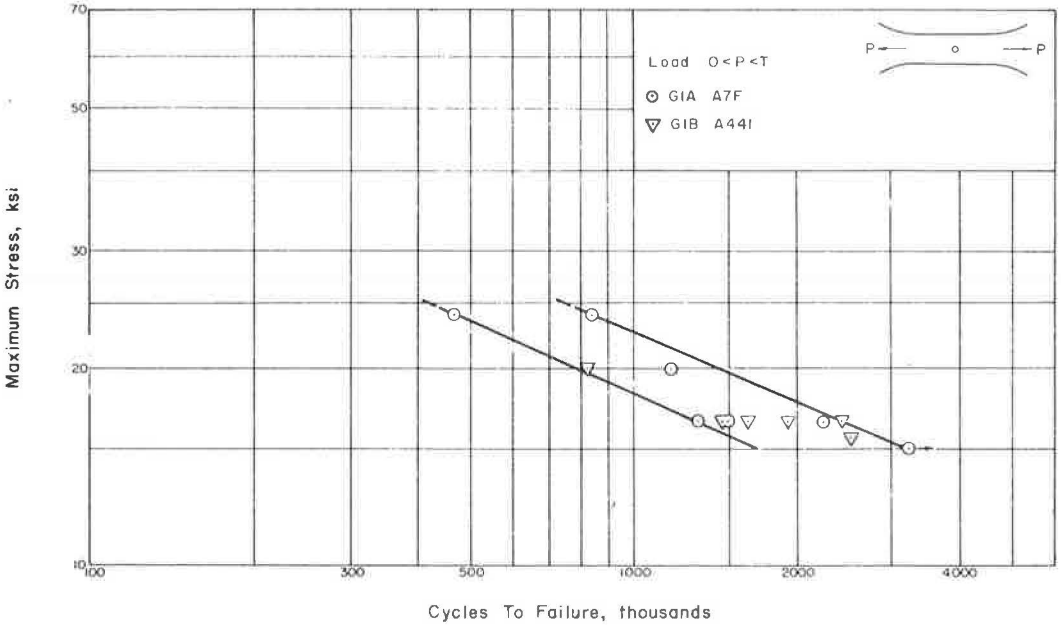

Figure 10. Effect of type of steel on fatigue life, zero-to-tension stress cycle.

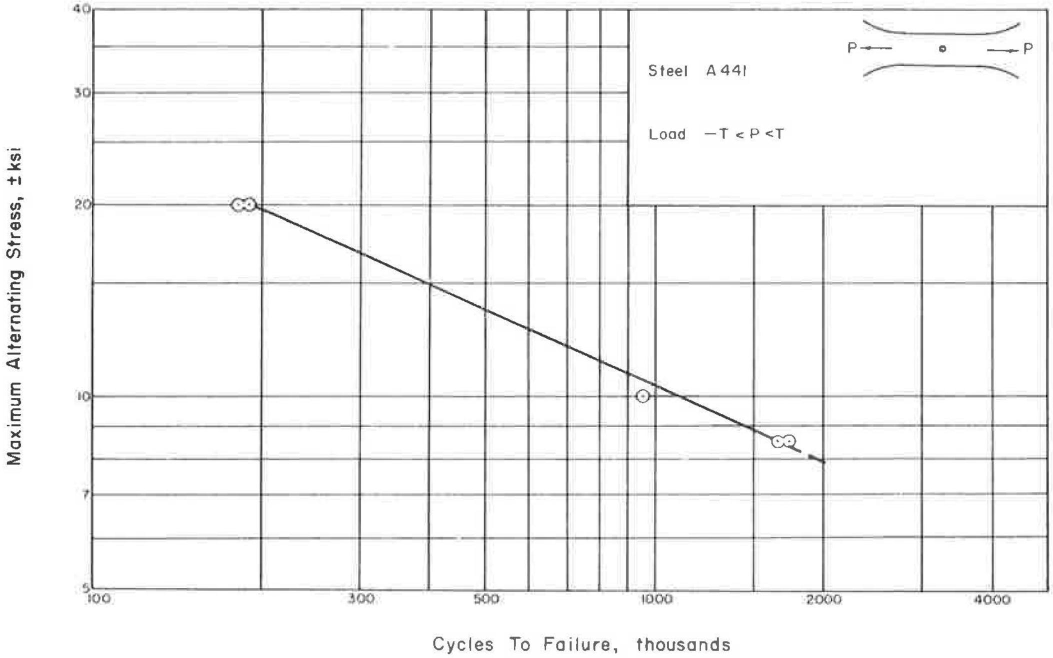

Figure 11. Fatigue results for GIB specimens, complete reversal stress cycle.

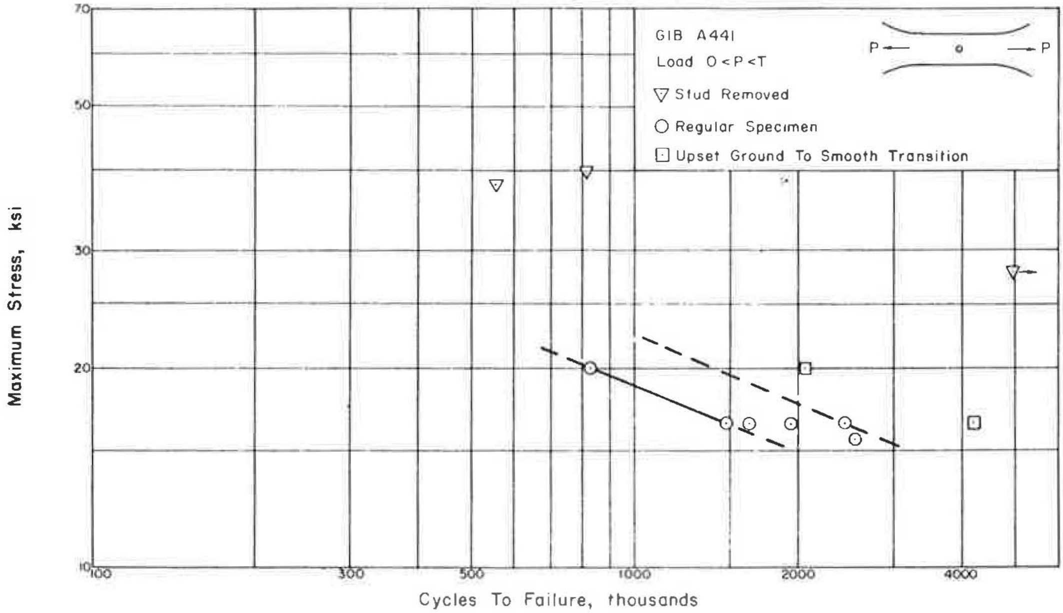

Figure 12. Geometrical effect on fatigue results, zero-to-tension stress cycle.

no significant difference could be observed. The remaining two specimens with the modified welding procedure, GIB19 and GIB20, were subjected to special tests which are reported later.

On the basis of the tests conducted it can be concluded that, within the limits studied, the variations in welding procedure had no significant effect on the fatigue life.

Effect of Upset Geometry

To study the effect of geometry in the region of the upset, four specimens of the GIB series were subjected to treatments altering this geometry. Two specimens, GIB11 and GIB12, were ground so that their upsets formed a smooth transition from the plate surface to the stud. Each was tested at a different zero-to-tension stress cycle for which results were available for specimens with the as-produced geometry. The results of these tests are presented in Table 3 and Figure 12. Figure 12 indicates that the fatigue life of these treated specimens was approximately double that of the as-produced specimens.

The studs of two other specimens of this series, GIB19 and GIB20, were completely removed and the surface smoothness was ground to approximate that of the surrounding plate. This alteration should remove completely the geometrical effect and, therefore, any difference in fatigue life between these specimens and plain plate specimens could be attributed to the effect of welding on the base metal. The results of the tests conducted on these two specimens are given in Table 3. The specimens proved to be significantly more fatigue resistant than all other types of specimens in this program. These test results are not quite as good as the results obtained in previous investigations for plain plate specimens of A441 steel. Therefore, one can conclude that even when the stud is completely removed from the plate to which it is attached, some effect of the welding remains and the fatigue resistance is slightly less than that obtained for plain plate material.

Significance of Stud Spacing

The effect of stud spacing can be studied by comparing several different series of tests. In one case, the effect of plate width can be studied for the various specimens provided with a single stud. Series GIB, GIC, and GID all contain test results for single-stud specimens subjected to a one-half tension-to-tension stress cycle. The results of these tests are given in the individual tables and have been presented for purposes of comparison in Figure 13. These results indicate that a slight increase in fatigue life is obtained when the width of the plate is increased. Although the plate to which the stud is attached is continuous, the stud acts somewhat like a hole in a flat-plate specimen. The stress concentration effect increases as the width of the plate decreases, which is directly in line with what would be expected for a plate with a hole.

The effect of stud spacing can also be studied by examining the results of the GID series (Table 6, Fig. 14). All tests in this series were conducted on a stress cycle which varied from one-half tension-to-tension. The specimens were all 10 in. wide and were provided with one, three, or five studs. In the multi-studded specimens, it might easily be reasoned that since the plate is heated and cooled more slowly when several studs are attached in succession, the plate should contain residual stresses of a lower magnitude and the studs should represent less of a stress concentration. However, one could easily argue in favor of a reduced fatigue life because of the increased number of stress concentrations where fatigue fracture could initiate.

An examination of the test results indicate that neither of these factors is very dominant. As seen in Figure 14, the single-studded specimens are slightly more resistant to fatigue failure. However, a study of the results presented in Figure 13 reveal that the results for a single stud attached to a 3½-in. wide plate, corresponding to a stud spacing of 3½ in., and the results for the single stud attached to a 5-in. wide plate, corresponding to a stud spacing of 5 in., give results in line with those presented in Figure 14. Although there is a slight decrease in fatigue life as the number of studs in any one line is increased, this difference is not significant when converted to stress levels which would produce failure at the same number of cycles.

It is interesting to note at this time that the specimens with more than one stud attached always had more than one failure surface occurring independently and almost

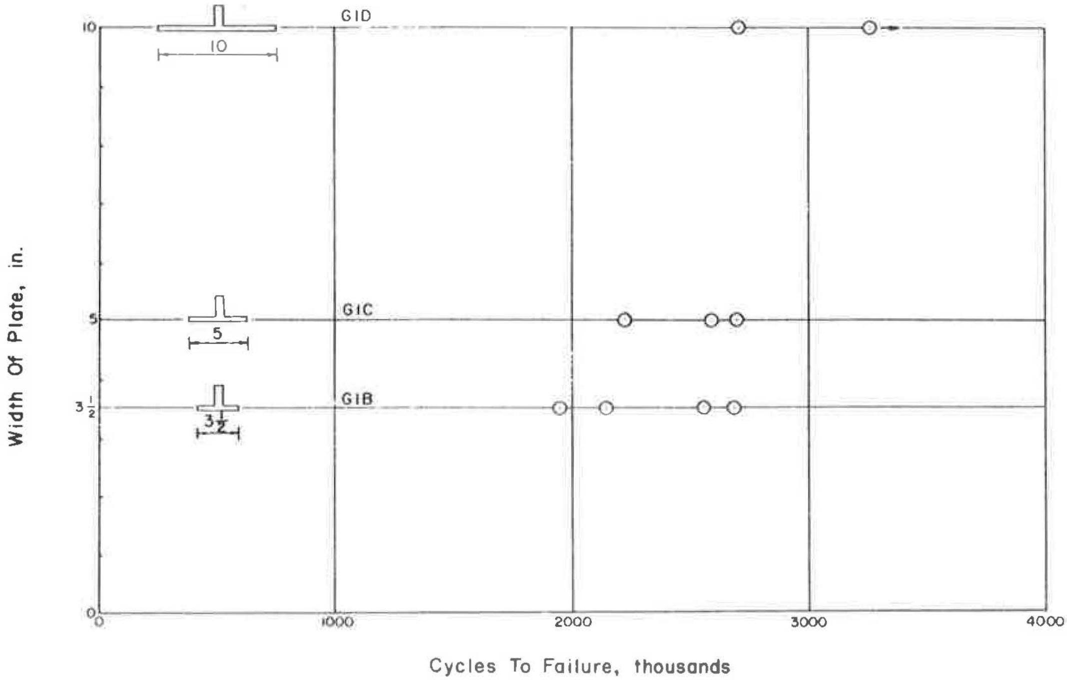

Figure 13. Width of plate vs fatigue life, stress cycle +14.0 to +28.0 ksi.

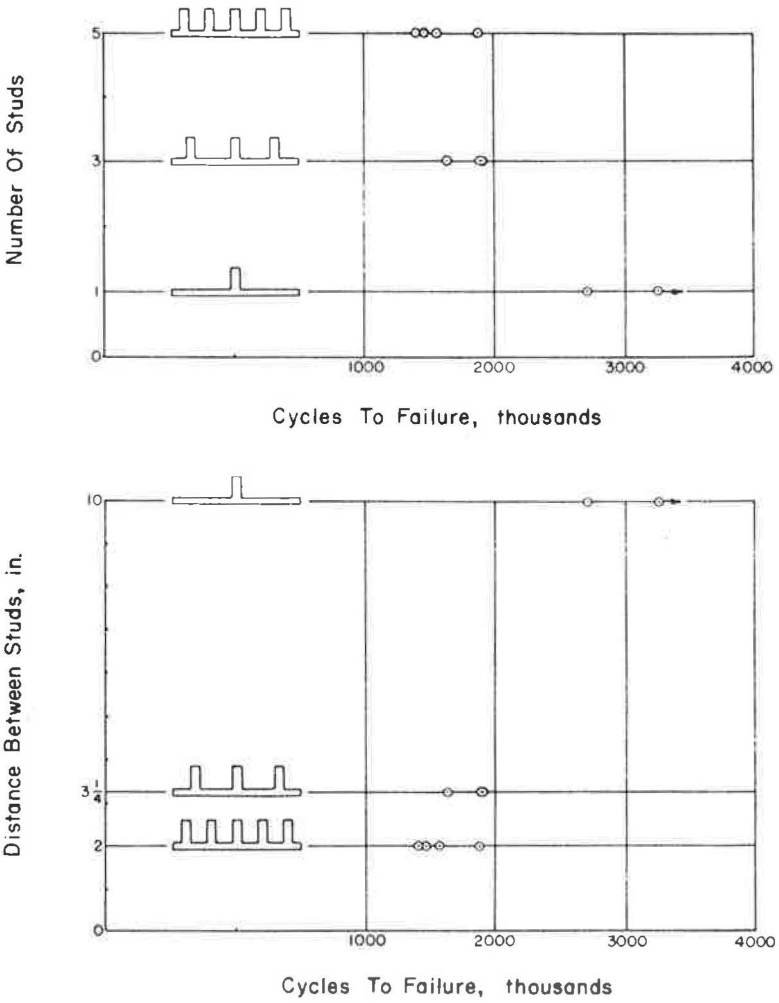

Figure 14. Stud spacing vs fatigue life, stress cycle +14.0 to +28.0 ksi.

simultaneously. In a number of cases, failures occurred above and below the same stud. These fractures indicate that failure is not precipitated by one particular weak spot, but that the effect of the studs is extremely consistent and that failures initiate at a number of independent locations and propagate individually.

Comparison with Other Test Results

Table 7 gives test results obtained in this and previous investigations (2, 3) with similar materials. Previous tests have been conducted on plain-plate material of A441 and A7, double-V butt-welded joints in A441 steel and plate material with a single hole. These results indicate that the attachment of studs is a somewhat more severe condition than the presence of a hole or of a double-V butt weld. On the basis of the results for plain-plate specimens of A441, the plate with studs has an effective stress concentration factor in fatigue of approximately 2.5.

Static Tests

During the course of the investigation several static tests on plain-plate specimens with a single attached stud were conducted. The results of these tests (Table 8)

TABLE 7

EFFECT OF VARIOUS STRESS RAISERS ON FATIGUE LIFE OF PLATE SPECIMENS[a]

Specimen	$F_{2,000,000}$ (ksi)
Plain plate (A441)	0 to +40
Plain plate (A7)	0 to +35
Double-butt weld (A441)	0 to +28
Plate with hole (A441)	0 to +24
Plate with stud (A441)	0 to +16

[a] Zero-to-tension, axial loading.

TABLE 8

RESULTS OF STATIC TESTS

Specimen	ASTM Designation	Yield Point (ksi)	Ultimate Strength (ksi)
GIA7	A7F[a]	31.6	53.9
GIA8	A7F[a]	29.6	53.6
GIB10	A441	-	80.4

[a] Failed to meet ASTM A7 tensile requirements.

indicate that the presence of the stud did not in any way influence either the yield point or the ultimate strength of the base material. A comparison of these results with those presented in Table 1 indicates that the average of the yield point obtained is at least as high as that obtained on the coupon tests and the ultimate strength is somewhat higher. With the A441 specimen no yield point was recorded, but the ultimate strength is very close to that obtained in the coupon tests and is well in excess of that required by the specifications.

BEHAVIOR OF BEAM SPECIMENS

The purpose of this series of tests was to provide a correlation between the results of the flat-plate specimens and the stress conditions as they actually occur in composite construction. In addition, as previously noted, this series of specimens was divided into three groups: one subjected to flexural loading without any load being transmitted through the stud shear connector, one subjected to flexural loading with a shear loading applied by special mechanical adapters and a final group in which the stud was embedded in a concrete slab and subjected to shear force transmitted by the composite action obtained. All tests on beam specimens were conducted on a stress cycle which ranged from approximately one-half tension-to-tension with the stress range chosen so as to produce failure in approximately 2,000,000 cycles. The results are presented in Table 9.

Plain-Beam Tests

The results of the plain-beam tests, specimens GIE1 through GIE3, indicate that a stress cycle alternating between 16.4- and 32.8-ksi tension is required to produce failure in approximately 2,000,000 cycles. This stress range is slightly higher than the stress range which produced failure at this same life in the plain-plate specimens. Although no direct comparison can be made since the flange used in the beam tests was provided with two studs on a 6-in. wide plate and a spacing between studs of 2½ in., the results can be compared with specimens of the GIC series and the GID series. In the GIC series a single stud was attached to a 5-in. wide plate, in the GID series specimens providing stud spacings of 3¼ and 2 in. are included.

TABLE 9

FATIGUE RESULTS FOR BEAM SPECIMENS ONE-HALF TENSION-TO-TENSION, FLEXURAL LOADING

Specimen	Type[a]	Stress Cycle (ksi)	Life (cycles)
GIE1	PB	+15.0 to +29.9	2,780,000
GIE2	PB	+16.4 to +32.8	2,070,000
GIE3	PB	+16.5 to +32.9	1,940,000
GIE4	SF	+11.5 to +24.2	2,020,000
GIE5	SF	+12.4 to +24.6	2,210,000
GIE6	SF	+12.7 to +25.2	1,830,000
GIE7	RC	+10.7 to +21.4[a]	1,480,000
		+15.0 to +30.0[a]	610,000
GIE8	RC	+15.0 to +30.0[a]	1,640,000
GIE9	RC	+15.3 to +30.0[a]	1,500,000

[a] PB - plain beam, SF - stud flexors, and RC - reinforced concrete.

[b] Based on Mc/I where I assumes concrete is cracked.

In all of the cases referred to, a stress cycle ranging from 14.0 to 28.0 ksi produced failure in approximately 2,000,000 cycles. This slight increase in stress cycle to produce failure in 2,000,000 cycles in the beam specimens is in all probability attributable to the stress gradient existing through the flange and the relief provided for the stress concentration effect of the stud. Even if one compares the average stress across the total flange area, the stress range for the beams in the current series of tests was from 15.7 to 31.4 ksi.

These results are extremely encouraging because they indicate that tests carried out on plain-plate specimens give an excellent indication of the strength which can be expected of similar installations on beams.

Beams with Stud Flexors

Specimens in this series were identical in all respects to those in the previous group, except that a shear force was applied to several of the stud shear connectors by a mechanical attachment. As mentioned earlier the heads of several studs near the center of the beam were removed so that mechanical flexors could be attached. Load in the flexors was adjusted by strain gages. A photograph of the flexor used for this purpose and a view of one beam with flexors in place are shown in Figure 15. The load applied was located approximately $^3/_4$ in. from the surface of the flange.

At the beginning of the fatigue test, the load in the flexor was adjusted so that at a maximum flexural load the shear stress in the studs to which the flexor was attached had a nominal value of 15,000 psi. All beams were tested on a stress cycle which varied from one-half tension-to-tension. The load in the flexor, however, remained nearly constant at the magnitude applied at the beginning of the test. The load in the flexor could be monitored during the individual test cycles and also at various stages during the progress of the test. Such monitoring indicated that at no time during the course of a test on any specimen did the load in the flexor drop below a value of 80 percent of the maximum value set. In only a few cases did the load on the flexor drop to this value. In the other cases, the load in the flexor did not drop below a value of 85 percent of the maximum value. This fact is particularly significant because the stress levels reported in Table 9 are computed on the basis of the section properties of the base beam at the location of the failure. No account has been taken of the effect of the stud flexor on the distribution of stress through the depth of the beam. The local effect of the load transmitted through the stud has also been neglected in the stresses reported.

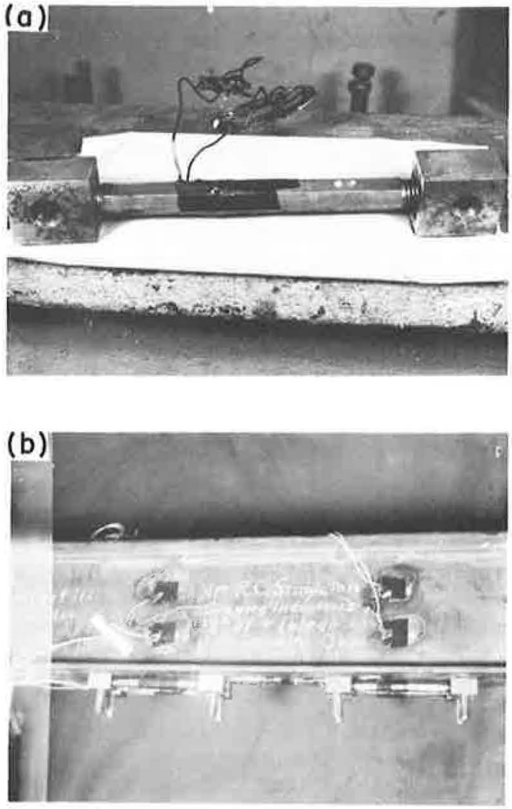

Figure 15. Mechanical stud flexors: (a) flexor, and (b) beam with stud flexors in position.

All failures in this series of beam specimens occurred on the side of the stud away from the flexor used to apply load to the stud. Two failures occurred at the centerline of the beam where the moment and corresponding flexural stress have the maximum value. The other failure occurred at a stud at a distance of 10 in. from the centerline of the beam. At this point, the moment and flexural stress have a value equal to 91 percent of the maximum value at midspan. Since these values are based on nominal stress calculations and neglect the local effect of the load in the stud, the actual difference in stresses for these two fracture locations must be even smaller than that indicated by simple flexural calculations.

The foregoing discussion serves to explain why the stresses reported in Table 9 for this particular series appear to be somewhat low. With the load transmitted through the stud, however, these beams still required a stress range of about 12.5 ksi on a one-half tension-to-tension stress cycle to produce failure in 2,000,000 cycles.

Beams with Reinforced Concrete Cover

All beams in this series were provided with a reinforced concrete cover. The amount of reinforcement placed in the concrete was calculated to produce in the studs a maximum shear force equal in magnitude to the maximum load applied in the previous series by the mechanical flexors. The reinforcement was placed in one layer near the tension flange, resulting in the proper magnitude of shear force in the studs and a distribution of flexural stresses in the base beam to insure failure under the applied loads in approximately 2,000,000 cycles.

Specimens in this series, as in the previous series, were provided with strain gages at several locations along the length of the beam. The strain gages were distributed through the depth of the beam to indicate the extent to which the concrete and the reinforcement acted as a composite section. These gages were located at cross-sections corresponding to the location of studs and at the section midway between the studs.

On application of load during the progress of the fatigue test, cracks appeared at each row of studs. These were the only visible concrete cracks which formed during the course of the fatigue tests; their presence caused fluctuations in the location of the neutral axis as determined from the strain gages.

In the region between studs where the concrete was not cracked, the neutral axis was shifted toward the flange to which the shear connectors were attached. At the stud locations where the concrete was cracked, the neutral axis shifted slightly away from the tension flange of the beam. Near the ends of the span, between the rows of studs, the neutral axis shifted to a location which indicated that the concrete in this region is almost completely effective.

For beams in this series the nominal stress on the extreme fiber of the tension flange can be computed in several different ways, depending on the basis used for these calculations. One can assume that only the steel beam resists the bending moment, in which case the stress cycle for beams GIE7, GIE8 and GIE9 in the fatigue test was from +21,800 to +43,800 psi for a total range of 22,000 psi.

The stress cycles reported in Table 9 were calculated on the basis of a cracked section for all of the concrete slab. On the basis of the results of the strain gage studies, this is the most reasonable assumption for the actual state of stress. A very reasonable check on these stresses was obtained by the strain gages. These gages indicated a linear strain distribution throughout the web of the beam. In both flanges the strain recorded by the gages was less than the value which would be expected if the web strains are extrapolated. This nonlinearity is caused by local effects on both flanges. In one flange the indicated strains are affected by the presence of the loading heads used in the fatigue machine. On the other flange the strains are very strongly affected by the proximity of the gages to a section where the concrete is cracked and also by the local effects of the load transmitted by the stud shear connector.

If the linear strain distribution recorded in the web is extrapolated to the flanges, the moment determined from this distribution is in almost complete agreement with that determined on the basis of statics for the beam structure. This would certainly seem to verify the fact that deviations from this distribution, as recorded by the strain gages, are caused by the local circumstances noted previously.

All beams in this series failed by propagation of a fatigue crack through the tension flange. These cracks initiated on the edge of the stud shear connectors, as in all previous tests conducted on beams and plate specimens. The fractures initiated at the row of studs just removed from the pure moment region of the beam span. This location agrees with that expected since between the support point and the point of load application, the beam is subjected to a constant value of shear and a linear increase in bending moment. All studs in this region, therefore, are required to transmit the same shear force and the one row of studs nearest the point of maximum moment is the most likely point for any fatigue failure to initiate. Although the row of studs at midspan is subjected to a slightly higher moment, they are not subjected to any shear force and are, therefore, not the most critical.

On the basis of all beam tests conducted, it would appear that the fatigue resistance of beams with reinforced concrete cover is the same as that obtained from the plate tests. A comparison of the beam tests indicates that the presence of the reinforced concrete produces a condition which is slightly more severe than the plain beam but not quite as severe as when the studs are loaded by the mechanical flexors.

FRACTURE SURFACES

The fracture surfaces obtained in all fatigue tests followed the same pattern with the fracture initiating at or near the edge of the stud which is first encountered by the axial stress flow. Initial cracks occurred at either one of these locations or at both of them, more or less simultaneously. As the test progressed, one of the cracks, in those cases where two cracks initiated, propagated more rapidly and caused the other crack to stop propagating.

Typical fracture surfaces for the various specimens tested are shown in Figures 16 through 19. The general features of the fractures shown in Figure 16 are very similar and indicate the general nature of all fracture surfaces encountered in the test

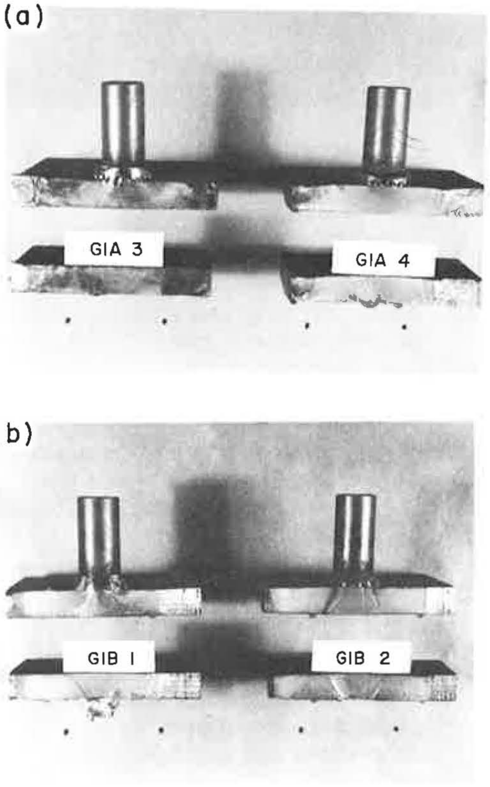

Figure 16. Typical fracture surfaces of single-stud specimens: (a) A7F steel, and (b) A441 steel.

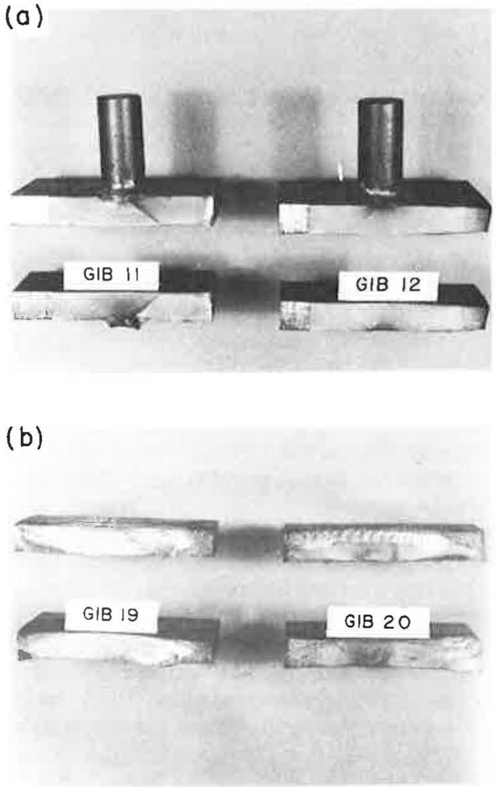

Figure 17. Fracture surfaces of specimens with altered geometry: (a) ground upset, and (b) stud completely removed.

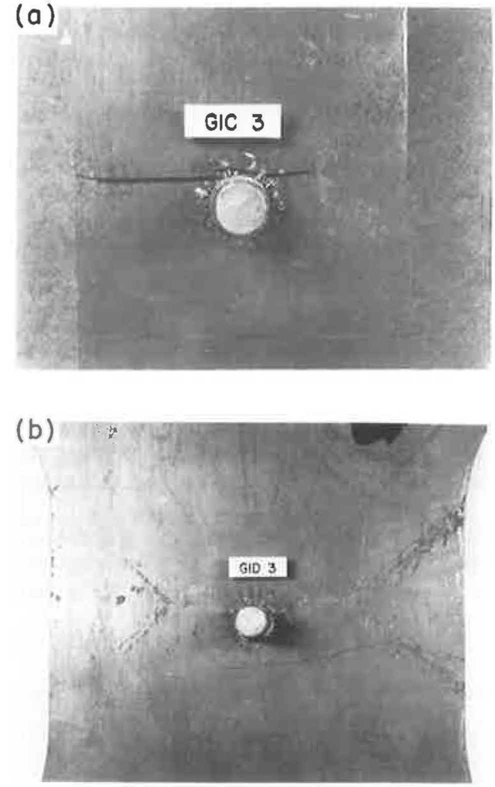

Figure 18. Fractures of single-stud wide-plate specimens: (a) 5 in. wide, and (b) 10 in. wide.

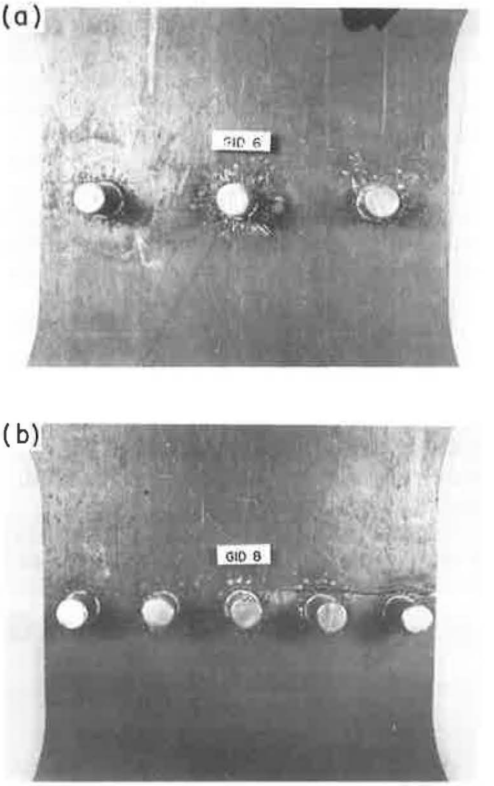

Figure 19. Fractures of multiple-stud wide-plate specimens: (a) three studs, and (b) five studs.

program. Typical features include a region generally referred to as the "thumbnail," where the rate of propagation is relatively slow. As the crack grows in size, the rate of propagation increases and the fracture surface is somewhat rougher. The final stage of fracture is a static failure of the remaining area of the test specimen.

Particular note should be taken of Figure 16b which shows the fracture surface for GIB1. In this specimen the fracture actually initiated under the upset. As the crack propagated, it cut across the upset as well as the parent plate, so that when final fracture occurred a portion of the upset was torn from around the stud. This type of failure was encountered in a few of the cases in this study and was primarily affected by the extent to which the upset was bonded to the parent plate. When the upset was not completely bonded, the critical location was actually under the upset and the fracture propagated from this point.

Figure 17 shows the fracture surfaces which resulted when the geometry of the upset was altered. The top portion of this figure shows the result when the upset was ground to a smooth transition between the parent plate and the stud. Failure surfaces in this case are very similar to those previously presented except that the region of slow propagation is somewhat larger than when the upset is subjected to no treatment. Figure 17b shows the fracture surfaces which resulted in the two cases where the stud was completely removed. Here again the fracture surface is not greatly different from that previously reported, except that the region of slow propagation is somewhat larger. The failures initiated at locations corresponding to where the edge of the stud would have been, had it not been removed. This would indicate that the metallurgical structure in this area is weaker as a result of the changes occurring during the welding process. The fatigue test results indicate, however, that the influence of this metallurgical change is not nearly as great as the geometrical effect of the presence of the upset.

Figure 18 shows the fracture locations for the cases where a single stud was attached to a wider plate. The fracture surfaces in these cases were similar to those previously presented. A very interesting feature of the multiple stud specimens is shown in Figure 19, where typical failures of wide plates with multiple studs are presented. Close examination of the photograph of specimen GID6 reveals several independent cracks which have initiated in a manner identical to that obtained for the plate specimens with a single stud. The photograph of specimen GID8 shows how these cracks which initiate and propagate independently join up to form a continuous crack which eventually causes final fracture.

Although it is not readily apparent in the photographs of the specimens with multiple studs, close examination of the specimens revealed that a large number of independent cracks had actually initiated. In the case of the specimens with three studs, at least three independent cracks were initiated. In the case of the specimens with five studs, the number of independent cracks varied from six to eight, indicating that in all cases at least some cracks were initiated on both sides of the studs. This observation is of particular importance since it indicates that the fatigue resistance of such installations is not a case of the weakest link but rather that the fatigue resistance of all of the studs is virtually the same and that fracture initiates at all studs at very nearly the same number of cycles. Some further indication of this fact is contained in the following section.

METALLURGICAL STUDIES

As a part of the program it was essential that detailed metallurgical studies be carried out to determine the nature of the microstructure as influenced by base material, heat input and amount of material available to absorb the heat input during the welding process. A total of five different specimens was subjected to detailed examination. Most of these specimens were examined after completion of the fatigue test. In one case the specimen was subjected to metallurgical study in the as-produced condition to verify that at the examination section the fatigue loading had produced no change.

Both macro- and micrographs of areas of interest were taken for all specimens studied. The studies also included detailed hardness traverses from baseplate material to unaffected base-stud material, across the heat-affected zones and the weld-metal microstructure.

Microstructures

The general microstructural features of the stud welds are typical of welds in general: a columnar weld-metal zone, with ferrite outlining of the prior austenite matrix. This weld-metal zone is a mixture of tempered martensite, ferrite and pearlite at room temperature. The next portion of the microstructure is the heat-affected zone which possesses an austenite grain size gradient (largest grains near the fusion line), resulting in the presence of martensite near the fusion line. Away from the fusion line the amount of martensite decreases and the amount of pearlite and ferrite increases. Adjacent to this region is the unaffected base-metal zone which consists of Widmanstätten ferrite and pearlite in a banded structure due to the hot rolling process.

Detailed macro- and micrographs of a variety of specimens are contained in Figures 20 through 24. Hardness surveys from the baseplate material across the heat-affected zone and weld metal to the base material of the stud are contained in Figures 25 through 28. The specific microstructures vary somewhat in width of the heat-affected and weld-metal zones. The relative amount of martensite in the heat-affected and weld-metal zones and the fineness of the columnar structure of the weld metal vary as a result of the difference in the heat input to the various specimens. The amount of weld metal increases with the amount of heat input to the specimens, as does the width

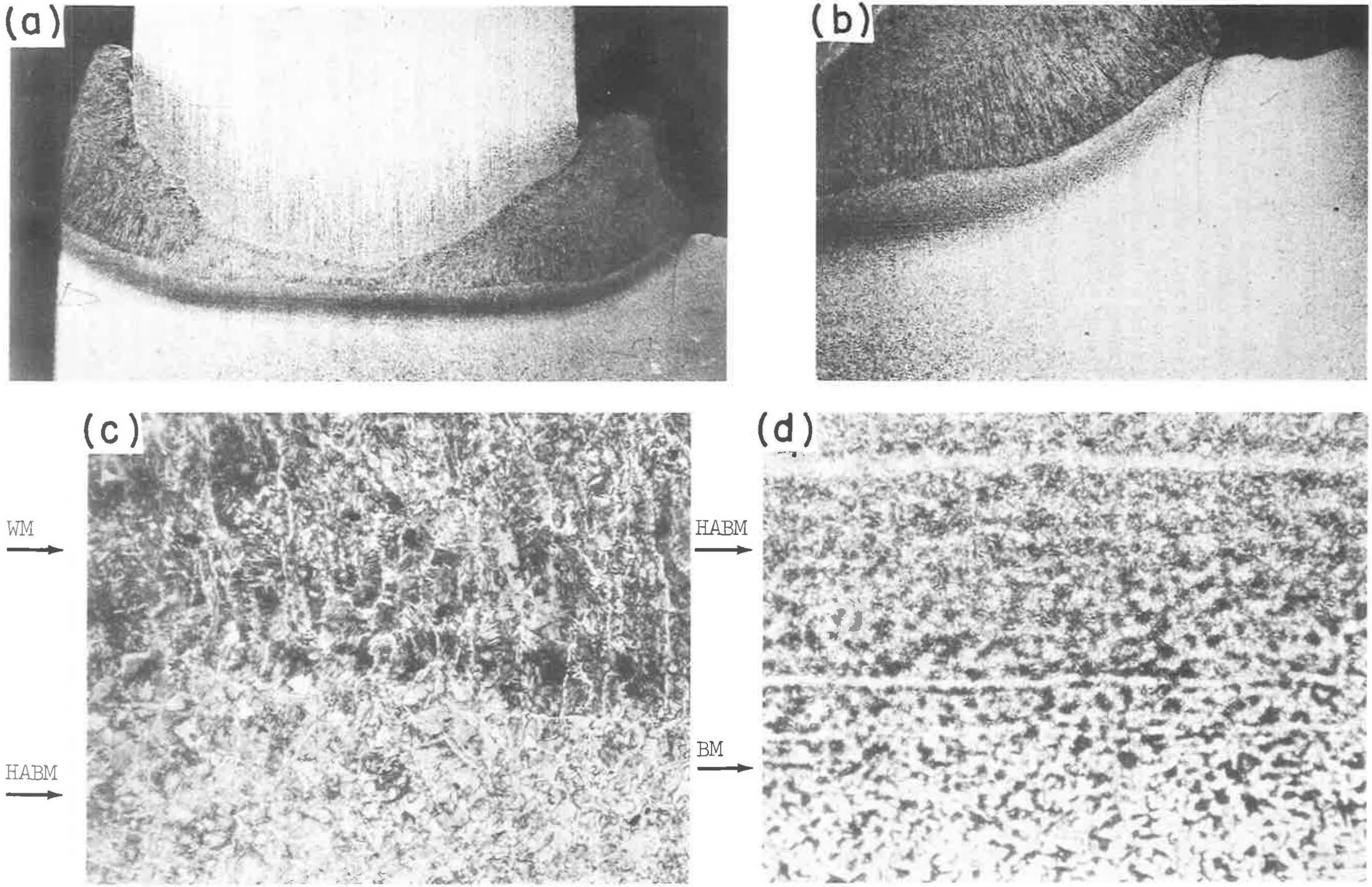
(a)
(b)
(c)
(d)
WM
HABM
HABM
BM

Figure 20. Specimen GIA2: (a) macrograph 3X; (b) macrograph 6X; (c) and (d) micrographs 72X.

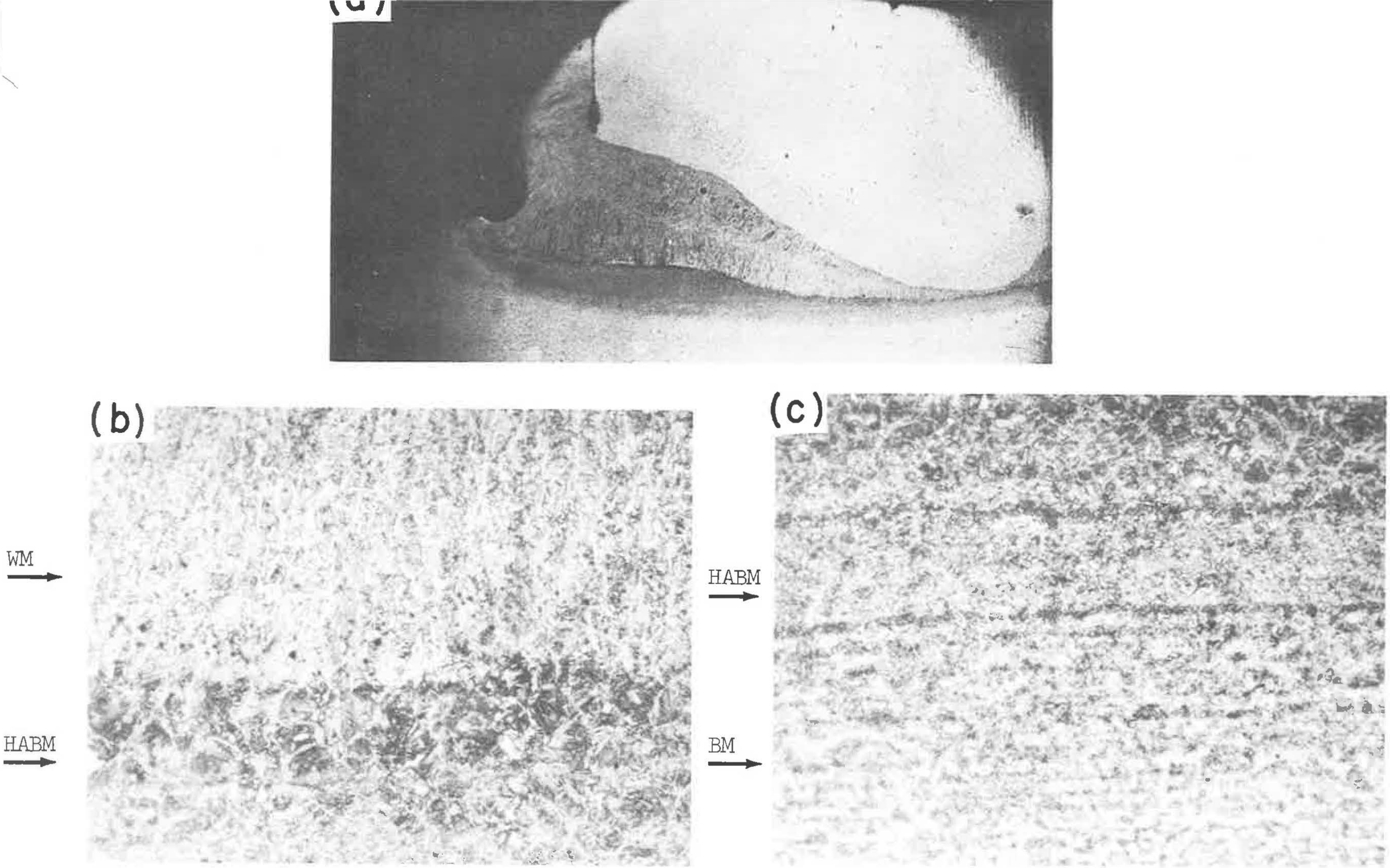
(b)
(c)
WM
HABM
HABM
BM

Figure 21. Specimen GIB1: (a) macrograph 5X; (b) and (c) micrographs 72X.

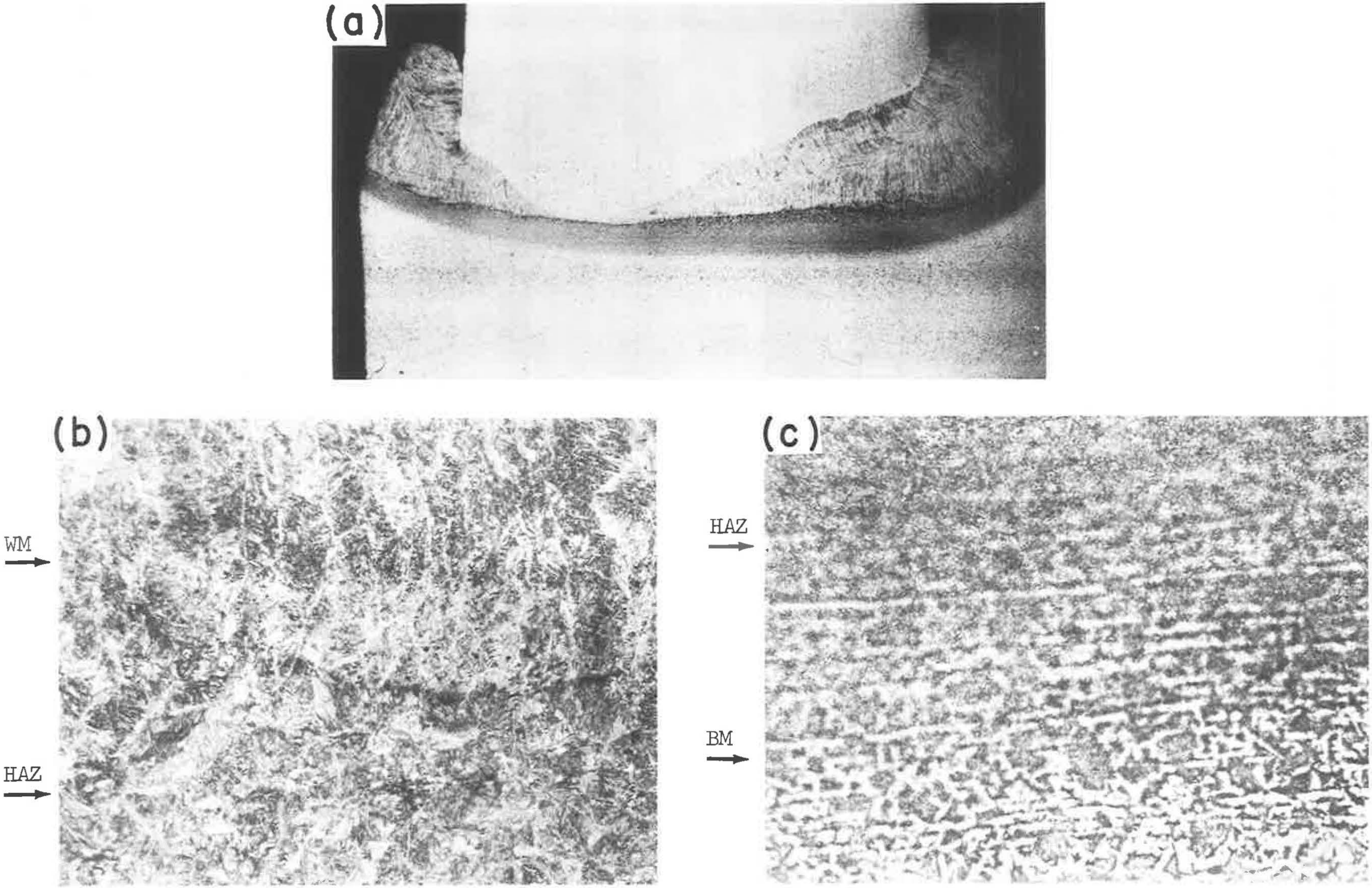
(a)
(b)
WM
HAZ
(c)
HAZ
BM

Figure 22. Specimen GIB16: (a) macrograph 3X; (b) and(c) micrographs 75X.

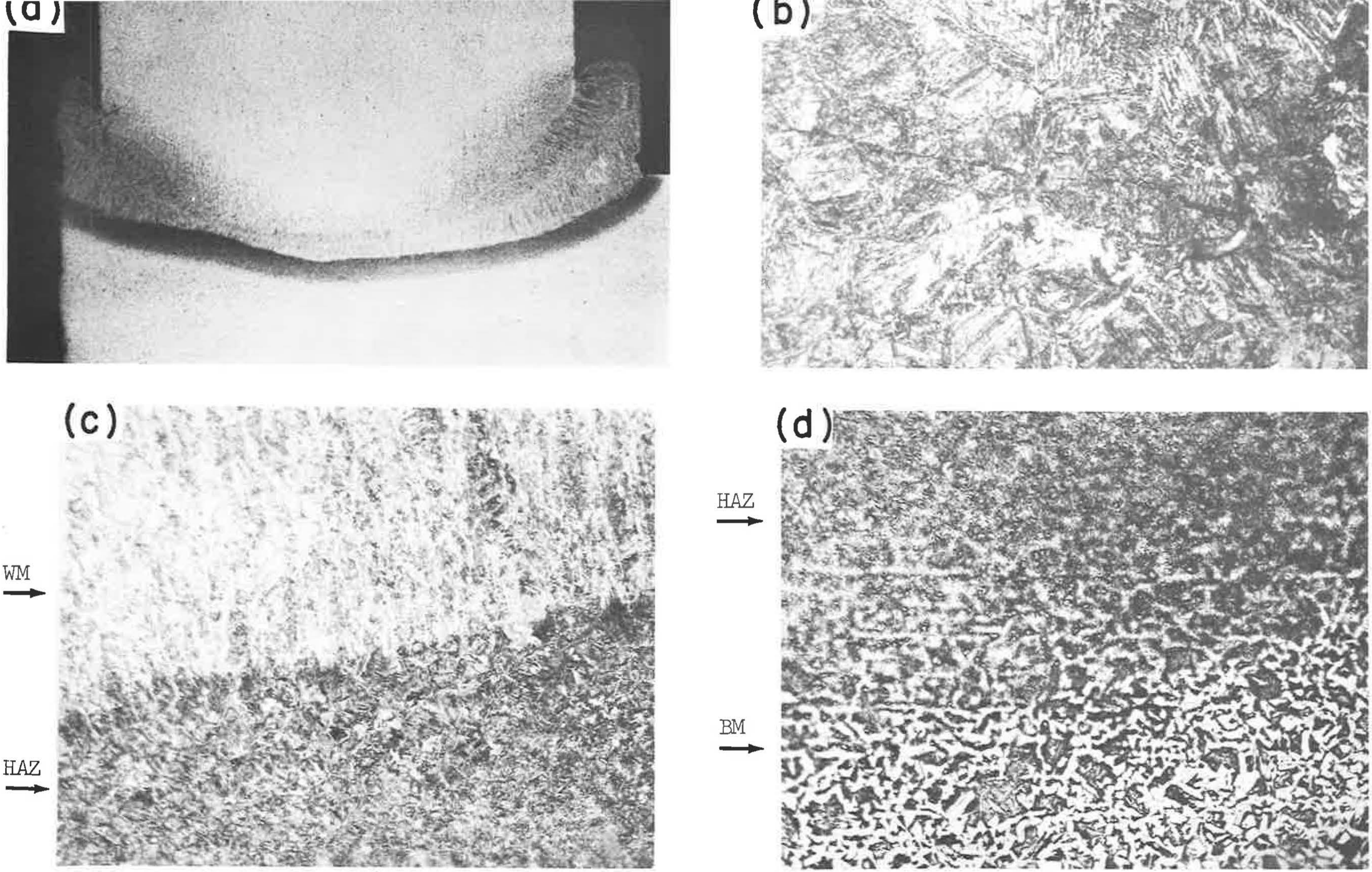
(a)
(b)
(c)
WM
HAZ
(d)
HAZ
BM

Figure 23. Specimen GIC2: (a) macrograph 3X; (b) micrograph 500X, showing crack in HAZ; (c) and (d) micrographs 75X.

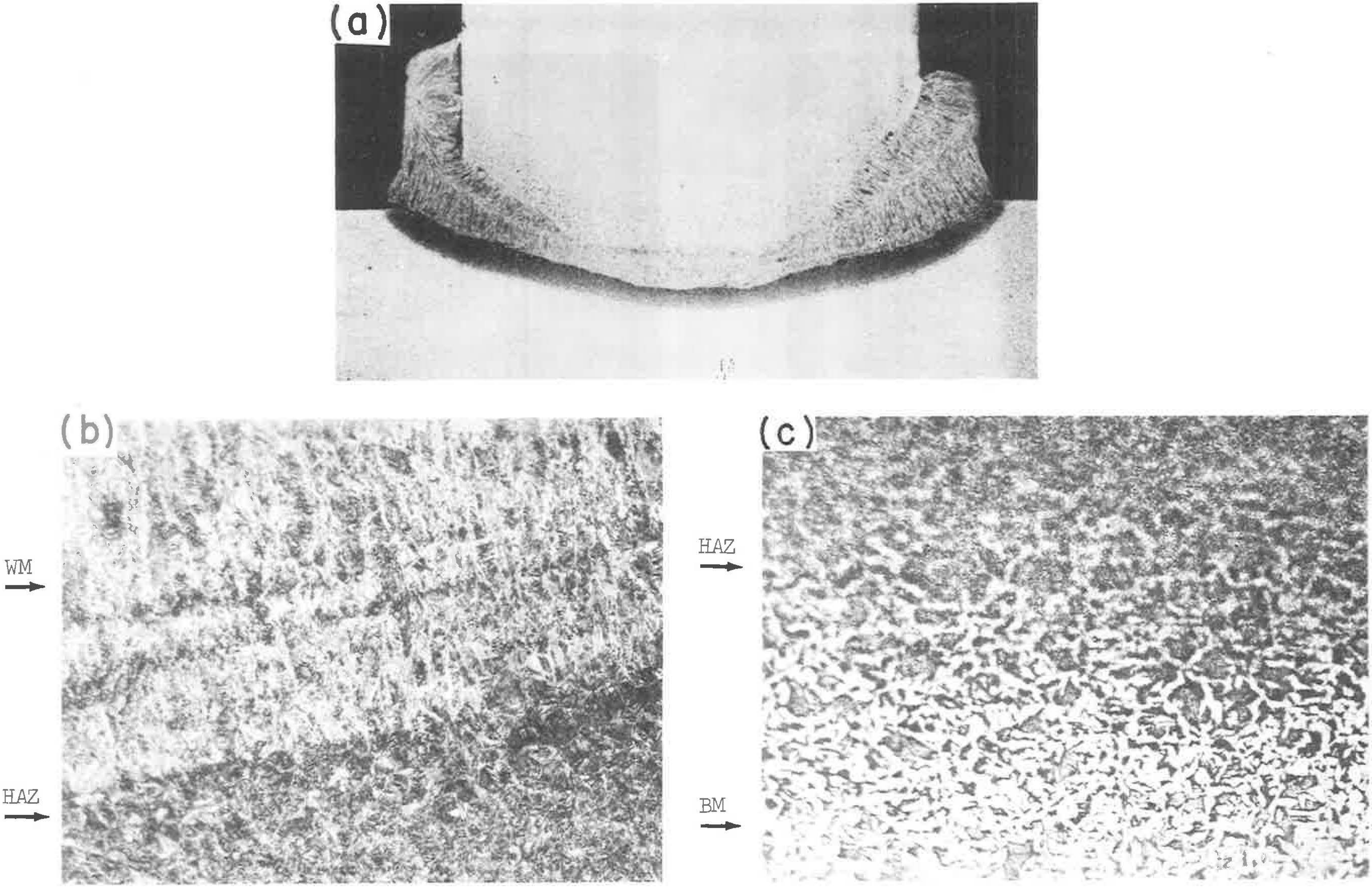
(a)
(b)
(c)
WM
HAZ
HAZ
BM

Figure 24. Specimen GIC5: (a) macrograph 5X; and (b) and (c) micrographs 75X.

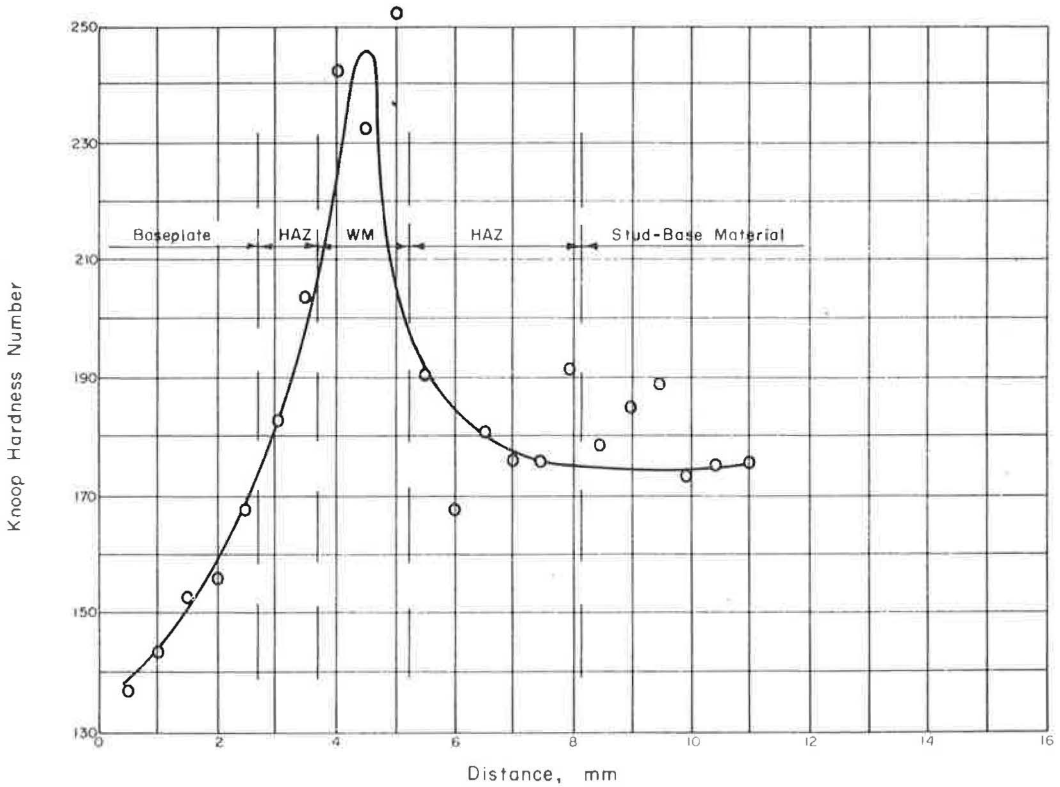

Figure 25. Hardness survey, specimen GIA2.

of the heat-affected zone. Consequently, GIA2 and GIC5 have the narrowest weld-metal and heat-affected zones, followed by GIB1 and GIB16, and the fineness of the weld-metal structure decreases in the same order. Specimen GIB16 has a higher percentage of martensite in the heat-affected zone than GIB1.

Although an increase in heat input generally decreases the hardenability, the opposite is true for this material. The presence of the strong carbide former, vanadium, ties up some carbon and long solution times are required to take the carbon back into solution. As a result, more carbon is in solution in GIB16 than in GIB1, which accounts for the increased amount of martensite. Specimen GIB1 would be expected to have a smaller amount of martensite than GIC5 due to the lower heat input, and GIA2 would have less martensite due to the decreased hardenability of A7F steel as compared to A441 steel. Since the weld metal is formed by melting the base metal, the same trends observed in the heat-affected zone should be observed in the weld-metal zones.

Hardness Surveys

As would be expected on the basis of metallographic observation, the hardness of the material increases as the percent of martensite increases. As a result, the hardness of the heat-affected zone of the plate GIB16 is considerably higher than that of GIB1, and the same is true of the weld-metal zones. It is also true that the hardness of the heat-affected zone of the plate and the weld-metal zone of GIB1 is considerably higher than the corresponding hardness in these regions of GIA2, due to the increased alloy content of A441 steel as compared to A7F. Table 10 contains a summary, from four different specimens, of the size and average hardness of the various zones which result from the welding operation.

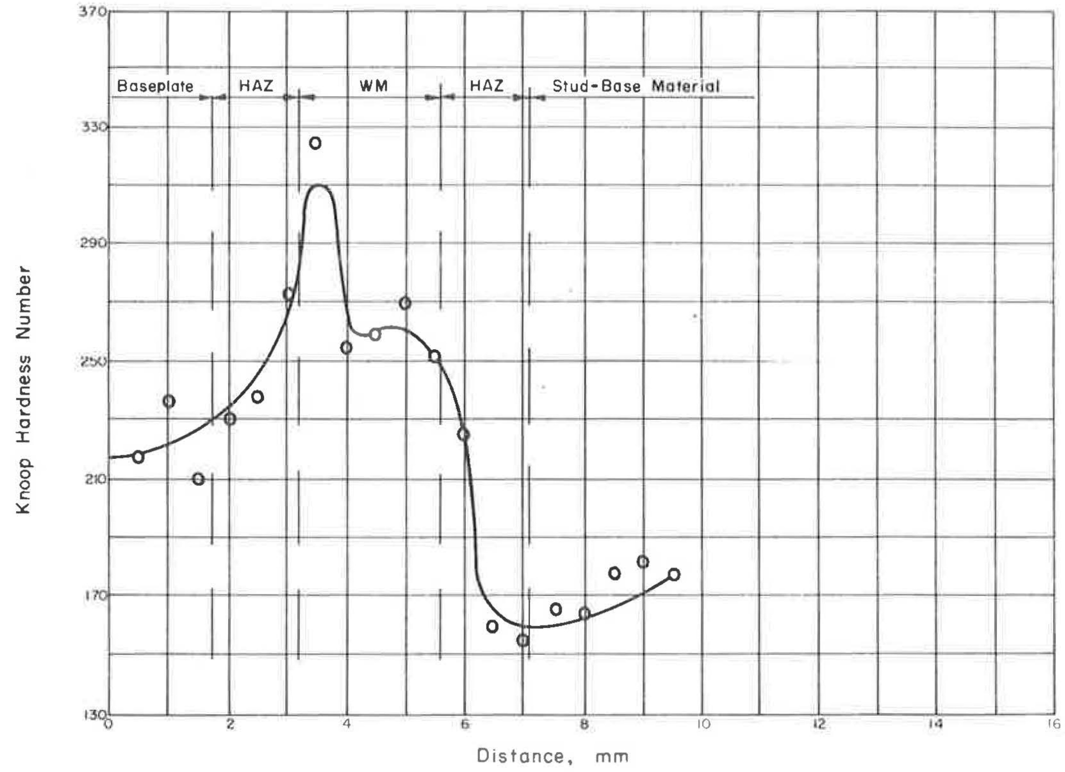

Figure 26. Hardness survey, specimen GIB1.

Mode of Failure

Typical failure of all specimens is evidenced in GIA2. Both of the macrographs in Figure 20 shows a fatigue crack on the right-hand edge of the stud which initiated at the fusion line and traversed the heat-affected zone. This is not the crack which resulted in final failure of the specimen but is rather 180° away from the source of ultimate failure. Propagation of the crack is transgranular as seen in GIA2.

SUMMARY

The tests reported give a very good indication of the effect of base material, number of stud connectors, spacing of stud connectors and welding procedure on the fatigue resistance. On the basis of the flat-plate test series, the following conclusions have been drawn:

1. In all cases, the fracture initiated at the edge of the upset and propagated radially through the thickness of the plate. Almost without exception the multi-studded specimens featured more than one independent fracture surface. All multiple fractures occurred almost simultaneously.
2. The stress range to produce failure in 2,000,000 cycles varied from 16,000 psi in complete reversal to 14,000 psi in a half tension-to-tension stress cycle.
3. There was no noticeable difference in fatigue life between specimens fabricated from A7F or A441 base material.
4. Altering the stud-welding procedure to supply more heat to the weld had no effect on the fatigue life.
5. Changing the stud geometry by grinding the upset to a smooth transition doubled the fatigue life. Complete removal of the studs provided an even greater resistance to

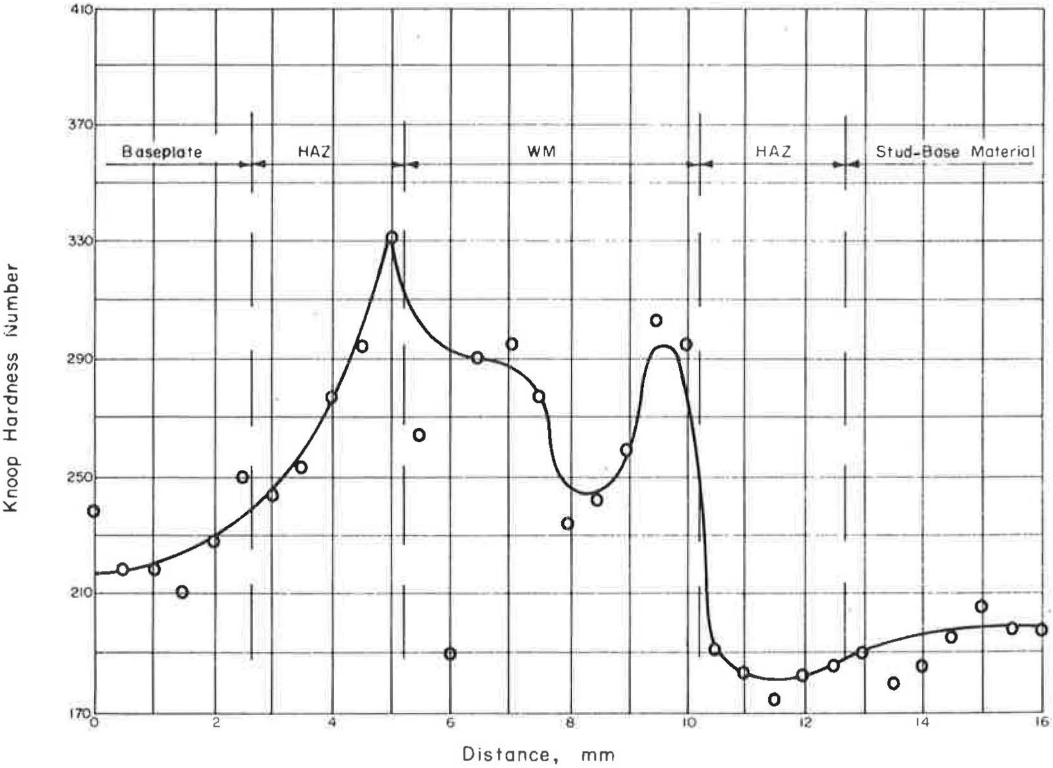

Figure 27. Hardness survey, specimen GIB16.

fatigue loading. With the stud removed, however, the fatigue life was not as great as has been reported earlier for plain-plate specimens of similar material.

6. The number of studs in a line transverse to the direction of stress and the spacing of the studs has some effect on the fatigue resistance but the effect is not very large.

The behavior of the beam specimens in all three series was very similar to what was obtained for the flat-plate specimens. Excellent correlation is obtained between the flat-plate specimens and the beam specimens, not only in overall behavior but also in terms of stress levels required to produce failure in 2,000,000 cycles. The following observations have been made on the basis of the beam tests:

1. Fractures in the beam specimens were similar to those obtained in the flat-plate specimens. In flat-plate specimens the fracture might occur on either side of the stud, whereas in the beam specimens, the fractures occurred on the side of the stud where secondary tensile stresses, due to the loading of the stud, were added to the primary tensile flexural stresses.

2. Cracking occurred in the concrete at every row of studs and only at the studs. Although the slab used in these tests was narrow, there is reason to believe that shear connectors in the negative moment regions might prove to be an effective means of crack control.

3. The half tension-to-tension stress cycle to produce failure in 2,000,000 cycles for the various groups of beams tested was plain beams, 16.4 to 32.8 ksi; beams with flexors, 12.5 to 25.0 ksi; and beams with concrete, 14.0 to 28.0 ksi. In view of the extent of the agreement between the results of the flat-plate and beam specimens, it would certainly appear that the flat-plate tests give a satisfactory indication of the behavior of similar beam tests.

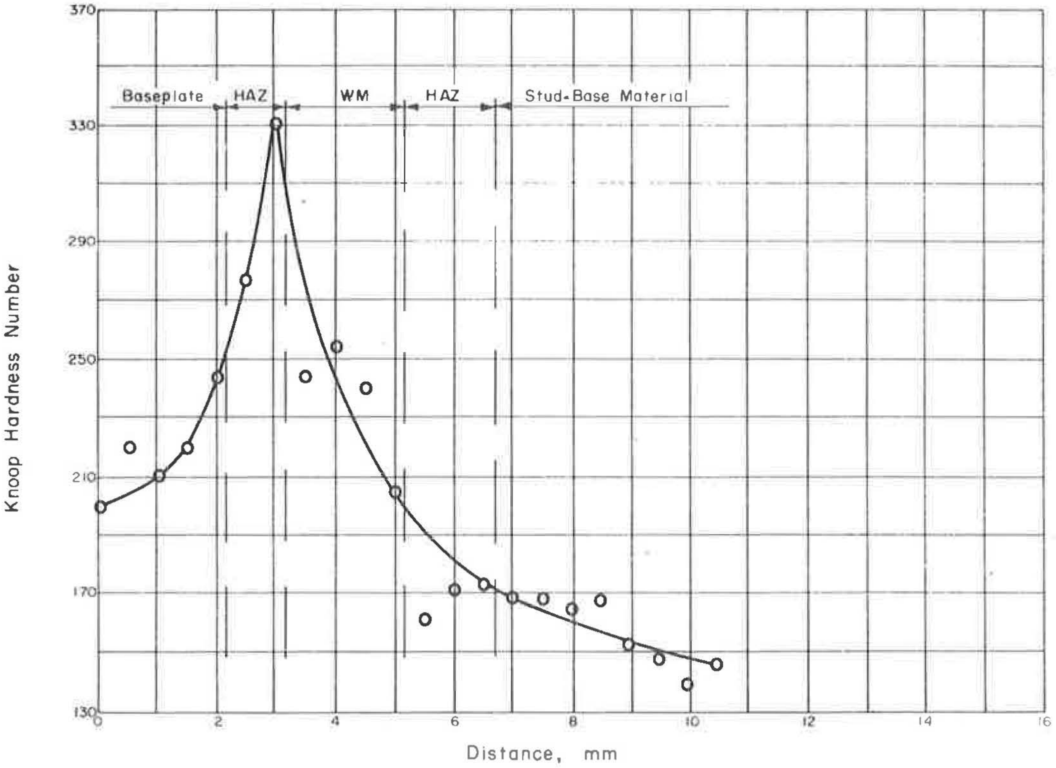

Figure 28. Hardness survey, specimen GIC5.

TABLE 10

EFFECT OF STUD-WELDING PROCEDURE

Item	Value			
Specimen	GIA2	GIB1	GIB16	GIC5
Type of steel	A7F	A441	A441	A441
Heat input[a]:				
Weld current (amp)	1,500	1,500	1,450	1,750
Arc voltage (volts)	33	33	33	31
Weld time (cycles)	58	58	76	43
Heat (KVA cycles)	2,870	2,870	3,630	2,330
Zone widths (mm):				
Heat-affected zone stud	3.0	1.5	2.5	1.5
Weld metal	1.5	2.5	5.0	2.0
Heat-affected zone plate	1.0	1.5	2.5	1.0
Avg. zone hardness (Knoop):				
Base metal stud	180	171	195	157
Heat-affected zone stud	181	179	184	169
Weld metal	143	255	266	237
Heat-affected zone plate	194	248	283	305
Base metal plate	150	222	228	215

[a] Lift of 3/32 in. and plunge of 3/16 in. used.

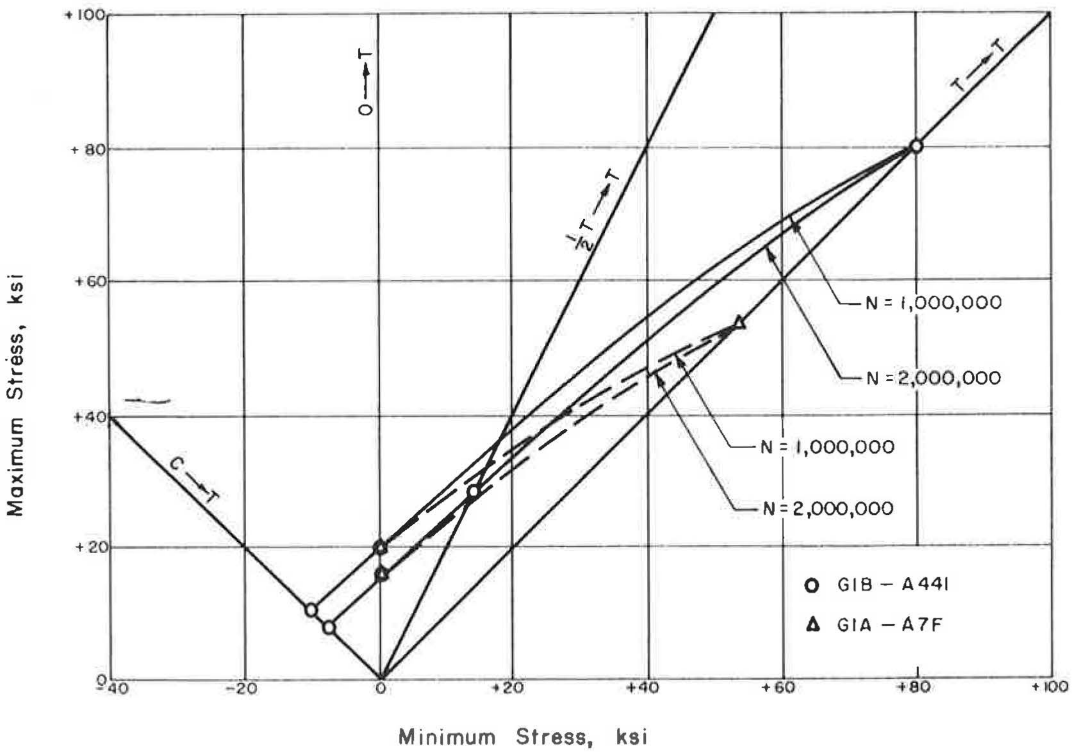

Figure 29. Modified Goodman diagram for GIA and GIB specimens.

With this as a basis, the modified Goodman diagram presented in Figure 29 should serve for the development of suitable provisions for fatigue in the case of designs which utilize stud shear connectors for composite action in negative moment regions. This diagram yields a stress range of 16,000 psi for complete reversal, 16,000 psi for zero-to-tension, and 14,000 psi for half tension-to-tension for failure in 2,000,000 cycles. A somewhat smaller range would be required for stress cycles above this level. Applying a factor of safety of approximately 1.6 on these stresses results in permissible stress cycles of approximately 10,000 psi.

ACKNOWLEDGMENTS

The tests described herein were conducted in the structural laboratories of the Civil Engineering Department at the University of Illinois under the sponsorship of Gregory Industries, Inc. The tests were conducted by K. A. Selby, at the time research assistant in Civil Engineering. The authors wish to express their appreciation to W. T. Becker, Research Assistant, who conducted the metallurgical studies, and the members of the Civil Engineering Shop who prepared the test members.

REFERENCES

1. Viest, I. M. Review of Research on Composite Steel Concrete Beams. Jour. ASCE, Vol. 86, No. ST6, June 1960.

2. Stallmeyer, J. E., Nordmark, G. E., Munse, W. H., and Newmark, N. M. Fatigue Strength of Welds in Low-Alloy Structural Steel. Suppl. to Welding Jour., June 1956.
3. Wilson, W. M., and Thomas, F. P. Fatigue Tests of Riveted Joints. Univ. of Illinois Eng. Exper. Sta. Bull. 302, 1938.

Field Dynamic Loading Studies of Highway Bridges in the U. S., 1948–1965

R. F. VARNEY and C. F. GALAMBOS
Bridge Engineers, Structures and Applied Mechanics Division, U. S. Bureau of Public Roads

A compilation of pertinent information is presented for all highway bridges on which experimental dynamic load data have been gathered in this country since 1948. The bridges are grouped as simple, continuous or cantilever span types in three general superstructure categories: steel girder, concrete and miscellaneous. The tabulation provides a brief summary of construction details, dynamic measurements taken and the velocities, positions, and magnitudes of test loads. This compilation of dynamic bridge research test parameters provides the bridge design and research engineer a ready guide to field bridge study information not previously available in one source.

•THE FOLLOWING tabulation of highway bridges provides a reference to bridge types and parameters on which dynamic vehicular loading performance data are available for the use of highway bridge design and research engineers. The tabulation was compiled from published and unpublished reports on completed studies and from advance information available on current studies.

The bridge descriptions are presented in three groups: simple, continuous and cantilever spans. In each group the bridges are listed by superstructure category: steel girder, concrete and miscellaneous. Within each category the listing is alphabetically by State. For additional detail the reader is referred to the pertinent publications available.

Bridges on which the personnel and equipment of the U. S. Bureau of Public Roads Structures and Applied Mechanics Division have been employed in a cooperative field endeavor with a State Highway Department are indicated by an asterisk. These studies bear a relationship to one another because of the uniformity of research procedures followed and, in recent years, the nearly identical loadings with a vehicle whose dynamic characteristics are carefully measured. The same continuity of research holds true for many of the bridges studied by the Michigan Highway Department and for the AASHO Road Test bridges studied.

The format is designed to permit a quick comparison of the essentials of the bridge studies. Related field studies on which only static data are sought have not been included. The information contained in the tabulation is somewhat varied due to the diverse scope of the different reports. The information has been tabulated for publication at the request of C. P. Siess, Chairman of Highway Research Board Committee on Bridge Dynamics, and L. T. Oehler, Chairman of Highway Research Board Committee on Field Testing of Bridges.

Paper sponsored by Committee on Bridges.

TABLE 1A

SIMPLE SPANS

Steel Girder Superstructures

Site/Date	Specifications	Measurements	Loading	Ref.
Illinois (AASHO Road Test, 10 bridges) 1958-1961	All 50' span 1-lane bridges of 15' roadway; 8 non-composite (5 with cover plates) and 2 composite; 3 18 WF- or 21 WF-beams with $6^1/_2$" slab; designed for 27,000- and 35,000-psi stress level under applied loadings.	Deflections; top and bottom flange strains at midspan, at ends of cover plates and other sections; wheelpath profiles taken.	One vehicle path generally; various 2- and 3-axle loads; induced impact; extensive vehicle instrumentation; tests to failure; speeds from creep to 50 mph	15
*Maryland (Shawan Rd.) 1962	A 100' composite welded deck plate girder span; 3-lane 33' roadway on 7 beams of 54" depth; 7" slab with 2" bituminous wearing surface; H20-S16 design; on 3% grade; flange thickness transitioned.	Deflections; top and bottom flange strains at midspan; shear strains near bearing; fixed bearing reactions; strains at bottom flange transitions; wheelpath profiles taken.	BPR test vehicle; speeds to 50 mph on 9 paths for creep and 4 paths for other runs; induced impact; 73 K on axles (10, 33 and 30 K, at 13' and 20' spacing; axle housing gages calibrated by incremental loading.	23
Massachusetts (Conway-Shirkshire) 1953	A 69' non-composite rolled I-beam span; H15 design; 14' roadway with $6^1/_2$" slab on 4 33WF141 beams.	Midspan deflection at one point.	Speeds to 40 mph; 44 K on 2 axles (7 and 37 K) at 13' spacing; vehicle spring constants and natural frequency measured; centerline runs.	
Massachusetts (Gilbertville-	A 114' non-composite deck plate girder span; 24' roadway with	As above.	As above.	7

	60° skew; H20 design.			
Massachusetts (Ware-Malboeuf) 1953	A 77' non-composite through plate girder span; 18' roadway with $2^{1}/_{2}$" open steel-grating deck on 16WF45 floor beams carried on 2 54" deep girders.	As above.	As above.	7
Massachusetts (Townsend-South St.) 1953	An 86' non-composite through plate girder span; 24' roadway with 7" slab on two 84" deep beams; 17° skew; H15 design.	As above.	As above except 43 K on 2 axles (8 and 35 K) at 13' spacing.	7
Massachusetts (Townsend-Main St.) 1953	An 89' composite rolled I-beam span; 7" slab; 30' roadway on 8 36WF170 beams; 21° skew; H20 design; cover plated.	As above.	As above.	7
Michigan (Fennville) 1950, 1953	Six 60' spans; 5 non-composite, 1 composite; 28' roadway with 7" min. slab on 7 36WF182 beams.	First test: strains and deflections at midspan, all spans; strains in lateral deck reinforcing bars; strains in diaphragms. Second test: midspan deflections only; 1 gage per span except 2 spans with 1 gage per beam.	First test: three vehicle paths; induced impact; simulated load in 1 lane; 72 K on 3 axles (18, 32 and 32 K) at 14' spacings; speeds to 12 mph; also 38 K on 3 axles (8 and 30 K tandem) at 12' and 4' spacing; speeds to 25 mph. Second test: speeds to 50 mph on centerline only; 50 K on 3 axles (10, 18 and 22 K) at 14' spacings; 28 K on 2 axles (10 and 18 K) at 14' spacing.	2, 8
Michigan (B8-58-7-26) 1956	Three composite spans of 70', 60' and 72'; 36WF150 to 230 stringers spaced at 6' centers with 7" min. slab; 28° skew.	Deflections.	39 K on three axles (6, 15 and 18 K) at 13' and 14' spacings; speeds to 25 mph; axle housing gages calibrated under incremental loading.	24

TABLE 1A (Continued)

Site/Date	Specifications	Measurements	Loading	Ref.
Michigan (B2-39-3-8) 1957	A 45' non-composite span with $7\frac{1}{2}$" slab on 30WF108 beams at 58" centers; a 49' non-composite span with $7\frac{1}{2}$" slab on 30WF124 beams at 58" centers.	One midspan deflection gage in each of 2 spans.	40 K on 3 axles (6, 16 and 18 K) at 13' and 14' spacing; speeds to 45 mph on 1 path; axle housing gages calibrated under incremental loading.	13
Michigan (X3-33-6-1) 1957	Three 61' composite spans; $7\frac{1}{2}$" slab on 36WF170 beams at 64" centers.	One midspan deflection gage in each of 3 spans.	As above.	13
*Missouri (Burris Fork) 1955	A 45' non-composite span; 22' roadway; $6\frac{1}{4}$" slab on two 27WF94 exterior beams and two 27WF102 interior beams; H15 design.	Deflections; top and bottom flange strains at midspan and quarter point; wheelpath profiles taken.	Three vehicle paths; 65 K on four axles (6, 27 and 32 K tandem) at 13', 20' and 4' spacing; spring constants determined; speeds to 48 mph; induced impact.	14
*South Dakota (James R.) 1955	A 55' composite span; 24' roadway of 6" slab on 4 30WF108 beams; level grade; welded connections; H15 design.	As above.	Two vehicle paths; 71 K on 5 axles (7 K, 32 K tandem and 32 K tandem) at 11', 4', 17' and 4' spacing; 32 K on 2 axles (14 and 18 K) at 12' spacing; speeds to 40 mph; axle housing gages calibrated under incremental loading; induced	23

(P. & S. F.) 1962	framed grid on random spaced columns; 3° curve and 2% grade; 9 lines of 30WF108 and 30WF116 beams; transverse 30WF108 and 30WF132 members at 39', 30', 37', 39' and 34' spacing; two 24' roadways and 4' median; $6\frac{1}{2}$" slab; H20 design.	various points on longitudinal and transverse beams; column bending strains; wheelpath profiles taken.	vehicle paths; 68 K on 3 axles (9, 31 and 28 K) at 13' and 20' spacing; axle housing gages calibrated under incremental loading; speeds to 50 mph; some uncontrolled commercial traffic recorded.	
*Virginia (Weyers Cave) 1961	Three 67' composite spans; 24' roadway of $7\frac{1}{2}$" slab on 4 36WF160 cover plated beams; H20 design; 1.7% grade.	Deflections; top and bottom flange strains at midspan; pier top longitudinal deflections; flange strains at ends of cover plates and near bearing; wheelpath profiles taken.	BPR test vehicle; 3 vehicle paths; speeds to 45 mph; induced impact; 58 K on 3 axles (10, 24 and 24 K) at 13' and 20' spacing; 73 K on 3 axles 10, 32 and 31 K) at 13' and 20' spacing; spring constants determined.	19
*Virginia (Hazel R.) 1962	Two 63' and 1 67' composite spans; H20 design; nearly level grade; 24' roadway with $7\frac{1}{2}$" slab on 4 36WF150 beams in 63' spans and 36WF160 beams in 67' span; latter is an identical superstructure to Weyers Cave bridge above; all beams in all spans cover plated.	As above.	BPR test vehicle; 74 K on 3 axles (10, 32 and 32 K) at 13' and 20' spacing; axle housing gages calibrated under incremental loading; speeds to 30 mph; induced impact; 5 vehicle paths.	22

TABLE 1B

SIMPLE SPANS

Concrete Superstructures

Site/Date	Specifications	Measurements	Loading	Ref.
California (Harrison St.) 1960	80' span 4-cell box girder; H20-S16 design; 28' roadway; 2" asphalt wearing surface on 6$^{3}/_{8}$" deep slab; box 4' 10" deep; 2% grade and superelevated.	Concrete and steel flexural strains; shear strains near bearings; temperatures; tested before and after adding intermediate diaphragm.	58 K on 2 axles (12 and 46 K) at 13' spacing; speeds to 20 mph; induced impact; minor vehicle instrumentation.	23
Illinois (AASHO Road Test, 8 bridges) 1958 to 1961	All 50' span 1-lane bridges with 6$^{1}/_{2}$" slab and 15' roadway; four prestressed bridges, each with 3 24" deep I-beams; 2 post- and 2 pretensioned; designed for 300- and 800-psi tensile stress; 4 T-beam bridges, each with 3 11$^{1}/_{2}$" wide by 20" monolithic beams; variable reinforcement; designed for 30,000- and 40,000-psi tensile stress in reinforcing bars.	Deflections; strains on reinforcing and prestressing steel; surface strains on prestressed concrete; wheelpath profiles taken.	One vehicle path generally; various 2- and 3-axle loads; induced impact; extensive vehicle instrumentation; tests to failure; speeds from creep to 50 mph.	15
Iowa (Des Moines R.) 1958	A 100' prestressed post-tensioned span; 30' roadway on 6 60" deep I-beams; level grade; 2 intermediate diaphragms; 6$^{1}/_{4}$" slab.	Strains on bottom surface of beams at midspan; additional strains on web for neutral axis determination.	Four vehicle paths; speeds to 25 mph; 41 K on 3 axles (9 K and 32 K tandem) at 13' and 4' spacing; 74 K on 5 axles (9 K, 32 K tandem and 33 K tandem) at 11', 4', 19' and 4' spacing.	12
*Maryland	A 100' prestressed, post-	Deflections; surface strains	BPR test vehicle; 73	23

	centers; 3% grade; H20-S16 design.		speeds to 45 mph; induced impact; axle housing gages calibrated by incremental loading.	
*New York (Chili Ave.) 1965	A 66' T-beam span with 48' roadway and 7" slab on 7 beams 10" wide by 59" deep; H20-S16 design; 14° skew; A432 reinforcement; 3% grade; monolithic beams and slab.	Deflections; strain gages on tensile reinforcement; strain gages in slab; wheelpath profiles to be taken.	BPR test vehicle; 74K on 3 axles (10, 32 and 32 K) at 13' and 20' spacing; other factors to be determined; axle housing gages calibrated under incremental loading.	25
Pennsylvania (Centerport Cr.) 1954	A 33' span of 9 pretensioned, prefabricated 21" by 36" beams, each with 2 12$^1/_2$" diameter hollow cores; level grade; 2" asphalt wearing course; 25' roadway; shear keys for lateral load distribution; designed for 80% of H20-S16 wheel load to each beam.	Deflections of center and edge beam at midspan and quarter span for dynamic runs.	Speeds to 25 mph; induced impact; 57 K on 3 axles (5, 18 and 34 K) at 13' and 22' spacing; centerline and curb lane vehicle paths.	5
*Pennsylvania (Little Schuylkill R.) 1964	A 61' span of 5 prestressed pretensioned box beams at 83" centers with 7$^1/_2$" slab; 30' roadway; H20-S16 design; 5 hollow rectangular beams, 48" wide and 33" deep with 5" walls; level grade; neoprene bearing pads.	Deflections; strain at various levels on beam sides, on bottom surface of beam, on top and bottom of slab and on curb and parapet all at 3.55' from midspan; similar strain measurements at a section 18' from bearing.	BPR test vehicle; 74 K on 3 axles (10, 32 and 32 K) at 13' and 20' spacing; also second vehicle with 74 K on 3 axles (9, 32 and 33 K) at 14' and 22' spacing; both run in parallel at 20 mph; speeds to 35 mph with BPR vehicle; 3 high-speed and 7 creep vehicle paths; induced impact.	23

TABLE 1C
SIMPLE SPANS
Miscellaneous Superstructures

Site/Date	Specifications	Measurements	Loading	Ref.
California (Vacaville) 1964	A 26', 34' wide orthotropic deck plate span; 30° skew; longitudindal stiffeners at 18" centers; transverse stiffeners at 12" centers; one free edge; one elastically supported.	Deflections and strains under outside wheel track of curb lane.	Dynamic loading by random truck traffic; wheelbases and axle loads measured at weigh station.	23
Michigan (B2-61-3-21) 1956	A 108' and 110' through truss span; fabricated bridge floor on 16WF46 floor beams at 39" centers.	Deflections.	39 K on 3 axles (6, 15 and 18 K) at 13' and 14' spacings; speeds to 35 mph; axle housing gages calibrated under incremental loading.	24
Pennsylvania (Ft. Loudon) 1948	A 14' deep, 111' span riveted Warren through truss, H20 design; 23' roadway on I-beam stringers; 7" slab and 4" bituminous wearing course; 2% grade.	Strains and deflections at critical points on truss members, floor beams and stringers.	Speeds to 50 mph; 8 test vehicles; most loading by 96 K on 5 axles (9 K, 42 K tandem and 45 K tandem) at 14', 4', 15' and 4' spacing; centerline runs, both directions; braking runs.	1
Virginia (Statewide)	35 composite steel girder bridges of varying length and	Vibrations measured with a portable accelerometer at	Runs of 10 and 20 mph in several lanes; 20 K	16

*Virginia (Reynolds Bridge) 1963	Aluminum modified semimonocoque of 5 modules in a 97' span; H20 and H15-S12 design; 28' roadway; 1% grade; 4' 10" deep modules; lateral bracing at 8' centers; longitudinally stiffened webs; 7¼" composite slab of lightweight concrete.	Deflections and strains at midspan for each module; fixed bearing reactions; wheelpath profiles taken; shear strains.	BPR test vehicle; 75 K on 3 axles (10, 33 and 32 K) at 13' and 20' spacing; speeds to 30 mph; axle housing gages calibrated under incremental load; 4 vehicle paths; induced impact.	23
*Maryland (Fairchild Bridge) 1964	Aluminum semimonocoque of 5 modules in 93' span; H20-S16 design; 30' roadway; 5' 7" deep modules; 6" composite slab of lightweight concrete; on 3% portion of vertical curve.	Deflections and longitudinal strains at midspan for each module; shear strains at section 8' from bearing; wheelpath profiles taken.	BPR test vehicle; 75 K on 3 axles (10, 33 and 32 K) at 13' and 20' spacing; axle housing gages calibrated under incremental load; speeds to 63 mph on 3 vehicle paths; slower runs on 8 vehicle paths; induced impact.	23

The following bridges described in the continuous or cantilever span sections also include simple span portions:

Michigan - Jackson Bypass
Michigan - (B1-81-1-13)
Michigan - (B1-77-20-11)
Michigan - (B1-33-6-4)
Michigan - (B1-56-12-6)
Michigan - (B1-11-18-7)

TABLE 2A

CONTINUOUS SPANS

Steel Girder Superstructures

Site/Date	Specifications	Measurements	Loading	Ref.
California (San Leandro Cr.)	63' continuous spans; every third span has 46' suspended portion; 3 non-composite 36WF230 beams; 28' roadway; 8" slab; H20-S16 design; on 3% grade; cover plates over bearings.	Deflections; top and bottom flange strains in 1 continuous and 1 suspended span; positive and negative moment sections gaged; Carlson strain meters in concrete; strains on columns, diaphragms and girder webs; tested with diaphragms connected and disconnected.	Five vehicle paths; speeds to 25 mph; induced impact; 67 K on 2 axles (17 and 50 K) at 14' spacing; 85 K on 5 axles (9 K, 32 K tandem, and 44 K tandem) at 14', 4', 23' and 4' spacing.	3
Indiana (Purdue) 1953	63'-75'-63' non-composite continuous spans; 6 33WF130 beams; 28' roadway; 7" slab; H20 design; level grade.	Top and bottom flange strains in 3 positive and 2 negative moment sections; slip between slab and steel; deflections on 2 beams; concrete surface strains; web strains.	Two vehicle paths; speeds to 35 mph; induced impact; 49 K on 5 axles (5 K, 20 K tandem and 24 K tandem) at 12', 4', 12' and 4' spacing; also H15 and H20 loadings; sprung load frequency measured.	6
*Iowa (Miller's Cr.) 1956	55'-70'-55' composite continuous spans; 2 27WF94 exterior and 2 30WF116 interior beams; 28' roadway; 8" slab; H20-S16 design; level grade; cover plated at midspan and at bearings.	Deflections; top and bottom flange strains at positive and negative moment sections; wheelpath profiles taken.	Centerline, curb and normal lane vehicle paths; speeds to 55 mph; induced impact; 23 K on 2 axles (5 and 18 K) at 12' spacing; 64 K on 5 axles (7 K, 25 K tandem and 32 K tandem) at 11', 4', 18', and 4' spacing; axle housing gages calibrated by incremental	11

Iowa (Wapsipinicon R.) 1956	73'-94'-94'-94'-73' non-composite continuous spans; 2 33WF125 exterior and 2 36WF160 interior beams; 24' roadway; 8 " slab; H15 design; level grade; cover plated at bearings.	Positive moment section deflections and top and bottom flange strains in first 3 spans; negative moment top and bottom flange strains near interior pier; wheelpath profiles measured.	Centerline, curb and normal lane paths; speeds to 50 mph; induced impact; same vehicles as for Miller's Creek bridge above.	11
Iowa (Skunk River) 1957	73'-94'-73' composite continuous spans; 2 33WF141 and -152 exterior beams; 4 36WF194 interior beams; 48' roadway; $8\frac{1}{8}$" slab; cover plated at bearings.	Bottom flange strains at 1 positive and 1 negative moment section and near ends of cover plate.	Speeds to 50 mph; 14 creep-speed vehicle paths; 4 paths at higher speeds; 41 K on 3 axles (9 K and 32 K tandem) at 13' and 4' spacing.	10
Iowa (Ashworth Rd.) 1958	53'-67'-67'-53' composite continuous spans; 2 30WF108 exterior beams; 2 33WF130 interior beams; 28' roadway; $7\frac{1}{4}$" slab; level grade; cover plated at bearings.	Bottom flange strains at 2 positive and 2 negative moment sections; additional strains on web for neutral axis location.	Dynamic runs on centerline and on regular traffic lanes; speeds to 40 mph; 41 K on 3 axles (9 K and 32 K tandem) at 13' and 4' spacing; 74 K on 5 axles (9 K, 32 K tandem and 33 K tandem) at 11', 4', 19' and 4' spacing.	12
Michigan (Jackson Bypass) 1953	A 73'-92'-74' continuous portion and 5 76' to 84' simple spans; 2 29' roadways, each on 6 50" deep plate girders; cover plates; light vertical and horizontal curvature.	One point deflection at midspan of each span.	Speeds to 45 mph on 1 vehicle path in each roadway; induced impact; 28 K (10 and 18 K) on 2 axles at 14' spacing; 50 K on 3 axles (10, 18 and 22 K) at 14' spacings; also weighed and measured commercial traffic.	8
Michigan (B1-34-13-8) 1956	A 101' non-composite end span of a 3-span continuous deck plate girder bridge with floor beams and stringers; 7" min slab on 18WF50 stringers at 5' centers.	Deflections.	Speeds to 35 mph; 39 K on 3 axles (6, 15 and 18 K) at 13' and 14' spacings; axle housing gages calibrated under incremental loading.	24

TABLE 2A (Continued)

Site/Date	Specifications	Measurements	Loading	Ref.
Michigan (B1-70-7-3) 1957	A 69' end span of a 3-span non-composite skewed continuous plate girder; $7^1/_2$'' slab on 66'' deep girders at 94'' centers.	One midspan deflection gage.	Speed to 45 mph on 1 path; 40 K on 3 axles (6, 16 and 18 K) at 13' and 14' spacings; axle housing gages calibrated under incremental loading.	13
Michigan (B2-38-1-14) 1957	42'-80'-42' non-composite continuous spans; $7^1/_4$'' slab on 36WF170 beams at 62'' centers.	One midspan deflection gage in center and 1 end span.	As above.	13
Minnesota (No. 6440) 1952	Two 85' end spans, 4 100' center span with 70' suspended portion on 15' cantilevers; continuous composite H20 design; 3-lane 27' roadway; $6^1/_2$'' slab on 8 36WF150 beams.	Strains at 116 points.	One vehicle path in each direction; 51 and 30 K 2-axle vehicles; natural frequencies of sprung load determined; 50 mph for lighter and 20 mph for heavier vehicle; static loadings; induced impact; vehicles also run in tandem.	4
*Missouri (Burris Fork) 1955	60'-80'-60' non-composite continuous spans; 22' roadway of $6^1/_4$'' slab on 4 beams; 33WF130 exterior, 33WF130 interior in end spans, and 33WF141 interior in center span; H15 design.	Deflections; top and bottom flange strains at 3 midspan sections; wheelpath profiles taken.	65 K on 4 axles (6, 27 and 32 K tandem) at 13', 20' and 4' spacings; spring constants determined; speeds to 51 mph; induced impact; 3 vehicle paths.	18
*Oregon (N. Dillard) 1953	121'-160'-121' composite continuous spans; 30' roadway of $6^1/_2$'' slab on two variable depth (70'' to 110'') plate girders; nearly level grade; cover plated at positive and negative moment sections; 3 longitudinal lines of 16WF-stringers on	Series I: deflections and top and bottom flange girder strains in positive moment sections; Series II: negative moment girder strains; Series III: stringer strains; Series IV: floor beam strains; wheelpath profiles taken.	Two vehicle paths, curb lane and centerlane; 69 K on 5 axles (6 K, 31 K tandem and 32 K tandem) at 13', 3', 13', and 3' spacings; speeds to 30 mph; 71 K on 5 axles (9 K, 32 K tandem and 30 K tandem) at	9

			weighed and measured commercial traffic.	
*Oregon (Troutdale) 1953	As above.	Deflections; top and bottom flange girder strains in 2 positive moment sections; wheelpath profiles taken.	As above.	9
*South Dakota (James R.) 1955	70'-90'-70' composite continuous spans; 24' roadway of 6" slab on 4 30WF108 beams; H15 design; level grade; welded connections; cover plated in negative moment sections.	Deflections and top and bottom flange strains at positive moment sections; wheelpath profiles taken.	Two vehicle paths; 71 K on 5 axles (7 K, 32 K tandem and 32 K tandem) at 11', 4', 17' and 4' spacings; 32 K on 2 axles (14 and 18 K) at 12' spacing; speeds to 40 mph; induced impact; axle housing gages calibrated under incremental loading.	23
*Texas (P. & S. F.) 1962	40'-51'-40' non-composite continuous spans; 2 24' roadways and 4' median on 9 27WF94 beams; $6^{1}/_{2}$" slab; 4% grade and 3° curve; cover plated over piers; H20 design.	Deflections; positive and negative moment section top and bottom flange strains; pier top longitudinal deflections; wheelpath profiles taken.	BPR test vehicle; 68 K on 3 axles (9, 31 and 28 K) at 13' and 20' spacing; 8 creep speed paths; 4 paths at other speeds up to 50 mph; axle housing gages calibrated under incremental loading; some uncontrolled commercial traffic recorded.	20
*Texas (T. & N. O.) 1962	50'-65'-65'-50' continuous composite spans; H20-S16 design with 43° skew; 52' roadway of $6^{1}/_{2}$" slab on 7 beams; 33WF130 in end spans and 33WF141 in interior spans; level grade; cover plated over piers.	Top and bottom flange strains and deflections at midspan of end and intermediate spans on skewed and normal sections; top and bottom flange negative moment strains; slab soffit strains; pier top longitudinal deflections; wheelpath profiles taken.	BPR test vehicle; 68 K on 3 axles (9, 31 and 28 K) at 13' and 20' spacing; 3 vehicle paths; centerline and each curb lane; speeds to 35 mph; axle housing gages calibrated under incremental loading.	21

TABLE 2B

CONTINUOUS SPANS

Concrete Superstructures

Site/Date	Specifications	Measurements	Loading	Ref.
*Alabama (Auburn Univ.) 1965	44'-55'-44' continuous T-beam spans with 6" slab on 2 $16\frac{3}{4}$" wide haunched beams at 8' centers; 16' roadway; no curbs; for testing only; level grade.	Positive and negative moment section steel reinforcement strains; temperatures; deflections; concrete strains; reactions; all measurements on one-half of bridge; wheelpath profiles to be taken.	BPR test vehicle; 74 K on 3 axles (10, 32 and 32 K) at 13' and 20' axle spacing; other factors to be determined; axle housing gages calibrated by incremental loading.	25
Iowa (Cumming Interchange) 1958	43'-56'-56'-43' pretensioned, prestressed spans made partially continuous by poured diaphragms at bearings and by continuous slab; 6 28" deep I-beams; 24' roadway with $5\frac{1}{2}$" slab; at crest of vertical curve; 1 interior diaphragm per span.	Strains on bottom surface of each beam at 2 positive and 2 negative moment sections; additional strains on web for neutral axis determination.	Four vehicle paths; speeds to 35 mph; 41 K on 3 axles (9 K and 32 K tandem) at 13' and 4' spacing; 74 K on 5 axles (9 K, 32 K tandem and 33 K tandem) at 11', 4', 19' and 4' spacing.	12
Michigan (B1-38-11-25)	42'-58'-42' continuous T-beam spans; beams on $81\frac{1}{2}$" centers; 8" slab; beams 33" deep at midspan.	Deflections at midspan in center and 1 end span.	Speeds to 45 mph in 1 lane; 39 K on 3 axles (6, 15 and 18 K) at 13' and 14' spacing; axle housing gages calibrated by incremental loading.	13
Michigan (B5-81-11-8) 1957	39'-53'-53'-39' continuous T-beam spans; 28" midspan depth; beams at $74\frac{1}{4}$" centers; 8" slab.	Deflections at midspan in 2 spans.	As above.	
*New York (Elmwood Ave.) 1964	35'-60'-60'-35' continuous T-beam spans; 4° skew; 7" slab; 48' roadway on 10 beams 10" wide by 37" deep; H20-S16 design; A432 reinforcement; monolithic beam and slab; on V.C. with 4% ascending	Deflections; strain in one quarter of bridge layout at 2 positive and 2 negative moment sections; strains measured on reinforcing steel; wheelpath profiles taken; deck and web concrete surface strains.	BPR test vehicle; 73 K on 3 axles (10, 32 and 31 K) at 13' and 20' spacing; 5 vehicle paths; speeds to 30 mph; induced impact; axle housing gages cali	23

*Texas (Hillsboro) 1963	55'-88'-88'-55' continuous T-beam spans; 7" slab; 30° skew; 24' roadway on 3 $28\frac{1}{2}$" wide haunched girders 20" deep at midspan; on 0 to 5% V. C.; H15 design with A432 reinforcement in superstructure only.	Numerous positive and negative moment section reinforcing steel strain gages throughout; gages at top and bottom of columns on vertical bars; deflections in all spans; crack surveys at regular intervals.	BPR test vehicle; speeds to 25 mph; 5 vehicle paths; induced impact; first, 50 K on 3 axles (10, 25 and 25 K) at 13' and 20' spacings and then 73 K (10, 33 and 30 K).	23

TABLE 2C

CONTINUOUS SPANS

Miscellaneous Superstructures

Site/Date	Specifications	Measurements	Loading	Ref.
Iowa (Clive Rd.) 1958	41'-69'-69'-41' continuous composite aluminum plate girder spans; 30' roadway with 8" slab on 2 36" deep interior and 2 34" deep exterior girders at 9' 6" centers; cover plates at bearings; diaphragms at 13' centers; H20-S16 design.	Bottom flange strains at 2 positive and 2 negative moment sections; additional web strains for neutral axis location.	Speeds to 40 mph on 4 paths; 41 K on 3 axles (9 K and 32 K tandem) at 13' and 4' spacings; 74 K on 5 axles (9 K, 32 K tandem and 33 K tandem) at 11', 4', 19' and 4' spacings.	12

TABLE 3

CANTILEVER SPANS

Steel Girder Superstructures

Site/Date	Specifications	Measurements	Loading	Ref.
Michigan (B1-81-1-13) 1956	Two 98' non-composite anchor spans of cantilever deck plate girder with floor beams and stringers; 7" min slab; 53" min. girder depth; 66' non-composite suspended span on 26' cantilevers; 7" min. slab on 53" girders; 2 60' composite simple spans with 7½" min. slab on 36WF182 beams at 6' centers.	Deflections.	Speeds to 25 mph; 39 K on 3 axles (6, 15 and 18 K) at 13' and 14' spacings; axle housing gages calibrated under incremental loading.	24
Michigan (X3-56-7-26) 1956	A 65' composite center anchor span; 7" min. slab on 36WF170 beams at 6' centers; 53' composite end span on 5.5' cantilever with 7" min. slab on 36WF230 beams at 6' centers; 67' composite end span on 5.5' cantilever with 7" min. slab on 36WF230 beams at 6' centers; 30° skew.	Deflections.	As above; speeds to 40 mph.	24
Michigan (B1-77-20-11) 1956	A 100' non-composite anchor span of a cantilever deck plate girder with floor beams and stringers; 78" min. girder depth; 7" min. slab on 18WF50 stringers at 61" centers; 18° skew; two 60' non-composite simple spans; 7" min. slab on	Deflections.	As above; speeds to 30 mph.	24

Michigan (B1-64-10-11) 1956	A 84' non-composite anchor span of cantilever deck plate girder of 67" min. depth with floor beams and stringers; stringers at 55" centers; 60' non-composite suspended span on 21' cantilevers; 7" min. slab.	Deflections.	As above.	24
Michigan (B1-18-12-2) 1956	A 67' composite anchor span of cantilever bridge; 7" min. slab on 36WF160 beams at 5' centers; 69' composite suspended span on 8.5' cantilevers; 7" min. slab on 36WF194 beams at 5' centers.	Forty strain gage positions at midspan and over pier; deflections.	Speeds to 50 mph on 7 paths; 39 K on 3 axles (6, 15 and 18 K) at 13' and 14' spacings; induced impact; axle housing gages calibrated under incremental loading.	24
Michigan (B1-18-12-2) 1957	As above.	One midspan deflection gage in each of 2 spans.	Speeds to 45 mph on 1 path; 40 K on 3 axles (6, 16 and 18 K) at 13' and 14' spacing; axle housing gages calibrated under incremental loading.	13
Michigan (B1-33-6-4) 1957	One composite 70' anchor span of cantilever bridge; 7" slab on 36WF230 beams at 5' centers; 4 composite 65' simple spans with 7" slab on 36WF170 beams at 5' centers.	One midspan deflection gage in each of 5 spans.	As above.	13
Michigan (B1-34-6-1) 1957	A 74' non-composite anchor span of cantilever bridge; 7" slab on 48" deep plate girders at 6' centers; 47' non-composite suspended span on 14' cantilevers; 7" slab on 36WF160 beams at 6' centers.	One midspan deflection gage in each of 2 spans.	As above.	13

TABLE 3 (Continued)

Site/Date	Specifications	Measurements	Loading	Ref.
Michigan (B1-73-20-2) 1957	A composite 74' end anchor span of 5-span cantilever bridge with 36WF182 beams at 60" centers; 58' suspended span with 33WF141 beams at 60" centers on 8.5' cantilevers; 75' center anchor span with 36WF170 beams; 7" slab.	One midspan deflection gage in each of 3 spans.	As above.	13
Michigan (B1-39-5-8) 1957	A 57' non-composite anchor span of a cantilever bridge; 7" slab on 36WF150 beams at 58" centers; 61' non-composite suspended span on 9' cantilevers; 7" slab on 36WF160 beams at 58" centers.	One midspan deflection gage in each of 2 spans.	As above.	13
Michigan (B1-56-12-6) 1957	A 74' anchor span of a non-composite deck cantilever plate girder; 7" slab on 2 66" min. deep plate girders; two composite 56' simple spans with 7" slab on 36WF150 beams at 66" centers.	One midspan deflection gage in each of 3 spans.	As above.	13
Michigan (B1-62-12-1) 1957	A 97' anchor span of non-composite deck cantilever plate girder; 7" slab; 24' roadway on 2 81' min. deep plate girders.	One midspan deflection gage.	As above.	13
Michigan (B2-73-20-2) 1957	A 74' anchor span of 3-span composite cantilever; 7" slab on 36WF182 beams at 60" centers; 58' suspended span with 33WF150 beams at 60" centers on 8.5 cantilevers.	One midspan deflection gage in each of 2 spans.	As above.	13
Michigan	A 50' anchor span of 3-span	As above.	As above.	13

	48'' centers; a 65' composite suspended span with 36WF160 beams on 7.5' cantilevers.			
Michigan (B1-11-18-7) 1958	A 128' non-composite anchor span of a bascule bridge; a deck plate girder with floor beams and stringers; 7'' min. slab on stringers spaced at 63'' centers; a 68' non-composite simple span with 7'' min. slab on 36WF182 beams at 54'' centers.	Deflections.	Speeds to 3 mph; 26 K on two axles (6 and 20 K) at 14' spacing; differential pressure cell on rear tires for dynamic axle load measurements; some commercial traffic records taken.	24
*Nebraska (Center Cr.) 1956	A 3-span non-composite cantilever bridge; 26' roadway of $6^{1}/_{2}$'' slab on 5 30WF132 beams; 62' anchor span; 54' suspended span on 11' cantilevers; H15 design; level grade.	Deflections; top and bottom flange strains at midspan sections of suspended and anchor span; strains at negative moment section and through both hanger links; wheelpath profiles taken.	Two vehicle paths, centerline and curb, in each direction; speeds to 50 mph; 35 K on 2 axles (8 and 27 K) at 14' spacing; 53 K and 62 K on 4 axles (5 K, 24 K and 24 K tandem, also 4 K, 26 K and 32 K tandem) at 14', 12' and 4' spacing; axle housing gages calibrated by incremental loading.	17
*Nebraska (Loup R.) 1956	A 7-span non-composite cantilever bridge; 21' roadway of $7^{1}/_{2}$'' slab on 4 beams; 72' end span beams 36WF150 second span beams 36WF194 with 68' suspended span on 14.5' and 22.5' cantilevers; 105' third span beams 36WF230; fourth span beams 36WF230 with 73' suspended span on 21' cantilevers; H12.5 design.	Deflections; top and bottom flange strains at center of suspended span; strains on hangers; strains at center and near bearing on 105' span; wheelpath profiles taken.	Two vehicle paths, centerline and curb, in each direction; 53 K 4-axle vehicle above; 30 K on 2 axles (6 and 24 K) at 14' spacing; axle housing gages calibrated by incremental loading; speeds to 50 mph.	

REFERENCES

1. Van Eenam, N. Live-Load Stress Measurements on Fort Loudon Bridge, Final Report. Highway Research Board Proc., Vol. 31, pp. 36-61, 1952.
2. Foster, G. M. Tests on Rolled Beam Bridge Using H20-S16 Loading. Highway Research Board Res. Rept. 14-B, pp. 10-38, 1952.
3. Lin, T. Y. Horonjeff, R., Clough, R. W., and Scheffey, C. F. Investigation of Stresses in the San Leandro Creek Bridge. Univ. of California, Inst. of Transportation and Traffic Eng., Res. Rept. No. 13, May 1953.
4. Wise, J. A. Dynamics of Highway Bridges. Highway Research Board Proc., Vol. 32, pp. 180-187, 1953.
5. Roesli, A., Smislova, A., Ekberg, C. E., Jr., and Eney, W. J. Field Tests on a Prestressed Concrete Multi-Beam Bridge. Highway Research Board Proc., Vol. 35, pp. 152-171, 1956.
6. Hayes, J. M., and Sbarounis, J. A. Vibration Study of a Three-Span Continuous I-Beam Bridge. Highway Research Board Bull. 124, pp. 47-78, 1956.
7. Biggs, J. M., and Suer, H. S. Vibration Measurements on Simple-Span Bridges. Highway Research Board Bull. 124, pp. 1-15, 1956.
8. Foster, G. M., and Oehler, L. T. Vibration and Deflection of Rolled-Beam and Plate-Girder Bridges. Highway Research Board Bull. 124, pp. 79-110, 1956.
9. Edgerton, R. C., and Beecroft, G. W. Dynamic Studies of Two Continuous Plate-Girder Bridges. Highway Research Board Bull. 124, pp. 33-46, 1956.
10. Hulsbos, C. L., and Linger, D. A. Dynamic Tests of a Three-Span Continuous I-Beam Highway Bridge. Highway Research Board Bull. 279, pp. 18-46, 1961.
11. Prentzas, E. G. Dynamic Behavior of Two Continuous I-Beam Bridges. Iowa Highway Research Board Bull. No. 14, Iowa State Highway Commission, Ames, 1958.
12. Linger, D. A., and Hulsbos, C. L. (a) Forced Vibration of Continuous Highway Bridges. Highway Research Board Bull. 339, pp. 1-22, 1962; (b) Dynamic Load Distribution in Continuous I-Beam Highway Bridges. Highway Research Record No. 34, pp. 47-69, 1963.
13. Oehler, L. T. Vibration Susceptibilities of Various Highway Bridge Types. Proc. ASCE, Jour. Structural Div., Vol. 83, No. ST4, July 1957.
14. Impact Study of a Simple I-Beam Span of a Highway Bridge. Missouri State Highway Dept., Div. of Bridges, Jefferson City, Aug. 1958.
15. Highway Research Board Spec. Repts. 61D, 71 and 73, 1962.
16. Kinnier, H. L., and Slepetz, J. M. Vibration Survey of Composite Bridges, Progress Report No. 1. Virginia Council of Highway Invest. and Res., Charlottesville, April 1961.
17. Dynamic Tests of Two Cantilever Type Deck Steel Girder Bridges. Nebraska Dept. of Roads, Bridge Design Sect., Lincoln, Aug. 1961.
18. Baldwin, J. W., Jr. Impact Study of a Steel I-Beam Highway Bridge. Univ. of Missouri Bull., Eng. Exp. Sta. Ser., No. 58, Oct. 1964.
19. Kinnier, H. L. Vibration Survey of Composite Bridges, Progress Report No. 2—A Dynamic Stress Study of the Weyer's Cave Bridge. Virginia Council of Highway Invest. and Res., Charlottesville, Aug. 1963.
20. Gersch, B. C. Dynamic Test of P. & S. F. Railroad Overpass, El Paso, Texas. Texas Highway Dept. Res. Rept. No. 64-2, Sept. 1964.
21. Gersch, B. C. Dynamic Testing Program of the T. & N. O. Railroad Overpass, El Paso County, Texas. Texas Highway Dept. Res. Rept. No. 64-5, Sept. 1964.
22. Kinnier, H. L., and McKeel, W. T., Jr. Virbration Survey of Composite Bridges, Progress Report No. 3—A Dynamic Stress Study of the Hazel River Bridge. Virginia Council of Highway Invest. and Res. Charlottesville, Sept. 1964.
23. Reports in prepartion by the following groups:
    Maryland - Univ. of Maryland, Dept. of Civil Eng., College Park.
    Virginia - Virginia Council of Highway Invest. and Res., Charlottesville.
    California - California Div. of Highways, Sacramento.
    Pennsylvania - Lehigh Univ., Dept. of Civil Eng., Bethlehem.

New York - New York State Dept. of Public Works, Bureau of Phys. Res., Albany.
Texas - Texas Highway Dept. (D-5), Austin.
South Dakota - South Dakota Dept. of Highways, Pierre.

24. Report unpublished to date.
25. Dynamic field study pending.